

Catch the Sun:

New Ancillary Ligands in Copper(I) Dye-Sensitized Solar Cells Lead to Panchromatic Light Harvesting

Inauguraldissertation

zur

Erlangung der Würde eines Doktors der Philosophie

vorgelegt der

Philosophisch-Naturwissenschaftlichen Fakultät

der Universität Basel

von

Frederik J. Malzner

aus Waldshut-Tiengen, Deutschland

Basel, 2018

Originaldokument gespeichert auf dem Dokumentenserver der Universität Basel

edoc.unibas.ch



Catch the Sun: New Ancillary Ligands in Copper(I) Dye-Sensitized Solar Cells Lead to
Panchromatic Light Harvesting by Frederik J. Malzner

is licensed under a *Creative Commons Attribution 4.0 International License*.

Genehmigt von der Philosophisch-Naturwissenschaftlichen Fakultät

auf Antrag von

Prof. Dr. Edwin C. Constable und Prof. Dr. Marcel Mayor

Basel, den 24.04.2018

Prof. Dr. Martin Spiess

Dekan

University of Basel

Department of Chemistry

Constable/Housecroft Research Group

Mattenstrasse 24a

4058 Basel

Switzerland

Frederik J. Malzner

2018

Parts of this work have been published:

B. Bozic-Weber, S. Y. Brauchli, E. C. Constable, S. O. Fürer, C. E. Housecroft, F. J. Malzner, I. A. Wright and J. A. Zampese, *Dalton Trans.*, 2013, **42**, 12293.

F. J. Malzner, S. Y. Brauchli, E. C. Constable, C. E. Housecroft and M. Neuburger, *RSC Advanced*, 2014, **4**, 48712.

S. Y. Brauchli, F. J. Malzner, E. C. Constable and C. E. Housecroft, *RSC Advanced*, 2014, **4**, 62728.

S. Y. Brauchli, F. J. Malzner, E. C. Constable and C. E. Housecroft, *RSC Advanced*, 2015, **5**, 48516.

F. J. Malzner, A. Prescimone, E. C. Constable, C. E. Housecroft and M. Willgert, *J. Mater. Chem. A*, 2017, **5**, 4671.

F. J. Malzner, M. Willgert, E. C. Constable and C. E. Housecroft, *J. Mater. Chem. A*, 2017, **5**, 13717.

F. J. Malzner, C. E. Housecroft and E. C. Constable, *Inorganics*, 2018, **6**, 57.

At the beginning there's always a dream.

ABSTRACT

The world population is increasing. More people demand better living conditions and the boom in the developing countries continues apace. The story of human progress is also the story of energy. Energy was and will be the key feature of progress. Nowadays, three energy transitions have taken place. These have developed our society from wood burning to coal-powered steam engines to a dependence on electricity which involved burning fossil fuels. All energy transitions up to now have included burning materials that produce not only energy but also air pollution and so-called greenhouse gases. The CO₂ concentration in Earth's atmosphere is not at an acceptable level and the effects affect everyone on Earth. However, since the oil crisis in the 1970s and nuclear disasters such as Chernobyl and Fukushima, public awareness has been raised and the demand for alternative energy sources has increased. Renewable energy sources that disappeared over a long period, such as wind power, have made their comeback and a topical example of new renewable resources is photovoltaics. Photovoltaics produce renewable, sustainable and eco-friendly energy. Most commercial solar cells are based on silicon. Since their development in 1953, new generations of solar cells have been investigated in order to make them cheaper, more environmentally friendly and more efficient. Dye-sensitized solar cells are one cutting edge technology. They had their breakthrough in 1991 with the developments of Michael Grätzel and Brian O'Regan¹. A dye is adsorbed onto a semiconductor surface that is adhered to a conducting glass substrate. The electrical circuit is closed with a counter electrode and an electrolyte. Several types of dyes have been investigated but only a few have shown promising results. A new and exciting area encompasses copper(I)-based dyes. They consist of copper(I) complexes which incorporate a ligand with functional groups to anchor to the semiconductor surface and an ancillary ligand which can be structurally tuned to optimize light harvesting. Most of the ancillary ligands are based on a 2,2'-bipyridine core. Investigations aimed at improving cell performance had, in 2015, "got stuck" at photoconversions of around 2%. This thesis describes the path to new types of simple ancillary ligands that surpass the performance of the most optimized 2,2'-bipyridine-based ligands. The path includes the development of general methods that improve the economical part of the fabrication of the solar cells and the regeneration of destroyed dye. The new families of ancillary ligand lead to the development of panchromatic co-sensitized copper(I) dye-sensitized solar cells. For the first time, a copper(I) dye has been combined with a commercially available and cheap organic dye and the remarkable performance has shown the exciting potential of copper(I) dye-sensitized solar cells. Catch the Sun.

TABLE OF CONTENTS

ABSTRACT	III
TABLE OF CONTENTS	V
ABBREVIATIONS	XI
INTRODUCTION	1
1. MOTIVATION AND AIM	2
2. GLOBAL ENERGY	5
2.1. Yesterday	5
2.2. Today	7
2.3. Tomorrow	9
3. RENEWABLE ENERGY	10
3.1. Water	11
3.2. Wind	12
3.3. Sun	13
4. PHOTOVOLTAIC TECHNOLOGIES	16
5. DYE-SENSITIZED SOLAR CELLS	18
COPPER(I) DYE-SENSITIZED SOLAR CELLS	21
6. COPPER – PHOTOPHYSICALLY ACTIVE, EARTH-ABUNDANT, CHEAP	22
7. DESIGN AND WORKING PRINCIPLE OF N-TYPE DYE-SENSITIZED SOLAR CELLS	25
7.1. Components	25
7.1.1. Working Electrode	25
7.1.2. Photosensitizer	29
7.1.3. Counter Electrode	36
7.1.4. Electrolyte	36
7.2. Working Principle	38
7.2.1. n-Type Dye-Sensitized Solar Cells	38
8. CHARACTERISATION	42
8.1. UV-Vis Spectroscopy	42
8.1.1. Instrumental Details	42
8.1.2. Solid-state UV-Vis Spectroscopy	43
8.2. Solar Simulator	44
8.2.1. Instrumental Details	44
8.2.2. <i>J-V</i> Measurements	46
8.3. External Quantum Efficiency	49
8.3.1. Instrumental Details	49
8.3.2. EQE Measurements	50

TABLE OF CONTENTS

8.4.	Electrical Impedance Spectroscopy	52
8.4.1.	Instrumental Details	52
8.4.2.	EIS Measurements	53
SYNTHETIC STRATEGY AND CHARACTERIZATION		57
9.	TARGET MOLECULES	58
9.1.	2,2'-Bipyridine-Based Ligands	58
9.2.	Heterocyclic N [^] NX Ancillary Ligands	61
10.	SYNTHETIC STRATEGY	63
11.	CHARACTERIZATION	67
11.1.	NMR Spectroscopy	67
11.2.	UV-Vis Spectroscopy	76
11.3.	Mass Spectrometry	82
11.4.	Electrochemistry	84
11.5.	Crystal Structures	87
11.5.1.	Crystal Structure Data	92
11.6.	DFT calculations	93
DEVICE FABRICATION		97
12.	EQUIPMENT DETAILS	98
13.	GENERAL DEVICE FABRICATION	100
FROM BPY TO N[^]NX		103
14.	2,2'-BIPYRIDINE ANCILLARY LIGANDS	106
14.1.	Prologue: Substituents and Halogens	107
14.2.	Minimizing the Excess of Ancillary Ligand and the Total Process Time in the Dye-Assembly Process	113
14.3.	Combination of the Best Performing Substituent and Halogen	123
14.4.	Influence of the Co-adsorbent Cheno on the Efficiency	127
14.5.	Regeneration of the Dye on the Semiconductor Surface	139
14.6.	2,2'-Bipyridine-Based Ligands with Different Functional Groups	143
15.	N [^] NX ANCILLARY LIGANDS	147
15.1.	A New Type of Ancillary Ligand for Copper(I)-Based Dye-Sensitized Solar Cells: N [^] NX	148
15.2.	Outlook: Optimization of the N [^] NS Ligand	171

PANCHROMATIC CO-SENSITIZED COPPER(I) DYE-SENSITIZED SOLAR CELLS	179
16. CO-SENSITIZATION PRE-TESTS WITH A COPPER(I)-DYE AND N719	183
17. THE HISTORY OF “BLORANGE”	196
EXPERIMENTAL PART	233
18. GENERAL INSTRUMENTS AND METHODS	234
19. ANCILLARY LIGAND SYNTHESIS	235
19.1. 2,2'-Bipyridine-Based Ligands	235
19.1.1. 4,4'-Di-(4-bromophenyl)-6,6'-dimethyl-2,2'-bipyridine (L-Br)	235
19.1.2. 4,4'-Di-(4-iodophenyl)-6,6'-dimethyl-2,2'-bipyridine (L-I)	236
19.1.3. 4,4'-Di-(4-iodophenyl)-6,6'-diphenyl-2,2'-bipyridine (^{Ph}L-I)	238
19.1.4. 4,4'-Di-(4-dimethylaminophenyl)-6,6'-diphenyl-2,2'-bipyridine (L-NMe₂)	239
19.1.5. 4,4'-Di-(4-phenoxyphenyl)-6,6'-diphenyl-2,2'-bipyridine (L-OPh)	240
19.1.6. 4,4'-Di-(4- <i>tert</i> -butylphenyl)-6,6'-diphenyl-2,2'-bipyridine (L-t-Bu)	242
19.2. Heterocyclic N [^] NX Ancillary Ligands	244
19.2.1. 2-(6-Methylpyridin-2-yl)-1 <i>H</i> -benzo[<i>d</i>]imidazole (N[^]NNH)	244
19.2.2. 1-Methyl-2-(6-methylpyridin-2-yl)-1 <i>H</i> -benzo[<i>d</i>]imidazole (N[^]NNMe)	244
19.2.3. 2-(6-Methylpyridin-2-yl)benzo[<i>d</i>]oxazole (N[^]NO)	245
19.2.4. 2-(6-Methylpyridin-2-yl)benzo[<i>d</i>]thiazole (N[^]NS)	246
19.2.5. 2-(6-Phenylpyridin-2-yl)benzo[<i>d</i>]thiazole (^{Ph}N[^]NS)	246
19.2.6. 2-(Quinolin-2-yl)benzo[<i>d</i>]thiazole (^{qui}N[^]NS)	247
19.2.7. 2-(6-(Difluoromethyl)pyridin-2-yl)benzo[<i>d</i>]thiazole (^{CHF₂}N[^]NS)	248
19.2.8. 2-(6-(Trifluoromethyl)pyridin-2-yl)benzo[<i>d</i>]thiazole (^{CF₃}N[^]NS)	248
19.2.9. 2-(6-Methylpyridin-2-yl)-6-nitrobenzo[<i>d</i>]thiazole (N[^]NS(NO₂))	249
19.2.10. 2-(6-Methylpyridin-2-yl)benzo[<i>d</i>]thiazole-6-amine (N[^]NS(NH₂))	250
19.2.11. <i>N</i> -Methyl-2-(6-methylpyridin-2-yl)benzo[<i>d</i>]thiazole-6-amine (N[^]NS(NHMe))	251
19.2.12. <i>N,N</i> -Dimethyl-2-(6-methylpyridin-2-yl)benzo[<i>d</i>]thiazole-6-amine (N[^]NS(NMe₂))	252
20. COPPER(I) COMPLEX SYNTHESIS	254
20.1. 2,2'-Bipyridine-Ligand-Based Complexes	254
20.1.1. [Cu(L-I) ₂][PF ₆]	254
20.1.2. [Cu(L-NMe₂) ₂][PF ₆]	255
20.1.3. [Cu(L-OPh) ₂][PF ₆]	256
20.1.4. [Cu(L-t-Bu) ₂][PF ₆]	257
20.2. Heterocyclic N [^] NX Ancillary Ligands-Based Complexes	258
20.2.1. [Cu(N[^]NNH) ₂][PF ₆]	258
20.2.2. [Cu(N[^]NNMe) ₂][PF ₆]	259
20.2.3. [Cu(N[^]NO) ₂][PF ₆]	259
20.2.4. [Cu(N[^]NS) ₂][PF ₆]	260

TABLE OF CONTENTS

20.2.5.	[Cu(^{Ph} N [^] NS) ₂][PF ₆]	261
20.2.6.	[Cu(^{qui} N [^] NS) ₂][PF ₆]	262
20.2.7.	[Cu(^{CHF₂} N [^] NS) ₂][PF ₆]	262
20.2.8.	[Cu(^{CF₃} N [^] NS) ₂][PF ₆]	263
20.2.9.	[Cu(N [^] NS(NO ₂) ₂) ₂][PF ₆]	264
20.2.10.	[Cu(N [^] NS(NH ₂) ₂) ₂][PF ₆]	265
20.2.11.	[Cu(N [^] NS(NHMe) ₂) ₂][PF ₆]	265
20.2.12.	[Cu(N [^] NS(NMe ₂) ₂) ₂][PF ₆]	266
21.	ANCHORING LIGAND SYNTHESIS	267
21.1.	((6,6'-Dimethyl-[2,2'-bipyridine]-4,4'-diyl)-bis(4,1-phenylene))bis(phosphonic acid) (ALP1)	267
21.2.	((6,6'-Diphenyl-[2,2'-bipyridine]-4,4'-diyl)-bis(4,1-phenylene))bis(phosphonic acid) (^{Ph} ALP1)	269
	CONCLUSION & OUTLOOK	271
	ACKNOWLEDGEMENTS	275
	REFERENCES	279
	CURRICULUM VITAE	289

TABLE OF CONTENTS

ABBREVIATIONS

ABBREVIATIONS

General Units

A	ampere	mL	millilitre
Å	angstrom	mm	millimetre
a.u.	arbitrary units	mM	millimolar
AM	air mass	mmol	millimole
BTU	British thermal units	ms	millisecond
cm	centimetre	mV	millivolt
d	day	mW	milliwatt
dm	decimetre	nm	nanometre
eq.	equivalents	ppm	parts per million
eV	electron volt	ps	picosecond
G	global	s	second
g	gram	TWh	terawatt hour
h	hour	US\$	US dollar
Hz	hertz	V	volt
K	degree Kelvin	W	watt
kg	kilogram	%	percentage
M	molar	°	degree
m	metre	°C	degrees Celsius
m/z	mass to charge ratio	µF	microfarad
mA	milliampere	µm	micrometre
mg	milligram	µs	microsecond
MHz	megahertz	δ	chemical shift
min	minute	Ω	Ohm

Chemicals

Ac	acetate	ITO	indium-doped tin oxide
b-AlO _x	basic aluminium oxide	Me	methyl
bpy	2,2'-bipyridine	MeCN	acetonitrile
CdS	cadmium sulphide	MeOH	methanol
Cheno	chenodeoxycholic acid	n-Bu	<i>n</i> -butyl
CIGS	copper indium gallium selenide	n-Hex	<i>n</i> -hexyl
CO ₂	carbon dioxide	NiO	nickel oxide

ABBREVIATIONS

CuSe ₂	copper selenide (mineral marcasite)	PEN	polyethylene naphthalate
dmbpy	6,6'-dimethyl-2,2'-bipyridine	PET	polyethylene terephthalate
DMF	dimethylformamide	Ph	phenyl
dmp	4,7-dimethyl-1,10-phenanthroline	phen	1,10-phenanthroline
DMSO	dimethyl sulfoxide	PPA	polyphosphoric acid
Et	ethyl	qui	2-quinoline
Et ₂ O	diethyl ether	SnO ₂	tin oxide
Fc	ferrocene	TBA	tert-butylammonium cation
FTO	fluorine-doped tin oxide	t-Bu	<i>tert</i> -butyl
GaAs	gallium arsenide	TiO ₂	titanium dioxide
H ₂ O	water	TMS	tetramethylsilane
InP	indium phosphide	ZnO	zinc oxide
iso-Bu	<i>iso</i> -butyl		

Analysis & Experimental

aq. sat.	aqueous saturated	MALDI	matrix assisted laser desorption ionisation
calc.	calculated	MS	mass spectrometry
cat.	catalytic amount	NIR	near infrared
cos	cosine	NMR	nuclear magnetic resonance
COSY	correlation spectroscopy	NOESY	nuclear Overhauser effect spectroscopy
CV	cyclic voltammetry	r.t.	room temperature
d	doublet	s	singlet
dd	doublet of doublets	sec	secant
DFT	density functional theory	t	triplet
ESI	electrospray ionisation	TOF	time of flight
HMBC	heteronuclear multiple bond correlation	tt	triplet of triplets
HMQC	heteronuclear multiple quantum correlation	UV-Vis	Ultra-Violet Visible

ABBREVIATIONS

HPLC	high performance liquid chromatography	>	greater than
HR	high resolution	≤	less then or equal
J	coupling constant	ε	extinction coefficient
m	multiplet	Θ_z	zenith angle
M	parent ion	λ_{max}	wavelength at which maximum absorption occurs

Chemistry

LUMO	lowest unoccupied molecular orbital	CB	conduction band
HOMO	highest occupied molecular orbital	E_F	Fermi level
MO	molecular orbital	$L_{ancillary}$	ancillary ligand
HETPHEN	heteroleptic bisphenanthroline complexes	L_{anchor}	anchoring ligand
MLCT	metal-to-ligand charge transfer	co-sens.	co-sensitized

Photovoltaics

DSC	dye-sensitized solar cell	P	power
CPE	constant phase element	P_{in}	power density of the incident light
$C_{P\mu}$	chemical capacitance at the cathode	P_{mpp}	maximum power point
C_μ	chemical capacitance	R_d	diffusion resistance
EIS	electrochemical impedance spectroscopy	R_{Pt}	cathode/electrolyte charge transfer resistance
EQE	external quantum efficiency	R_{rec}	recombination resistance
EQE_{max}	maximum external quantum efficiency	R_s	series resistance
ff	fill factor	R_{tr}	transport resistance
I	current	V	voltage

ABBREVIATIONS

<p>I_{sc} short-circuit current</p> <p>J current density</p> <p>J_{mpp} maximum-power-point current density</p> <p>J_{sc} short-circuit current density</p> <p>$J-V$ current-voltage</p> <p>L_D length of diffusion</p>	<p>V_{mpp} maximum-power-point voltage</p> <p>V_{oc} open-circuit voltage</p> <p>Ws Warburg diffusion element</p> <p>η overall photoconversion efficiency</p> <p>τ electron lifetime</p>
Others	
<p>AD anno domini</p> <p>ATT American Telephone & Telegraph Company</p> <p>BC before Christ</p> <p>BP British Petroleum</p> <p>Fig. figure</p> <p>LED light emitting diode</p>	<p>R&D research and development</p> <p>S.&Cent. Southern and Central America America</p> <p>US United States</p> <p>USA United States of America</p> <p>USSR Union of Soviet Socialist Republics</p>

ABBREVIATIONS

INTRODUCTION

1. Motivation and Aim

The world in 2018 is faced with a problem of how the future will emerge. International as well as national political tensions are present all over the globe, ecological calamities and an imbalance of climate, famines, onset of diseases that have been combatted decades ago and the increase of the gap between rich and poor are present in our daily lives. There are challenges for us to overcome to ensure a sustainable future for mankind. The main problems of human kind are security, environment, water, food, health, poverty and energy. The numbers of people which affect these problems are steadily increasing. At the beginning of 2018, 7.6 billion people live on Earth² and projections compiled by the United Nations forecast that in 2100 the global population will be around 13.2 billion people³ (Fig. 1).

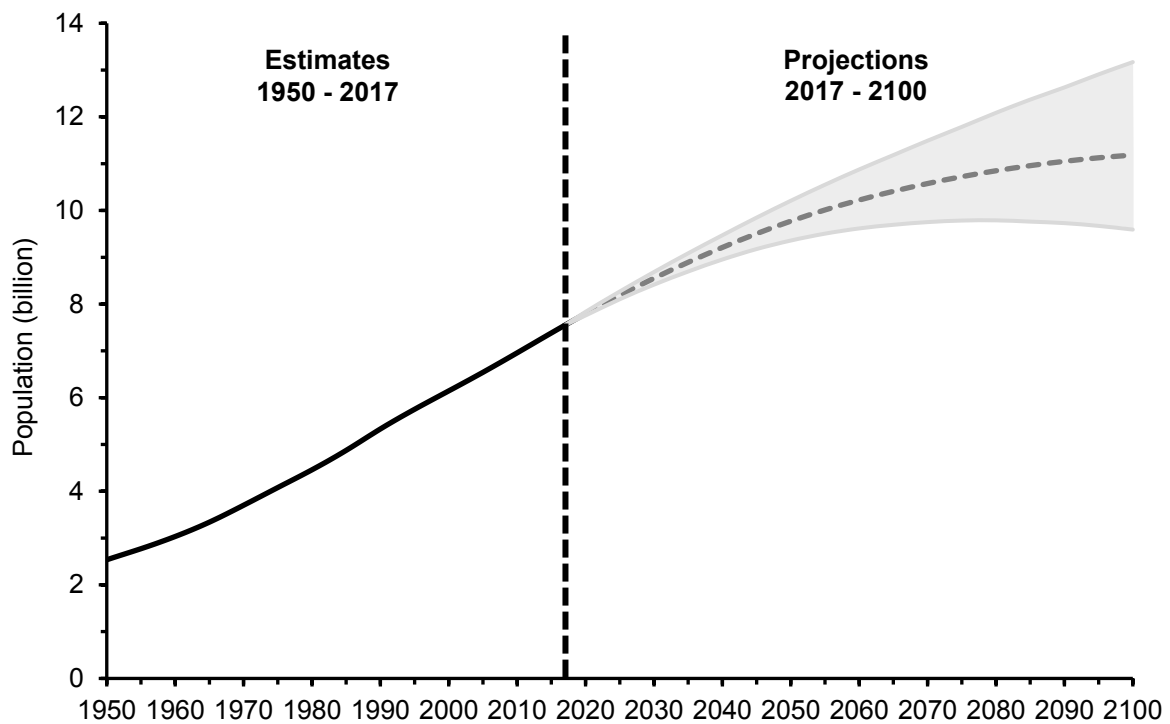


Fig. 1 Population of the world: estimated values from 1950 - 2017 (black line) and projections until 2100 (medium variant: grey dotted line, upper/lower 95% prediction intervals: grey area). [Data: United Nations³]

With increased global population, the demand for energy increases and in developing countries, the demand for energy is especially great. Everyone wants to improve his or her standard of living and as a consequence, an increased supply of energy is needed. The most essential resource that endorses the progress, evolution and prosperity of human societies has always been energy.⁴ Today, this mainly relies on fossil energy fuels such as coal, oil or natural gas. However, when they are burned, greenhouse gases such as CO₂ are produced. The CO₂ concentration in the atmosphere has almost doubled since the transition from organic biomass to fossil fuels at the beginning of the 19th century (Fig. 2).

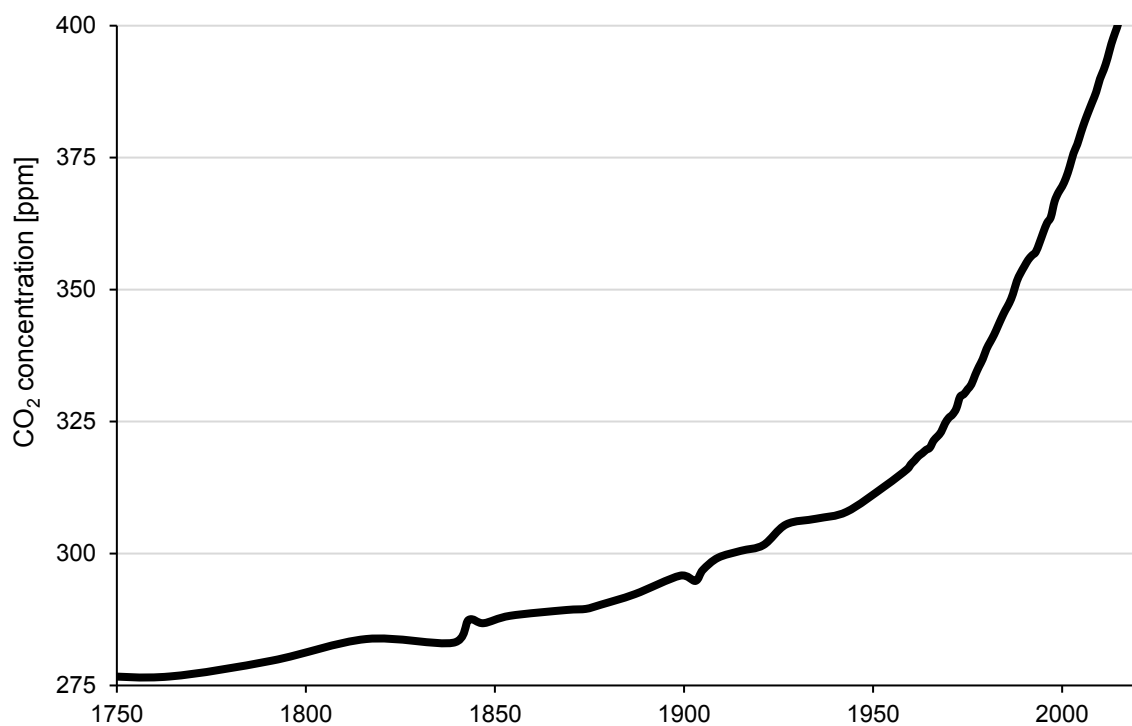


Fig. 2 CO₂ concentration in the atmosphere since 1750 (1750-1953: data from measurements of air occluded in a 200-m core drilled at the Siple Station in the Antarctica, 1959-2017: data from daily measurements). [Data: NOAA⁵, CDIAC⁶]

A proven effect of the increased CO₂ concentration is the climate change that affects everyone on the planet. The year 2016 has been the hottest year since the annual average temperature has been recorded at the beginning of the 19th century. Alternatives such as nuclear energy are not the best course for human kind to follow. Production of even more harmful products under dangerous conditions cannot be the future of energy production. Because of this, the transition

INTRODUCTION

from fossil fuels to renewable energy sources such as wind, hydropower or photovoltaics has to be promoted. The biggest potential is with photovoltaics. All types of photovoltaic modules have to be improved and alternatives have to be investigated in order to use the energy of the greatest energy source available on Earth: the Sun.

2. Global Energy

The Sun is the ultimate energy source. Almost all available energy on the Earth comes from the energy of the Sun.⁴ Sunlight offers heat and light that is captured by plants which can be eaten or burned for light and heat. Some of the sunlight also evaporates water that rises into the atmosphere. From there, it falls as rain. The rain that falls on land on very high places can be used due to gravity. Gravity pulls the rain into streams and rivers that run towards lakes and oceans. This running water is essentially stored sunlight that can be used through its mechanical energy. Uneven distributions of solar energy in the atmosphere leads to temperature variations. This results in motion of air masses meaning winds are stored sunlight, too. The wind also causes waves which contribute to the mechanical energy of water. Fossil fuels are, of course also, stored sunlight. Derived from biological deposition that has been accumulated for millions of years, coal and oil are the most concentrated forms of stored sunlight available on Earth.⁷ Almost all organisms rely on solar energy to survive. Life on Earth would be impossible without photosynthesis which converts solar energy into plant biomass.⁸ In the food chain, this energy is transferred to the muscles of human body which have been the first used energy source by humankind on Earth.

2.1. Yesterday

At the beginning of human kind on Earth, the only energy that could be used was the energy the body could generate. But with the mastery of fire 400 000-500 000 years⁹ ago, the Organic Energy Economy began.¹⁰ Fire could be used for cooking and heating by using biomass as fuel. The additional created light improved safety in human settlements and promoted the expansion of habitation.^{10,11} Also the development of ovens which permitted the early forms of crafting, made it possible to produce pottery and to refine metals from ore.⁴ The next milestone in global energy was the Agricultural Revolution.¹² With the introduction of agriculture, more food was available and permanent settlements increased the human population. The next essential steps were water and wind power. The first windmills were built about 2500 years ago.¹³ To master water and wind power using water and windmills led to an improved energy use. Nevertheless, most produced energy originated from biomass which resulted in intensive land use with rapid growth of population. In conclusion, the Organic Energy Economy was limited to the consumption of

energy at the rate that solar energy can be converted into useful goods.⁴ With the growth of population and limited land availability a transition to another energy source was crucial: fossil fuels.^{10,14}

The milestone that determined the transition from an organic economy to the fossil fuel economy was the invention of the steam engine (Fig. 3). This was the beginning of the "Industrial Revolution" and the conversion of heat directly into mechanical energy was now possible.¹⁵ The early steam engines were used to pump water out of coal mines to facilitate the mining of coal. But with improvements over time, steam engines became a powerful tool which replaced human muscle and animal power to extract more coal, move ships and trains and lead to a manufacturing industry that is the foundation of today's complex and energy intensive economy system.¹⁰

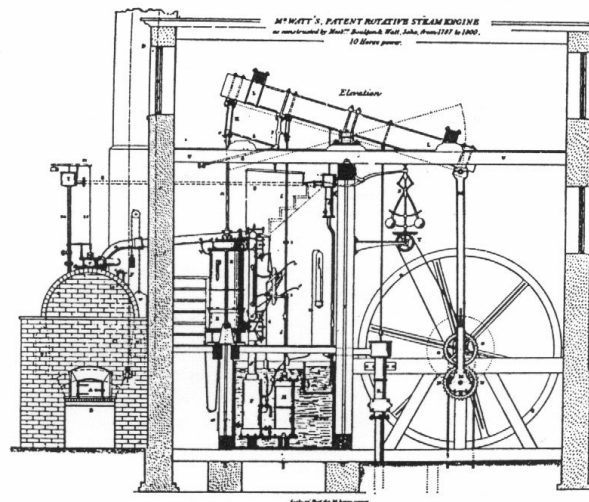


Fig. 3 Drawing of James Watt's steam engine.¹⁶

During the 18th century many industries transferred from wood-fuels to coal while heating services made this transition by the beginning of the 19th century. With increased prices for wood-fuel the transition to coal was encouraged additionally especially at a time when the harvesting of forest trees had to be regulated and sometimes even restricted.⁴ The growing demand for coal in the 19th century was achieved by new technological improvements.¹⁰ The introduction of other fossil fuels like petroleum enhanced the usage of fossil energy sources. The invention of the internal combustion engine really promoted the use of refined oil that was discovered in the 1850s.⁴ The oil age was reached in the 1960s and concerns about maintaining a constant energy supply after the oil crises of 1973 and 1979 (Fig. 4) led to an increase of the use of natural gas.⁴

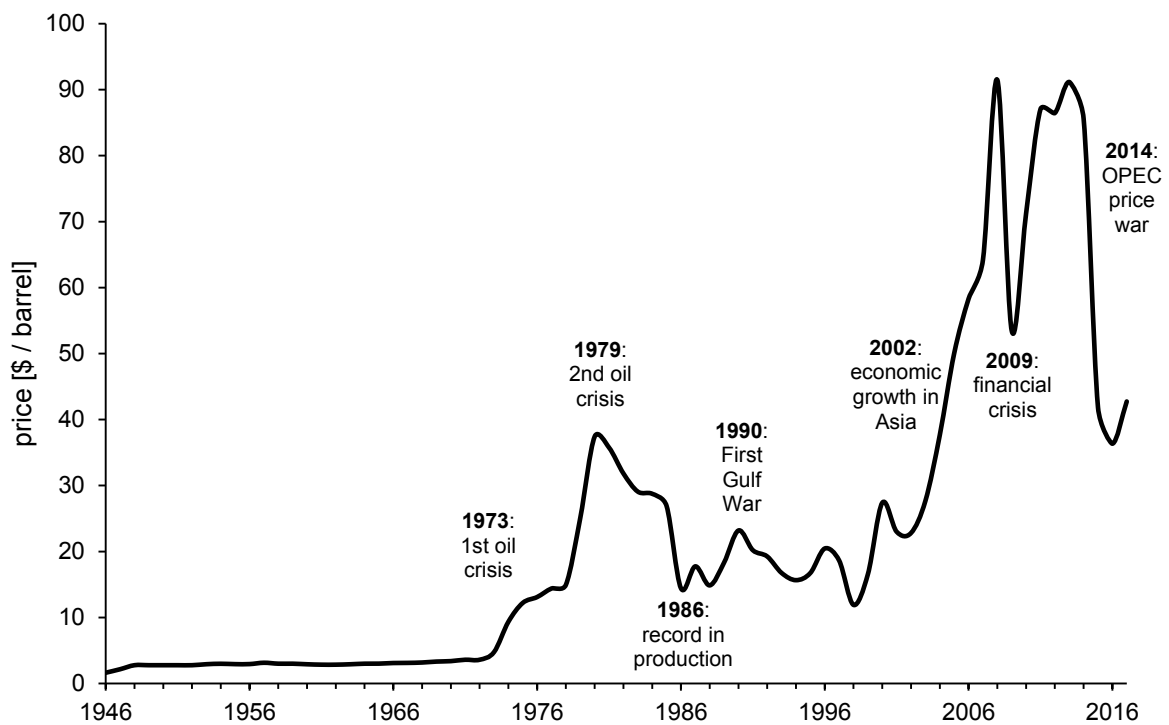


Fig. 4 Oil price in dollar per barrel from 1946 until 2017 with notable events that influenced the price.^{17,18}

Each energy transition has taken 50 to 60 years. First from wood to coal and then from coal to oil. Still ongoing is a transition from oil to natural gas. The year when energy provided by fossil fuels surpassed wood and charcoal was in the US 1885, 1875 in France and 1901 in Japan. It is remarkable that this transition took place in the USSR in 1930, 1965 in China and in the late 1970s in India. The 20th century was therefore still a century of coal. A similar pacing of three global energy transitions over two centuries is remarkable. Especially because of the different production techniques, distribution channels and machinery to convert them into usable power.¹⁹

2.2. Today

Nowadays, the share of energy consumption is still mainly based on fossil fuels (Fig. 5). 85% of the energy in the world comes from oil (33%), coal (28%) and natural gas (24%), 5% from nuclear energy and only 10% from renewable energy sources and hydropower. The share of renewables has increased over the last decades and the energy transition to natural gas is still taking place. In

Europe, the share of fossil fuels is still 75% but due to government-sponsored projects²⁰ renewable energies have the share of 15%. 10% of the consumed energy in Europe is produced by nuclear power stations. This is mainly due to France, which produces 39% of their energy using nuclear power stations.²¹

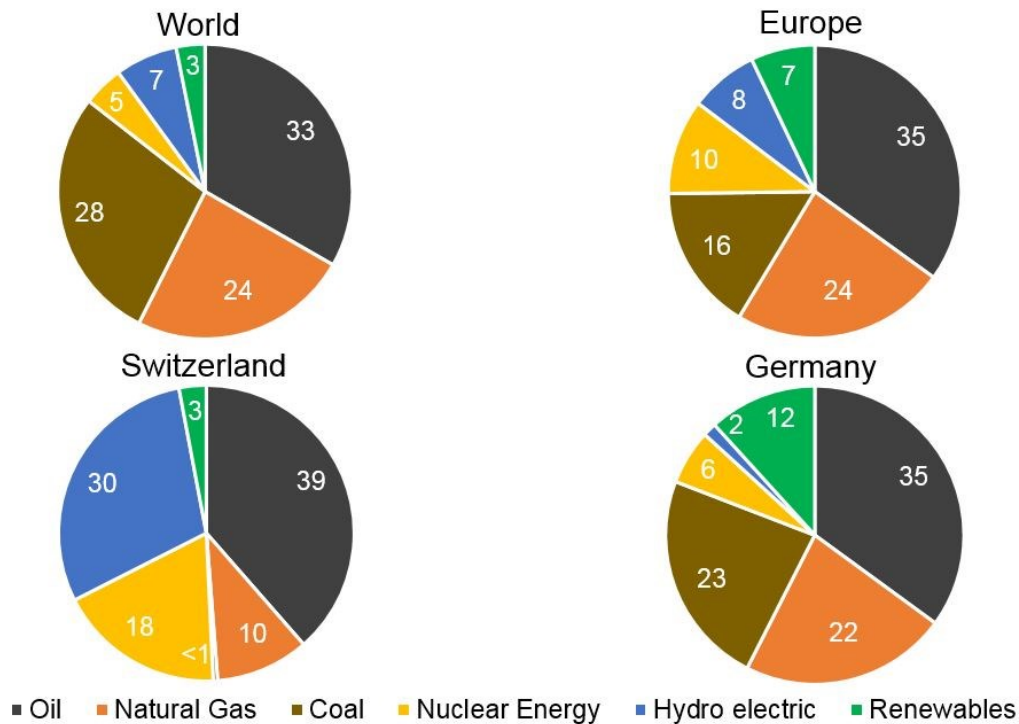


Fig. 5 Share of energy consumption by fuel in the world, Europe, Switzerland and Germany in 2016 (values in percent). [Data: BP Statistical Review 2017²¹]

The share of energy consumption in Switzerland is attributed to its geographical location. Many high mountains and a lot of water favours the usage of hydropower. 30% of consumed energy comes from hydropower in Switzerland. Only oil with 39% has a bigger share. The high ratio of nuclear energy (18%) provides a huge amount of the basic energy supply but the future should be based on water and Sun.²² Today, the share of renewable energy in the world is only 3%. In Germany the installation of renewable energies has been promoted by the government and the share of renewables is 12%. This is the highest value for renewable energy consumption in Europe.²¹ The main part comes, of course, from fossil fuels but the transition from fossil fuels to renewables is a time- and cost-intensive process.

2.3. Tomorrow

The goal of future global energy must be the reduction of fossil fuels and increase of renewable and eco-friendly energy sources. This can be done by using more efficient energy transition pathways from fossil fuels to energy. This can be achieved by using modern, more efficient heating systems or by insulating houses with triple-glazed windows to lower energy loss.²³ Simple things can be done to consume less energy. However, because CO₂ production or radioactive waste cannot be a burden for our descendants, it is important to make the switch to renewables. This change is challenging for several reasons. First of all, it is the scale. The amount of fossil fuels being used now is 20 times greater than during the 1890s when coal was overtaking wood. Therefore, it is most important to lower overall energy use to speed up the gradual transition to renewables. The faster the global demand rises, the more difficult it is to increase the share of renewable energies. Second of all, it is the demand for uninterrupted supply of energy throughout the whole day. Wind and solar can contribute to the base load of power, but they cannot supply all of it. The wind does not blow and the Sun is not shining all the time. On days with perfect weather conditions, Germany is able to supply 100% of consumed energy by renewable energy sources.²⁴ But in order to cover the peaks of energy demand especially in the evening additional power is needed. One possibility is the storage of excess power generated by renewables when demand is low. This has to be inexpensive and efficient. Unfortunately, the only good, large-scale solution is pumping water up to an elevated reservoir so it can flow back through a turbine when the power is needed.^{8,23} The change to many small, decentralized renewable sources contains also the construction of new transmission lines. But this is expensive and often faces stiff local oppositions. The complete energy infrastructure has to be reshaped, and this results in a more challenging transition to renewables than the prior shifts from coal to oil and natural gas.⁸ But in order to achieve this transition everyone do his bit. With decreased consumption, the energy transition off fossil fuels can be achieved.

3. Renewable Energy

The future of world-wide energy production must rely on renewable energy sources: water, wind, Sun and others like biomass and geothermal energy. Most of these renewable forms of energy have been used for thousands of years but passed out of mind after they have been replaced by other energy sources. Nevertheless, events such as the oil crisis or nuclear disasters have resulted in a great demand for alternatives, and these alternatives must be renewable, eco-friendly and everywhere available. Political efforts like the decisions from the United Nations Climate Change Conference in Paris 2015 contributed to the increased promotion of renewable energy sources.

5878 TWh of renewable energies were consumed in the world in 2016 (Fig. 6). This is 10% of the total amount of consumed energy in the world. The main share originates from hydropower, but wind power, solar power and other renewable energy sources are on the increase.

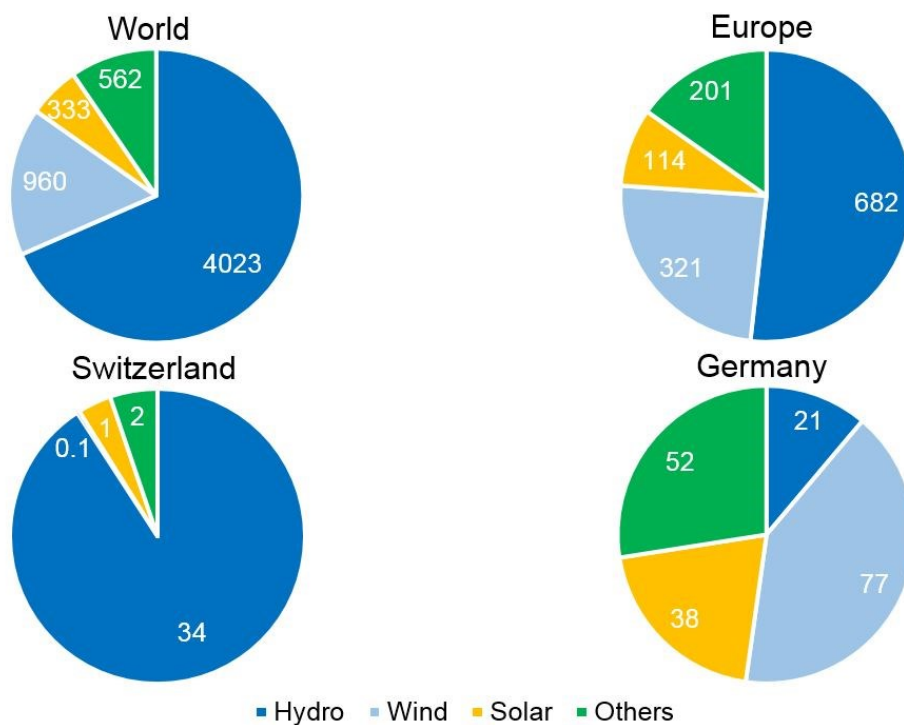


Fig. 6 Share of energy consumption of renewable energies in the world, Europe, Switzerland and Germany in 2016 (values in TWh; Others: geothermal, biomass and others). [Data: BP Statistical Review 2017²¹]

Europe is a pioneer in the use of renewable energy and here, only about one half of the share of renewable energy consumption comes from hydropower. The share of wind power is about 25% and photovoltaics 10%. That the usage of each energy source has to be adapted to the geographical location of the country is clear to see using the example of Switzerland. Hydropower arising from plentiful mountains and water results in a share of hydropower of over 90% in Switzerland. Germany is the country with the highest share of solar energy consumption in Europe (20%). Other renewable energy sources are now contributing significantly.²¹

3.1. Water

The oldest renewable energy source is water. Since the third century BC, people have used water as a source of energy.²⁵ At the beginning hydropower was used to drive scoop wheels in order to water the fields. This technique is known from Mesopotamia but also India or China.²⁶ The ancient Greeks used simple water mills to drive grindstones. This technique came to Europe by the Romans in the first millennium AD.²⁵ The first known water mills were built in Germany in the 6th century²⁶ and by the end of the 11th century, water power was used all over Western Europe to mill grain, process cloth, tan leather, saw wood and crush ore.²⁵ Until the 19th century, water wheels had been one of the mainly used power sources, but was phased out to some extent with the advent of the steam machine. However, so as coal was expensive, hydropower stations were still used. At the time when coal became cheaper and cheaper, many factories changed to steam machines. The first water turbine was invented in 1827 and with the invention of the electrodynamic generator by Werner von Siemens in 1866 the first electricity was produced by hydropower. The first hydropower stations were built in Great Britain in 1880 and at the Niagara Falls in 1895 (Fig. 7).²⁶ From that point on more and more hydropower stations were built globally, and especially after the oil-price shock of 1973, many countries looked for alternative energy sources. Those that could harness hydropower,²⁵ and the biggest hydropower stations are in China today.

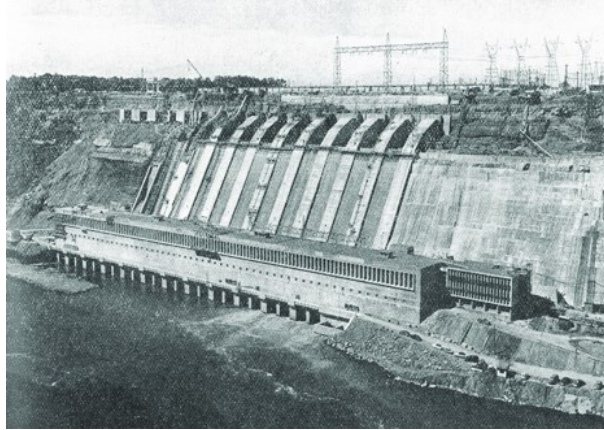


Fig. 7 First hydropower station at the Niagara Falls in 1895.²⁷

3.2. Wind

Wind power has always been important throughout the history of humanity.²⁸ Starting with sailboats over 4000 years ago the power of the wind was used to transport goods on rivers.²⁹ Around 700 BC the first wind wheels were built and the technique was used until ancient times, when windmills were used to mill grain or pump water. The first wind machines were manufactured in the 12th century in Europe and continued to be used until the 19th century.²⁹ Windmills were used until the Industrial Revolution when steam machines replaced them at the end of the 19th century. In 1853, the first model of a pure wind wheel with a vertical axis and blades was invented by Halladay in the US (Fig. 8), and at the world fair in Illinois in 1876 had an international breakthrough.³⁰

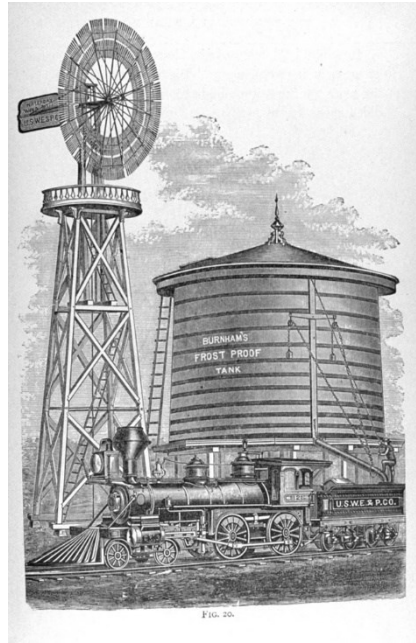


Fig. 8 Halladay windmill used as a water pump in 1885.³¹

The first electricity from wind was produced in 1887 by Blyth in Scotland and the first pilot plant was built in 1891 in Denmark.²⁸ Wind turbines were developed over time but never had a big share of the energy production. This changed with the oil crises in the 1970s. The first wind farm in the world was constructed in New Hampshire in 1980 and eleven years later, 1991, Denmark built the first offshore wind farm.²⁵ Today, wind energy is gradually coming to the forefront all over the world²⁸ and over 200 000 plants now produce electricity. Most of the installed wind power is located in China, USA and Germany.

3.3. Sun

The power of the Sun is the origin of life on Earth, and for this reason, each ancient civilization had a god of the Sun. The Sun is the main part of daily life and the orientation of buildings with respect to the Sun has been important since ancient times. Solar energy is one of the very few sources that is completely clean and free.³² The power of the Sun has mainly been harnessed in the form of heat, and conversion to electricity was not realized until 1839 when Becquerel discovered the photovoltaic effect.³³ The term photovoltaic comes from the Greek “phos” meaning “light” and the term “voltaic”, meaning “electric”, from the Italian physicist Volta.³⁴ The

solar cell is the only device that converts the energy of the sunlight directly into electricity without pollution, sound or moving parts.³² More solar energy reaches the Earth in one hour than all the energy consumed on the planet in one year.³⁵ The current global energy consumption could be provided by covering an area equivalent to approximately 1% of Earth's surface with solar cells with an efficiency of 10%. Photovoltaics are the most important energy source because solar energy is very abundant.³²

Photovoltaics has the most rapid growth out of all renewable energy sources. It is almost exponential and countries such as Japan, China and Germany are great pioneers (Fig. 9). From 2010 to 2016, the number of photovoltaic power installations on Earth has increased sixfold. With the introduction of the renewable energy law, Germany was the first country that promoted photovoltaics in the 2000s. But other countries, especially in Europe, participated the upturn. Japan and China installed photovoltaic modules quite early, but the rapid growth of installed photovoltaic power started in 2012. The US started the expansion of their photovoltaic systems only in the last few years.²¹

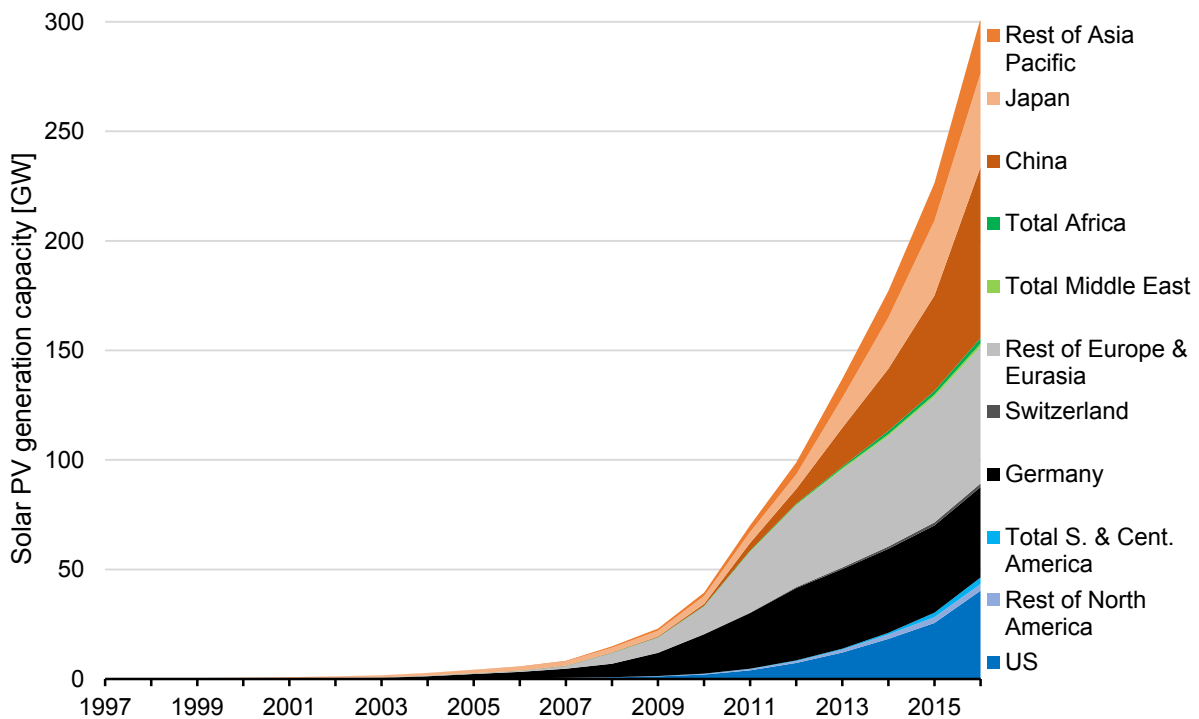


Fig. 9 Growth of photovoltaic power installations from 2000 to 2016. [Data: BP Statistical Review 2017²¹]

Today, the pioneering countries China, Japan and Germany still have the highest share of installed photovoltaic power of the world (Fig. 10). In the year 2016, China had a share of 26%, Japan and Germany 14%. It is remarkable that the whole Asia Pacific part has almost half of all installed photovoltaic power, Europe one third. The US is still behind. The big country USA has comparable installed photovoltaics like Germany or Japan. The most notable fact is that regions such as South America, Africa or the Middle East where the amount of sunlight strikes the Earth is the biggest on Earth, have such a low share of installed photovoltaics.²¹

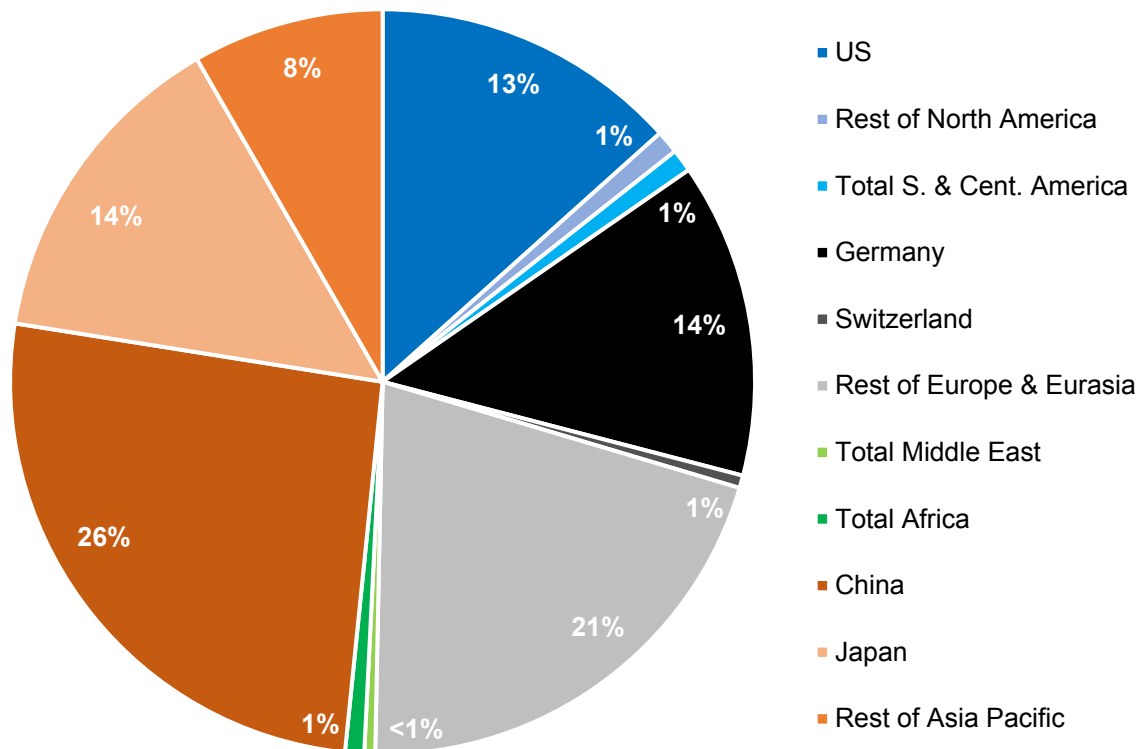


Fig. 10 Share of installed photovoltaic power in 2016. [Data: BP Statistical Review 2017²¹]

These data show that the great potential of solar power is still unexhausted. Great improvements have been investigated in the photovoltaic technologies but there will be a lot more to come.

4. Photovoltaic Technologies

The story of photovoltaics started with the discovery of the photovoltaic effect by Becquerel in 1839.³³ After the discovery of the photoelectric effect, researchers including Smith (1873), Adams and Day (1876) and Fritts (1893 and 1894) investigated several materials that generate an electrical current when irradiated. After this pioneering work in the 19th century, Hallwachs observed photosensitivity by combination of copper and cuprous oxide.³⁶ Einstein was the first person who gave the scientific world a more detailed view on the photovoltaic effect. He described how photon absorption causes the photoelectric effect in 1905 and was awarded with the Nobel Prize for this discovery in 1921. This work is the theoretical basis for all photovoltaic devices and semiconductors, in which electrons are excited by absorbed photons.³² A number of early thin film cells were investigated in the 1930s.³³ But the first generation solar cells which are the conventional solar cell of today are based on Silicon.³⁷ The silicon solar cell was discovered by Pearson, Chapin and Fuller at ATT Bell Laboratories in 1953³³ and had a photoconversion efficiency of 6%.³²



Fig. 11 The inventors of the first silicon solar cell Pearson, Chapin and Fuller at ATT Bell Laboratories in 1953.³⁸

INTRODUCTION

The second generation of solar cells are based on thin film technologies. In the 1970s scientist developed thin films of crystalline Si and a whole range of new semiconductor materials like copper indium gallium selenide (CIGS), cadmium sulphide (CdS), indium phosphide (InP), copper selenide (CuSe₂) or gallium arsenide (GaAs). Beside polycrystalline and amorphous silicon and organic semiconductors, these are almost all alternative materials used by today's new photovoltaic industry. In 1967, the first thin film CdS cell deposited on plastic was developed. Already at that time multiple bandgap designs and tandem cells were established.³³ The first research laboratory for photovoltaic research was founded in 1972 at the University of Delaware.³⁶ The investigations of Barnett and Green in the early 1980s led to 20% efficient cells.³³ The third generation solar cell devices are promising technologies. Multijunction cells, dye-sensitized solar cells (DSCs), organic solar cells or perovskite solar cells belong to the third generation of solar cells.³⁷ A lot of research was done for every generation and the highest efficiencies are summarized in Table 1.

Table 1 List of independently confirmed highest efficiency of solar cells.³⁹

Classification	η [%]	Reference
Si (crystalline)	26.7	40
GaAs	28.8	41
CIGS	21.7	42
Multijunction	38.8	43
DSC	11.9	44
Organic	11.2	45
Perovskite	20.9	46

5. Dye-Sensitized Solar Cells

Since the 1970s, attempts have been made to use the principle of photosynthesis for solar cells. Early attempts tried to cover crystals of TiO_2 with a layer of chlorophyll, but the efficiency of this first sensitized solar cells was about 0.01%.³³ The first official reference for dye-sensitized solar cells was reported in a US patent submitted in 1977.⁴⁷ A scientist in Switzerland, Michael Grätzel (Fig. 12), and his co-worker, Brian O'Regan, discovered in 1991 that nanoparticles could enhance the efficiency.¹ They used a sponge of small nanoparticles, each about 20 nm in diameter, and sensitized them with a thin layer of a dye. This increased the surface area available for absorbing sunlight by the factor of 1000³³ and the photoconversion efficiency of about 700%.

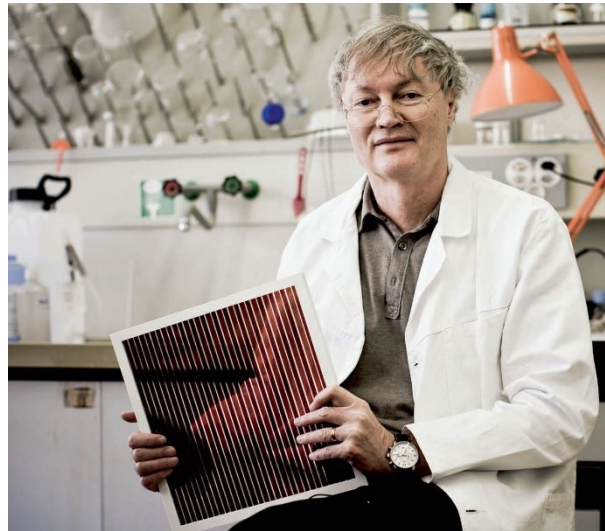


Fig. 12 The inventor of the dye-sensitized solar cell Michael Grätzel.⁴⁸

Since the investigations by Grätzel and O'Regan an impressive amount of work has been carried out in order to improve the efficiency of DSCs. A lot of research has been done to optimize every single component of the device in terms of material, structure and activity.³⁵ Compared to conventional photovoltaics, in DSCs the functions of light absorption, charge generation and transport are separated and carried out by different components. Because of this, it is possible to tune every single component with a large number of technical options in order to optimize and improve the performance of the complete device.⁴⁹ Because DSCs work in a wide range of lighting conditions and orientation and are less sensitive to partial shadowing and a low level of

illumination, they are well suited for several applications. The main advantages of DSCs are also low cost, available environmental-friendly raw materials and semi-transparent and multicolour range possibilities.³⁴ They can be used outdoors as well as indoors. The coloured DSCs are excellent multifunctional building elements that generate electricity either from outdoor daylight or indoors, while acting as Sun, heat and noise insulator.³³ DSCs can be used with flexible and light-weight substrates which is an essential advantage with respect to other technologies.⁴⁹ The deep interest in DSCs can be observed in the number of scientific publication (Fig. 13). Until the development of the new type of perovskite solar cells in 2014 there was an almost exponential growth in number of publications dealing with the topic of DSCs.

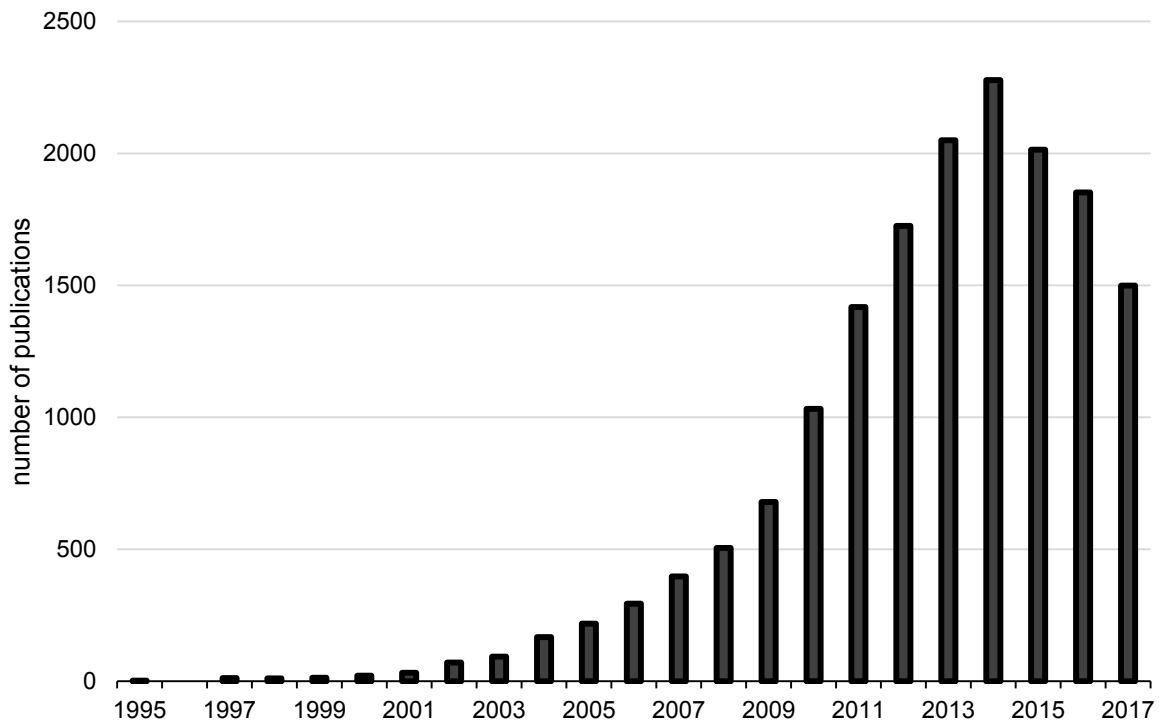


Fig. 13 Number of publications annually dealing with the topic “dye-sensitized solar cell” [Data: Web of Science]

But DSCs have moved out the R&D stage and are on the verge of approaching the thin film photovoltaics market.⁴⁹ Many companies worldwide are working in the field of DSCs. They entered the global market in 2003 when the first commercial modules were installed in Australia.³³ The market has a growing interest due to their applicability to indoor facilities and in

portable devices. The forecast of the growth of the DSC market by the year 2030 is over 130 million US\$.³⁵

The highest achievable theoretical efficiency for DSCs has been estimated to be 32%⁵⁰ and the highest achieved efficiency in lab conditions is 14.3%⁵¹ to date.



Fig. 14 Indoor and outdoor applications of DSCs.⁵²⁻⁵⁴

Nowadays, DSCs are divided into two parts: n-type DSCs and p-type DSCs. n-type DSCs deal with an n-type semiconductor and a dye that injects electrons into the semiconductor to start the electrical circuit. On the other hand, p-type DSCs are using p-type semiconductors like NiO and dyes that can take electrons from the semiconductor and inject holes into the semiconductor.⁵⁵⁻⁵⁸ One goal is to combine both parts in one tandem cell to achieve increased performances.⁵⁹

**COPPER(I)
DYE-SENSITIZED
SOLAR CELLS**

6. Copper – Photophysically Active, Earth-Abundant, Cheap

Since the pivotal work of McMillin⁶⁰ in the late 1970s, copper has emerged as a promising candidate for an Earth-abundant metal in dye-sensitized solar cells. He has shown that $[\text{Cu}(\text{dmp})_2]^+$ (dmp = 4,7-dimethyl-1,10-phenanthroline) can undergo a light induced redox reaction wherein it acts as a reductant under the presence of a Co(III) species. The knowledge gained from McMillin's pioneering work can be transferred to a DSC where a Cu(I) complex interacts with the incoming photons and injects the excited electron to the conduction band of the semiconductor (the detailed working principle is described in *7.2 Working Principle*). But copper has other important properties that make it a promising candidate for DSCs.

Amaroli has shown that the photophysical properties of copper(I) complexes are convenient for the usage in DSCs.⁶¹ Copper(I) complexes prefer a tetrahedral coordination environment which allows more structural distortions than other complexes with a higher coordination number (like octahedral Ru(II) complexes, for example). Therefore, they can be tuned in photophysical and electrochemical properties and contain good oxidation and reduction parameters.

Most of the best performing inorganic dyes are based on Ru(II) complexes (see later: *7.1.2 Photosensitizer*). But the natural abundance of ruthenium is very low (0.001 ppm in Earth's crust). It sits alongside Rh, Pd, Ag, Os, Ir, Pt and Au as the eight precious metals on Earth. Copper (60 ppm in Earth's crust) is about four orders of magnitude more abundant on Earth in contrast to ruthenium (Fig. 15). Copper also belongs to the group of major industrial metals which include Mg, Al, Ti, Cr, Mn, Fe, Ni, Zn, Mo, Sn, W and Pb. The metals Cu, Mn, Fe, Ni and Zn have been used in inorganic dyes in the quest to find an Earth-abundant alternative to Ru, but with the exception of metalloporphyrin dyes which typically contain Zn, Cu has shown the highest potential.⁶²

Natural abundance of the metal has of course an impact on the price. Because of its much higher abundance, copper is much cheaper than ruthenium. In the beginning of 2018, 1 kg ruthenium costs about 6300 US\$, whereas copper only about 7 US\$/kg (Fig. 16)

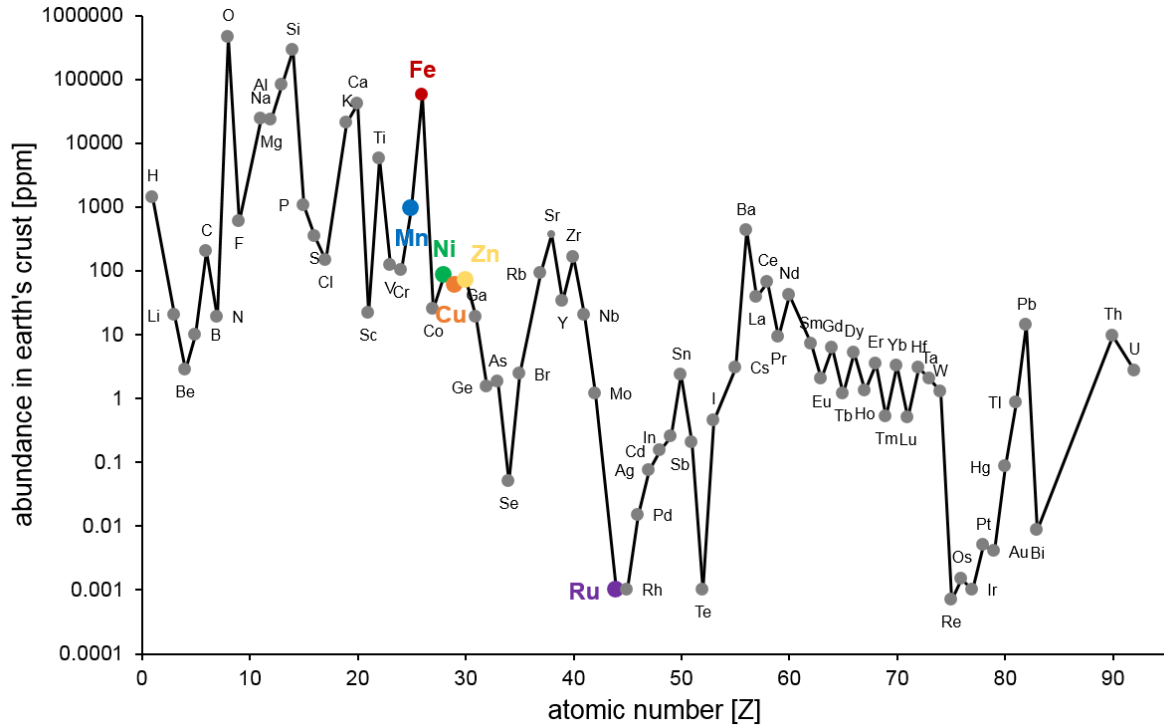


Fig. 15 Abundance of elements in the upper Earth crust (in DSCs used major industrial metals and ruthenium in colour). [Data: Jefferson Lab⁶³]

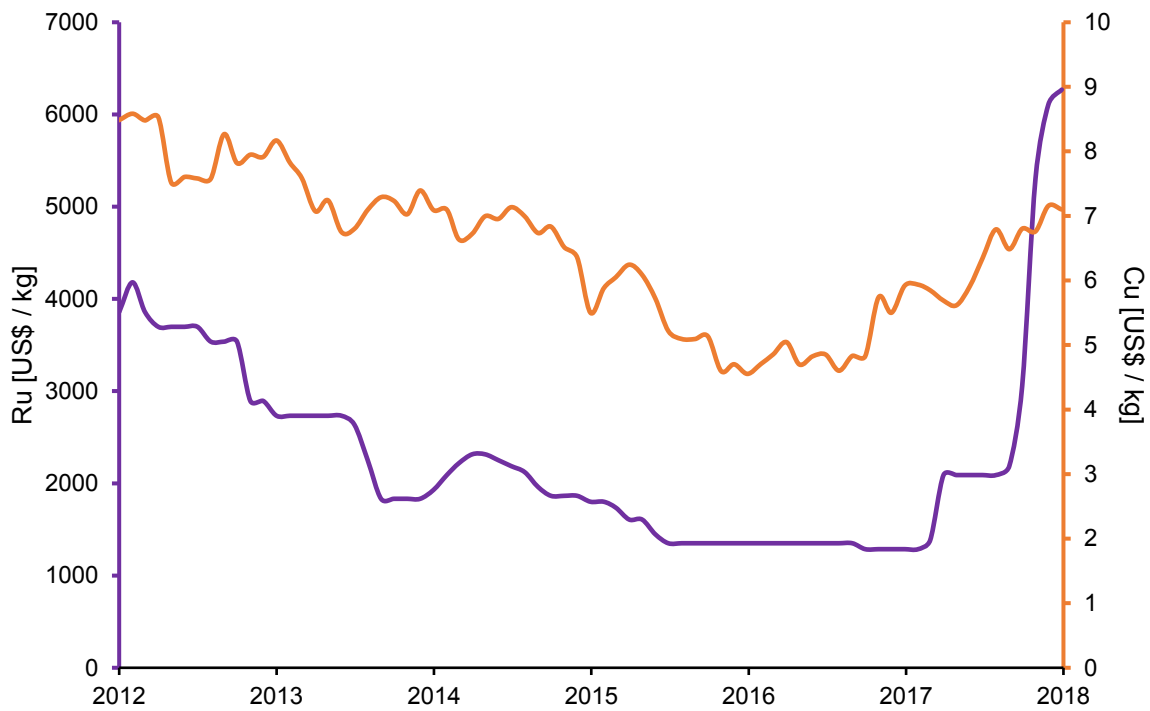


Fig. 16 Development of the ruthenium and copper price over the period of all described investigations. [Data: Quandl^{64,65}]

The ability to recycle copper from disposed electronics and other discarded metal makes the usage of copper also more environmentally friendly. Almost one third of the used copper in 2015 came from recycled copper.⁶⁶ Copper belongs to the materials that do not degrade or lose their chemical or physical properties in the recycling process. Its recycling value is so substantial that premium-grade scrap copper holds around 95% of the value of the original primary metal. The recycling also saves a huge amount of energy. Recycling saves 85% of energy compared to the manufacturing of the metal from scratch. If the metal is extracted from copper ore it takes about 95 million BTU per tonne whereas recycling only 10 million. Because copper is recycled by smelting and the extraction is done with addition of coal followed by burning at high temperatures, recycling copper also reduces the CO₂ emission by 65%.⁶⁷ There are also new methods that operate at ambient temperatures such as the leach-solvent extraction-electrowinning (SX/EW) process or a bioleaching process using bacteria.⁶⁸

With its tuneable photophysical properties and the simplicity to synthesize homoleptic bis(diamine) copper(I) complexes (see *10 Synthetic Strategy*), Cu(I) complexes (heteroleptic complexes as discussed later) are a serious alternative to Ruthenium dyes in DSCs (details see: *7.1.2 Photosensitizer*).

7. Design and Working Principle of n-type Dye-Sensitized Solar Cells

7.1. Components

The DSC consists of two conducting substrates with an electron conducting material in between (Fig. 17). In general, the substrate is glass but other materials like plastics are investigated. The glass sheets are coated with a conducting oxide. One part, the working electrode, bears a semiconductor, the other one, the counter electrode, is covered with a catalyst. The dye is designed to anchor on the semiconductor surface to sensitize the solar cell. The electrolyte handles the electron transport between both electrodes to close the circuit.

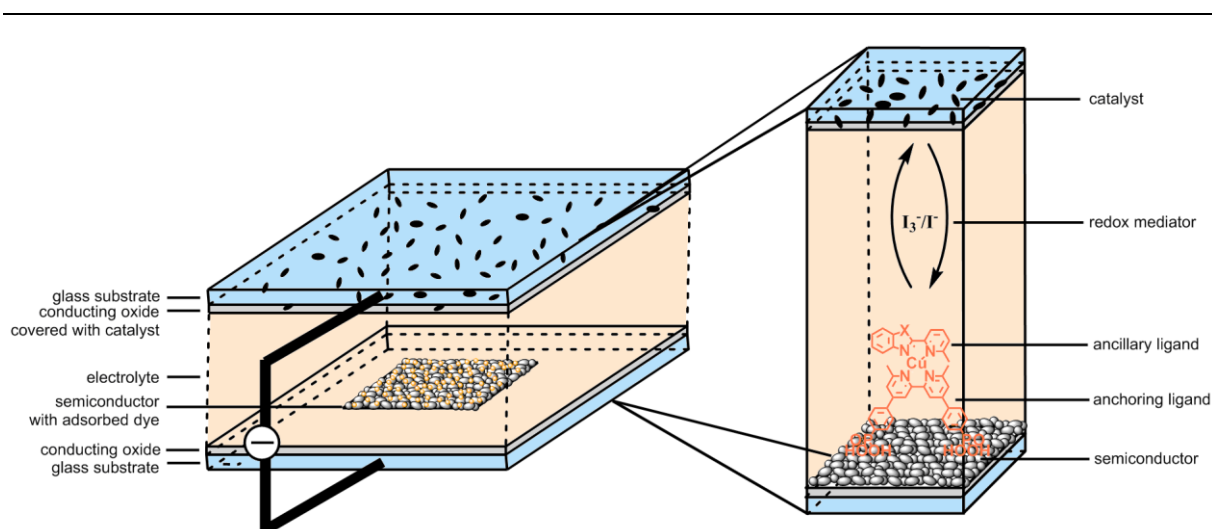


Fig. 17 Schematic representation of a DSC with zoom-in example of a copper(I) sensitizer in a DSCs.

7.1.1. Working Electrode

The electrode that interacts directly with the incoming photons is the working electrode. It consists of a substrate where a semiconductor is applied. The most commonly used substrate is glass. It is used because it is cheap, readily available and highly transparent in the visible spectrum.³² But in order to investigate flexible DSCs plastics have been used. The most common plastic substrates are polyethylene terephthalate (PET) and polyethylene naphthalate (PEN).⁶⁹

The substrate has to be coated with a conducting layer in order to receive a conductive substrate. This layer has to be transparent as well. Another property it has to fulfil is the resistance to high temperatures. During the sintering process of the whole electrode with the applied semiconductor, temperatures up to 500 °C are reached. To guarantee a high conductivity, low resistance is also required. Based on these requirements transparent conducting oxides such as indium-doped tin oxide (ITO) and fluorine-doped tin oxide (FTO) have been investigated.

On top of this conductive substrate a semiconductor is deposited. Until today several oxide semiconductors have been used in DSCs. The most commonly used n-type semiconductor is TiO₂ but ZnO, SnO₂ or chalcogenides have also been investigated.^{32,36} A major breakthrough in DSC technology came from Grätzel and O'Regan with the use of a nanocrystalline TiO₂ instead of a bulk crystal. Thereby the surface area was increased about 1000 times with the consequence that much more dye could anchor to the semiconductor.⁷⁰ This critical change improved the photoconversion efficiency by about 700%. Because a high surface area is important to reach highly efficient DSCs, nanoparticles, -rods, -fibres and -channels of several semiconductors have been investigated to increase the surface area.^{34,37,71-74} Further investigations to enhance the performance were done by using light scattering particles, transparent electrodes or other surface engineering technics.⁷³⁻⁷⁵ Also the implementation of doping of the semiconductor or using composites can improve the DSC performance.^{73,74}

TiO₂ became the most used semiconductor because of its low-cost, market abundance, non-toxicity and biocompatibility.⁷⁶ TiO₂ is also used in everyday life in white paint, toothpaste or Sun cream for example.³⁶ TiO₂ has many advantages for sensitized photochemistry and photoelectrochemistry. It is stable under visible irradiation and in electrochemical systems under extreme operating conditions.³² In DSCs, TiO₂ semiconductors exhibit higher performance than other semiconductor oxides.⁷⁶ Generally, TiO₂ occurs in three natural crystalline forms: anatase, rutile and brookite (Fig. 18).

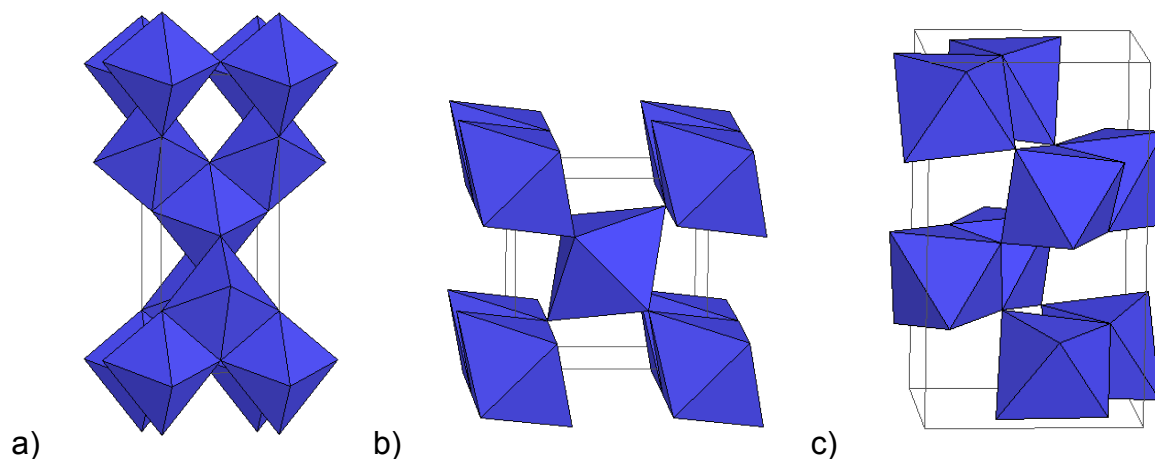


Fig. 18 Natural crystalline forms of TiO_2 : (a) anatase, (b) rutile and (c) brookite.⁷⁷

Brookite is difficult to prepare and only anatase and rutile are possible candidates for bulk applications. Rutile is more stable than anatase, but of the three polymorphs of TiO_2 the anatase phase has the best photocatalytic activity. Anatase occurs as pyramid-like crystals and is stable at low temperature, while rutile occurs as needle-like crystals and forms in high-temperature processes. Anatase (3.2 eV) has a larger band gap than rutile (3.0 eV) (Fig. 20). The anatase band gap corresponds to an absorption of incident light at a wavelength of 388 nm while the rutile band gap corresponds to 413 nm where it absorbs 4% of the incident light (Fig. 19). With a larger band gap and a higher conduction band edge energy also higher open-circuit voltages (see *8.2.2 J-V Measurements*) can be obtained what results in higher efficiencies.

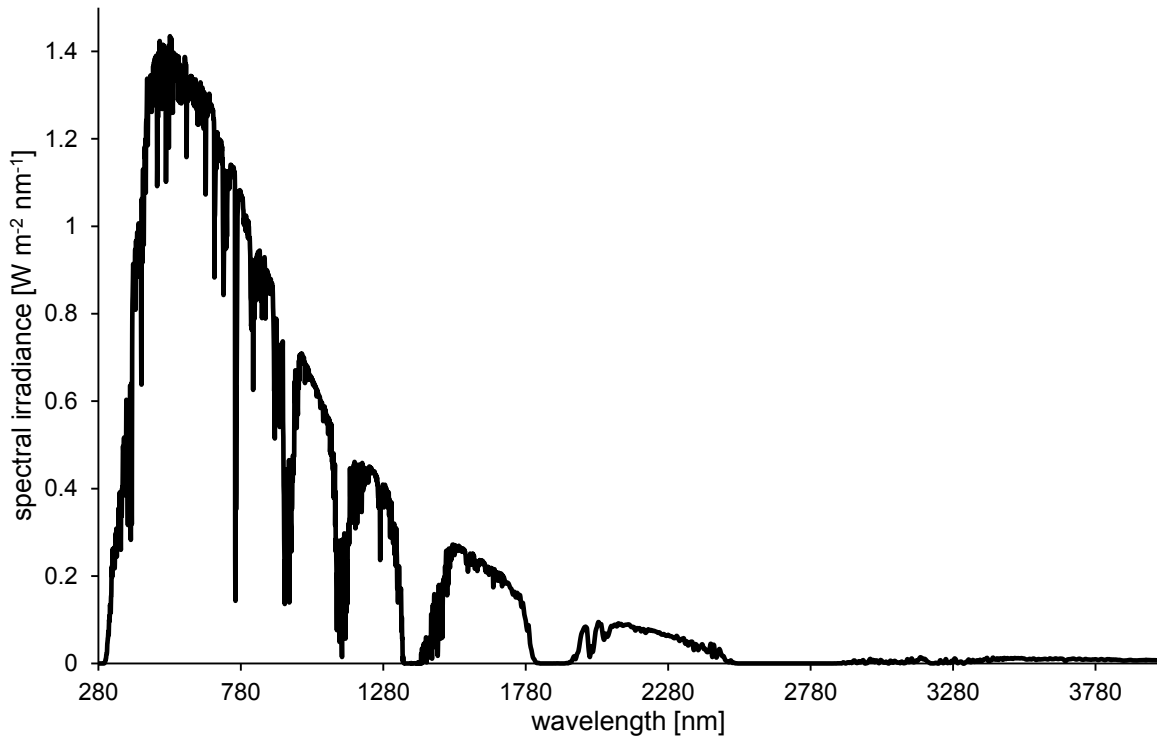


Fig. 19 Solar spectrum on the surface of the Earth.⁷⁸

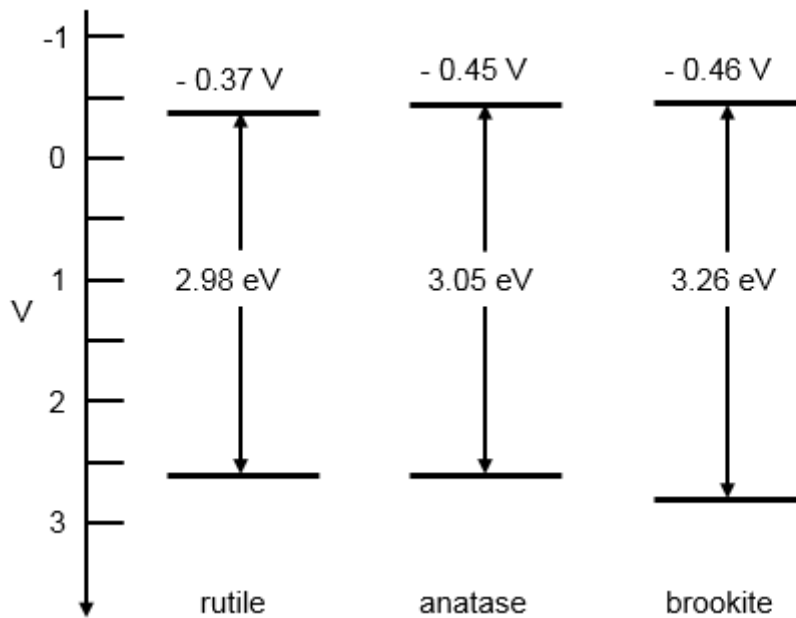


Fig. 20 Band gaps of the three natural crystalline forms of TiO₂ at pH = 7.⁷⁹

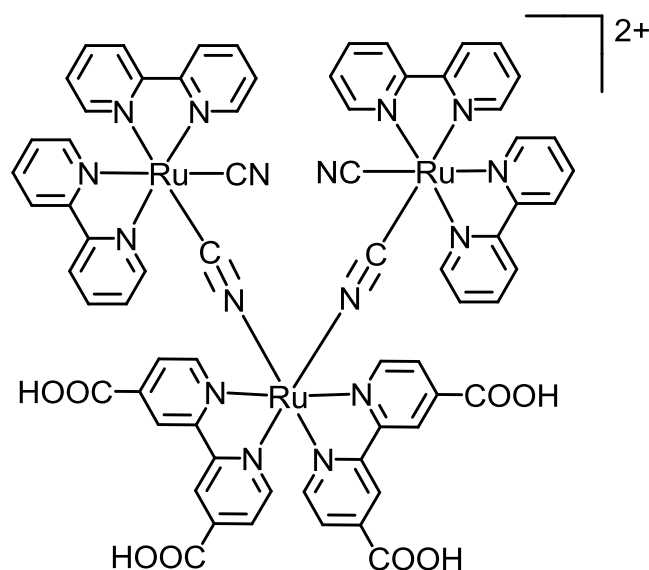
For the electron injection of the excited dye in the semiconductor it is important that the conduction band edge coincides with the excited electron level of the dye.³² That means that the LUMO (lowest unoccupied molecular orbital) energy level of the sensitizer must be lower than the conduction band of the metal oxide.⁷⁶ Anatase belongs to the indirect band gap semiconductor category. This means that it is impossible for photoexcited electrons to undergo direct transition from the conduction band to the valence band. This results in a longer lifetime of the electron.⁷⁴ TiO₂ also has a high dielectric constant that provides a shielding of the injected electrons and recombination is prevented.³² This improves the performance of the DSC because one of the most important factors is the electron transport across the TiO₂ electrode.⁷⁶

7.1.2. Photosensitizer

The key component of a DSC is the photosensitizer (dye). The investigation of the dye and its application in DSCs is the main topic of this thesis. The dye interacts directly with the incoming photons and injects excited electrons into the conduction band of the semiconductor. With these two objectives, the main requirements for a dye are obvious. First of all, the photosensitizer should have a broad absorption range in the visible range of the solar spectrum. Ideally it covers the whole visible solar spectrum and also the near infra-red region. The extinction coefficient of the sensitizer should be high to absorb as many photons as possible. In order to inject electrons efficiently into the conduction band of the semiconductor, the excited state level must be sufficiently higher than the conduction band edge. Another requirement is that the highest occupied molecular orbital (HOMO) is more positive than the redox potential of the redox mediator to guaranty the regeneration of the dye.⁸⁰

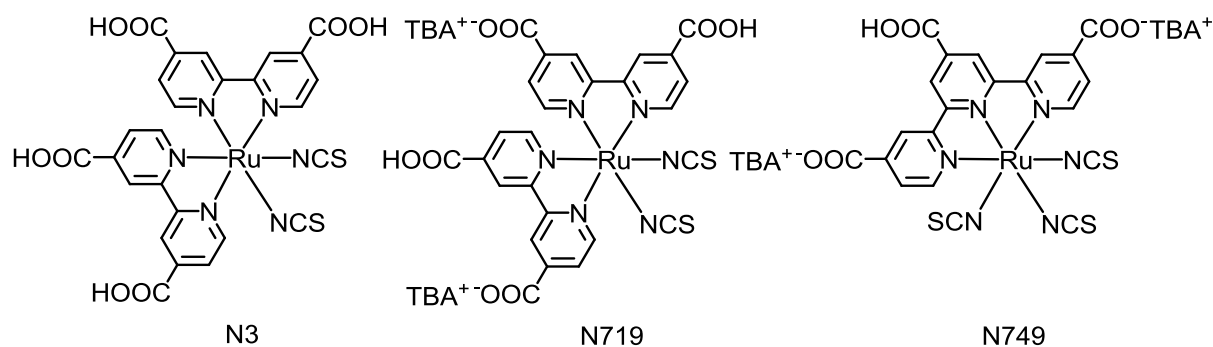
Photosensitizers can be divided into two groups: metal-organic coordination complexes and metal-free organic compounds. Both groups of dyes are applied to the semiconductor surface by immersing the photoanode into a solution of the dye. Therefore, the dye has to be soluble. And that it binds to the surface anchoring groups are necessary that interact strongly with the semiconductor surface.

Metal-organic complexes are the originally used sensitizers. Grätzel and O'Regan used a ruthenium-based dye (Scheme 1) and reached an efficiency of 7.1 - 7.9%.¹



Scheme 1 The ruthenium-based dye reported by Grätzel and O'Regan in their breakthrough Nature paper in 1991.¹

The Ru-based dyes have been further developed by M. K. Nazeeruddin in the group of Grätzel. The dyes **N3**⁸¹, **N749**⁸² and in particular **N719**⁸³ (Scheme 2) are often used reference dyes when screening new sensitizers. In this thesis **N719** is used as a reference dye. A maximum efficiency of 11.2% has been reached with **N719**.⁸⁴



Scheme 2 Ruthenium dyes **N3**, **N719** and **N749** (TBA = tert-butylammonium cation).

N719 shows an extraordinary quantum efficiency (Fig. 21) (details about EQE see 8.3 *External Quantum Efficiency*). It has a wide range of efficient photon-to-power conversion efficiency between 370 and 700 nm and an external quantum efficiency (EQE) maximum about 80%.

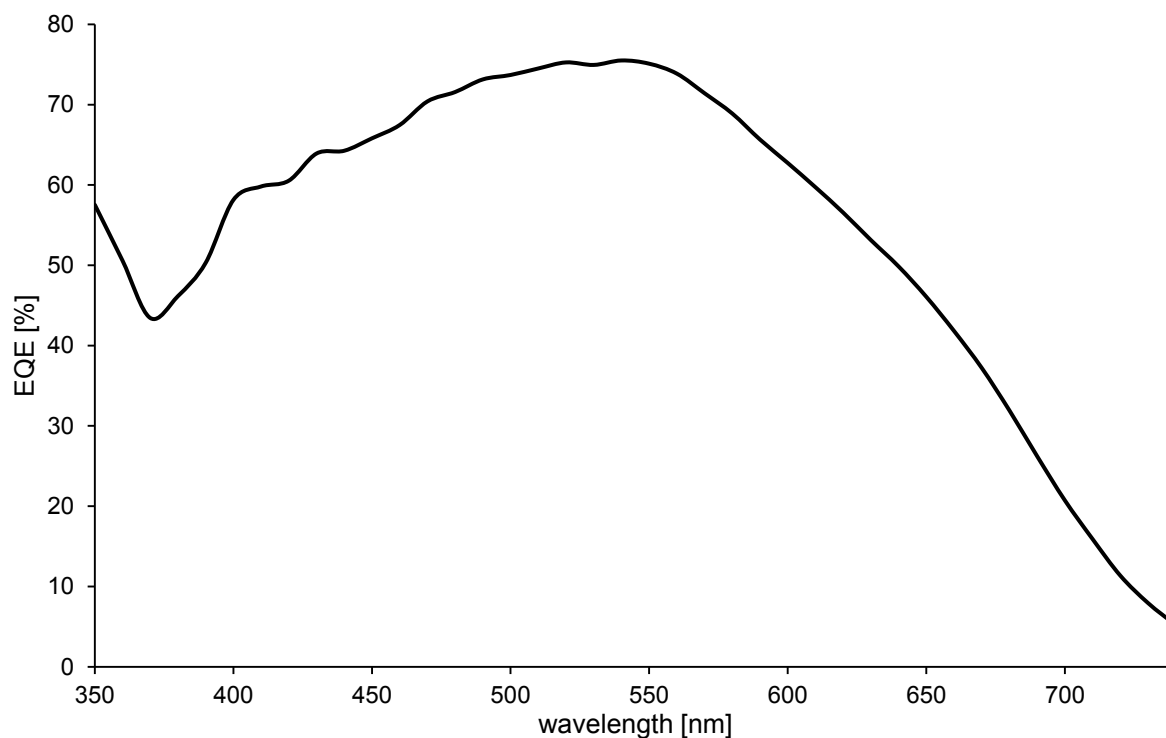
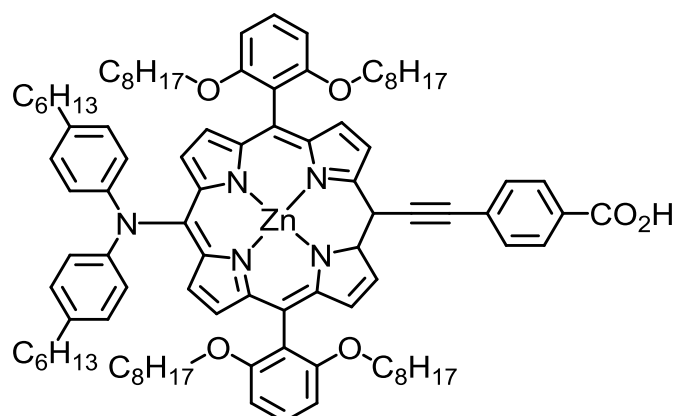


Fig. 21 EQE curve of the ruthenium dye N719.

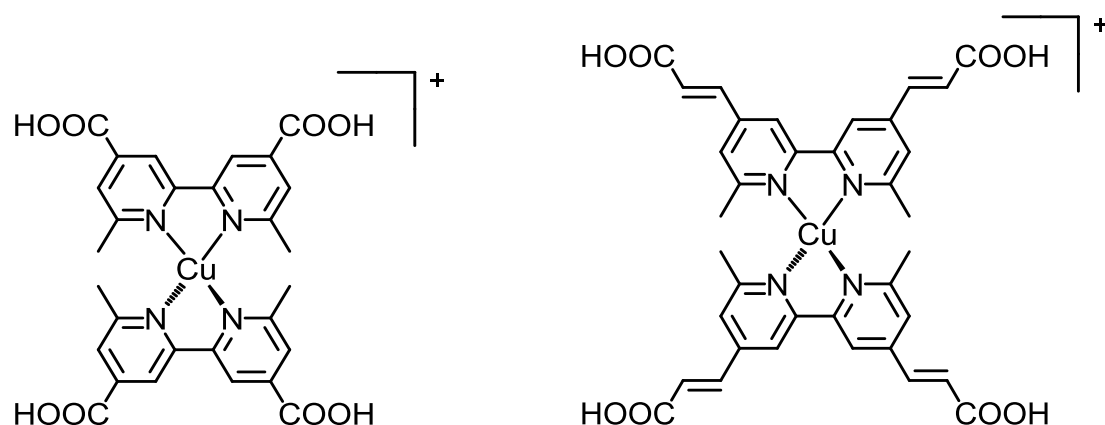
However, other Earth-abundant metals such as Mn, Fe, Ni or Zn have been investigated as well.⁶² Mn has been investigated as the central metal ion in metalloporphyrins but depending on the porphyrin very low efficiencies were obtained (0.01⁸⁵ - 1.50%⁸⁶). Metalloporphyrins with Zn have shown promising results.^{87,88} A DSC with a Zn porphyrin (Scheme 3) is one of the best performing device to date with an efficiency of 12.1% when combined with a Co(II/III) electrolyte.⁸⁹



Scheme 3 Dye of one of the best performing DSC with an efficiency of 12.1%.⁸⁹

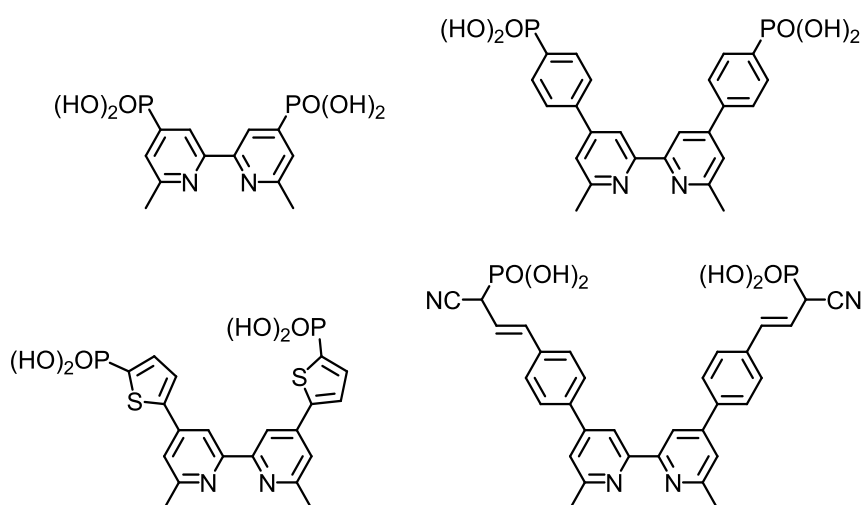
Heteroleptic complexes of Zn(II) have also been used as dyes. Efficiencies up to 0.71% were reached in the study by Hostettler and co-workers.⁹⁰ Ni does not perform in porphyrins or coordination polymers⁶² but coordination complexes have shown efficiencies about 1%.⁹¹ Photosensitizers with Fe have been investigated over the last 20 years but efficiencies over 1% have not yet been reached.⁶²

The most promising Earth-abundant metal is copper. It has been investigated in dyes in DSCs since the pivotal work of Sauvage in 1994⁹². In the beginning of the research homoleptic Cu(I) complexes (Scheme 4) were used and efficiencies up to 2.3%⁹³ were obtained with unmasked cells. It is relevant here to mention on the fact that DSCs should be masked during measurements to prevent overestimation of their performance. This point was discussed in detail by Snaith in 2012.^{94,95} Even with these critical comments, it remains a fact that many groups continue to report data for unmasked cells. This makes comparison of literature data difficult. Recently, Dragonetti and co-workers reported that masking lead to a 25-30% decrease in photoconversion efficiency.⁹⁶



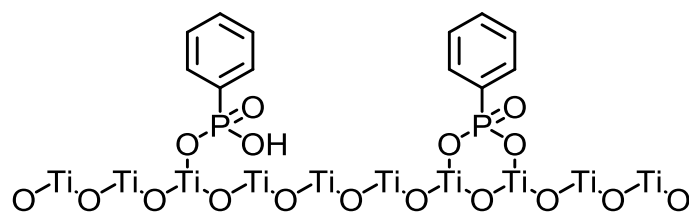
Scheme 4 Homoleptic copper(I) dye used by A. Hernandez Redondo.⁹³

The use of heteroleptic Cu(I) dyes has been the breakthrough needed to produce an increase in efficiency. Here, the dye consists of an anchoring ligand and an ancillary ligand. The anchoring ligand has to have anchoring groups to adsorb on the semiconductor surface. Typical anchoring groups are carboxylic acids and phosphonic acids but also a wide range of other anchoring groups have been tested.⁹⁷⁻⁹⁹ Investigations have shown that phosphonic acid anchoring groups perform better than carboxylic acids.¹⁰⁰ Several anchoring ligands have been investigated in the Constable/Housecroft research group but the best performing one is the anchoring ligand **ALP1** that is also used in this thesis as the anchoring ligand. Scheme 5 shows several phosphonic anchoring ligands investigated in our research group with **ALP1** in the top right corner.¹⁰⁰⁻¹⁰²



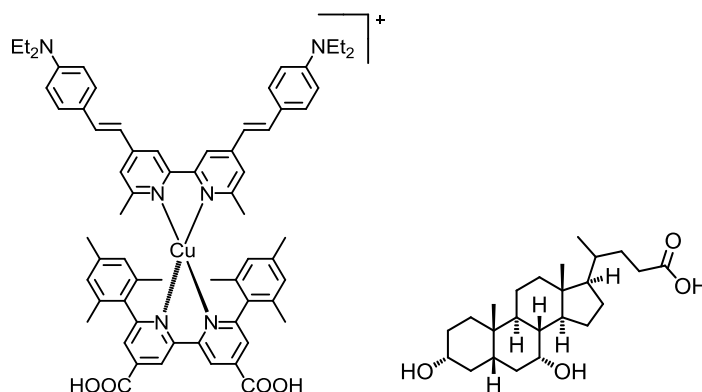
Scheme 5 Some anchoring ligands for Cu(I)-based DSCs with phosphonic acid anchoring groups.¹⁰⁰⁻¹⁰²

Experiments have shown that the phosphonic acid binds in two possible binding modes to the TiO₂ surface. In the end a mixture of monodentate and bidentate binding mode after deprotonation of the phosphonate hydroxyl groups is proposed. Scheme 6 represents a schematic presentation of both binding modes.¹⁰³



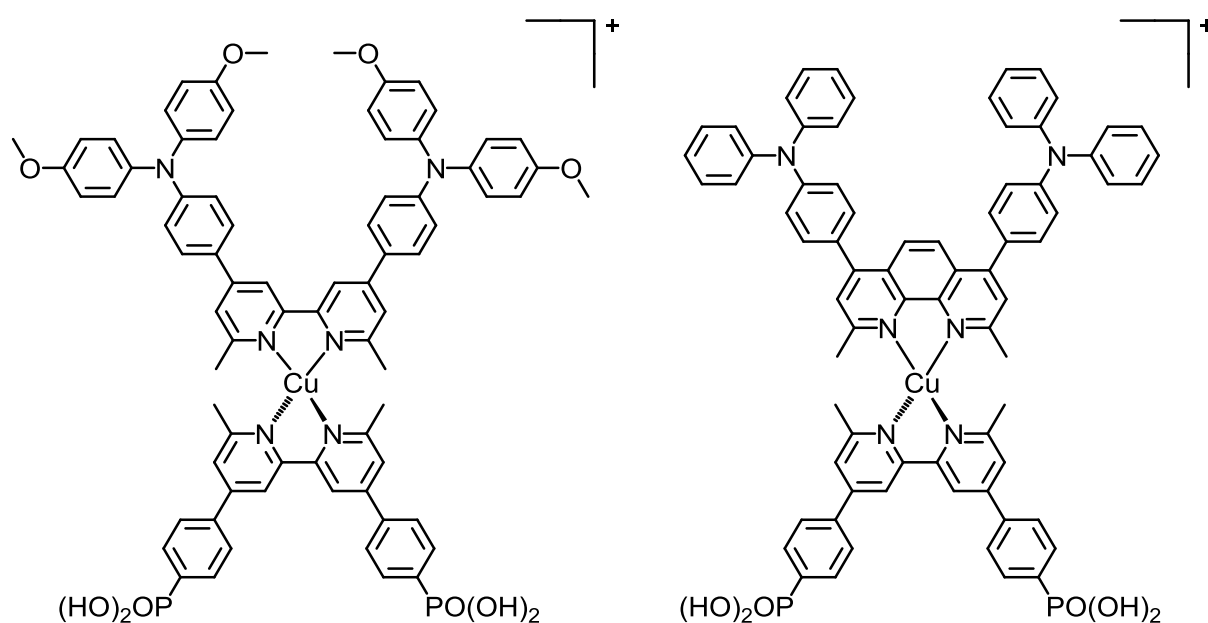
Scheme 6 Schematic representation of the proposed binding modes of phosphonic acid anchoring groups on anatase TiO₂.

Schmittl and co-workers investigated the HETPHEN (heteroleptic bisphenanthroline complexes) strategy to synthesize heteroleptic Cu(I) complexes. But highly sterically demanding diamine ligands are necessary to obtain stable complexes.¹⁰⁴ The biggest problem is the formation of mixtures of homoleptic and heteroleptic complexes that are hardly to separate. The group of Odobel used this strategy to synthesize the Cu(I) complex in Scheme 7. This complex lead to photoconversion efficiency of 4.66% in combination with a co-adsorbent and appears to be the most efficient Cu(I)-based DSC to date.¹⁰⁵ However, these results were with unmasked DSCs. It remains a problem in the literature that both masked and unmasked DSCs are reported, making comparisons difficult.



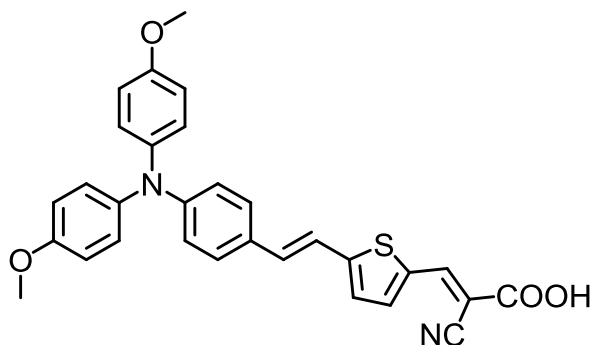
Scheme 7 The Cu(I) dye investigated by the group of Odobel reaching an overall efficiency of 4.66% (left) with the co-adsorbent chenodeoxycholic acid (**Cheno**) (right).

Within the Constable/Housecroft research group, we have developed a stepwise method (details see *13 General Device Fabrication*) of assembling heteroleptic dyes on the semiconductor surface and this gives an easy method to screen different ancillary ligands without the need for isolation of the heteroleptic complex. The isolation of the heteroleptic complex would be difficult because of an equilibrium of homo- and heteroleptic complexes in solution. Several ancillary ligands have been tested and with a 2,2'-bipyridine-based ligand (Scheme 8) an efficiency of 3.77% with unmasked cells was reached.¹⁰⁰ A DSC with a 1,10-phenanthroline-based ligand (Scheme 8) had an efficiency of 3.69% with a Co(II/II) redox couple.¹⁰⁶



Scheme 8 Cu(I) dyes with a 2,2'-bipyridine-¹⁰⁰ and a 1,10-phenanthroline-based¹⁰⁶ ancillary ligand.

The second group of dyes are metal-free organic compounds. They have with a donor part, a π -bridge and an acceptor part all in the same structure. A big advantage is that they are completely organic whereby they are inexpensive, environmental friendly and have no problem with limited resources.³² Common donor groups are arylamines¹⁰⁷ and the π -bridge often consists of at least one thiophene unit. The acceptor part bears the anchoring group that is most often a cyanoacrylate.^{32,36,108} The absorption range of the dyes can be tuned to achieve organic dyes with visible- or with near-infrared light absorption.¹⁰⁹ Optimized devices can reach efficiencies over 10.0%.^{32,109,110} A simple organic dye is shown in Scheme 9.



Scheme 9 Simple organic dye with a triarylamine donor part, a π -bridge with a thiophene unit and an acceptor part with a cyanoacrylate anchoring group.

7.1.3. Counter Electrode

The substrate of the counter electrode has the same requirements as the working electrode. Here, glass is the commonly used but investigations towards flexible DSCs have used a plastic substrate. The electrode is made conductive with the help of FTO or ITO as seen for the working electrode. But the counter electrode has the purpose to handle the electron transfer to the electrolyte (see detailed working principle in 7.2 *Working Principle*). Because of this, the conducting substrate is coated with a catalyst to obtain sufficiently fast reaction kinetics for the redox couple reduction reaction. Generally, a platinum-coated electrode is used. But with the usage of iodine-based electrolytes corrosion of Pt is observed. Here, a reaction of I_3^- and Pt leads to PtI_4 which decreases the long-term stability of the device.⁷⁶ Pt is also one of the most expensive components of a DSC (about 30.000 US\$/kg¹¹¹).¹¹² Thus, the replacement of Pt is a goal to enhance the performance of DSCs. An interesting alternative are carbon-based materials. Investigations with graphene, graphite, carbon nanotubes, carbon black and hard carbon spherules are carried out.^{32,76} They are cheap and combine heat-resistance, sufficient conductivity, electrocatalytic activity for the I_3^- reduction reaction and corrosion resistance.³² Other alternatives are conducting polymers, metals like aluminium, metal compounds with carbides, sulphides, nitrides, phosphides, oxides, tellurides and selenides or cobalt sulphide nanoparticles for example.^{32,76,112}

7.1.4. Electrolyte

The connection between the working and the counter electrode is built by an electrolyte. The electrolyte plays an important role in a DSC. It transfers the charge between the two electrodes

(see detailed working principle in *7.2 Working Principle*). It always contains a redox couple that is able to be reduced by the counter electrode and can reduce the oxidized dye itself. A good redox couple should have fast electron transfer kinetics, small visible light absorption, good stability and slow electron recombination kinetics at the dye surface. The main feature that limits the performance of the DSC are the diffusion properties.³² This is most important when a liquid medium is used. But there are also solid-state and quasi-solid electrolytes.^{112,109} A high stability and non-corrosiveness are necessary to achieve long-term stability.³²

Since the breakthrough by Grätzel and O'Regan, a liquid electrolyte containing an I^-/I_3^- redox couple is used as a standard. It fulfils most of the required properties to be a good electrolyte. It has a high conversion efficiency and a high stability.³² But it also absorbs light in the visible spectrum (around 430 nm¹¹²) why the concentration has to be low.¹¹³ As a solvent a mixture of acetonitrile and valeronitrile or pure *N*-methoxypropionitrile is used. It is important to use solvents with a low viscosity to guaranty fast diffusion of the charge through the electrolyte. The main problem of the low viscose solvents is their high vapour pressure. Temperatures over 50 °C can be reached under illumination of one Sun.¹¹² When temperatures over the boiling point of the solvent are reached dissolution of the sealing can occur.

Additives have been investigated to enhance the photovoltaic performance. Cations like guanidium or alkali cations are used to increase the short-circuit current. They adsorb on the TiO_2 semiconductor surface and lead to a shift in the conduction band toward more positive potentials that increases the electron injection dynamics. On the other hand, nitrogen-containing heterocyclic compounds as 4-*tert*-butylpyridine are used to improve the open-circuit voltage.³²

Beside the medium of the electrolyte and additives also new redox couples have been investigated. The electrolyte has an impact on all key parameters of a DSC. Redox couples are mainly influencing factors on the open-circuit voltage. It can be tuned by the redox potential of alternative redox couples. Here, especially iodine-free alternatives have been investigated. Several transition metal-based complexes like ferrocene/ferricenium, cobalt(II/III), nickel(III/IV) and copper(I/II)^{97,99} have been studied. The performance of iodine-containing electrolytes has been optimized since the development of the first DSC by Grätzel and O'Regan.³⁶

7.2. Working Principle

The perfect interaction of all components in a DSC leads to an electron flow. As already mentioned, the field of DSCs is divided into n-type DSCs and p-type DSCs. In p-type DSCs the photosensitizer takes up the electron from the p-type semiconductor to induce a hole into the semiconductor and starts the electrical circuit. In an n-type DSC, an electron from the excited state of the dye is injected into an n-type semiconductor that is the reverse process of that occurs at the semiconductor/dye interface in a p-type device.

7.2.1. n-Type Dye-Sensitized Solar Cells

Fig. 22 displays the working principle of an n-type DSC. The optimal sequence of electron-transfer steps starts with photons hitting the photosensitizer (S) incoming from the working electrode side. The dye absorbs photons within the visible or near infrared region. This interaction leads to the excitation of the sensitizer to its excited state (S*). The excited sensitizer injects an electron to the conduction band (E_{cond}) of the semiconductor where it travels through to reach the back-collector electrode.

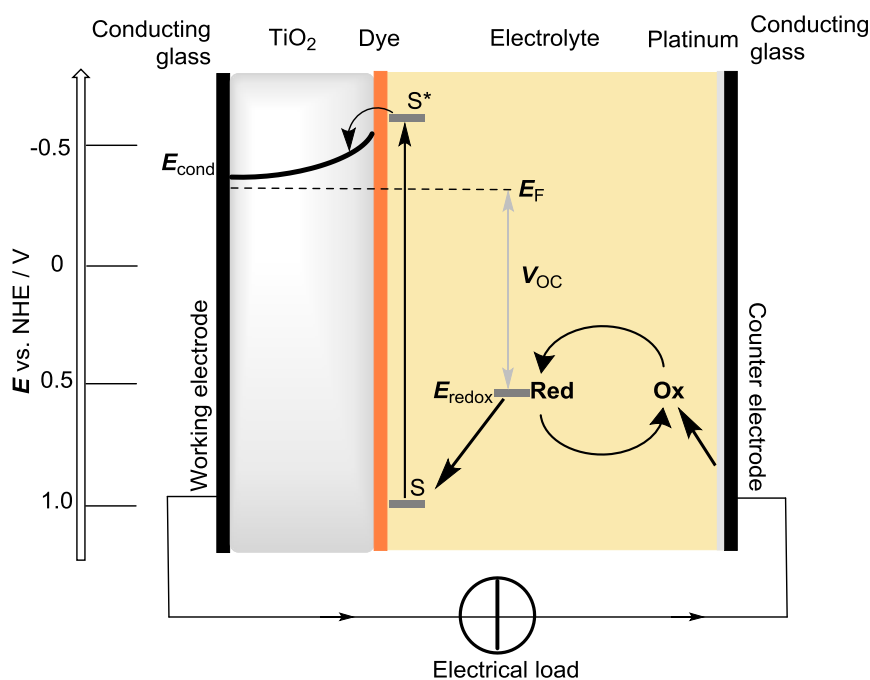
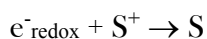
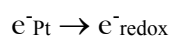
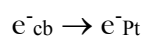
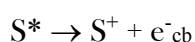
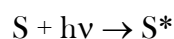


Fig. 22 Working principle and energy level diagram of an n-type DSC.

After the electrons have passed through the electrical load they reach the counter electrode. Here, the platinum catalyses the reduction of the oxidized species of the redox mediator. The redox mediator diffuses through the electrolyte to the working electrode side of the DSC and regenerates the oxidized sensitizer. In this fashion the cycle is closed and the electrical current occurs. Scheme 10 summarizes all electron-transfer steps of a DSC.



Scheme 10 Sequence of electron-transfer steps of a DSC (S = sensitizer in its ground state; S* = sensitizer in its excited state; S+ = sensitizer in its oxidized state; e⁻_{cb} = electron in the conduction band of the semiconductor; e⁻_{Pt} = electron at the Pt counter electrode, e⁻_{redox} = electron in the redox couple).

But the system has to be tuned individually because of undesired electron-transfer pathways in every electron-transfer step. Most of the undesired back reactions occur at the working electrode. At the semiconductor/dye/electrolyte-interface most of the back reactions take place (Fig. 23).

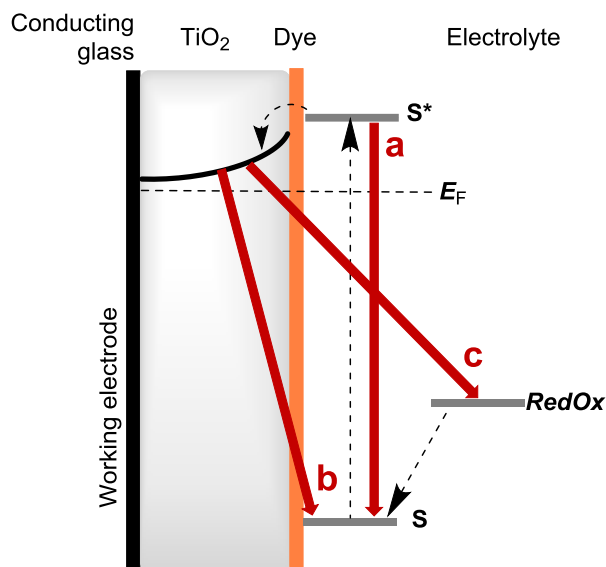


Fig. 23 Summary of back-reactions at the semiconductor/dye/electrolyte-interface (**a**) decay of excited state dye back to the ground state; **b**) recombination of the injected electron with the oxidized dye; **c**) recombination of the injected electron with the oxidized electrolyte; optimal electron transfers in dashed lines).

After excitation of the sensitizer no injection can take place because of decay of the excited state to the ground state of the dye. And if injection took place, undesired electron-transfer pathways can still occur. Recombination of the injected electrons with the oxidized dye or the redox shuttle can be observed. Also, accumulation of electrons in trap states of the semiconductor can decrease the performance of the DSC. However, the counter electrode and the electrolyte have to be tuned to guarantee optimal electron transport.

All electron-transfer reactions compete with each other and the DSC components have to be tuned to guarantee the optimal pathway. After excitation of the dye, the injection into the semiconductor must be faster than decay or recombination processes. In measurements of an exemplary Ru-sensitized DSC (Fig. 24) this is the case.

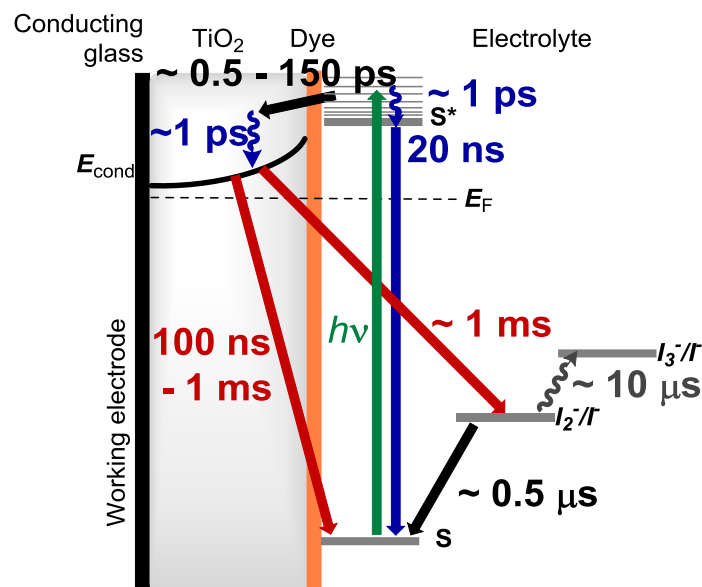


Fig. 24 Kinetics of a Ru-sensitized DSC with I^-/I_3^- redox mediator: typical time constants under irradiation (green) of the desired electron-transfer processes (black), recombination processes (red), nonradiative decays (blue) and disproportionation reaction (grey).¹¹³

Depending on the dye, the time constant of injection is between 0.5 and 150 ps and recombination reactions occur at a time scale of nanoseconds to milliseconds.¹¹³ Nonradiative decay occurs in the conduction band of the semiconductor and from higher energy levels of the excited state of the dye to the ground state in picoseconds to nanoseconds timescale. But as long as injection and travel through the semiconductor takes place these are not performance decreasing processes. The regeneration of the oxidized dye by an iodine redox shuttle is the slowest electron-transfer process.

8. Characterisation

8.1. UV-Vis Spectroscopy

The absorption characteristics of the working electrode can be measured using solid-state UV-Vis spectroscopy.

8.1.1. Instrumental Details

All measurements have been performed on a *VARIAN Cary-5000 spectrophotometer*. This instrument can be operated in single- and double beam method. For the investigations of the working electrode the single beam method has been used (Fig. 25).

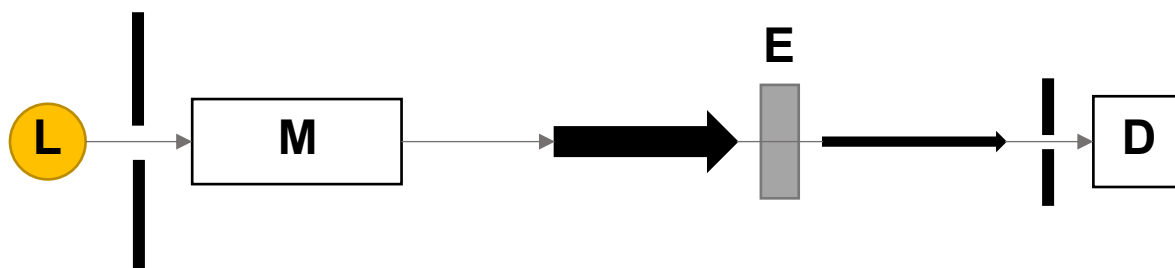


Fig. 25 Schematic representation of a UV-Vis spectrophotometer used with single beam method (L = light source; M = monochromator; E = working electrode; D = detector).

The light generated is modulated by a monochromator. The light with a specific wavelength and intensity hits the dye-functionalized working electrode at the semiconductor side. The working electrode has to be a transparent electrode, as opposed to electrodes using in the DSCs which have a scattering layer applied on the surface. A certain part of this light is absorbed by the working electrode and the intensity is referred to the reference intensity. The reference intensity is defined by the absorption of an unfunctionalized working electrode without scattering layer.

The controlling and data acquisition was done by the *VARIAN Cary Win UV Scan Application* software.

8.1.2. Solid-state UV-Vis Spectroscopy

After the instrument has been switched on, the background is measured. First, a transparent working electrode is measured and afterwards a measurement with zero transmittance. Finally, the absorption spectrum of a dye-functionalized working electrode without scattering layer is recorded. The absorption maximum can be determined but the intensity of the signal is in arbitrary units of absorbance. Because it is not possible to quantify the dye loading on the electrode, no extinction coefficients can be obtained. For ruthenium dyes it is usual practice to desorb the dye, dissolve in a solvent and measure the absorption spectrum in solution. The concentration of the solution can be backcalculated from the extinction coefficient of the known complex. In the case of heteroleptic copper dyes desorption followed by redissolving results in an equilibrium mixture of homo- and heteroleptic complexes. It is therefore not possible to use the Beer-Lambert-law to quantify the amount of dye.

8.2. Solar Simulator

The key measurement of a DSC is the investigation of the overall efficiency (η) by a solar simulator.

8.2.1. Instrumental Details

The solar simulator used in all following investigations is a *Solaronix SolarSim 150*. It consists of a metallic box in which a light source is mounted on the upper, inside surface (Fig. 26a). The light source consists of three light bulbs. One light bulb is a *Philips MSR 200 HR 1CT* and two are *Osram HLX 64623 XENOPHOT* Xenon light bulbs. The light spectrum is adjusted to the solar spectrum via a filter glass that is placed between the light source and the sample table. The temperature-controlled and height-adjustable sample table is placed on the bottom of the box. The temperature is regulated to 25 °C in order to give stable measurement conditions. Otherwise the sample table would be heated up steadily during the measurements.

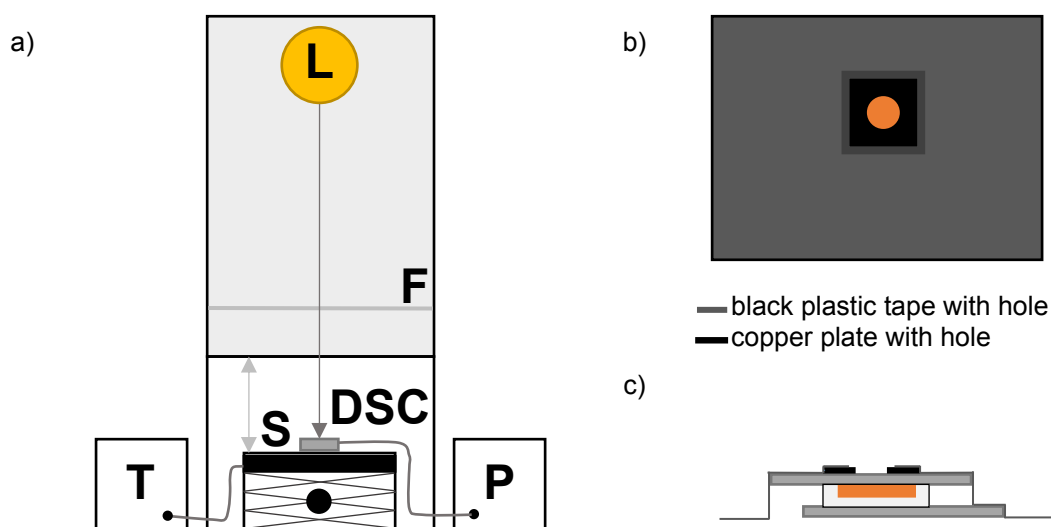


Fig. 26 a) Schematic representation of solar simulator (L = light source; F = filter glass; S = height-adjustable temperature controlled sample table; T = temperature controller; DSC = dye-sensitized solar cell; P = potentiostat), b) on-top view of a fully masked DSC, c) section-view of a fully masked DSC.

The sample table is height-adjustable because the distance to the light source regulates the light intensity. The international standard solar spectrum that is used for solar cell measurements is AM 1.5 G (AM = air mass; G = global). This standard spectrum corresponds to a light intensity of 1000 mW cm^{-2} .

The AM is defined as the path length of the sunlight through the atmosphere. When the Sun is in zenith the light intensity at the entry point into atmosphere is defined as AM 0 (Fig. 27).

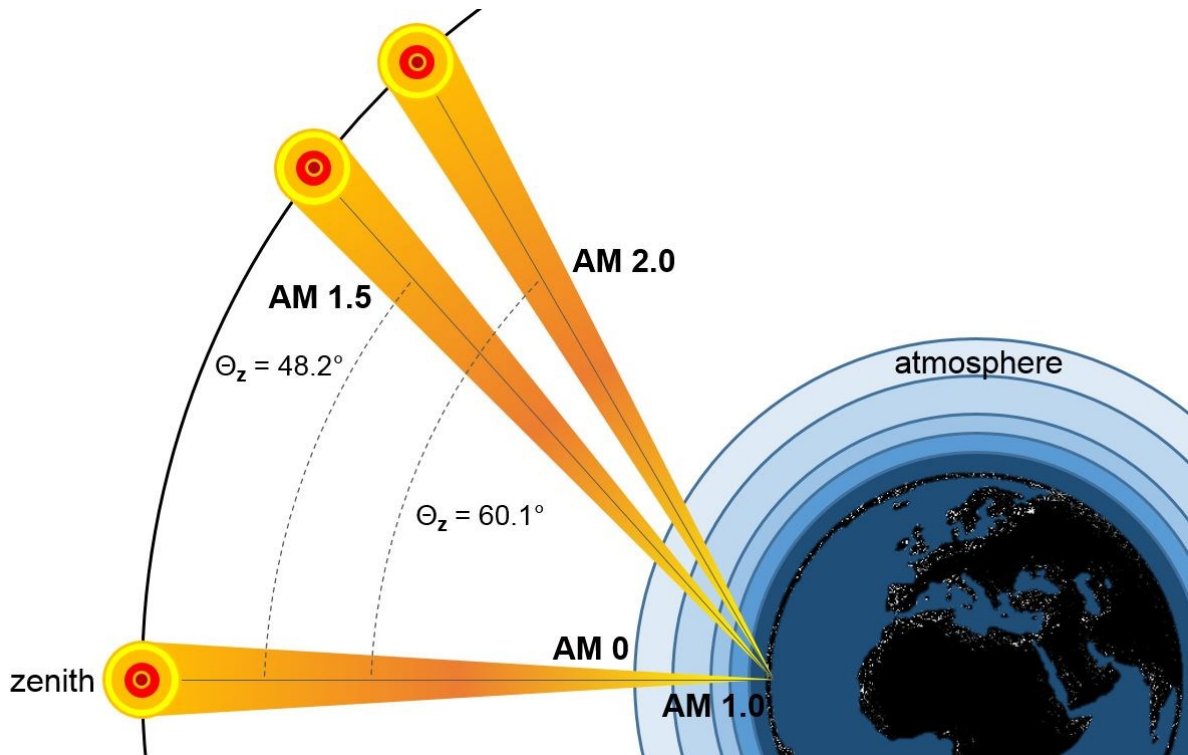


Fig. 27 Schematic representation of the influence of the zenith angle on the AM value.

When absorption, reflection and scattering of the atmosphere is taken into account, the light intensity is defined as AM 1.0 on the global surface. The influence of the zenith angle on AM can be described by Equation 1.

$$AM \approx \sec \Theta_z \approx \frac{1}{\cos \Theta_z}$$

Equation 1 Influence of the zenith angle on the AM value.

The definition of global spectrum (G) is a cell that is mounted to the ground without a concentration system under the blue sky. This implies that standard AM 1.5 G is equal to an irradiation at the surface of the globe with a zenith angle of about 48.2° to a cell that is mounted on the ground without a concentration system under the blue sky.

In order to guarantee the identical irradiation energy, the solar simulator is referenced with a silicon solar cell before each series of measurements. This reference cell has been calibrated by a standard cell under standard conditions in a research centre. Here, crystalline silicon cells are used because they are currently the only solar devices with a high stability over a long period of time.

All measurements are carried out by an external potentiostat (*Keithley 2400* series source meter). It can apply a defined voltage and measures the generated current output.

In order to determine the irradiated active area of the DSC a mask is placed on top of the working electrode side of the DSC (Fig. 26b, Fig. 26c). Therefore, a copper plate with a calibrated hole is placed on top and in the end a black plastic tape with a hole is glued over the complete DSC. In this way, the DSC is fully masked during the measurement and the influence of scattered light is minimized. Working with unmasked DSCs leads to an overestimation of their performance.^{94,95}

To control the measurement and for the data acquisition the software *ReRa Tracer 2* from *ReRa Solutions* was used.

8.2.2. *J-V* Measurements

The key parameters short-circuit current density (J_{sc}) and open-circuit voltage (V_{oc}) are determined by a *J-V* measurement. To record the *J-V* curve, first of all, the light source is switched on. After a period of 30 minutes a constant light intensity has been reached. In the meantime, the reference cell is placed on the sample table. Before the measurement of the DSC, the light intensity is regulated to 1000 mW cm^{-2} by modulating the height of the sample table and control the light intensity with the help of the reference cell. The DSC is then placed on the sample table for at least 20 minutes before measurement. The working and the counter electrodes are connected to the potentiostat and the DSC is fully masked as described above. A voltage range is applied to the irradiated DSC and the corresponding current output is measured. With this data, an I-V curve is plotted (Fig. 28). The connection between current density (J) and the current (I) is described by Equation 2.

$$J = \frac{I}{\text{irradiated active area}}$$

Equation 2 Conversion of the current I to the current density J .

Solar cell measurements are displayed in J - V curves due to the better comparability of the data, because the irradiated active area is taken into account.

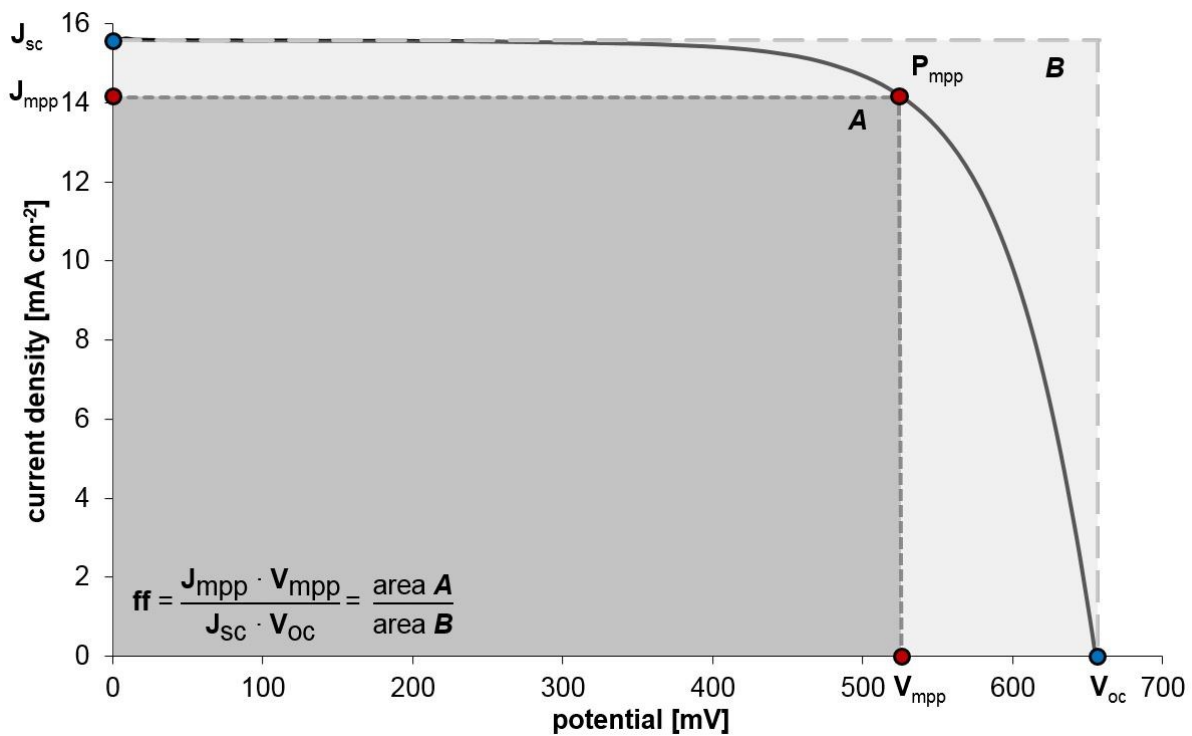


Fig. 28 J - V curve experiment with key parameters (J_{sc} : short-circuit current density; J_{mpp} : maximum-power-point current density; V_{oc} : open-circuit voltage; V_{mpp} : maximum-power-point voltage; P_{mpp} : maximum power point; ff : fill factor).

Based on the J - V curve, several key parameters of a solar cell can be obtained. The first parameter is J_{sc} . This is the interception of the J - V curve with the current density-axis. This is the highest obtainable current generated by the DSC. The next parameter is V_{oc} . It can be determined by the interception with the voltage-axis. Here, no current flux is measurable. The third key parameter is the fill factor (ff). It is essentially a measure of the quality of the cell. To calculate

the ff , the maximum power point has to be determined. Since the power is determined by Equation 3, the maximum power point can be calculated with the I-V data.

$$P = I \cdot V$$

Equation 3 Definition of the power P.

The corresponding current- and voltage values are the maximum-power point current (I_{mpp}) or the corresponding current density (J_{mpp}) and the maximum-power point voltage (V_{mpp}). The graphical expression of the ff is the ratio of the area of the dark-grey rectangular A defined by J_{mpp} and V_{mpp} to the area of the light-grey rectangular B defined by J_{sc} and V_{oc} (Fig. 28). The value is given in percentages from 0 to 100%. Subsequently, the value of ff can be calculated by Equation 4.

$$ff = \frac{J_{mpp} \cdot V_{mpp}}{J_{sc} \cdot V_{oc}}$$

Equation 4 Definition of the fill factor ff .

With the key parameters J_{sc} , V_{oc} and ff and the power density of the incident light (P_{in}) one can finally calculate η with Equation 5.

$$\eta = \frac{P_{out}}{P_{in}} = \frac{J_{sc} \cdot V_{oc} \cdot ff}{P_{in}}$$

Equation 5 Definition of the overall efficiency η .

Considering Equation 5, one can conclude that high efficiencies are obtained from cells that give high J_{sc} , V_{oc} and ff values. A relative efficiency compared to the standard dye **N719** was introduced in literature because no identical measurement conditions are given for all published investigations.

Stability tests were done with DSCs that are stored in the dark.

8.3. External Quantum Efficiency

The external quantum efficiency measurement investigates the performance of a DSC at a specific wavelength and determines the most efficient wavelength range.

8.3.1. Instrumental Details

A *Spe-Quest quantum efficiency setup* EQE system from *ReRa Solutions* was used for external quantum efficiency measurement. The system consists of a 100 W halogen light source that is coupled with an *Omni-lambda 300* grating monochromator from *Lot Oriel* in order to generate monochromatic light (Fig. 29). The light beam is then carried through an optical chopper from *ThorLabs* to modulate the frequency of irradiation to 3 Hz. In the end, the frequency modulated light hits the unmasked DSC that is irradiated by a bias light consisting of standard white LEDs. The response of the DSC was amplified with a large dynamic range IV converter from *CVI Melles Griot* and afterwards measured with a *SR830 DSP Lock-In amplifier* from *Stanford Research*.

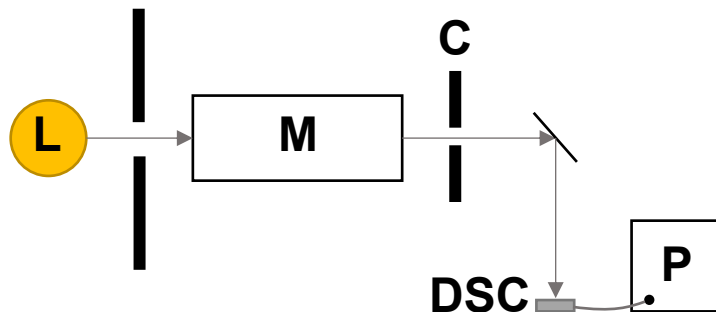


Fig. 29 Schematic representation of an external quantum efficiency system (L = light source; M = monochromator; C = chopper; DSC = dye-sensitized solar cell; P = potentiostat).

The measurement was controlled by the *Photor3* software from *ReRa Solutions*.

8.3.2. EQE Measurements

EQE measurements are the second important measurement type performed to investigate the performance of a DSC. The EQE curve displays how many percent of the incoming photons is converted to electrical power (Fig. 30). It can be described by the number of electrons that are generated by a specific number of incident photons as a function of wavelength (Equation 6).

$$EQE(\lambda) = \frac{\text{number of electrons}}{\text{number of photons}}$$

Equation 6 The ratio of number of generated electrons to the number of incident photons as a function of the wavelength gives EQE.

After the instrument has been calibrated with a reference cell, the DSC can be measured. Therefore, it is connected to the potentiostat and bias light is applied and the measurement is made under short-circuit working conditions. Afterwards, frequency regulated monochromatic light is shone on the cell and the EQE curve is recorded.

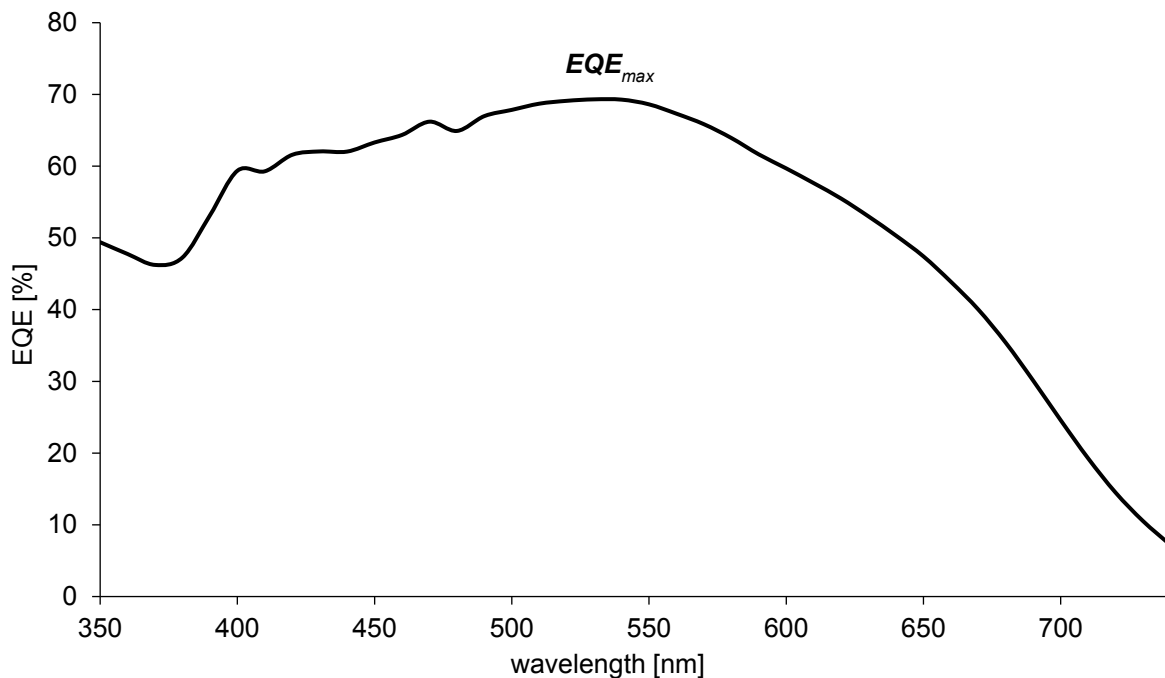


Fig. 30 EQE curve experiment with key parameter (EQE_{max} : maximum external quantum efficiency).

The maximum of the EQE curve is determined with the maximum percentage and the corresponding wavelength. The curve gives also information about the wavelength range the DSC is working. A well performing DSC shows a high curve over a wide wavelength range.

From the EQE curve one can also calculate the I_{sc} by integration over the whole spectrum (Equation 7).

$$I_{sc} = \int_0^{\infty} \text{EQE}(\lambda) \cdot I_{\text{sun}}(\lambda) d\lambda$$

Equation 7 Calculation of I_{sc} via integration over the wavelength range of the whole EQE spectrum.

8.4. Electrical Impedance Spectroscopy

With the help of electrical impedance spectroscopy (EIS), electrochemical processes within the DSC can be investigated and additional parameters can be extracted.

Starting with the foundations of Oliver Heaviside at the end of the 19th century, electrochemical impedance spectroscopy has become a remarkable tool in the last 40 years to investigate the mechanisms of electrochemical reactions, measuring dielectric and transport properties of materials and exploring the properties of porous electrodes.¹¹⁴ Besides the study of biosensors, complex reaction mechanisms, corrosion reactions, surface changes, semiconductor materials, batteries and fuels¹¹⁵, EIS plays an important role in the investigations of physical processes within DSCs.¹¹⁶⁻¹¹⁸ For instance, key parameters like recombination resistance (R_{rec}), transport resistance (R_{tr}) and chemical capacitance (C_{μ}) can be extracted to name a few.

8.4.1. Instrumental Details

The impedance measurements have been carried out on a *ModuLab XM PhotoEchem* photoelectrochemical measurement system from *Solartron Analytical*. The DSC is mounted on an optical bench where a laser beam with a wavelength of 590 nm is focused on the working electrode. The light source is modulated by a *DC2100* controller from *ThorLabs* (Fig. 31). In this way, measurements at different light intensities can be performed

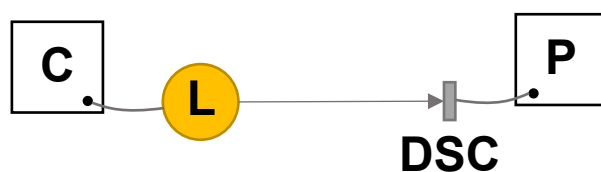


Fig. 31 Schematic representation of an electrochemical impedance spectroscopy system (C = light controller; L = light source; DSC = dye-sensitized solar cell; P = potentiostat).

The DSC is connected to a potentiostat with a frequency response analyser.

The measurement setup was controlled by the *xm studio photochem* software from *Solartron analytical* and the EIS data was analysed by the *ZView* software from *Scribner Associates Inc.*

8.4.2. EIS Measurements

The measurements may be performed with an adjustable light source in order to measure at different illumination intensities and a potentiostat to apply a small AC current of varied frequency. The impedance was measured in the frequency range of 0.05 Hz to 400 kHz using an amplitude of 10 mV. While measuring at open-circuit voltage (V_{oc}), the resulting impedance response depending on the light intensity and the applied frequency is recorded. The data is usually represented in a Nyquist plot (Fig. 32).

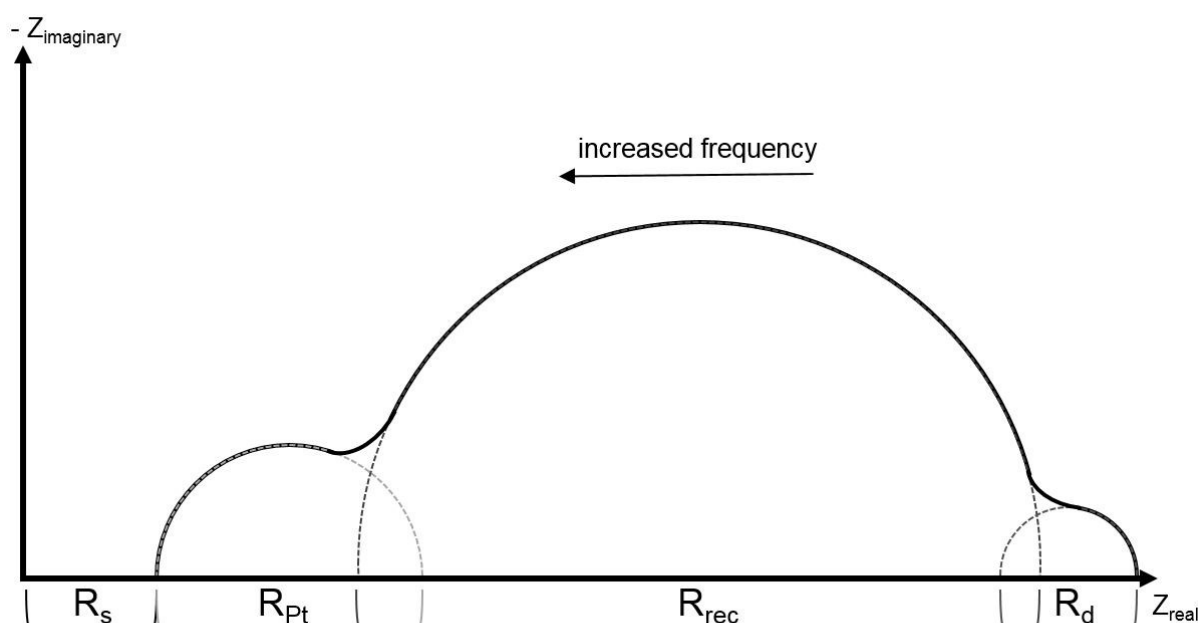


Fig. 32 A schematic diagram of a Nyquist plot of a well-functioning DSC at high light intensity showing overlapping semi-circles which have been extrapolated for clarity.

Ideally, three separate semi-circles should be observed in this plot. Each semi-circle corresponds to the impedance of a specific interfacial charge transfer process which takes place at a given frequency. Starting at the origin of the Nyquist plot, the distance from zero to the start of the first semi-circle describes the series resistance (R_s) within the whole measurement. It arises mainly from the charge resistance of the TiO_2/FTO interface.¹¹⁹ The first semi-circle displays the cathode/electrolyte charge transfer resistance (R_{pt}), the second one the recombination resistance of the active layer/electrolyte interface (R_{rec}) and the third semi-circle corresponds to the diffusion

resistance of the charge carriers within the electrolyte (R_d). The semi-circle of R_d may or may not be seen depending on how large it is and on the magnitude of R_{rec} which may lead to overlapping of the two semi-circles.¹⁰²

After measuring the EIS spectra of the solar cells, a model of the measured system has to be developed. This model is used to verify that the measured data can be fitted to the model. Subsequently, the key parameters mentioned before can be extracted. In order to extract these parameters from the measurement, two different equivalent circuit models were used for the different applied light intensities.

Fig. 33 displays a standard equivalent circuit used for fitting the measured DSCs at a light intensity of 2.2 mW cm^{-2} . In this case, the fitting model consists of five elements. First, a series resistance (R_s) was introduced to model the series resistance of the whole measurement. An extended distributed element (DX) was used for fitting of the active layer/electrolyte interface according to the transition line model.¹²⁰ With this extended distributed element it is possible to take R_r into account. A Warburg diffusion element (W_s) has been introduced to model the diffusion impedance of the charge carrier through the electrolyte close to the photoactive semiconductor surface. The circuit containing a series resistance (R_{Pt}) and a constant phase element (CPEPt) models the Pt counter electrode. The constant phase element was used instead of a capacitor because of the high porosity of interfaces, while a conventional capacitor describes the capacitance over a completely smooth surface.¹²¹

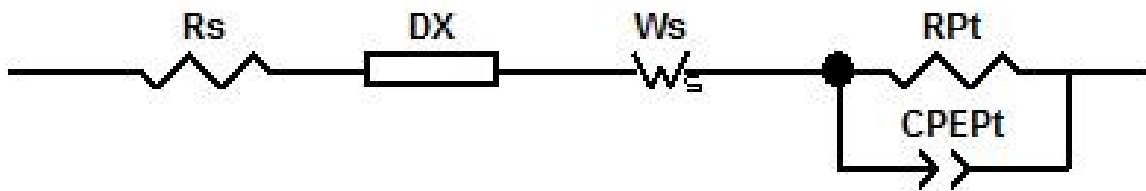


Fig. 33 Fitting model for EIS measurements at a light intensity of 2.2 mW cm^{-2} .

Because of the lower R_r a model with two Randles-type circuits were used for EIS measurements at 22 mW cm^{-2} light intensity (Fig. 34).

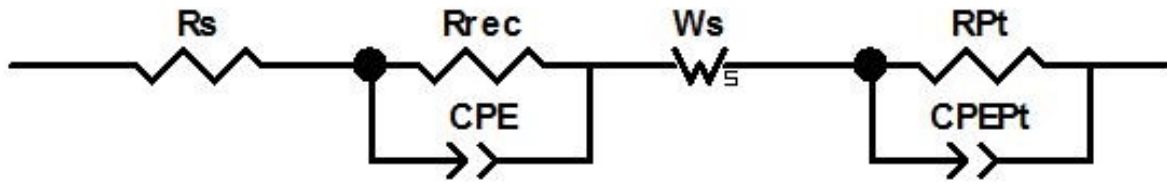


Fig. 34 Fitting model for EIS measurements at a light intensity of 22 mW cm⁻².

The equivalent circuit used for fitting the measured DSCs is displayed in Fig. 34. The fitting model consists of the series of two Randles-type circuits, a Warburg resistance (Ws) and a further series resistance (Rs). The Warburg diffusion element has been introduced to model the diffusion of the charge carrier through the electrolyte. Each circuit characterizes one electrode interface. The first circuit models the TiO₂/dye/electrolyte interface and the second one the electrolyte/Pt/FTO interface.

With the extracted values of the EIS parameters more information can be obtained. When a constant phase element is used in the equivalent circuit the capacitance has to be corrected (Equation 8).

$$C_{\text{corr}} = (R_{\text{rec}}^{1-n} \cdot C)^{\frac{1}{n}}$$

Equation 8 Calculation of the corrected capacitance when a constant phase element is used (n is the constant phase element factor).¹²²

With the corrected capacitance and the recombination resistance the lifetime τ of an electron in the semiconductor can be calculated (Equation 9). The longer the lifetime the higher the chance that the electron surpasses the semiconductor and reaches the back to reach the external circuit.

$$\tau = R_{\text{rec}} \cdot C_{\text{corr}}$$

Equation 9 Calculation of the lifetime τ of an electron in the semiconductor.¹²³

The length of diffusion L_D of an electron in the semiconductor can be calculated with the help of the ratio of the recombination resistance and the transport resistance (Equation 10). The length of diffusion L_D should be longer than the thickness of the semiconductor L .

$$L_D = L \sqrt{\frac{R_{\text{rec}}}{R_{\text{tr}}}}$$

Equation 10 Calculation of the length of diffusion of an electron in the semiconductor (L is the thickness of the semiconductor).¹²⁰

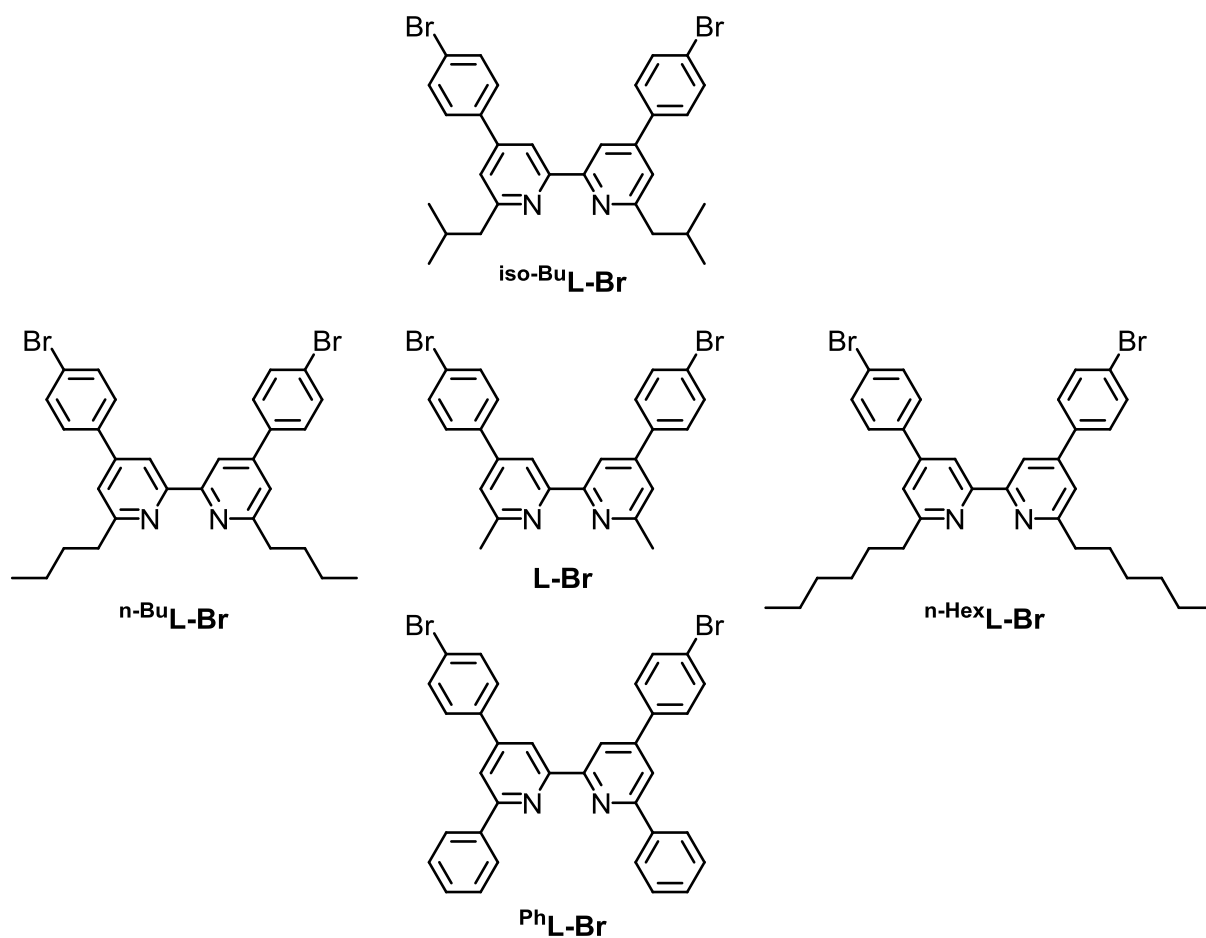
SYNTHETIC STRATEGY
AND
CHARACTERIZATION

9. Target molecules

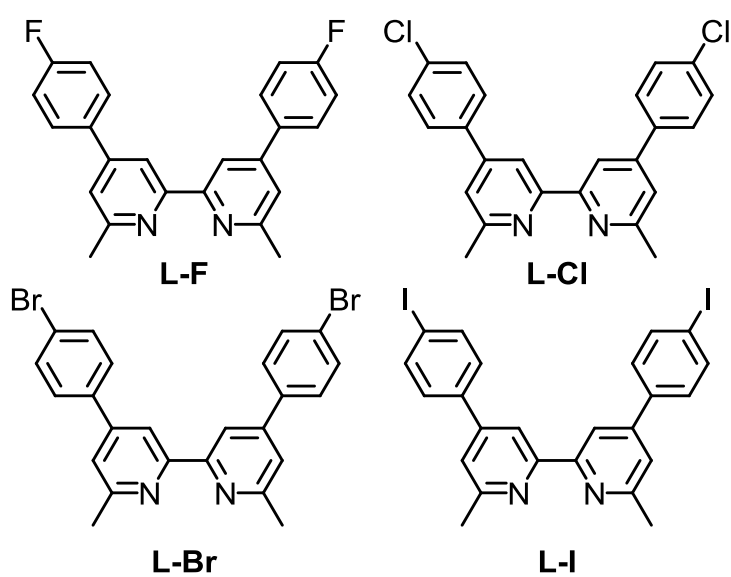
During the studies to optimize the performance of copper(I) dye-sensitized solar cells, several series of ligands were synthesized. Starting with 2,2'-bipyridine (bpy) based ligands, the influence of different substituents in the 4,4'- and 6,6'-positions of the bpy-core was investigated. The corresponding target molecules are summarized in Section 9.1. New heterocyclic $N^{\wedge}N^{\times}$ ligands have been developed and the influence of different heteroatoms was investigated. Based on these investigations, further structural modifications to the ligands were made. The corresponding target molecules of this new family of ancillary ligand are detailed in Section 9.2.

9.1. 2,2'-Bipyridine-Based Ligands

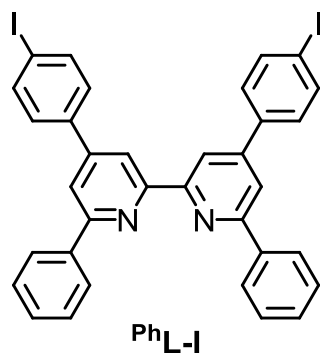
The 2,2'-bipyridine-based ancillary ligands with different steric groups in the 6,6'-positions investigated during the Master studies are displayed in Scheme 11. Ancillary ligands with peripheral halo-substituents in the 4,4'-positions investigated during the Master studies are shown in Scheme 12. The combination of the best performing steric group and peripheral halo-substituent is the first ligand investigated in the PhD studies (Scheme 13). Ligands with different functional groups in the 4,4'-positions of the bpy-core were synthesized and summarized in Scheme 14. The anchoring ligand **ALP1** is bpy-based and displayed in Scheme 15.



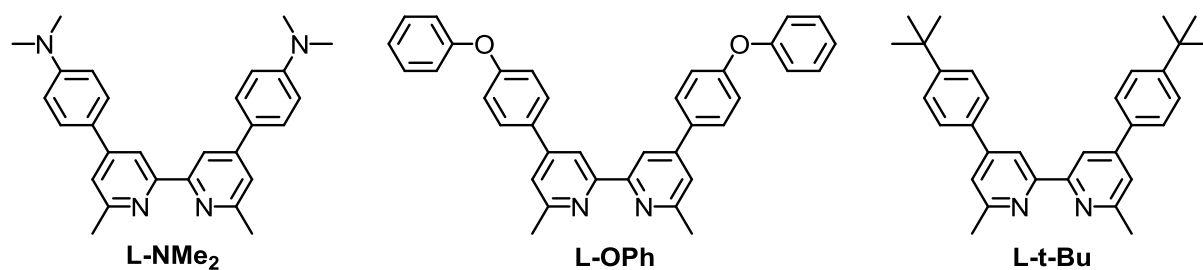
Scheme 11 Ligands with 6,6'-substituents of different steric properties: R^1L-Br .



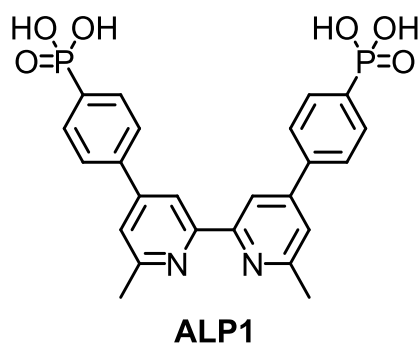
Scheme 12 Ligands with peripheral halo-substituents: $L-X$.



Scheme 13 Ligand with phenyl groups in the 6,6'-positions and iodine as peripheral halo-substituent: **PhL-I**.



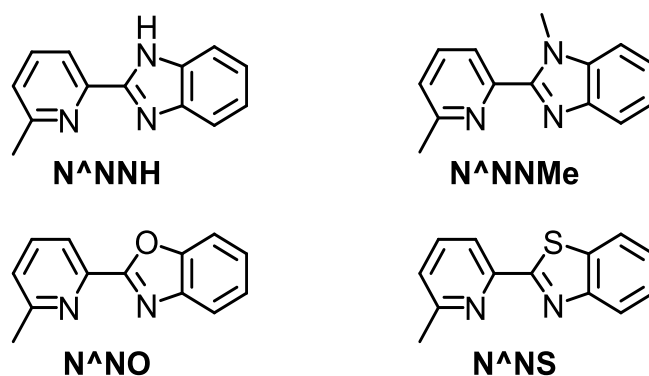
Scheme 14 Ligands with different functional groups in the 4,4'-positions: **L-X**.



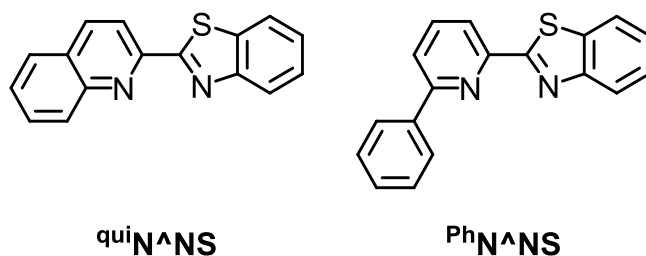
Scheme 15 Anchoring ligand with a phenyl spacer and phosphonic acid anchoring group: **ALP1**.

9.2. Heterocyclic N[^]NX Ancillary Ligands

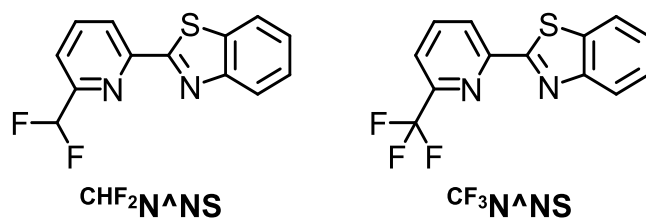
The new generation of heterocyclic N[^]NX ancillary ligands is displayed in Scheme 16. The structural functionalisations of the N[^]NS ligand with extended π -systems (Scheme 17), fluorine-containing substituents (Scheme 18) and different functional groups in the benzothiazole domain (Scheme 19) were synthesized.



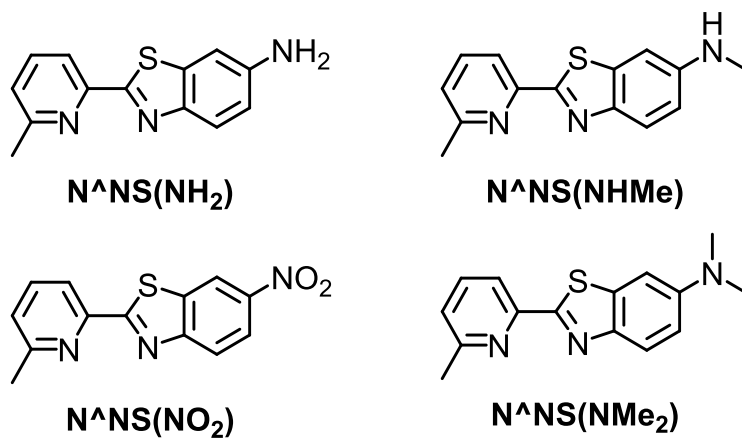
Scheme 16 Ligands containing different heterocyclic units: N[^]NX.



Scheme 17 Ligands with extended π -systems: R^{N^}NS.



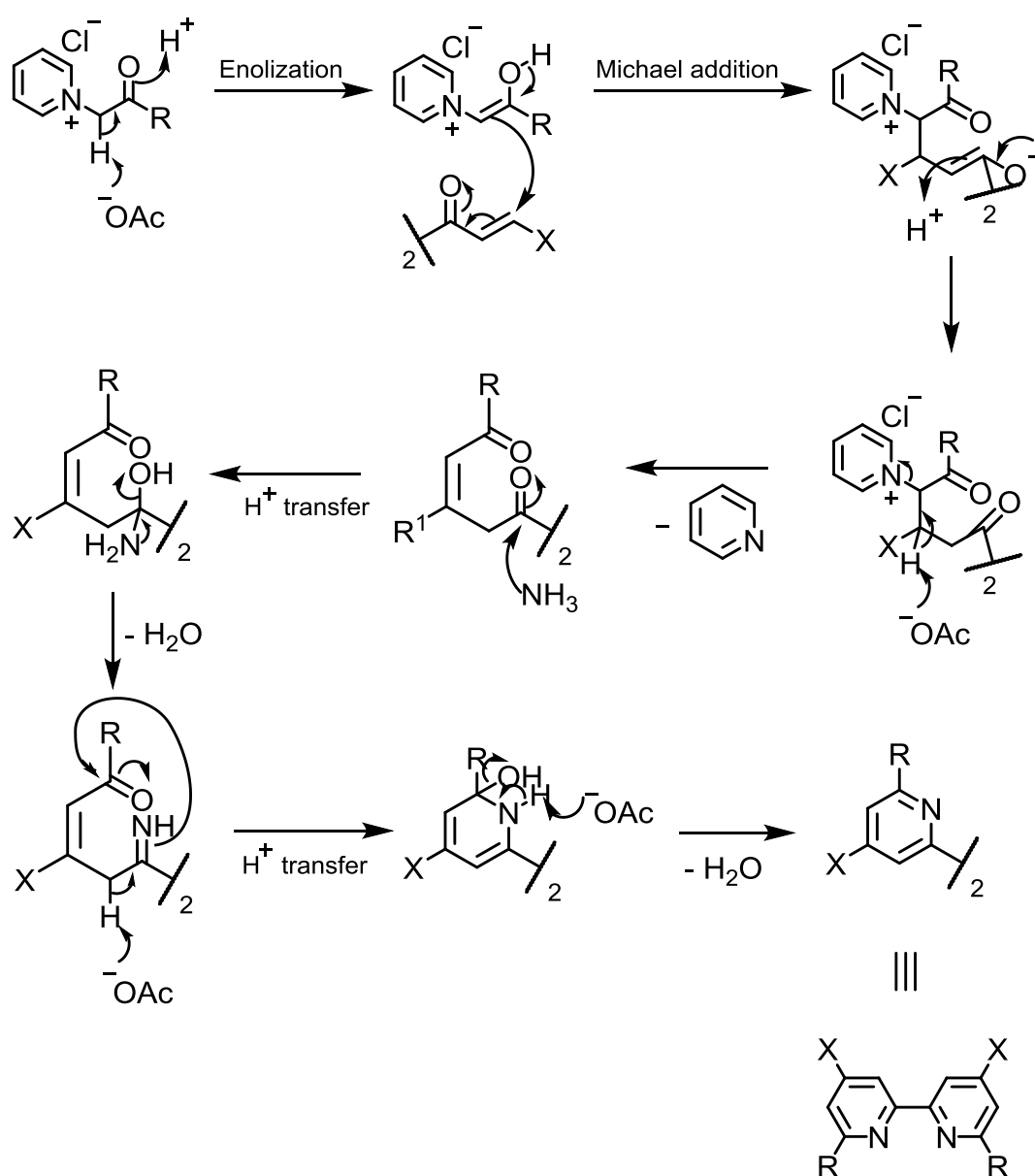
Scheme 18 Ligands with fluorine-containing substituents: CH_xF_yN[^]NS



Scheme 19 Ligands with different functional groups: N^{*}NS(X).

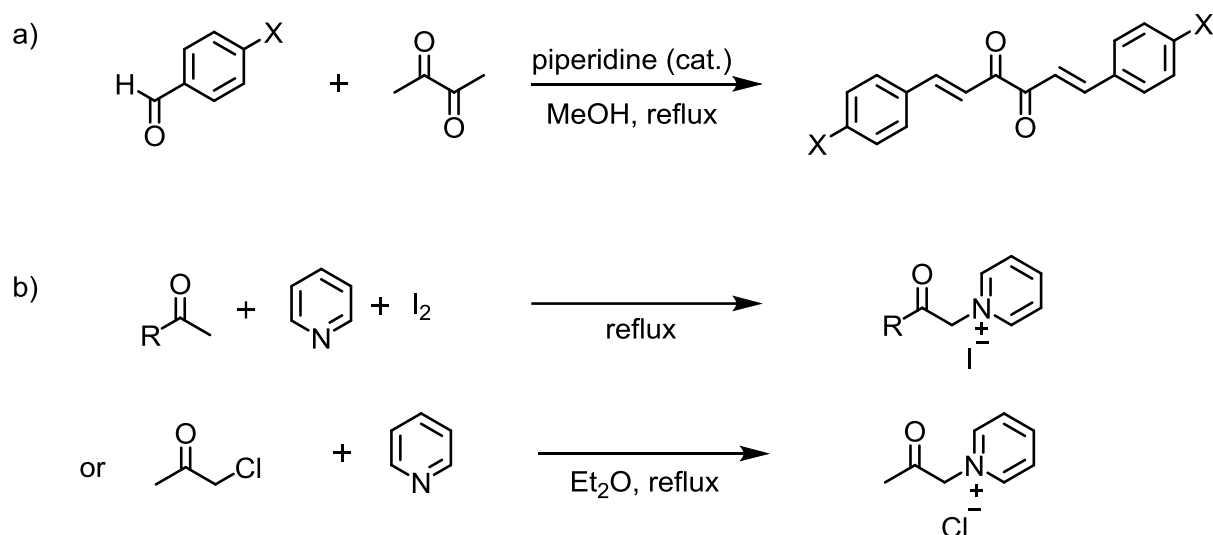
10. Synthetic Strategy

The first group of ancillary ligands is based on a 2,2'-bipyridine (bpy) core with different substituents in the 4,4'- and 6,6'-positions. Fritz Kröhnke developed a method in 1976 to synthesize 2,4,6-trisubstituted pyridines.¹²⁴ But he also developed methods to synthesize bipyridines. One of the methods starts with a pyridinium salt that reacts with a doubly unsaturated ketone and ammonium acetate as the nitrogen source to give the corresponding bipyridine (Scheme 20).

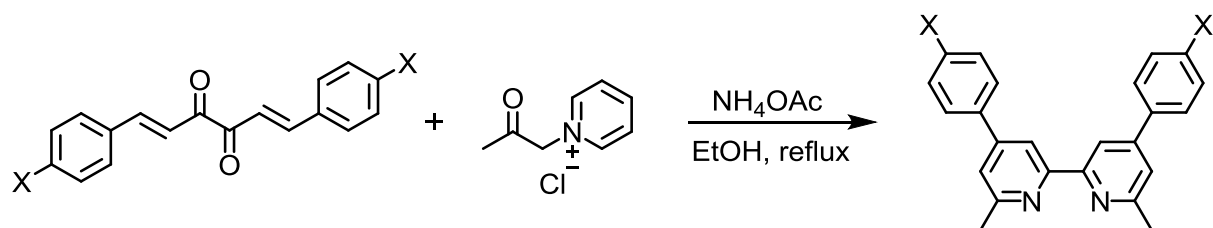


Scheme 20 General reaction mechanism of the Kröhnke pyridine synthesis.

The Kröhnke synthesis is one of the cheapest, easiest and most versatile methods to synthesize a bpy. It needs only two precursors that are synthesized in a one-step reaction (Scheme 21). The first precursor is a pyridinium salt that can be easily synthesized with pyridine and chloroacetone or a ketone and iodine. The design of the pyridinium salt accounts for the substituent in the 6,6'-positions of the bpy. The 4,4'-positions of the bpy can be tuned by the second precursor. A α,β -unsaturated diketone is synthesized by the reaction of 2,3-butanedione and a benzaldehyde with catalytic amounts of piperidine. Depending on the reaction partners yields of over 60% can be obtained for the last step of the bpy synthesis (Scheme 22).

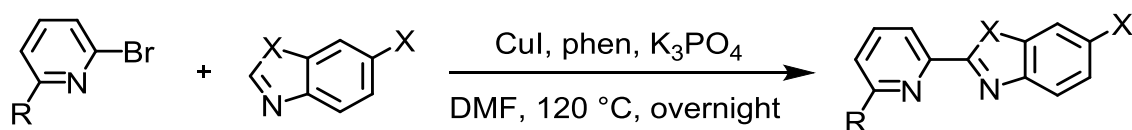


Scheme 21 General reaction conditions for the synthesis of a (a) diketone and a (b) Kröhnke salt for the Kröhnke pyridine synthesis.

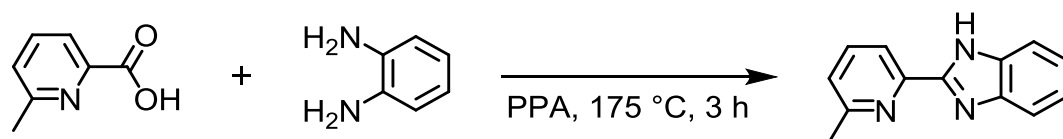


Scheme 22 General reaction conditions for the Kröhnke bipyridine synthesis with the example of methyl groups in the 6,6'-positions.

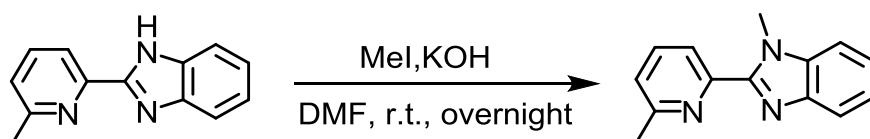
The new group of heterocyclic ancillary ligands was mainly synthesized by adaption of a literature reported Cu(I)-catalysed coupling reaction (Scheme 23).¹²⁵ Starting from a bromopyridine and a benzothiazole or benzooxazole the corresponding **N[^]NNX** ligand was synthesized. The **N[^]NNH** ligand was synthesized following a reported literature procedure¹²⁶ by condensation reaction of o-phenylenediamine and 6-methylpicolinic acid in polyphosphoric acid (PPA) (Scheme 24). The conversion of **N[^]NNH** to **N[^]NNMe** was done by a standard methylation reaction with MeI (Scheme 25).¹²⁷ The methylation reaction was also adapted for the synthesis of the benzothiazole precursors of **N[^]NS(NHMe)** and **N[^]NS(NMe₂)**. Therefore, benzothiazol-6-amine was methylated under basic conditions with MeI. The mono- and dimethylated amine were separated by column chromatography. The **N[^]NS(NH₂)** ligand was synthesized by reduction of the **N[^]NS(NO₂)** ligand with activated zinc and hydrazine adapting the literature procedure¹²⁸ (Scheme 26).



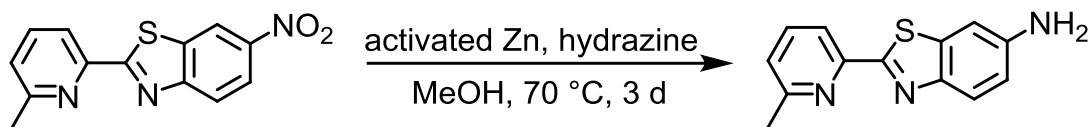
Scheme 23 General reaction conditions for the synthesis of **N[^]NNX** ligands.



Scheme 24 Reaction conditions for the synthesis of **N[^]NNH**.

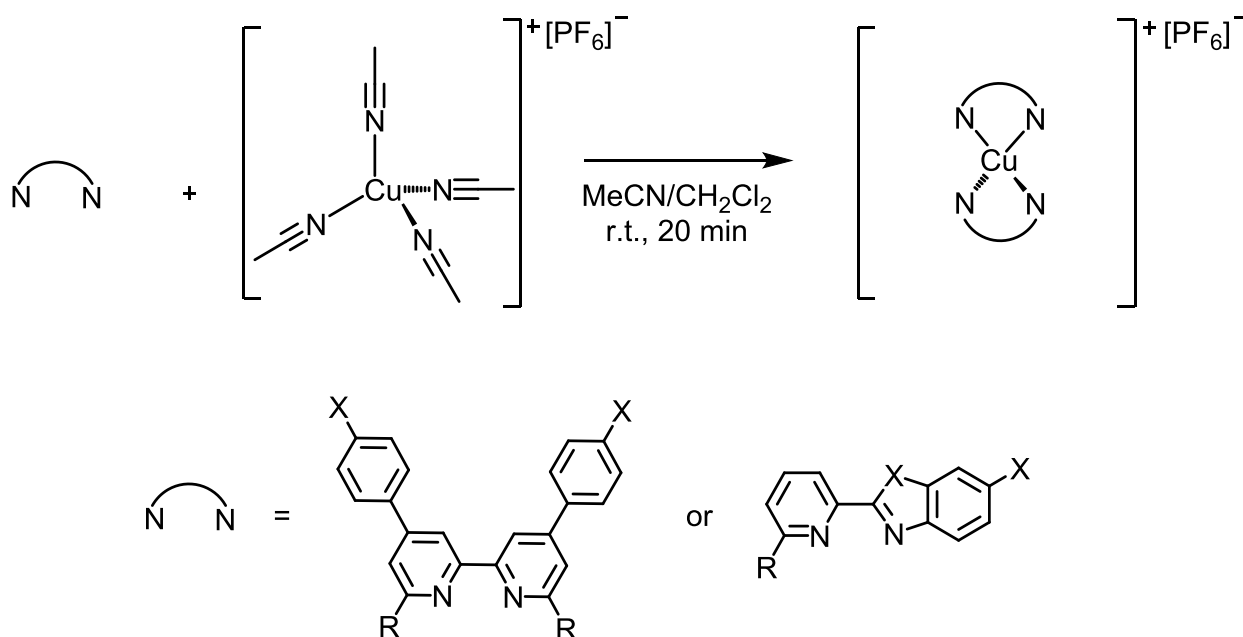


Scheme 25 Reaction conditions for the methylation of **N[^]NNH** to **N[^]NNMe**.



Scheme 26 Reaction conditions for the reduction of $N^{\wedge}NS(NO_2)$ to $N^{\wedge}NS(NH_2)$.

The synthesis of all the homoleptic Cu(I) complexes was done by complexation of the ligand with $[Cu(MeCN)_4][PF_6]$ (Scheme 27). Two equivalents of the ligand and one of $[Cu(MeCN)_4][PF_6]$ were used.



Scheme 27 General reaction conditions for the synthesis of the homoleptic Cu(I) complexes.

11. Characterization

11.1. NMR Spectroscopy

The ^1H and ^{13}C NMR spectra of ligands and homoleptic complexes were assigned using COSY, NOESY, HMQC and HMBC.

For the **L-I** ligand, the ^1H NMR resonances for protons $\text{H}^{\text{A}5}$ and $\text{H}^{\text{A}3}$ were distinguished by the appearance of a cross peak in the HMBC spectrum between signals for C^{a} and $\text{H}^{\text{A}5}$. Broadening of the signals for $\text{H}^{\text{A}3}$ and $\text{H}^{\text{A}5}$ is most likely associated with rotation of the 4-iodophenyl groups on the NMR timescale. The biggest influence of the halogen can be observed for the protons $\text{H}^{\text{B}2}$ and $\text{H}^{\text{B}3}$. Compared to the other halogen-containing ligands¹²⁹, $\text{H}^{\text{B}3}$ of **L-I** is the most low-field shifted and the only case where $\text{H}^{\text{B}3}$ is more low-field shifted than $\text{H}^{\text{B}2}$.

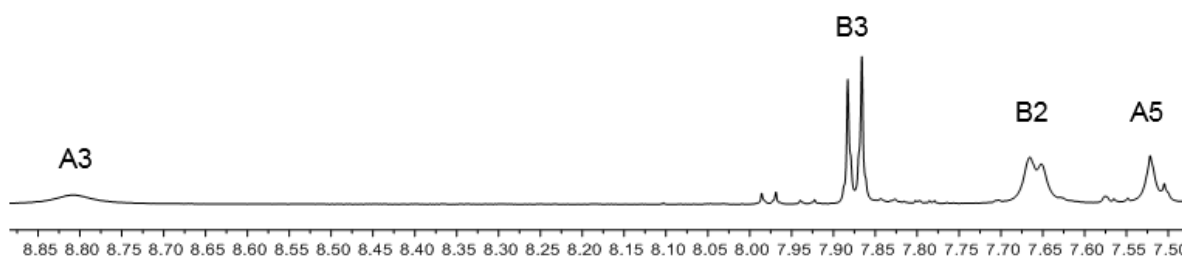
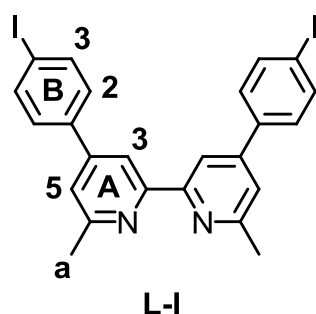
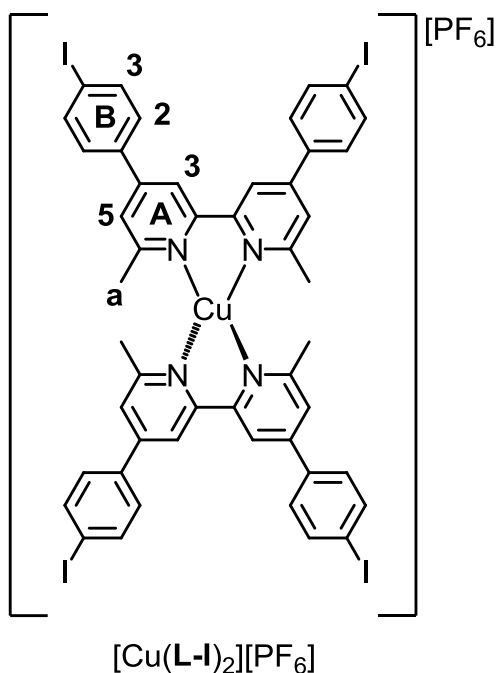


Fig. 35 400 MHz ^1H NMR spectrum of a CDCl_3 solution of ligand **L-I** (chemical shifts in δ/ppm).

The complexation of **L-I** with $[\text{Cu}(\text{MeCN})_4][\text{PF}_6]$ resulted in a mixture of two species. X-ray crystallographic data confirmed that $[\text{Cu}(\text{L-I})(\text{MeCN})_2][\text{PF}_6]$ was one of the species (see *11.5 Crystal Structures*). The second species was the desired homoleptic complex $[\text{Cu}(\text{L-I})_2][\text{PF}_6]$.



This can also be observed in the ^1H NMR spectrum. The spectrum in Fig. 36 was obtained at low-temperature (240 K). Variable temperature NMR spectroscopic experiments showed splitting of the broad signals observed at 298 K into two separate proton signals for each species. Only the signals for H^{A5} are overlapping. The black coloured peaks in Fig. 36 correspond to the homoleptic $[\text{Cu}(\text{L-I})_2][\text{PF}_6]$ complex and the blue coloured peaks to the heteroleptic Cu(I) complex with one L-I ligand and two coordinated MeCN ligands.

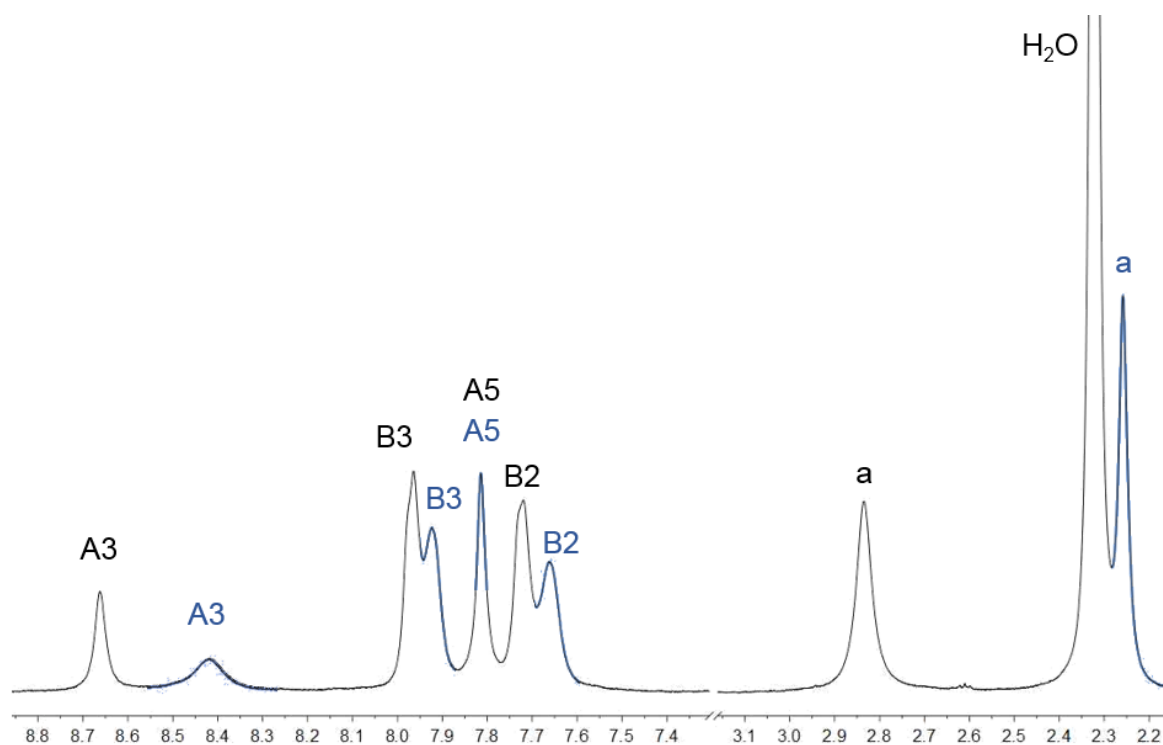
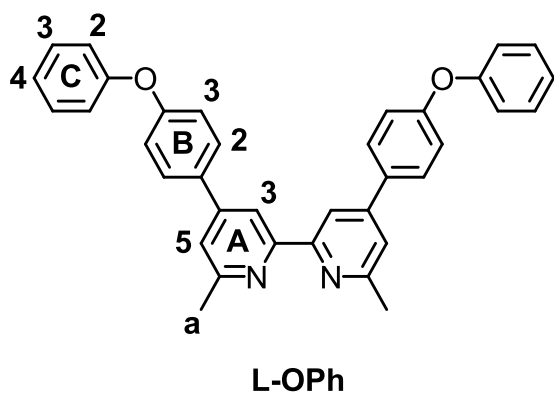


Fig. 36 Low-temperature ^1H NMR spectrum of the mixture of $[\text{Cu}(\text{L-I})_2][\text{PF}_6]$ (black) and $[\text{Cu}(\text{L-I})(\text{MeCN})_2][\text{PF}_6]$ (blue) at 240 K (chemical shifts in δ/ppm).

The ^1H NMR spectra of the L-X ligands with different functional groups are comparable to the other bpy-based ancillary ligands. The aromatic region of the ^1H NMR spectrum of L-t-Bu is



displayed in the bottom part of Fig. 37. Four aromatic signals for the protons H^{A3} , H^{B2} , H^{B3} and H^{A5} are observed. Two signals in the aliphatic region arise from the protons of the methyl and the *tert*-butyl group. The introduction of the phenoxy-group leads to additional aromatic signals in the 1H NMR spectrum (Fig. 37, top).

For the homoleptic copper(I) complexes of the R^1L-Br and $L-X$ ligands, the 1H and ^{13}C NMR spectra were consistent with the single ligand environment in each complex. The spectra were fully assigned using routine 2D methods. The 1H NMR spectrum of a CD_3CN solution of $[Cu(L-t-Bu)_2][PF_6]$ is shown in Fig. 38 as a representative spectrum. All aromatic peaks are shifted to lower field with respect to the 1H NMR spectrum of the ligand (Fig. 37, bottom). The signal of proton H^{A5} is affected the most. The methyl groups give rise to a sharp singlet.

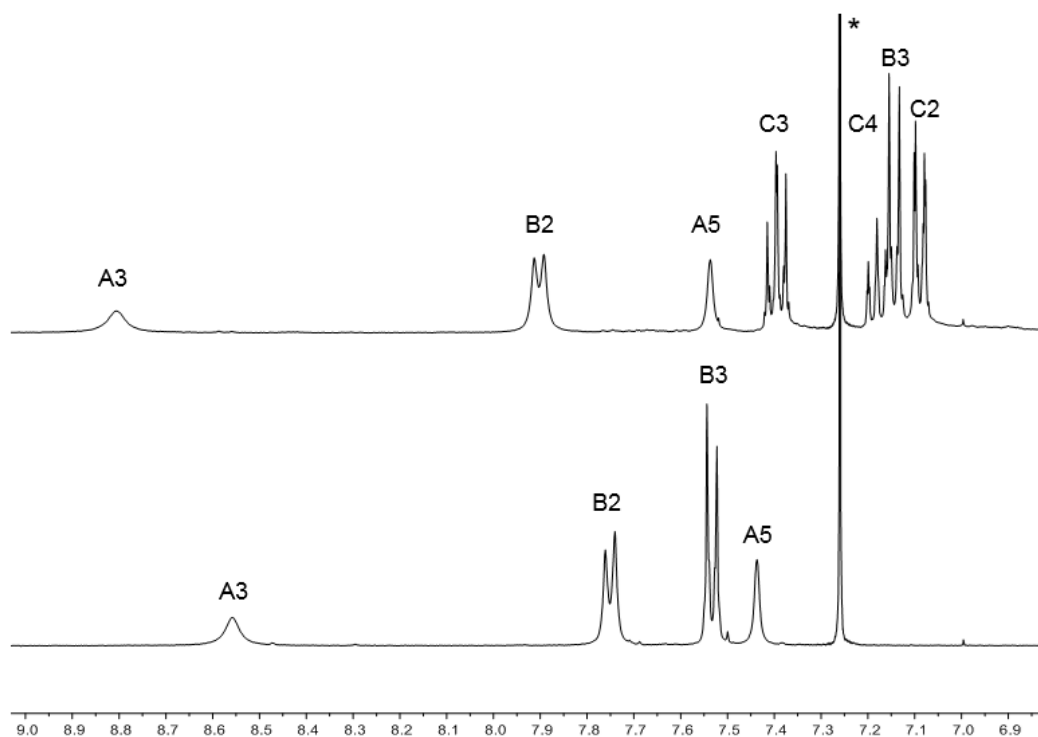


Fig. 37 400 MHz 1H NMR of $CDCl_3$ solution of ligands **L-OPh** (top) and **L-t-Bu** (bottom) (* = residual $CHCl_3$, chemical shifts in δ/ppm).

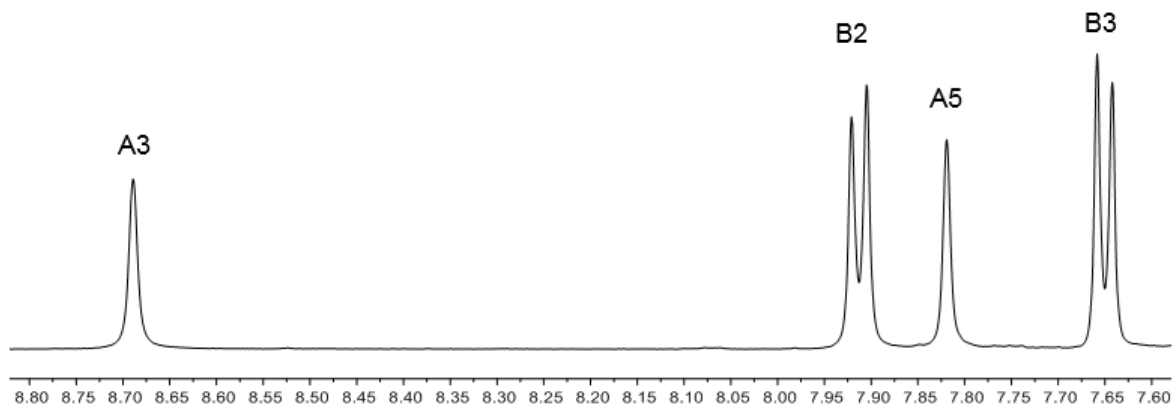
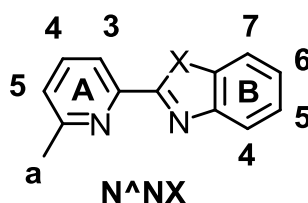


Fig. 38 500 MHz ^1H NMR of CD_3CN solution of $[\text{Cu}(\text{L-}t\text{-Bu})_2][\text{PF}_6]$ (chemical shifts in δ/ppm).

The 500 MHz ^1H NMR spectra of CDCl_3 solutions of the $\text{N}^{\wedge}\text{NX}$ ligands with $\text{X} = \text{NH}, \text{O}, \text{S}$ are published¹³⁰⁻¹³² and are displayed in Fig. 39. The influence of the heteroatom is mainly visible for the signals arising from protons in ring B. The peaks of the pyridine ring A are all within a shift range of 0.1 ppm for each individual proton. Going from $\text{N}^{\wedge}\text{NNH}$, $\text{N}^{\wedge}\text{NO}$ to $\text{N}^{\wedge}\text{NS}$ proton signals of $\text{H}^{\text{B}4}$, $\text{H}^{\text{B}5}$ and $\text{H}^{\text{B}6}$ are shifted low-field. Proton $\text{H}^{\text{B}7}$ is in *ortho*-position to the heteroatom and is only shifted for the ligand $\text{N}^{\wedge}\text{NS}$ with respect to $\text{N}^{\wedge}\text{NNH}$ and $\text{N}^{\wedge}\text{NO}$. An overlapping of the signals of protons $\text{H}^{\text{B}5}$ and $\text{H}^{\text{B}6}$ is not observed only for $\text{N}^{\wedge}\text{NS}$.



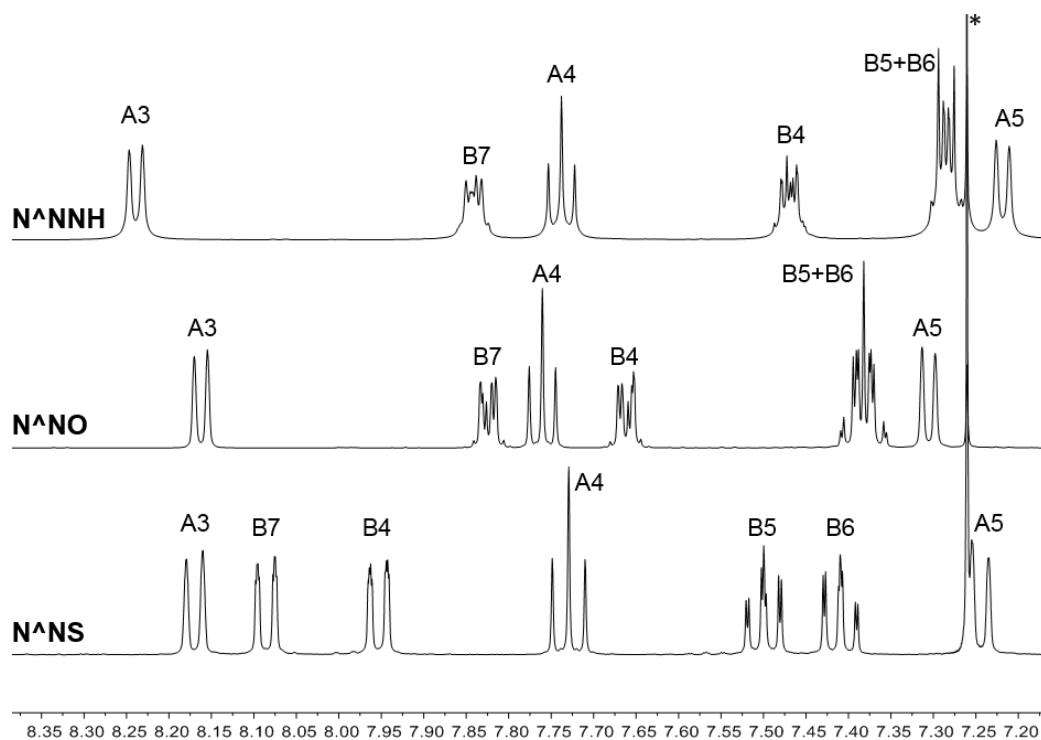
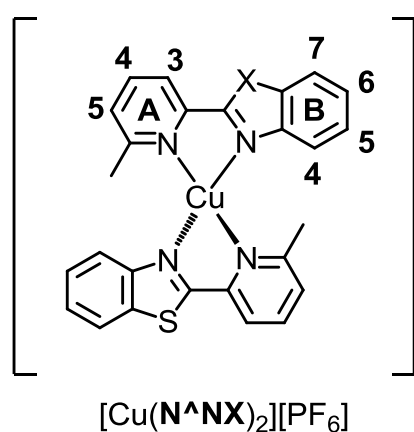


Fig. 39 500 MHz ^1H NMR spectra of CDCl_3 solutions of $\text{N}^{\text{A}}\text{NX}$ ligands with $\text{X} = \text{NH}$, O , S (* = residual CHCl_3 , chemical shifts in δ/ppm).

^1H and ^{13}C NMR spectra of CD_3CN solutions of the complexes were assigned using 2D methods



$[\text{PF}_6]$ (COSY, NOESY, HMQC and HMBC); for $[\text{Cu}(\text{N}^{\text{A}}\text{NNH})_2][\text{PF}_6]$, the correlations were made at 220 K (see below). The ^1H NMR spectra of $[\text{Cu}(\text{N}^{\text{A}}\text{NO})_2][\text{PF}_6]$ and $[\text{Cu}(\text{N}^{\text{A}}\text{NS})_2][\text{PF}_6]$ are shown in Fig. 40 and are well resolved at 295 K.

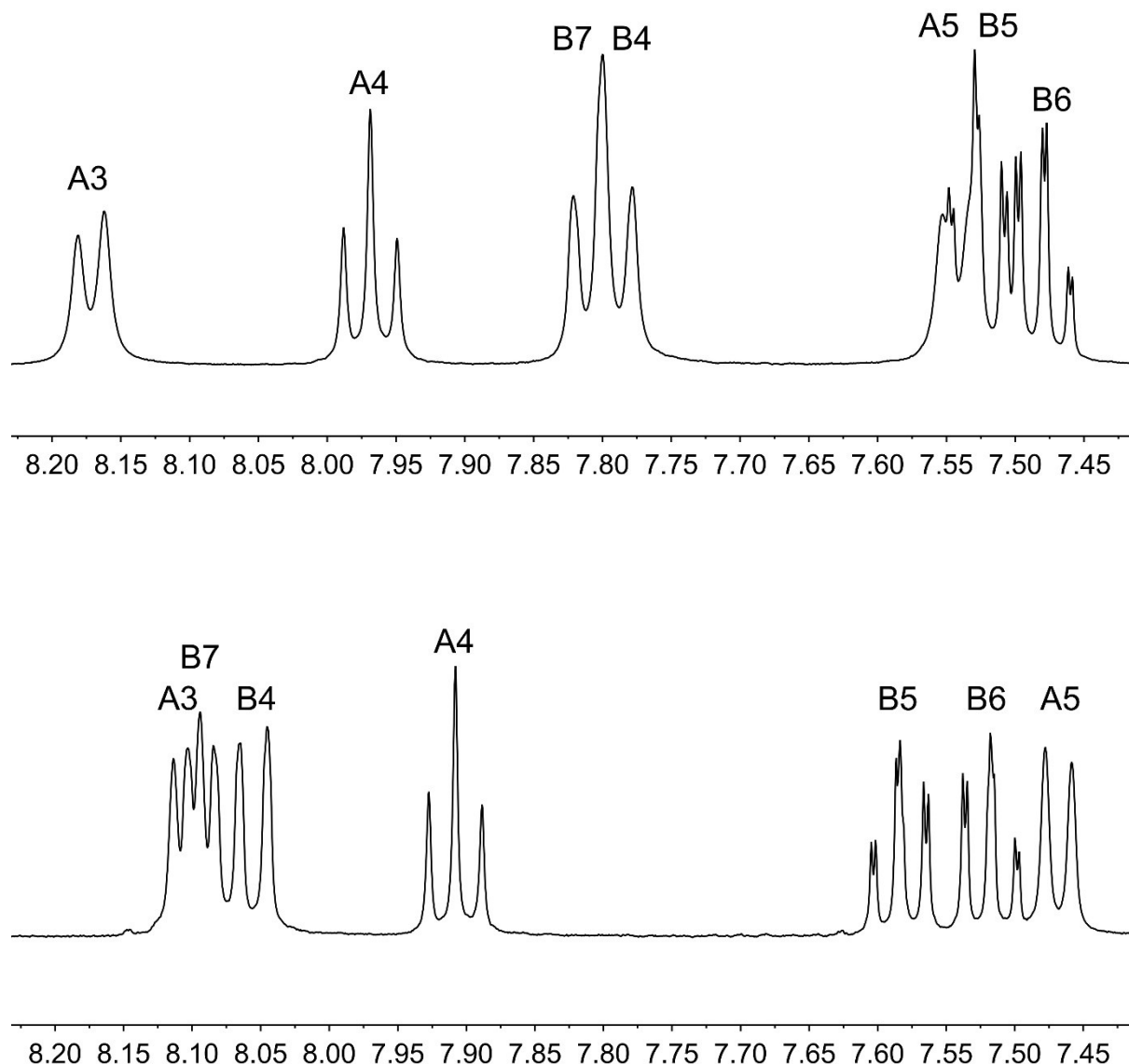


Fig. 40 Aromatic regions of the 500 MHz ¹H NMR spectra of [Cu(N^ANO)₂][PF₆] (top) and [Cu(N^ANS)₂][PF₆] (bottom) in CD₃CN at 295 K (chemical shifts in δ/ppm).

For [Cu(N^ANNH)₂][PF₆] which contains an imidazolyl NH, all the signals in the room temperature ¹H NMR spectrum (in CD₃CN or acetone-*d*₆) are broad; the NH group gives rise to a broad signal centred at δ 11.7 ppm. The signals sharpen upon cooling to 220 K (Fig. 41), and we propose that the temperature dependence of the spectrum arises from a dynamic process (on-off coordination) involving tautomers of the imidazole unit coupled with rotation about the C_{pyridine}-C_{imidazole} bond. The ¹H NMR spectra recorded below 245 K show evidence for a minor component (Fig. 41).

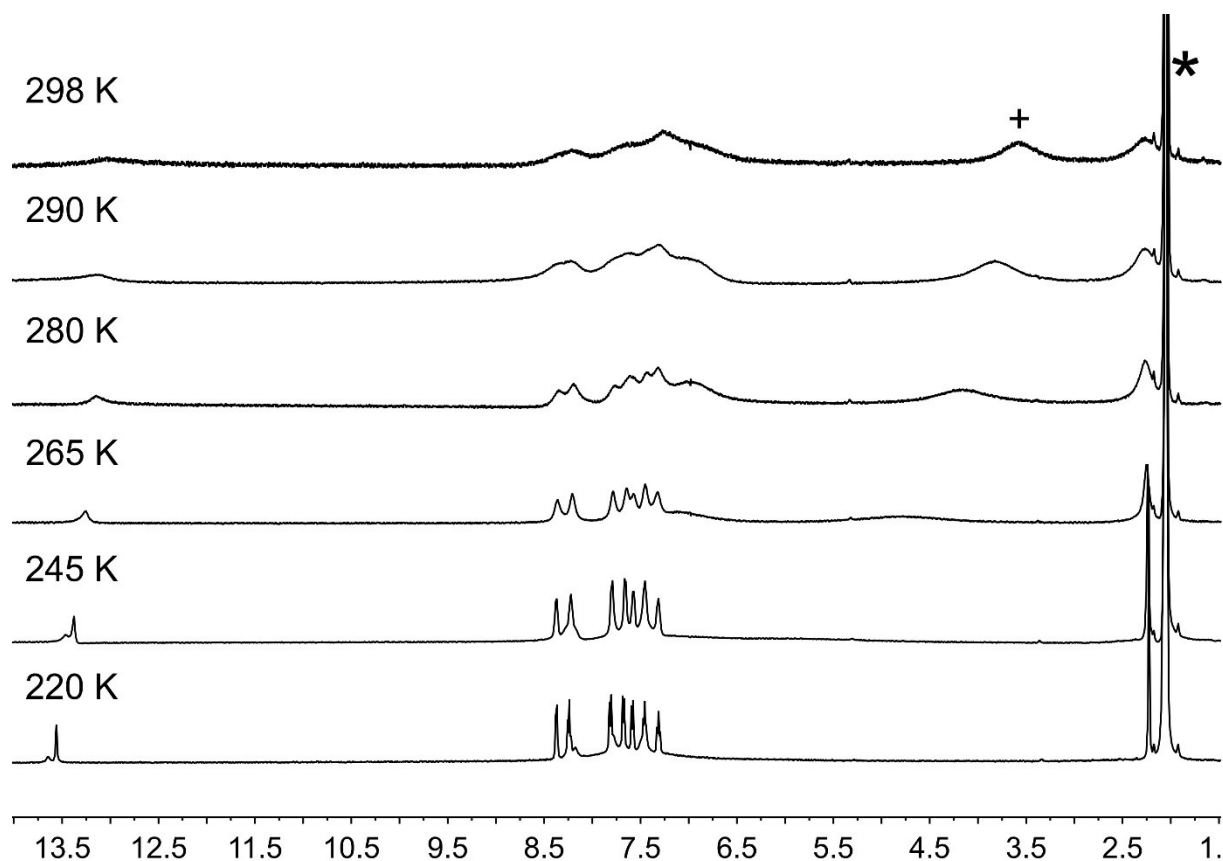


Fig. 41 Variable temperature 500 MHz ^1H NMR spectra of an acetone- d_6 solution of $[\text{Cu}(\text{N}^{\wedge}\text{N}^{\wedge}\text{NH})_2][\text{PF}_6]$. (* = residual CHCl_3 , + = water, chemical shifts in δ/ppm).

Fig. 42 shows a comparison of the spectra of acetone- d_6 solution of $[\text{Cu}(\text{N}^{\wedge}\text{N}^{\wedge}\text{NH})_2][\text{PF}_6]$ at 220 K and of $\text{N}^{\wedge}\text{N}^{\wedge}\text{NH}$ at 295 K. The coincidence between the broad signal at δ 8.18 ppm in Fig. 42a with the doublet at δ 8.20 ppm in Fig. 42b suggests that the subspectrum arises from dissociated ligand; the shift in the signal for the NH proton (Fig. 42a vs. b) probably indicating the differing hydrogen bonding environment. Replacing the NH by NMe on going from $[\text{Cu}(\text{N}^{\wedge}\text{N}^{\wedge}\text{NH})_2][\text{PF}_6]$ to $[\text{Cu}(\text{N}^{\wedge}\text{N}^{\wedge}\text{NMe})_2][\text{PF}_6]$ leads to a well resolved ^1H NMR spectrum at 295 K, and this supports the proposal that the dynamic behaviour in $[\text{Cu}(\text{N}^{\wedge}\text{N}^{\wedge}\text{NH})_2][\text{PF}_6]$ involves the imidazole NH group.

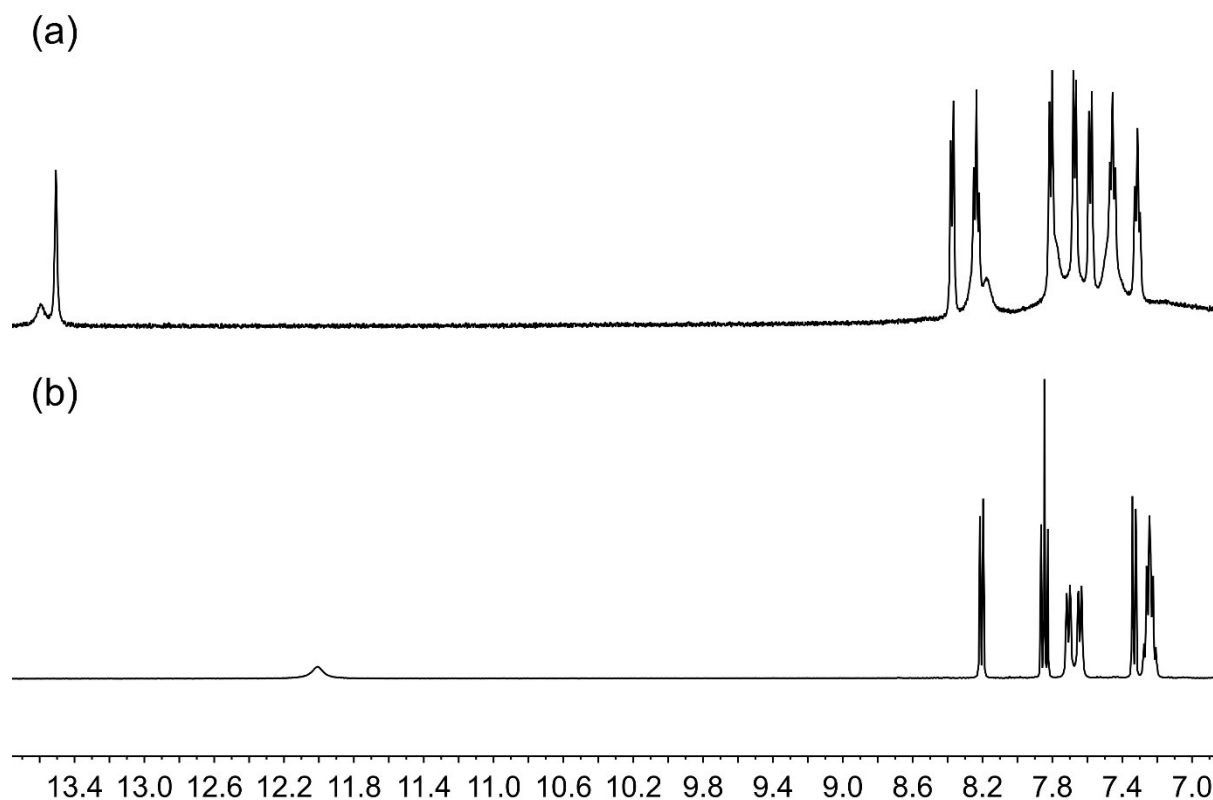
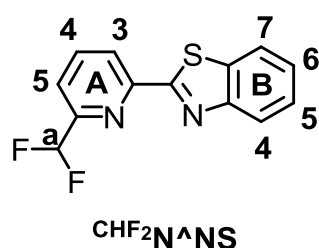


Fig. 42 Comparison of the aromatic regions of the 500 MHz ^1H NMR spectra of (a) $[\text{Cu}(\text{N}^{\text{ANNH}})_2][\text{PF}_6]$ at 220 K and (b) N^{ANNH} at 295 K, both in acetone- d_6 (chemical shifts in δ/ppm).

A new family of ancillary ligands was prepared in which functional groups were introduced into either the pyridine-ring or the benzothiazole domain. The ^1H and ^{13}C NMR spectra of the N^{ANS}



ligands were assigned using COSY, NOESY, HMQC and HMBC methods. Fig. 43 shows the 500 MHz ^1H NMR spectrum of a CDCl_3 solution of the ligand $\text{CHF}_2\text{N}^{\text{ANS}}$. The chemical shifts of ring B are comparable to those of the N^{ANS} ligand (Fig. 39). Due to the influence of the CHF_2 group, all peaks of ring A are shifted to

low-field. This is especially noticeable for proton H^{A5} which is next the CHF_2 group. The triplet at δ 6.73 ppm is assigned to the proton of the CHF_2 group which couples to the NMR active ^{19}F with a spin of $\frac{1}{2}$. ($J_{\text{HF}} = 55.2$ Hz).

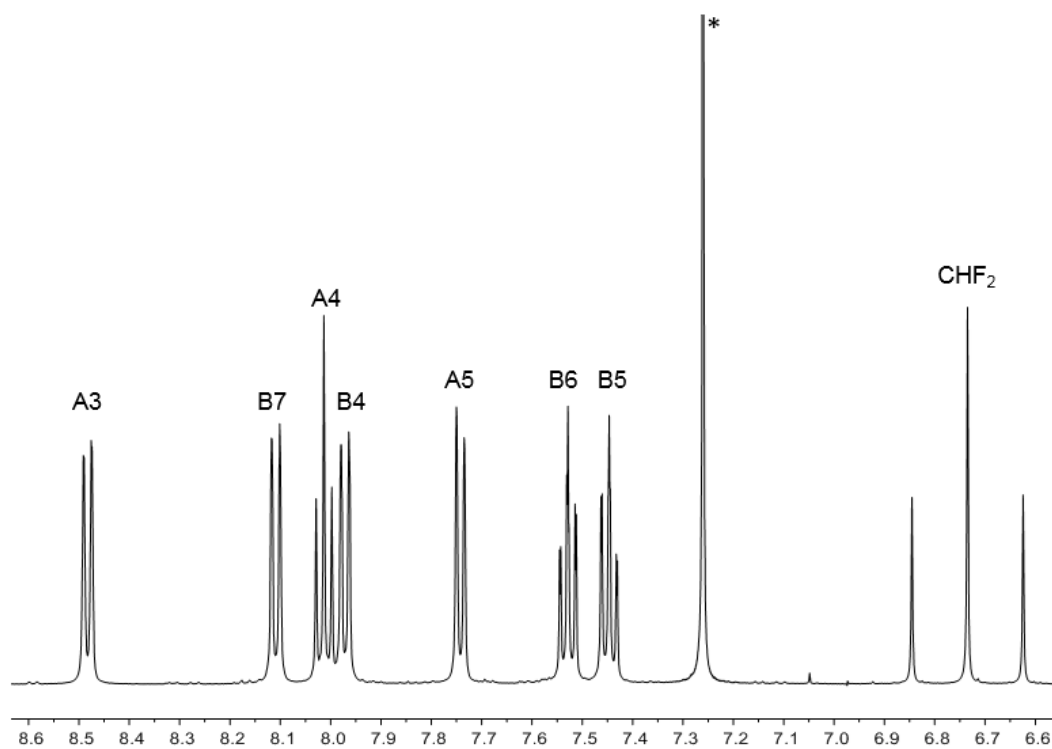


Fig. 43 500 MHz ^1H NMR spectrum of CDCl_3 solutions of $\text{CHF}_2\text{N}^+\text{NS}$ (* = residual CHCl_3 , chemical shifts in δ/ppm).

11.2. UV-Vis Spectroscopy

The solution electronic absorption spectra of homoleptic $[\text{Cu}(\text{R}\text{L-Br})_2][\text{PF}_6]$ complexes with $\text{R} = \text{Me}, n\text{-Bu}, \text{iso-Bu}, n\text{-Hex}, \text{Ph}$ have previously shown¹³³ that the absorption range of the complex containing the phenyl substituents is broader than with the other substituents (Fig. 44). Two broad absorption bands in the visible region of the spectrum and a red-shift of the MLCT band to 573 nm are observed. The spectrum of $[\text{Cu}(\text{Ph}\text{L-Br})_2][\text{PF}_6]$ also displays an enhanced spectral response in the higher energy bands.

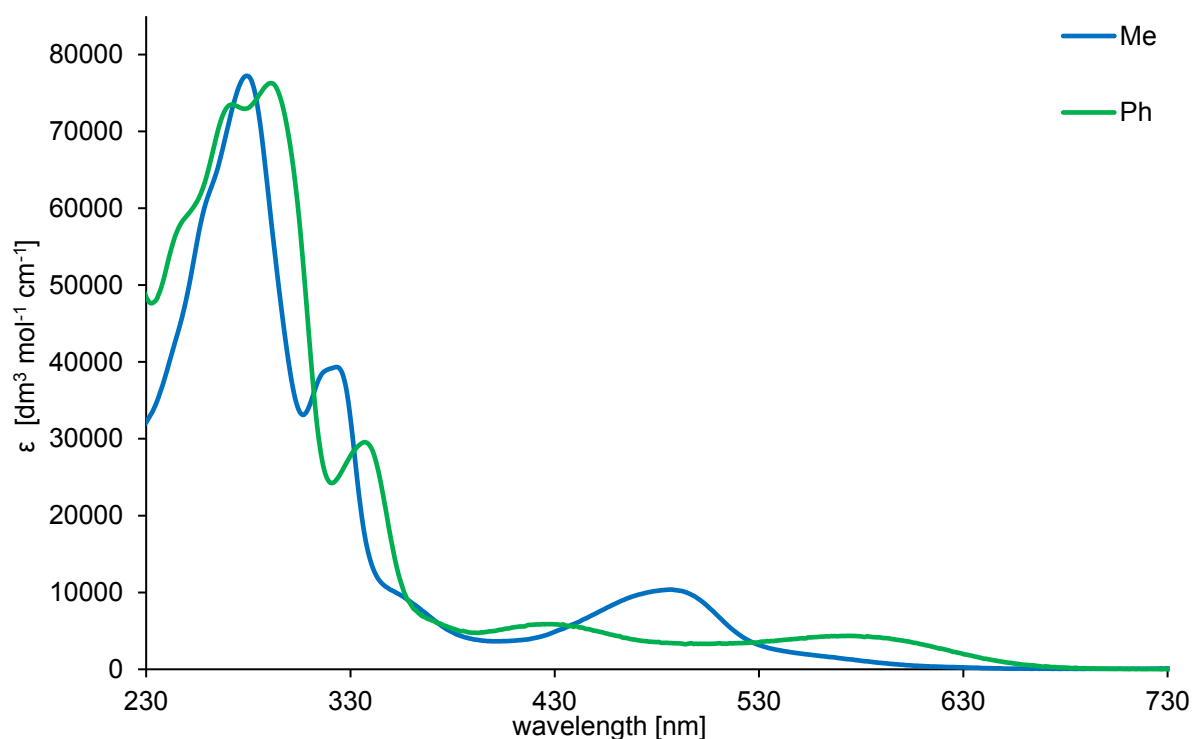


Fig. 44 Solution UV-Vis spectra in CH_2Cl_2 of $[\text{Cu}(\text{L-Br})_2][\text{PF}_6]$ and $[\text{Cu}(\text{Ph}\text{L-Br})_2][\text{PF}_6]$.

The solution absorption spectra of the L-X ligands are compared in Fig. 45, the intense high energy bands arising from $\pi^* \leftarrow \pi$ and $\pi^* \leftarrow n$ transitions. The highest energy absorption shifts from 248 nm in L-F to 260 nm in L-I .

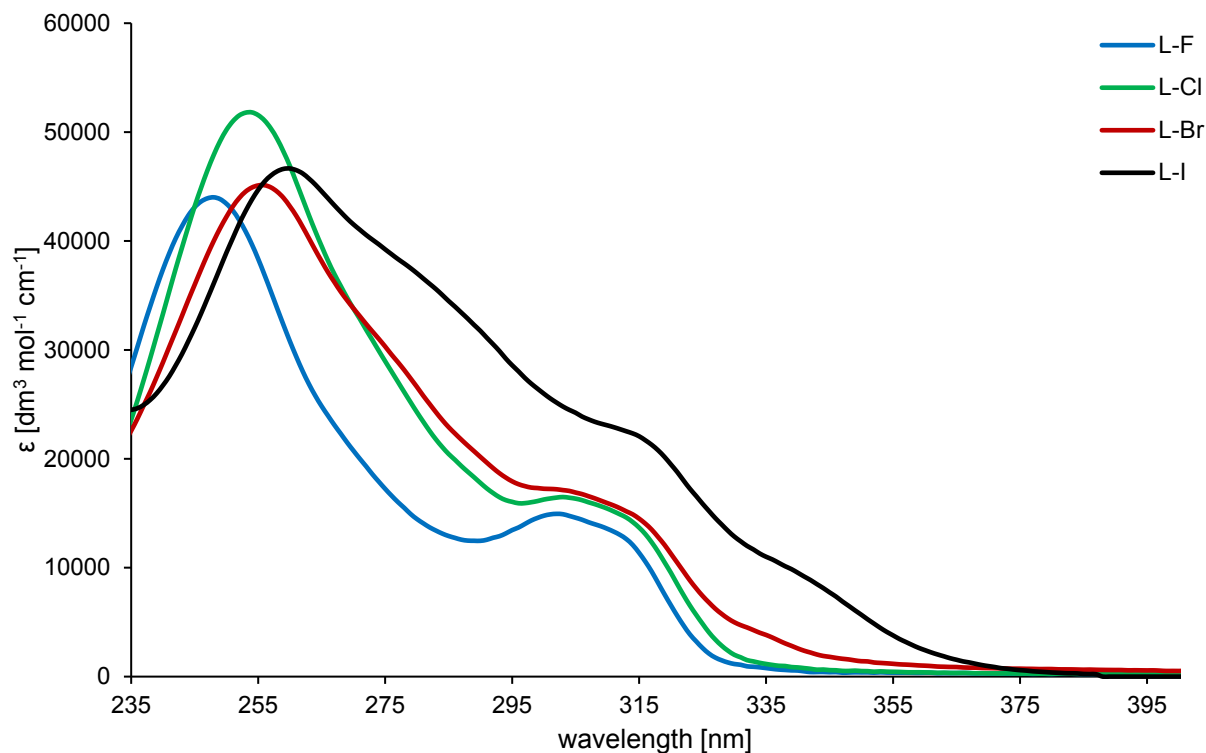


Fig. 45 Solution UV-Vis spectra in CH_2Cl_2 of the L-X ligands with $\text{X} = \text{F}, \text{Cl}, \text{Br}, \text{I}$.

The difficulties isolating the homoleptic $[\text{Cu}(\text{L-I})_2][\text{PF}_6]$ complex resulted in it being impossible to measure the UV-Vis absorption spectrum of this complex. The UV-Vis spectra of the homoleptic Cu(I) complex of the ligands **L-F**, **L-Cl** and **L-Br** have previously been reported¹²⁹ and have shown a metal-to-ligand charge transfer (MLCT) band from 483 nm for $[\text{Cu}(\text{L-F})_2][\text{PF}_6]$ to 488 nm for $[\text{Cu}(\text{L-Br})_2][\text{PF}_6]$. The mixture of $[\text{Cu}(\text{L-I})_2][\text{PF}_6]$ and $[\text{Cu}(\text{L-I})(\text{MeCN})_2][\text{PF}_6]$ has an MLCT maximum at 488 nm.

The UV-Vis spectra of the $[\text{Cu}(\text{L-X})_2][\text{PF}_6]$ complexes with $\text{X} = \text{NMe}_2, \text{OPh}, \text{t-Bu}$ (Fig. 46) show an identical MCLT maximum at 484 nm. The intensity of the MLCT band is greatest with the ligand **NMe₂**. The $\pi^* \leftarrow \pi$ and $\pi^* \leftarrow n$ (for the ligand **L-OPh**) transitions at the wavelength range between 230 and 400 nm are different for each complex. An expanded π -system for $[\text{Cu}(\text{L-OPh})_2][\text{PF}_6]$ leads to a more intense absorption at 320 nm whereas the introduction of **L-NMe₂** results in reduced absorbance and a red shift. The absorption spectrum of $[\text{Cu}(\text{L-t-Bu})_2][\text{PF}_6]$ is comparable to the spectrum of $[\text{Cu}(\text{L-Br})_2][\text{PF}_6]$ in Fig. 44.

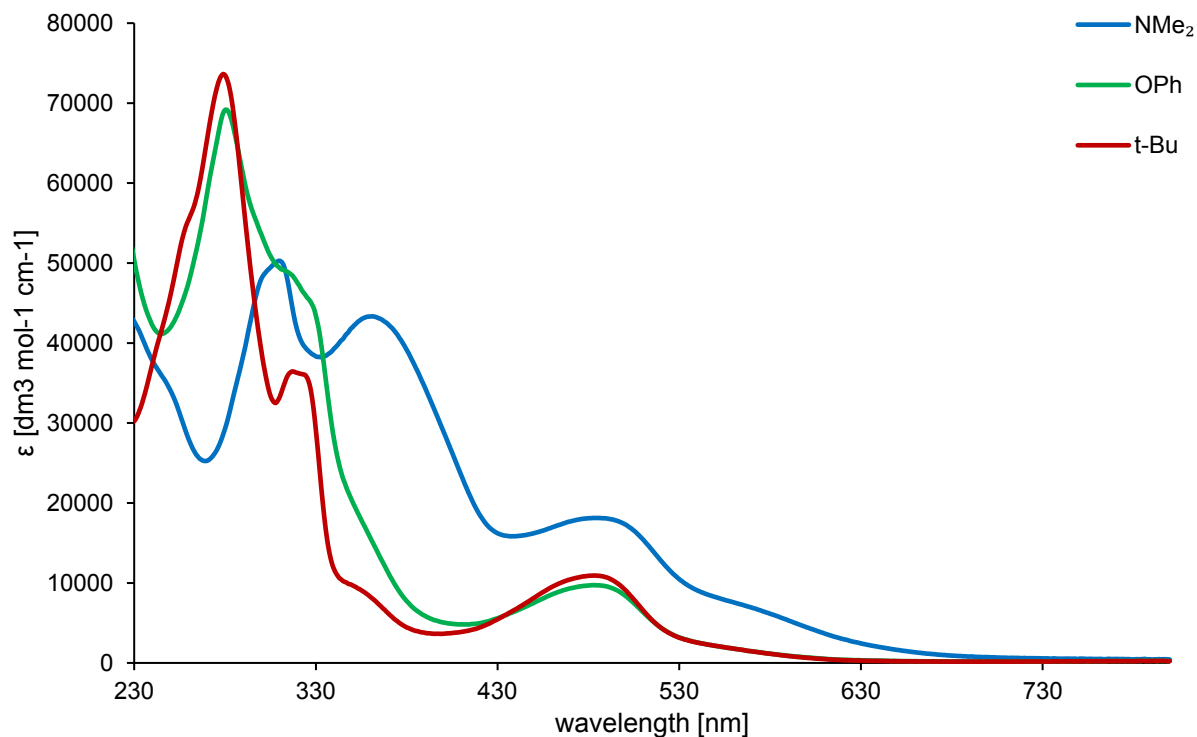


Fig. 46 Solution UV-Vis spectra in CH₂Cl₂ of the homoleptic [Cu(L-X)₂][PF₆] complexes with X = NMe₂, OPh, t-Bu.

Fig. 47 shows the solution absorption spectra of the four homoleptic [Cu(N[^]NX)₂][PF₆] complexes. High-energy bands arise from ligand-based $\pi^* \leftarrow \pi$ and $\pi^* \leftarrow n$ transitions, and the broad absorption between 400 and 520 nm is assigned to a MLCT band. The MLCT absorption maxima, λ_{max} , shift significantly to lower energy as the heteroatom in the ligand is changed: [Cu(N[^]NO)₂][PF₆], 424 nm; [Cu(N[^]NNH)₂][PF₆], 435 nm; [Cu(N[^]NNMe)₂][PF₆], 446 nm; [Cu(N[^]NS)₂][PF₆], 465 nm. The intensity of the MLCT band is greatest with the benzothiazole ligand N[^]NS.

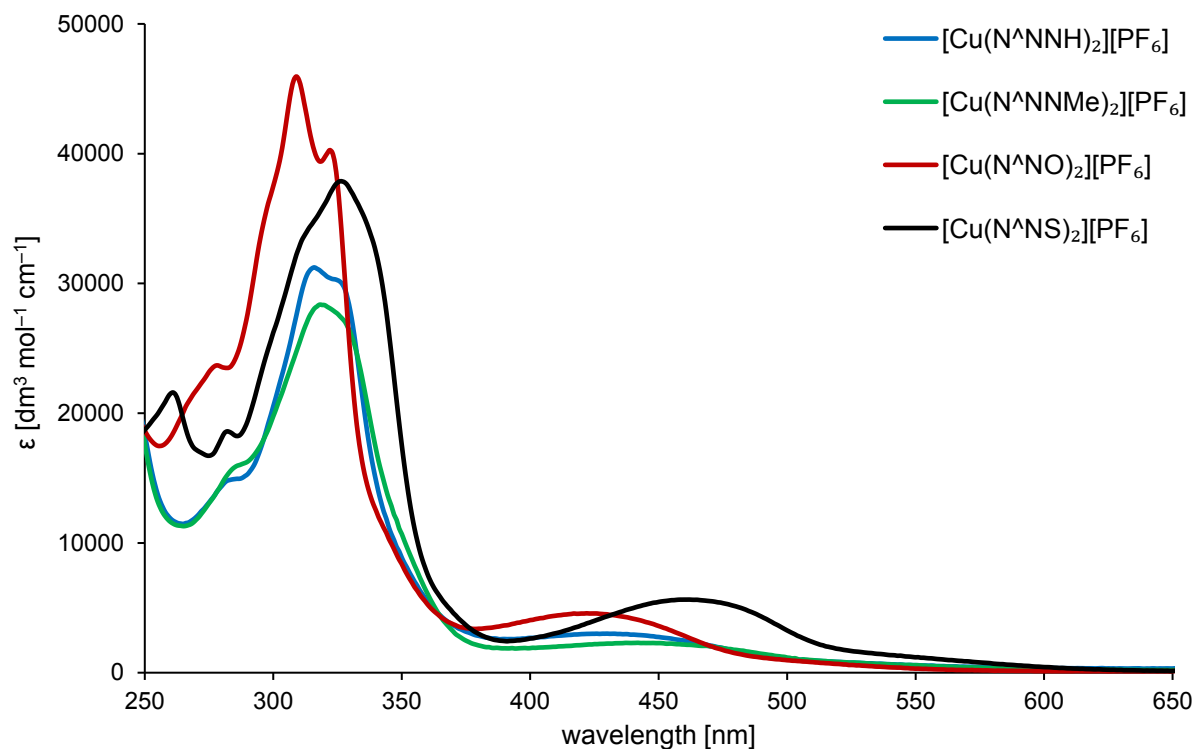


Fig. 47 Solution UV-Vis spectra in CH_2Cl_2 of the homoleptic $[\text{Cu}(\text{N}^{\text{X}}\text{NS})_2][\text{PF}_6]$ complexes with $\text{X} = \text{NH}, \text{NMe}, \text{O}, \text{S}$.

The solution UV-Vis spectra of the copper(I) complexes containing the modified $\text{N}^{\text{X}}\text{NS}$ ligands are displayed in Fig. 48-Fig. 50. The introduction of an amine-group at the benzothiazole ring results in decreased $\pi^* \leftarrow \pi$ transitions between 230 and 360 nm (Fig. 48). The MLCT absorption maxima are blue shifted with respect to the MCLT absorption of $[\text{Cu}(\text{N}^{\text{NS}})_2][\text{PF}_6]$ (N^{NS} : $\lambda_{\text{max}} = 465$ nm, $\text{N}^{\text{NS}}(\text{NH}_2)$: $\lambda_{\text{max}} = 385$ nm, $\text{N}^{\text{NS}}(\text{NHMe})$: $\lambda_{\text{max}} = 409$ nm, $\text{N}^{\text{NS}}(\text{NMe}_2)$: $\lambda_{\text{max}} = 442$ nm). A red shift is observed for the MLCT band of $[\text{Cu}(\text{N}^{\text{NS}}(\text{NO}_2))_2][\text{PF}_6]$ ($\lambda_{\text{max}} = 476$ nm). The absorption spectra of the copper(I) complexes containing $\text{N}^{\text{X}}\text{NS}$ ligands with an extended π -system (Fig. 49) show that the introduction of a quinoline unit enhances the absorption over the whole wavelength range. The MLCT absorption maximum is at 506 nm and for $[\text{Cu}(\text{Ph}^{\text{NS}})_2][\text{PF}_6]$ at 445 nm, respectively. The homoleptic copper(I) complexes of fluorine-containing ligands $^{\text{CHF}_2}\text{N}^{\text{NS}}$ and $^{\text{CF}_3}\text{N}^{\text{NS}}$ in Fig. 50 have almost identical MLCT absorption bands with a λ_{max} at 449 nm. The $\pi^* \leftarrow \pi$ transitions occur at comparable wavelength whereby the spectrum of $[\text{Cu}(^{\text{CF}_3}\text{N}^{\text{NS}})_2][\text{PF}_6]$ shows higher intensities.

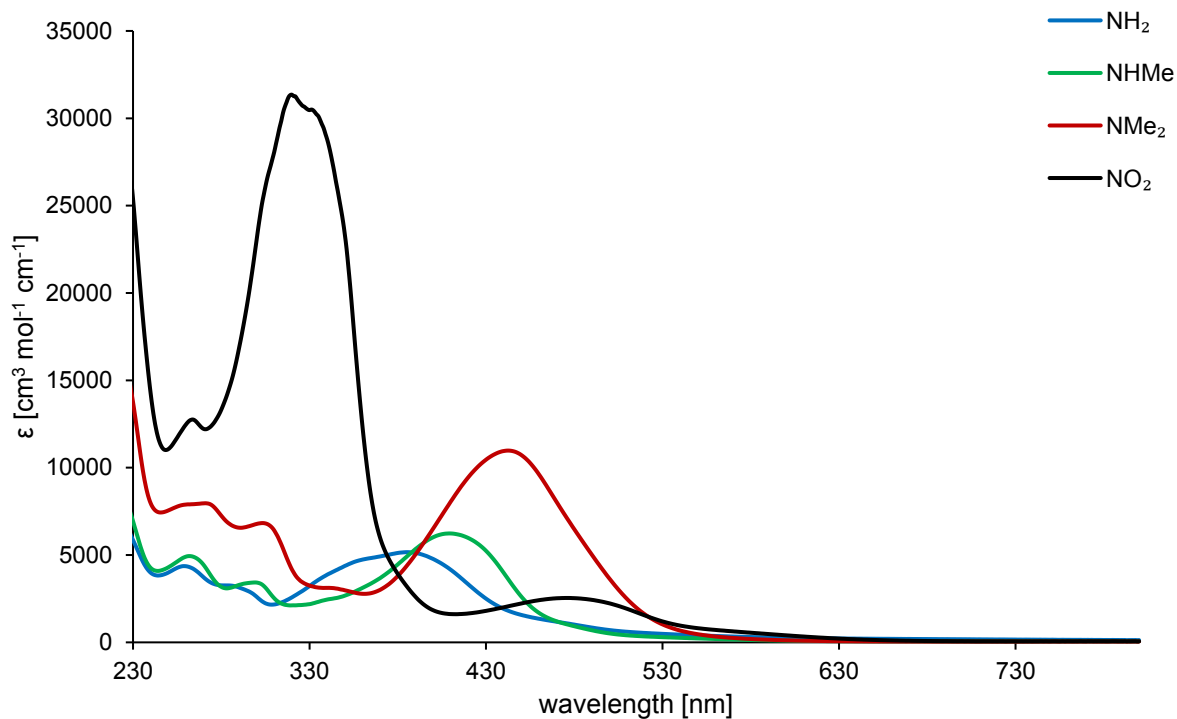


Fig. 48 Solution UV-Vis spectra in CH_2Cl_2 of the homoleptic $[\text{Cu}(\text{N}^{\text{NS}}(\text{X}))_2][\text{PF}_6]$ complexes with $\text{X} = \text{NH}_2, \text{NHMe}, \text{NMe}_2, \text{NO}_2$.

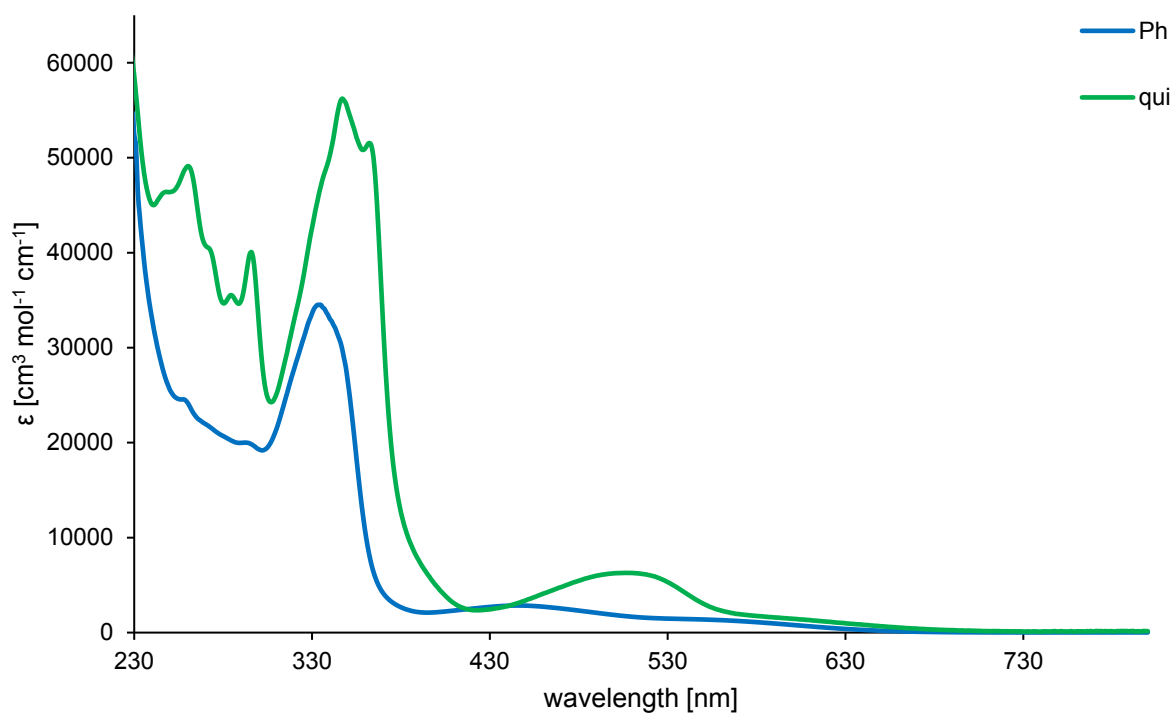


Fig. 49 Solution UV-Vis spectra in CH_2Cl_2 of the homoleptic $[\text{Cu}(\text{RN}^{\text{NS}})_2][\text{PF}_6]$ complexes with $\text{R} = \text{Ph}, \text{qui}$.

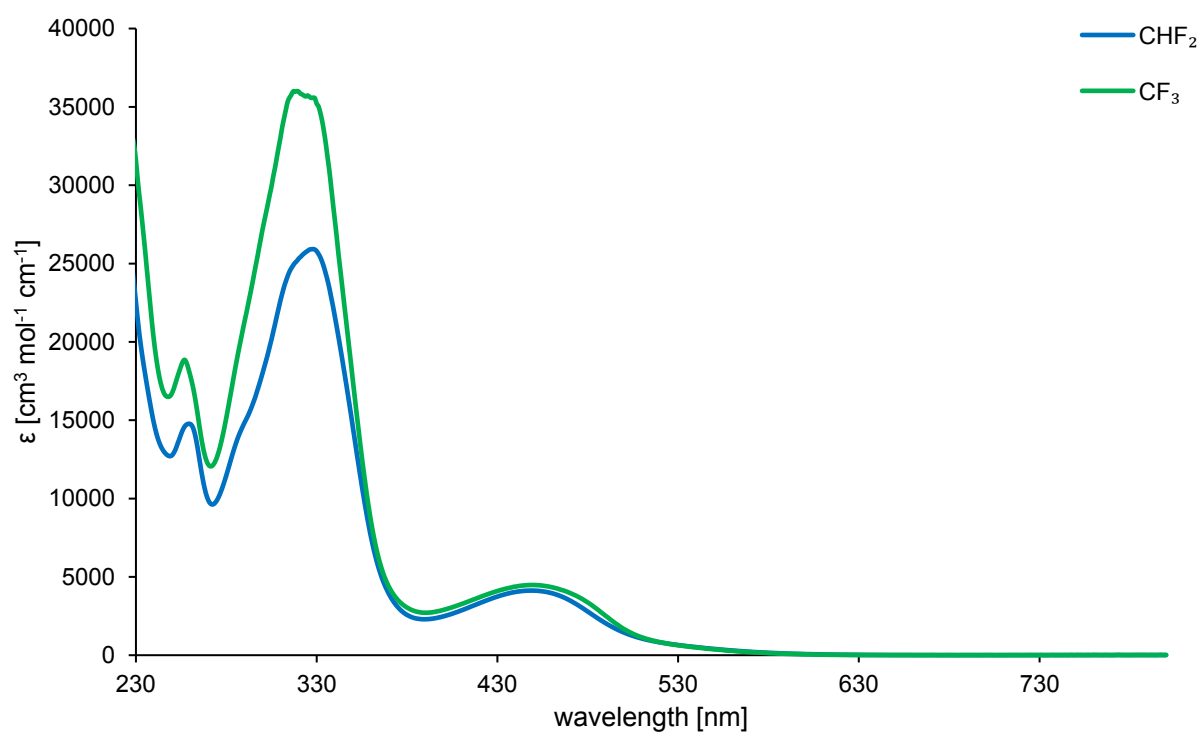


Fig. 50 Solution UV-Vis spectra in CH_2Cl_2 of the homoleptic $[\text{Cu}(\text{R}^{\text{N}}\text{NS})_2][\text{PF}_6]$ complexes with $\text{R} = \text{CHF}_2, \text{CF}_3$.

11.3. Mass Spectrometry

The mass of the compounds was verified by ESI-MS or MALDI TOF mass spectrometry. The ligands were measured in the positive mode and the $[M + H]^+$ ion was observed as the base peak in each case. The homoleptic copper(I) complexes were measured in positive and negative modes. In positive mode, the ESI-MS spectra of the compounds showed a base peak corresponding the $[M - PF_6]^+$. In the negative mode, a peak at $m/z = 149$ corresponds to the $[PF_6]^-$ counter ion. For the homoleptic copper(I) complexes of the $N^{\wedge}NX$ ligands HR ESI-MS spectra were obtained (Fig. 51 - Fig. 54).

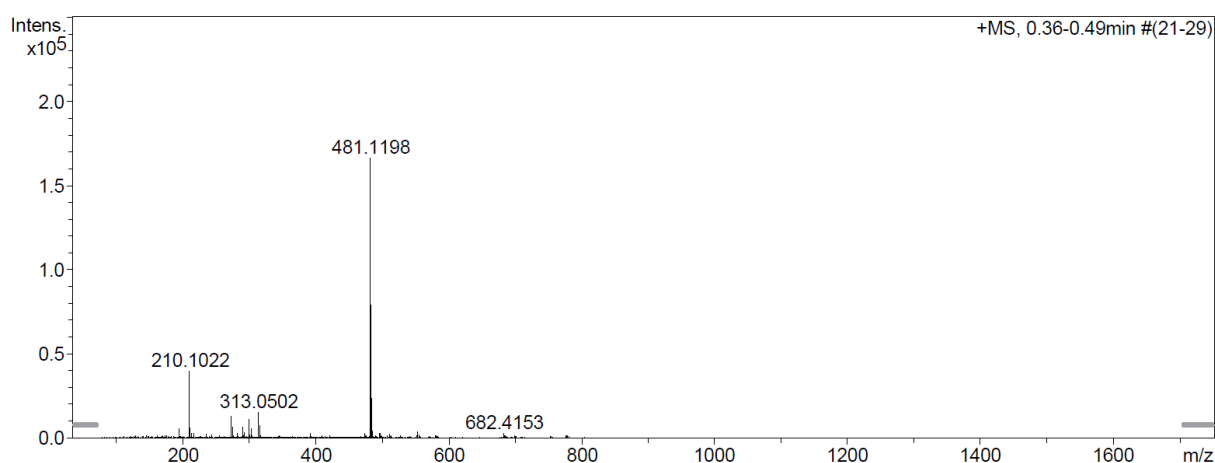


Fig. 51 HR ESI-MS spectrum of $[Cu(N^{\wedge}NNH)_2][PF_6]$ (calc. 481.1196).

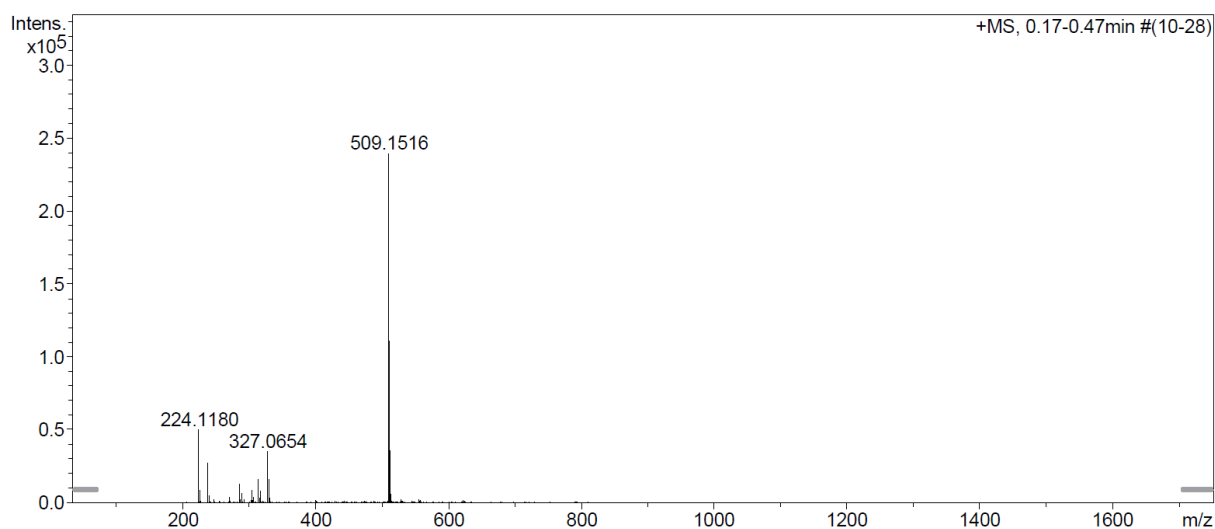


Fig. 52 HR ESI-MS spectrum of $[Cu(N^{\wedge}NNMe)_2][PF_6]$ (calc. 509.1509).

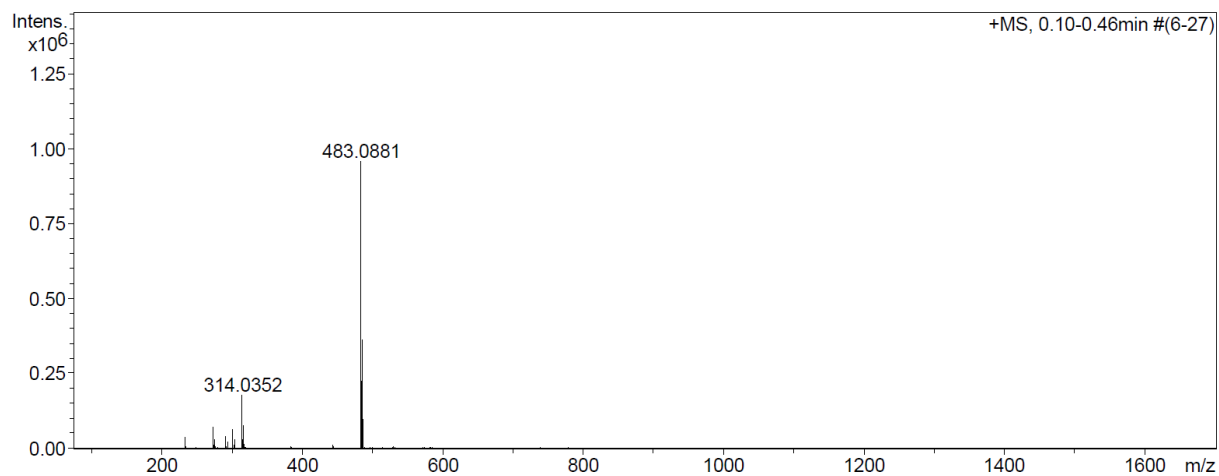


Fig. 53 HR ESI-MS spectrum of $[\text{Cu}(\text{N}^{\text{NO}})_2][\text{PF}_6]$ (calc. 483.0877).

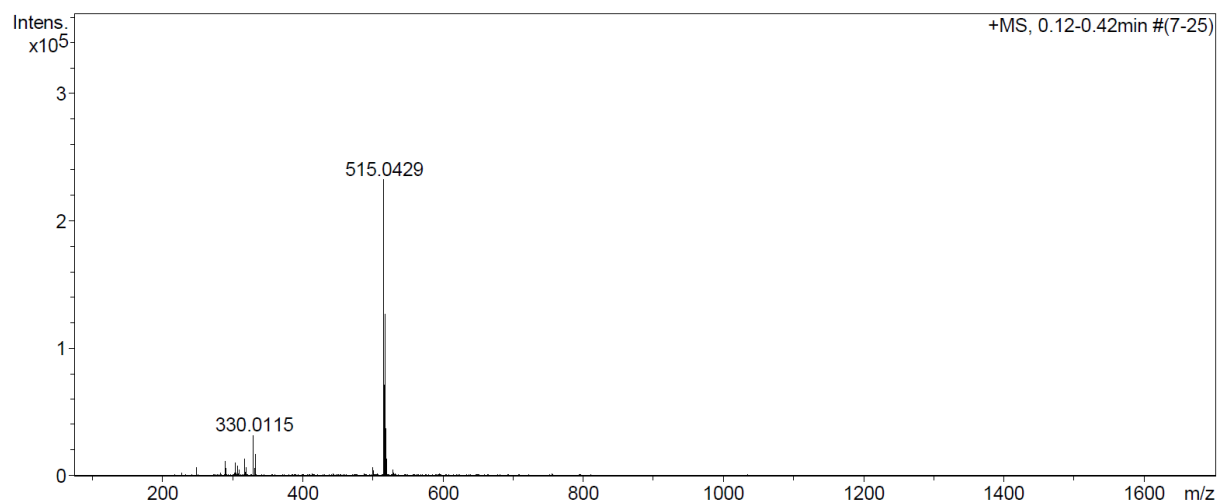


Fig. 54 HR ESI-MS spectrum of $[\text{Cu}(\text{N}^{\text{NS}})_2][\text{PF}_6]$ (calc. 515.0420).

11.4. Electrochemistry

The electrochemical behaviours of $[\text{Cu}(\text{L-F})_2][\text{PF}_6]$, $[\text{Cu}(\text{L-Cl})_2][\text{PF}_6]$ and $[\text{Cu}(\text{L-Br})_2][\text{PF}_6]$ are compared in Table 2, and a representative cyclic voltammogram (with internal Fc/Fc^+ reference) is shown in Fig. 55. Each complex exhibits a copper-centred oxidation process and the introduction of the F, Cl or Br substituents has only a small effect on its potential. In each of $[\text{Cu}(\text{L-F})_2][\text{PF}_6]$ and $[\text{Cu}(\text{L-Cl})_2][\text{PF}_6]$, the irreversible ligand-centred reduction process ca. -2.0 V is more pronounced in the first cycle than in subsequent scans.

Table 2 Cyclic voltammetric data for $[\text{Cu}(\text{L-X})_2][\text{PF}_6]$ with X = F, Cl, Br with respect to Fc/Fc^+ ; CH_2Cl_2 solutions with $[\text{tBu}_4\text{N}][\text{PF}_6]$ as supporting electrolyte and scan rate of 0.1 V s^{-1} . Processes are reversible unless otherwise stated (ir = irreversible).

Complex	$E_{1/2}^{\text{ox}}$ [V]	$E_{\text{pc}} - E_{\text{pa}}$ [mV]	$E_{1/2}^{\text{red}}$ [V]	$E_{1/2}^{\text{red}}$ [V]
$[\text{Cu}(\text{L-F})_2][\text{PF}_6]$	+0.39	74	-2.08 ^{ir}	-2.42 ^{ir}
$[\text{Cu}(\text{L-Cl})_2][\text{PF}_6]$	+0.43	67	-2.06 ^{ir}	-2.42 ^{ir}
$[\text{Cu}(\text{L-Br})_2][\text{PF}_6]$	+0.42	94	-2.16 ^{ir}	

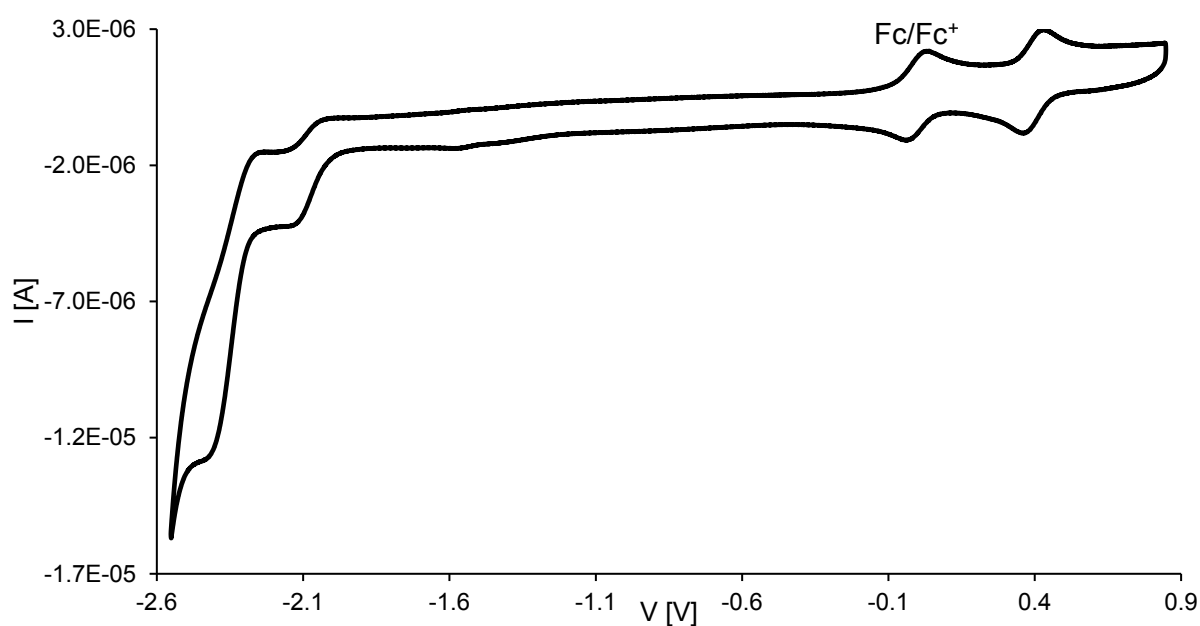


Fig. 55 Cyclic voltammogram for a CH_2Cl_2 solution of $[\text{Cu}(\text{L-F})_2][\text{PF}_6]$; scan rate 0.1 V s^{-1} and referenced internally to Fc/Fc^+ .

The redox activities of $[\text{Cu}(\text{N}^{\wedge}\text{NX})_2][\text{PF}_6]$ ($\text{X} = \text{NH}, \text{NMe}, \text{O}, \text{S}$) were investigated by cyclic voltammetry of CH_2Cl_2 solutions and a representative cyclic voltammogram (CV) for the oxidation process is depicted in Fig. 56. Each complex shows a reversible metal-centred oxidation process (Table 3) assigned to the $\text{Cu}^+/\text{Cu}^{2+}$ redox couple. The potentials for $[\text{Cu}(\text{N}^{\wedge}\text{NNH})_2][\text{PF}_6]$ and $[\text{Cu}(\text{N}^{\wedge}\text{NNMe})_2][\text{PF}_6]$ are similar, and are also similar to that for $[\text{Cu}(\text{dmbpy})_2][\text{PF}_6]$ (+0.17 V in CH_3CN)¹³⁴. Introduction of O or S heteroatoms on going to $[\text{Cu}(\text{N}^{\wedge}\text{NO})_2][\text{PF}_6]$ or $[\text{Cu}(\text{N}^{\wedge}\text{NS})_2][\text{PF}_6]$, respectively, shifts the copper(I) oxidation to higher potential (Table 3), indicating a better π -acceptor ability, consistent with the red shift in the absorption spectrum of $\text{N}^{\wedge}\text{NS}$. The four copper(I) complexes show poorly defined reduction processes. For $[\text{Cu}(\text{N}^{\wedge}\text{NNH})_2][\text{PF}_6]$ and $[\text{Cu}(\text{N}^{\wedge}\text{NNMe})_2][\text{PF}_6]$, no significant changes in the CV were observed through three successive cycles, whereas both $[\text{Cu}(\text{N}^{\wedge}\text{NO})_2][\text{PF}_6]$ and $[\text{Cu}(\text{N}^{\wedge}\text{NS})_2][\text{PF}_6]$ developed an additional irreversible process at positive potential in subsequent scans.

Table 3 Cyclic voltammetric data for $[\text{Cu}(\text{N}^{\wedge}\text{NX})_2][\text{PF}_6]$ with $\text{X} = \text{NH}, \text{NMe}, \text{O}, \text{S}$ with respect to Fc/Fc^+ ; CH_2Cl_2 solutions with $[\text{Bu}_4\text{N}][\text{PF}_6]$ as supporting electrolyte and scan rate of 0.1 V s^{-1} . Processes are reversible unless otherwise stated (ir = irreversible).

Complex	$E_{1/2}^{\text{ox}}$ [V]	$E_{pc} - E_{pa}$ [mV]
$[\text{Cu}(\text{N}^{\wedge}\text{NNH})_2][\text{PF}_6]$	+0.15	77
$[\text{Cu}(\text{N}^{\wedge}\text{NNMe})_2][\text{PF}_6]$	+0.13	105
$[\text{Cu}(\text{N}^{\wedge}\text{NO})_2][\text{PF}_6]$	+0.41	93
$[\text{Cu}(\text{N}^{\wedge}\text{NS})_2][\text{PF}_6]$	+0.43	82

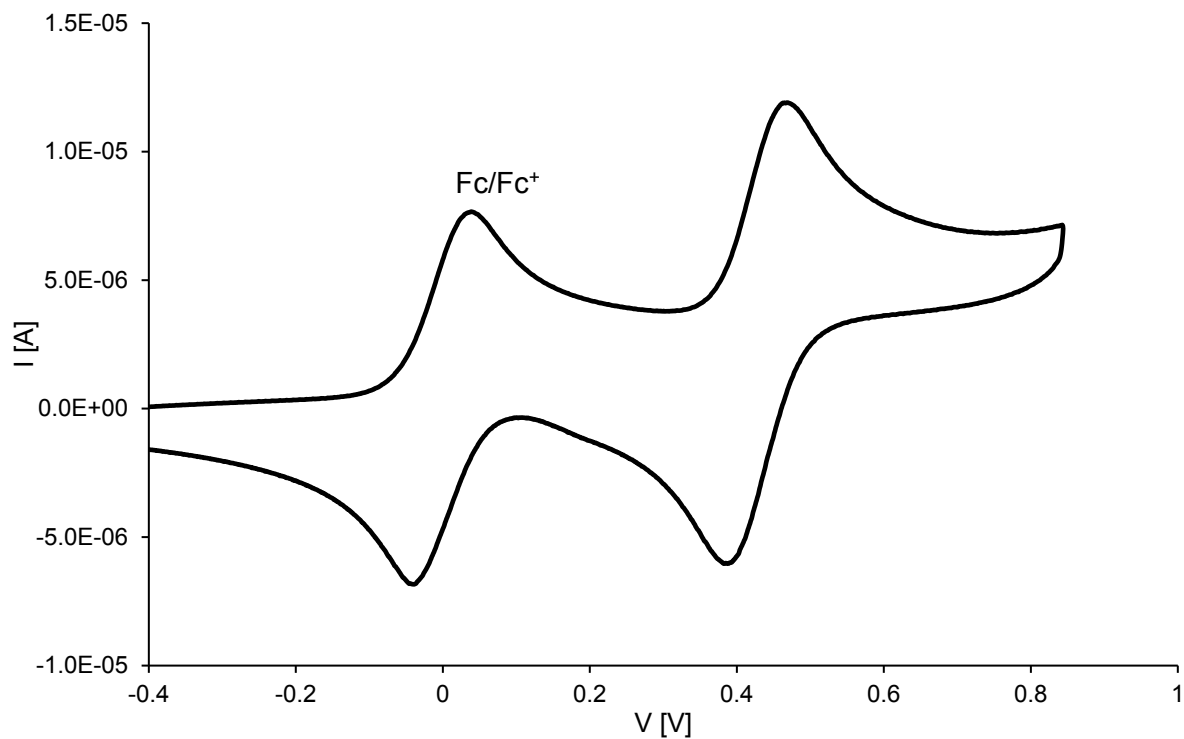


Fig. 56 Cyclic voltammogram of the oxidation process for a CH_2Cl_2 solution of $[\text{Cu}(\text{N}^{\wedge}\text{NS})_2][\text{PF}_6]$; scan rate 0.1 V s^{-1} and referenced to Fc/Fc^+ .

11.5. Crystal Structures

All X-ray crystallographic measurements were carried out by Dr. Markus Neuburger and Dr. Alessandro Prescimone.

The homoleptic copper(I) complex of **L-I** could not be isolated and, as described earlier, a mixture of $[\text{Cu}(\mathbf{L-I})_2][\text{PF}_6]$ and $[\text{Cu}(\mathbf{L-I})(\text{MeCN})_2][\text{PF}_6]$ was obtained. X-ray quality crystals of the latter grew from an MeCN solution of the mixture of compounds layered with Et₂O. The presence of $[\text{Cu}(\mathbf{L-I})(\text{MeCN})_2][\text{PF}_6]$ was verified by X-ray crystallographic measurements. Fig. 57 shows the structure of the $[\text{Cu}(\mathbf{L-I})(\text{MeCN})_2]^+$ cation in $[\text{Cu}(\mathbf{L-I})(\text{MeCN})_2][\text{PF}_6]$.

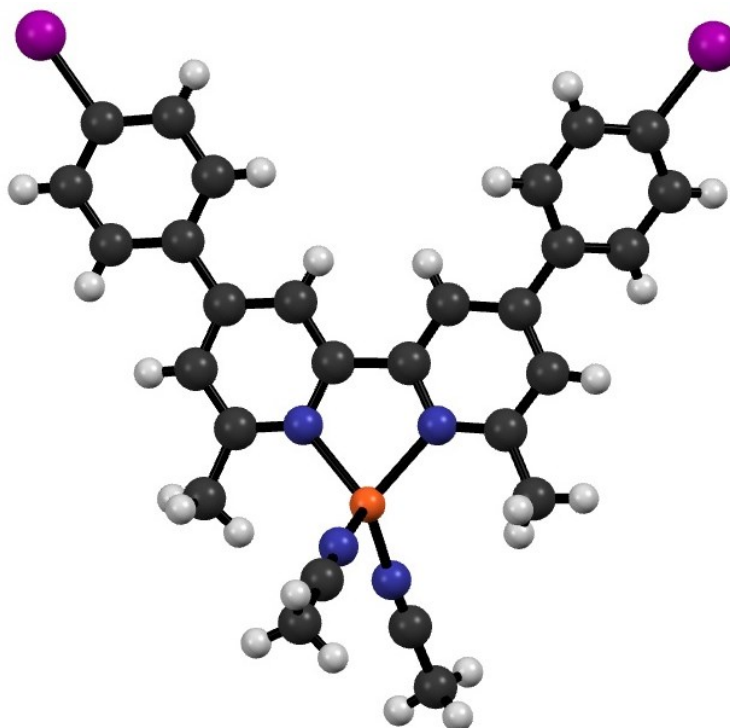


Fig. 57 Ball and stick representation of the $[\text{Cu}(\mathbf{L-I})(\text{MeCN})_2]^+$ cation.

The complex crystallizes in the monoclinic space group $C2/c$. Atom Cu1 (Fig. 58) is in a distorted tetrahedral environment; the bite angle of the bpy unit is $81.06(7)^\circ$, and other N-Cu-N bond angles range from $106.24(9)$ to $124.31(8)^\circ$. The bpy domain deviates from planarity with the angle between the planes of the pyridine rings being 13.8° . The phenyl ring containing C12 is twisted

through 15.5° with respect to the plane of the pyridine ring with N1, while the corresponding angle for the rings containing C18 and N2 is 38.7° .

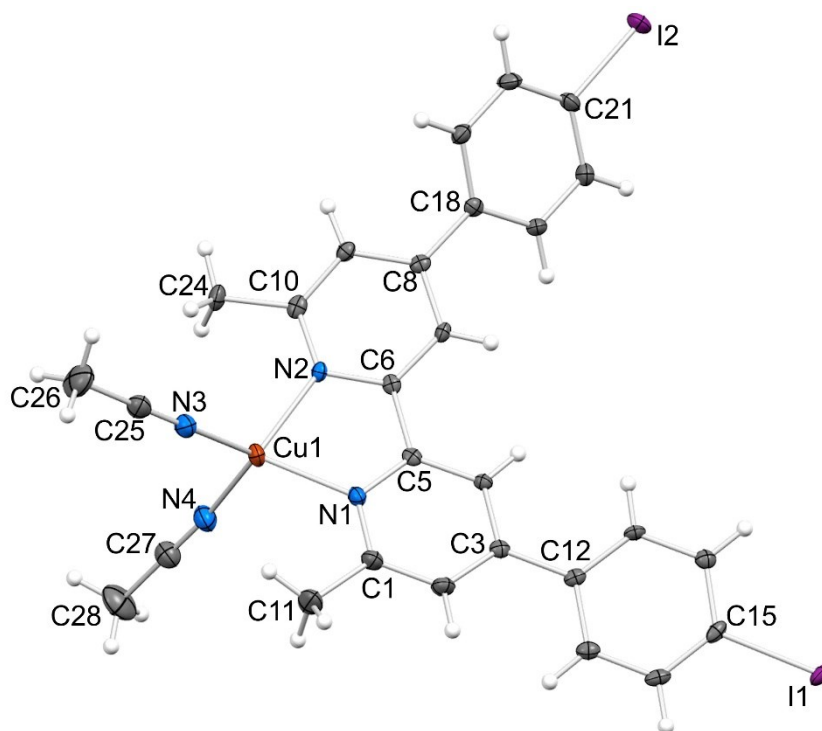


Fig. 58 Structure of the $[\text{Cu}(\mathbf{L-I})(\text{MeCN})_2]^+$ cation in $[\text{Cu}(\mathbf{L-I})(\text{MeCN})_2][\text{PF}_6]$ with ellipsoids plotted at 50% probability level (reprinted with permission of the Royal Society of Chemistry).

The difference in twist angles is associated with the packing of the cations. Face-to-face π -stacking occurs between phenylbpy domains involving the phenyl ring containing atom C12 and this leads to infinite columns of cations running parallel to the c -axis (Fig. 59a). The stacks are built up by alternating operations of a 2-fold axis followed by an inversion centre. The asymmetric unit contains two half-anions; each $[\text{PF}_6]^-$ is ordered, and atoms P1 and P2 are each located on a 2-fold axis. Cation \cdots anion interactions involve extensive $\text{CH}\cdots\text{F}$ contacts. For the anion containing P1 (green in Fig. 59b), these contacts involve arene CH units; in addition this anion exhibits a short $\text{F}\cdots\text{I}$ contact ($\text{F3}\cdots\text{I2}^i = 3.406(1) \text{ \AA}$, symmetry code $i = 1/2 - x, -1/2 + y, 1/2 - z$). In contrast, the anion containing P2 (red in Fig. 59b) sits between the π -stacked cations and interacts with methyl groups of both coordinated ligands $\mathbf{L-I}$ and MeCN.

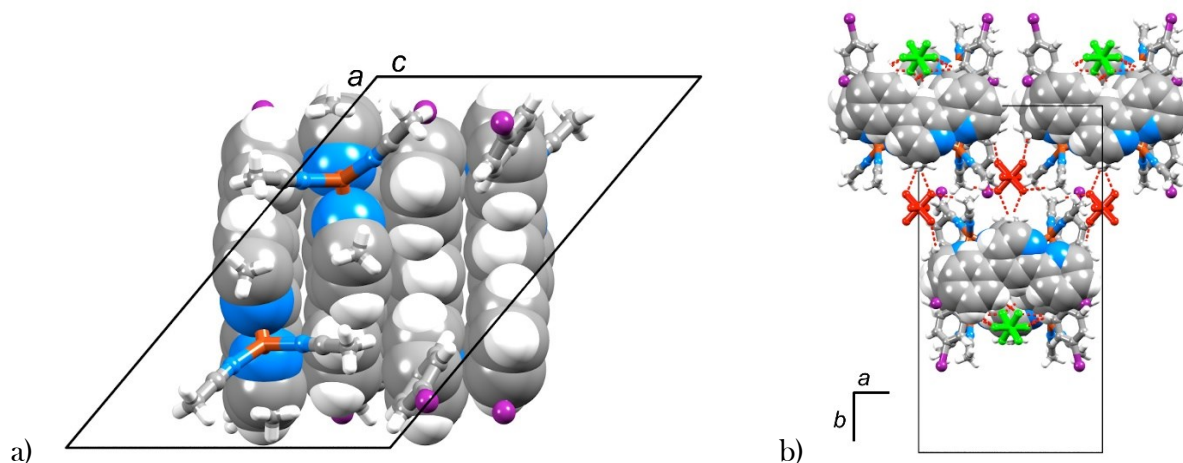


Fig. 59 (a) Face-to-face π -stacking of phenylbpy domains (spacefilling representation) involving the phenyl ring with C12 leading to infinite assemblies following the c -axis. View down the c -axis showing the two different $[\text{PF}_6]^-$ environments. Anion with P1 is shown in green, and with P2, in red; $\text{CH}\cdots\text{F}$ contacts are shown by red hashed lines (reprinted with permission of the Royal Society of Chemistry).

Single crystals of $[\text{Cu}(\text{N}^{\wedge}\text{NO})_2][\text{PF}_6]\cdot 0.5\text{CH}_2\text{Cl}_2$ and $[\text{Cu}(\text{N}^{\wedge}\text{NS})_2][\text{PF}_6]$ were grown by slow diffusion of Et_2O into CH_2Cl_2 solutions of the compounds. The compounds crystallize in the monoclinic space groups $C2/c$ and $P2_1/c$, respectively, and the structures of the $[\text{Cu}(\text{N}^{\wedge}\text{NO})_2]^+$ and $[\text{Cu}(\text{N}^{\wedge}\text{NS})_2]^+$ cations are shown in Fig. 60.

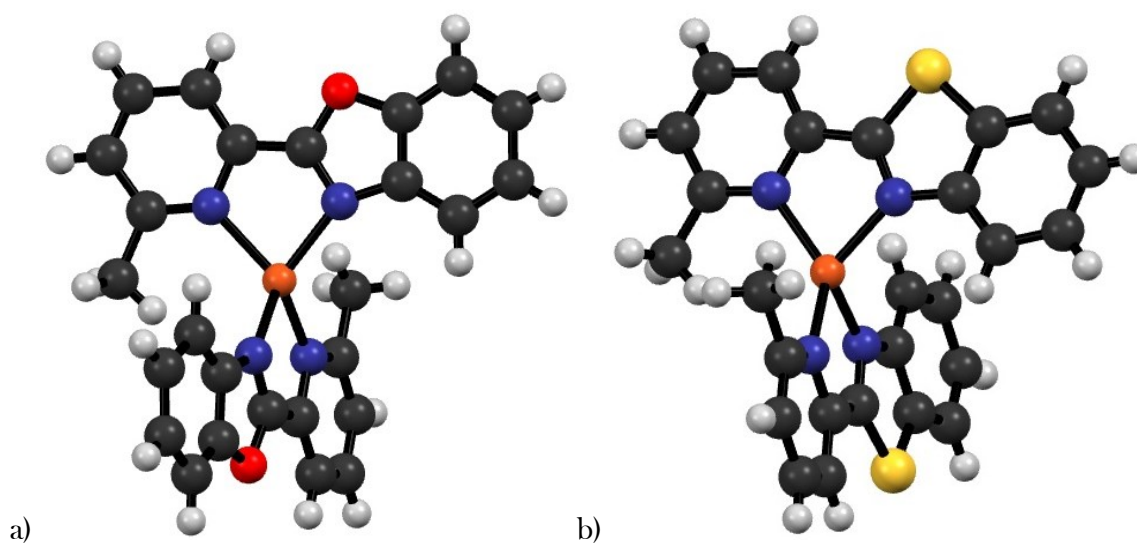


Fig. 60 Ball and stick representations of the (a) $[\text{Cu}(\text{N}^{\wedge}\text{NO})_2]^+$ and (b) $[\text{Cu}(\text{N}^{\wedge}\text{NS})_2]^+$ cations.

The structure determinations confirm that each of $N^{\wedge}NO$ and $N^{\wedge}NS$ coordinates in an N,N' -chelating mode. Atom Cu1 in each cation is tetrahedrally sited (Fig. 61). The Cu–N bond lengths are typical (range 2.033(4) to 2.074(5) Å) and the angle between the least squares planes through the individual ligands in $[Cu(N^{\wedge}NO)_2]^+$ is 76.7° and the corresponding angle in $[Cu(N^{\wedge}NS)_2]^+$ is 86.1°.

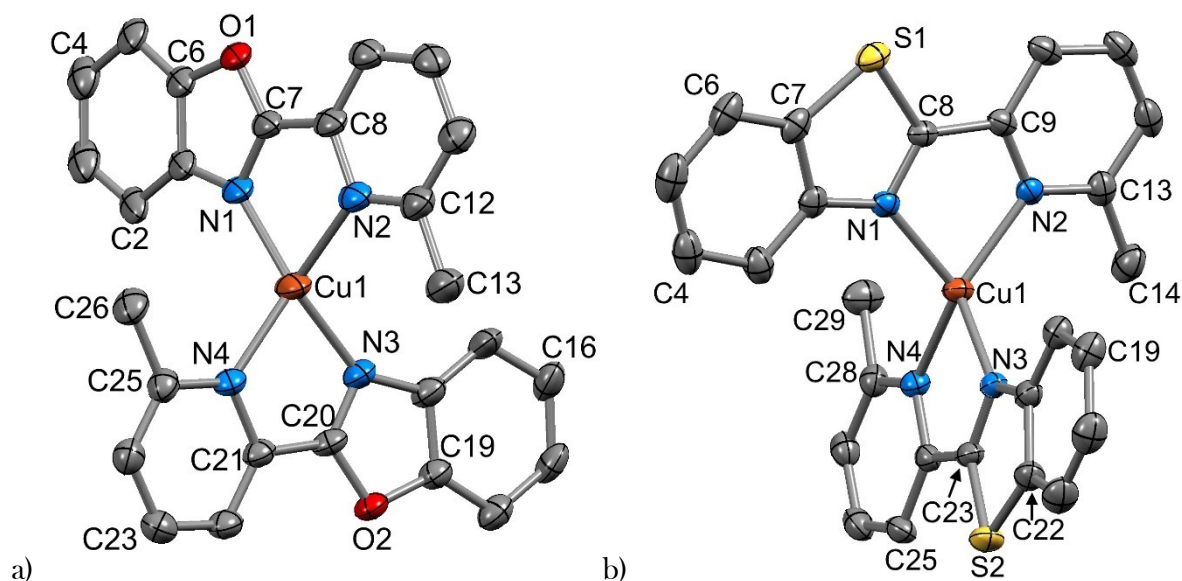


Fig. 61 The structures of the (a) $[Cu(N^{\wedge}NO)_2]^+$ cation in $[Cu(N^{\wedge}NO)_2][PF_6] \cdot 0.5CH_2Cl_2$ and (b) the $[Cu(N^{\wedge}NS)_2]^+$ cation in $[Cu(N^{\wedge}NS)_2][PF_6]$; ellipsoids are plotted at 30% probability level and H atoms and solvent molecules are omitted (reprinted with permission of the Royal Society of Chemistry).

The $[Cu(N^{\wedge}NO)_2]^+$ cations form columns along the c -axis with face-to-face π -interactions between 1,3-benzoxazole units (Fig. 62a). Adjacent pairs of 1,3-benzoxazoles are mutually offset and are related, alternately, by inversion or a 2-fold axis. For the former π -stacking interaction, the distance between the least squares planes through the 1,3-benzoxazoles is 3.23 Å, and the centroid...centroid distance is 3.51 Å. For the latter, the angle between least squares planes is 3.7°, and centroid...plane and centroid...centroid distances are 3.25 and 3.61 Å. The packing of cations in $[Cu(N^{\wedge}NS)_2][PF_6]$ involves centrosymmetric embraces of cations in which the methyl groups point into the thiazole rings (Fig. 62b); the closest $CH \cdots$ thiazole_{centroid} distance is 3.17 Å.¹³⁵ In addition, the pyridine ring containing N4 engages in a weak π -stacking contact with the arene ring containing C19^{*i*} (symmetry code $i = 1 - x, -1/2 + y, 1/2 - z$) in the adjacent molecule; interaction

is not optimal, with centroid···centroid and centroid···plane separations of 3.84 and 3.47 Å, respectively, and an angle between the ring planes of 9.9°.

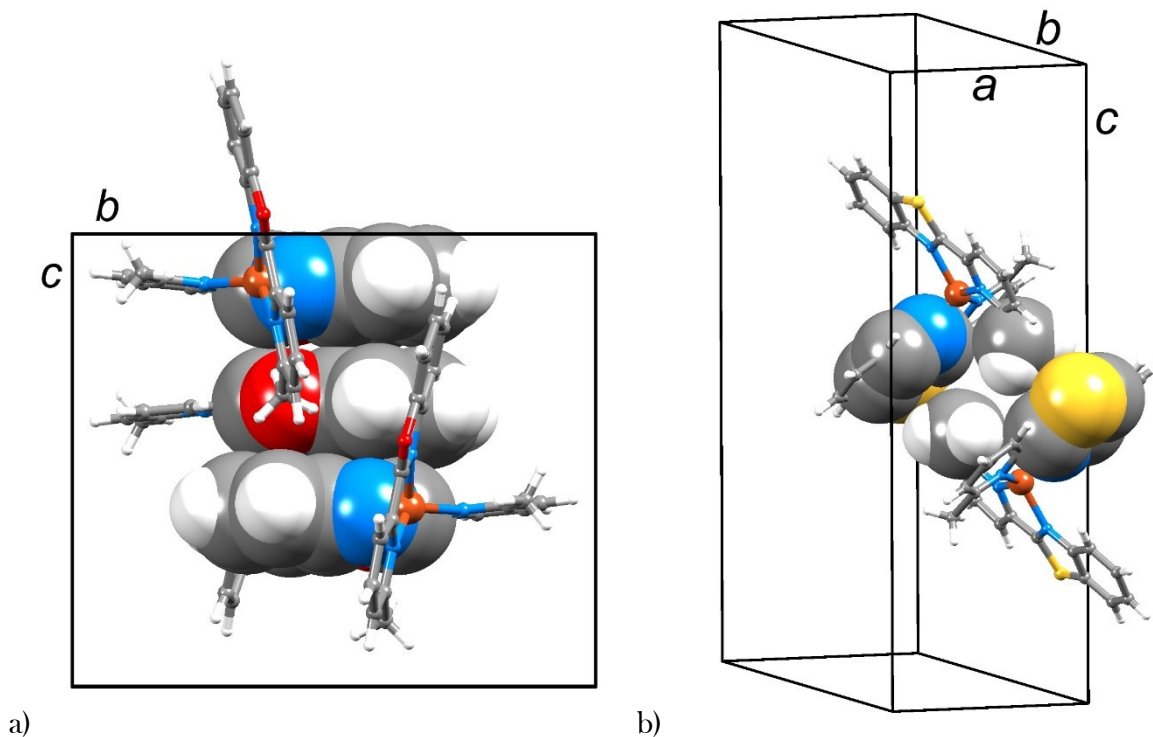


Fig. 62 (a) View down the a-axis of the unit cell in $[\text{Cu}(\text{N}^{\wedge}\text{NO})_2][\text{PF}_6] \cdot 0.5\text{CH}_2\text{Cl}_2$ showing stacked cations. (b) Centrosymmetric embrace of cations in $[\text{Cu}(\text{N}^{\wedge}\text{NS})_2][\text{PF}_6]$ (reprinted with permission of the Royal Society of Chemistry).

11.5.1. Crystal Structure Data



$\text{C}_{28}\text{H}_{24}\text{CuF}_6\text{I}_2\text{N}_2\text{P}$, $M = 878.84$, orange block, monoclinic, space group $C2/c$, $a = 9.9980(4)$, $b = 29.1275(18)$, $c = 13.5247(8)$ Å, $\beta = 130.048(2)^\circ$, $U = 6080.0(7)$ Å³, $Z = 8$, $D_c = 1.920$ mg m⁻³, $\mu(\text{Cu-K}\alpha) = 18.021$ mm⁻¹, $T = 123$ K. Total 28 350 reflections, 5520 unique, $R_{\text{int}} = 0.027$. Refinement of 5460 reflections (380 parameters) with $I > 3\sigma(I)$ converged at final $R_1 = 0.0250$ (R_1 all data = 0.0251), $wR_2 = 0.0261$ (wR_2 all data = 0.0263), $\text{gof} = 1.0853$.



$\text{C}_{26.50}\text{H}_{21}\text{ClCuF}_6\text{N}_4\text{O}_2\text{P}$, $M = 671.44$, orange block, monoclinic, space group $C2/c$, $a = 29.0226(18)$, $b = 14.9554(10)$, $c = 12.9437(9)$ Å, $\beta = 90.929(4)^\circ$, $U = 5617.4(6)$ Å³, $Z = 8$, $D_c = 1.59$ Mg m⁻³, $\mu(\text{Cu-K}\alpha) = 3.172$ mm⁻¹, $T = 123$ K. Total 19 041 reflections, 5039 unique, $R_{\text{int}} = 0.030$. Refinement of 4013 reflections (361 parameters) with $I > 2\sigma(I)$ converged at final $R_1 = 0.1000$ (R_1 all data = 0.1171), $wR_2 = 0.2272$ (wR_2 all data = 0.2359), $\text{gof} = 1.0095$. CCDC 1497681.



$\text{C}_{26}\text{H}_{20}\text{CuF}_6\text{N}_4\text{PS}_2$, $M = 661.11$, orange block, monoclinic, space group $P2_1/c$, $a = 8.1188(3)$, $b = 13.8910(5)$, $c = 23.9522(9)$ Å, $\beta = 92.0462(17)^\circ$, $U = 2699.57(17)$ Å³, $Z = 4$, $D_c = 1.627$ Mg m⁻³, $\mu(\text{Cu-K}\alpha) = 3.752$ mm⁻¹, $T = 123$ K. Total 34 879 reflections, 4984 unique, $R_{\text{int}} = 0.027$. Refinement of 4925 reflections (361 parameters) with $I > 2\sigma(I)$ converged at final $R_1 = 0.0883$ (R_1 all data = 0.0888), $wR_2 = 0.2242$ (wR_2 all data = 0.2243), $\text{gof} = 0.9825$. CCDC 1497682.

11.6. DFT calculations

All DFT calculations were carried out by Prof. Dr. Catherine Housecroft.

DFT calculations on the ground state, energy minimized structures of $[\text{Cu}(\text{ALP1})(\text{L-F})]^+$, $[\text{Cu}(\text{ALP1})(\text{L-Cl})]^+$, $[\text{Cu}(\text{ALP1})(\text{L-Br})]^+$ and $[\text{Cu}(\text{ALP1})(\text{L-I})]^+$ showed that the energies and characteristics of the LUMO and LUMO+1 of the four complexes are similar. The LUMO is centred on the anchoring ligand while the LUMO+1 is principally localized on the bpy domain of the ancillary ligand. These MOs are shown for the iodo-complex in Fig. 63a and b.

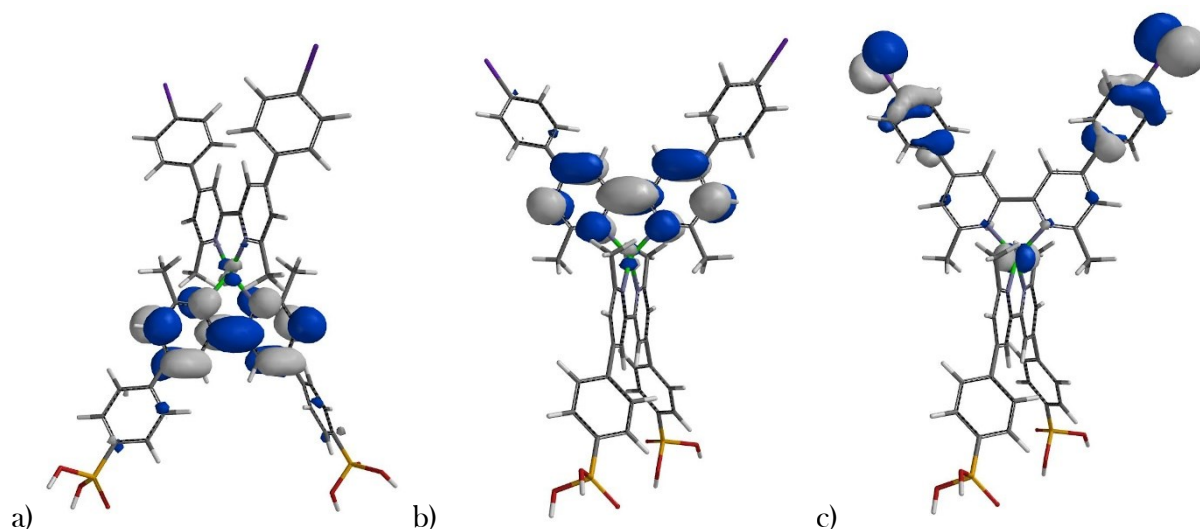


Fig. 63 (a) LUMO, (b) LUMO+1, and (c) HOMO-3 of $[\text{Cu}(\text{ALP1})(\text{L-I})]^+$ (ligand **L-I** is at the top of each diagram).

The DFT calculations indicate that the HOMO of each ground-state dye is mainly based on copper, as are the next two highest occupied MOs. Ancillary ligand character is present in HOMO-3 and HOMO-4 in $[\text{Cu}(\text{ALP1})(\text{L-I})]^+$, with a dominant contribution from the iodophenyl substituent (Fig. 63c). Significantly, the corresponding contributions by ligands **L-F**, **L-Cl** or **L-Br** to these MOs is smaller.

DFT calculations on the ground state, energy minimized structures of $[\text{Cu}(\text{ALP1})(\text{N}^{\wedge}\text{NNMe})]^+$ (Fig. 64), $[\text{Cu}(\text{ALP1})(\text{N}^{\wedge}\text{NO})]^+$ (Fig. 65) and $[\text{Cu}(\text{ALP1})(\text{N}^{\wedge}\text{NS})]^+$ (Fig. 66) showed that the

energies and characteristics of the HOMO and LUMO of the complexes are similar. HOMO and HOMO-1 are mainly metal character; the HOMO-2 and HOMO-3 are also mainly copper-based. LUMO and LUMO+1 are close in energy and have similar orbital characters. Going from $[\text{Cu}(\text{ALP1})(\text{N}^{\wedge}\text{NNMe})]^+$ to $[\text{Cu}(\text{ALP1})(\text{N}^{\wedge}\text{NO})]^+$ or $[\text{Cu}(\text{ALP1})(\text{N}^{\wedge}\text{NS})]^+$ lowers the LUMO and the HOMO energies but the anchor character remains in the LUMO manifold. The HOMO is mainly localized on the copper.

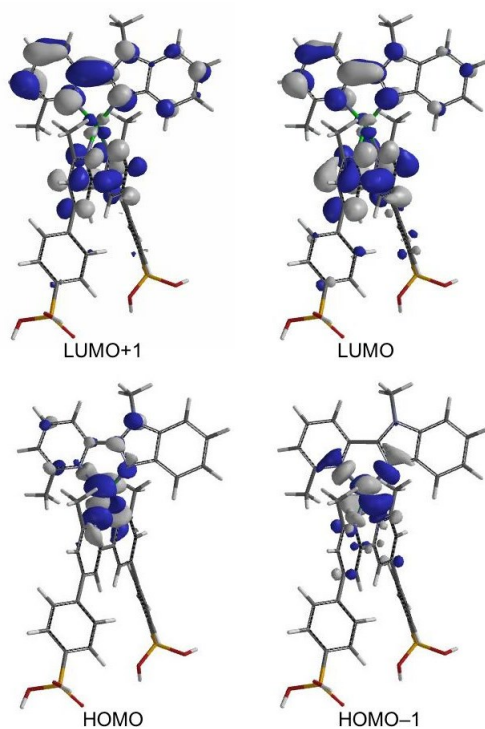


Fig. 64 LUMO, LUMO+1, HOMO and HOMO-1 of $[\text{Cu}(\text{ALP1})(\text{N}^{\wedge}\text{NNMe})]^+$ (ligand $\text{N}^{\wedge}\text{NNMe}$ is at the top of each diagram).

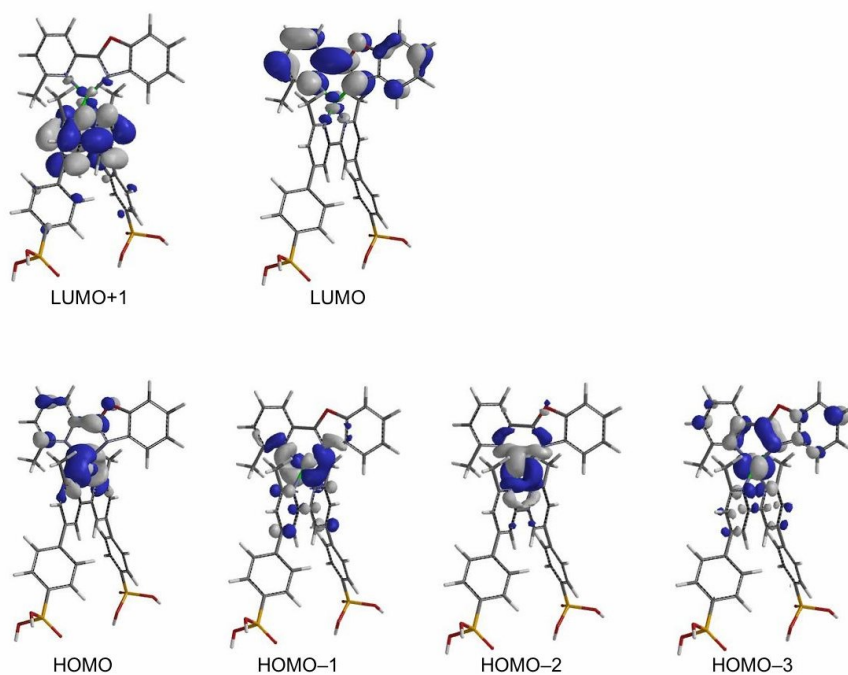


Fig. 65 LUMO, LUMO+1, HOMO, HOMO-1, HOMO-2 and HOMO-3 of $[\text{Cu}(\text{ALP1})(\text{N}^{\wedge}\text{NO})]^+$ (ligand $\text{N}^{\wedge}\text{NO}$ is at the top of each diagram).

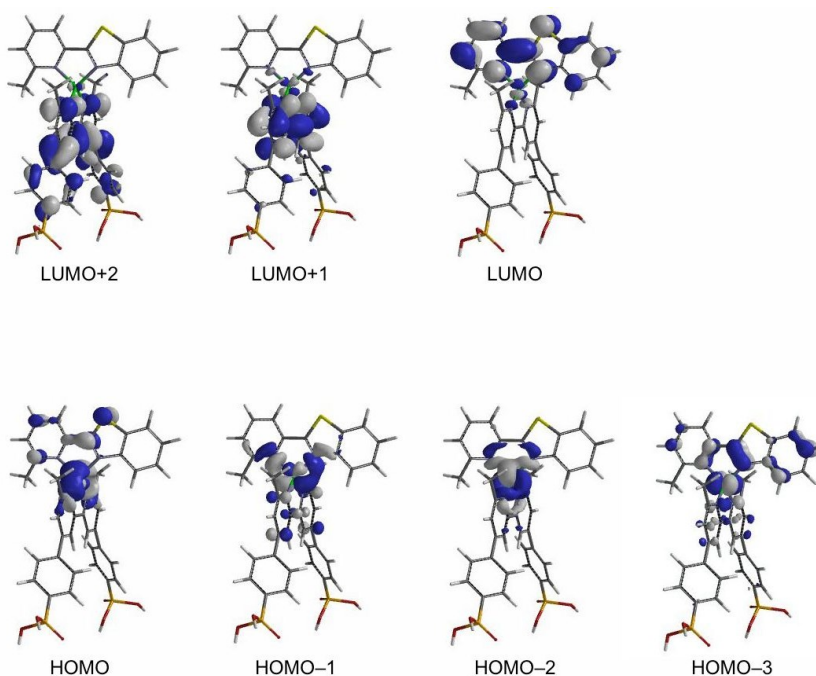


Fig. 66 LUMO, LUMO+1, LUMO+2, HOMO, HOMO-1, HOMO-2 and HOMO-3 of $[\text{Cu}(\text{ALP1})(\text{N}^{\wedge}\text{NS})]^+$ (ligand $\text{N}^{\wedge}\text{NS}$ is at the top of each diagram).

DEVICE FABRICATION

12. Equipment Details

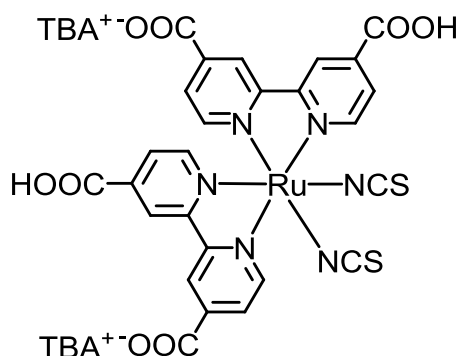
Commercially available equipment was used for the assembly of the DSCs.

The main components were supplied in a *Solaronix Test Cell Kit* (Ref. 74991) consisting of Titania Electrodes, opaque (Ref. 74101, FTO coated glass, screen-printed TiO₂ nanoxide paste, active area: 6 x 6 mm, thickness: 9 μm + 3 μm scattering layer), Platinum Electrodes, drilled (Ref. 74201, FTO coated glass, screen-printed Platisol T/SP precursor), Gaskets (Ref. 74301, Meltonix 1170-60 sealing film, dimensions: 14 x 14 mm (outer), 8 x 8 mm (inner), thickness: 60 μm), Sealings (Ref. 74401, Meltonix 1170-60 sealing film, dimensions: 8 x 8 mm, thickness: 60 μm) and Caps (Ref. 74501, thin glass lid, diameter: 6 mm).

For the heating of the electrodes a *Schott Instruments SLK2* heating plate was used.

As dye-bath vials *FAUST Weithalsflasche* (30 mL, ArtNr. 6287779) with screw-cap (ArtNr. 9072164) were used.

The reference dye **N719** (Scheme 28) was purchased from *Solaronix* (Ref. 21651, Solaronix Ruthenizer 535-bisTBA).



Scheme 28 Reference Ruthenium-dye **N719** (TBA = tetra-butylammonium).

The dye baths consisted of either a 1 mM DMSO solution of the anchoring ligand **ALP1**, or a 0.1 mM CH₂Cl₂ solution of a homoleptic copper(I) complex. Additional details for co-sensitized DSCs or treated with co-adsorbents are described in the corresponding part.

The electrolyte comprised LiI (0.1 mol dm^{-3}), I₂ (0.05 mol dm^{-3}), 1-methylbenzimidazole (0.5 mol dm^{-3}) and 1-butyl-3-methylimidazolium iodide (0.6 mol dm^{-3}) in methoxypropionitrile.

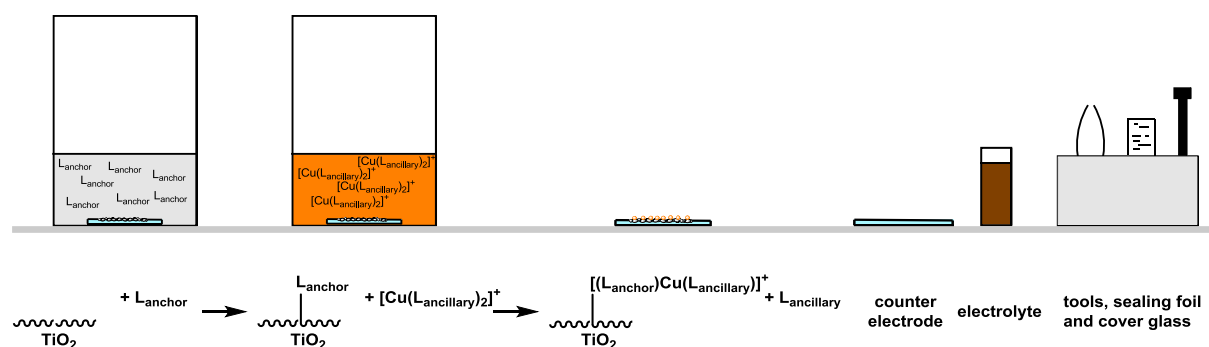
The working and the counter electrode of the DSC were assembled with a *Digital Solder Station ST-50D* from *Toolcraft* equipped with a home-made tip.

For better conductivity a high purity silver paste was used on the contacts.

13. General Device Fabrication

The following method was used for the fabrication of all the single-dye copper(I)-based DSCs (Scheme 29).

The photoelectrodes were rinsed with HPLC-grade EtOH and sintered at 450 °C for 30 min. The electrodes were cooled to about 80 °C and immersed into a 1 mM anchoring ligand solution in DMSO (extra pure) for 1 day. The colourless electrodes were removed from the solution and washed with extra-pure DMSO and HPLC-grade EtOH. Afterwards, the electrodes were dried with a heat gun at about 80 °C. The anchoring ligand functionalized electrodes were immersed into a 0.1 mM homoleptic copper(I) complex solution in HPLC-grade CH₂Cl₂ of the respective ancillary ligand for 3 days. During this time, ligand exchange on the electrode surface took place and the electrodes turned red-orange. The electrodes were removed from the dye-bath solution, washed with HPLC-grade CH₂Cl₂ and dried with a heat gun at about 80 °C.



Scheme 29 Schematic representation of the stepwise method of assembling copper(I) dyes in n-type dye-sensitized solar cells and the required equipment.

The counter electrode was washed with HPLC-grade EtOH and residual organic impurities were removed by heating for 30 min at 450 °C on a heating plate.

The dye-covered photoelectrode and the counter electrode were assembled using thermoplast hot-melting sealing foil gaskets by heating them with the soldering iron while applying moderate pressure. The electrolyte was introduced into the DSC by vacuum backfilling. The hole in the counter electrode was finally sealed with sealing foil and a cover glass.

On each electrode a small amount of silver paste was applied to provide a higher conductivity.

Fig. 67 displays a schematic representation of a completely assembled DSC.

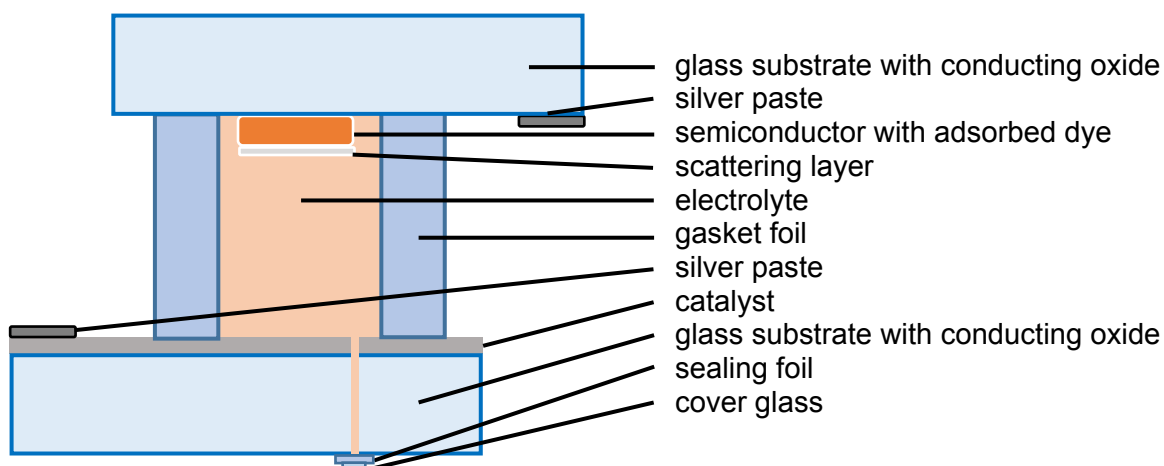


Fig. 67 Section-view of a schematic representation of a completely assembled DSC.

The **N719** reference cell was assembled with the same procedure described above with the only difference that a 0.3 mM dye-bath solution in HPLC-grade EtOH was used. The electrode was immersed into the dye-bath solution for 3 days. After removing from the dye-bath solution it was washed with HPLC-grade EtOH and dried with a heat gun at about 80 °C. Afterwards, the DSC was assembled by the procedure described above.

For the 1:1 dye-assembly process the same method as for the general method for single-dye copper(I) DSCs was used. The only difference is the usage of a dye-bath solution in CH₂Cl₂ of a 1 : 1 mixture of [Cu(MeCN)₄][PF₆] and the responding ancillary ligand in the second dipping step.

For the investigations of the influence of the co-adsorbent **Cheno** to the DSC efficiency, **Cheno** was added to the respective solution in later described ratio. The procedure of the cell assembly was the same like for the single-dye copper(I)-based DSCs.

The panchromatic co-sensitized copper(I) DSCs were assembled by different dipping procedures described in detail later in the corresponding chapter (*17 The History of “Blorange”*).

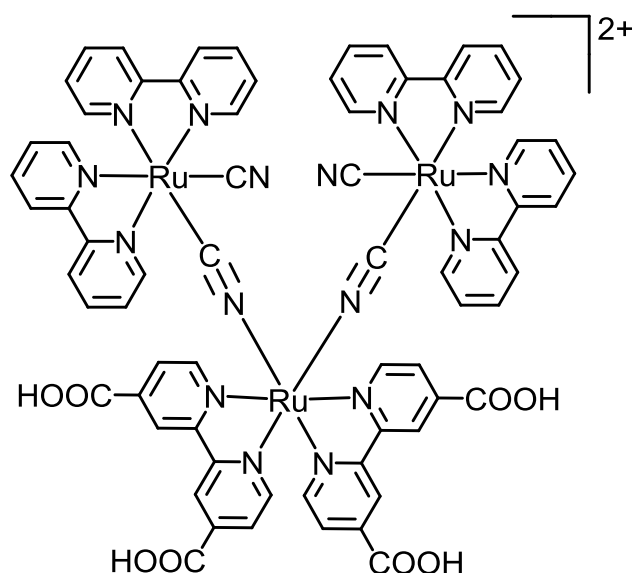
For each set of DSCs duplicate cells were assembled to confirm the reproducibility.

FROM BPY TO $N^{\wedge}NX$

The dye itself is the most important part in a dye-sensitized solar cell. Without the dye no harvesting of the sunlight in the visible spectrum is possible. The key role of all processes in a DSC has the dye. Everything starts with the dye and ends with it.

At the beginning of the history of DSCs, the knowledge about the interaction of semiconductors with photons have led to the basics of a DSC (see *4 Photovoltaic Technologies*).

But the tremendous achievement of Grätzel and O'Regan¹ was the sensitization of the nanocrystalline semiconductor with a dye. With this simple change an increase of 700% of cell efficiency was achieved. The solar cells had an efficiency of 7% while with before used bulk materials efficiencies of only 1% were achieved.

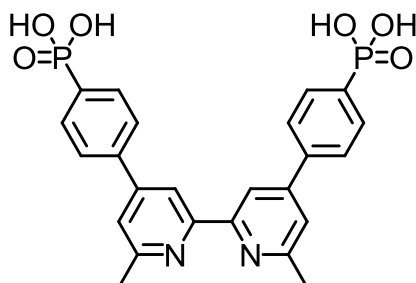


Scheme 30 Trinuclear ruthenium complex used by Grätzel & O'Regan in the breakthrough *Nature* paper from 1991.¹

This breakthrough in 1991 started the success story of the DSCs. As mentioned in the introduction, several different types of dyes have been investigated - from organic dyes over porphyrins to coordination complexes of different metals.

This research is based on copper(I) coordination complexes and their application as sensitizers in DSCs. Each heteroleptic complex consists of the Cu(I) metal ion and two different ligands. One ligand, the anchoring ligand, has functionalities that can interact with the semiconductor surface. Possible anchoring groups are carboxylic acids and phosphonic acids for example, as

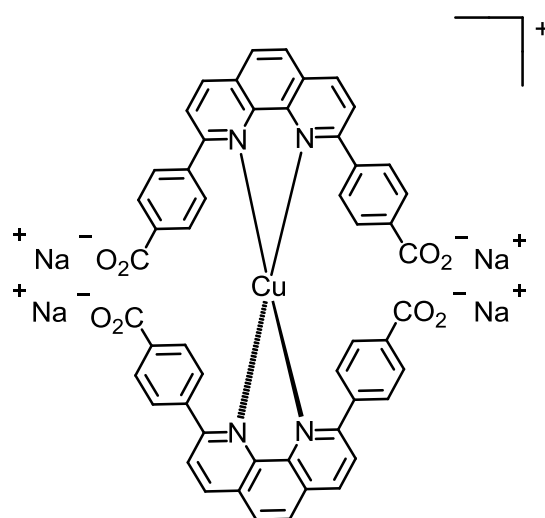
mentioned in 7.1.2 *Photosensitizer* (Scheme 5). Previously, it has been shown that for copper(I) dyes, phosphonic acid anchors lead to better DSC performances than carboxylic acid anchors. Therefore, in all investigations, **ALP1** was used for consistency and comparability (Scheme 31).



Scheme 31 Anchoring ligand **ALP1**

The second ligand is the ancillary ligand, and it is the structural and electronic properties of this ligand that are used to improve the DSC performance. Since the beginning of the research about Cu(I)-based DSCs in 1994 by Sauvage and co-workers⁹², bis(diimine) metal binding domains such as 2,2'-bipyridines and 1,10-phenanthrolines have been the ligands of choice.

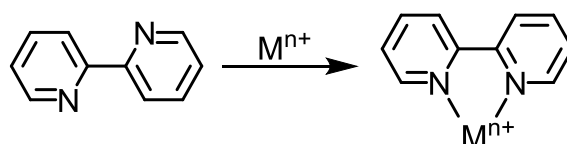
Sauvage and co-workers investigated a 1,10-phenanthroline based ligand (Scheme 32) with substituents in the positions next to the *N,N'*-coordination site to hinder flattening of the tetrahedral copper(I) coordination sphere and anchoring domains appended as peripheral substituents.



Scheme 32 Copper(I) complex for the first Cu(I)-based DSC by Sauvage and co-workers.

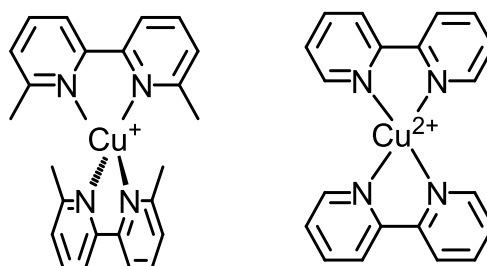
14. 2,2'-Bipyridine Ancillary Ligands

The state of the art ancillary ligands in copper-based DSCs are based on 2,2'-bipyridines (bpy). The free bpy ligand has a preferred *trans* conformation and undergoes a conformational change to *cis* caused by a chelate formation with a metal (Scheme 33). With the rotation around the C-C axis between the rings, bpy is able to act as a bidentate ligand. To simplify the reading all ligands in this thesis are presented in the final *cis* conformation.



Scheme 33 2,2'-Bipyridine in the preferred *trans* conformation and the conformational change to *cis* caused by chelate formation with a metal.

The ease of introducing different substituents in the 6,6'- and the 4,4'-positions of the bpy core (see 10 *Synthetic Strategy*) makes bpy a candidate for tuning the properties in electrochemical, photophysical and steric issues. The classical, easy and cheap Kröhnke pyridine synthesis method can be adapted to synthesise bipyridines with different substituent in 6,6'- and 4,4'-positions of the bpy core.¹²⁴ When using copper(I) complexes it is important to introduce at least methyl groups in the 6,6'-positions to introduce steric hindrance in order to hinder the flattening of the complex to the square planar configuration that is favoured by copper(II). This exhibits robust redox stability and the copper(I) complex stays in its preferred tetrahedral configuration (Scheme 34).

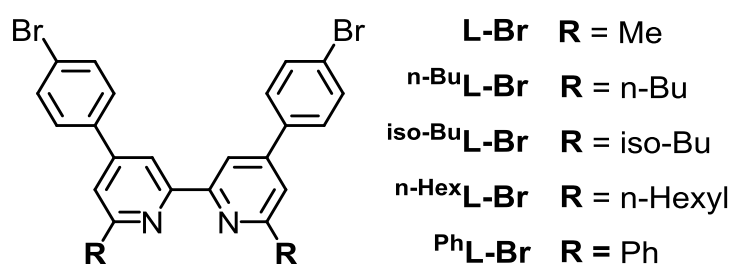


Scheme 34 Preferred configuration of a Cu(I) (tetrahedral) and a Cu(II) (square planar) complex.

14.1. Prologue: Substituents and Halogens

The initial investigations formed a part of a Master's project under the supervision of Dr. Sven Y. Brauchli. The project focused on the influence of the substituent in the 6,6'-positions of the bpy. In order to stabilize the Cu(I) oxidation state, bulky substituents in these positions have to be introduced. A short summary of this work is given here as it sets the scene for an investigation of peripheral halo-groups and rationalizes the choice of 6,6'-dimethyl substitution pattern in the bpy unit.

The standard substituent in the 6,6'-positions of bpy is methyl and has been used for several investigations in the Constable/Housecroft research group.^{100-102,106,129,133} The benefits of an extended π -system in the 4,4'-positions in the bpy unit have been shown by comparison to 6,6'-dimethylbipyridine.^{133,136} A standard ligand was therefore the ligand **L-Br** (Scheme 35). To investigate the influence of the substituent in the 6,6'-positions of (4-bromophenyl)-6,6'-dialkyl-2,2'-bipyridine, three ligands with a *n*-butyl- (**n-BuL-Br**), *iso*-butyl- (**iso-BuL-Br**) or *n*-hexyl-substituent (**n-HexL-Br**) (Scheme 35), respectively, were synthesized. In addition, Dr. Sven Y. Brauchli developed a (4-bromophenyl)-6,6'-diaryl-2,2'-bipyridine ligand where the substituent in the 6,6'-positions is phenyl (**PhL-Br**) (Scheme 35).



Scheme 35 Ancillary ligands **R^LL-Br** with different alkyl- or aryl-groups in the 6,6'-positions of bpy (R = Me, *n*-Bu, *iso*-Bu, *n*-Hexyl, Ph).

The corresponding copper(I) complexes [Cu(**R^LL-Br**)₂][PF₆] were synthesized and single crystal structures of [Cu(**L-Br**)₂][PF₆], [Cu(**n-BuL-Br**)₂][PF₆], [Cu(**iso-BuL-Br**)₂][PF₆] and [Cu(**PhL-Br**)₂][PF₆] were determined (Fig. 68). The space-filling representation emphasizes the need of a substituent in the 6,6'-positions to protect the Cu(I) centre and hinder the conformation

change to square-planar. Phenyl groups in the 6,6'-positions give π -stacking that leads to flattening (Fig. 68d).

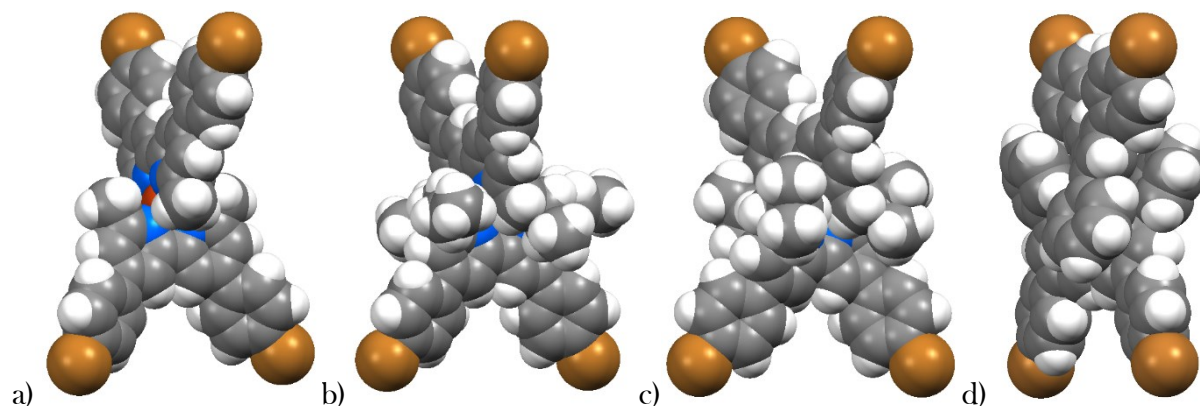


Fig. 68 Space-filling representations of the molecular structures (determined by X-ray crystallography) of the homoleptic copper(I) complexes of the ligands a) **L-Br**, b) ***n*-BuL-Br**, c) ***iso*-BuL-Br** and d) **PhL-Br** (C = grey; H = white; N = blue; Cu = red; Br = brown).

The typical UV-Vis absorption spectrum of a Cu(I) complex contains ligand-based $\pi^* \leftarrow \pi$ transitions in the UV region up to a wavelength of 400 nm and a characteristic metal-to-ligand charge transfer (MLCT) band at around 480 nm (Fig. 69).

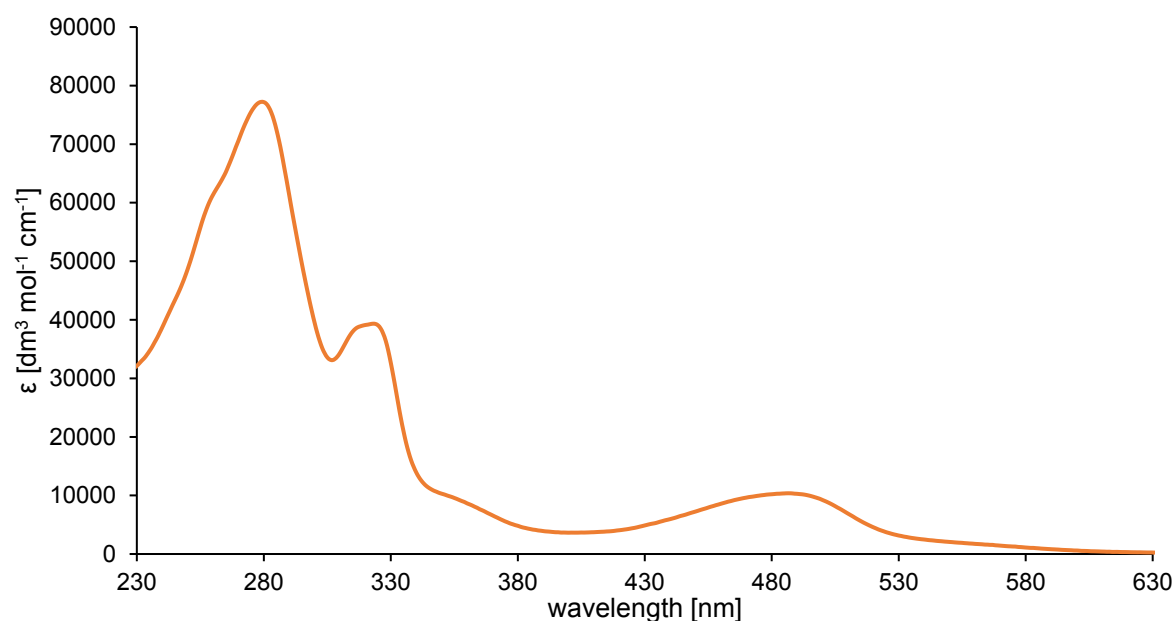


Fig. 69 UV-Vis absorption spectra of the homoleptic $[\text{Cu}(\text{L-Br})_2][\text{PF}_6]$ complex.

The complexes were used to assemble DSCs with the anchoring ligand **ALP1**. Table 4 summarizes the performance data of the DSCs on the day of sealing the cell and 2 days later.

Table 4 DSC performance data for DSCs containing dyes with the anchoring ligand **ALP1** and the ancillary ligands **^RL-Br** on the day of sealing the cells and 2 days after sealing the cell.

Dye	J_{sc} [mA cm ⁻²]	V_{oc} [mV]	ff [%]	η [%]	Relative η [%]
On the day of sealing the cell					
[Cu(ALP1)(L-Br) ⁺	4.77	503	73	1.76	24.9
[Cu(ALP1)(^{n-Bu} L-Br) ⁺	4.22	482	74	1.49	21.1
[Cu(ALP1)(^{iso-Bu} L-Br) ⁺	6.42	555	73	2.60	36.7
[Cu(ALP1)(^{n-Hex} L-Br) ⁺	4.80	502	72	1.74	24.6
[Cu(ALP1)(^{Ph} L-Br) ⁺	3.97	605	69	1.67	23.6
N719	15.37	648	71	7.08	100.0
2 days after sealing the cell					
[Cu(ALP1)(L-Br) ⁺	5.93	525	74	2.31	27.8
[Cu(ALP1)(^{n-Bu} L-Br) ⁺	5.42	501	73	1.99	24.0
[Cu(ALP1)(^{iso-Bu} L-Br) ⁺	6.91	576	72	2.87	34.6
[Cu(ALP1)(^{n-Hex} L-Br) ⁺	5.51	521	73	2.09	25.2
[Cu(ALP1)(^{Ph} L-Br) ⁺	6.96	606	74	3.10	37.4
N719	17.20	684	71	8.30	100.0

All cells show a gain in values of J_{sc} and V_{oc} what is likely due to dye aggregation and reorganization on the surface over time¹³⁷⁻¹³⁹. The highest energy conversion efficiencies were obtained for DSCs with sterically ancillary ligands like ^{iso-Bu}**L-Br** and ^{Ph}**L-Br**. They had an overall efficiency η of 2.87 and 3.10%, respectively. The DSCs with ancillary ligands containing straight chains (**L-Br**, ^{n-Bu}**L-Br** and ^{n-Hex}**L-Br**) had an η between 1.99 and 2.31% on day 2 after sealing the cell. The best EQE_{max} value of 50% at 470 nm was obtained by a DSC containing ^{iso-Bu}**L-Br** (Fig. 70). All other DSCs had an EQE_{max} value between 38 and 46%.

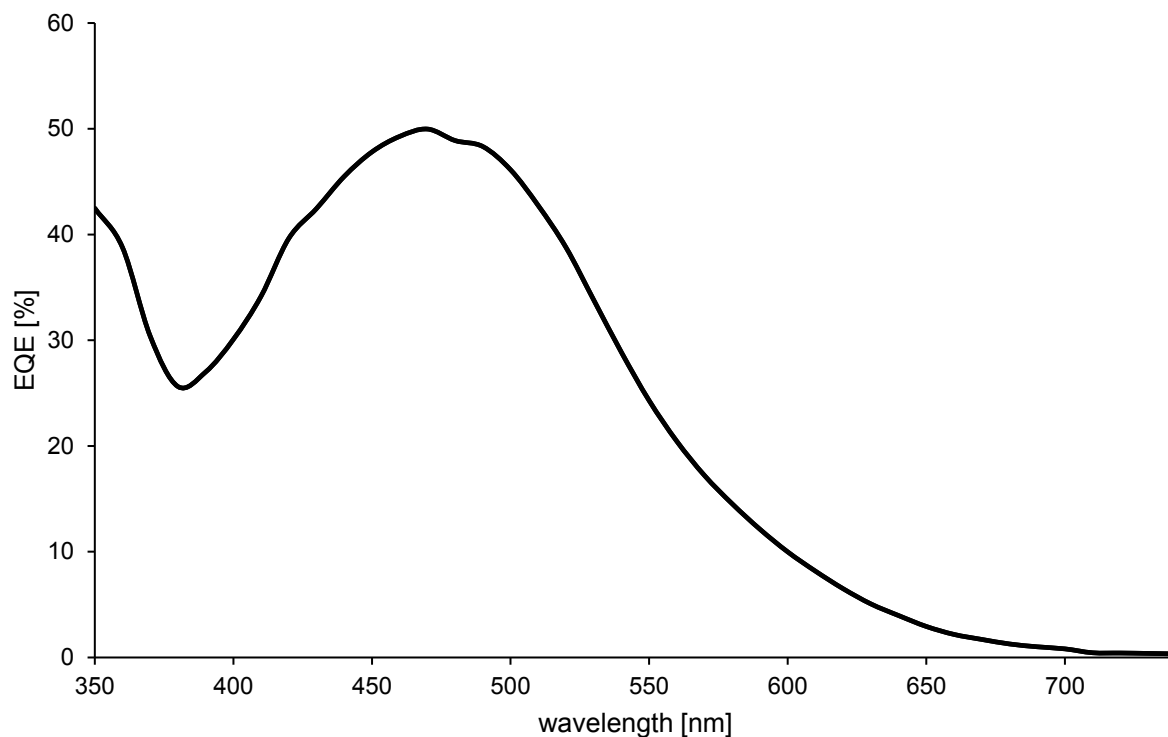
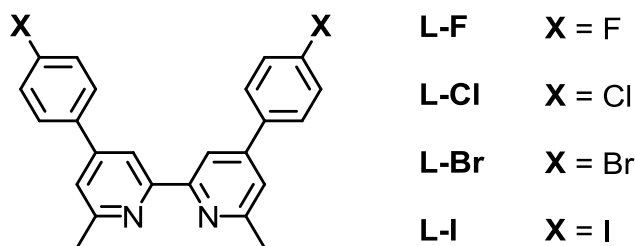


Fig. 70 EQE curve on the day of sealing the cell for a DSC containing a copper(I) dye with the anchoring ligand **ALP1** and the ancillary ligand ^{iso-Bu}**L-Br**.

Not only do substituents in the 6,6'-positions have an impact on the efficiency of the DSC, the halogen on the phenyl rings in the 4,4'-positions of the bpy core also affects the performance.

The relatively good photoconversion efficiencies obtained using the ancillary ligand **L-Br** lead to a systematic study of halo-substituted ligands, and a comparison of the effects of introducing peripheral fluorine (**L-F**), chlorine (**L-Cl**), bromine (**L-Br**) and iodine (**L-I**) substituents (Scheme 36).



Scheme 36 Ancillary ligands **L-X** with different halogens (X = F, Cl, Br, I).

DSC performance measurements with the anchoring ligand **ALP1** and the ancillary ligands **L-F**, **L-Cl**, **L-Br** and **L-I** have shown that after a period of one week all three halogen-containing ancillary ligands are better than the DSC with the ancillary ligand **L-Br** (Table 5).

Table 5 DSC performance data for DSC containing copper(I) dyes with the anchoring ligand **ALP1** and the ancillary ligands **L-X** on the day of sealing the cells and 7 days after sealing the cell.

Dye	J_{sc} [mA cm ⁻²]	V_{oc} [mV]	ff [%]	η [%]	Relative η [%]
On the day of sealing the cell					
[Cu(ALP1)(L-F) ⁺	6.70	527	68	2.41	33.8
[Cu(ALP1)(L-Cl) ⁺	6.00	522	70	2.18	30.6
N719 ^a	16.66	637	67	7.13	100.0
[Cu(ALP1)(L-Br) ⁺	6.49	525	72	2.45	33.0
[Cu(ALP1)(L-I) ⁺	6.68	582	74	2.88	38.8
N719 ^b	16.08	641	72	7.43	100.0
7 days after sealing the cell					
[Cu(ALP1)(L-F) ⁺	6.62	556	69	2.54	33.7
[Cu(ALP1)(L-Cl) ⁺	6.95	565	66	2.60	34.5
N719 ^a	16.42	692	66	7.53	100.0
[Cu(ALP1)(L-Br) ⁺	6.46	561	68	2.45	32.1
[Cu(ALP1)(L-I) ⁺	7.10	604	74	3.16	41.4
N719 ^b	16.21	662	71	7.63	100.0

^a**N719** reference cell used in conjunction with DSCs containing dyes [Cu(**ALP1**)(**L-F**)⁺ and [Cu(**ALP1**)(**L-Cl**)⁺. ^b**N719** reference cell used in conjunction with DSCs containing dyes [Cu(**ALP1**)(**L-Br**)⁺ and [Cu(**ALP1**)(**L-I**)⁺.

The highest η value was obtained by a DSC with **L-I** as the ancillary ligand. The cell had an efficiency of 3.16% what was the highest ever measured for copper(I)-based DSCs at the time. It had a J_{sc} value of 7.10 mA cm⁻², an V_{oc} value of 604 mV and reached an EQE_{max} value of 51%.

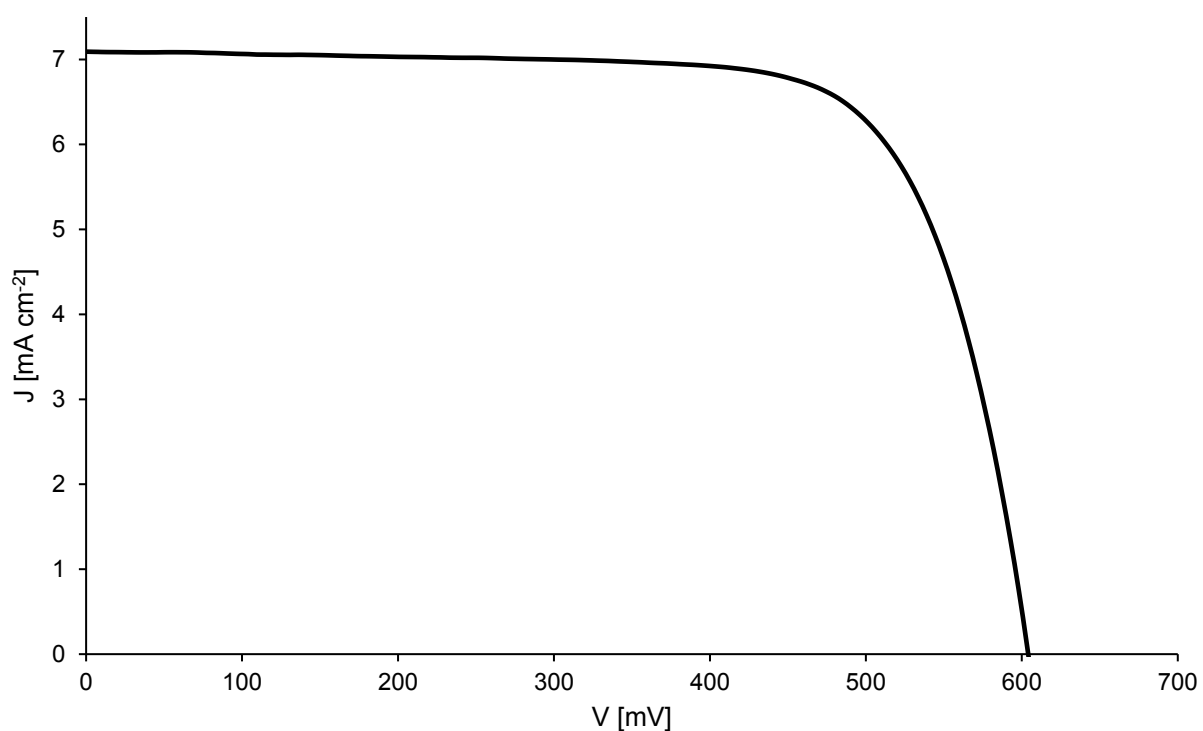


Fig. 71 *J-V* curve of the best performing DSC out of all halogen containing ancillary ligands ([Cu(ALP1)(L-I)]⁺) on day 7 after sealing the cell.

Both Master studies, that with the 6,6'-dialkyl or 6,6'-diaryl substitution patterns and that with the halo-substituted compounds, demonstrated that J_{sc} values of 7.0 mA cm^{-2} , an V_{oc} of 600 mV, an EQE_{max} value of 50% and a relative overall efficiency of 40% are threshold values for optimal performing copper(I)-based DSCs. It is important to note that DSC parameters vary with the solar simulator instrument used¹³⁶, and that all measurements in this thesis employed the same instrument.

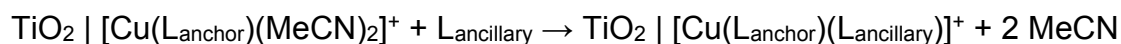
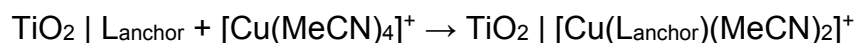
14.2. Minimizing the Excess of Ancillary Ligand and the Total Process Time in the Dye-Assembly Process

The standard ligand-exchange dye-assembly process consists of two dipping steps. In the first dipping step, the anchoring ligand is applied to the semiconductor surface. The final heteroleptic Cu(I) complex is achieved by ligand exchange during the second dipping step where the anchoring ligand functionalized photoelectrode is immersed in a homoleptic [Cu(L_{ancillary})₂][PF₆] complex solution (Equation 11). This dye-assembly process was also adopted by the research group of Robertson at the University of Edinburgh.¹⁴⁰



Equation 11 Ligand-exchange dye-assembly process with a homoleptic [Cu(L_{ancillary})₂][PF₆] complex.

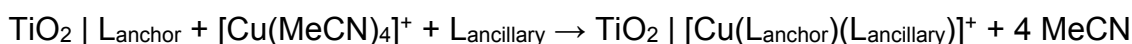
But in this dye-assembly process, one ancillary ligand is wasted due to ligand exchange. In order to optimize the atom economy, Dr. Nik Hostettler developed a dipping procedure using a sequential approach of the metal ion and the ancillary ligand.⁹⁰ In this latter investigation, a Zn(II) metal ion and a terpyridine-based ancillary ligand was used. The DSCs worked with the new strategy. Dr. Sven Y. Brauchli adapted this method to Cu(I) DSCs (Equation 12). After the photoelectrode had been dipped into the anchoring ligand solution for 1 day, the functionalized electrode was immersed in a Cu(I) solution for 1 day. [Cu(MeCN)₄][PF₆] was used as the source of copper(I). This step converts the bound anchoring ligand into [Cu(L_{anchor})(MeCN)₂]⁺ (the coordination of the MeCN ligands is assumed). In the final dipping step, the ancillary ligand is added by dipping the photoelectrode in an ancillary ligand solution for 3 days.



Equation 12 Stepwise dye-assembly process with sequential approach of anchoring ligand, the metal ion and the ancillary ligand.

In this stepwise dye-assembly process the synthesis of the homoleptic $[\text{Cu}(\text{L}_{\text{ancillary}})_2][\text{PF}_6]$ complex is not needed. This is a clear advantage when the homoleptic Cu(I) complex is too labile and cannot be isolated. But in the stepwise dye-assembly process an additional dipping step is introduced that prolongs the total process time.

In order to combine the minimization of excess of ancillary ligand and a short total process time a new dye-assembly process was developed. Here, the anchoring ligand functionalized photoelectrode is immersed in a 1 : 1 mixture of the Cu(I) source $[\text{Cu}(\text{MeCN})_4][\text{PF}_6]$ and the ancillary ligand. Both stock solutions in CH_2Cl_2 have a concentration of 0.1 mM and is consistent with the dye-bath concentration of the general ligand-exchange dye-assembly process. In this dye-assembly process the need to prepare the homoleptic copper(I) complex is also eliminated. The whole heteroleptic complex is assembled *in situ* in one dipping step after the semiconductor has been functionalized with the anchoring ligand (Equation 13).



Equation 13 1:1 dye-assembly process with a 1 : 1 mixture of $[\text{Cu}(\text{MeCN})_4][\text{PF}_6]$ and the ancillary ligand in the second dipping step.

The investigations were executed with the anchoring ligand **ALP1** and the ancillary ligand **L-I**. This combination was chosen because low-temperature NMR studies (Fig. 36) gave the evidence of a second species and a crystal grown from the solution turned out to be the heteroleptic $[\text{Cu}(\text{L-I})(\text{MeCN})_2][\text{PF}_6]$ complex. In conclusion, the dye-bath solution of **L-I** in *Part 14.1* consisted of a mixture of homoleptic $[\text{Cu}(\text{L-I})_2][\text{PF}_6]$ complex and heteroleptic $[\text{Cu}(\text{L-I})(\text{MeCN})_2][\text{PF}_6]$ complex (Fig. 72).

The anchoring ligand functionalized photoelectrode was dipped in a 1 : 1 CH_2Cl_2 solution of $[\text{Cu}(\text{MeCN})_4][\text{PF}_6]$ and **L-I** for 3 days. The electrode became pale red-orange and the colour persisted after drying. The DSC performance data of duplicate cells over a period of one week is summarized in Table 6.

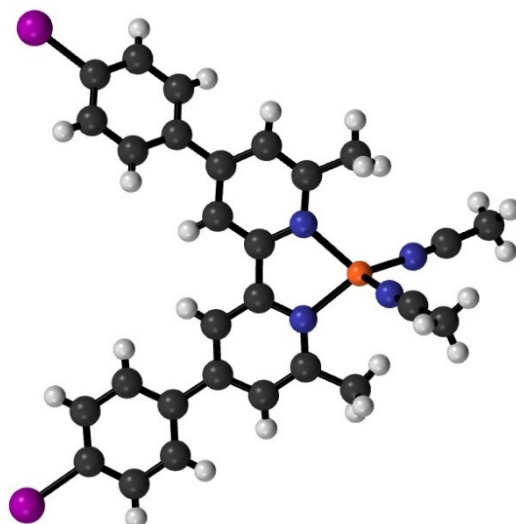


Fig. 72 X-ray crystallographic structure of the $[\text{Cu}(\mathbf{L-I})(\text{MeCN})_2]^+$ cation in $[\text{Cu}(\mathbf{L-I})(\text{MeCN})_2][\text{PF}_6]$.

Table 6 DSC performance data for two independent DSCs containing of the anchoring ligand **ALP1** and the ancillary ligand **L-I** assembled in the by the 1:1 dye-assembly process on the day of sealing the cells, 3 days and 7 days after sealing the cell.

Dye	J_{sc} [mA cm ⁻²]	V_{oc} [mV]	FF [%]	η [%]	Relative η [%]
On the day of sealing the cell					
$[\text{Cu}(\mathbf{ALP1})(\mathbf{L-I})]^+$	6.82	551	69	2.59	34.4
$[\text{Cu}(\mathbf{ALP1})(\mathbf{L-I})]^+$	7.01	559	70	2.75	36.5
N719	16.88	641	70	7.54	100.0
3 days after sealing the cell					
$[\text{Cu}(\mathbf{ALP1})(\mathbf{L-I})]^+$	6.97	584	70	2.83	37.3
$[\text{Cu}(\mathbf{ALP1})(\mathbf{L-I})]^+$	6.93	588	68	2.75	36.3
N719	16.54	671	68	7.58	100.0
7 days after sealing the cell					
$[\text{Cu}(\mathbf{ALP1})(\mathbf{L-I})]^+$	6.85	587	70	2.80	36.0
$[\text{Cu}(\mathbf{ALP1})(\mathbf{L-I})]^+$	6.96	587	66	2.71	34.9
N719	16.55	684	69	7.77	100.0

The performances of both DSCs are comparable. They have J_{sc} values of 6.82 and 7.01 mA cm⁻² on the day of sealing the cell, and values $V_{oc} = 551$ and 559 mV, respectively, are similar. With a good f of 69 and 70%, respectively, they reach overall efficiencies of 2.59 and 2.75%. Comparable results with regard to the DSC with the ligand-exchange dye-assembly process ($\eta = 2.88\%$, Table 5) are achieved with the 1:1 dye-assembly process. The DSCs are also stable over a period of 7 days. As seen in the J - V curves in Fig. 73, the J_{sc} stays on a constant level whereas the V_{oc} improves from 551 or 559 mV, respectively, to 587 mV on day 7 after sealing the cell. On day 7 after sealing the cell both DSCs show good efficiencies ($\eta = 2.80$ and 2.71%, Table 6). They do not reach the efficiency of 3.16% of the DSC assembled by the ligand-exchange dye-assembly process (Table 5) but are still at the same good level of performance.

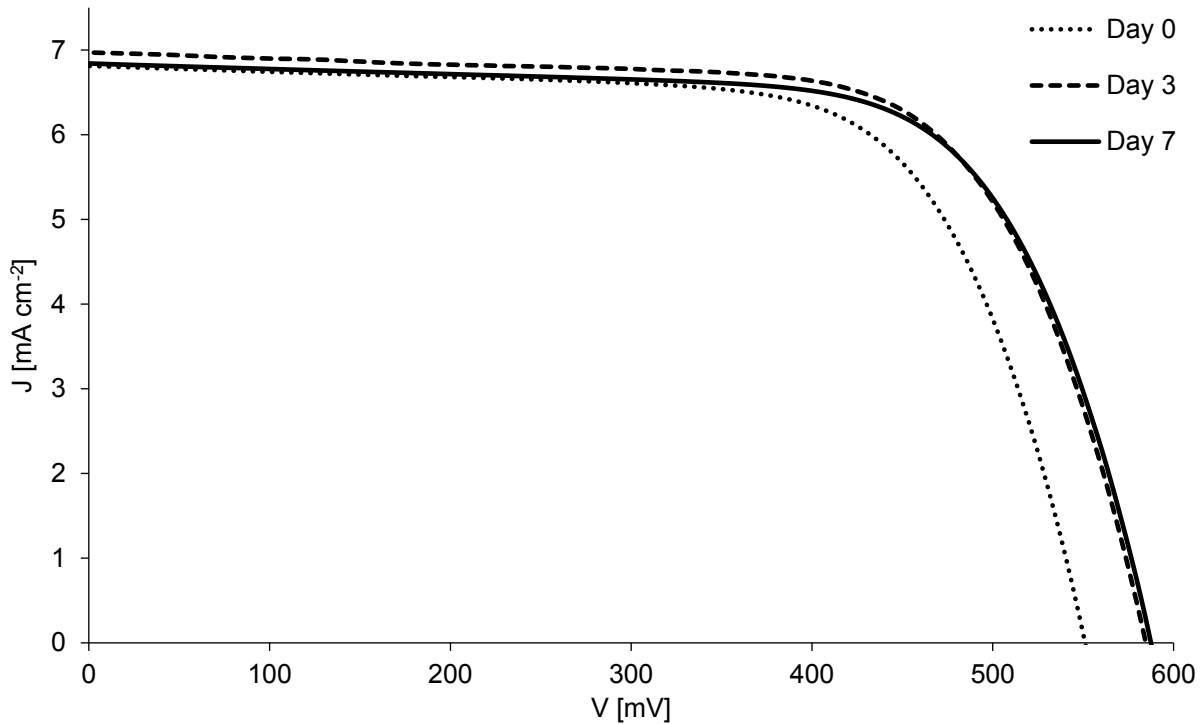


Fig. 73 J - V curves of DSCs assembled by the 1:1 dye-assembly process on the day of sealing the cell, 3 days and 7 days after.

Because there is little change in J_{sc} , the EQE spectra vary little over a 7 day period (Fig. 74). They have with 470 nm the identical wavelength of the EQE_{max} value than all Cu(I) DSCs (compare Fig. 70). The shape of the curve varies little and show maxima at around 46% on the day of cell

fabrication. They drop by maximum 0.5% what confirms the stability of the J_{sc} over one-week period.

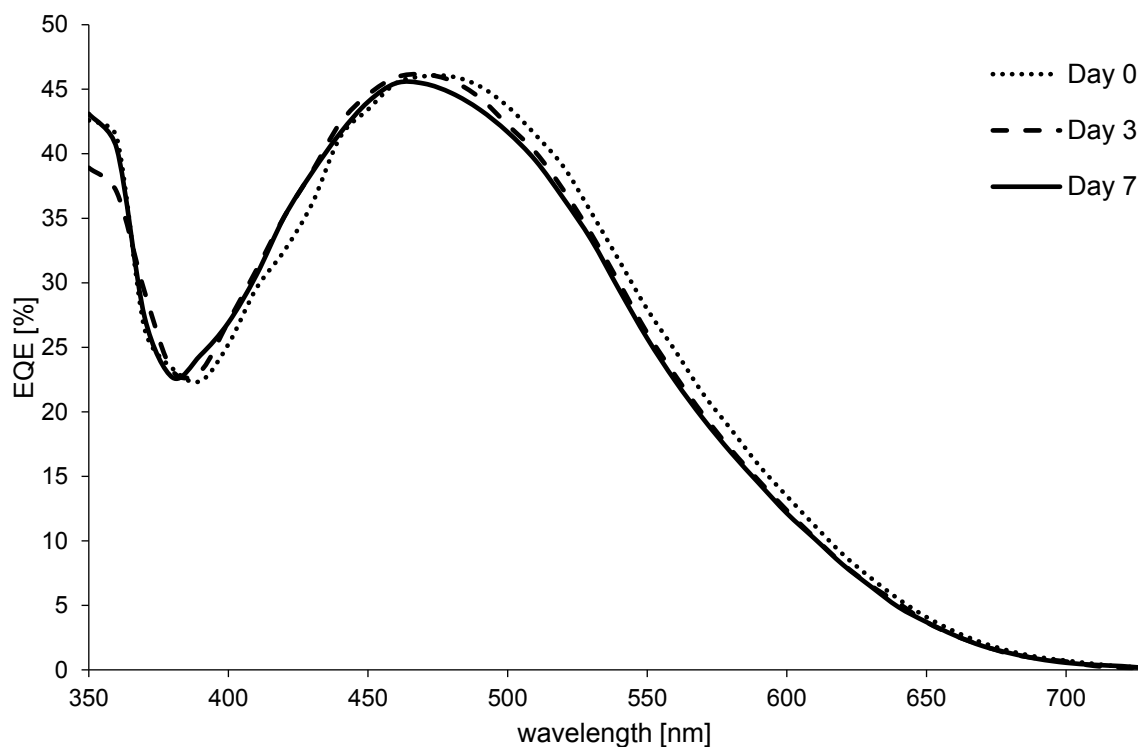


Fig. 74 EQE spectra of DSCs assembled by the 1:1 dye-assembly process on the day of sealing the cell, 3 days and 7 days after.

Overall, comparable performances are achieved for DSCs assembled by the ligand-exchange or the 1:1 dye-assembly process. The differences are not significant and the necessity of the synthesis of the homoleptic $[\text{Cu}(\text{L}_{\text{ancillary}})_2][\text{PF}_6]$ complex is not needed. This dye-assembly process also prevents the wastage of one equivalent of ancillary ligand and shortens the total process time with regard to the stepwise dye-assembly process from 5 days to 4 days. With this 1:1 dye-assembly process the excess of ancillary ligand is minimized and the total process time is at the level of the standard ligand-exchange dye-assembly process.

Whether or not the total process time could be shortened even more was next investigated. The newly developed 1:1 dye-assembly process was used but the dipping time of the second dipping step was altered. The typical soaking time for the second dipping step in a homoleptic $[\text{Cu}(\text{L}_{\text{ancillary}})_2][\text{PF}_6]$ complex solution is 3 days. In the ligand-exchange dye-assembly process it is

necessary because of the required time for the complete ligand-exchange on the semiconductor surface. However, less time should be needed for the ligand exchange (MeCN for ancillary ligand) in the 1:1 dye-assembly process as in the ligand-exchange dye-assembly process involving the homoleptic complex. The applicability of a shorter dipping time was investigated by immersing the anchoring ligand functionalized photoelectrode in a 1 : 1 mixture of [Cu(MeCN)₄][PF₆] and the ancillary ligand for 3 days or only 1 day.

The same ligand combination of **ALP1** and **L-I** was used. The dye-bath conditions were constant. Only the dipping time was adjusted. Table 7 compares the DSC performance data of DSCs assembled by the 1:1 dye-assembly process with a dipping time of 1 day and 3 days, respectively.

Table 7 DSC performance data for DSCs containing of the anchoring ligand **ALP1** and the ancillary ligand **L-I** assembled in the by the 1:1 dye-assembly process with a dipping time of 1 or 3 days for the second dipping step on the day of sealing the cells, 3 days and 7 days after sealing the cell.

Dye	dipping time [days]	J_{sc} [mA cm ⁻²]	V_{oc} [mV]	ff [%]	η [%]	Relative η [%]
On the day of sealing the cell						
[Cu(ALP1)(L-I) ⁺	1	5.53	530	71	2.09	28.3
[Cu(ALP1)(L-I) ⁺	3	7.01	559	70	2.75	37.2
N719		15.93	647	72	7.39	100.0
3 days after sealing the cell						
[Cu(ALP1)(L-I) ⁺	1	5.71	583	71	2.37	32.0
[Cu(ALP1)(L-I) ⁺	3	6.93	588	68	2.75	37.1
N719		15.40	677	71	7.40	100.0
7 days after sealing the cell						
[Cu(ALP1)(L-I) ⁺	1	5.75	578	71	2.36	32.7
[Cu(ALP1)(L-I) ⁺	3	6.96	587	66	2.71	37.5
N719		15.18	685	69	7.22	100.0

Both dipping times resulted in working DSCs. The DSC with a dipping time of 1 day has an overall efficiency of 2.09% and a ff of 71% (Table 7). The good ff implies the good performance of the cell also with shorter dipping times. The DSC with a dipping time has an η of 2.75% as seen before. The biggest difference is observable in the J_{sc} . The 3 day dipping time gave a

J_{sc} value over 7 mA cm^{-2} . But the DSC with a dipping time of 1 day only has a J_{sc} value of 5.53 mA cm^{-2} . The difference in J_{sc} stays constant over a period of 7 days. On day 7 after sealing the cell the DSC with a dipping time of 3 days still had a J_{sc} value of 6.96 mA cm^{-2} whereas the DSC with a dipping time of 1 day still had a J_{sc} of just 5.75 mA cm^{-2} . In the V_{oc} the DSC with 3 days dipping time gained from 530 to 578 mV. At the day of sealing the cell the difference in V_{oc} was almost 30 mV. But on day 3, the values of 583 and 588 mV are almost identical. After a period of 7 days both DSCs have comparable V_{oc} values (578 mV for 1 day dipping time; 587 mV for 3 days dipping time). In the end, the DSC with a dipping time of 3 days performs better than the DSC with a dipping time of 1 day ($\eta = 2.36\%$ for 1 day dipping time, $\eta = 2.75\%$ for 3 days dipping time). A longer dipping time results in improvement of the J_{sc} value and slightly better V_{oc} values.

The enhanced absorption of DSCs with a longer dipping time can also be observed by solid-state absorption spectroscopy. A transparent electrode was dipped in the bath by the 1:1 dye-assembly process and the before investigated dipping times of 1 and 3 days was used for the second dipping step. The solid-state UV-Vis absorption spectra were recorded and are displayed in Fig. 75.

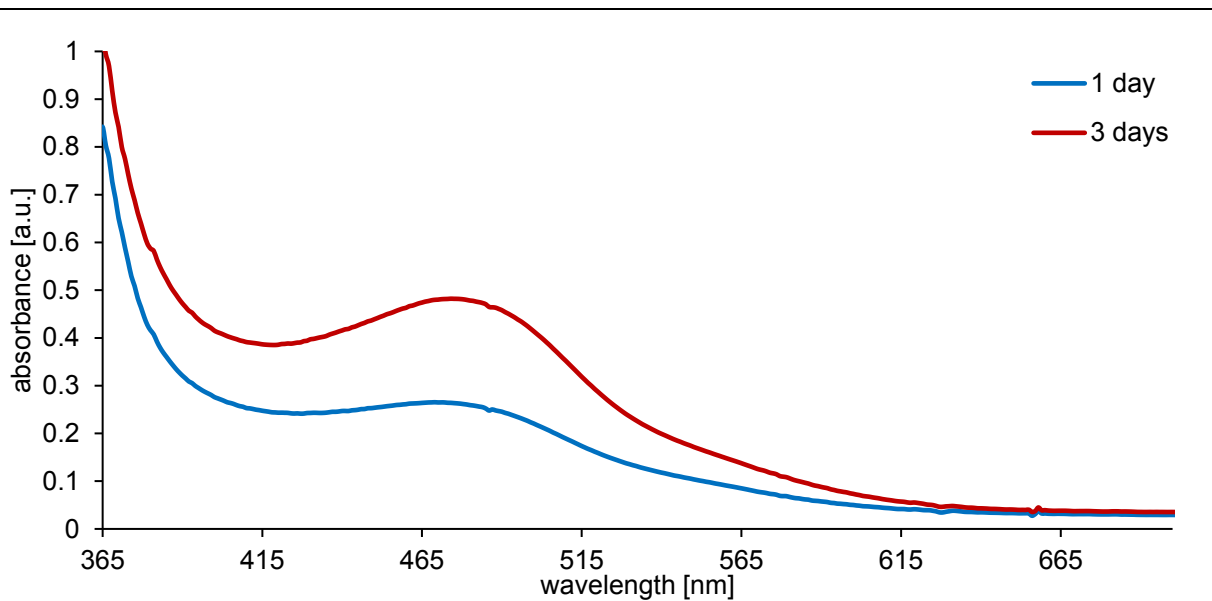


Fig. 75 Solid-state UV-Vis spectra of dye-functionalized transparent photoelectrodes with the 1:1 dye-assembly process with dipping times of 1 or 3 days in the second dipping step.

Both curves had an absorption maximum at 480 nm which is consistent with other Cu(I) dye-functionalized photoelectrodes^{141,142}. But the difference in intensities is significant. The electrode that was immersed for 1 day had an absorbance of 0.26 a.u. at its maximum and the

electrode that was immersed for 3 days had an absorbance of 0.48 a.u. at its maximum. The higher absorption for the longer dipping time was consistent over the whole spectrum and the difference is also visible by eye (Fig. 76) with photoelectrode with a dipping time of 3 days (Fig. 76 b) having a much darker colour.

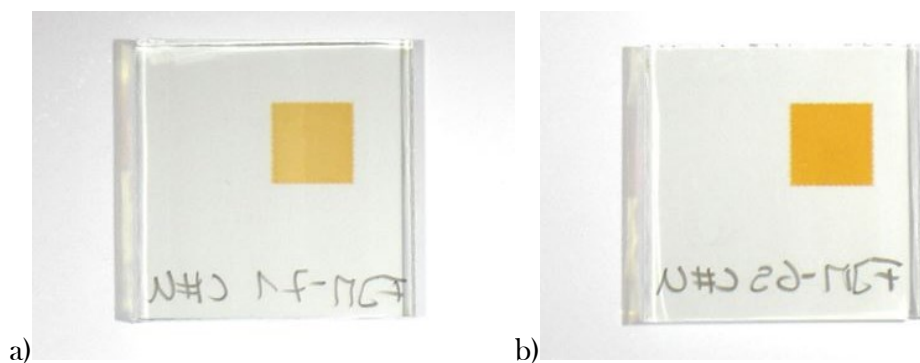


Fig. 76 Photographs of dye-functionalized transparent photoelectrodes with the 1:1 dye-assembly process with dipping times of (a) 1 or (b) 3 days in the second dipping step.

The difference in absorption and J_{sc} can also be expressed by the results of the EQE measurements. The spectra of the 7 day old DSCs are displayed in Fig. 77. The DSC with a dipping time of 1 day had an EQE_{max} value of 47.8% at 480 nm. The EQE_{max} value of the DSC that had been 3 days in the dye bath is lower ($EQE_{max} = 44.7\%$ at 470 nm). However, increased response at higher and lower energies in the EQE spectrum for the 3 day soaking time were observed. The overall EQE response is higher with the longer dipping time as can be seen from the higher value of J_{sc} (7.01 mA cm^{-2} vs 5.53 mA cm^{-2} , Table 7). The results show that in a DSC, not only are the absorption properties of the dye significant, other processes also influence the DSC performance.

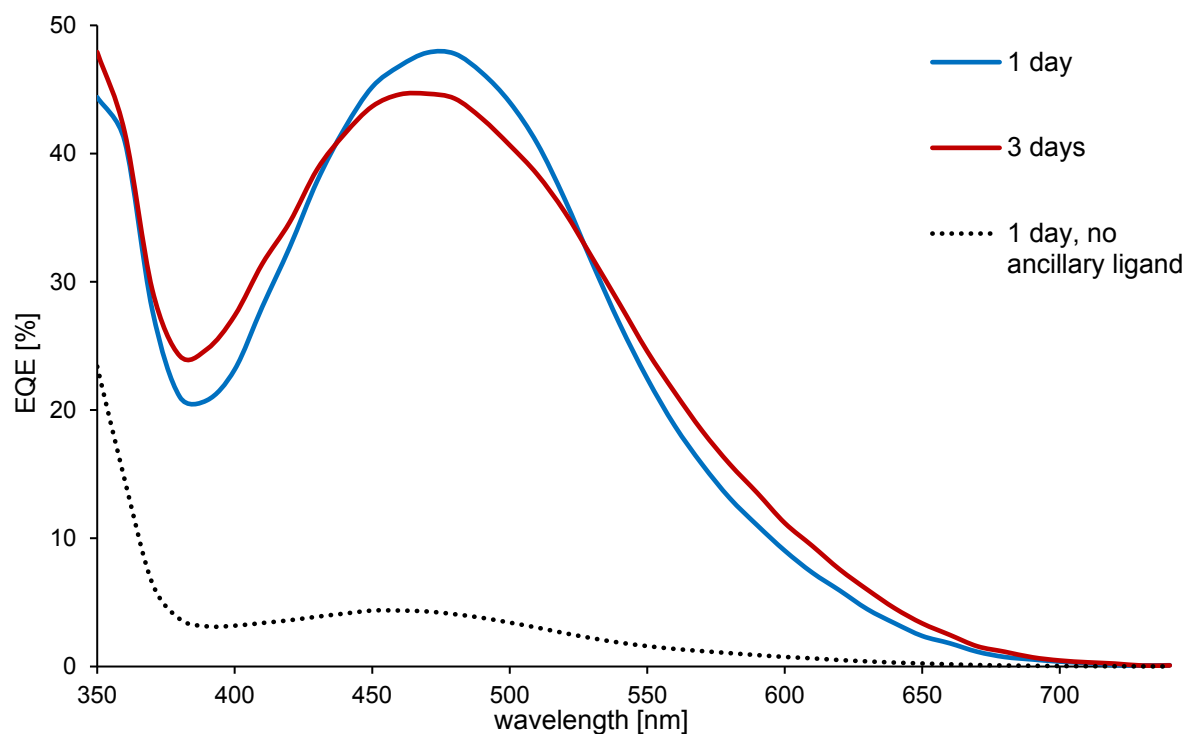


Fig. 77 Comparison of the EQE spectra of DSCs assembled by the 1:1 dye-assembly process with dipping times of 1 or 3 days in the second dipping step 7 days after sealing the cell. The dotted line displays the EQE spectra of a DSC without addition of the ancillary ligand in the second dipping step.

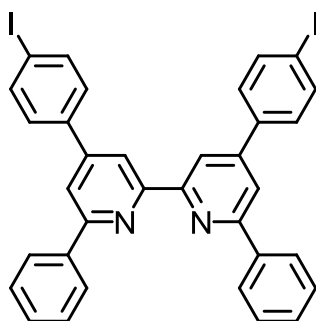
A control experiment was carried out in order to verify the role of the ancillary ligand. An anchoring ligand functionalized photoelectrode was dipped in a $[\text{Cu}(\text{MeCN})_4][\text{PF}_6]$ solution for 1 day. After washing and drying, the electrode had a pale-yellow colour. It is assumed at this stage that the surface bound complex is $[\text{Cu}(\text{ALP1})(\text{MeCN})_2]^+$ (The isolated $[\text{Cu}(\text{L-I})(\text{MeCN})_2][\text{PF}_6]$ is pale-orange.). The DSC was assembled and the EQE spectrum was measured (Fig. 77, dotted black). The EQE spectrum of this cell was very poor and had an EQE_{max} value of 4.4% at 460 nm. This demonstrates that the heteroleptic bis-diimine complex is required in order to achieve a good functioning DSC.

In conclusion, the 1:1 dye-assembly process gives comparable DSC performance to the standard ligand-exchange dye-assembly process and a dipping time of 3 days in the second dipping step is necessary to achieve higher efficiencies. The excess of ancillary ligand can be minimized and a total process time of 4 days is required for well performing Cu(I) DSCs. But it has to be noted,

that each individual dye-assembly process has to be adjusted to the ligand combination as is discussed later in the thesis.

14.3. Combination of the Best Performing Substituent and Halogen

Based on the investigations of the Master studies, and the subsequent investigations using ancillary ligand **L-I**, an obvious target was to combine the most promising peripheral halogen with the most effective 6,6'-substituent. This led to ancillary ligand **PhL-I** (Scheme 37).



Scheme 37 Ancillary ligand **PhL-I**.

The synthesis of the ligand **PhL-I** was straight forward by the Kröhnke method (Scheme 20). But the complexation with $[\text{Cu}(\text{MeCN})_4][\text{PF}_6]$ in MeCN or CH_2Cl_2 was not successful. No stable homoleptic complex was achieved. It has to be noted, that this cannot be due to steric hindrance of the four phenyl substituents around the Cu(I) ion because the bromo-analogue had been isolated previously (Fig. 68d).

Because of that the standard ligand-exchange dipping procedure could not be used. However, the stepwise - or the 1:1 dipping procedures have been developed exactly for a case like this. In both dipping procedures the homoleptic Cu(I) complex is not needed and the individual usage of the ligand and the Cu(I) source $[\text{Cu}(\text{MeCN})_4][\text{PF}_6]$ is necessary. The DSCs were assembled once by the 1:1 dipping procedure and once by the stepwise dipping procedure. The 1:1 dipping procedure involves the functionalization of the semiconductor surface with the anchoring ligand **ALP1** and dipping of this electrode into a solution of the 1:1 mixture of the ancillary ligand **PhL-I** and $[\text{Cu}(\text{MeCN})_4][\text{PF}_6]$. In the stepwise method the anchoring ligand-functionalized electrode is immersed first in a $[\text{Cu}(\text{MeCN})_4][\text{PF}_6]$ solution and afterwards in a solution containing the ancillary ligand **PhL-I**.

Table 8 summarizes the DSC data of both dipping procedures. It is first of all obvious that the 1:1 dipping procedure cannot be used for this ligand combination. On the day of sealing the cell a J_{sc} value of 0.61 mA cm⁻² and an V_{oc} value of 438 mV was measured. With a fill factor of only 39%, an overall efficiency of 0.10% is achieved. An increase in performance over a period of one week due to dye aggregation and reorganisation is also observed for this DSC. On day 7 all key factors increased ($J_{sc} = 1.87$ mA cm⁻², $V_{oc} = 507$ mV, $ff = 59\%$) and an efficiency of 0.56% was achieved.

Table 8 DSC performance data for DSC containing of the anchoring ligand **ALP1** and the ancillary ligand **^{Ph}L-I** assembled by a 1:1 or stepwise dipping procedure on the day of sealing the cells, 3 days and 7 days after sealing the cell.

Dye	procedure	J_{sc} [mA cm ⁻²]	V_{oc} [mV]	ff [%]	η [%]	Relative η [%]
On the day of sealing the cell						
[Cu(ALP1)(^{Ph}L-I) ⁺	1:1	0.61	438	39	0.10	1.4
[Cu(ALP1)(^{Ph}L-I) ⁺	stepwise	7.73	517	68	2.71	37.4
N719		16.41	635	69	7.23	100.0
3 days after sealing the cell						
[Cu(ALP1)(^{Ph}L-I) ⁺	1:1	1.41	520	49	0.36	5.0
[Cu(ALP1)(^{Ph}L-I) ⁺	stepwise	7.77	545	64	2.69	37.0
N719		15.79	665	69	7.28	100.0
7 days after sealing the cell						
[Cu(ALP1)(^{Ph}L-I) ⁺	1:1	1.87	507	59	0.56	7.8
[Cu(ALP1)(^{Ph}L-I) ⁺	stepwise	8.10	561	58	2.61	36.5
N719		15.85	656	69	7.16	100.0

In contrast to the 1:1 dipping procedure the stepwise dipping procedure resulted in a well performing DSC. On the day of sealing the cell a high J_{sc} value ($J_{sc} = 7.73$ mA cm⁻²) was measured. With a moderate V_{oc} of 517 mV and a ff of 68%, an overall efficiency of 2.71% was achieved. Over a period of one week the key parameters J_{sc} and V_{oc} increased. The J_{sc} value of 8.10 mA cm⁻² is the highest J_{sc} value of all bpy-based ancillary ligands in this thesis. The high J_{sc} is equivalent to a good EQE response. Fig. 78 displays the EQE curves of a DSC assembled by the stepwise dipping procedure.

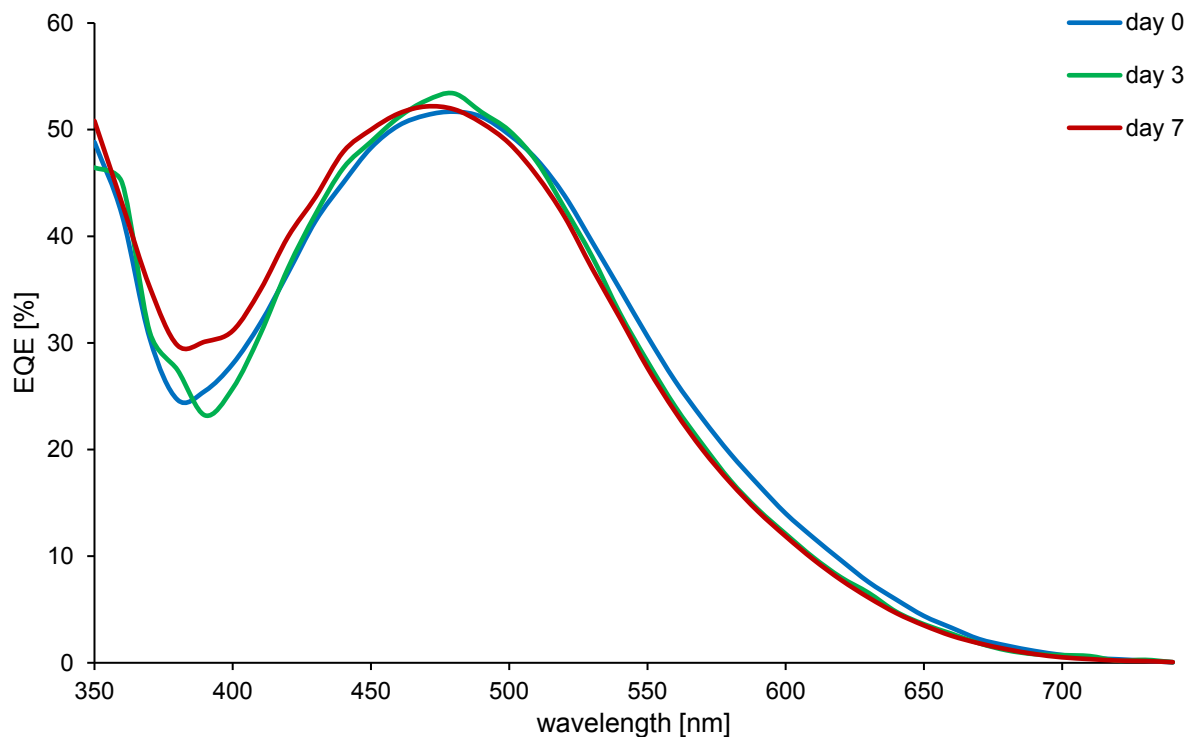


Fig. 78 EQE curves of a DSC assembled by the stepwise dipping procedure containing the dye $[\text{Cu}(\text{ALP1})(\text{PhL-I})]^+$ on the day of sealing the cell, 3 days after and 7 days after sealing the cell-

EQE_{max} values over 50% at $\lambda_{max} = 480$ nm were measured. The V_{oc} is still moderate ($V_{oc} = 561$ mV vs 588 mV for a DSC with the dye $[\text{Cu}(\text{ALP1})(\text{L-I})]^+$) but the ff dropped to 58%. The non-optimal fill factor meant that a high η could not be achieved. On day 3 after sealing the cell a η of 2.69% and on day 7 after sealing the cell one of 2.61% were measured. In contrast to the best performing DSCs containing dyes with the ^RL-Br and L-X ancillary ligands, efficiencies over 3.00% were not observed ($\eta = 3.10\%$ for ^{Ph}L-Br, Table 4; $\eta = 3.16\%$ for L-I, Table 5). However, the high J_{sc} value did result in a high EQE_{max} value (Fig. 79). The curve has a typical shape for Cu(I)-based DSCs and a maximum of 52.2% at 470 nm on day 7 after sealing the cell.

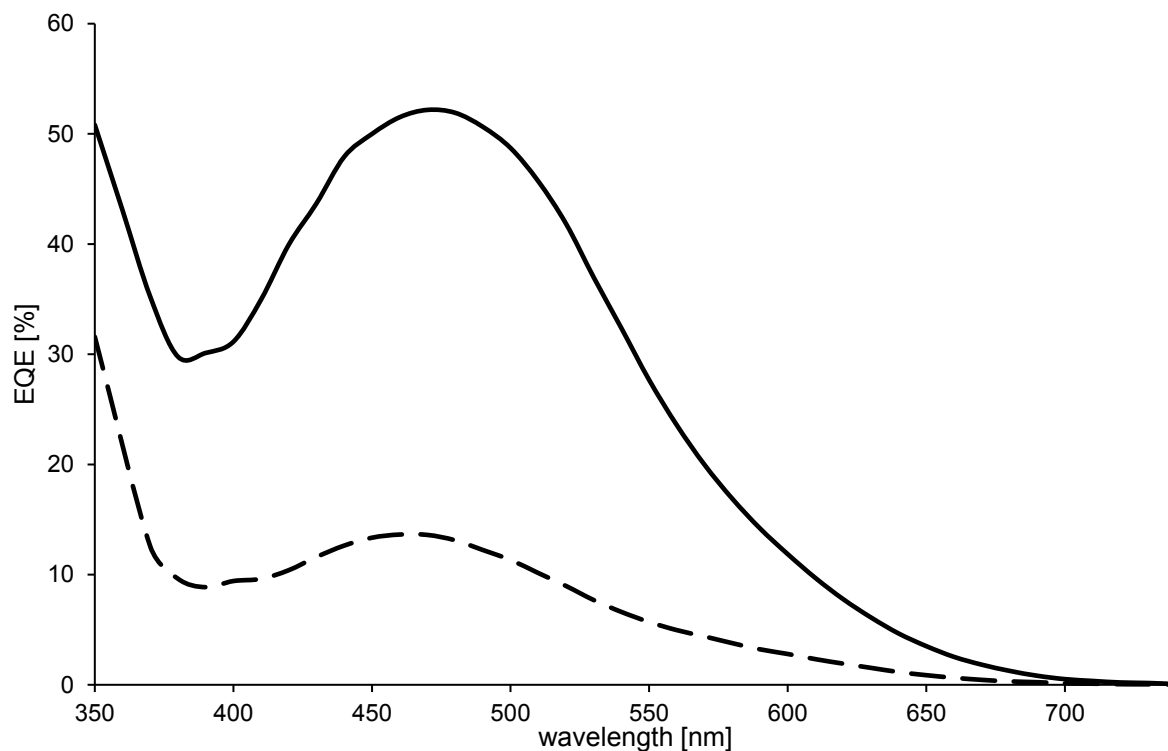


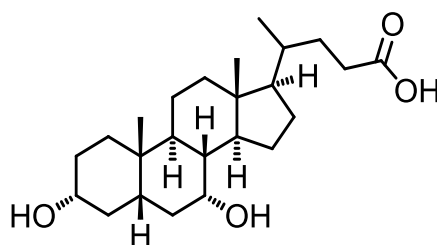
Fig. 79 EQE curves of DSCs containing of the anchoring ligand **ALP1** and the ancillary ligand **P^hL-I** assembled by the 1:1 dipping-procedure (dashed) or stepwise dipping-procedure (solid) on day 7 after sealing the cell.

All in all, the ancillary ligand **P^hL-I** is a promising candidate to optimize the performance of Cu(I)-based DSCs. High J_{sc} and moderate V_{oc} values are obtained but the biggest problem is the ff . In both dipping-procedures ff of only 58 to 59% were measured (Table 8, day 7 after sealing the cell) and these values are very low for Cu(I) DSCs.

This ligand combination shows also that the choice of the dipping-procedure has to be done individually for every ligand combination. When the ligand-exchange dipping-procedure is possible this should be the used. When the 1:1 - or the stepwise dipping-procedure have to be used because no homoleptic $[\text{Cu}(\text{L}_{\text{ancillary}})_2][\text{PF}_6]$ complex can be synthesised, both dipping-procedures have to be tested to ensure that the best possible DSCs are obtained.¹⁴³

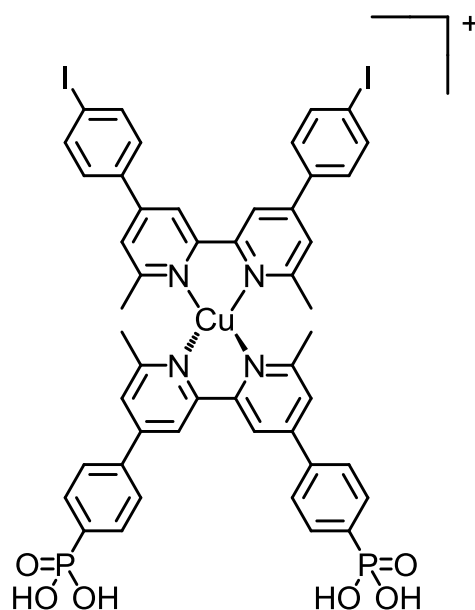
14.4. Influence of the Co-adsorbent Cheno on the Efficiency

The best-performing copper(I)-based DSC so far reported has an overall efficiency of 4.66% and contains a heteroleptic copper(I) complex with an anchoring ligand and an ancillary ligand (Scheme 7) and the co-adsorbent chenodeoxycholic acid (**Cheno**).¹⁰⁵ However, the overall efficiency of the DSC without the co-adsorbent is 2.93%. By adding **Cheno** an increase in efficiency of 60% is obtained. Although this possible positive impact of **Cheno** on the performance of the DSC is known, few studies have investigated the effects of **Cheno** on Cu(I) dyes. It is well known that **Cheno** enhances the V_{oc} due to passivation of the semiconductor surface and lead to a reduction in the recombination of Ru(II)-containing dyes such as **N719**¹⁴⁴ and zinc(II) porphyrin dyes^{145,146}. Hernandez Redondo and co-workers have reported that the addition of **Cheno** to a homoleptic Cu(I) dye does not enhance the performance of the DSC⁹³, whereas the group of Robertson report improved photocurrents when **Cheno** is added to a heteroleptic dye¹⁴⁷. These results imply that the influence of **Cheno** on the efficiency of a DSC can be positive but this is not necessarily the case. Therefore, the use of **Cheno** has to be tested individually for each dye.



Scheme 38 Co-adsorbent chenodeoxycholic acid (**Cheno**).

For the investigations of the influence of the co-adsorbent **Cheno** on the efficiency of Cu(I)-based DSCs, a dye containing ancillary ligand **L-I** and the anchoring ligand **ALP1** were used (Scheme 39). After it has been shown that a 1 : 1 mixture of $[\text{Cu}(\text{MeCN})_4][\text{PF}_6]$ and **L-I** give comparable results to the stepwise dipping method with the homoleptic $[\text{Cu}(\text{L-I})_2]^+$ complex this method was used for the following investigations as well.



Scheme 39 The surface-bound heteroleptic copper(I) complex containing **ALP1** as anchoring ligand and **L-I** as ancillary ligand for the investigations of the impact of **Cheno** on the DSC efficiency.

The effect of **Cheno** on the DSC performance was investigated in two different ways. First of all, **Cheno** was added to the ancillary ligand solution in different molar ratios and the performance of the completely assembled DSCs were measured. In the second part, **Cheno** was added to the anchoring ligand solution in different ratios and also the influence on the DSC performance was measured.

For the cells where **Cheno** was added to the ancillary ligand solution, anchoring ligand-functionalized photoelectrodes were immersed in a CH₂Cl₂ solution of [Cu(MeCN)₄][PF₆], **L-I** and **Cheno** in molar ratios of 1 : 1 : 0, 1 : 1 : 1, 1 : 1 : 3, 1 : 1 : 6, and 1 : 1 : 10 for a period of 3 days. The stock solution of all three components had a concentration of 0.1 mM. The DSCs were assembled as described in the experimental section and performance data were measured on the day of sealing the cells and after 3 and 7 days. Table 9 summarizes the DSC performance data.

Table 9 DSC performance data for DSCs containing a copper(I) dye with the anchoring ligand **ALP1** and the ancillary ligand **L-I** and with the co-adsorbent **Cheno** on the day of sealing the cells, 3 days and 7 days after sealing the cell. **Cheno** was introduced to the dye-bath in a specified ratio to [Cu(MeCN)₄][PF₆] and **L-I**.

Dye	Ratio of Cu : L-I : Cheno	J_{sc} [mA cm ⁻²]	V_{oc} [mV]	ff [%]	η [%]	Relative η [%]
On the day of sealing the cell						
[Cu(ALP1)(L-I) ⁺	1 : 1 : 0	7.01	559	70	2.75	42.4
[Cu(ALP1)(L-I) ⁺	1 : 1 : 1	6.74	573	70	2.69	41.5
[Cu(ALP1)(L-I) ⁺	1 : 1 : 3	5.66	563	73	2.33	36.0
[Cu(ALP1)(L-I) ⁺	1 : 1 : 6	6.27	568	72	2.57	39.7
[Cu(ALP1)(L-I) ⁺	1 : 1 : 10	6.48	564	71	2.58	39.8
N719		16.55	636	62	6.48	100.0
3 days after sealing the cell						
[Cu(ALP1)(L-I) ⁺	1 : 1 : 0	6.93	588	68	2.75	38.2
[Cu(ALP1)(L-I) ⁺	1 : 1 : 1	6.78	574	70	2.71	37.7
[Cu(ALP1)(L-I) ⁺	1 : 1 : 3	6.36	593	70	2.64	36.7
[Cu(ALP1)(L-I) ⁺	1 : 1 : 6	6.56	584	72	2.76	38.4
[Cu(ALP1)(L-I) ⁺	1 : 1 : 10	6.82	586	71	2.83	39.4
N719		16.35	675	65	7.19	100.0
7 days after sealing the cell						
[Cu(ALP1)(L-I) ⁺	1 : 1 : 0	6.96	587	66	2.71	36.0
[Cu(ALP1)(L-I) ⁺	1 : 1 : 1	6.84	571	70	2.72	36.1
[Cu(ALP1)(L-I) ⁺	1 : 1 : 3	6.33	590	69	2.59	34.4
[Cu(ALP1)(L-I) ⁺	1 : 1 : 6	6.47	581	73	2.75	36.5
[Cu(ALP1)(L-I) ⁺	1 : 1 : 10	6.82	584	71	2.84	37.7
N719		16.16	677	69	7.53	100.0

The DSC without the co-adsorbent **Cheno** had an efficiency of 2.75% on the day of sealing the cell, as investigated before (*14.2 Minimizing the Excess of Ancillary Ligand and the Total Process Time in the Dye-Assembly Process*). This cell is also the best performing one on day 0 compared the DSCs with **Cheno** (Table 9). The best performing DSC out of the cells where **Cheno** was added is the one with a molar ratio of 1 : 1 : 1 ([Cu(MeCN)₄][PF₆] : **L-I** : **Cheno**). It has with 573 mV a higher V_{oc} than the DSC without **Cheno** - which is the case for all DSCs with **Cheno**

(563 - 573 mV vs. 559 mV). However, the J_{sc} is lower compared to the DSC without **Cheno** (6.74 vs 7.01 mA cm⁻²). This is also a general observation for all DSCs with **Cheno**. These cells have a J_{sc} value between 5.66 and 6.74 mA cm⁻² which is lower than that for the DSC without **Cheno** (7.01 mA cm⁻²). No trend in the effect of the amount of **Cheno** that was added to the ancillary solution was observed. However, while the performance of the DSC without **Cheno** is constant over a period of one week, all DSCs with **Cheno** gain in J_{sc} and V_{oc} resulting in higher η values. The cell without **Cheno** still had an efficiency of 2.71% after one week and with 6.96 mA cm⁻², this cell had the highest J_{sc} value. But the DSCs with **Cheno** have J_{sc} values from 6.33 to 6.84 mA cm⁻² and the difference to the DSC without **Cheno** is now smaller. On the day of sealing the cell, the worst performing cell had a J_{sc} value of 5.66 mA cm⁻² and the one without **Cheno** 7.01 mA cm⁻². But 7 days later, the worst performing cell had a J_{sc} value of 6.33 mA cm⁻² and the one without **Cheno** 6.96 mA cm⁻², what is a difference of 0.63 mA cm⁻². The gain in the V_{oc} value of the DSCs where **Cheno** was added to the ancillary ligand solution was so big that after 7 days a higher V_{oc} was measured than for the cell without **Cheno**. The DSC with a molar ratio of 1 : 1 : 3 had an V_{oc} of 590 mV and the one without **Cheno** an V_{oc} of 587 mV. The trends for day 7 after sealing the cells in J_{sc} and V_{oc} can also be observed in the J - V curves (Fig. 80).

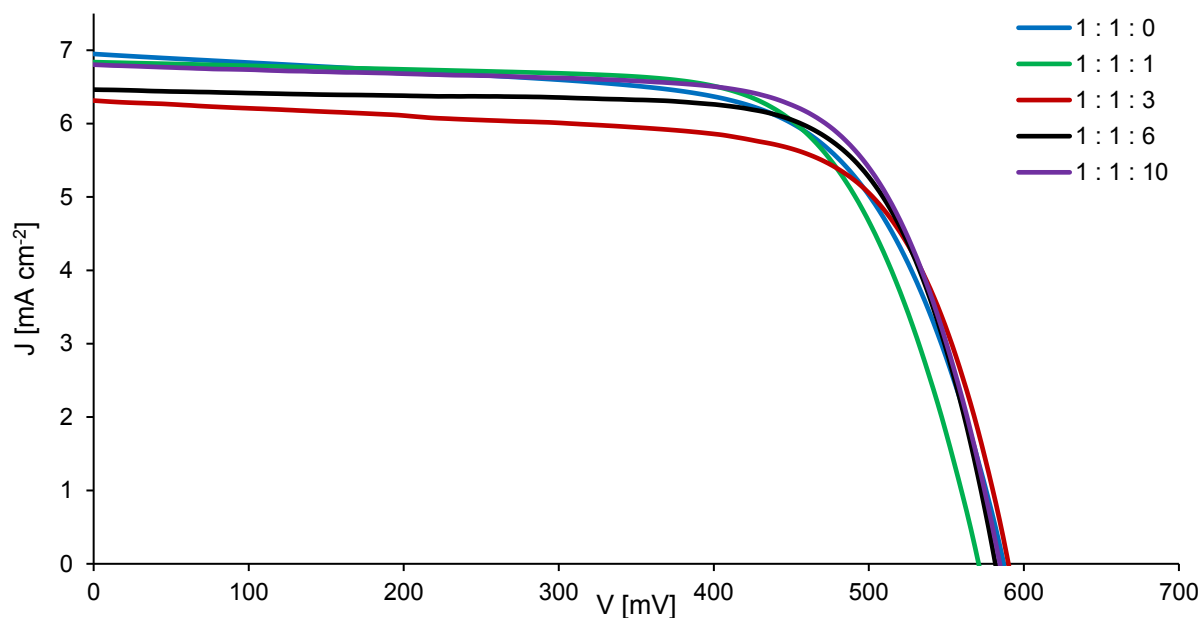


Fig. 80 J - V curves of DSCs 7 days after sealing the cell in which the anchoring ligand functionalized photoelectrode was dipped into a $[\text{Cu}(\text{MeCN})_4][\text{PF}_6]$: **L-I** : **Cheno** dye bath with different ratios (1 : 1 : 0, 1 : 1 : 1, 1 : 1 : 3, 1 : 1 : 6, 1 : 1 : 10).

The fill factors of all DSCs during a period of one week were always good, around 70% which shows low current leakage inside the cells (Table 9). In the end, the DSCs treated with **Cheno** in the ancillary ligand solution had an overall efficiency in the range of 2.59 to 2.84% whereas the cell without **Cheno** had an η of 2.71% (Table 9).

The same trend was observed in the EQE data of the DSCs. Table 10 summarizes the EQE maximum values of DSCs treated with different ratios of **Cheno** in the ancillary ligand solution. All DSCs have an EQE_{max} value between 39.7 and 47.1% at around 470 nm after the period of one week.

Table 10 EQE maximum data of DSC treated with different ratios of **Cheno** in the ancillary ligand solution on the day of sealing the cell, 3 days and 7 days after sealing the cell.

molar ratio [Cu(MeCN) ₄][PF ₆] : L-I : Cheno	Day 0		Day 3		Day 7	
	λ_{max} [nm]	EQE_{max} [%]	λ_{max} [nm]	EQE_{max} [%]	λ_{max} [nm]	EQE_{max} [%]
1 : 1 : 0	480	46.1	470	45.6	470	44.7
1 : 1 : 1	470	45.5	470	45.6	470	45.9
1 : 1 : 3	470	42.7	470	41.2	470	39.7
1 : 1 : 6	480	43.3	470	45.5	470	45.2
1 : 1 : 10	470	46.0	470	47.1	470	46.6

On the day of sealing the cells the DSC without **Cheno** has the highest EQE_{max} value with 46.1% at 480 nm. The changes in EQE_{max} values during the period of one week is negligible for all DSCs. **Cheno** also has no impact on the wavelength of the EQE_{max} value. All DSCs have their highest photon-to-electrical power conversion efficiency at 470 nm. Fig. 81 displays the EQE curves of the cells on day 7 after sealing the cell. All curves have the same shape and identical wavelength at their maxima. No trend of the influence of the ratio of added EQE_{max} is observable.

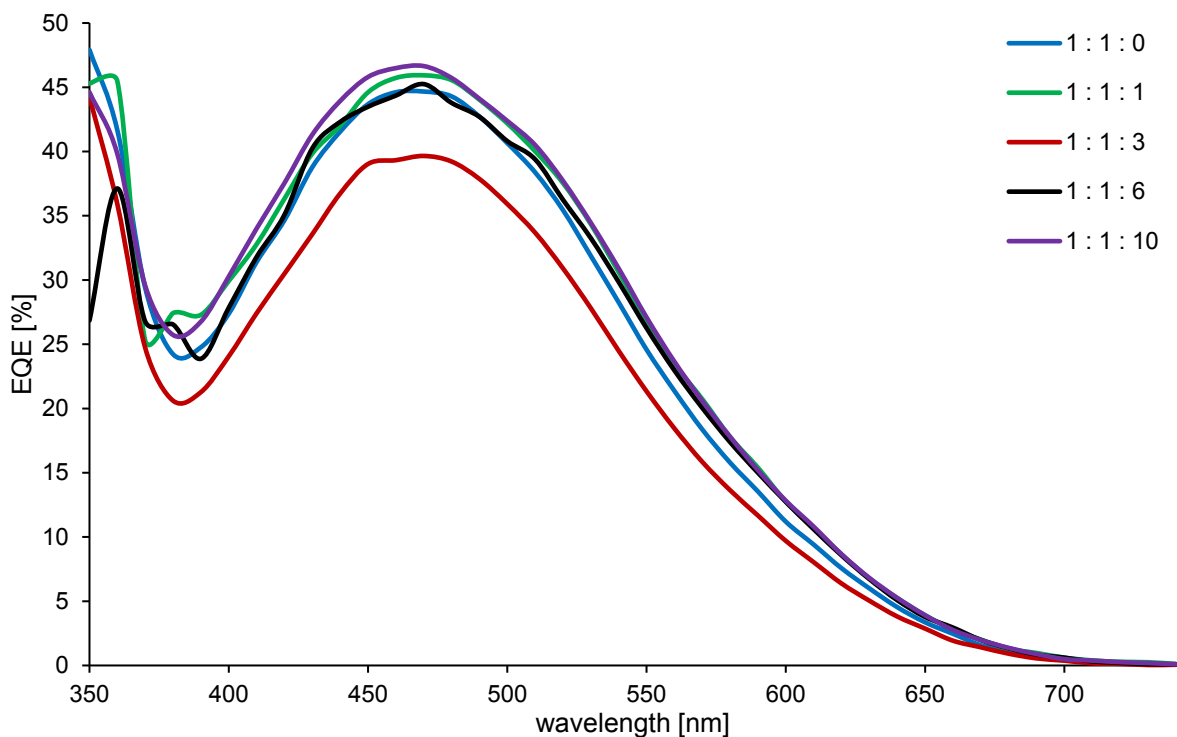


Fig. 81 EQE curves of DSCs 7 days after sealing the cell in which the anchoring ligand functionalized photoelectrode was dipped into a $[\text{Cu}(\text{MeCN})_4][\text{PF}_6] : \text{L-I} : \text{Cheno}$ dye bath with different ratios (1 : 1 : 0, 1 : 1 : 1, 1 : 1 : 3, 1 : 1 : 6, 1 : 1 : 10).

No noticeable improvement in performance is observed when **Cheno** is added to the ancillary ligand solution. No π -stacking can occur between the single dye-molecules which **Cheno** should suppress. This can be due to the fact that the dye possesses little steric crowding. This suggests that optimal dye-coverage of the semiconductor is already achieved without **Cheno**. That can be seen in the fact, that the DSC without **Cheno** has the highest J_{sc} value during the whole measurements in a period of one week. But **Cheno** should also hinder the recombination of electrons in the semiconductor with the electrolyte (Fig. 82).

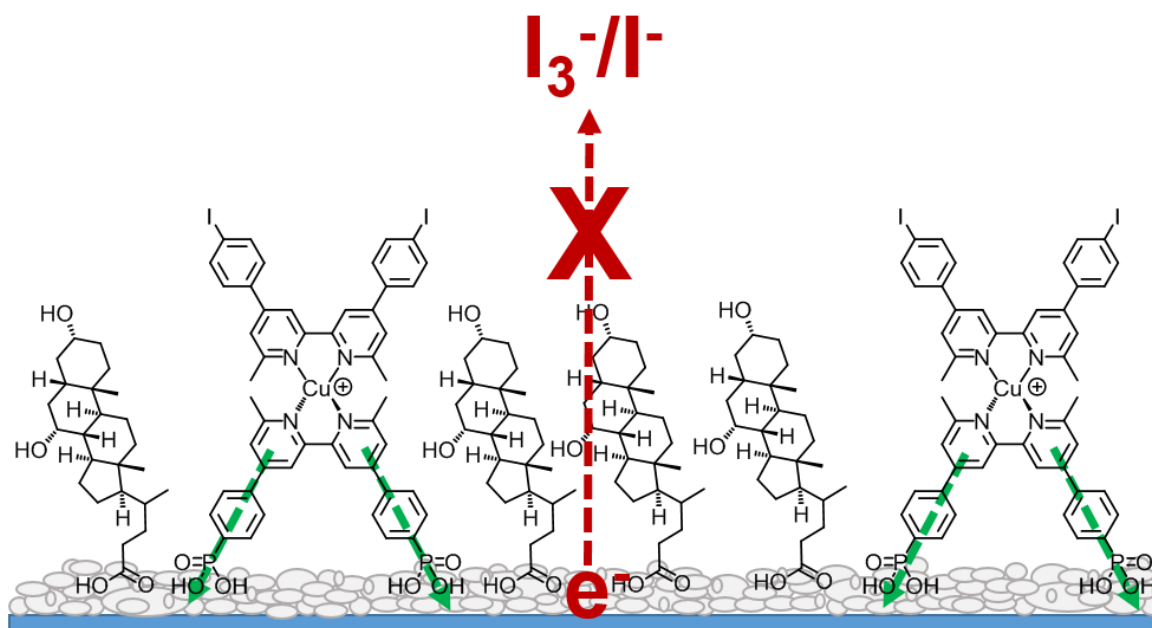


Fig. 82 Schematic representation of the blocking effect of co-adsorbed **Cheno**: the electrolyte is blocked from reaching the semiconductor surface and injection (green) is favoured over recombination (red).

With reduced recombination, a higher density of charge carriers in the semiconductor can be achieved. This has an impact on the conduction band level of the semiconductor and subsequently on the Fermi level. With a negative shift of the Fermi level, higher V_{oc} values are achieved. This can be observed in the gain in V_{oc} . V_{oc} values over 600 mV were measured during this investigation with the duplicate cells assembled with a molar ratio of 1 : 1 : 3 of the ancillary ligand solution (611 mV on day 3 after sealing the cell).

Due to the stepwise dye-assembly on the semiconductor surface, the anchoring ligand **ALP1** is introduced in the first dipping step and **Cheno** was added to the ancillary ligand solution in the second dipping step. But if the semiconductor is already covered with **ALP1** less binding sites for **Cheno** are available. Therefore, **Cheno** is added to the anchoring ligand solution in the first dipping step to see the effect on the DSC performance. In this case, competitive binding of **ALP1** and **Cheno** occurs.

For the investigation of the influence on the DSC performance of **Cheno** added to the anchoring ligand solution, the dye-functionalized photoelectrodes were prepared by dipping the washed and

sintered electrode into a DMSO solution containing the anchoring ligand **ALP1** and **Cheno** in molar ratios of 1 : 1, 1 : 3 and 1 : 6 for one day. The stock solution of each component has a concentration of 1 mM. Afterwards, the electrodes were removed from the solution, washed with DMSO and EtOH and dried with a heat gun at about 80 °C. For the second dipping step the functionalized photoelectrodes were immersed in a solution of [Cu(MeCN)₄][PF₆] and **L-I** with a ratio of 1 : 1. The stock solutions have a concentration of 0.1 mM. The DSCs are assembled in the general method and the DSC performance is measured under solar simulator conditions.

The DSC performance measurements were made at the day of sealing the cell, 3 days later and after a period of one week (Table 11). The results of the measurements indicate that adding **Cheno** to the anchoring ligand solution is detrimental. Already on the day of sealing the cells this observation is obvious. All cells where **Cheno** was added during the first dipping step performed worse well than the DSC without **Cheno** (Table 11). They had an overall efficiency between 2.11 and 2.23% on the day of sealing the cell and the DSC without **Cheno** has an η of 2.75%. **Cheno** has no impact on the ff (68 - 70% for all cells) and the V_{oc} value. But the J_{sc} is significant lower when **Cheno** is added (5.43 - 5.92 mA cm⁻² vs 7.01 mA cm⁻²). During a period of one week this trend is constant. The DSC without **Cheno** had the highest efficiency with $\eta = 2.71\%$ (Table 11). The cells with **Cheno** had an overall efficiency of 2.27 to 2.52%. On day 7 after sealing the cells, it was observed that higher amounts of **Cheno** have a negative effect. The DSC where **Cheno** was added in a ratio of 1 : 6 has the lowest J_{sc} (5.75 mA cm⁻²) and the poorest η (2.27%). This trend is perfectly displayed in the J - V curves for 7 day old DSCs (Fig. 83). The untreated cell has the highest J_{sc} as well as the highest V_{oc} and the introduction of **Cheno** results in the drop of all key parameters.

Table 11 DSC performance data for DSCs containing a dye with the anchoring ligand **ALP1** and the ancillary ligand **L-I** and with the co-adsorbent **Cheno** on the day of sealing the cells, 3 days and 7 days after sealing the cell. **Cheno** was introduced to the anchoring ligand-bath in specified ratio to **ALP1**.

Dye	Ratio of ALP1 : Cheno	J_{sc} [mA cm ⁻²]	V_{oc} [mV]	ff [%]	η [%]	Relative η [%]
On the day of sealing the cell						
[Cu(ALP1)(L-I) ⁺	1 : 0	7.01	559	70	2.75	36.3
[Cu(ALP1)(L-I) ⁺	1 : 1	5.43	566	69	2.12	28.0
[Cu(ALP1)(L-I) ⁺	1 : 3	5.92	558	68	2.23	29.4
[Cu(ALP1)(L-I) ⁺	1 : 6	5.73	536	69	2.11	27.8
N719		16.18	656	71	7.58	100.0
3 days after sealing the cell						
[Cu(ALP1)(L-I) ⁺	1 : 0	6.93	588	68	2.75	36.2
[Cu(ALP1)(L-I) ⁺	1 : 1	6.02	570	70	2.40	31.6
[Cu(ALP1)(L-I) ⁺	1 : 3	6.45	538	69	2.39	31.4
[Cu(ALP1)(L-I) ⁺	1 : 6	5.79	562	70	2.28	30.0
N719		16.18	671	70	7.60	100.0
7 days after sealing the cell						
[Cu(ALP1)(L-I) ⁺	1 : 0	6.96	587	66	2.71	34.3
[Cu(ALP1)(L-I) ⁺	1 : 1	6.15	574	71	2.49	31.5
[Cu(ALP1)(L-I) ⁺	1 : 3	6.59	547	70	2.52	31.9
[Cu(ALP1)(L-I) ⁺	1 : 6	5.75	564	70	2.27	28.7
N719		16.14	697	70	7.91	100.0

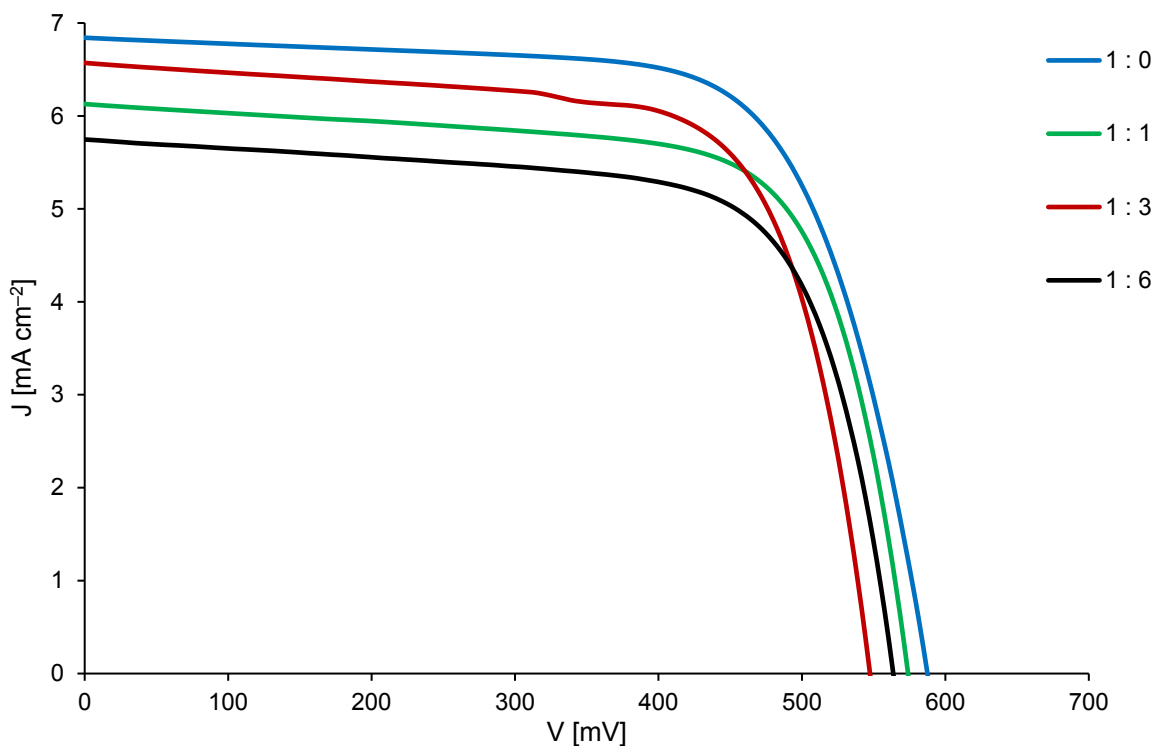


Fig. 83 J - V curves of DSCs 7 days after sealing the cell in which the photoelectrode was dipped into anchoring ligand solution containing **ALP1** and **Cheno** in different ratios (1 : 0, 1 : 1, 1 : 3, 1 : 6) followed by treatment with ancillary ligand solution containing of $[\text{Cu}(\text{MeCN})_4][\text{PF}_6]$: **LI** (1 : 1).

The biggest drop is observed in the J_{sc} value. This can be explained by competitive binding of the anchoring ligand **ALP1** and **Cheno**. Here, also the anchoring domain has an impact. **ALP1** has a phosphonic anchoring group whereas **Cheno** has a carboxylic acid anchor. The anchoring group is connected with the core via an alkyl chain which increases the conformational flexibility of **Cheno**. Less binding sites for **ALP1** are available. This results in a poorer surface coverage of the Cu(I) dye. From this, one can infer that a lower current flow is present which decreases the J_{sc} . With lower current flow, a lower current density in the semiconductor is present as well. Although **Cheno** blocks the recombination of injected electrons with the electrolyte the current density in the semiconductor is lower than in DSCs without **Cheno**. In the end, lower V_{oc} values are obtained when **Cheno** is added.

Lower EQE_{max} values are obtained when **Cheno** is added to the anchoring ligand solution on the day of sealing the cell (Table 12). The DSCs with **Cheno** gain in the EQE_{max} value during a period of one week and reach comparable values on day 7.

Table 12 EQE maximum data of DSC treated with different ratios of **Cheno** in the anchoring ligand solution on the day of sealing the cell, 3 days and 7 days after sealing the cell.

molar ratio ALP1 : Cheno	Day 0		Day 3		Day 7	
	λ_{max} [nm]	EQE_{max} [%]	λ_{max} [nm]	EQE_{max} [%]	λ_{max} [nm]	EQE_{max} [%]
1 : 0	480	46.1	470	45.6	470	44.7
1 : 1	470	39.9	470	43.1	470	42.8
1 : 3	470	42.5	470	46.6	470	45.9
1 : 6	480	45.6	480	44.6	470	46.0

But although there is no obvious trend in the shape of the spectra it can be observed that the highest amount of **Cheno** (1 : 6, black curve) results in a loss of quantum efficiency at both lower and higher wavelength of EQE_{max} .

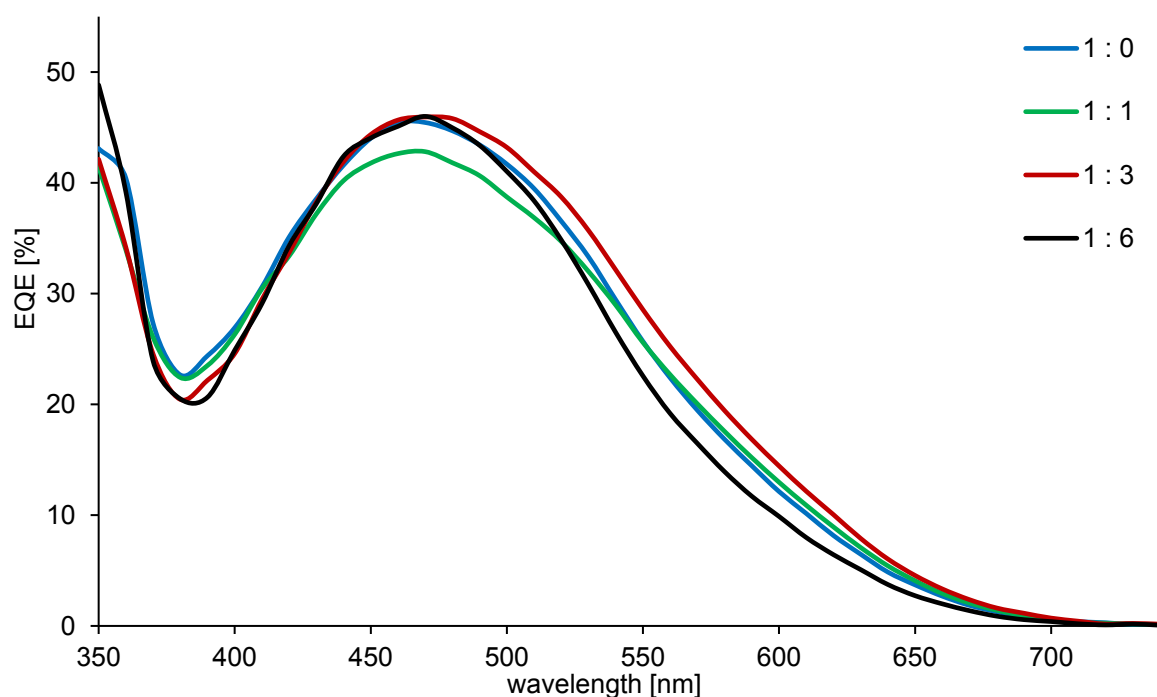


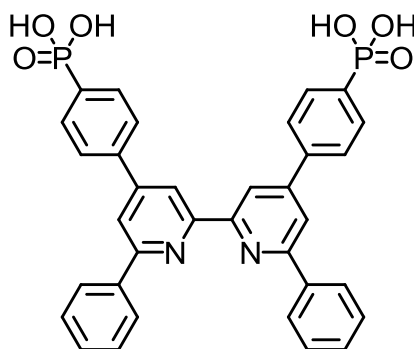
Fig. 84 EQE curves of DSCs 7 days after sealing the cell in which the photoelectrode was dipped into anchoring ligand solution containing of **ALP1** and **Cheno** in different ratios (1 : 0, 1 : 1, 1 : 3, 1 : 6) followed by treatment with ancillary ligand solution containing of $[Cu(MeCN)_4][PF_6] : LI$ (1 : 1).

In conclusion, the introduction of **Cheno** to a small Cu(I) dye has no positive influence on the efficiency. The key parameters drop in both cases: either when **Cheno** is added to the **ALP1** anchoring ligand solution in the first dipping step or to the ancillary ligand solution in the second dipping step. When **Cheno** is added to the ancillary ligand solution the negative effect is not as significant as when it is added to the anchoring ligand solution.

14.5. Regeneration of the Dye on the Semiconductor Surface

A problem that occurs occasionally with Cu(I)-based DSCs is the bleaching of the electrode under exposure to iodine-based electrolyte. The photoelectrodes become paler over a period of time and the cell performance drops noticeably. The question was whether the whole dye is cleaved off the semiconductor surface or if only the ancillary ligand and/or the {Cu(L_{ancillary})} unit.

The anchoring ligand ^{Ph}ALP1 developed by Dr. Sven Y. Brauchli was used for this investigation where this phenomenon occurred (Scheme 40). It is an anchoring ligand with a phosphonic acid anchoring group like ALP1 but has a 6,6'-diphenyl substituent pattern instead of a 6,6'-dimethyl substitution pattern in bpy. **L-Br** was used as the ancillary ligand.



Scheme 40 Anchoring ligand ^{Ph}ALP1.

The heteroleptic [Cu(^{Ph}ALP1)(**L-Br**)]⁺ complex on the photoelectrode was assembled in the stepwise manner and a dark orange-coloured photoelectrode was observed. But when it was exposed to the I⁻/I₃⁻ electrolyte during the cell assembly process, the dye bleached (Fig. 85) and the DSC performance was poor ($\eta = 0.59\%$ or 10.0% relative to **N719**).

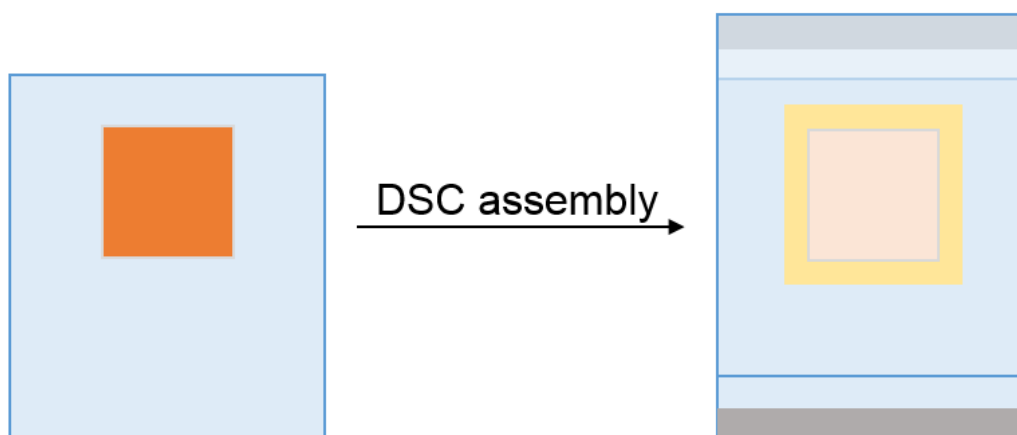


Fig. 85 Bleaching of the photoelectrode after contact with I^-/I_3^- electrolyte during DSC assembly process.

Two strategies were used to investigate the problem: firstly, solid-state absorption spectroscopy and secondly, the impact of iodide by using LiI solution.

For this investigation transparent TiO₂ electrodes (Solaronix Test Cell Titania Electrodes Transparent) were washed with HPLC EtOH and sintered at 450 °C for 30 min. The cooled electrodes were dipped into the anchoring ligand and ancillary ligand solution stepwise as described for the dipping process of the DSCs. Afterwards, solid-state absorption spectra of both electrodes were measured (Fig. 86, blue curves). Then, one electrode was dipped into the I^-/I_3^- electrolyte and one into a 0.1 M solution of LiI in 3-methoxypropionitrile for 15 min. The composition of the LiI-solution was used to guarantee identical iodide concentrations as in the I^-/I_3^- electrolyte. After soaking, the electrodes were washed with 3-methoxypropionitrile and dried with a heat gun at about 80 °C. The solid-state absorption spectra of both electrodes were measured. The bleaching of the electrolyte exposed electrode was clearly observed by the decreased absorption (Fig. 86, solid red curve). The same effect was observed when the dye-functionalized electrode was exposed to the LiI-solution (Fig. 86, dotted red curve). If only I^- is present in the solution as in the LiI-solution and there are no additional additives (as in the electrolyte), a bigger drop in absorption was observed, apparently because the attack of I^- to the surface-bound dye is more readily achieved. This observation results in the suggestion that the bleaching is caused by the attack of I^- at the copper(I) centre.

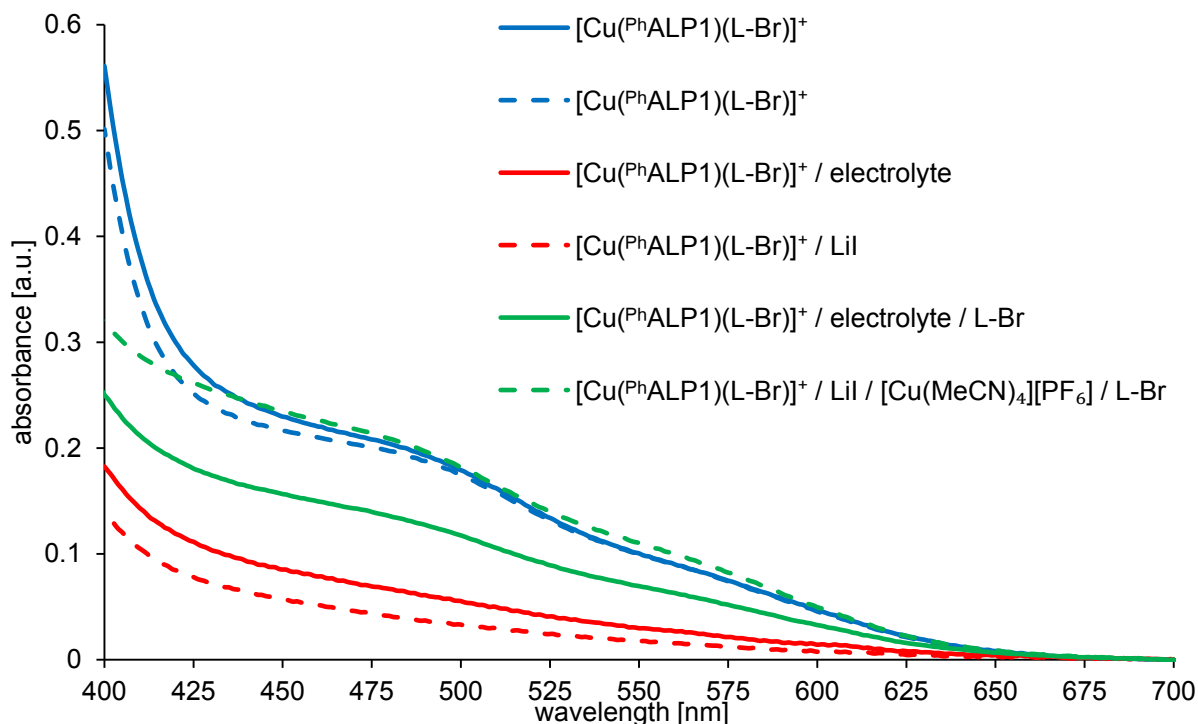


Fig. 86 Solid-state absorption spectra of electrodes containing the dye $[\text{Cu}(\text{PhALP1})(\text{L-Br})]^+$ (blue), after treatment with the I^-/I_3^- - electrolyte or LiI solution (red) and after dye regeneration (green).

However, the question as to whether the whole dye is cleaved off the surface or if only the ancillary ligand and/or the metal ion are removed has not yet been answered. The fact that an absorption between 450 and 650 nm is still observed implies that some dye remains on the surface (Fig. 86, red curves). To investigate if only the ancillary ligand is cleaved off the semiconductor surface, the electrolyte treated electrode was soaked in a 0.1 mM CH_2Cl_2 solution of **L-Br** for 15 min, was then removed, washed with CH_2Cl_2 and dried with a heat gun at about 80 °C (Fig. 86, red to green continuous curves). The solid-state absorption spectrum was measured once again. A clear increase in absorption in comparison to the bleached electrode is observed. However, a full regeneration to the pristine dye-loading before the bleaching of the electrode was not achieved. The result implies that the anchoring ligand is not cleaved off the surface and in some cases the copper centre is still bound to the anchoring ligand. Otherwise, the dye could not be regenerated by treatment with the ancillary ligand. However, loss of some copper must take place otherwise a full regeneration would have been observed. To underline this statement the second bleached electrode was dipped into a 2.0 mM MeCN solution of $[\text{Cu}(\text{MeCN})_4][\text{PF}_6]$ for 15 min. After

removing the electrode, it was washed with MeCN and dried with a heat gun at about 80 °C. Finally, the electrode was dipped into the 0.1 mM CH₂Cl₂ solution of **L-Br** for 15 min, washed with CH₂Cl₂ and dried with a heat gun (Fig. 86, dotted green curve) The solid-state absorption spectrum is consistent with the proposal, because a complete regeneration of the dye is now observed and an almost congruent absorption spectra of the untreated and regenerated electrode are achieved.

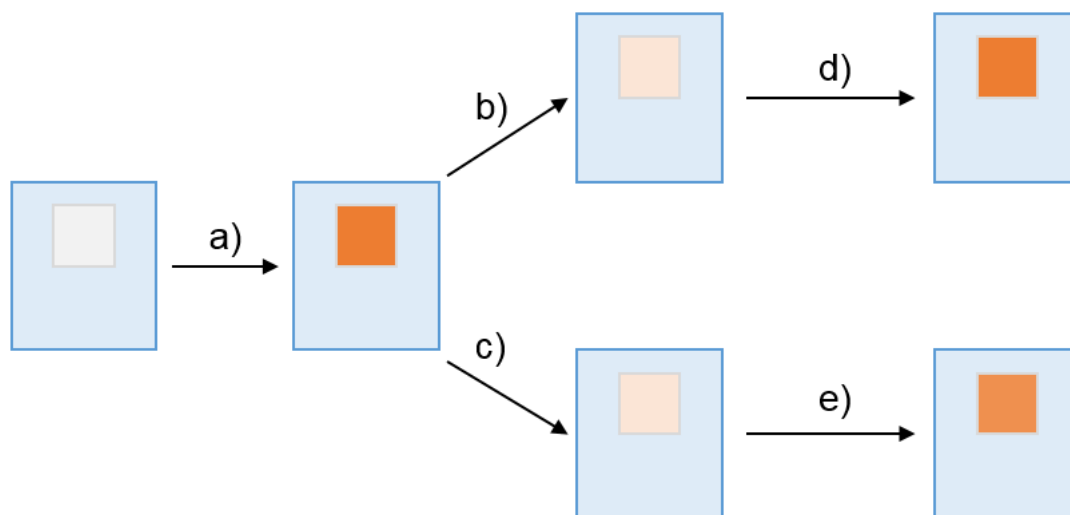
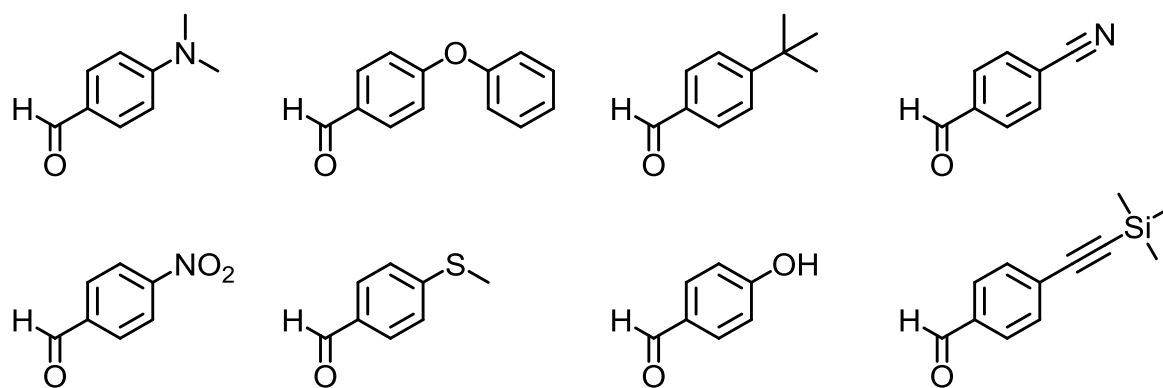


Fig. 87 Regeneration of the copper(I) dye on the photoelectrode: a) dye-sensitization of a photoelectrode; b) treatment with LiI; c) treatment with I⁻/I₃⁻ electrolyte; d) treatment with first [Cu(MeCN)₄][PF₆] and afterwards with the ancillary ligand **L-I**; e) treatment with **L-I**.

In conclusion, bleaching occurs by cleavage of the ancillary ligand and also in some cases of the copper-centre from the surface-anchored complex. The dye is readily regenerated by soaking a bleached electrode in a Cu(I)-solution and an ancillary ligand solution (Fig. 87). This bleaching effect justifies the need of more investigations about alternative electrolytes that are not based on iodine to replace the I⁻/I₃⁻ electrolyte in copper(I)-based DSCs.

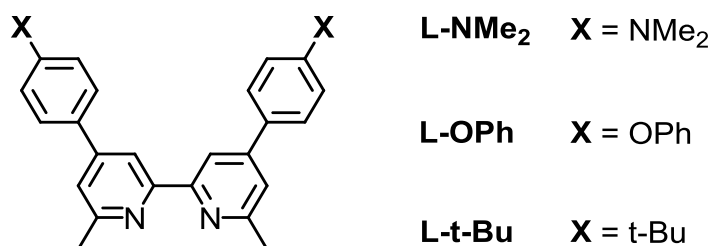
14.6. 2,2'-Bipyridine-Based Ligands with Different Functional Groups

After it had been shown that halo-phenyl substituents in the 4,4'-positions of the bpy core can increase the performance of a DSC, the chemical inventory of the Constable/Housecroft group was examined for 4-substituted benzaldehydes with different functional groups. No specific character of the functional group was considered, only the substitution pattern of the molecule. Possible candidates are shown in Scheme 41.



Scheme 41 4-Substituted benzaldehydes with different functional groups from the chemical inventory of the Constable/Housecroft research group.

4-Substituted benzaldehydes with the functional groups dimethylamine (NMe₂), phenoxy (OPh), tert-butyl (t-Bu), cyano (CN), nitro (NO₂), methylthio (SMe), hydroxy (OH) and trimethylsilylethynyl (CCSiMe₃) were selected. These 4-substituted benzaldehydes were used in the Kröhnke pyridine synthesis (see *10 Synthetic Strategy*) for the synthesis of the diketone-precursor. However, only the diketone-precursors with the functional groups NMe₂, OPh and t-Bu could be isolated. The synthesis of the corresponding **L-X** ligands (X = NMe₂, OPh, t-Bu) via the Kröhnke methodology resulted in the desired 2,2'-bpy-based ligands (Scheme 42) in moderate yields (yield = 35 - 46%).



Scheme 42 2,2'-Bpy-based ancillary ligands **L-X** with different functional groups (X = NMe₂, OPh, t-Bu).

After the synthesis of the homoleptic copper(I) complexes, the ligands were tested as ancillary ligands in DSCs. The anchoring ligand **ALP1** was used in the ligand-exchange dye-assembly procedure. The performance data for the DSCs on the day of sealing the cell, 3 days and 7 days after sealing the cell are summarized in Table 13.

Table 13 DSC performance data for DSCs containing copper(I) dyes with the anchoring ligand **ALP1** and the ancillary ligands **L-X** with X = NMe₂, OPh, t-Bu on the day of sealing the cells, 3 days and 7 days after sealing the cell.

Dye	J_{sc} [mA cm ⁻²]	V_{oc} [mV]	ff [%]	η [%]	Relative η [%]	EQE_{max} [nm], [%]
On the day of sealing the cell						
[Cu(ALP1)(L-NMe₂) ⁺	4.49	504	66	1.50	20.7	480, 28.3
[Cu(ALP1)(L-OPh) ⁺	6.08	527	68	2.19	30.2	470, 41.9
[Cu(ALP1)(L-t-Bu) ⁺	5.08	525	71	1.90	26.2	470, 39.1
N719	16.07	636	71	7.25	100.0	530, 73.4
3 days after sealing the cell						
[Cu(ALP1)(L-NMe₂) ⁺	5.33	353	71	2.01	26.8	480, 33.9
[Cu(ALP1)(L-OPh) ⁺	6.19	545	69	2.33	31.1	470, 44.5
[Cu(ALP1)(L-t-Bu) ⁺	4.33	548	70	1.66	22.1	470, 36.4
N719	15.74	676	71	7.50	100.0	520, 72.6
7 days after sealing the cell						
[Cu(ALP1)(L-NMe₂) ⁺	5.26	539	71	2.02	27.3	480, 35.0
[Cu(ALP1)(L-OPh) ⁺	6.07	554	69	2.31	31.2	470, 44.6
[Cu(ALP1)(L-t-Bu) ⁺	4.56	547	68	1.70	22.9	470, 38.8
N719	15.57	682	70	7.41	100.0	540, 72.6

On the day of sealing the cells J_{sc} values of 4.49 mA cm^{-2} for the **L-NMe** ancillary ligand, 5.08 mA cm^{-2} for **L-t-Bu** and 6.08 mA cm^{-2} for **L-OPh** were obtained. The measured V_{oc} values were low ($V_{oc} = 504 \text{ mV}$ for **L-NMe**₂, $V_{oc} = 525 \text{ mV}$ for **L-t-Bu**, $V_{oc} = 527 \text{ mV}$ for **L-OPh**). Although the DSCs showed good f values, the combinations of low V_{oc} and relatively J_{sc} values resulted in low overall efficiencies for all the DSCs. Fig. 88 displays the J - V curves for the cells on days 0 and 7. While the DSC with **L-NMe**₂ showed an enhancement in performance over the seven-day period; use of ancillary ligand **L-OPh** lead to a smaller ripening effect. Ripening effects are not uncommon and originate from reorganization of dye molecules on the surface.¹³⁷⁻¹³⁹ Over a period of one week all DSCs increased in V_{oc} ($V_{oc} = 539 \text{ mV}$ for **L-NMe**₂, $V_{oc} = 547 \text{ mV}$ for **L-t-Bu**, $V_{oc} = 554 \text{ mV}$ for **L-OPh**, Table 13). The variations in the J_{sc} values of the DSCs (Table 13 and Fig. 88) are also reflected in the trends observed in the EQE curves of the DSCs in Fig. 89.

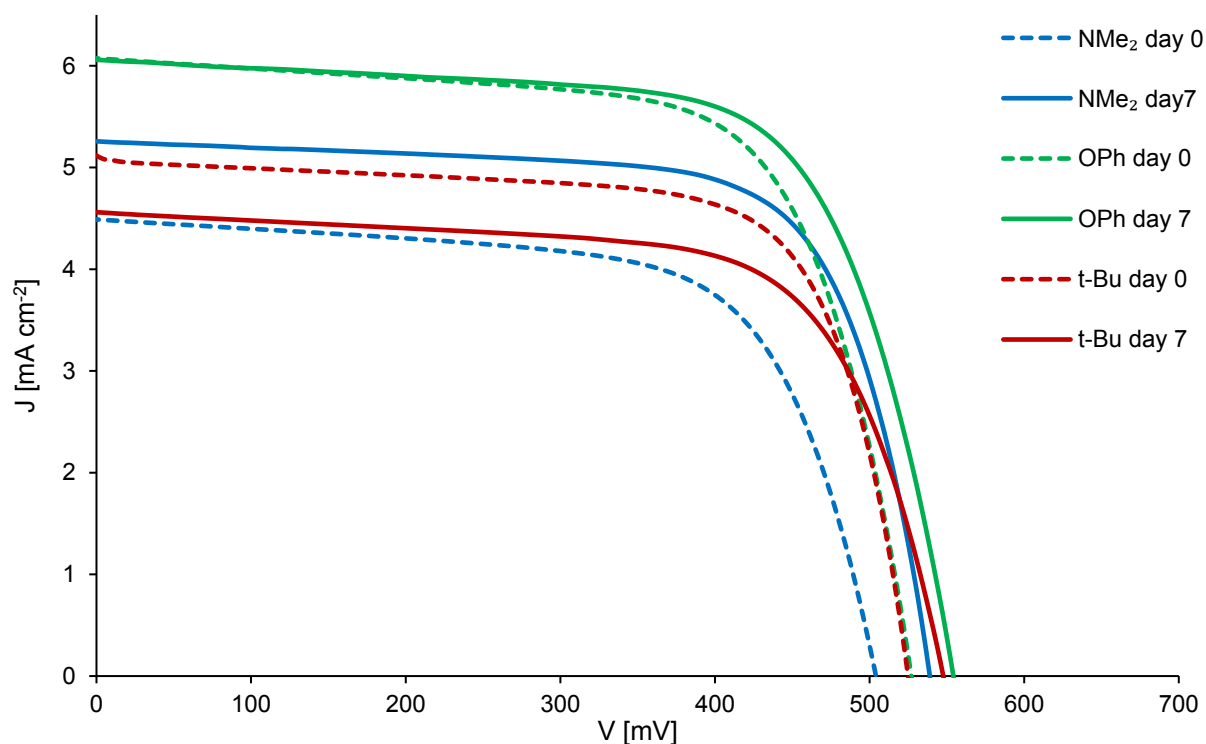


Fig. 88 J - V curves for the DSCs containing of the anchoring ligand **ALP1** and the ancillary ligands **L-X** with $X = \text{NMe}_2, \text{OPh}, \text{t-Bu}$ on the day of sealing the cells and 7 days after sealing the cell.

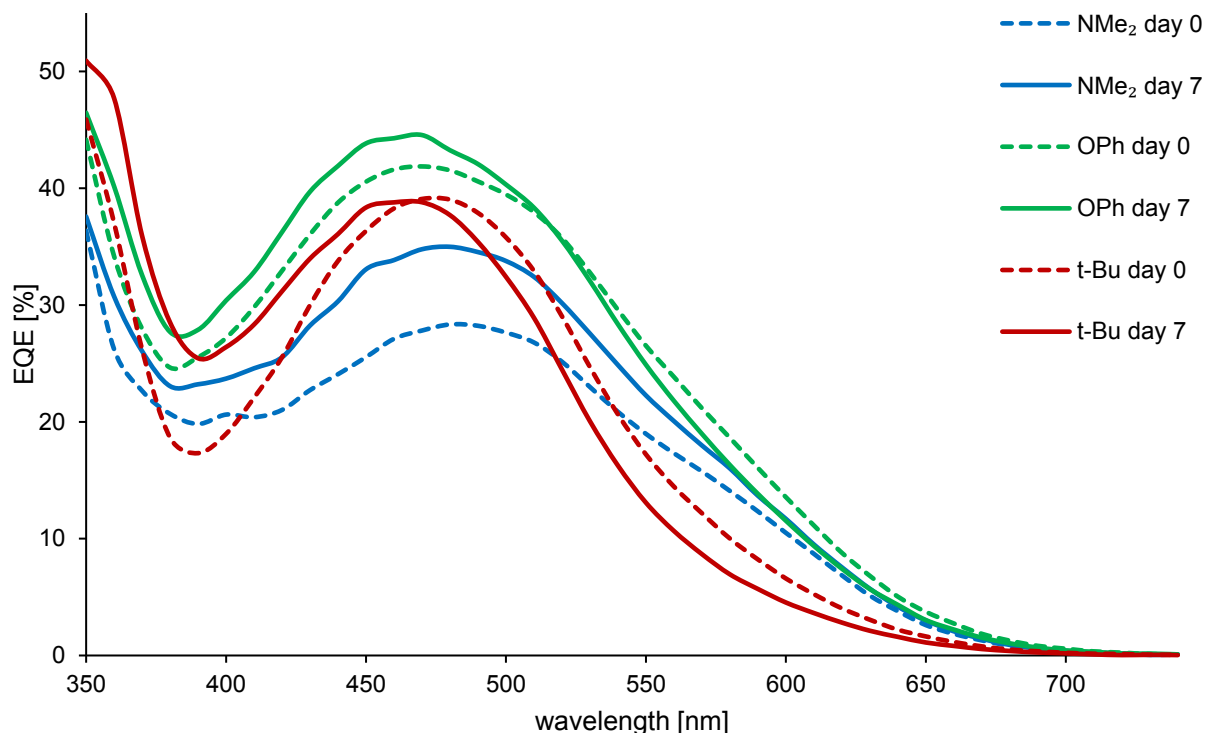


Fig. 89 EQE curves for the DSCs containing of the anchoring ligand **ALP1** and the ancillary ligands **L-X** with X = NMe₂, OPh, t-Bu on the day of sealing the cells and 7 days after sealing the cell.

The highest EQE response is observed for the DSC with the ancillary ligand **L-OPh**. The EQE_{max} for the DSC containing of the dye $[\text{Cu}(\text{ALP1})(\text{L-NMe}_2)]^+$ is not as high as for the DSC containing of the dye $[\text{Cu}(\text{ALP1})(\text{L-t-Bu})]^+$ but the response of the DSC with **L-NMe₂** is much broader. The increased EQE response of the DSC containing of the dye $[\text{Cu}(\text{ALP1})(\text{L-NMe}_2)]^+$ is clearly visible in Fig. 89.

In conclusion, the performance of all DSCs was relatively poor and the performance could not be improved compared to the halogen-containing **L-X** ligands. A new type of ancillary ligands should be investigated to improve the performance of Cu(I)-based DSCs.

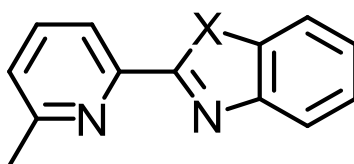
15. N^NX Ancillary Ligands

The state of the art ancillary ligands have been 2,2'-bipyridine-based ligands. Many investigations to optimize the performance of copper(I)-based DSCs have been done by changing the substituents in the 4,4'- and/or 6,6'-positions of the bpy. Bulky groups, bigger π -systems or other groups have been introduced into the 6,6'-positions. And phenyl-groups with simple halogens or big π -conjugated systems and other functional groups in the 4,4'-positions of the bpy-core have been tested. But all investigations resulted in mainly comparable results with a few positive outliers with efficiencies $> 3\%$.

In the area of ruthenium and organic dyes, many of the good performing dyes are structurally rather simple. This should, therefore, also be the goal for copper(I)-based dyes. Ligands with simple architectures and with as few as possible synthetic steps should be investigated. New ancillary ligands with N^N binding sites are needed to make the next generation Cu(I)-based dye-sensitized solar cells.

The requirements for the new type of ancillary ligands are a N^N binding site, a big enough π -system, bulky substituent(s) near to the coordination site to stabilize the copper(I) complex, simple synthesis and the possibility to be modified in subsequent investigations.

With the help of literature¹⁴⁸⁻¹⁵⁷, DFT calculations of possible candidates and the knowledge of the synthesis of different N^N ligands in the Constable/Housecroft research group this new type of ancillary ligands was examined: N^NX (Scheme 43).

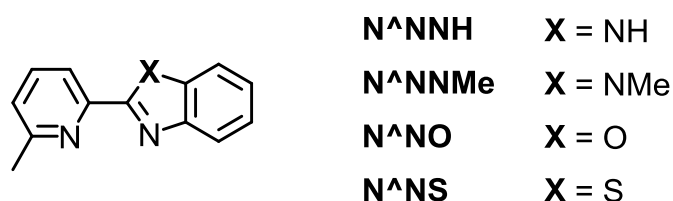


Scheme 43 The new type of ancillary ligands: N^NX.

First of all, the influence of different heteroatoms was investigated in order to determine the best performing ligand that can act as a building block in subsequent optimizations.

15.1. A New Type of Ancillary Ligand for Copper(I)-Based Dye-Sensitized Solar Cells: N[^]NX

The synthesis of the ancillary ligands N[^]NNH¹²⁶, N[^]NO and N[^]NS¹²⁵ (Scheme 44) is a reported condensation reaction or a one-step coupling reaction (see 9.2 *Heterocyclic N[^]NX Ancillary Ligands*) and the transformation of N[^]NNH to N[^]NNMe is a standard methylation. The complexation with [Cu(MeCN)₄][PF₆] to the corresponding copper(I) complexes is straight forward. All Cu(I) complexes are stable under ambient conditions except [Cu(N[^]NNH)₂][PF₆]. Solutions of red [Cu(N[^]NNH)₂][PF₆] which are left standing in air slowly oxidize to the corresponding green copper(II) complex. The presence of the [Cu(N[^]NNH)₂]²⁺ cation is supported by ESI MS at m/z 240.4 showing a characteristic isotope pattern with peaks at half-mass separations consistent with the 2+ charge. Because of this observation all solid compounds and solutions of [Cu(N[^]NNH)₂][PF₆] have to be stored under argon.



Scheme 44 Investigated ancillary ligands N[^]NX with different heteroatoms (X = NH, NMe, O, S).

The N[^]N-chelating mode was confirmed by crystallographic data. Single crystals of [Cu(N[^]NO)₂][PF₆]·0.5CH₂Cl₂ (Fig. 90) and [Cu(N[^]NS)₂][PF₆] (Fig. 91) were grown by slow diffusion of Et₂O into CH₂Cl₂ solutions of the compounds. Both show the complexation via the nitrogen atoms and that the other heteroatoms O and S are not involved.

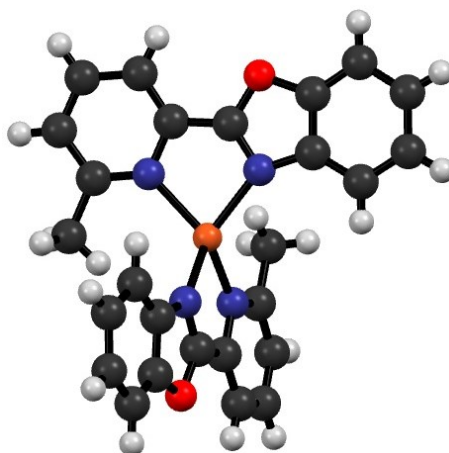


Fig. 90 X-ray crystallographic structure of the [Cu(N[^]NO)₂]⁺ cation.

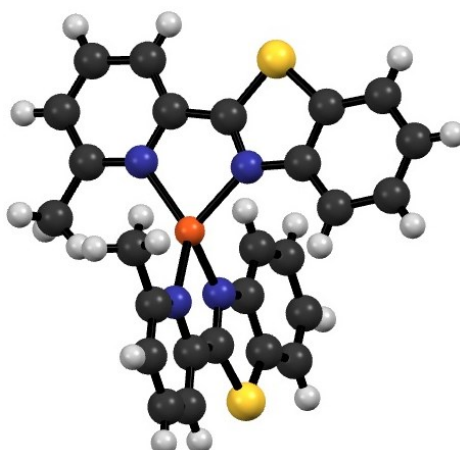


Fig. 91 X-ray crystallographic structure of the [Cu(N[^]NS)₂]⁺ cation.

The solution absorption spectra of the four homoleptic Cu(I) complexes (Fig. 92) show the typical metal-to-ligand charge transfer (MLCT) band between 400 and 520 nm for all complexes. High-energy bands arise from ligand-based $\pi^* \leftarrow \pi$ and $\pi^* \leftarrow n$ transitions as also seen in the 2,2'-bipyridine-based ligands (Fig. 69). That implies that the new N[^]NX ligands have comparable absorption characteristics to the bpy ligands.

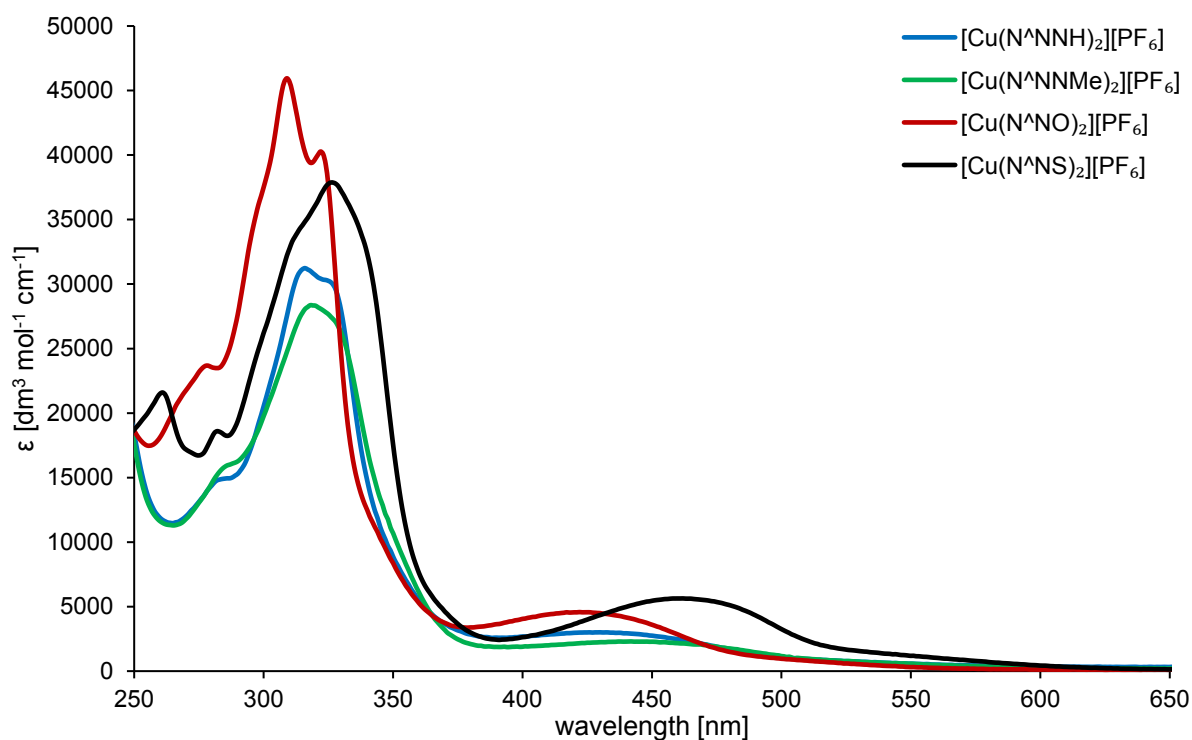


Fig. 92 UV-Vis absorption spectra of $[\text{Cu}(\text{N}^{\text{NNH}})_2][\text{PF}_6]$, $[\text{Cu}(\text{N}^{\text{NNMe}})_2][\text{PF}_6]$, $[\text{Cu}(\text{N}^{\text{NO}})_2][\text{PF}_6]$ and $[\text{Cu}(\text{N}^{\text{NS}})_2][\text{PF}_6]$.

The copper(I) complexes of N^{NNH} and N^{NNMe} have comparable UV-Vis absorption spectra. $[\text{Cu}(\text{N}^{\text{NNH}})_2][\text{PF}_6]$ has a higher extinction coefficient than $[\text{Cu}(\text{N}^{\text{NNMe}})_2][\text{PF}_6]$ over the whole wavelength range. $[\text{Cu}(\text{N}^{\text{NO}})_2][\text{PF}_6]$ has the highest extinction coefficient between 250 and 350 nm, whereas the most intense MLCT is observed for $[\text{Cu}(\text{N}^{\text{NS}})_2][\text{PF}_6]$. For the application in a DSC, the MLCT band is the most important one. The MLCT absorption maxima of all complexes shift significantly to lower energy as the heteroatom in the N^{NX} ligand is changed. The greatest intensity is measured with $[\text{Cu}(\text{N}^{\text{NS}})_2][\text{PF}_6]$. It also has the most red-shifted MLCT band energy of 465 nm. The MLCT absorption maximum of $[\text{Cu}(\text{N}^{\text{NNMe}})_2][\text{PF}_6]$ is at 446 nm, of $[\text{Cu}(\text{N}^{\text{NNH}})_2][\text{PF}_6]$ at 435 nm and for $[\text{Cu}(\text{N}^{\text{NO}})_2][\text{PF}_6]$ at 424 nm (Fig. 93).

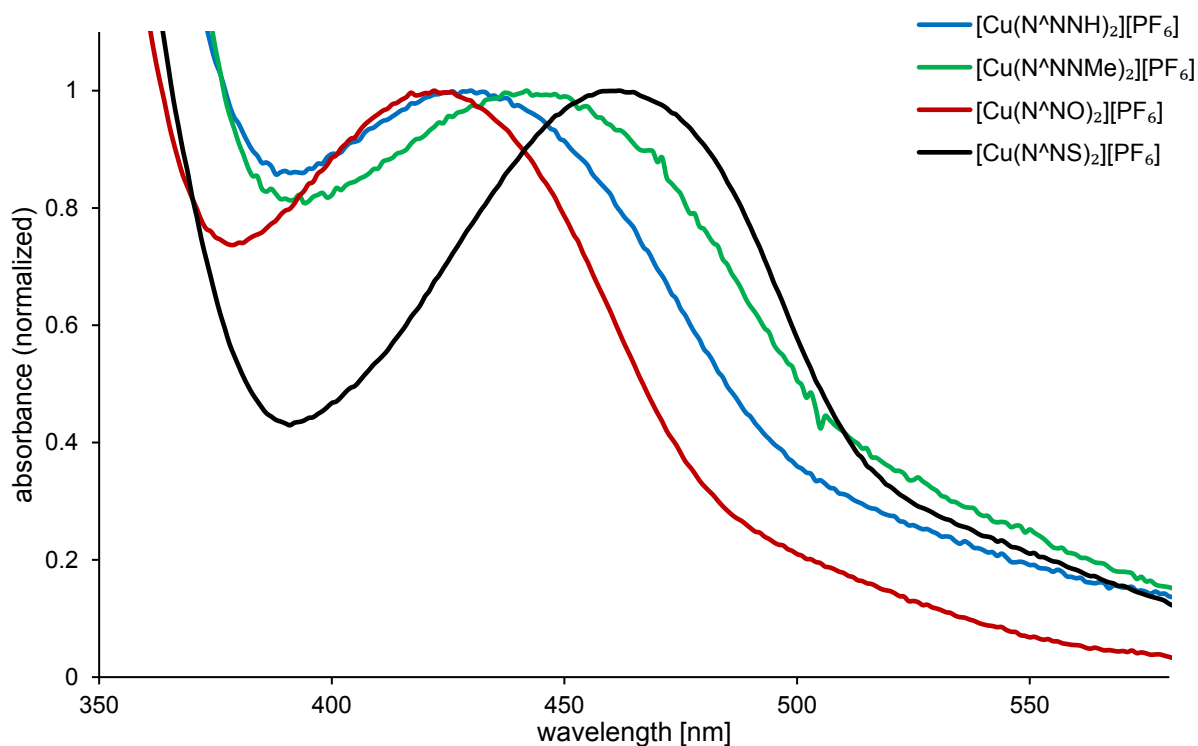


Fig. 93 Normalized UV-Vis absorption spectra of the MLCT band of the [Cu(N[^]NX)₂][PF₆] complexes.

In order to investigate the performance of the N[^]NX ligands in copper(I)-based dyes, transparent photoelectrodes were functionalized with the anchoring ligand **ALP1** and finally dipped in the homoleptic Cu(I) complex solution of the corresponding N[^]NX ligands. The heteroleptic [Cu(**ALP1**)(N[^]NX)]⁺ complex was formed by ligand exchange. The solid-state absorption spectra of all four dyes were measured (Fig. 94).

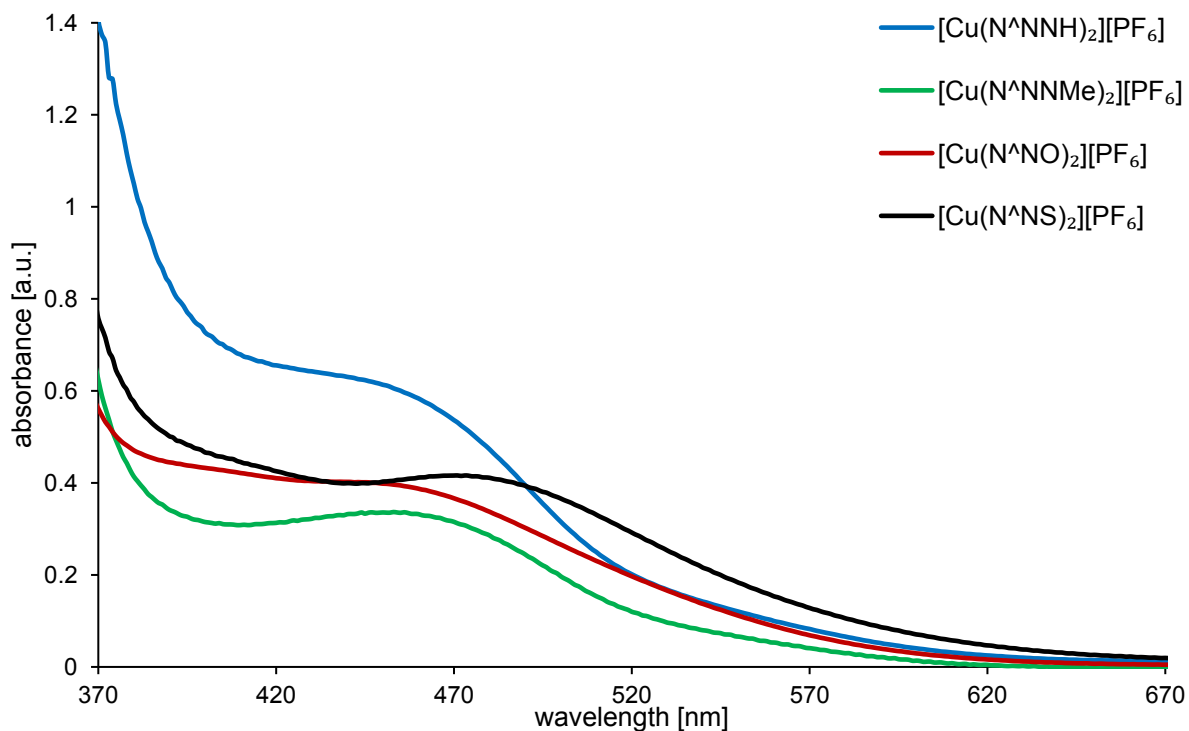


Fig. 94 Solid-state absorption spectra of electrodes containing the N[^]NX dyes.

The absorption maxima of the MLCT bands of the surface-adsorbed heteroleptic dyes is visible in all four spectra. They are all red-shifted with respect to the solution UV-Vis spectra of the homoleptic complexes (Fig. 93). The MLCT absorption maxima are at 443 nm for $[\text{Cu}(\text{ALP1})(\text{N}^{\text{^}}\text{NNH})]^+$, at 453 nm for $[\text{Cu}(\text{ALP1})(\text{N}^{\text{^}}\text{NNMe})]^+$, at 445 nm for $[\text{Cu}(\text{ALP1})(\text{N}^{\text{^}}\text{NO})]^+$ and at 471 nm for $[\text{Cu}(\text{ALP1})(\text{N}^{\text{^}}\text{NS})]^+$. Thus, the heteroleptic $\text{Cu}(\text{ALP1})(\text{N}^{\text{^}}\text{NS})^+$ dye has the lowest energy MLCT band with an absorption tail to about 630 nm (Fig. 94).

With a knowledge of the absorption spectroscopic properties of the heteroleptic complexes in hand, DSCs were assembled by the standard ligand-exchange dye-assembly process. The DSC performance of single-dye DSCs containing the heteroleptic surface-bound dyes $[\text{Cu}(\text{ALP1})(\text{N}^{\text{^}}\text{NNH})]^+$, $[\text{Cu}(\text{ALP1})(\text{N}^{\text{^}}\text{NNMe})]^+$, $[\text{Cu}(\text{ALP1})(\text{N}^{\text{^}}\text{NO})]^+$ or $[\text{Cu}(\text{ALP1})(\text{N}^{\text{^}}\text{NS})]^+$ were measured. Table 14 summarizes the DSC performance data on the day of assembling the cell and 3 days and 7 days after sealing the cell.

Table 14 DSC performance data for DSCs containing copper(I) dyes with the anchoring ligand **ALP1** and the ancillary ligands N[^]NX on the day of sealing the cells and 7 days after sealing the cell.

Dye	J_{sc} [mA cm ⁻²]	V_{oc} [mV]	ff [%]	η [%]	Relative η [%]
On the day of sealing the cell					
[Cu(ALP1)(N [^] NNH)] ⁺	6.93	608	72	3.03	40.1
[Cu(ALP1)(N [^] NNMe)] ⁺	6.99	558	70	2.71	35.9
[Cu(ALP1)(N [^] NO)] ⁺	6.91	531	71	2.62	34.7
[Cu(ALP1)(N [^] NS)] ⁺	7.76	530	70	2.88	38.1
N719	16.57	630	72	7.55	100.0
3 days after sealing the cell					
[Cu(ALP1)(N [^] NNH)] ⁺	6.88	604	72	2.97	41.2
[Cu(ALP1)(N [^] NNMe)] ⁺	6.38	555	71	2.51	34.8
[Cu(ALP1)(N [^] NO)] ⁺	6.19	568	69	2.44	33.8
[Cu(ALP1)(N [^] NS)] ⁺	6.77	542	70	2.58	35.8
N719	15.03	660	73	7.21	100.0
7 days after sealing the cell					
[Cu(ALP1)(N [^] NNH)] ⁺	7.16	607	72	3.12	45.4
[Cu(ALP1)(N [^] NNMe)] ⁺	6.74	552	70	2.60	37.8
[Cu(ALP1)(N [^] NO)] ⁺	6.40	579	67	2.47	36.0
[Cu(ALP1)(N [^] NS)] ⁺	7.42	558	63	2.59	37.7
N719	14.47	650	73	6.87	100.0

The performance data confirm that all DSCs are stable over a period of one week. The slight improvement in efficiency for some of the cells over a period of one week follows trends also observed for bpy-based DSCs. It is most likely associated with the initial formation of aggregates of the dye molecules on the surface followed by molecular reorganization over periods of days.¹³⁷¹³⁸¹³⁹ On the day of sealing the cell the DSC containing the dye [Cu(**ALP1**)(N[^]NNH)]⁺ has with 3.03% the best overall efficiency of the set of cells. It has a remarkably high V_{oc} of 608 mV. All other cells have an V_{oc} value between 530 and 558 mV. The cell containing the dye [Cu(**ALP1**)(N[^]NS)]⁺, has a J_{sc} value of almost 8 mA cm⁻² ($J_{sc} = 7.76$ mA cm⁻²) which has only been surpassed (at the time of study) by a DSC containing the ancillary ligand **PhLI** ($J_{sc} = 8.10$ mA cm⁻², Table 8). Although this is the highest measured J_{sc} value of this set, it is

noteworthy that all other cells also have a high J_{sc} value of almost 7 mA cm^{-2} ($J_{sc} = 6.93 \text{ mA cm}^{-2}$ for $[\text{Cu}(\text{ALP1})(\text{N}^{\wedge}\text{NNH})]^+$, $J_{sc} = 6.99 \text{ mA cm}^{-2}$ for $[\text{Cu}(\text{ALP1})(\text{N}^{\wedge}\text{NNMe})]^+$, $J_{sc} = 6.91 \text{ mA cm}^{-2}$ for $[\text{Cu}(\text{ALP1})(\text{N}^{\wedge}\text{NO})]^+$).

The good J_{sc} values are also represented in the EQE curves (Fig. 95). The shape of the curves is comparable to bpy-based DSCs (Fig. 70) what confirms the usefulness of the new N[^]NX ancillary ligands in Cu(I)-based dyes. EQE measurements on the day of sealing the cell give EQE_{max} values over 50% for all cells (Table 15). The EQE spectra all exhibit λ_{max} of 480 nm, despite the variation (443–471 nm) observed in the broad MLCT solid-state absorption spectra of the dyes (Fig. 94). All DSCs obtain EQE_{max} values higher ($EQE_{max} = 53.0 - 55.3\%$, Table 15) than the EQE_{max} value of the most intensively optimized bpy-based dye **PhLI** ($EQE_{max} = 52.2\%$, Fig. 79).

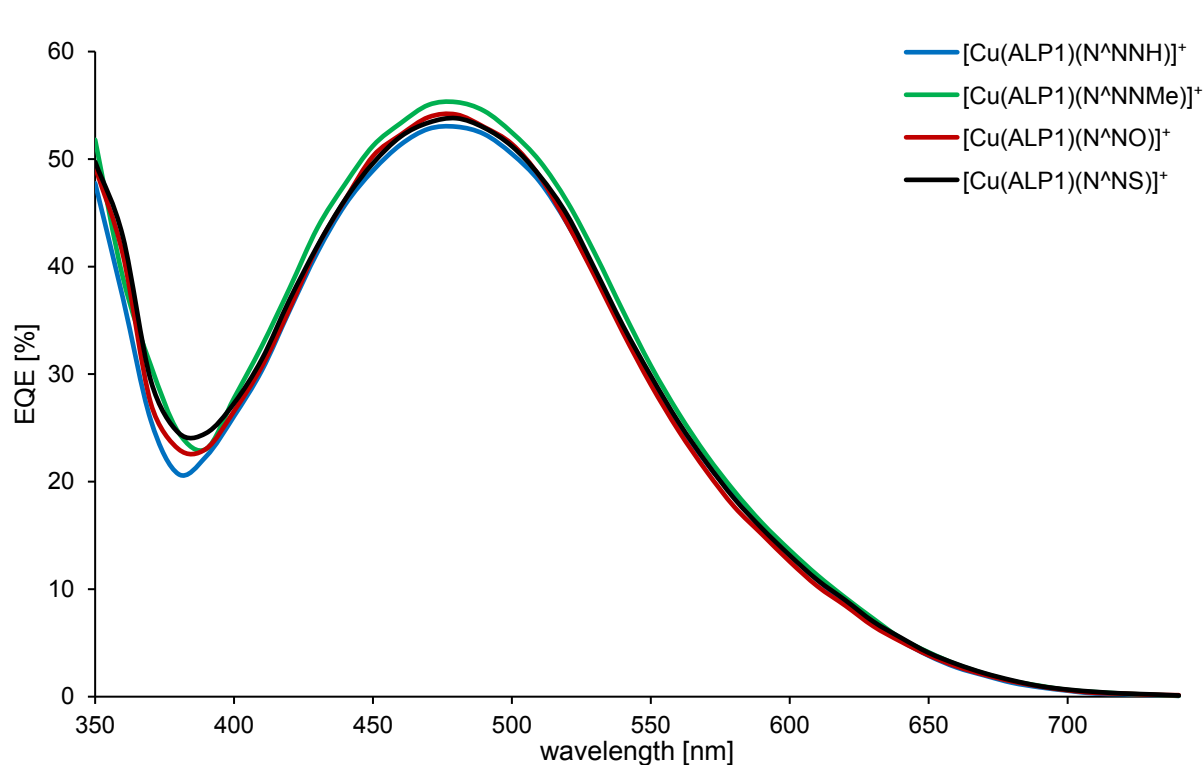


Fig. 95 EQE spectra of DSCs containing the dyes $[\text{Cu}(\text{ALP1})(\text{N}^{\wedge}\text{NNH})]^+$ recorded on the day of cell assembly.

Table 15 EQE data for DSC containing copper(I) dyes with the anchoring ligand **ALP1** and the ancillary ligands N[^]NX on the day of sealing the cells, 3 and 7 days after sealing the cell.

Dye	Day 0		Day 3		Day 7	
	λ_{max} [nm]	EQE_{max} [%]	λ_{max} [nm]	EQE_{max} [%]	λ_{max} [nm]	EQE_{max} [%]
[Cu(ALP1)(N [^] NNH)] ⁺	480	53.0	480	53.1	480	54.7
[Cu(ALP1)(N [^] NNMe)] ⁺	480	55.3	480	53.4	480	54.0
[Cu(ALP1)(N [^] NO)] ⁺	480	54.1	470	50.5	470	50.2
[Cu(ALP1)(N [^] NS)] ⁺	480	53.8	480	50.8	470	46.2

All DSCs have a ff over 70% which implies a good working cell with low resistance within the cell which will be discussed later with the implementation of the new method electrochemical impedance spectroscopy (details see: *8.4 Electrical Impedance Spectroscopy*). The high J_{sc} and V_{oc} values for [Cu(**ALP1**)(N[^]NS)]⁺ and [Cu(**ALP1**)(N[^]NNH)]⁺, respectively, can also be observed in the J - V curves of the DSCs (Fig. 96).

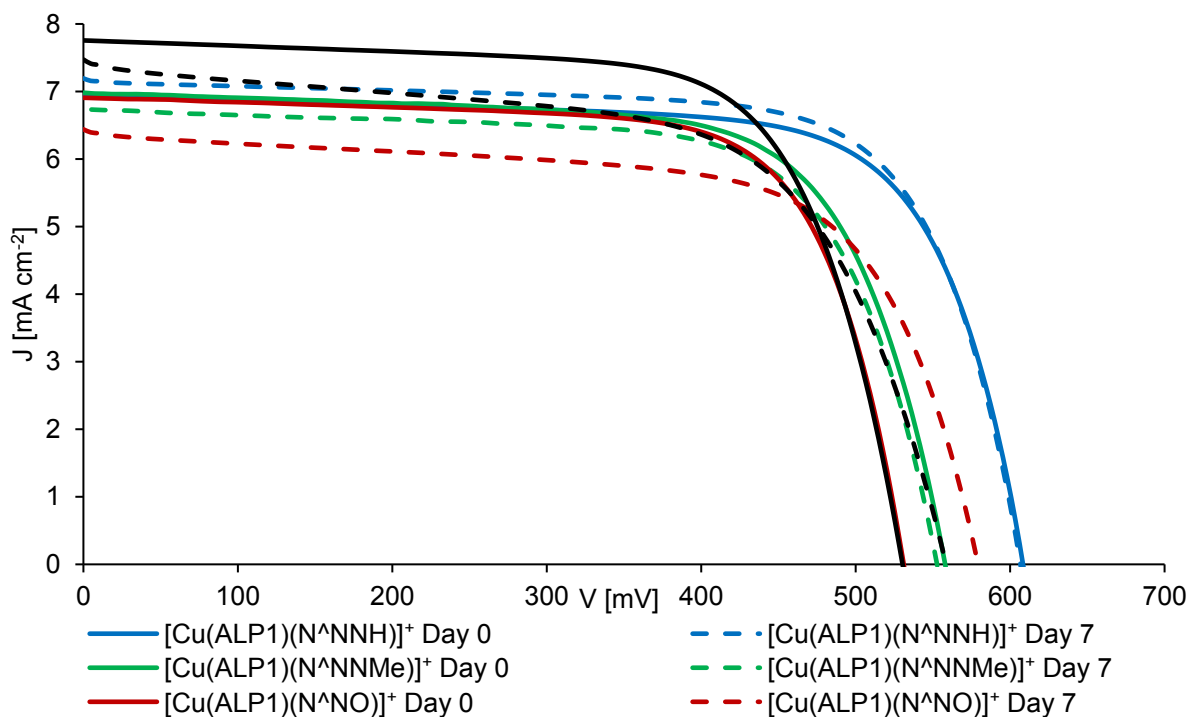


Fig. 96 J - V curves for the DSCs containing of the anchoring ligand **ALP1** and the ancillary ligands N[^]NX on the day of sealing the cells and 7 days after sealing the cell.

The trends in performance are constant over a period of 7 days. The cell containing the dye [Cu(ALP1)(N[^]NS)]⁺ has the highest J_{sc} value ($J_{sc} = 7.42 \text{ mA cm}^{-2}$) and the cell containing the dye [Cu(ALP1)(N[^]NNH)]⁺ has the highest V_{oc} value ($V_{oc} = 607 \text{ mV}$). The performance of the DSC containing [Cu(ALP1)(N[^]NO)]⁺ was tested after the cell had been stored in the dark for 9 months. After this period, the cell had a J_{sc} value of 4.86 mA cm^{-2} , an V_{oc} value of 605 mV and an η of 2.15% emphasizing the long-term stability of the device.

The ancillary ligands N[^]NNH and N[^]NNMe only differ in replacing the imidazolyl NH by NMe. This results in small change in the values of J_{sc} ($J_{sc} = 6.93 \text{ mA cm}^{-2}$ for [Cu(ALP1)(N[^]NNH)]⁺, $J_{sc} = 6.99 \text{ mA cm}^{-2}$ for [Cu(ALP1)(N[^]NNMe)]⁺, Table 14). However, the change from NH to NMe results in a drop in V_{oc} of about 50 mV. As a consequence, the DSC containing [Cu(ALP1)(N[^]NNH)]⁺ has a higher overall efficiency.

It is very satisfying that these simple unmodified N[^]NX ancillary ligands show comparable results to the best tuned bpy ancillary ligands.

The fact that N[^]NS leads to the highest short-circuit current density ($J_{sc} = 7.76 \text{ mA cm}^{-2}$), while the open-circuit voltage is optimized with N[^]NNH ($V_{oc} = 608 \text{ mV}$), resulted in the suggestion to combine the benefits of both by using a co-sensitized approach.

Three different procedures were used to combine both dyes on the semiconductor surface. The first procedure was dipping the anchoring ligand functionalized photoelectrode into a 1 : 1 mixture of the homoleptic copper(I) complexes [Cu(N[^]NNMe)₂][PF₆] and [Cu(N[^]NS)₂][PF₆] (1:1); this method is termed the 1:1 co-sensitization procedure. The other two possibilities are the stepwise dipping procedure. The functionalized photoelectrode was first immersed in the [Cu(N[^]NNH)₂][PF₆] and then in the [Cu(N[^]NS)₂][PF₆] solution (N/S procedure) or first in the [Cu(N[^]NS)₂][PF₆] and then in the [Cu(N[^]NNH)₂][PF₆] solution (S/N procedure). The stock solutions have a concentration of 0.1 mM in CH₂Cl₂. After each dipping step, the photoelectrode was washed with CH₂Cl₂ and dried with a heat gun at about 80 °C.

In order to investigate the behaviour of both dyes on the semiconductor surface the procedures were tested using transparent electrodes. Fig. 97 displays the solid-state absorption spectra of the single-dye DSCs and the DSC assembled by the 1:1 co-sensitization procedure.

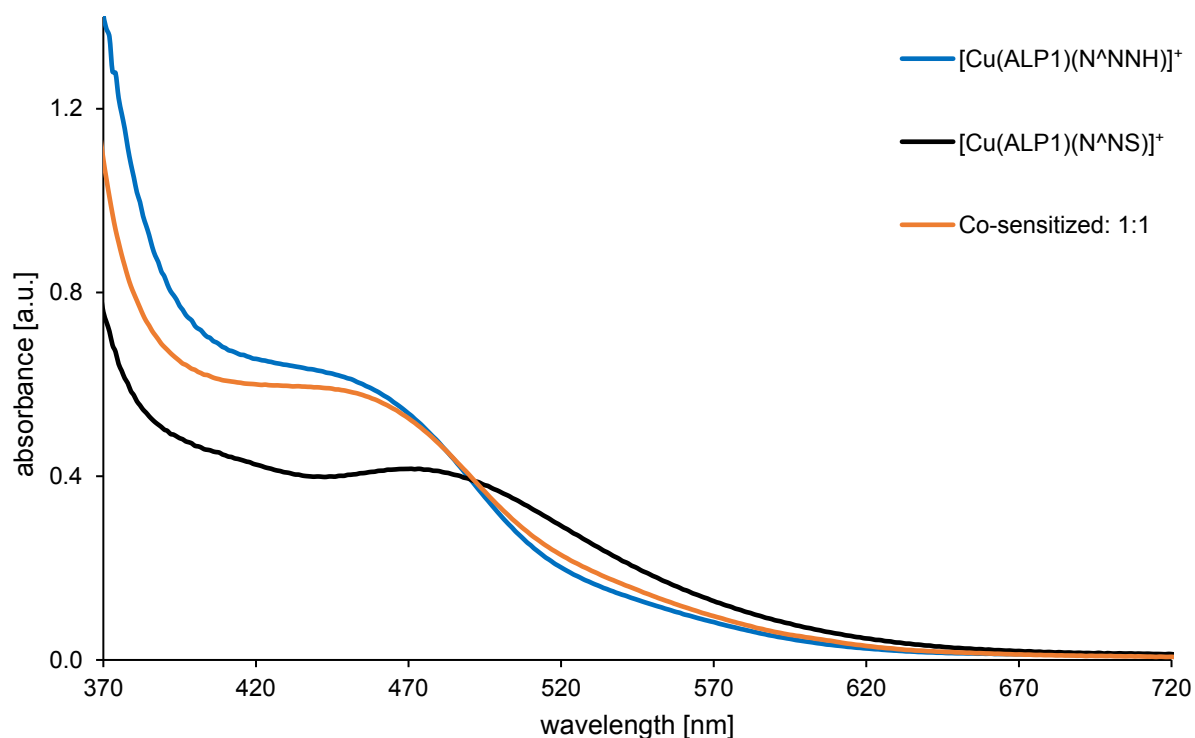


Fig. 97 Solid-state absorption spectra of transparent photoelectrodes functionalized with single dyes $[\text{Cu}(\text{ALP1})(\text{N}^{\text{^}}\text{NNH})]^+$ and $[\text{Cu}(\text{ALP1})(\text{N}^{\text{^}}\text{NS})]^+$, respectively, compared with co-sensitized photoelectrodes treated by the 1:1 procedure.

Compared to values of λ_{max} of 443 for $[\text{Cu}(\text{ALP1})(\text{N}^{\text{^}}\text{NNH})]^+$ and 471 nm for $[\text{Cu}(\text{ALP1})(\text{N}^{\text{^}}\text{NS})]^+$, respectively, for the single dyes, the co-sensitized surface has an absorption maximum at about 440 nm. This implies that the dye $[\text{Cu}(\text{ALP1})(\text{N}^{\text{^}}\text{NNH})]^+$ is more dominant on the surface. The only slightly more intense absorption of the co-sensitized photoelectrode with respect to the single-dye between 480 and 570 nm (Fig. 97) shows that little $[\text{Cu}(\text{ALP1})(\text{N}^{\text{^}}\text{NS})]^+$ is present on the semiconductor surface. This suggested that competition between the dyes in the 1 : 1 mixture leads to preferential coverage with $[\text{Cu}(\text{ALP1})(\text{N}^{\text{^}}\text{NNH})]^+$ rather than a mixture of $[\text{Cu}(\text{ALP1})(\text{N}^{\text{^}}\text{NNH})]^+$ and $[\text{Cu}(\text{ALP1})(\text{N}^{\text{^}}\text{NS})]^+$ and that dye-bath solution composition is not reflected in the composition of dyes on the surface.

Next, the S/N and N/S co-sensitization procedures were tested and the results proved to be different (Fig. 98). For the electrode that was co-sensitized by the S/N procedure the solid-state absorption spectrum maximum was at 442 nm what replicates that of the single dye $[\text{Cu}(\text{ALP1})(\text{N}^{\text{^}}\text{NNH})]^+$ (443 nm). This is consistent with the higher affinity of $\text{N}^{\text{^}}\text{NNH}$ than $\text{N}^{\text{^}}\text{NS}$. In the last dipping step $\text{N}^{\text{^}}\text{NNH}$ apparently displaces coordinated $\text{N}^{\text{^}}\text{NS}$.

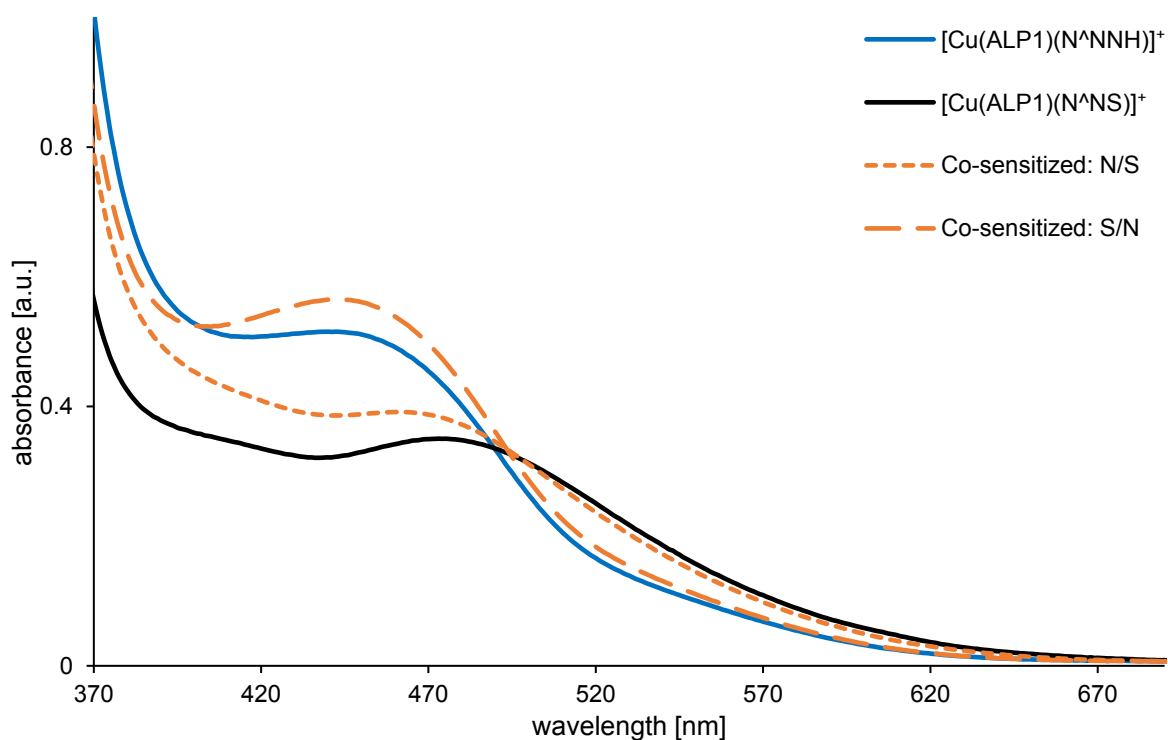


Fig. 98 Solid-state absorption spectra of transparent photoelectrodes functionalized with single dyes $[\text{Cu}(\text{ALP1})(\text{N}^{\text{NNH}})]^+$ and $[\text{Cu}(\text{ALP1})(\text{N}^{\text{NS}})]^+$, respectively, compared with co-sensitized photoelectrodes treated sequentially by the N/S and S/N procedure, respectively.

In contrast, the broad MLCT absorption for the electrode co-sensitized by the N/S procedure surface with λ_{max} at 460 nm suggests that both dyes $[\text{Cu}(\text{ALP1})(\text{N}^{\text{NNH}})]^+$ and $[\text{Cu}(\text{ALP1})(\text{N}^{\text{NS}})]^+$ are bound to the TiO_2 surface. This suggests that N^{NNH} is a significantly stronger σ -donor than N^{NS} and the Cu(I) complex $[\text{Cu}(\text{ALP1})(\text{N}^{\text{NNH}})]^+$ is more stable with respect to ligand displacement than $[\text{Cu}(\text{ALP1})(\text{N}^{\text{NS}})]^+$.

The results obtained from the solid-state absorption spectroscopy data were then applied to the DSC assembly. The photoelectrodes were co-sensitized using the 1:1, N/S and S/N procedures, respectively, and an I^-/I_3^- electrolyte was used. The DSC performance data are summarized in Table 16.

Table 16 DSC performance data for DSCs co-sensitized by the different procedures containing copper(I) dyes with the anchoring ligand **ALP1** and the ancillary ligands **N[^]NNH** and **N[^]NS** on the day of sealing the cells, 3 days and 7 days after sealing the cell.

co-sensitization procedure ^a	J_{sc} [mA cm ⁻²]	V_{oc} [mV]	ff [%]	η [%]	Relative η [%]
On the day of sealing the cell					
1:1	7.20	592	71	3.02	40.0
S/N	6.91	588	73	2.96	39.2
N/S	6.35	528	73	2.44	32.3
N719	16.57	630	72	7.55	100.0
3 days after sealing the cell					
1:1	7.34	593	71	3.07	42.6
S/N	6.18	583	72	2.61	36.2
N/S	5.93	519	72	2.20	30.5
N719	15.03	660	73	7.21	100.0
7 days after sealing the cell					
1:1	7.30	600	71	3.10	45.1
S/N	6.24	586	72	2.63	38.3
N/S	5.95	521	72	2.22	32.3
N719	14.47	650	73	6.87	100.0

a) see text for description of co-sensitization procedures.

First, the use of the 1:1 co-sensitization procedure is considered. A comparison of the performances of the single-dye DSC (Table 14) with the performance of the co-sensitized cell shows that the high V_{oc} values of DSC sensitized with only [Cu(**ALP1**)(**N[^]NNH**)]⁺ is also observed for the co-sensitized cell. The small gain in J_{sc} (6.93 (Table 14) to 7.20 mA cm⁻² (Table 16)) is consistent with a small increase in EQE_{max} (53.0%, Table 15 to 56.8%, Table 17).

Table 17 EQE data for DSCs co-sensitized by the different procedures containing of the anchoring ligand **ALP1** and the ancillary ligands **N[^]NNH** and **N[^]NS** on the day of sealing the cells, 3 days and 7 days after sealing the cell.

Dye	Day 0		Day 3		Day 7	
	λ_{max} [nm]	EQE_{max} [%]	λ_{max} [nm]	EQE_{max} [%]	λ_{max} [nm]	EQE_{max} [%]
1:1	480	56.8	470	56.9	470	56.8
S/N	480	51.3	470	47.6	480	48.5
N/S	460	40.6	470	46.9	480	46.4

The latter is maintained over a period of a week after fabricating the cells. While the overall efficiencies of 3% (Table 16) are satisfyingly 40% that of the **N719** reference DSC and the cells are stable over a period of a week (Fig. 99, solid curves), there is no noticeable enhancement with respect to the DSCs sensitized with $[\text{Cu}(\text{ALP1})(\text{N}^{\wedge}\text{NNH})]^+$ alone and, taken with the solid-state absorption data, suggest that surface-coverage by $[\text{Cu}(\text{ALP1})(\text{N}^{\wedge}\text{NNH})]^+$ is dominant when the electrode functionalized with anchor **ALP1** is exposed to both $[\text{Cu}(\text{N}^{\wedge}\text{NNH})_2]^+$ and $[\text{Cu}(\text{N}^{\wedge}\text{NS})_2]^+$.

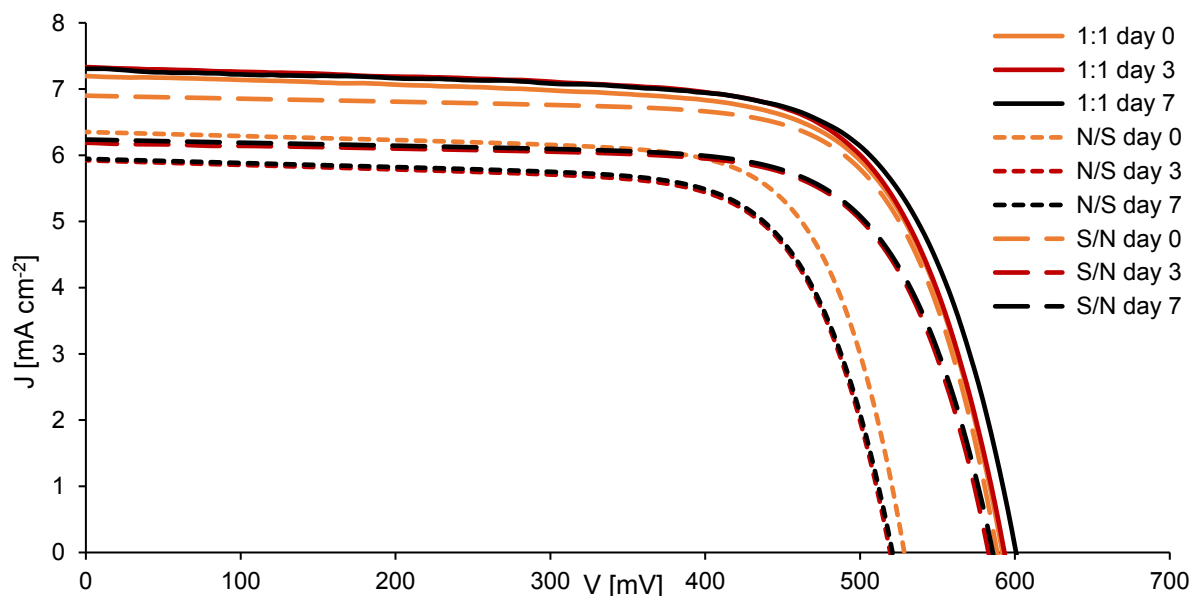


Fig. 99 J - V curves for the DSCs containing mixtures of the dyes $[\text{Cu}(\text{ALP1})(\text{N}^{\wedge}\text{NNH})]^+$ and $[\text{Cu}(\text{ALP1})(\text{N}^{\wedge}\text{NS})]^+$ on the day of sealing the cells, 3 days and 7 days after sealing the cell.

Next, we consider electrodes functionalized with **ALP1** that are treated sequentially with $[\text{Cu}(\text{N}^{\wedge}\text{NS})_2]^+$ and then $[\text{Cu}(\text{N}^{\wedge}\text{NNH})_2]^+$. The performances of these DSCs are rather similar to those fabricated using the mixed dye-bath (Table 16). Again, values of J_{sc} and V_{oc} , the EQE_{max} and solid-state absorption spectra are all consistent with the dominant dye being $[\text{Cu}(\text{ALP1})(\text{N}^{\wedge}\text{NNH})]^+$. Exposing the anchor-functionalized electrodes to the homoleptic copper(I) complexes in the reverse order, (i.e. $[\text{Cu}(\text{N}^{\wedge}\text{NNH})_2]^+$ then $[\text{Cu}(\text{N}^{\wedge}\text{NS})_2]^+$) results in poorer performing DSCs. The high values of J_{sc} that were characteristic of the single S-containing dye $[\text{Cu}(\text{ALP1})(\text{N}^{\wedge}\text{NS})]^+$ are not observed for the mixed dye system. The values of V_{oc} for DSCs with dyes assembled by the S/N procedure are close to those obtained when the dyes are assembled using the 1 : 1 mixture of $[\text{Cu}(\text{N}^{\wedge}\text{NNMe})_2][\text{PF}_6]$ and $[\text{Cu}(\text{N}^{\wedge}\text{NS})_2][\text{PF}_6]$ in the dye-bath (Fig. 99). Moreover, the V_{oc} values replicate those observed for the DSCs with the single dye $[\text{Cu}(\text{ALP1})(\text{N}^{\wedge}\text{NNH})]^+$. In contrast, V_{oc} values for the DSC with dyes assembled by the N/S method are similar to those of the DSC with single dye $[\text{Cu}(\text{ALP1})(\text{N}^{\wedge}\text{NS})]^+$. The results from this part of the investigation are consistent with competition for surface binding-sites with ligand **N[^]NH** dominating over **N[^]NS**, both in binding and in contribution to the overall photoresponse.

In order to investigate the electrochemical processes within the DSC and extract additional parameters electrochemical impedance spectroscopy (EIS) (see *8.4 Electrical Impedance Spectroscopy*) of the DSCs were measured.

First of all, DSCs containing the single surface-bound dyes $[\text{Cu}(\text{ALP1})(\text{N}^{\wedge}\text{NNH})]^+$, $[\text{Cu}(\text{ALP1})(\text{N}^{\wedge}\text{NNMe})]^+$, $[\text{Cu}(\text{ALP1})(\text{N}^{\wedge}\text{NO})]^+$ or $[\text{Cu}(\text{ALP1})(\text{N}^{\wedge}\text{NS})]^+$ are considered in the following discussion. The influence of the heteroatom is initially investigated, and then the impact of replacing a proton by a methyl group on going from ligand **N[^]NH** to **N[^]NNMe**. Finally, the different co-sensitized DSCs are considered. All EIS measurements were conducted 3 days after sealing the cell. All DSCs utilize the same anchoring ligand **ALP1** and have identical electrolyte composition as well as TiO₂ semiconductor and counter electrodes.

EIS for DSCs containing $[\text{Cu}(\text{ALP1})(\text{N}^{\wedge}\text{NNH})]^+$, $[\text{Cu}(\text{ALP1})(\text{N}^{\wedge}\text{NNMe})]^+$, $[\text{Cu}(\text{ALP1})(\text{N}^{\wedge}\text{NO})]^+$ or $[\text{Cu}(\text{ALP1})(\text{N}^{\wedge}\text{NS})]^+$ are discussed in the following part. The key parameters of the EIS measurement at a light intensity of 22 mW cm⁻² are given in Table 18, and those for a light intensity of 2.2 mW cm⁻² in Table 19.

Table 18 EIS data obtained from measurements at a light intensity of 22 mW cm⁻² of DSCs containing the dye [Cu(ALP1)(N[^]NX)]⁺.

dye	V_{oc}^a [mV]	R_{rec} [Ω]	C_{μ} [μF]	R_{Pt} [Ω]	$C_{Pt\mu}$ [μF]	τ^b [ms]
[Cu(ALP1)(N [^] NNH)] ⁺	621	159	337	9	6	54
[Cu(ALP1)(N [^] NNMe)] ⁺	590	189	244	16	5	46
[Cu(ALP1)(N [^] NO)] ⁺	587	210	298	15	6	62
[Cu(ALP1)(N [^] NS)] ⁺	554	178	322	20	6	57

a) V_{oc} values obtained from the EIS measurement at a given light intensity.

b) calculated from Equation 9

Table 19 EIS data obtained from measurements at a light intensity of 2.2 mW cm⁻² of DSCs containing the dye [Cu(ALP1)(N[^]NX)]⁺.

dye	V_{oc}^a [mV]	R_{rec} [Ω]	C_{μ} [μF]	R_{Pt} [Ω]	$C_{Pt\mu}$ [μF]	R_r [Ω]	τ^b [ms]	L_d [μm]
[Cu(ALP1)(N [^] NNH)] ⁺	552	974	170	6	12	124	166	34
[Cu(ALP1)(N [^] NNMe)] ⁺	504	1014	131	21	6	160	133	30
[Cu(ALP1)(N [^] NO)] ⁺	538	1076	168	13	9	129	180	35
[Cu(ALP1)(N [^] NS)] ⁺	510	893	187	19	7	106	167	35

a) V_{oc} values obtained from the EIS measurement at a given light intensity.

b) calculated from Equation 9

c) calculated from Equation 10

The data in Table 18 demonstrate that DSCs with [Cu(ALP1)(N[^]NNH)]⁺, [Cu(ALP1)(N[^]NO)]⁺ and [Cu(ALP1)(N[^]NS)]⁺ have a higher chemical capacitance (C_{μ}) and lower recombination resistance (R_{rec}). The higher the capacitance, the higher the total charge density in the TiO₂ semiconductor, and the more electrons reside in the conduction band prior to collection. When the transport resistance (R_r) is also low, a higher J_{sc} is observed because of the higher mobility of electrons and shorter transit times in the semiconductor. The fact that R_r is rather low relative to R_{rec} in all of the DSCs (Table 24) is shown by the good separation of the first and second semi-circles in the Nyquist plot shown in Fig. 100.

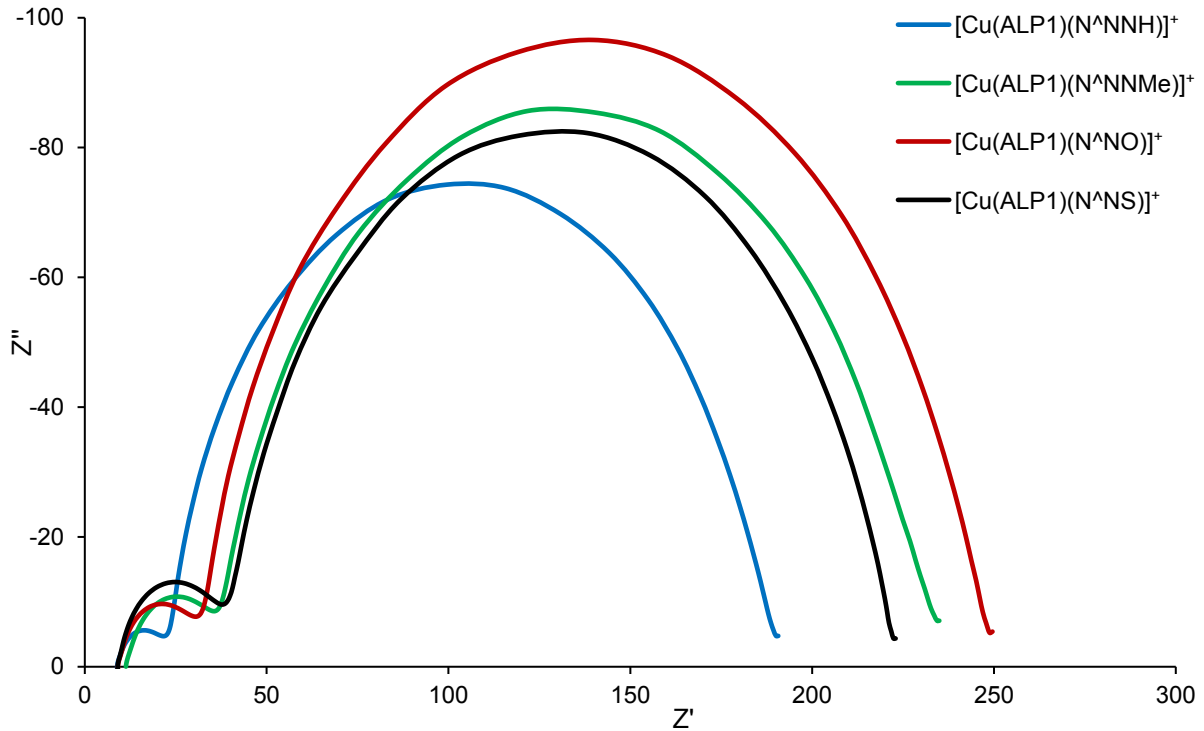


Fig. 100 Nyquist plots of DSCs containing the dyes $[\text{Cu}(\text{ALP1})(\text{N}^{\text{NX}})]^+$ at a light intensity of 22 mW cm^{-2} .

A comparison of the DSCs containing dyes $[\text{Cu}(\text{ALP1})(\text{N}^{\text{NNH}})]^+$ and $[\text{Cu}(\text{ALP1})(\text{N}^{\text{NO}})]^+$ is instructive. At high light intensities, $[\text{Cu}(\text{ALP1})(\text{N}^{\text{NNH}})]^+$ leads to a higher C_{μ} and a lower R_{rec} . However, in this case the negative influence on the performance of the DSC of a low R_{rec} is partly offset by a low R_r (Table 19) with the result that the electrons are easily transported through the semiconductor. This results in the high J_{sc} (6.88 mA cm^{-2} on day 3, Table 14) of the DSCs containing the dye $[\text{Cu}(\text{ALP1})(\text{N}^{\text{NNH}})]^+$. The R_r values are extracted from the EIS measurements at low light intensities (Table 19), because R_r is more dominant at moderate voltages, as is seen in Fig. 101.

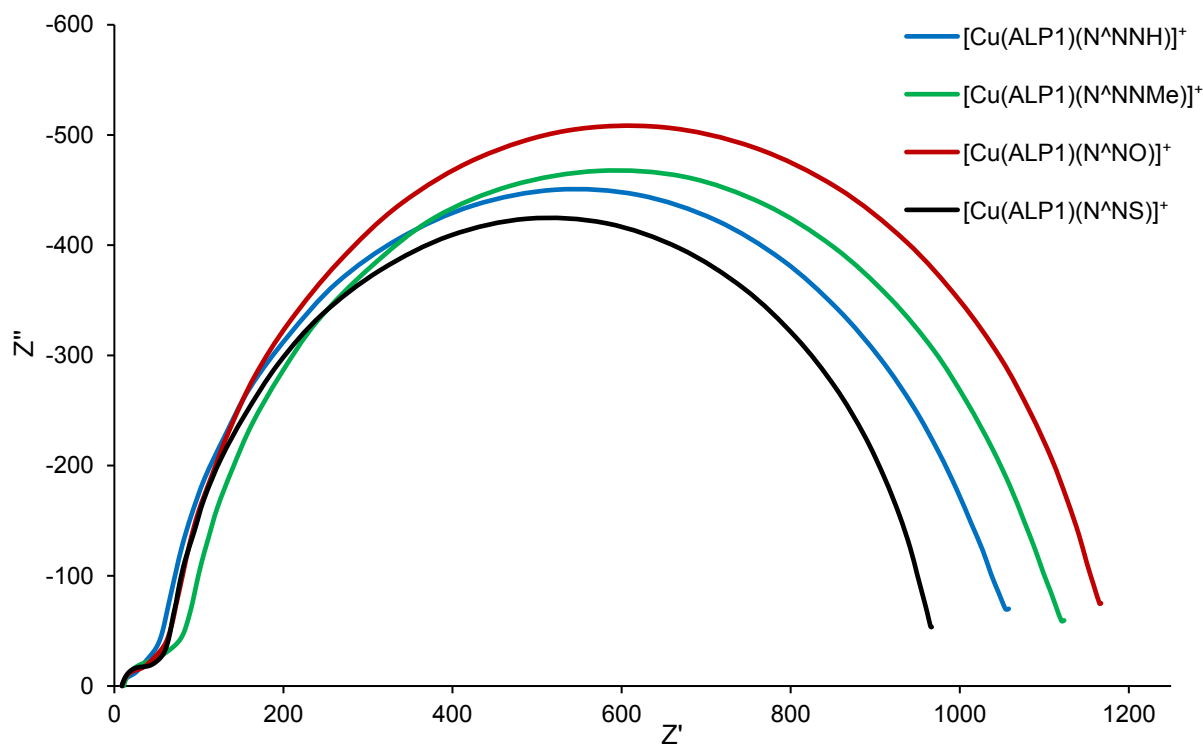


Fig. 101 Nyquist plots of DSCs containing the dyes $[\text{Cu}(\text{ALP1})(\text{N}^{\text{NX}})]^+$ at a light intensity of 2.2 mW cm^{-2} .

On the other hand, DSCs with ancillary ligand **N[^]NO** have a low C_μ and a high R_{rec} in conjunction with a comparable R_{tr} . Here, the lowest J_{sc} value (6.19 mA cm^{-2} on day 3, Table 14) is observed because fewer electrons are injected into the semiconductor, whilst the electron transport remains comparable to DSCs with ligand **N[^]NNH**. DSCs with **N[^]NS** have the lowest R_{tr} of all single dye DSCs (see Table 19) but the C_μ and R_{rec} lie in between those of **N[^]NNH** and **N[^]NO** at high light intensities (see Table 18). This trend is observed in the rather high J_{sc} (6.77 mA cm^{-2} on day 3, Table 14) of the DSCs containing the dye $[\text{Cu}(\text{ALP1})(\text{N}^{\text{NS}})]^+$ found in the J - V measurements (Table 14). In a DSC, the theoretical V_{oc} is the difference between the energy level of the redox couple in the electrolyte and the Fermi level (E_F) of the semiconductor. The latter may be altered by increasing or decreasing the conduction band (CB) level; a more negative CB leads to an increase in V_{oc} and vice versa. In this study, the I^-/I_3^- electrolyte is constant and observed changes in V_{oc} arise from changes to the CB level of the semiconductor brought about by the variation in dye. As seen in Table 14, the highest V_{oc} is observed with a DSC containing $[\text{Cu}(\text{ALP1})(\text{N}^{\text{NNH}})]^+$ and the lowest with $[\text{Cu}(\text{ALP1})(\text{N}^{\text{NS}})]^+$. The trends in the J - V curves are also observed in the EIS measurements at a light intensity of 22 mW cm^{-2} under

open-circuit voltage conditions. As stated above, more efficient electron injection may result in a higher C_μ . However, a better charge injection is favoured by a more extensive charge compensation which, in turn, results in a lower CB level and, consequently, a lower V_{oc} .¹⁵⁸ In addition to the influence of the charge compensation on the CB level, the electron recombination with the I_3^- in the electrolyte also has an impact. A relatively high C_μ and a high R_{rec} yield a good value for the electron lifetime (τ), calculated as the product of C_μ and R_{rec} . All DSCs show values of τ between 54 and 62 ms. A higher τ implies a lower charge loss in the semiconductor which keeps V_{oc} at a high value. The length of the diffusion path (L_d) for electrons in the semiconductor is also a good parameter to understand the functioning of the device. For a well-functioning cell, L_d should be greater than the thickness of the semiconductor layer. This is the case for all the DSCs studied, even at low light intensities. Table 19 shows that the DSCs have L_d values of 30–35 nm, about three times the thickness of the semiconductor of about 12 nm. In conclusion, the more electrons are accumulated in the semiconductor, the more likely it is that the CB level is shifted to more negative potential and the higher the resulting V_{oc} . The interplay of all of these parameters influences the V_{oc} , although the direct impact of individual parameters cannot be extracted. The effect of replacing the imidazolyl NH by NMe in comparing ancillary ligands N[^]NNH and N[^]NNMe is considered in the next part. When comparing the J-V curves of DSCs containing surface-bound dyes [Cu(ALP1)(N[^]NNH)]⁺ or [Cu(ALP1)(N[^]NNMe)]⁺ (blue and green curves in Fig. 96), the only significant differences are in V_{oc} (608 mV for [Cu(ALP1)(N[^]NNH)]⁺ and 558 mV for [Cu(ALP1)(N[^]NNMe)]⁺ on the day of sealing the DSCs, and 604 and 555 mV, respectively, on day 3, Table 14). The EIS measurements (Table 18 and Table 19) demonstrate that the DSC with [Cu(ALP1)(N[^]NNH)]⁺ has a higher C_μ but a lower R_{rec} and lower R_r than with [Cu(ALP1)(N[^]NNMe)]⁺. The higher C_μ and the lower R_r of DSCs containing [Cu(ALP1)(N[^]NNH)]⁺ versus [Cu(ALP1)(N[^]NNMe)]⁺ should result in a higher J_{sc} . On the other hand, the higher R_{rec} of [Cu(ALP1)(N[^]NNMe)]⁺ might lead to comparable J_{sc} values (Table 14). The only molecular difference between these dyes is the imidazolyl NH (in N[^]NNH) versus NMe (in N[^]NNMe). The higher R_{rec} of the DSC with [Cu(ALP1)(N[^]NNMe)]⁺ may be an effect of the methyl group shielding the semiconductor surface through increased steric hindrance compared to [Cu(ALP1)(N[^]NNH)]⁺. Consequently, less electrolyte can reach the surface to promote recombination reactions between the injected electrons and the electrolyte. The fact that neither a higher C_μ nor higher V_{oc} is associated with ancillary ligand N[^]NNMe suggests that the presence of the electron-donating Me group does not lead to better charge injection. As stated earlier, the only notable difference between the DSCs containing

[Cu(**ALP1**)(N[^]NNH)]⁺ and [Cu(**ALP1**)(N[^]NNMe)]⁺ is the V_{oc} . From an EIS point of view, the origin of this difference can be seen in the values of τ and L_d . Both parameters are higher for the DSC containing [Cu(**ALP1**)(N[^]NNH)]⁺. As already discussed, compared to the DSC with [Cu(**ALP1**)(N[^]NNMe)]⁺, that with [Cu(**ALP1**)(N[^]NNH)]⁺ benefits from a higher C_μ and lower R_{tr} . Consequently, less electron loss in the semiconductor results in a higher population of electrons in the CB, and as a consequence, a higher E_F and a higher V_{oc} . In conclusion, the high C_μ , low R_{tr} , and good L_d and τ values contribute to the high values of V_{oc} and J_{sc} observed for DSCs with the dye [Cu(**ALP1**)(N[^]NNH)]⁺ (Table 14).

The J - V measurements of the DSCs containing [Cu(**ALP1**)(N[^]NS)]⁺ and [Cu(**ALP1**)(N[^]NNH)]⁺ showed that use of ancillary ligand N[^]NNH or N[^]NS leads to the highest V_{oc} or J_{sc} , respectively. The results of co-sensitization experiments were significantly affected by the different dipping conditions used in the dye-baths, and the latter are expected to have an impact on the EIS parameters. EIS data for co-sensitized DSCs are presented in Table 20 and Table 21, and the nomenclature in the left-hand column is the same as in Table 16.

Table 20 EIS data obtained from measurements at a light intensity of 22 mW cm⁻² of DSCs co-sensitized by the different procedures containing of the anchoring ligand **ALP1** and the ancillary ligands N[^]NNH and N[^]NS.

dye	V_{oc}^a [mV]	R_{rec} [Ω]	C_μ [μF]	R_{Pt} [Ω]	$C_{Pt\mu}$ [μF]	τ^b [ms]
1:1	634	114	432	20	6	49
S/N	623	171	319	14	5	55
N/S	556	133	174	21	7	23

a) V_{oc} values obtained from the EIS measurement at a given light intensity.

b) calculated from Equation 9

Table 21 EIS data obtained from measurements at a light intensity of 2.2 mW cm⁻² of DSCs co-sensitized by the different procedures containing of the anchoring ligand **ALP1** and the ancillary ligands N[^]NNH and N[^]NS.

dye	V_{oc}^a [mV]	R_{rec} [Ω]	C_{μ} [μF]	R_{Pt} [Ω]	$C_{Pt\mu}$ [μF]	R_{tr} [Ω]	τ^b [ms]	L_d [μm]
1:1	552	635	238	20	7	71	152	36
S/N	562	893	180	15	7	65	161	45
N/S	487	-	-	-	-	-	-	^d

a) V_{oc} values obtained from the EIS measurement at a given light intensity.

b) calculated from Equation 9

c) calculated from Equation 10

d) EIS measurements was not fitted due to high R_{tr} (see text).

DSCs with electrodes functionalized with **ALP1** and then soaked in a dye-bath containing a 1 : 1 mixture of [Cu(N[^]NS)₂]⁺ and [Cu(N[^]NNH)₂]⁺ gave the highest C_{μ} (Table 20) of all measured DSCs. The high C_{μ} is consistent with the observed high J_{sc} (Table 16). The moderate value of R_{tr} facilitates improved electron transport in the semiconductor which, in turn, enhances J_{sc} . However, the relatively low R_{rec} militates against further enhancement of the value of J_{sc} . The EIS parameters for DSCs with electrodes functionalized with **ALP1** and then soaked sequentially in dye-baths containing [Cu(N[^]NS)₂]⁺ then [Cu(N[^]NNH)₂]⁺ are comparable with those using the 1 : 1 mixture of [Cu(N[^]NS)₂]⁺ and [Cu(N[^]NNH)₂]⁺ (Table 20 and Table 21). Of particular note is the increase in R_{rec} on going from the mixed to sequential dye-baths. Exposing the electrodes with adsorbed anchor **ALP1** to the homoleptic copper(I) complexes in the reverse order, (i.e. [Cu(N[^]NNH)₂]⁺ then [Cu(N[^]NS)₂]⁺) results in the lowest C_{μ} value in this study. In addition, R_{tr} is very high and R_{rec} is rather low. The very large R_{tr} meant that the data could not be fitted with the model in Fig. 15 at a low light intensity (Table 21); a Gerischer circuit element would have been needed in order to produce a good fit. However, this was not carried out since it was sufficient to establish that the R_{tr} of this cell is significantly larger than for the others in the series (Fig. 102). The high R_{tr} is reflected in the EIS measurements at high light intensities (Fig. 103) where the first and second semicircle overlap.

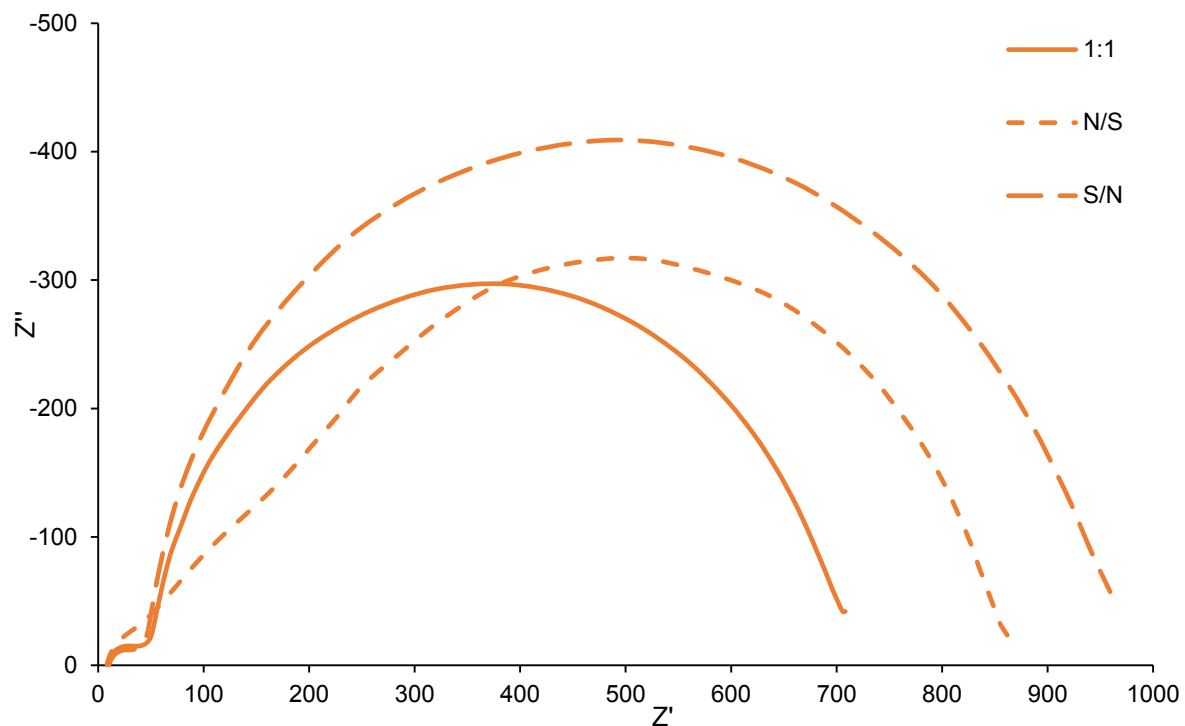


Fig. 102 Nyquist plots of DSCs containing mixtures of the dyes [Cu(ALP1)(N[^]NNH)]⁺ and [Cu(ALP1)(N[^]NS)]⁺ at a light intensity of 2.2 mW cm⁻².

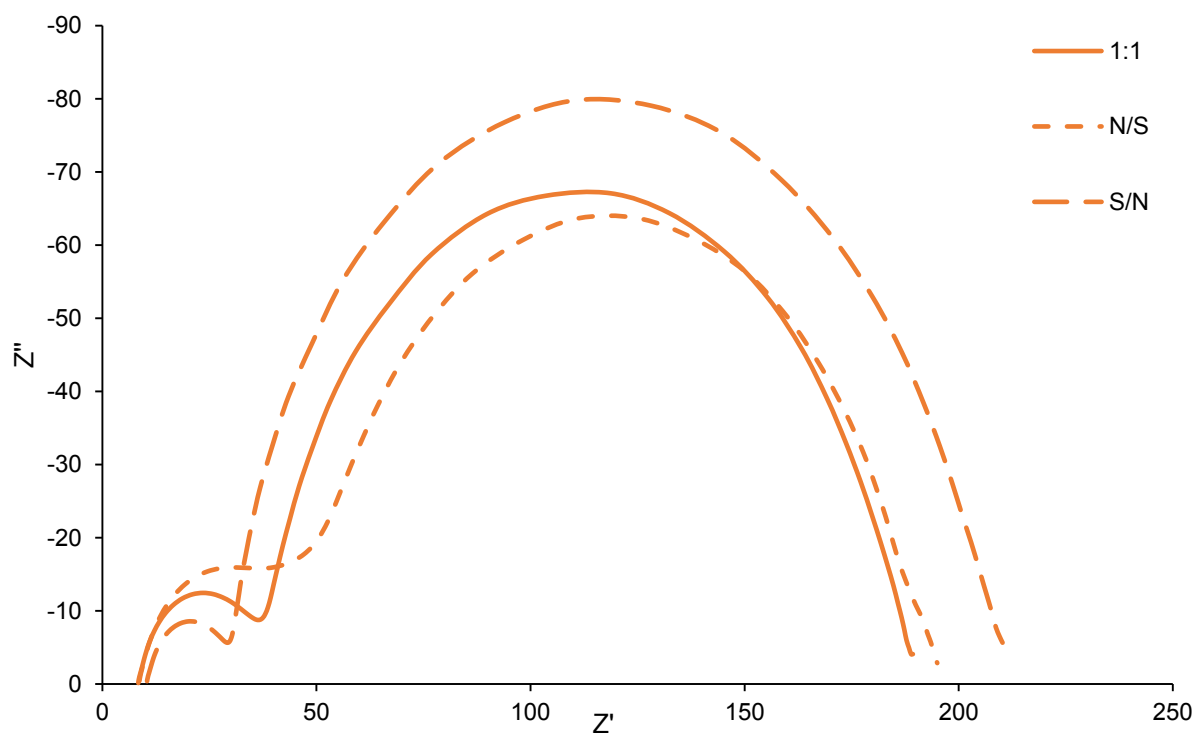


Fig. 103 Nyquist plots of DSCs containing mixtures of the dyes [Cu(ALP1)(N[^]NNH)]⁺ and [Cu(ALP1)(N[^]NS)]⁺ at a light intensity of 22 mW cm⁻².

Because of the high R_{tr} and low R_{rec} , the tendency for electron injection into the CB as well as the charge density in the semiconductor are reduced. Additionally, the recombination reaction with the electrolyte is dominant, and electrons in the semiconductor are lost by recombination. It follows that V_{oc} is low for DSCs assembled using the dye-baths in the sequence $[\text{Cu}(\text{N}^{\wedge}\text{NNH})_2]^+$ then $[\text{Cu}(\text{N}^{\wedge}\text{NS})_2]^+$ (Table 20). Once again, the impact of all EIS parameters on V_{oc} is apparent. The electron lifetime τ for N/S co-sensitized DSCs at high light intensity is 23 ms which is much shorter (Table 20) than those of DSCs made using S/N co-sensitization ($\tau = 55$ ms) or a 1 : 1 mixture of $[\text{Cu}(\text{N}^{\wedge}\text{NS})_2]^+$ and $[\text{Cu}(\text{N}^{\wedge}\text{NNH})_2]^+$ ($\tau = 49$ ms). The latter are in the same range as for the DSCs containing the single dyes $\text{N}^{\wedge}\text{NNH}$ or $\text{N}^{\wedge}\text{NS}$ (Table 18). Similar trends are observed at lower light intensities (Table 19 and Table 21). It has to be noted that L_d is, in the case of the DSCs made with a combination of dyes, higher than in the single dye DSCs. The cell with the S/N dipping procedure has a value of $L_d = 45$ mm which is the highest L_d in this study. The comparison of EIS data for DSCs made with a combination of dyes versus a single dye shows the dominant effect of ancillary ligand $\text{N}^{\wedge}\text{NNH}$ on the device performance. The data are consistent with the solid-state absorption measurements (Fig. 97 and Fig. 98) and the J - V measurements (Fig. 99) discussed above and indicate that ancillary ligand $\text{N}^{\wedge}\text{NNH}$ replaces $\text{N}^{\wedge}\text{NS}$ more efficiently than vice versa. When a S/N dipping procedure is used, the EIS parameters are comparable to single-dye DSCs containing the surface-bound dye $[\text{Cu}(\text{ALP1})(\text{N}^{\wedge}\text{NNH})]^+$. Both cells have the same R_{tr} , comparable R_{rec} and C_{μ} , as well as similar τ at a light intensity of 22 mW cm^{-2} . On the other hand, DSCs assembled by the N/S dipping method have a much lower C_{μ} than the single dye DSCs with single surface-bound dye $[\text{Cu}(\text{ALP1})(\text{N}^{\wedge}\text{NS})]^+$. Furthermore, R_{rec} is lower and R_{tr} is more than twice the value of the appropriate single dye DSC. Additionally, the electron lifetime τ at a light intensity of 22 mW cm^{-2} is only about the half of the single dye DSCs. This results in the lower overall efficiency of DSCs made using the N/S dipping procedure.

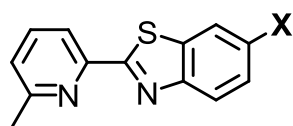
In conclusion, these new $\text{N}^{\wedge}\text{NX}$ ancillary ligands have a simple architecture and are easy to synthesize. The $\text{N}^{\wedge}\text{N}$ binding of the ligands was verified by X-ray crystallography. The $\text{N}^{\wedge}\text{NX}$ ancillary ligands perform well in copper(I)-based DSC. Even these simple unmodified ligands surpass the threshold values for bpy based ancillary ligands ($J_{sc} > 7 \text{ mA cm}^{-2}$, $V_{oc} > 600 \text{ mV}$). All DSCs have an EQE_{max} value over 50%. In the end an overall efficiency over 3% is reached with these simple new $\text{N}^{\wedge}\text{NX}$ ligands. The investigations show that the $\text{N}^{\wedge}\text{NX}$ ancillary ligands can replace the bpy-based ligands in copper(I)-based DSCs. The only problem is the air-sensitivity of

the homoleptic [Cu(N[^]NNH)₂][PF₆] complex. However, the homoleptic Cu(I)-complex bearing N[^]NS is stable under standard conditions and results in well performing DSCs. This is the first report of co-sensitization of DSCs using combinations of copper(I) dyes. In order to achieve an impact of both dyes the dipping order is important. This is an important development as it opens the way to a strategy for harvesting the full solar energy spectrum without the need for designing new panchromatic complexes.

15.2. Outlook: Optimization of the N[^]NS Ligand

The new types of N[^]NX ancillary ligands have shown promising results even with unmodified ligands. Out of the four heteroleptic copper(I) dyes containing of N[^]NNH, N[^]NNMe, N[^]NO and N[^]NS ligands, that with the N[^]NS ligand was performing well and was stable in air. In order to show the outstanding applicability of the N[^]NX ancillary ligands in copper(I)-based dye-sensitized solar cells, structurally modified N[^]NS ligands were synthesized and tested in DSCs. Functionalizations of the N[^]NS ligand can be done in the benzothiazole-unit or the pyridine-unit.

First of all, the electron donating groups NH₂, NHMe and NMe₂ were introduced in the position *para* to the nitrogen of the benzothiazole in order to introduce a "push-system" towards the metal centre (Scheme 45). Additionally, the ligand N[^]NS(NO₂) was synthesized to introduce an electron withdrawing group at the 6-position of the benzothiazole ring (Scheme 45).



N [^] NS(NH ₂)	X = NH ₂
N [^] NS(NHMe)	X = NHMe
N [^] NS(NMe ₂)	X = NMe ₂
N [^] NS(NO ₂)	X = NO ₂

Scheme 45 Ancillary ligands N[^]NS(X) with different substituents in the 6-position of the benzothiazole-ring (X = NH₂, NHMe, NMe₂, NO₂).

The DSCs were assembled by the ligand-exchange dye-assembly procedure with the anchoring ligand ALP1. The performance data of the DSCs containing the modified N[^]NS(X) ancillary ligands and the unmodified N[^]NS ligand on the day of sealing the cells are summarized in Table 22 and the corresponding *J-V* curves are displayed in Fig. 104. All cells with the modified N[^]NS(X) ligands have a lower *J_{sc}* value compared to the unmodified N[^]NS ligand. The DSC containing the dye [Cu(ALP1)(N[^]NS(NH₂))]⁺ has the lowest *J_{sc}* value of all cells (*J_{sc}* = 5.32 mA cm⁻²). The cells with the ancillary ligands N[^]NS(NHMe), N[^]NS(NMe₂) and N[^]NS(NO₂) have comparable *J_{sc}* values between 6.14 and 6.37 mA cm⁻² (Table 22).

Table 22 DSC performance data for DSC containing the copper(I) dye with the anchoring ligand **ALP1** and the ancillary ligands **N[^]NS(X)** with X = NH₂, NHMe, NMe₂, NO₂ and the unmodified **N[^]NS** ligand (from Table 14) on the day of sealing the cells.

Dye	J_{sc} [mA cm ⁻²]	V_{oc} [mV]	ff [%]	η [%]	Relative η [%]
On the day of sealing the cell					
[Cu(ALP1)(N[^]NS)] ⁺	7.76	530	70	2.88	38.1
[Cu(ALP1)(N[^]NS(NH₂))] ⁺	5.32	514	63	1.71	22.6
[Cu(ALP1)(N[^]NS(NHMe))] ⁺	6.37	522	66	2.20	29.1
[Cu(ALP1)(N[^]NS(NMe₂))] ⁺	6.30	531	66	2.21	29.3
[Cu(ALP1)(N[^]NS(NO₂))] ⁺	6.14	585	70	2.53	33.5
N719	16.57	630	72	7.55	100.0

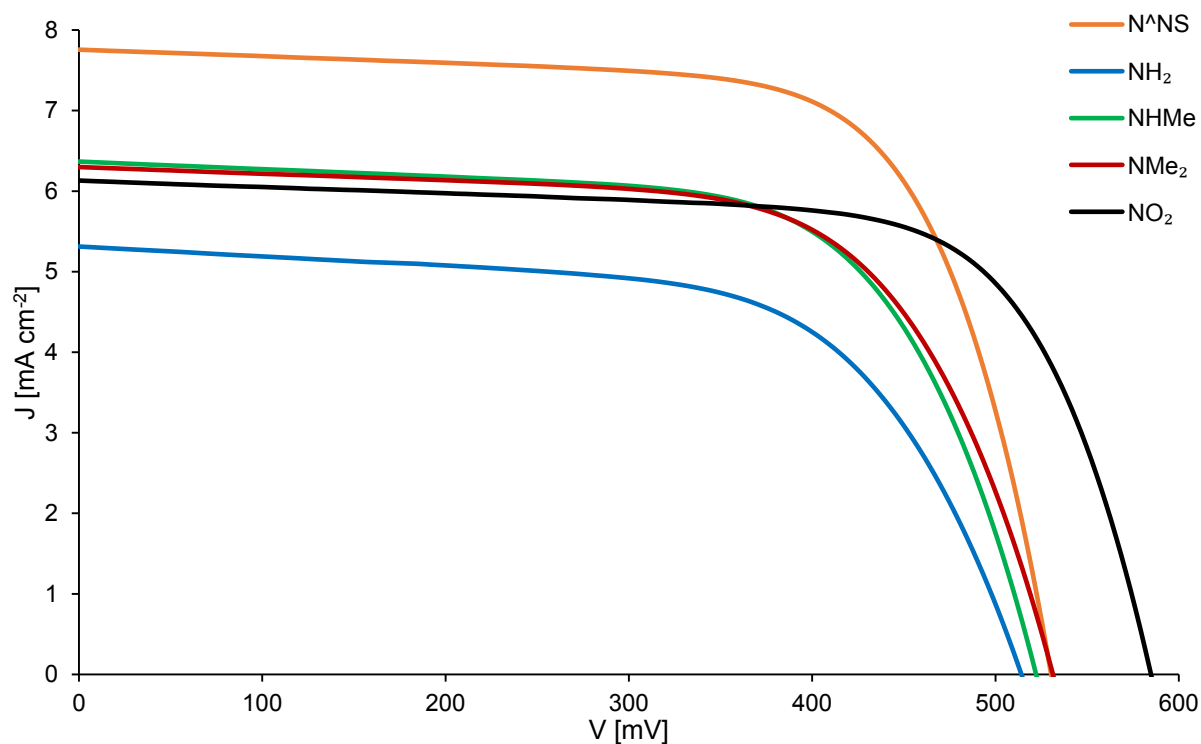
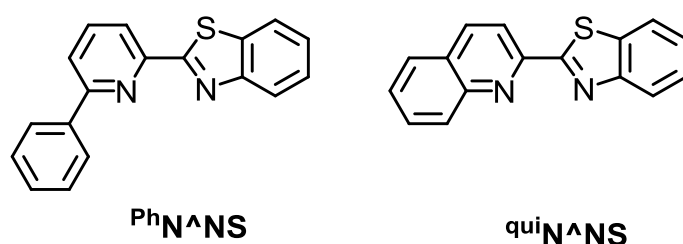


Fig. 104 J - V curves of DSC containing the dye [Cu(**ALP1**)(**N[^]NS(X)**)⁺ with X = NH₂, NHMe, NMe₂, NO₂ and the unmodified **N[^]NS** ligand on the day of sealing the cells.

The V_{oc} value of the cells containing the dyes with the ancillary ligands with electron-donating groups are comparable to the unmodified N[^]NS ligand ($V_{oc} = 530$ mV). The DSCs containing of the dye $[\text{Cu}(\text{ALP1})(\text{N}^{\wedge}\text{NS}(\text{NH}_2))]^+$, $[\text{Cu}(\text{ALP1})(\text{N}^{\wedge}\text{NS}(\text{NHMe}))]^+$ and $[\text{Cu}(\text{ALP1})(\text{N}^{\wedge}\text{NS}(\text{NMe}_2))]^+$ had V_{oc} values of 514 mV, 522 mV and 531 mV, respectively. The introduction of the nitro group in the N[^]NS(NO₂) ligand increases the open-circuit voltage. On the day of sealing the cell, an V_{oc} value of 585 mV is obtained. This might be due to the partially negative charge on the NO₂ group that blocks the recombination of injected electrons with the cations of the redox couple because of repulsion. With fill factors between 63 and 70%, overall efficiencies lower than the DSC with the unmodified N[^]NS ligand are achieved. The cell containing of the unmodified $[\text{Cu}(\text{ALP1})(\text{N}^{\wedge}\text{NS})]^+$ dye has an efficiency of 2.88%, whereas the cells containing the modified $[\text{Cu}(\text{ALP1})(\text{N}^{\wedge}\text{NS}(\text{X}))]^+$ dyes had an efficiency in the range of 1.71% to 2.53% (Table 22).

For the bpy-based ancillary ligands it has been shown that the introduction of a bigger π -system in the 6,6'-positions of the bpy-core can improve the performance of the DSCs. This observation is now transferred to the new family of ancillary ligands. Two new ancillary ligands with either a phenyl-substituent in 6-position of the pyridine (PhN[^]NS) or a quinoline instead of the pyridine (quiN[^]NS) (Scheme 46) were synthesized according to the procedure described in *10 Synthetic Strategy* and tested as ancillary ligands in Cu(I)-based DSCs.



Scheme 46 Ancillary ligands ^RN[^]NS with bigger π -systems (R = Ph, qui).

After assembling the DSCs by the standard ligand-exchange dye-assembly procedure, the performances were measured under solar simulator conditions. The DSC data are summarized in Table 23 and the J - V curves of the corresponding cells are displayed in Fig. 105. The short-circuit current density could not be improved by the introduction of the bigger π -system.

The DSC containing the dye [Cu(ALP1)(^{Ph}N[^]NS)]⁺ has a J_{sc} value of 7.21 mA cm⁻² and the one containing the dye [Cu(ALP1)(^{qui}N[^]NS)]⁺ has a J_{sc} value of 7.30 mA cm⁻² compared to 7.76 mA cm⁻² for the unmodified N[^]NS dye.

Table 23 DSC performance data for DSC containing copper(I) dyes with the anchoring ligand ALP1 and the ancillary ligands ^RN[^]NS with R = Ph, qui and the unmodified N[^]NS ligand (from Table 14) on the day of sealing the cells.

Dye	J_{sc} [mA cm ⁻²]	V_{oc} [mV]	ff [%]	η [%]	Relative η [%]
On the day of sealing the cell					
[Cu(ALP1)(N [^] NS)] ⁺	7.76	530	70	2.88	38.1
[Cu(ALP1)(^{Ph} N [^] NS)] ⁺	7.21	552	71	2.84	37.6
[Cu(ALP1)(^{qui} N [^] NS)] ⁺	7.30	561	72	2.95	39.1
N719	16.57	630	72	7.55	100.0

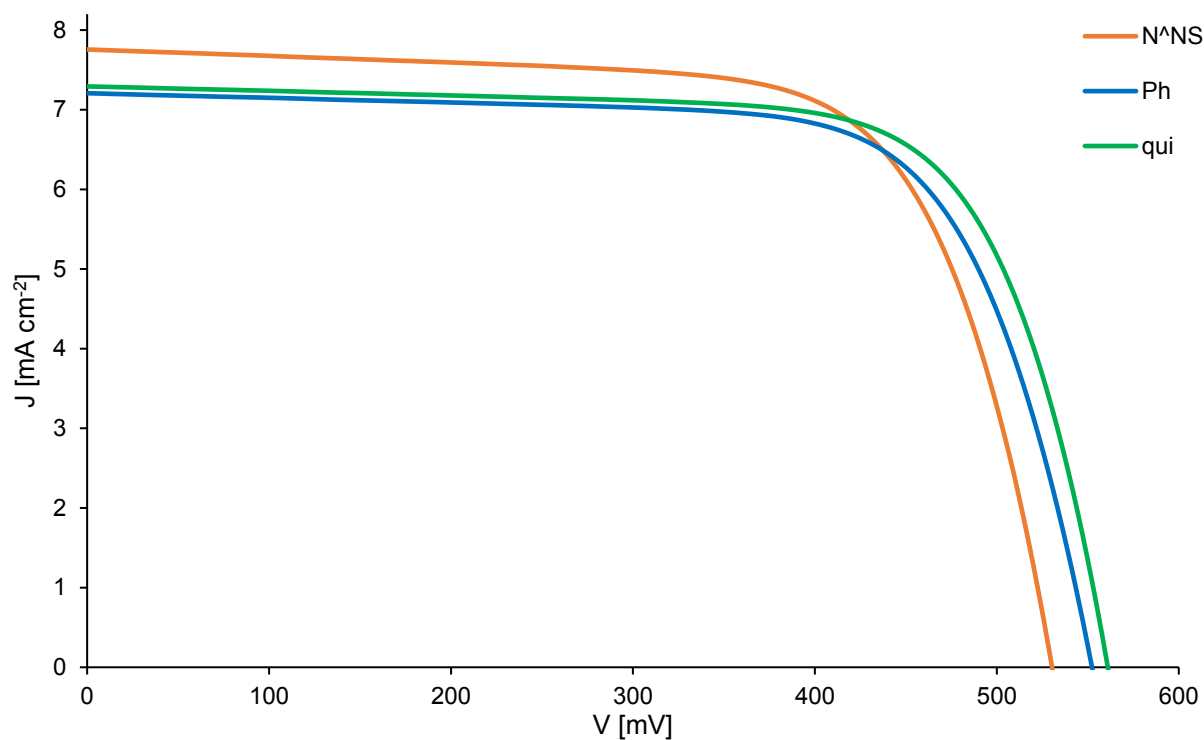
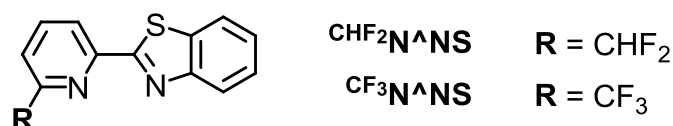


Fig. 105 J - V curves of DSC containing the dye [Cu(ALP1)(^RN[^]NS)]⁺ with R = Ph, qui and the unmodified N[^]NS ligand on the day of sealing the cells.

Although J_{sc} values were slightly lower for the dyes with the extended π -systems, higher V_{oc} values were obtained. The cell containing the dye [Cu(**ALP1**)(^{Ph}N[^]NS)]⁺ has an V_{oc} value of 552 mV and the one containing the dye [Cu(**ALP1**)(^{qui}N[^]NS)]⁺ has an V_{oc} value of 561 mV compared to 530 mV for the unmodified N[^]NS ligand. The fill factor of all cells is around 70%. Overall, comparable overall efficiencies are obtained for the modified ^RN[^]NS ligands ($\eta = 2.84\%$ for ^{Ph}N[^]NS; $\eta = 2.95\%$ for ^{qui}N[^]NS) with regard to the unmodified N[^]NS ligand ($\eta = 2.88\%$) on the day of sealing the cell.

Investigations of Brunner and co-workers have shown that the replacement of the methyl group by trifluoromethyl in the 6,6'-positions of bpy improves the performance of Cu(I)-based DSCs.¹⁵⁹ Therefore, the fluorine-containing substituents CHF₂ (^{CHF₂}N[^]NS) and CF₃ (^{CF₃}N[^]NS) were introduced in the 6-position of the pyridine ring (Scheme 47).



Scheme 47 Ancillary ligands ^RN[^]NS with fluorine-containing substituents (R = CHF₂, CF₃).

The performance data of the DSCs containing of the anchoring ligand **ALP1** and the modified ancillary ligands ^{CHF₂}N[^]NS and ^{CF₃}N[^]NS as well as the unmodified N[^]NS ligand are summarized in Table 24. The corresponding J - V curves are displayed in Fig. 106.

Table 24 DSC performance data for DSC containing copper(I) dyes the anchoring ligand **ALP1** and the ancillary ligands ^RN[^]NS with R = CHF₂, CF₃ and the unmodified N[^]NS ligand (from Table 14) on the day of sealing the cells.

Dye	J_{sc} [mA cm ⁻²]	V_{oc} [mV]	ff [%]	η [%]	Relative η [%]
On the day of sealing the cell					
[Cu(ALP1)(N [^] NS)] ⁺	7.76	530	70	2.88	38.1
[Cu(ALP1)(^{CHF₂} N [^] NS)] ⁺	7.97	567	71	3.20	42.4
[Cu(ALP1)(^{CF₃} N [^] NS)] ⁺	7.64	567	72	3.10	41.1
N719	16.57	630	72	7.55	100.0

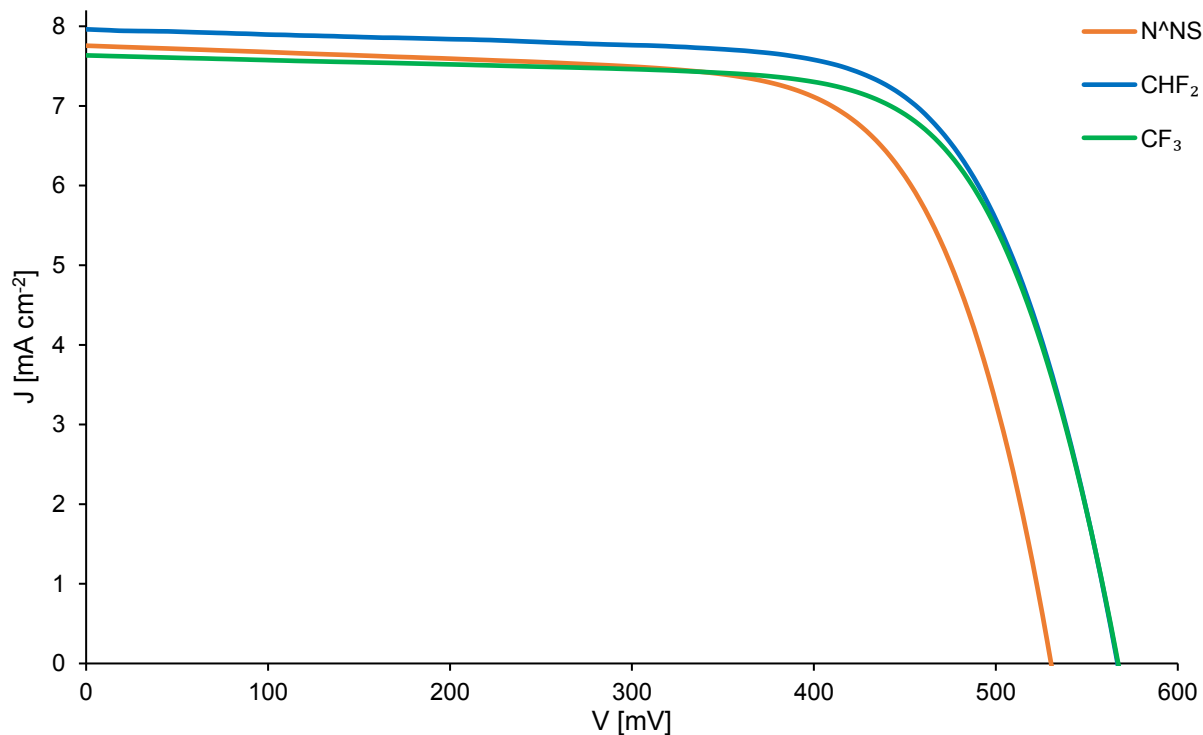


Fig. 106 J - V curves of DSCs containing the dye $[\text{Cu}(\text{ALP1})(\text{R}^{\text{N}^{\text{NS}}})]^+$ with $\text{R} = \text{CHF}_2$, CF_3 and the unmodified N^{NS} ligand on the day of sealing the cells.

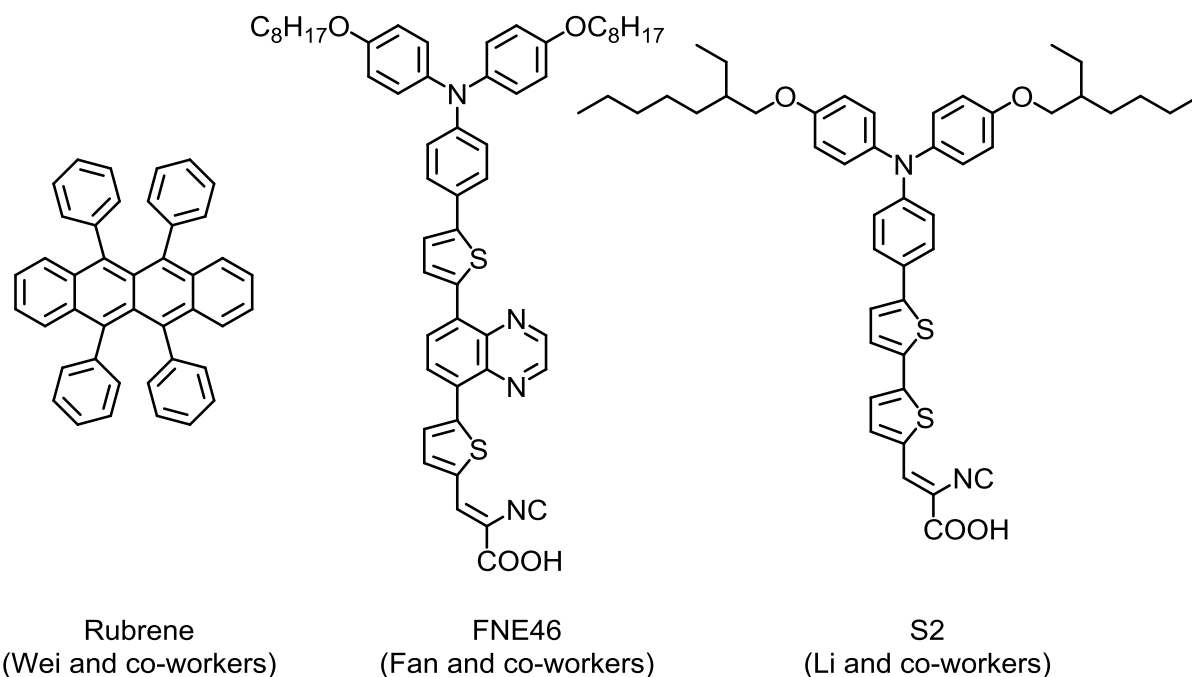
The DSCs containing the fluorine-containing ancillary ligands achieve comparable or even higher J_{sc} values than the unmodified N^{NS} ligand. The J_{sc} value of the cell containing the $\text{CF}_3\text{N}^{\text{NS}}$ ligand ($J_{sc} = 7.64 \text{ mA cm}^{-2}$) is slightly lower than the one for the N^{NS} ligand ($J_{sc} = 7.76 \text{ mA cm}^{-2}$). But the J_{sc} of the DSC containing the new ancillary ligand $\text{CHF}_2\text{N}^{\text{NS}}$ is, with 7.97 mA cm^{-2} , the highest measured J_{sc} value on the day of sealing the cell of all investigated DSCs in this thesis. The V_{oc} for both modified ancillary ligands ($V_{oc} = 567 \text{ mV}$ for $\text{CHF}_2\text{N}^{\text{NS}}$ and $\text{CF}_3\text{N}^{\text{NS}}$) is better than for the N^{NS} containing cell ($V_{oc} = 530 \text{ mV}$). With high fill factors of 71 and 72% both DSCs containing the modified ancillary ligands $\text{CHF}_2\text{N}^{\text{NS}}$ and $\text{CF}_3\text{N}^{\text{NS}}$ surpass the performance of the DSC containing the unmodified N^{NS} ligand. They exceed the efficiency level of 3% and have an overall efficiency of 3.10% for the DSC containing the $\text{CF}_3\text{N}^{\text{NS}}$ ligand and 3.20% for containing the $\text{CHF}_2\text{N}^{\text{NS}}$ ligand. The value of 3.20% is the highest measured overall efficiency for all single-dye copper(I)-based dye-sensitized solar cells in this thesis.

These preliminary tests to optimize the performance of the N[^]NS ligand show the great potential of the new N[^]NX ancillary ligands. Because of time constraints it was only possible to carry out initial screening of these new ancillary ligands. It is planned to complete this study by measuring EQE spectra and carrying out EIS measurements, so that a full assessment of these ligands can be made.

PANCHROMATIC
CO-SENSITIZED
COPPER(I)
DYE-SENSITIZED
SOLAR CELLS

Most of the copper(I) dyes used in DSCs have a narrow absorption region in the visible range. Hence, only a small part of the incoming sunlight is absorbed by the dye and the rest is unused. To overcome this problem with other dyes (e.g. organic dyes) much research has been done in the field of co-sensitization. However, molecules were used as co-adsorbents to fill the gaps and prevent aggregation of dye molecules. Different types of dyes have been investigated for co-sensitization. Additional molecules were investigated for co-adsorption. Inorganic dyes such as ruthenium complexes¹⁶⁰⁻¹⁷⁹, porphyrin dyes^{180,181}, and copper complexes^{105,182}, as well as organic dyes¹⁸³⁻¹⁹², have been investigated in co-sensitized solar cells or with co-adsorbents. Here, a second dye is absorbed on the semiconductor surface to overcome the deficiency of the absorption spectrum of the first dye and enhance the spectral response of the co-adsorbed TiO₂ film. Other advantages of co-sensitization are suppression of charge recombination, prolonging the electron lifetime and decreasing of the total resistance of the DSC.¹⁷⁰

Because of their tunable absorption maxima organic dyes as co-sensitizers have been examined for combination with all types of dyes. When co-sensitizing the ruthenium dye **N719** with an organic dye additional absorption between a wavelength of 300 and 600 nm is desired. With this, a higher short-circuit current density is achieved and thus a higher overall efficiency. Wei and co-workers used Rubrene (Scheme 48) as a simple organic co-sensitizer.¹⁶⁷ With the help of it they achieved additional absorption which lead to a higher short-circuit current density and even a higher open-circuit voltage, because the formation of a compact dye layer leads to less charge recombination and prolonged electron lifetime. The better charge-transport property of the organic dye promotes the electron transfer, too. The co-sensitized solar cell had an overall efficiency of 7.64%, which is 40% higher than without co-sensitization ($\eta = 5.46\%$). Adding an organic dye as co-sensitizer to a porphyrin dye gives even higher improvements. Fan and co-workers dipped the TiO₂ electrode first in a zinc porphyrin solution for 6 h and afterwards in an organic dye (Scheme 48) solution for 12 h ($\eta = 7.88\%$) and gained an improvement of 93% with respect to the porphyrin-sensitized DSC ($\eta = 4.09\%$).¹⁸¹ It is also possible to use two organic dyes in a co-sensitized DSC. Li and co-workers assembled a DSC with two organic dyes that absorbed in different regions and observed an improvement of up to 48%.¹⁸⁹ They designed several organic dyes (Scheme 48) to fill the absorption gap of the primary organic dye. With the help of the co-sensitizer they reached an efficiency of 6.5%. The DSC without the co-sensitizer had an efficiency of 4.4%.



Scheme 48 Molecules used for co-sensitization in literature.^{167,181,189}

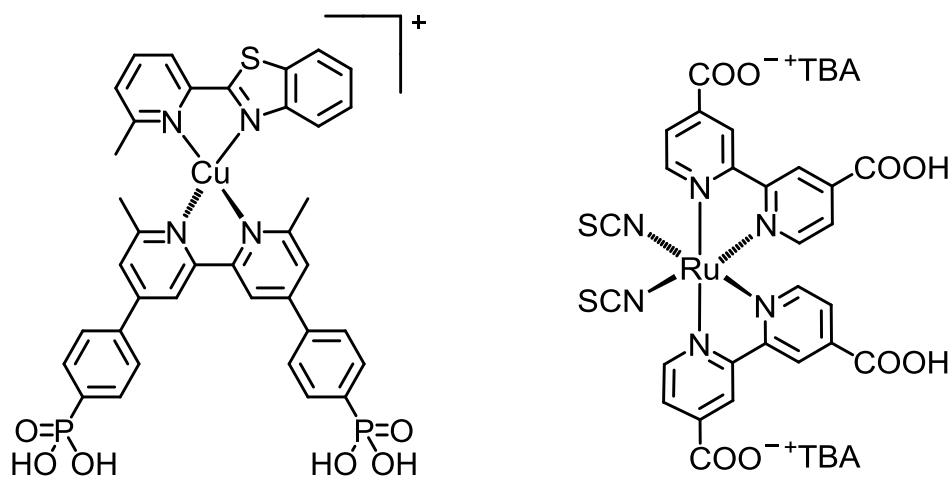
Not only have organic dyes been used as co-sensitizers, inorganic dyes also have been investigated in the field of co-sensitized DSCs. Gao and co-workers synthesized a cadmium complex as a co-sensitizer for **N719**.¹⁶¹ The cadmium complex has additional absorption in the wavelength region between 300 and 400 nm. After sequentially immersing the TiO₂ electrodes in solutions of the two dyes they observed higher short-circuit current densities as well as open-circuit voltages. Finally, they reached an overall efficiency of 8.27%, which is 27% better than the **N719** DSC ($\eta = 6.50\%$). In addition to cadmium complexes, Yadav and co-workers investigated zinc- and mercury complexes as co-sensitizers for DSCs.¹⁶² Ranasinghe and co-workers investigated the co-sensitization of **N719** with the other well-known ruthenium dye, the so-called black dye (**N749**, Scheme 2).¹⁶⁰ They chose these two ruthenium dyes because of their different UV-Vis absorption maxima. They mixed both dyes in a 1:1 cocktail and reached better short-circuit current density and open-circuit voltage than with either of the single dyes. They justify the improvement also with the fact that **N719** helps to prevent aggregation of molecules of the black dye. Co-sensitization with copper(I) dyes had not previously been reported in literature. Research was only done with the organic co-adsorbent Chenodeoxycholic acid as described in *14.4 Influence of the Co-adsorbent Cheno on the Efficiency*.

It has to be noted, that co-sensitization does not only has a positive effect. There are also examples where co-sensitization results in no big improvements¹⁶⁸ or even gives worse efficiency¹⁸⁹. All of the mentioned investigations focused on choosing a co-sensitizer with a different absorption region to gain a panchromatic DSC^{160-163,165-181,183,184,186-192}, use them as light scattering molecules to increase the light absorption¹⁶⁴ or to fill the gaps on the semiconductor surface to passivate the recombination sites and to prevent aggregation of dye molecules^{105,182}.

Now for the first time, co-sensitization with the combination of a copper(I)-based dye and an organic dye is investigated.

16. Co-sensitization Pre-tests with a Copper(I)-dye and N719

The co-sensitization with the two copper(I)-based dyes $[\text{Cu}(\text{ALP1})(\text{N}^{\wedge}\text{NS})]^+$ and $[\text{Cu}(\text{ALP1})(\text{N}^{\wedge}\text{NNH})]^+$ in *15.1 A New Type of Ancillary Ligand for Copper(I)-Based Dye-Sensitized Solar Cells: N[^]NX* demonstrated that the usage of two copper(I) dyes is possible and beneficial. In this case, both dyes have the same anchoring ligand **ALP1** with a phosphonic acid anchoring group. In this part the co-sensitization of a copper(I)-based dye and a ruthenium dye is investigated. The dyes chosen for the study are shown in Scheme 49. **N719** has been used because of the carboxylic acid anchoring group and a different absorption maximum than the Cu(I) dye (Fig. 107). Because the two dyes have different anchoring units (Scheme 49), there was the question as to whether both dyes could anchor simultaneously on the semiconductor surface. The usage of a phosphonic acid anchor and a carboxylic acid anchor leads to a competition of both anchoring groups.¹⁹³



Scheme 49 Copper(I) dye with anchoring ligand **ALP1** and ancillary ligand **N[^]NS** (left) and **N719**¹⁹⁴ (right) for the investigations of co-sensitization of photoelectrodes (TBA = tert-butylammonium).

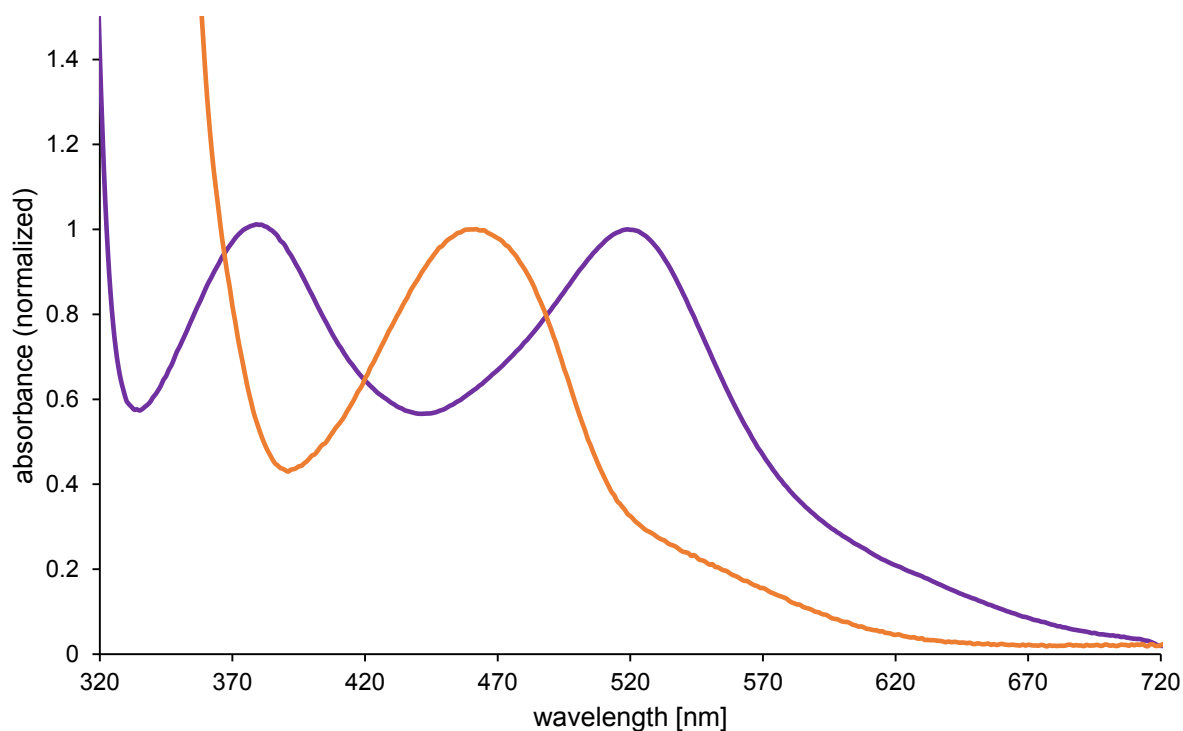


Fig. 107 Normalized UV-Vis absorption spectra of **N719** (purple) and $[\text{Cu}(\text{N}^{\text{NS}})_2][\text{PF}_6]$ (orange).

For the different dipping procedures a 1.0 mM DMSO solution of **ALP1**, a 0.1 mM CH_2Cl_2 solution of $[\text{Cu}(\text{N}^{\text{NS}})_2][\text{PF}_6]$ and a 0.3 mM EtOH solution of **N719** were used. The DSCs were assembled by the standard assembly procedure with the standard iodine-based electrolyte (see *12 Equipment Details* and *13 General Device Fabrication*). In the first dipping step the photoelectrode was always immersed in the anchoring ligand solution. **N719** was introduced before or after the Cu(I) dye assembly.

In the first dipping procedure (**N^{NS}/N719**) the heteroleptic Cu(I) complex was assembled on the TiO_2 surface by the ligand-exchange dye-assembly process and afterwards **N719** was introduced. The influence of the time the Cu(I) dye-functionalized photoelectrode is dipped into the **N719** solution was investigated by alternating the dipping time of **N719** from 10 min to 1 or 4 h to 1 d. Fig. 108 displays the J - V curves of the DSCs in comparison to the single-dye DSC from Fig. 96 and the corresponding Table 14. The J_{sc} value of all co-sensitized DSCs is lower than the single-dye DSC. A longer dipping time for the last dipping step in **N719** resulted in higher J_{sc} values. But the cells with a dipping time of 10 min and 1 h as well as the cells with dipping time of 4 h and 1 d had almost identical J_{sc} values. The V_{oc} for all co-sensitized DSCs

was larger than for the single-dye DSC. However, a trend in the influence of the dipping time was not observed.

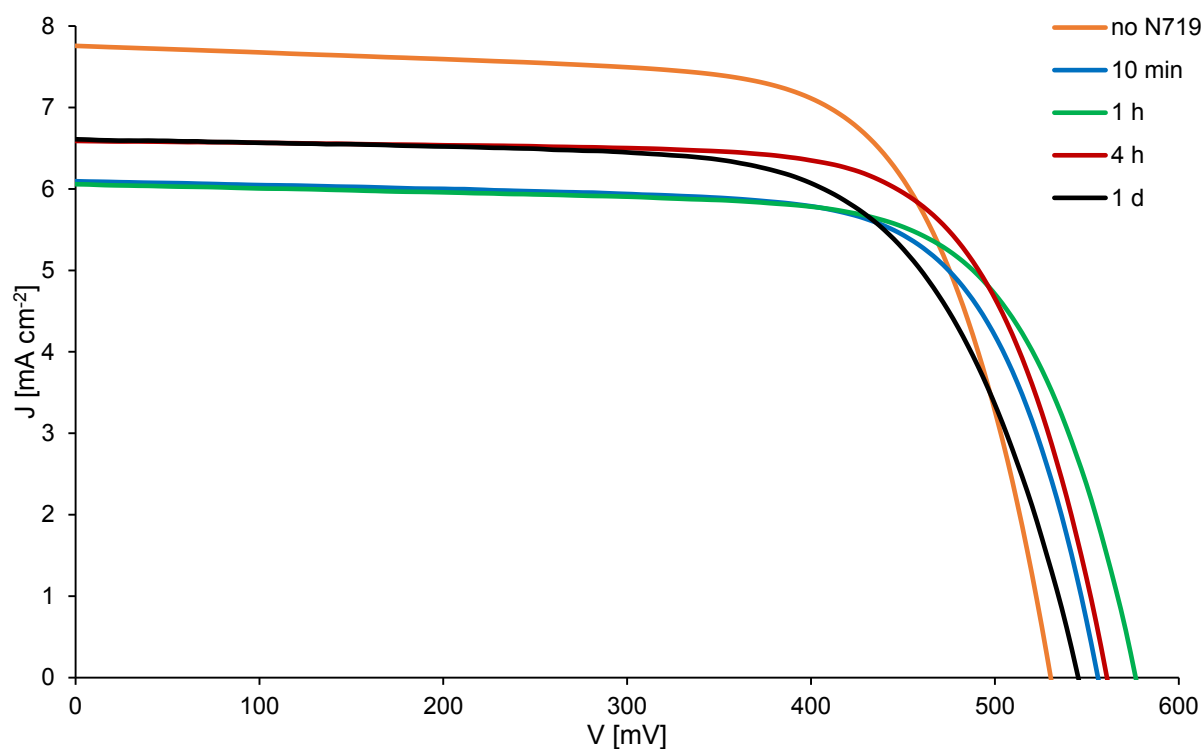


Fig. 108 J - V curves of DSC assembled by the N⁷¹⁹/N719 dipping procedure with different dipping times for N719 on the day of sealing the cells.

The confirmation that both dyes anchor on the TiO₂ surface came from the EQE curves (Fig. 109). With increased dipping time of N719 two phenomena were observed. The first was the reduction of the EQE_{max} of the Cu(I) dye at a wavelength of around 480 nm. Without a treatment of N719 an EQE_{max} value of 53.8% was measured (Table 26). But this value was reduced to 45.7% by only dipping the Cu(I) dye-functionalized photoelectrode into the N719 solution for 10 min. Dipping times of 4 h and 1 d resulted in almost identical EQE curves (Fig. 109). Here, EQE_{max} values of around 37% were measured. The second phenomenon was most obvious for those DSCs with a longer dipping time of N719. In contrast to the reduction of the EQE_{max} value of the Cu(I) dye the influence of N719 on the EQE spectra increases. The red and black curves in Fig. 109 both show shoulders in the EQE curve to lower and higher wavelengths compared to the EQE_{max} value increase with longer dipping times. At a wavelength range of 550 and 720 nm an increase in the EQE response is observable the longer the electrode

is dipped into the **N719** solution. The same trend is observed at a wavelength at 390 nm. For both shoulders, the DSC with the shortest dipping time of 10 min has the lowest EQE response whereas the DSC with the longest dipping time of 1 d has the highest EQE response. Subsequently one can clearly see that both dyes can anchor simultaneously on the semiconductor surface. There is as well not a huge difference between the absorption spectra of the electrodes with a dipping time of 4 h and 1 d. This shows that there is limited space available on the surface for **N719** and that it does not displace the phosphonic acid anchor. Table 27 summarizes the performance parameters and EQE maxima of the DSCs assembled by the **N^{NS}/N719** dipping procedure.

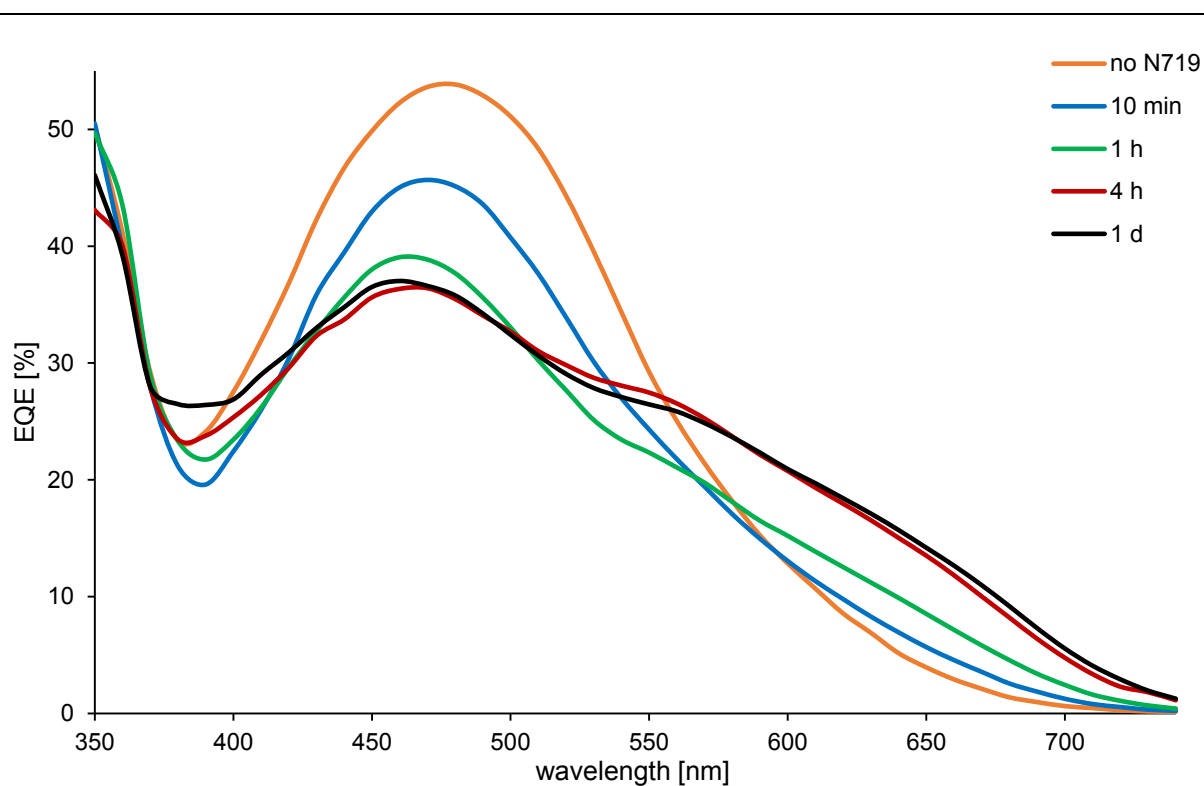


Fig. 109 EQE curves of DSC assembled by the **N^{NS}/N719** dipping procedure with different dipping times for **N719** on the day of sealing the cells.

Table 25 Performance parameters and EQE maxima of DSCs assembled by the N[^]NS/N719 dipping procedure with different dipping times for N719 on the day of sealing the cells.

dipping time	J_{sc} [mA cm ⁻²]	V_{oc} [mV]	ff [%]	η [%]	EQE_{max} [nm, %]
On the day of sealing the cell					
no N719	7.76	530	70	2.88	480, 53.8
10 min	6.10	556	72	2.45	470, 45.7
1 h	6.06	576	72	2.50	460, 39.1
4 h	6.59	561	73	2.68	470, 36.4
1 d	6.60	545	68	2.45	460, 37.0

The influence of the dipping order was investigated in the second dipping procedure. After the photoelectrode had been immersed into the ALP1 solution, it was dipped into the N719 solution, and different dipping times were investigated. Because it was observed in the first experiment that the dipping time of 4 h and 1 d gave comparable results, the longest dipping time of 1 d was omitted. Finally, the photoelectrodes were dipped into the [Cu(N[^]NS)₂][PF₆] solution and the DSCs were assembled. Fig. 110 displays the corresponding J - V curves of the DSCs without N719 and with a dipping time of 10 min, 1h or 4 h for the N719 dipping step. As in the first experiment (Fig. 108), the J_{sc} values were also lower compared to the untreated cell when a dipping step with N719 is introduced. Dipping times of 10 min and 1 h resulted in comparable J_{sc} values and the DSC with a dipping time of 4 h had the highest J_{sc} value of all N719 treated cells. The V_{oc} value is also in this dipping procedure higher than for the untreated cell, and for all DSCs it was around 560 mV (Table 28). But the impact of N719 on the performance of the DSCs is less than in the N[^]NS/N719 dipping procedure. This can be observed in the EQE curves in Fig. 111.

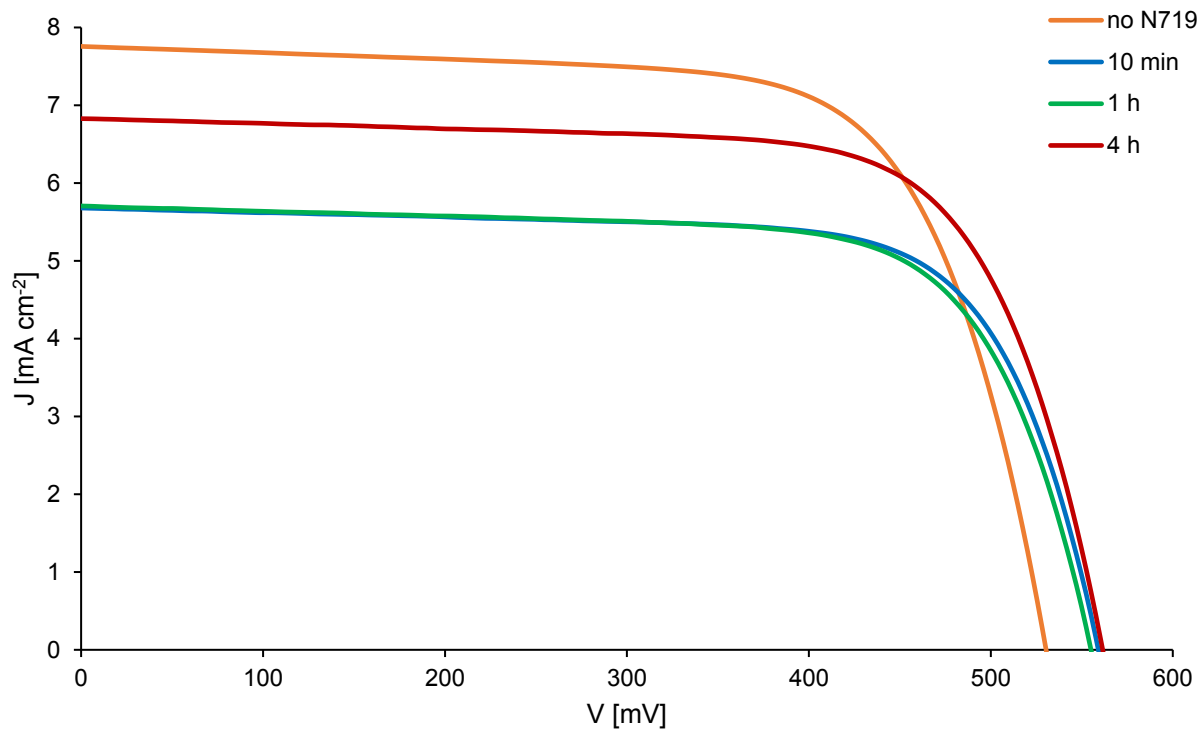


Fig. 110 J - V curves of DSC assembled by the N719/N^{NS} dipping procedure with different dipping times for N719 on the day of sealing the cells.

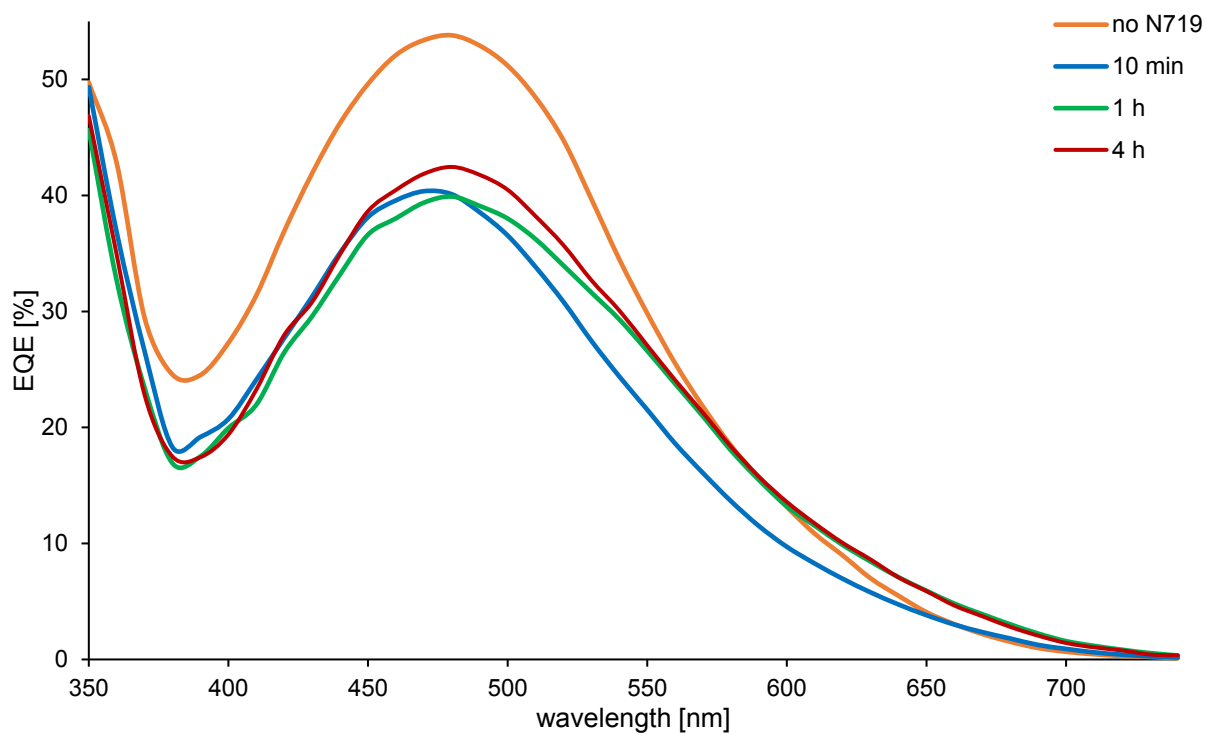


Fig. 111 EQE curves of DSC assembled by the N719/N^{NS} dipping procedure with different dipping times for N719 on the day of sealing the cells.

The EQE response decreases for all **N719** treated cells with respect to the untreated one. But the influence of the dipping time is not as big as seen before in the first **N[^]NS/N719** dipping procedure. A small shoulder between 550 and 700 nm can be observed but the EQE response at around 390 nm is not observable. The DSC with the longest dipping time of 4 h has the highest and the one with the shortest dipping time of 10 min has the lowest EQE response. The EQE_{max} value of all cells is over 40% (Table 26) and for the first dipping procedure, this value of EQE_{max} is only observed with an **N719** dipping time of 10 min (Table 25).

Table 26 Performance parameters and EQE maxima of DSCs assembled by the **N719/N[^]NS** dipping procedure with different dipping times for **N719** on the day of sealing the cells.

dipping time	J_{sc} [mA cm ⁻²]	V_{oc} [mV]	ff [%]	η [%]	EQE_{max} [nm, %]
On the day of sealing the cell					
no N719	7.76	530	70	2.88	480, 53.8
10 min	5.68	559	72	2.30	470, 40.7
1 h	5.70	555	72	2.26	470, 40.2
4 h	6.83	561	72	2.74	480, 42.5

With the **N719/N[^]NS** dipping procedure the decrease of the EQE response of the Cu(I) dye is not as dramatic as with the **N[^]NS/N719** dipping procedure. The comparison of the EQE curves of DSCs assembled by the different dipping procedures (Fig. 112) shows that with the **N[^]NS/N719** dipping procedure the EQE response of the [Cu(**ALP1**)(**N[^]NS**)]⁺ dye is lower whereas the **N719** response is much more pronounced. In contrast, the **N719/N[^]NS** dipping procedure results in a more pronounced EQE response of the [Cu(**ALP1**)(**N[^]NS**)]⁺ dye whereas the EQE response of **N719** is not so large. Both dipping procedures have shown that it is possible to simultaneously anchor a phosphonic acid anchor and a carboxylic acid anchor on the semiconductor surface with Cu(I)-based dyes containing the anchoring ligand **ALP1**.

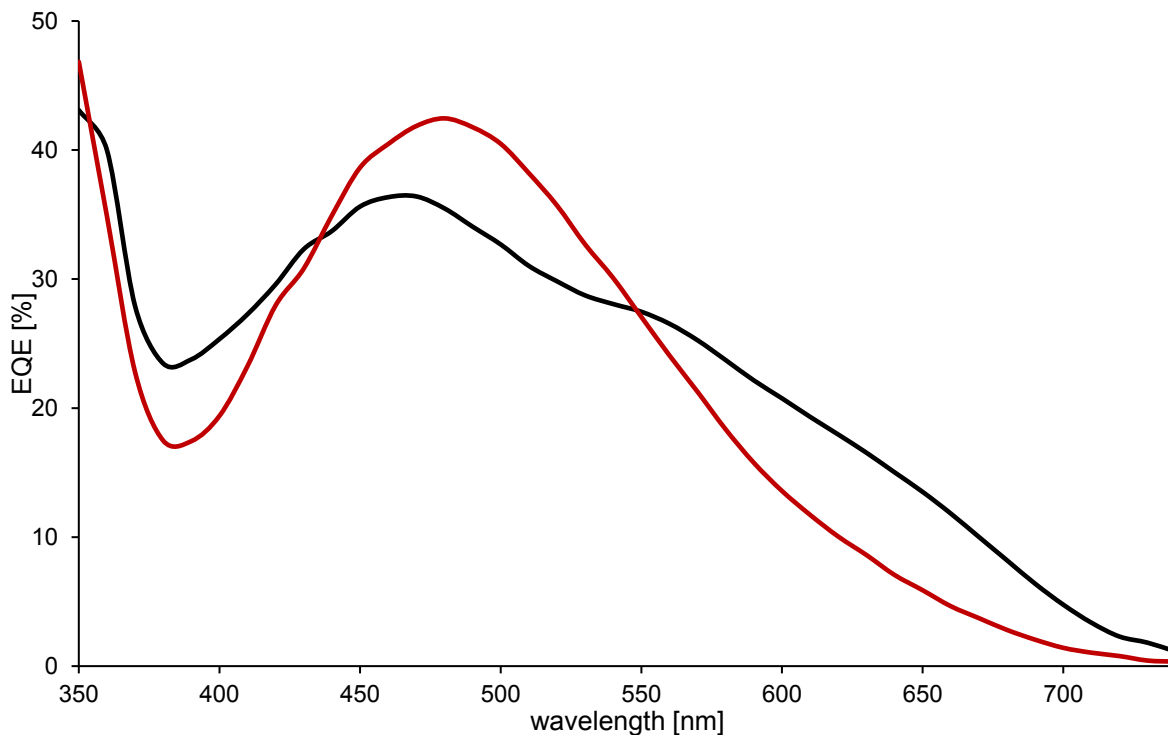


Fig. 112 Comparison of the EQE curves of DSCs assembled by the different dipping procedures with a dipping time of 4 hours for N719.

The observations in the DSC tests can be confirmed by solid-state UV-Vis spectroscopy. Here, identical dipping procedures to those described above were used to assemble the dyes on transparent photoelectrodes. The solid-state UV-Vis spectra of the N^{NS}/N719 dipping procedure are displayed in Fig. 113.

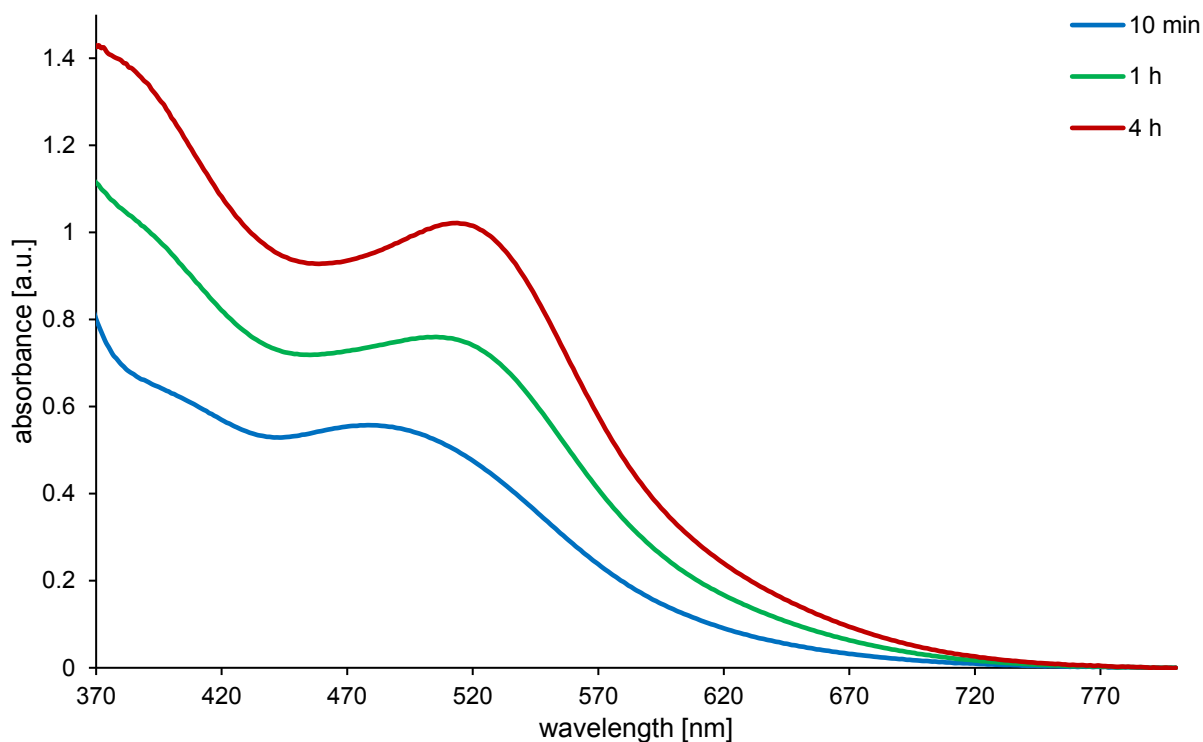


Fig. 113 Solid-state UV-Vis spectra of dye-functionalized photoelectrodes assembled by the $N^{NS}/N719$ dipping procedure with different dipping times for $N719$.

It was observed that a longer dipping time of $N719$ results first of all in higher absorption. The lowest absorption is measured for the electrode that was dipped into the $N719$ solution for 10 min. The spectrum has a maximum at 478 nm which corresponds to the $Cu(I)$ dye. With a dipping time of 1 h, the absorption increases and the maximum shifts to a wavelength of 505 nm. This is in the middle of the absorption maximum of the copper dye (480 nm) and the ruthenium dye (533 nm). The longest dipping time of 4 h results in an additional increase of absorption. The influence of $N719$ is here more dominant and the maximum shifts to 514 nm. This shift in absorption maximum shows the increased anchoring of $N719$ with increased dipping time and in conclusion the binding of both dyes on the semiconductor surface.

The observation that the impact of $N719$ is not so big in the $N719/N^{NS}$ dipping procedure was also verified by solid-state UV-Vis spectroscopy. Fig. 114 displays the absorption spectra of co-sensitized transparent photoelectrodes assembled by the $N719/N^{NS}$ dipping procedure. All spectra have a maximum at around 480 nm that corresponds to the absorption of the $Cu(I)$ dye (λ_{max} (10 min) = 480 nm, λ_{max} (1 h) = 478 nm, λ_{max} (4 h) = 481 nm). The shape of the spectra is identical. The only influence of the dipping time is that with longer dipping times a more intense

absorption is observed. However, the absorption of the electrodes with a dipping time of 1h and 4 h is almost identical.

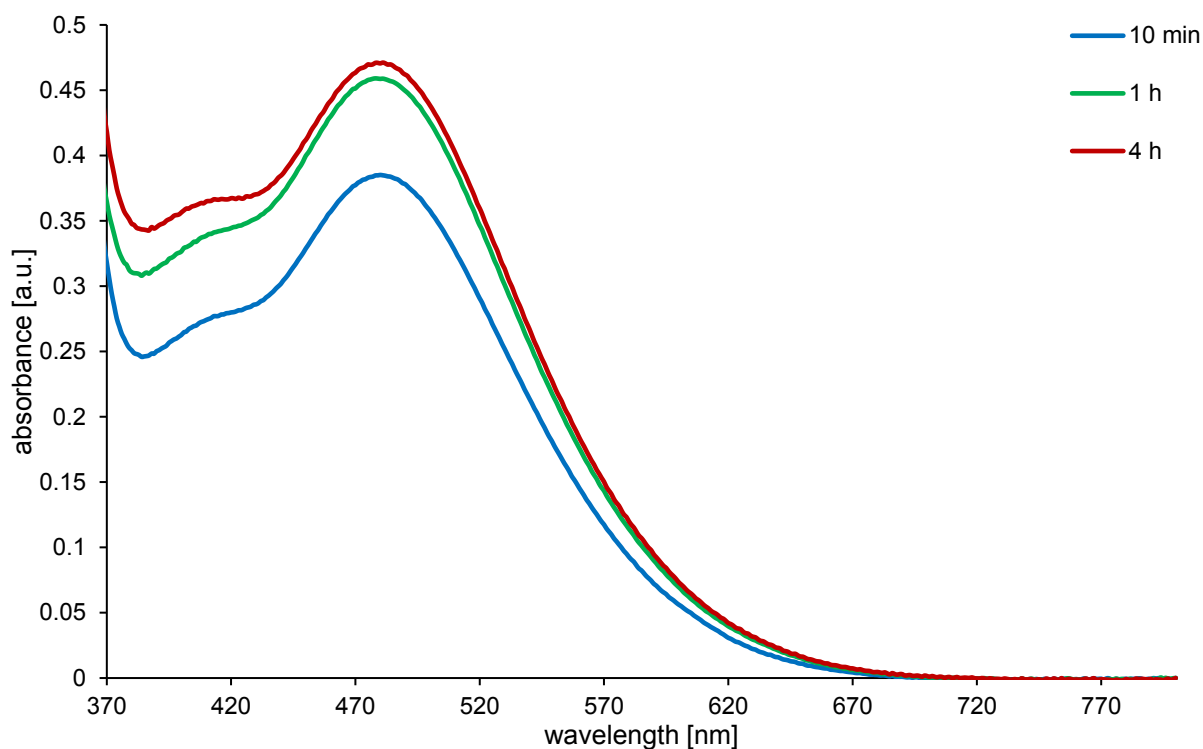


Fig. 114 Solid-state UV-Vis spectra of dye-functionalized photoelectrodes assembled by the N719/N^{NS} dipping procedure with different dipping times for N719.

The anchoring of N719 was investigated by solid-state UV-Vis spectra after each dipping step. The solid-state UV-Vis spectrum of a transparent photoelectrode that was immersed in an ALP1 solution for 1 d is displayed in Fig. 115. The observations of negative absorbance were reproducible and therefore has to be explained. In order to measure the baseline, the 100% transmission is measured by measuring the transmission of an untreated transparent photoelectrode. The 0% transmission is determined by blocking the light beam. That means that all measurements are referred to the absorption of an untreated electrode. However, the spectrum of the ALP1 treated photoelectrode has negative values with a minimum at 365 nm. This suggests that ALP1 removes parts of the TiO₂. Less TiO₂ is present on the electrode which leads to lower absorption. This can also be observed at the dye-assembly process of the DSCs. After dipping the photoelectrode in the ALP1 solution a small amount of white solid is observed from time to time on top of the electrode.

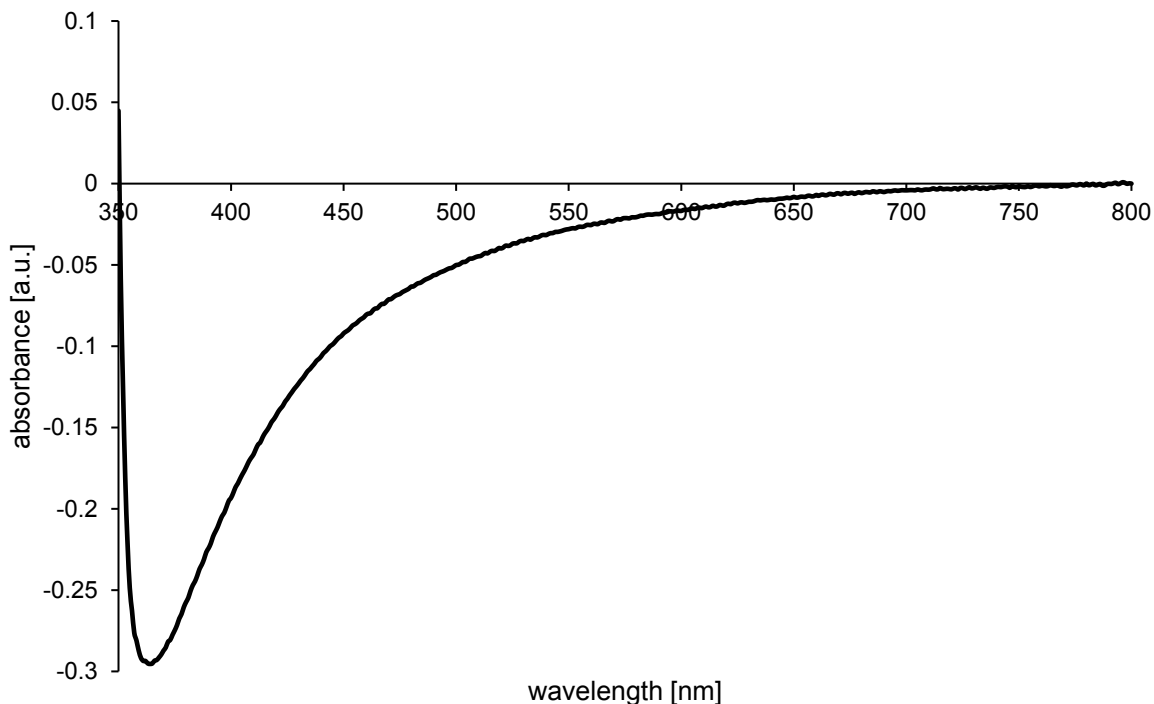


Fig. 115 Solid-state UV-Vis spectrum of a transparent photoelectrode dipped into an **ALP1** solution for 1 day.

In the second dipping step **N719** was introduced with different dipping times as described before. Fig. 116 displays the solid-state UV-Vis spectra. It can be observed that **N719** anchors to the semiconductor surface. The maximum of the spectra is at a wavelength of about 530 nm that corresponds to the absorption maximum of **N719**. The second absorption of **N719** at about 390 nm results in a less negative absorption value at the minimum of the spectra compared to the **ALP1** treated electrode (Fig. 115).

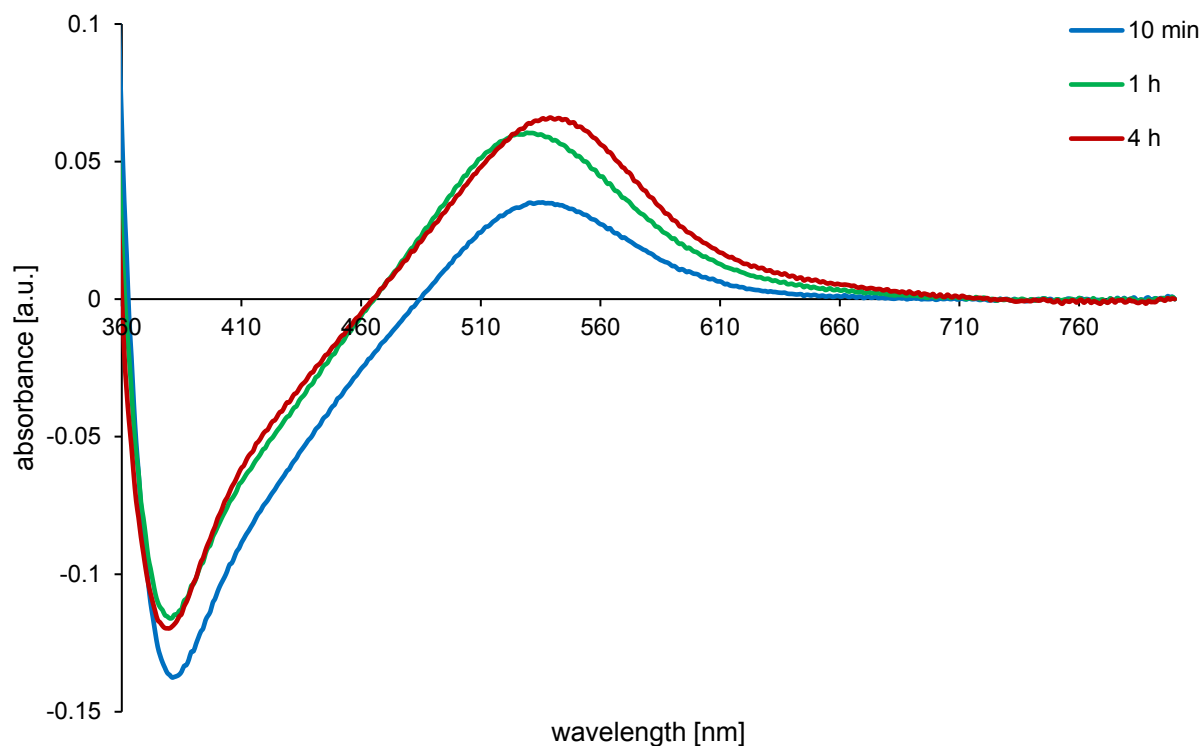


Fig. 116 Solid-state UV-Vis spectrum of a transparent photoelectrode dipped into an **ALP1** solution for 1 day and afterwards in a **N719** solution for different dipping times.

The absorption of **N719** is measurable but not very pronounced and it is also seen that the dipping time has no significant influence. The electrode that was immersed in the **N719** solution for 10 min had the lowest response. The absorption of the electrodes with longer dipping times is higher with respect to the one with 10 min but the difference is not as big as in the **N^{NS}/N719** dipping procedure (Fig. 113). This trend is constant after the last dipping step with $[\text{Cu}(\text{N}^{\text{NS}})_2][\text{PF}_6]$ (Fig. 114).

The comparison of the solid-state UV-Vis spectra of both dipping procedures in Fig. 117 shows that the order of the dipping steps is important. When **N719** was introduced after the Cu(I) dye had been assembled by the ligand-exchange dipping procedure, more **N719** appeared to be present on the surface. This is an assumption made purely on the visual appearance of the electrode. In the **N719/N^{NS}** dipping procedure the response of the Cu(I) dye is more dominant and is not as increased as in the **N^{NS}/N719** dipping procedure. But the response of **N719** is more intensive in the **N^{NS}/N719** dipping procedure than in the **N719/N^{NS}** dipping procedure.

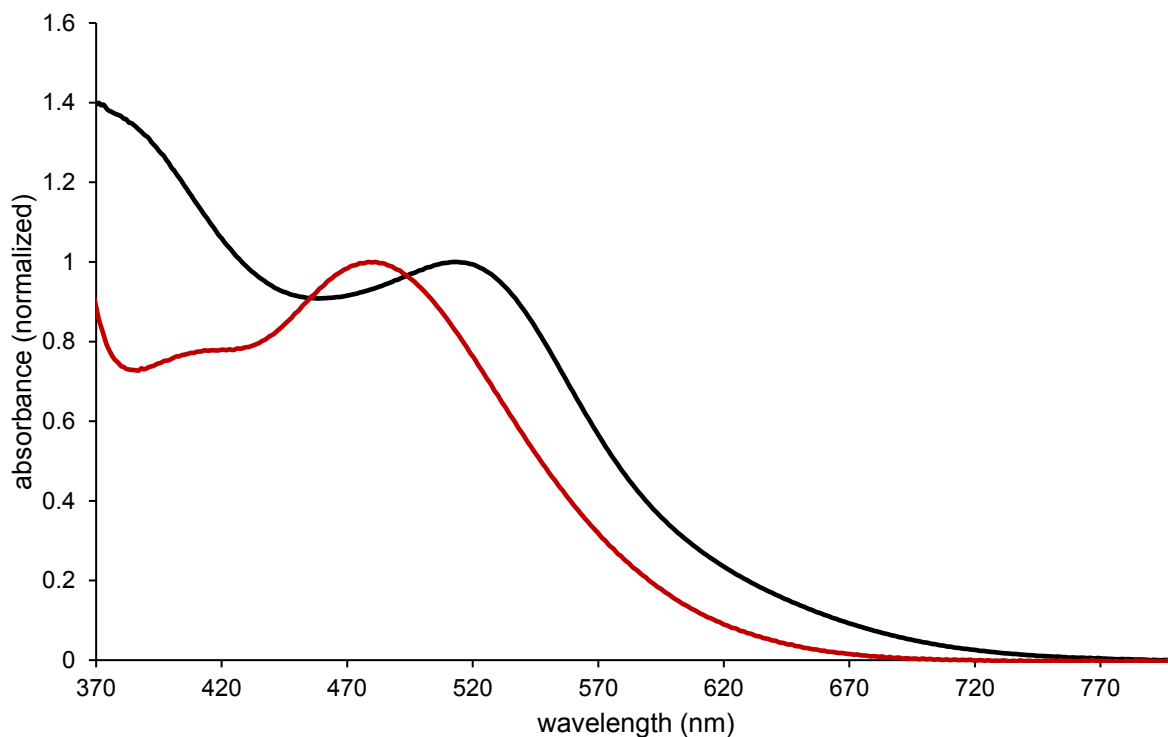
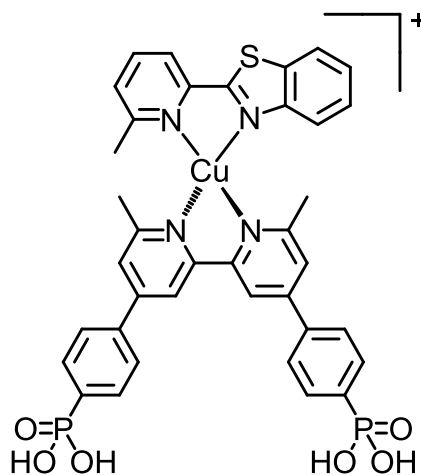


Fig. 117 Comparison of the solid-state UV-Vis spectra of transparent photoelectrodes treated by the different dipping procedures with a dipping time of 4 hours for N719.

In conclusion, a phosphonic acid anchor and a carboxylic acid anchor can anchor simultaneously on the semiconductor surface. The response of both dyes can be tuned by the order of the dipping steps. The dipping time can have an impact on the anchoring as well as on the influence of both dyes on the performance of the DSC.

17. The History of “Blorange”

The goal of this study was to achieve panchromatic co-sensitized copper(I)-based DSCs. For the copper part the $N^{\wedge}NX$ ligands have shown promising results (Table 14). The performance of DSCs containing the heteroleptic Cu(I)-dyes $[Cu(ALP1)(N^{\wedge}NH)]^{+}$ and $[Cu(ALP1)(N^{\wedge}NS)]^{+}$ was discussed in *15.1 A New Type of Ancillary Ligand for Copper(I)-Based Dye-Sensitized Solar Cells: N^{\wedge}NX*. They obtained remarkable performance data for such simple ancillary ligands. Although the dye with ancillary ligand $N^{\wedge}NH$ produced the highest open-circuit voltage ($V_{oc} = 608$ mV), use of $N^{\wedge}NS$ gave the highest J_{sc} (7.76 mA cm⁻²). The global efficiencies of the best performing DSCs with $[Cu(ALP1)(N^{\wedge}NH)]^{+}$ and $[Cu(ALP1)(N^{\wedge}NS)]^{+}$ were 3.03 and 2.88% on the day that the devices were fabricated *versus* 7.55% for the reference dye **N719** (Table 27). The standard ligand-exchange dye-assembly procedure relies upon the use of a homoleptic Cu(I)-complex of the ancillary ligand and $[Cu(N^{\wedge}NS)_2][PF_6]$ proved to be more air-stable in solution than $[Cu(N^{\wedge}NH)_2][PF_6]$. Thus, ancillary ligand $N^{\wedge}NS$ and anchoring ligand **ALP1** were chosen for the copper(I) part in the investigations to panchromatic DSCs (Scheme 50).



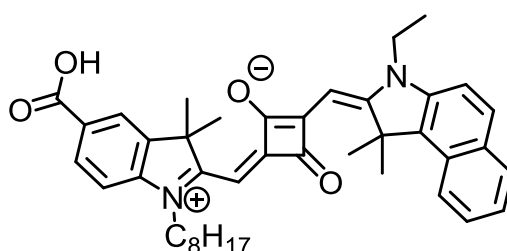
Scheme 50 Copper(I) dye with anchoring ligand **ALP1** and ancillary ligand $N^{\wedge}NS$ for the investigations of co-sensitization of photoelectrodes.

The performance of the DSC containing the dye $[Cu(ALP1)(N^{\wedge}NS)]^{+}$ combined with an I_3^-/I^- electrolyte investigated in *15.1 A New Type of Ancillary Ligand for Copper(I)-Based Dye-Sensitized Solar Cells: N^{\wedge}NX* is once again listed in Table 27 for convenience.

Table 27 Performance parameters and EQE maxima of a DSC containing the dye [Cu(ALP1)(N[^]NS)]⁺ from Table 14.

dye	J_{sc} [mA cm ⁻²]	V_{oc} [mV]	ff [%]	η [%]	Relative η [%]	EQE_{max} [nm, %]
On the day of sealing the cell						
[Cu(ALP1)(N [^] NS)] ⁺	7.76	530	69.9	2.88	38.1	480, 53.8
N719	16.57	630	72.4	7.55	100	540, 71.8
3 days after sealing the cell						
[Cu(ALP1)(N [^] NS)] ⁺	6.77	542	70.4	2.58	35.8	480, 50.8
N719	15.03	660	72.6	7.21	100	520, 70.8
7 days after sealing the cell						
[Cu(ALP1)(N [^] NS)] ⁺	7.42	558	62.6	2.59	37.7	470, 46.2
N719	14.47	650	73.0	6.87	100	540, 71.1

For co-sensitization of the copper(I)-dye, a dye was needed that had a complementary absorption range compared to that of [Cu(ALP1)(N[^]NS)]⁺. After the pre-tests with **N719**, a carboxylic acid anchoring domain is favoured and it should be commercially available. The overall efficiency should also be in the range of the Cu(I)- based DSC. Based on these requirements, the squaraine dye **SQ2**¹⁹⁵⁻²⁰⁰ (Scheme 51) was chosen as co-sensitizer.



Scheme 51 Organic squaraine dye **SQ2** used as co-sensitizer for panchromatic DSCs.

Fig. 118 displays the UV-Vis absorption spectra of **SQ2** in CH₂Cl₂. It has an absorption maximum at 658 nm and a narrow absorption range between 595 and 695 nm. The solid-state UV-Vis spectra of dye-functionalized FTO/TiO₂ surfaces with the two separate dyes are shown in Fig. 119 and demonstrate the wavelength range between 375 and 730 nm are covered by the dyes. The copper(I)-dye covers the absorption range from 425 nm to 575 nm whereas **SQ2** has

a complementary absorption range from 525 to 725 nm. **SQ2** has been used before in several studies of DSCs.^{191195,196,199-201} The reported results are summarized in Table 28. However, the use of CH₂Cl₂ as the **SQ2** dye-bath solvent has not yet been reported. CH₂Cl₂ is the standard solvent for copper-based dyes and the usage of CH₂Cl₂ as the solvent of **SQ2** was investigated first.

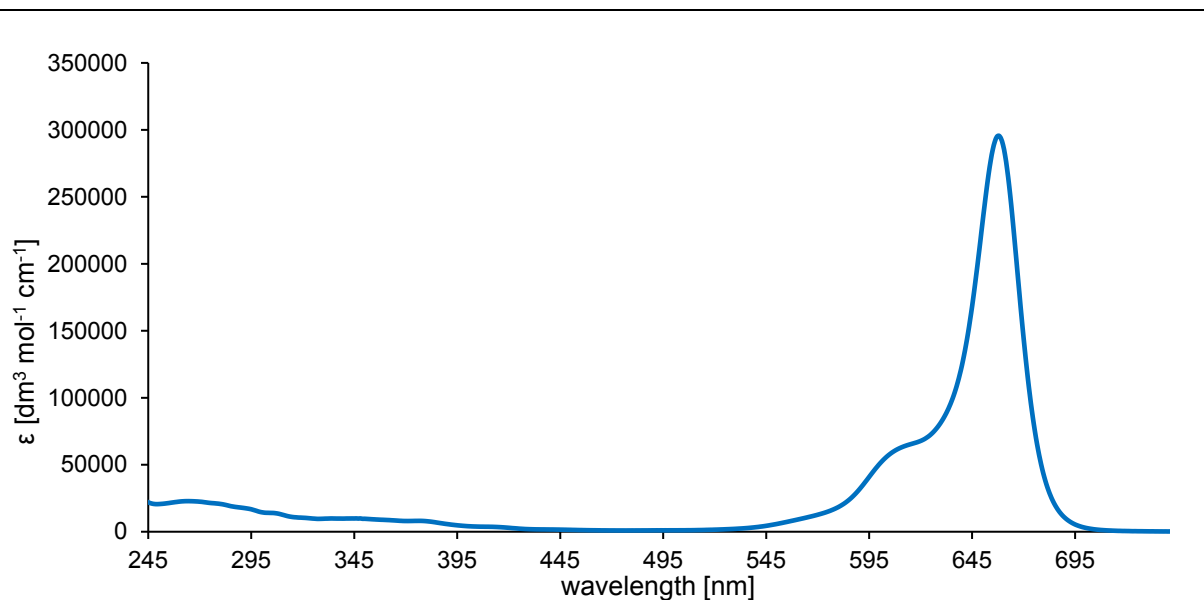


Fig. 118 UV-Vis spectrum of the organic dye **SQ2**.

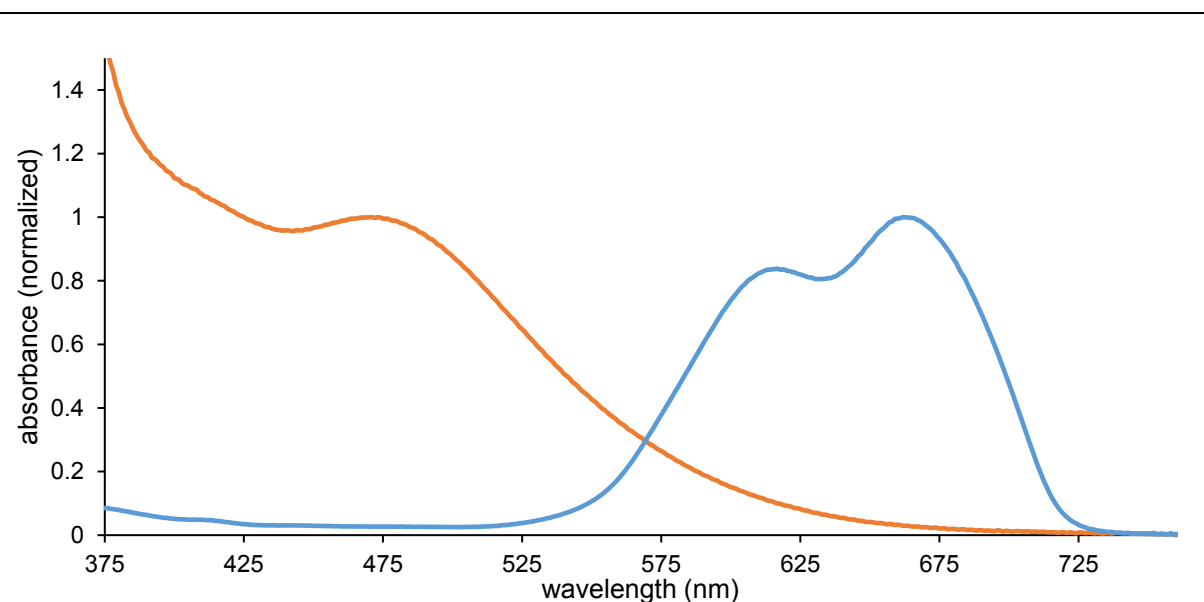


Fig. 119 Normalized solid-state absorption spectra of transparent photoelectrodes functionalized with the Cu(I)-dye [Cu(ALP1)(N^{NS})]⁺ (orange) and the organic dye **SQ2** (blue) (normalized to the absorption maximum of the respective dye).

Table 28 Performance parameters of DSCs containing the dye **SQ2** in literature compared to reference dye **N719**. In each case, an I^-/I_3^- -based electrolyte was used.

dye	solvent	J_{sc} [mA cm ⁻²]	V_{oc} [mV]	ff [%]	η [%]	η_{N719} [%]	Ref.
SQ2	MeCN : <i>t</i> -BuOH : DMSO (3.5 : 3.5 : 3)	11.05	600	60	3.98	7.97	201
SQ2	MeCN : <i>t</i> -BuOH (1:1)	10.38	600	66	4.11	- ^a	195
SQ2	MeCN : <i>t</i> -BuOH (1:1)	9.96	600	64	3.81	8.41	196
SQ2	MeCN : <i>t</i> -BuOH (1:1)	9.88	632	69	4.28	- ^a	191
SQ2	EtOH	9.00	640	72	4.16	- ^a	200
SQ2	THF	10.33	570	64	3.78	8.61	199

a) not reported.

DSCs with **SQ2** and an I^-/I_3^- redox shuttle were assembled. The photoelectrode was dipped in a 0.1 mM CH₂Cl₂ solution of **SQ2** for different dipping times (20 min, 1 h, 2 h, 24 h and 3 d, respectively). Table 29 displays the performance parameters of these devices.

Table 29 Performance parameters and EQE maxima of DSCs containing the dye **SQ2** with different dipping times of the photoanodes in the dye-bath before fabrication of the devices.

dye	dipping time	J_{sc} [mA cm ⁻²]	V_{oc} [mV]	ff [%]	η [%]	Relative η [%]	EQE_{max} [nm, %]
On the day of sealing the cell							
SQ2	20 min	6.99	521	72	2.62	34.7	670, 44.4
SQ2	2 h	7.91	491	67	2.62	34.7	580, 48.6
SQ2	4 h	9.46	504	699	3.28	43.4	560, 51.5
SQ2	24 h	9.44	494	68	3.17	42.0	560, 51.0
SQ2	3 d	8.32	503	68	2.85	37.7	560, 47.5
N719	1 d	16.57	630	72	7.55	100	540, 71.8
7 days after sealing the cell							
SQ2	20 min	9.18	531	70	3.40	49.5	660, 49.2
SQ2	2 h	10.73	529	67	3.77	54.9	560, 57.6
SQ2	4 h	11.84	544	69	4.44	64.6	550, 59.6
SQ2	24 h	12.24	529	67	4.32	62.9	550, 58.9
SQ2	3 d	10.95	529	67	3.89	46.6	550, 54.6
N719	1 d	14.47	650	73	6.87	100	540, 71.1

Despite the use of a different dye-bath solvent, the performances compare well with literature data (Table 28 *versus* Table 29). It was observed that with CH₂Cl₂ as the dye-bath solvent, higher J_{sc} values can be obtained (up to 12.24 mA cm⁻²), but V_{oc} values are lower compared to those in Table 28. It is significant that n-type DSCs containing the **SQ2** dye exhibit photoconversion efficiencies (2.62% to 3.28%, Table 29) which are comparable to those of DSCs sensitized with [Cu(**ALP1**)(**N[^]NS**)]⁺ (2.88%, Table 27).

The previously reported influence of aggregation of **SQ2** on the semiconductor surface and the impact on performance^{191,195-201} was also observed for DSCs where the **SQ2**-bath solvent is CH₂Cl₂. Longer dipping times lead to more aggregation resulting in a broader EQE spectrum, and a shift in the EQE maximum from 670 to 560 nm (Fig. 120 and Table 29). Extensive aggregation of **SQ2** molecules on the surface leads to greater quenching of the excited state of the dye and a lower recombination resistance (R_{rec}) at the TiO₂/dye/electrolyte-interface (see later). This results in lower J_{sc} values.^{191,195-201} However, some degree of aggregation is beneficial, leading to a broader absorption range and improved J_{sc} values. Fig. 120 demonstrates that a dipping time of 4 hours results in an optimum EQE curve on the day of cell fabrication, and longer dipping times lead to a decrease in DSC performance (Table 29).

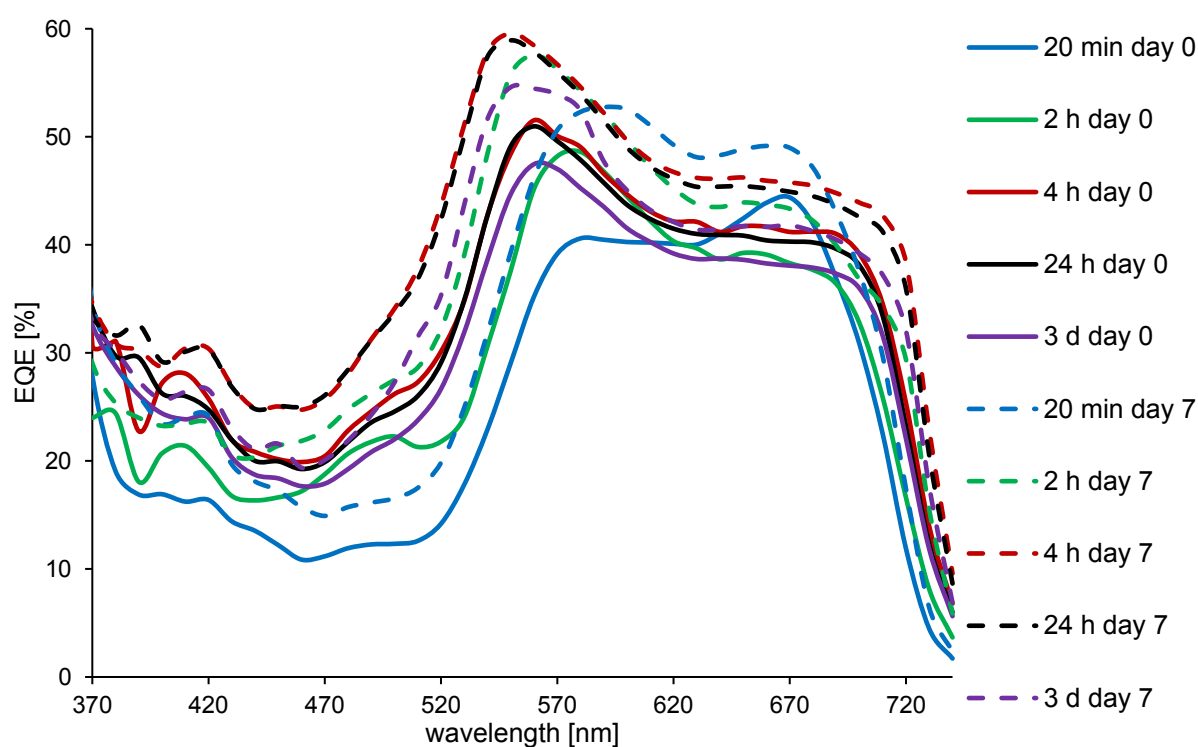


Fig. 120 EQE curves of a DSC containing the dye **SQ2** with different dipping times of the photoanodes in the dye-bath before fabrication of the devices.

Inspection of Fig. 121 and Table 29 confirms the influence of the dipping time in the **SQ2** dye-bath on J_{sc} and the overall cell performance. Significantly, there is a pronounced ageing effect, which is observed both in the EQE (Fig. 120) and the $J-V$ curves (Fig. 121). After the DSCs had been stored in the dark for 7 days, a maximum value of $\eta = 4.44\%$ (versus 6.87% for **N719**) was obtained (Table 29).

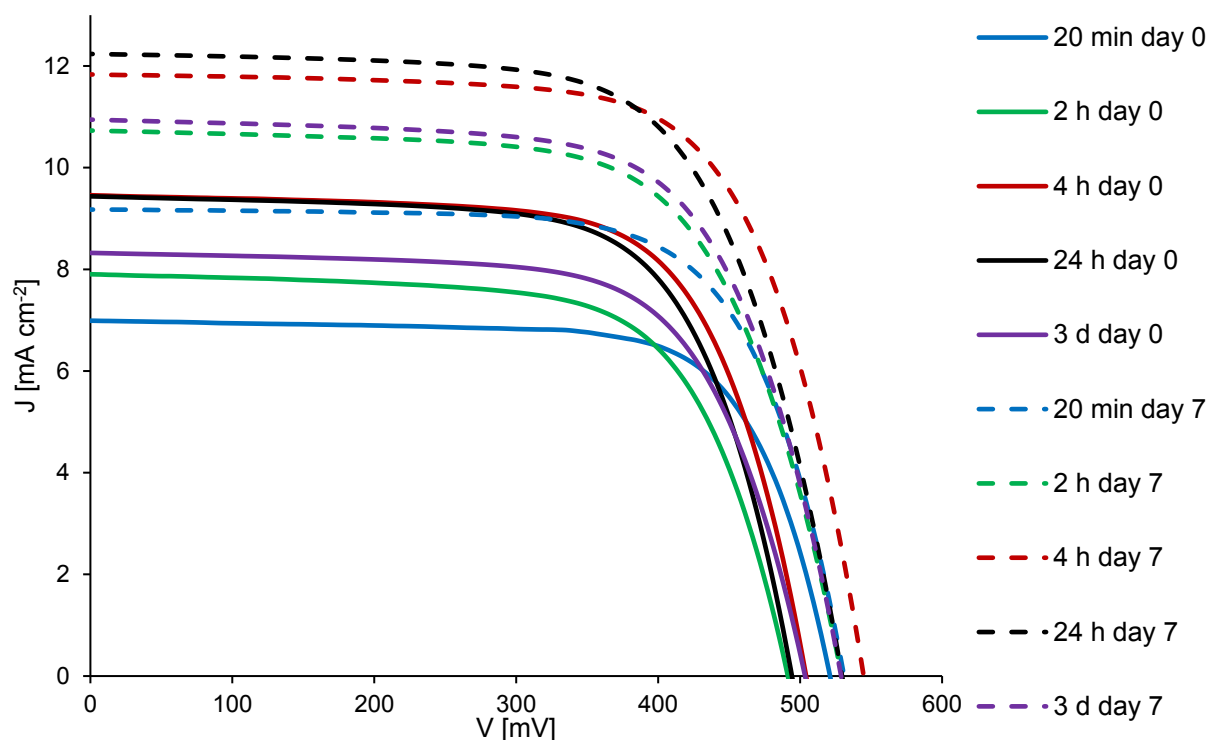


Fig. 121 $J-V$ curves of a DSC containing the dye **SQ2** with different dipping times of the photoanodes in the dye-bath before fabrication of the devices.

The structural differences between a phosphonic acid anchor (as in **ALP1**) and a carboxylic acid (as in **SQ2**) lead to different modes of bonding to the TiO_2 surface.^{98,202-204} It is also known that phosphonic acids bind more strongly to metal oxide surfaces than carboxylic acids.⁹⁸ Based on the pre-tests with the dyes $[\text{Cu}(\text{ALP1})(\text{L-Br})]^+$ (phosphonic acid anchor) and **N719** (carboxylic acid anchor) in *16 Co-sensitization Pre-tests with a Copper(I)-dye and N719* it can be anticipated that both dyes could be absorbed simultaneously onto the semiconductor surface. But the application of the investigated dipping procedures for **ALP1**, **L-Br** and **N719** in *16 Co-sensitization Pre-tests with a Copper(I)-dye and N719* need to be verified for optimal co-sensitization of the electrodes.

The optimal co-sensitization of the photoelectrodes was examined by EQE measurements. The goal was to optimize the EQE response for DSCs co-sensitized with $[\text{Cu}(\text{ALP1})(\text{N}^{\wedge}\text{NS})]^+$ and **SQ2**. The assembly of the heteroleptic $[\text{Cu}(\text{ALP1})(\text{N}^{\wedge}\text{NS})]^+$ using the ligand-exchange dye-assembly procedure requires that the photoanode is first immersed in a solution of anchoring ligand **ALP1**. In a second step, the functionalized photoanode was dipped into a CH_2Cl_2 solution of the homoleptic complex $[\text{Cu}(\text{N}^{\wedge}\text{NS})_2][\text{PF}_6]$. After ligand exchange, $[\text{Cu}(\text{ALP1})(\text{N}^{\wedge}\text{NS})]^+$ is bound to the semiconductor surface. Additionally, **SQ2** has to be introduced into this dipping procedure. Different dipping procedures were investigated to reach comparable values of EQE_{max} for DSCs containing both dyes. Table 30 summarizes the different dipping procedures with the sequences in which the photoanode was sequentially immersed into the dye-baths.

Table 30 Dipping procedures with anchoring ligand **ALP1**, homoleptic complex $[\text{Cu}(\text{N}^{\wedge}\text{NS})_2][\text{PF}_6]$ and the organic dye **SQ2**.

dipping procedure	1 st dipping step	2 nd dipping step	3 rd dipping step
<i>DPA</i>	ALP1 (dye-bath solvent: DMSO; concentration: 1 mM; dipping time: 1 d)	SQ2 (dye-bath solvent: CH_2Cl_2 ; concentration: 0.1 mM; dipping time: 20 min, 1 h, 2 h, 4 h)	$[\text{Cu}(\text{N}^{\wedge}\text{NS})_2][\text{PF}_6]$ (dye-bath solvent: CH_2Cl_2 ; concentration: 0.1 mM; dipping time: 3 d)
<i>DPB</i>	ALP1 (dye-bath solvent: DMSO; concentration: 1 mM; dipping time: 1 d)	$[\text{Cu}(\text{N}^{\wedge}\text{NS})_2][\text{PF}_6]$ (dye-bath solvent: CH_2Cl_2 ; concentration: 0.1 mM; dipping time: 3 d)	SQ2 (dye-bath solvent: CH_2Cl_2 ; concentration: 0.1 mM; dipping time: 20 min, 1 h, 2 h, 4 h)
<i>DP C</i>	ALP1 : SQ2 (dye-bath solvent: ALP1 in DMSO, SQ2 in CH_2Cl_2 ; concentration: ALP1 : 0.1 mM, SQ2 : 0.1 mM, 0.01 mM, 0.001 mM or 0.0001 mM; dipping time: 1 d)	$[\text{Cu}(\text{N}^{\wedge}\text{NS})_2][\text{PF}_6]$ (dye-bath solvent: CH_2Cl_2 ; concentration: 0.1 mM; dipping time: 3 d)	–
<i>DP D</i>	ALP1 : SQ2 (dye-bath solvent: ALP1 in DMSO, SQ2 in CH_2Cl_2 ; concentration: ALP1 : 0.1 mM, SQ2 : 0.1 mM, 0.01 mM, 0.001 mM or 0.0001 mM; dipping time: 1 d)	$[\text{Cu}(\text{N}^{\wedge}\text{NS})_2][\text{PF}_6]$ (dye-bath solvent: CH_2Cl_2 ; concentration: 0.1 mM; dipping time: 3 d)	SQ2 (dye-bath solvent: CH_2Cl_2 ; concentration: 0.1 mM; dipping time: 20 min)

The optimized dipping procedure from the pre-tests was used for the first experiment (Dipping Procedure A, *DPA*). First of all, the photoelectrode was dipped into the 1 mM DMSO solution of the anchoring ligand **ALP1** for 1 day. After washing with DMSO and EtOH the electrode was dried with a heat gun at about 80 °C. Afterwards, the functionalized photoelectrode was immersed in the **SQ2** solution (0.1 mM in CH_2Cl_2) for different dipping times (20 min, 1 h, 2 h, or 4h, respectively). After the corresponding dipping time the electrode was washed with

CH₂Cl₂ and dried. The last dipping step involved a dye bath containing the homoleptic [Cu(N[^]NS)₂][PF₆] (0.1 mM in in CH₂Cl₂) with a dipping time of 3 days (Fig. 122).

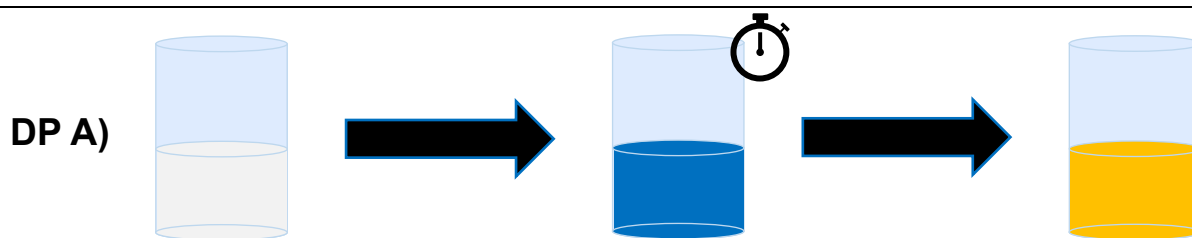


Fig. 122 Stepwise dipping procedure of photoanodes with the dipping procedure A (*DPA*) (stop watch = different dipping times; details see Table 30).

The best EQE response in *DPA* was measured with a dipping time of **SQ2** of 2 hours. But the dipping time has no influence on the EQE curve. Fig. 123 shows the EQE curve for all DSCs assembled by *DPA*. The EQE response of **SQ2** was low ($EQE_{max} = 28.7\%$, Table 31) and had the narrow shape characteristic of the solution UV-Vis spectrum of **SQ2** (Fig. 118).^{191,195,198,200,201} This indicates that there is little aggregation of **SQ2** on the surface. The copper(I)-dye [Cu(**ALP1**)(N[^]NS)]⁺ has a good EQE response with a maximum of 49.5% at $\lambda_{max} = 480$ nm (Table 31). It was observed that in the third dipping step, the [Cu(N[^]NS)₂][PF₆] dye-bath was initially orange but during the time that the electrode was in the bath, the colour of the solution changed from orange to greenish. This suggests that **SQ2** (which is blue) is partly washed off the surface.

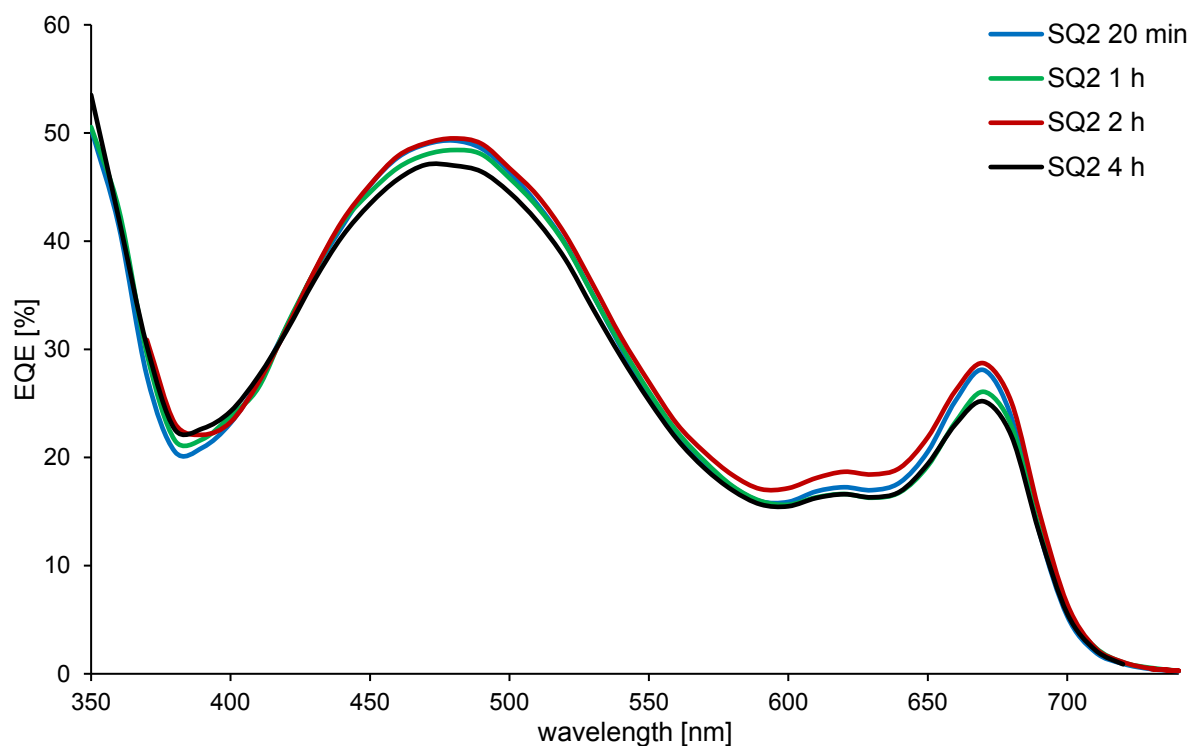


Fig. 123 EQE curves of DSCs assembled by the dipping procedure A (*DPA*) at the day of sealing the cell.

Table 31 EQE maxima of **SQ2** and $[\text{Cu}(\text{ALP1})(\text{N}^{\wedge}\text{NS})]^+$, respectively, of the DSCs assembled by the dipping procedure A (*DPA*).

dipping time	$[\text{Cu}(\text{ALP1})(\text{N}^{\wedge}\text{NS})]^+$		SQ2	
	λ_{max} [nm]	EQE_{max} [%]	λ_{max} [nm]	EQE_{max} [%]
20 min	480	49.3	670	28.1
1 h	480	48.4	670	26.1
2 h	480	49.5	670	28.7
4 h	470	47.1	670	25.2

In the next experiment (Dipping Procedure B, *DP B*), the sequence of the second and third dipping steps was changed with respect to *DP A*. First the heteroleptic copper(I)-dye $[\text{Cu}(\text{ALP1})(\text{N}^{\wedge}\text{NS})]^+$ was assembled on the TiO_2 surface by sequential exposure to anchor **ALP1**

for 1 day and then $[\text{Cu}(\text{N}^{\wedge}\text{NS})_2][\text{PF}_6]$ for 3 days. The standard washing and drying step between each step was done. In the third dipping step, **SQ2** was applied to the photoanode. Finally, the photoelectrode was washed with CH_2Cl_2 and dried (Fig. 124).

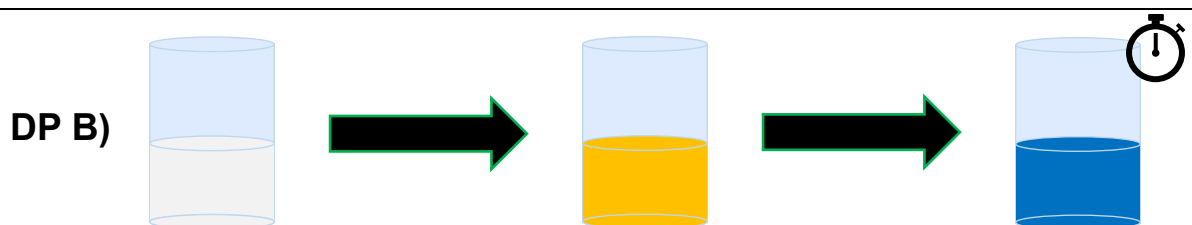


Fig. 124 Stepwise dipping procedure of photoanodes with the dipping procedure B (*DP B*) (stop watch = different dipping times; details see Table 30).

The EQE response due to the copper(I)-based dye ($EQE_{max} = 46.1\%$ at $\lambda_{max} = 480$ nm) is similar to that in *DP A* (Table 31 and Fig. 123). However, more **SQ2** was present on the surface with respect to *DP A*. This results in more aggregation and a broader and higher EQE curve between 580 and 720 nm (Fig. 125). The same trend in aggregation as in single-dye **SQ2** DSCs (Fig. 120) was also observed in *DP B* (Fig. 125). The longer the dipping time, the more aggregation is observed. The benefit of a certain level of aggregation (discussed earlier) is observed on increasing the dipping time from 20 minutes to 2 hours (at $\lambda_{max} = 670$ nm, EQE_{max} rises from 33.1 to 36.8%, Table 32). However, a longer dipping time of 4 hours results in higher aggregation and a low EQE_{max} of 28.7%. The best EQE response in *DP B* was obtained by a cell with a dipping time of **SQ2** of 1 hour.

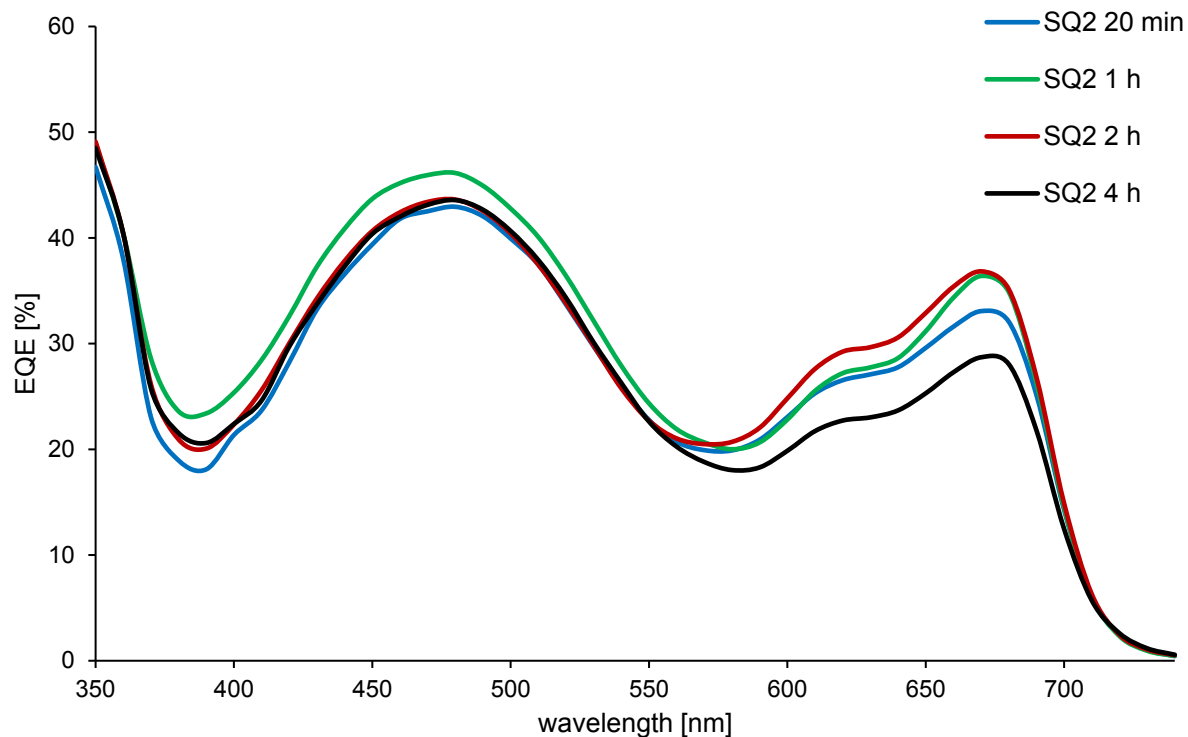


Fig. 125 EQE curves of DSCs assembled by the dipping procedure B (*DPB*) at the day of sealing the cell.

Table 32 EQE maxima of **SQ2** and $[\text{Cu}(\text{ALP1})(\text{N}^{\wedge}\text{NS})]^+$, respectively, of the DSCs assembled by the dipping procedure B (*DPB*).

dipping time	$[\text{Cu}(\text{ALP1})(\text{N}^{\wedge}\text{NS})]^+$		SQ2	
	λ_{max} [nm]	EQE_{max} [%]	λ_{max} [nm]	EQE_{max} [%]
20 min	480	42.9	670	33.1
1 h	480	46.1	670	36.4
2 h	470	47.8	670	36.8
4 h	480	43.6	670	28.7

DP A and *DP B* demonstrate that some degree of aggregation of **SQ2** on the TiO_2 surface is important in order to achieve a panchromatic DSC. In order to optimize the aggregation of **SQ2**, the organic dye was introduced with different concentrations (0.0001 to 0.1 mM) to the anchoring

ligand solution (0.1 mM) in the first dipping step. The very low concentrations of **SQ2** were used because of the higher extinction coefficient of **SQ2** (Fig. 118) with respect to the MLCT band of $[\text{Cu}(\text{ALP1})(\text{N}^{\wedge}\text{NS})]^+$ (Fig. 92). The mixture was prepared freshly before the photoelectrode was dipped in the solution for 1 day. In Dipping Procedure C (*DP C*), only a second dipping step with the homoleptic $[\text{Cu}(\text{N}^{\wedge}\text{NS})_2][\text{PF}_6]$ (0.1 mM in CH_2Cl_2) for 3 days was applied (Fig. 126).

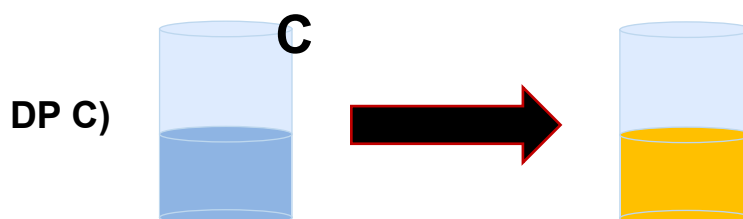


Fig. 126 Stepwise dipping procedure of photoanodes with the dipping procedure C (*DP C*) (c = different concentrations; details see Table 30).

The same problem as was encountered in *DPA* was observed for *DP C*. Dye **SQ2** anchored in the first immersion step was partly washed off during the second dipping cycle. Only the DSC with the highest **SQ2** concentration in the first dipping step (0.1 mM) showed a visible EQE response ($EQE_{max} = 3.0\%$) at $\lambda_{max} = 670$ nm (Table 33 and Fig. 127). Interestingly, the value of EQE_{max} of the copper(I)-dye (49.7%) in *DP C* is as high as in *DPA* (Table 31) in which **SQ2** was not present in the first dipping step. This is consistent with both **ALP1** and **SQ2** being able to bind simultaneously to the TiO_2 surface.

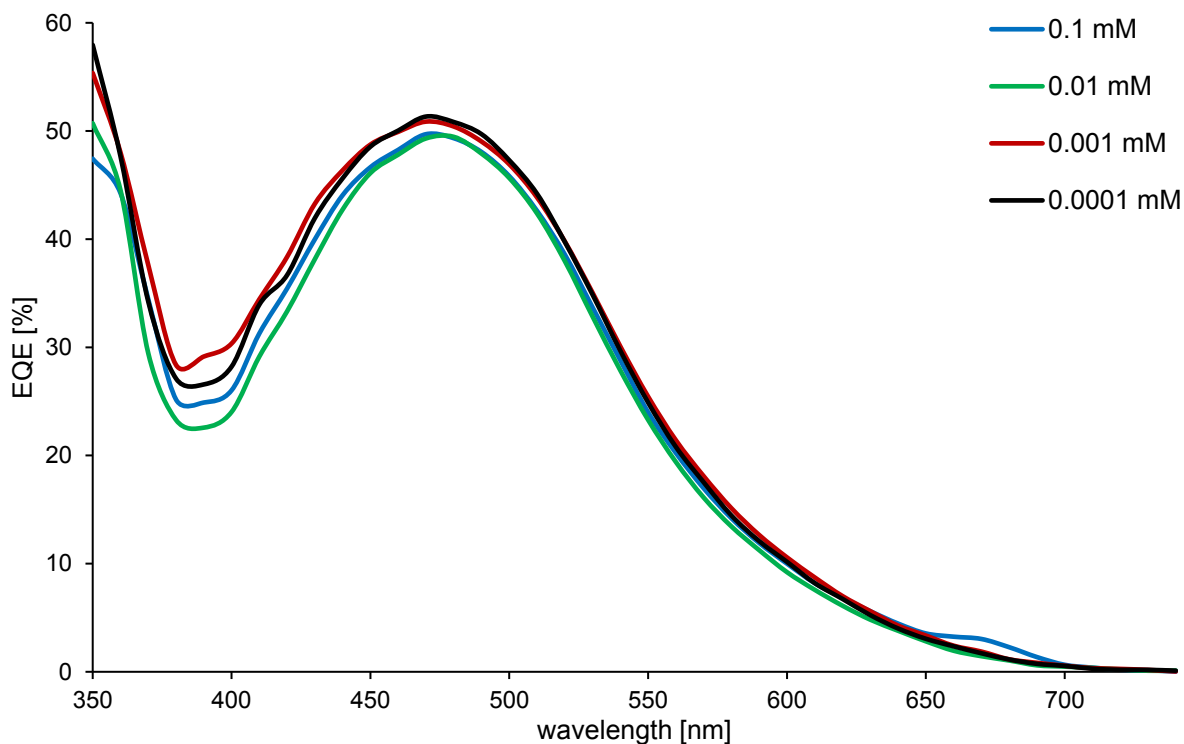


Fig. 127 EQE curves of DSCs assembled by the dipping procedure C (*DP C*) at the day of sealing the cell.

Table 33 EQE maxima of **SQ2** and $[\text{Cu}(\text{ALP1})(\text{N}^{\wedge}\text{NS})]^+$, respectively, of the DSCs assembled by the dipping procedure C (*DP C*).

concentration [mM]	$[\text{Cu}(\text{ALP1})(\text{N}^{\wedge}\text{NS})]^+$		SQ2	
	λ_{max} [nm]	EQE_{max} [%]	λ_{max} [nm]	EQE_{max} [%]
0.1	470	49.7	670	3.0
0.01	480	49.5	670	-
0.001	470	50.9	670	-
0.0001	470	51.3	670	-

In Dipping Procedure D (*DP D*) a final dipping step after the dipping procedure used in *DP C* was introduced. Here, the electrode was exposed to **SQ2** (0.1 mM in in CH_2Cl_2) for a second

time in the end of the whole dipping procedure. A short dipping time of 20 min was sufficient (Fig. 128).

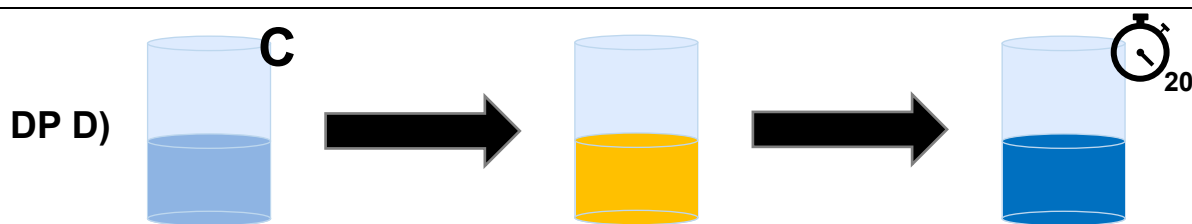


Fig. 128 Stepwise dipping procedure of photoanodes with the dipping procedure D (*DP D*) (*c* = different concentrations; 20 min stop watch = dipping time of 20 min; details see Table 30).

The aim was to refill the surface-vacancies created through loss of **SQ2** in the second dipping step (see above). Because of the introduction of **SQ2** in the first dipping step, more binding sites for **SQ2** are available and more aggregation can take place. This effect is visible in all measured DSCs of *DP D* (Fig. 129) in comparison to *DP C* (Fig. 127).

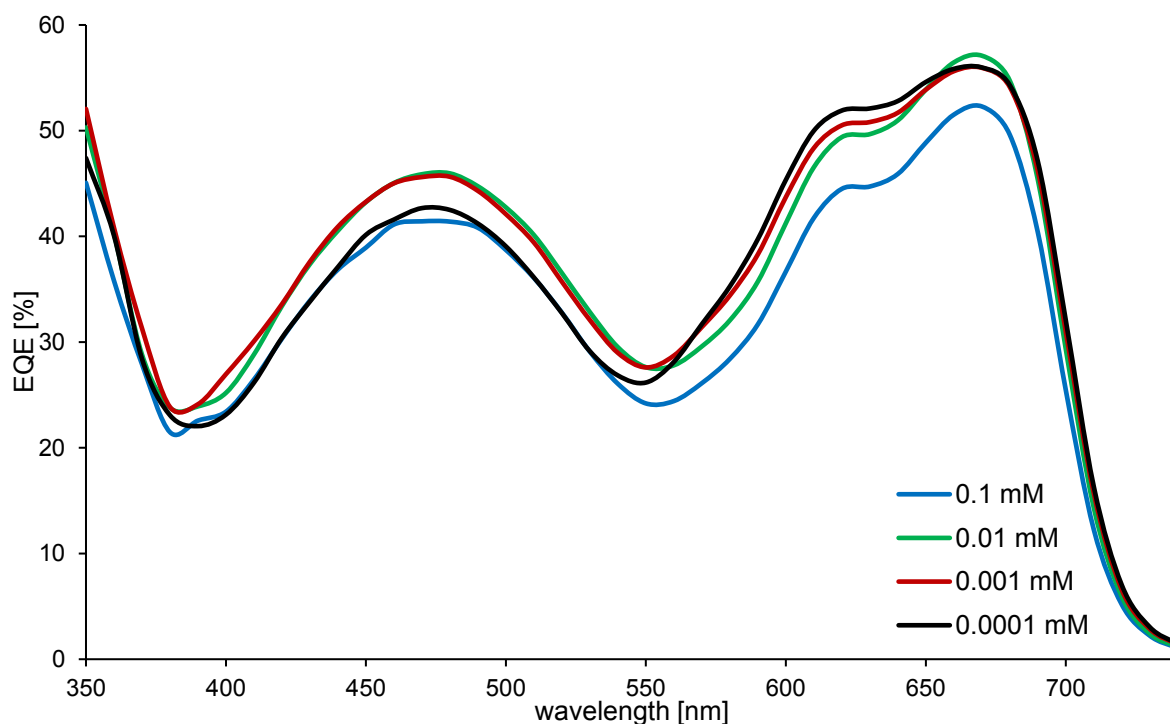


Fig. 129 EQE curves of DSCs assembled by the dipping procedure D (*DP D*) at the day of sealing the cell.

Table 34 EQE maxima of **SQ2** and $[\text{Cu}(\text{ALP1})(\text{N}^{\wedge}\text{NS})]^+$, respectively, of the DSCs assembled by the dipping procedure D (*DPD*).

concentration [mM]	$[\text{Cu}(\text{ALP1})(\text{N}^{\wedge}\text{NS})]^+$		SQ2	
	λ_{max} [nm]	EQE_{max} [%]	λ_{max} [nm]	EQE_{max} [%]
0.1	470	41.4	670	52.3
0.01	480	46.0	670	57.1
0.001	480	45.6	670	55.9
0.0001	470	42.7	670	56.0

The best panchromatic EQE response was recorded with a device from *DPD* with an **SQ2** concentration of 0.01 mM in the first dipping step (black curve in Fig. 129). Values of $EQE_{max} = 57.1\%$ ($\lambda_{max} = 670$ nm) for **SQ2** and $EQE_{max} = 46.0\%$ ($\lambda_{max} = 480$ nm) from $[\text{Cu}(\text{ALP1})(\text{N}^{\wedge}\text{NS})]^+$ were observed. The presence of **SQ2** in the first dipping step leads to more anchored **SQ2** on the final photoanode. In addition, the solubility of ligand **ALP1** is an important parameter; **ALP1** is poorly soluble in CH_2Cl_2 and some precipitation is observed when the CH_2Cl_2 solution of **SQ2** is added to the DMSO solution of **ALP1**.

In the history of the investigation of the dipping procedures (Fig. 130) it can be concluded that the phosphonic acid anchor (**ALP1**) binds more strongly to the semiconductor surface than the carboxylic acid anchor (**SQ2**). That is the reason why the copper(I)-dye $[\text{Cu}(\text{ALP1})(\text{N}^{\wedge}\text{NS})]^+$ has to be introduced before the organic dye **SQ2**. Otherwise **SQ2** gets washed off the surface during the next dipping step. The introduction of **SQ2** to the anchoring ligand solution increases the adsorption of **SQ2** when it is reintroduced in a final dipping step.

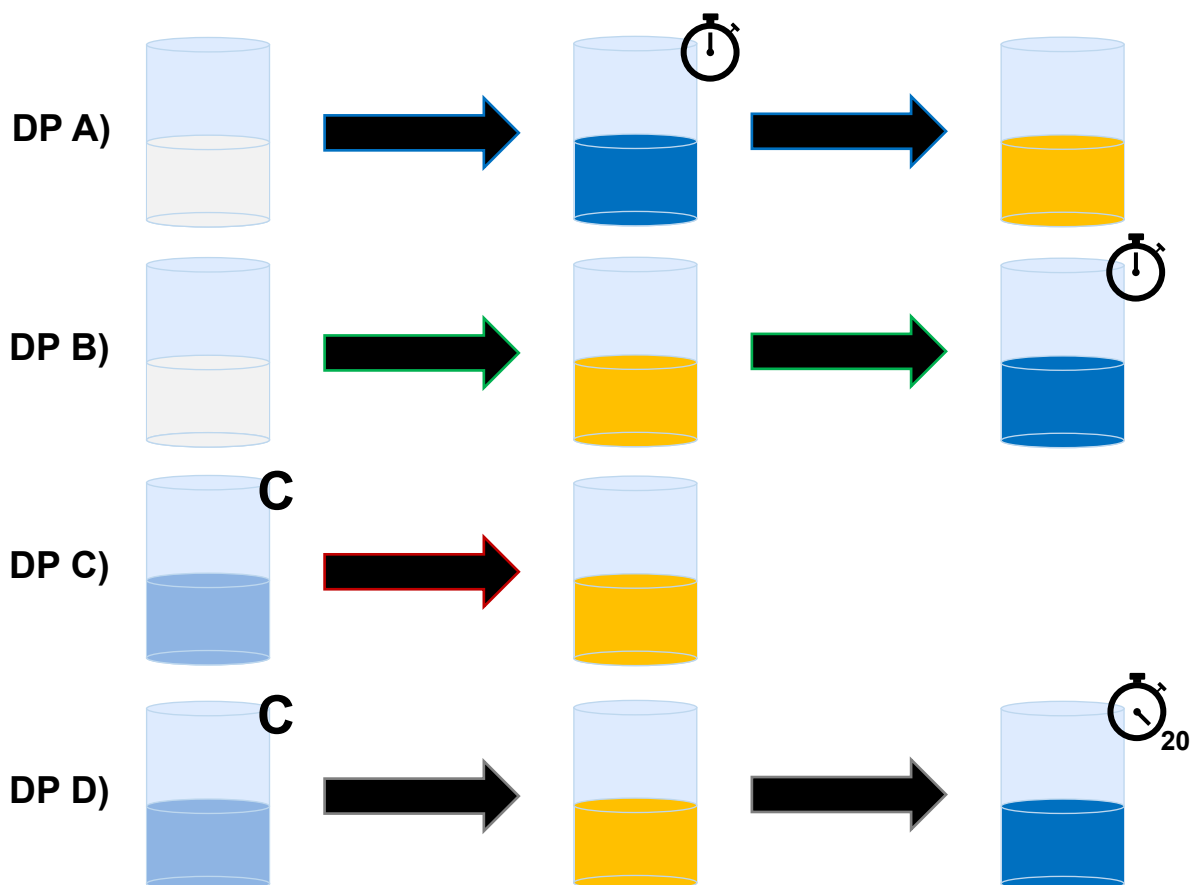


Fig. 130 Summary of stepwise dipping procedures of photoanodes with the dipping procedure A (*DP A*), B (*DP B*), C (*DP C*) and D (*DP D*) (stop watch = different dipping times; c = different concentrations; 20 min stop watch = dipping time of 20 min; details see Table 30).

The optimized EQE spectral response with matched values of EQE_{max} at 480 and 670 nm was obtained using the dipping procedure in *DP D* (Fig. 131) with the following sequence of steps:

first dipping step: **ALP1** in DMSO (0.1 mM) and **SQ2** in CH_2Cl_2 (0.01 mM) for 1 day,

second dipping step: $[Cu(N^{\wedge}NS)_2][PF_6]$ in CH_2Cl_2 (0.1 mM) for 3 days

third dipping step: **SQ2** in CH_2Cl_2 (0.1 mM) for 20 min.

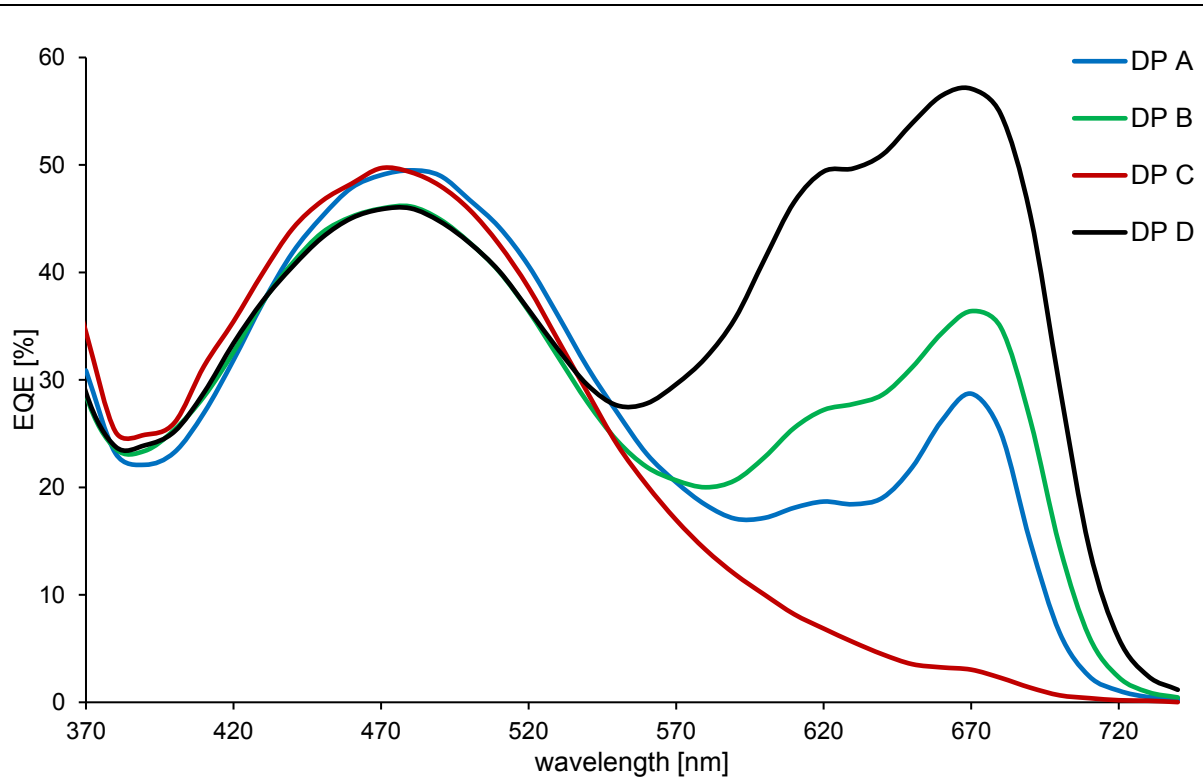


Fig. 131 EQE curves of the DSCs with the best EQE response for the different dipping procedures at the day of sealing the cell.

The performance of panchromatic co-sensitized DSCs is considered in the following part. The performance of the optimized co-sensitized DSC assembled by *DPD* with an **SQ2** concentration of 0.01 mM in the dye-bath of the first dipping step is listed in Table 35. The data of the single-dye DSCs is given for comparison.

Table 35 Performance parameters and EQE maxima of single-dye DSCs containing the dye [Cu(**ALP1**)(**N^{NS}**)]⁺ and **SQ2** with a dipping time of 20 minutes and the best-performing co-sensitized DSC on the day of sealing the cell, 3 days and 7 days later.

dye	J_{sc} [mA cm ⁻²]	V_{oc} [mV]	ff [%]	η [%]	Relative η [%]	EQE_{max} [nm, %]
On the day of sealing the cell						
[Cu(ALP1)(N^{NS})] ⁺	7.76	530	70	2.88	38.1	480, 53.8
SQ2	6.99	521	72	2.62	34.7	670, 44.4
co-sens. DSC	9.56	493	71	3.36	44.5	480, 46.0 670, 57.1
N719	16.57	630	72	7.55	100	540, 71.8
3 days after sealing the cell						
[Cu(ALP1)(N^{NS})] ⁺	6.77	542	70	2.58	35.8	480, 50.8
SQ2	9.25	537	70	3.45	47.9	670, 47.5
co-sens. DSC	11.86	515	72	4.39	60.9	480, 46.3 670, 58.1
N719	15.03	660	73	7.21	100	520, 70.8
7 days after sealing the cell						
[Cu(ALP1)(N^{NS})] ⁺	7.42	558	63	2.59	37.7	470, 46.2
SQ2	9.18	531	70	3.40	49.5	660, 49.2
co-sens. DSC	12.26	515	71	4.51	65.6	480, 47.1 670, 59.3
N719	14.47	650	73	6.87	100	540, 71.1

The initial value of J_{sc} for the co-sensitized DSC (9.56 mA cm⁻², Table 35) is higher than that of the single-dye DSCs (7.76 mA cm⁻² for [Cu(**ALP1**)(**N^{NS}**)]⁺ and 6.99 mA cm⁻² for **SQ2**). The V_{oc} of 493 mV is lower than single-dye DSCs (530 mV for [Cu(**ALP1**)(**N^{NS}**)]⁺ and 521 mV for **SQ2**), while the ff remains high (71%). The η of this device is 3.36% relative to 7.55% for **N719**. Fig. 132 displays the J - V curves of the co-sensitized device on the day of cell fabrication and after ageing; a comparison with single-dye DSCs is shown in Fig. 133. The EQE spectra of the device are shown in Fig. 134 and a comparison with the single-dye DSCs is made in Fig. 135.

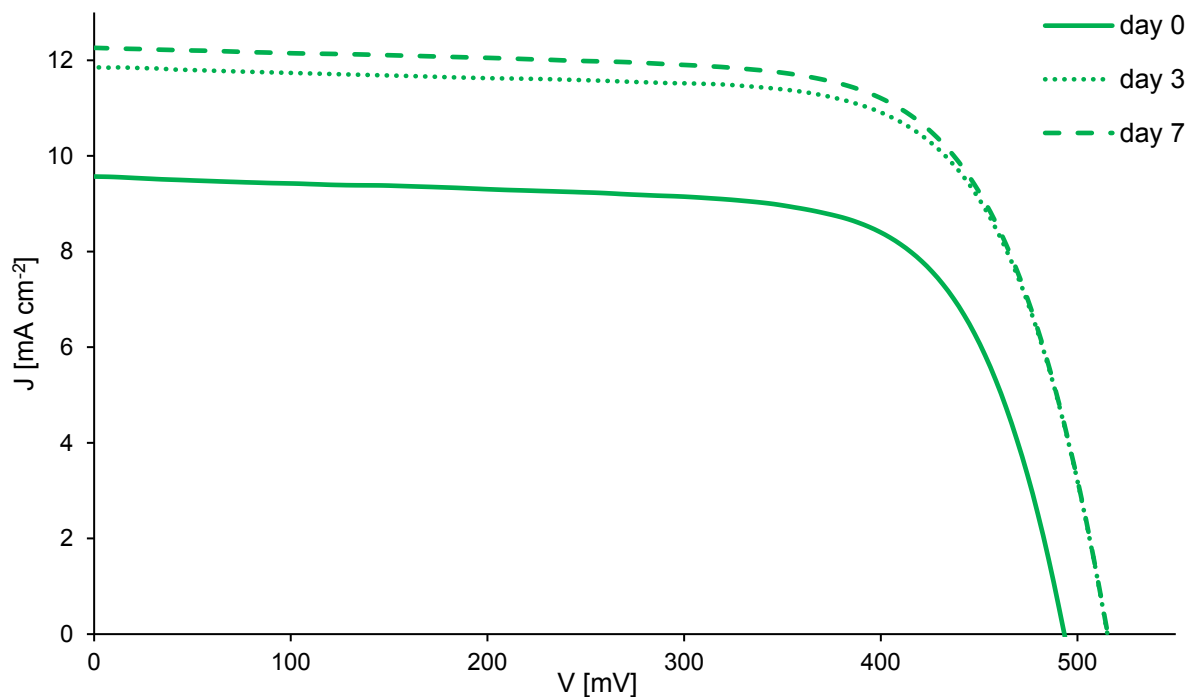


Fig. 132 J - V curves of the best performing co-sensitized DSC assembled with the dipping procedure D and a **SQ2**-concentration of 0.01 mM in the first dipping step on the day of sealing the cell, 3 days and 7 days later.

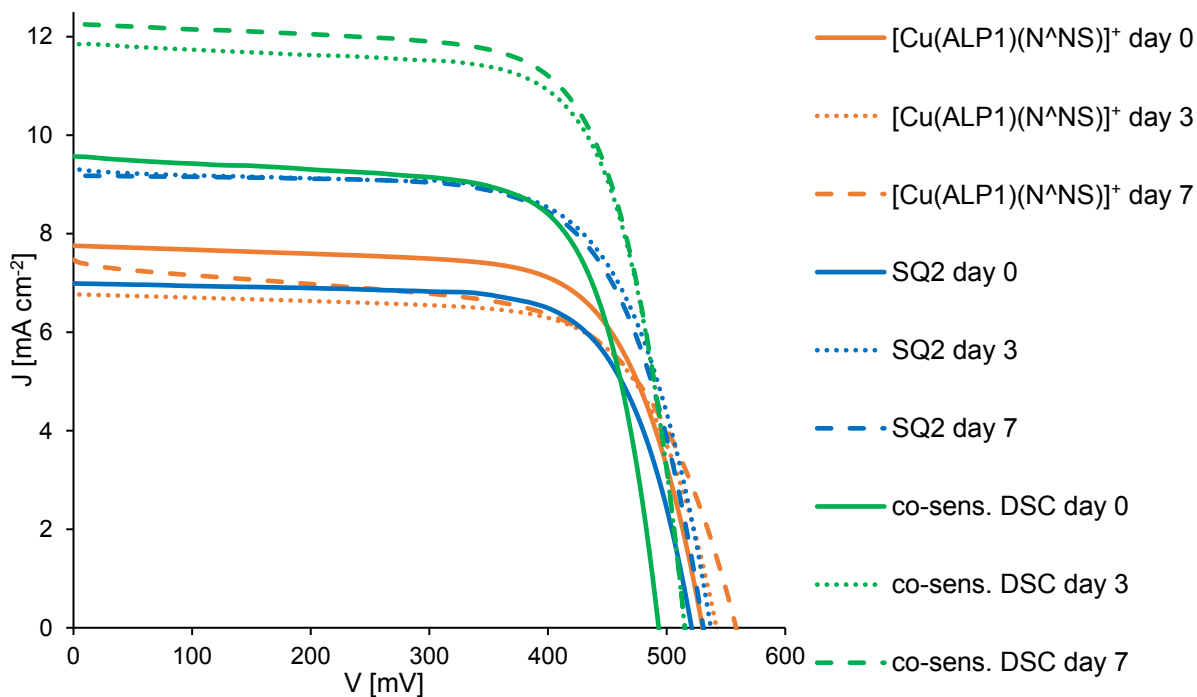


Fig. 133 J - V curves of the single-dye DSCs and the best co-sensitized DSC on day of sealing the cell, 3 days and 7 days later.

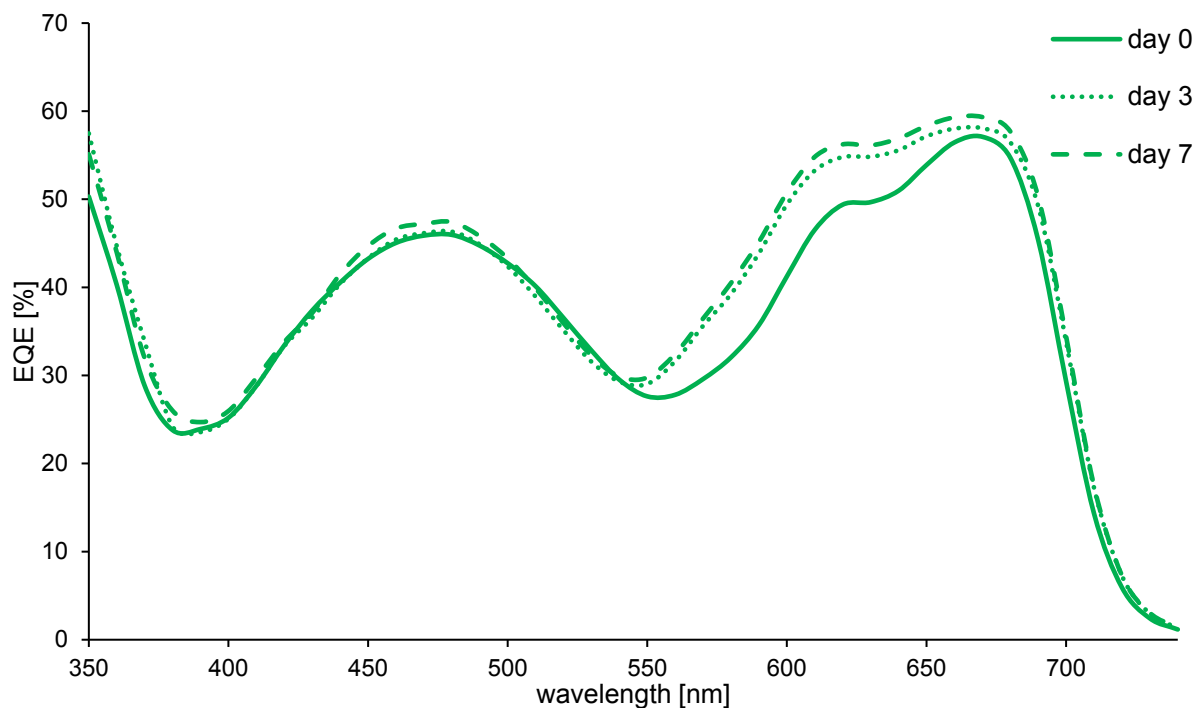


Fig. 134 EQE curves of the best performing co-sensitized DSC assembled with the dipping procedure D and a SQ2-concentration of 0.01 mM in the first dipping step on the day of sealing the cell, 3 days and 7 days later.

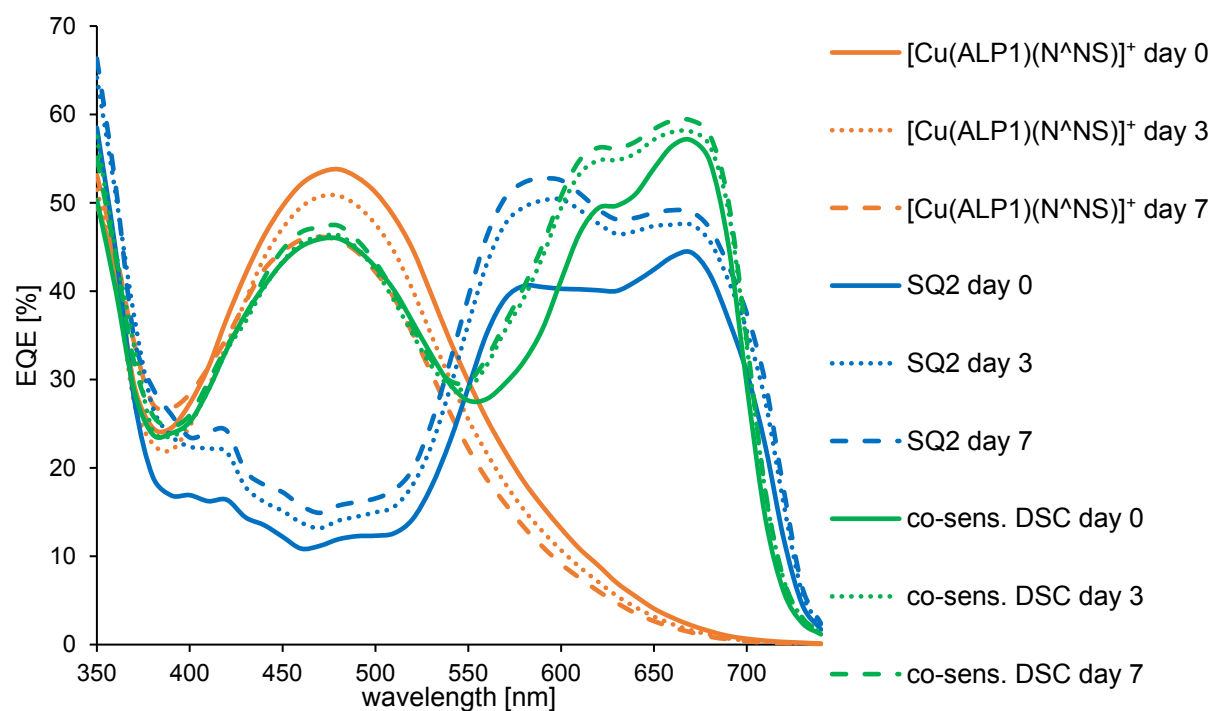


Fig. 135 EQE spectra of the single-dye DSCs and the best co-sensitized DSC on day of sealing the cell, 3 days and 7 days later.

The increase in J_{sc} over a 7 day period after cell fabrication (Fig. 132) is a known phenomenon and most probably arises from reorganization of the dye molecules on the TiO₂ semiconductor surface.¹³⁷⁻¹³⁹ The EQE maxima of both dyes in the co-sensitized cell also increase over a period of 7 days, but this is more pronounced for **SQ2** (Fig. 134). The value of EQE_{max} at $\lambda_{max} = 480$ nm (copper(I)-based dye) increases from 46.0% to 47.1% (Table 35). The EQE maximum at $\lambda_{max} = 670$ nm (from **SQ2**) increased from 57.1% to 59.3% over a period of 7 days and a higher level of aggregation resulted in a broader and higher EQE response between 540 and 740 nm (Fig. 134).^{191,195-201} It has to be remembered that the dipping times in the **SQ2** dye-bath required to achieve optimal EQE maxima are 4 hours for the single **SQ2** cell (59.6% at 550 nm, Table 29) *versus* only 20 minutes for the co-sensitized device (59.3% at 670 nm, Table 35). On day 7 after sealing the cell, a value of $J_{sc} = 12.26$ mA cm⁻² was obtained for the best performing DSC (Table 35). The V_{oc} increases over a period of 7 days from 493 to 515 mV and the ff stays constant. On day 7, a remarkable global efficiency of 4.51% was obtained relative to 6.87% for **N719** (Table 35). Setting **N719** to 100%, the co-sensitized DSC achieves a relative efficiency of 65.6%. This exceeds the previous record reported by Odobel and co-workers¹⁰⁵ for a copper(I)-based dye (4.66% *versus* 7.36% for **N719**, equivalent to a relative efficiency of 63.3%). Inspection of Table 35 demonstrates that the J_{sc} for the co-sensitized cell is always higher than the DSCs with single dyes. Although the V_{oc} is slightly lower for the co-sensitized *versus* single-dye DSCs, the value of η is always higher, confirming the benefit of co-sensitization. The performance of the DSC was tested again 14 days after assembling the device with the cell being stored in the dark; values of J_{sc} , V_{oc} and η were 12.85 mA cm⁻², 534 mV and 4.53%, emphasizing the stability of the device. Inspection of Table 36 reveals that all the DSCs fabricated using the procedure in *DP D* perform well and, in general, their performances improve with time.

Table 36 Performance parameters of DSCs assembled by the dipping procedure D (details see Table 30)

concentration	J_{sc} [mA cm ⁻²]	V_{oc} [mV]	ff [%]	η [%]
On the day of sealing the cell				
0.1	7.81	471	70	2.56
0.01	9.56	493	71	3.36
0.001	9.51	530	69	3.49
0.0001	10.19	484	67	3.28
3 days after sealing the cell				
0.1	10.51	520	69	3.77
0.01	11.86	515	72	4.39
0.001	9.11	560	65	3.33
0.0001	10.69	514	69	3.78
7 days after sealing the cell				
0.1	11.08	549	61	3.71
0.01	12.26	515	71	4.51
0.001	9.52	556	62	3.28
0.0001	11.33	524	69	4.11

For example, a co-sensitized DSC assembled by the dipping procedure of *DPD* (Table 30, **SQ2** concentration of 0.0001 mM in the first dipping step) had a photoconversion efficiency of 4.09% on day 7, 4.01% on day 28 and 3.75% on day 72 after sealing the cell (Fig. 136). This again emphasizes the benefits of the dipping procedure of *DPD* and the stability of the co-sensitized DSCs.

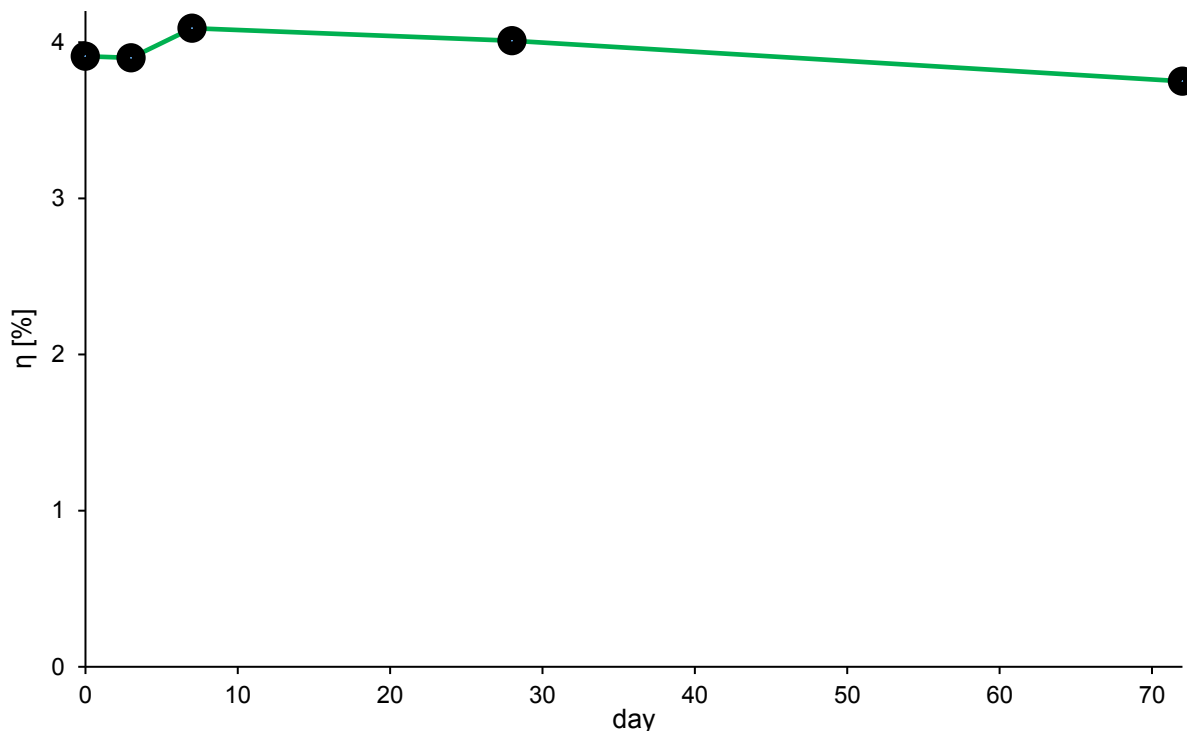


Fig. 136 Long-term stability of a co-sensitized DSC assembled by the dipping procedure D.

Electrochemical impedance spectroscopy (EIS) was measured for the single-dye DSCs and the panchromatic co-sensitized DSC. In order to extract the key parameters from the measurement, two different equivalent circuit models were used. At higher light intensities, a model with two Randles-type circuits were used for EIS measurements at 22 mW cm^{-2} light intensity (Fig. 137). The fitting model consists of two Randles-type circuits in series and a further series resistance (R_s). An additional Warburg diffusion element (W_s) has been introduced. Each circuit characterizes one electrode interface. The first circuit models the electrolyte/Pt/FTO interface and the second one the $\text{TiO}_2/\text{dye}/\text{electrolyte}$ interface.

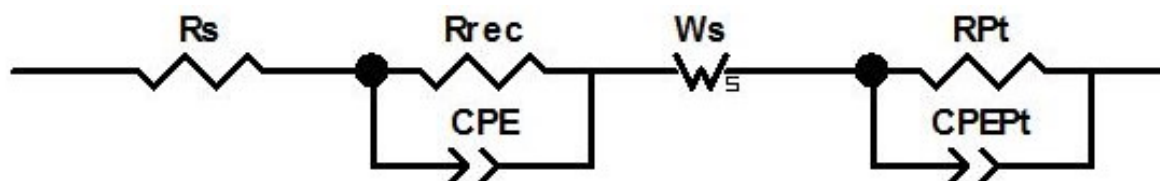


Fig. 137 Fitting model for EIS measurements at a light intensity of 22 mW cm^{-2} .

The fitting of the EIS measurements at a light intensity of 2.2 mW cm^{-2} were performed with the model displayed in Fig. 138. It consists of an extended distributed element (DX) to fit the $\text{TiO}_2/\text{dye}/\text{electrolyte}$ interface according to the transition line model. With this extended distributed element, it is possible to establish R_{tr} . The Warburg diffusion element (Ws) is again used to model the diffusion impedance of the charge carrier through the electrolyte close to the active surface. The Randles-type circuit containing R_{Pt} and CPE_{Pt} models the Pt counter electrode. The series resistance of the whole measurement is modelled by a series resistance (R_s).

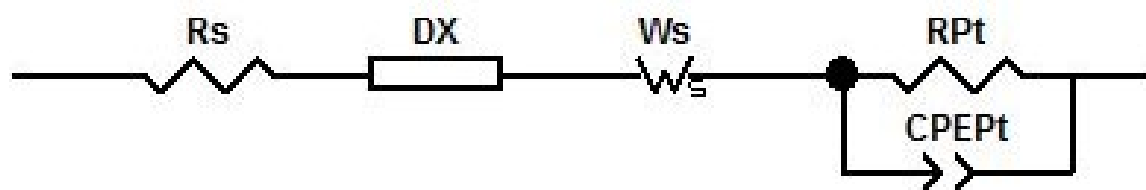


Fig. 138 Fitting model for EIS measurements at a light intensity of 2.2 mW cm^{-2} .

The following discussion compares single-dye DSCs containing $[\text{Cu}(\text{ALP1})(\text{N}^{\wedge}\text{NS})]^+$ or **SQ2**, and then considers the EIS results of the co-sensitized DSC with the best dipping procedure (*DPD*, Table 30) in comparison to the single-dye DSCs. The EIS measurements were conducted on DSCs that had aged for 3 days.

The EIS data for a DSC containing the dye $[\text{Cu}(\text{ALP1})(\text{N}^{\wedge}\text{NS})]^+$, was already discussed in *15.1 A New Type of Ancillary Ligand for Copper(I)-Based Dye-Sensitized Solar Cells: N^{\wedge}NX*. A single-dye **SQ2** DSC has been investigated by EIS by Fang and co-workers¹⁹¹ and values of $R_{rec} = 24.7 \Omega$ and the electron lifetime $\tau = 11.2 \text{ ms}$ were reported. These data are comparable with the EIS parameters measured at a light intensity of 22 mW cm^{-2} ($R_{rec} = 25.5 \Omega$, $\tau = 8.1 \text{ ms}$, Table 37). The low R_{rec} is a well-known disadvantage of organic DSCs and is one of the most crucial issues that needs to be addressed for organic DSCs in order to improve their performances.²⁰⁵⁻²¹⁰

Table 37 EIS data obtained from measurements at a light intensity of 22 mW cm^{-2} of DSCs containing the dye $[\text{Cu}(\text{ALP1})(\text{N}^{\wedge}\text{NS})]^+$, **SQ2** (dipping time 20 min) or the co-sensitization of both dyes by the best dipping procedure D.

dye	R_{rec} [Ω]	C_{μ} [μF]	R_{Pt} [Ω]	$C_{Pt\mu}$ [μF]	τ^a [ms]
$[\text{Cu}(\text{ALP1})(\text{N}^{\wedge}\text{NS})]^+$	178.8	319.4	30.6	16.3	57.1
SQ2	25.5	316.7	40.7	9.8	8.1
co-sens. DSC	24.2	362.4	10.4	12.1	8.8

a) calculated from Equation 9

A comparison of the EIS data (Table 37) for the $[\text{Cu}(\text{ALP1})(\text{N}^{\wedge}\text{NS})]^+$ and **SQ2** DSCs at a light intensity of 22 mW cm^{-2} shows that the C_{μ} is almost the same for both DSCs, but the R_{rec} is much higher for the DSC containing $[\text{Cu}(\text{ALP1})(\text{N}^{\wedge}\text{NS})]^+$. The longer electron lifetime, τ , observed for $[\text{Cu}(\text{ALP1})(\text{N}^{\wedge}\text{NS})]^+$ versus **SQ2** or the co-sensitized DSC (Table 37) is consistent with the much higher value of R_{rec} which militates against back reactions of the electrons in the conductance band. Fig. 139 displays the corresponding Nyquist plots at a light intensity of 22 mW cm^{-2} .

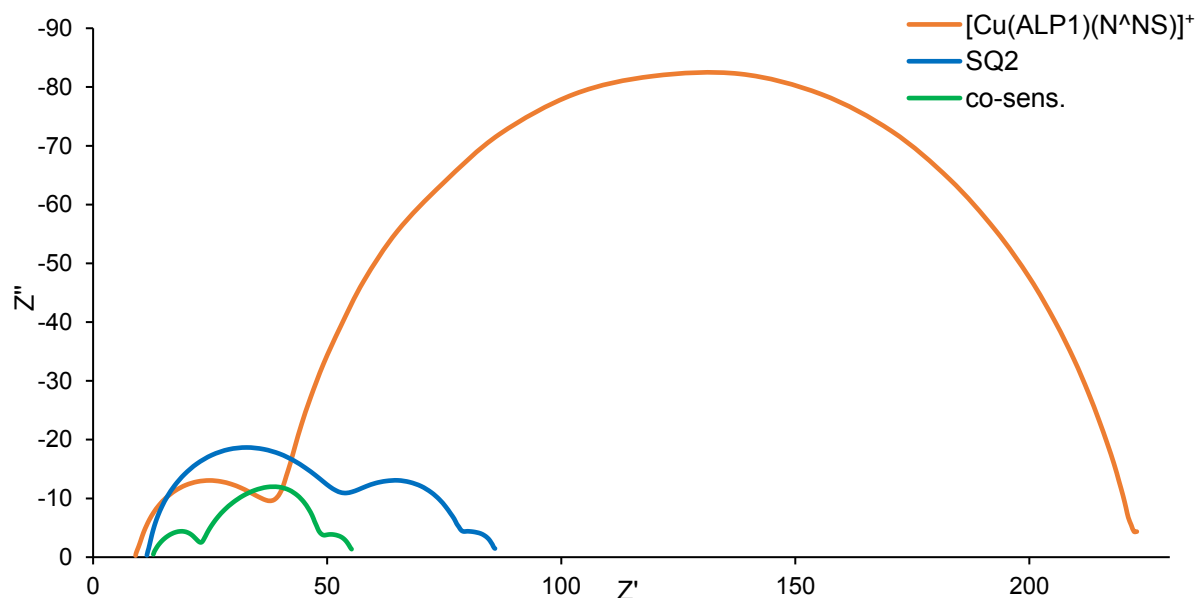


Fig. 139 Nyquist plots of DSCs containing the dye $[\text{Cu}(\text{ALP1})(\text{N}^{\wedge}\text{NS})]^+$, **SQ2** (dipping time 20 min) or the co-sensitization of both dyes by the best dipping procedure D at a light intensity of 22 mW cm^{-2} .

To obtain the transport resistance (R_{tr}), EIS measurements at low light intensity are required, and the fitted EIS parameters at a light intensity of 2.2 mW cm^{-2} are shown in Table 38. The Nyquist plots at light intensities 22 and 2.2 mW cm^{-2} are shown in Fig. 140.

Table 38 EIS data obtained from measurements at a light intensity of 2.2 mW cm^{-2} of DSCs containing the dye $[\text{Cu}(\text{ALP1})(\text{N}^{\wedge}\text{NS})]^+$, **SQ2** (dipping time 20 min) or the co-sensitization of both dyes by the best dipping procedure D.

dye	R_{rec} [Ω]	C_{μ} [μF]	R_{Pt} [Ω]	$C_{Pt\mu}$ [μF]	R_{tr} [Ω]	τ^a [ms]	L_d [μm]
$[\text{Cu}(\text{ALP1})(\text{N}^{\wedge}\text{NS})]^+$	893.3	186.7	19.4	7.2	105.9	166.7	34.9
SQ2	141.8	224.3	36.0	7.7	46.3	31.8	21.0
co-sens. DSC	151.0	195.3	10.6	8.6	50.3	29.5	20.8

a) calculated from Equation 9

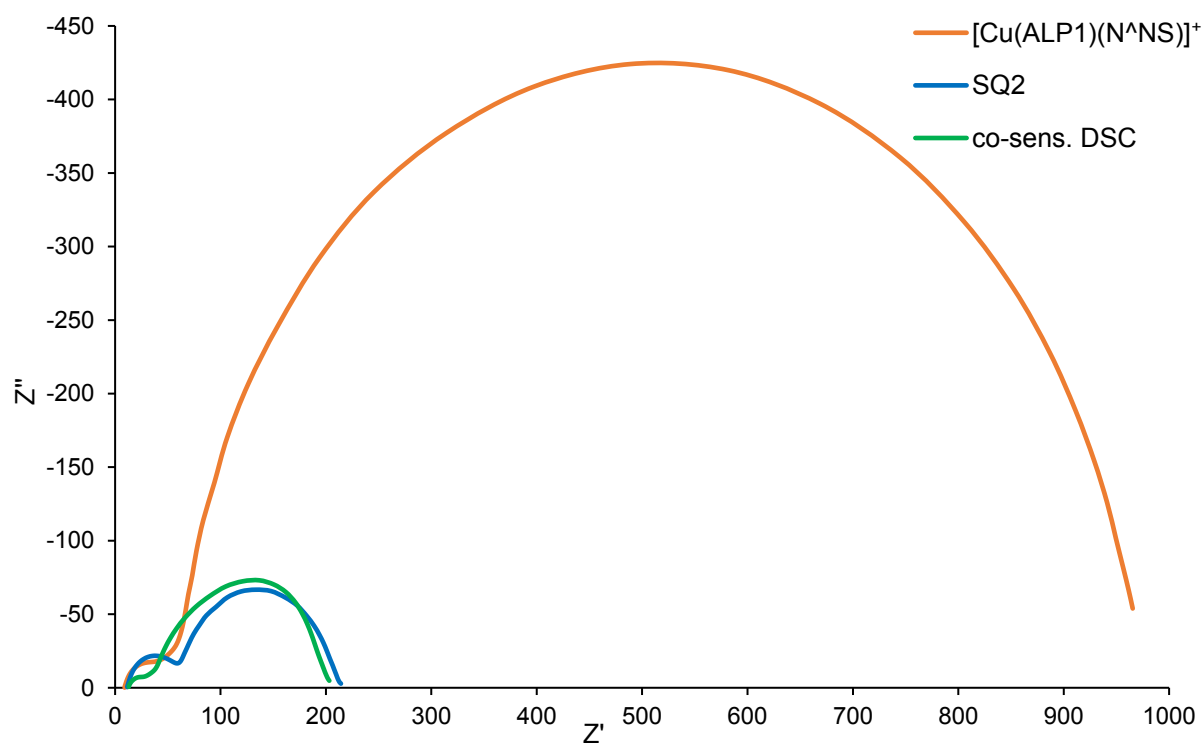


Fig. 140 Nyquist plots of DSCs containing the dye $[\text{Cu}(\text{ALP1})(\text{N}^{\wedge}\text{NS})]^+$, **SQ2** (dipping time 20 min) or the co-sensitization of both dyes by the best dipping procedure D at a light intensity of 2.2 mW cm^{-2} .

R_{tr} for the DSC sensitized by $[\text{Cu}(\text{ALP1})(\text{N}^{\wedge}\text{NS})]^+$ is considerably higher than for **SQ2**. This is consistent with the lower spectral response of the copper-based dye which leads to a lower number of absorbed photons.

An informative parameter to describe the interplay between R_{rec} and R_{tr} is the length of diffusion (L_d) which is calculated according to Equation 10. Although R_{rec} for the **SQ2** DSC is low (Table 37), it is a well performing cell, because R_{tr} must also to be taken into account. An efficient charge injection requires an L_d larger than the thickness of the semiconductor (here L is about 12 μm). As a consequence, when the ratio of R_{rec} to R_{tr} is greater than unity, the length of diffusion is long enough to minimize back reactions due to a long charge transit time. Here, the DSCs containing $[\text{Cu}(\text{ALP1})(\text{N}^{\wedge}\text{NS})]^+$ or **SQ2** both have an L_d two to three times larger than L .

When comparing the EIS measurements of the co-sensitized DSC with the single-dye DSCs (Table 37 and Table 38), it is observed that its characteristics resemble those of a pristine **SQ2** DSC. All parameters at a light intensity of 22 mW cm^{-2} are comparable to the single-dye **SQ2** DSC. The co-sensitized DSC has the highest C_{μ} of all the DSCs in this study. At the counter-electrode of the co-sensitized DSC, a low R_{Pt} is observed which enhances the charge transition at the cathode/electrolyte interface. R_{tr} for the co-sensitized DSC is as low as in the single-dye **SQ2** DSC. It has to be noted that **SQ2** can also partly bind to the scattering layer of the working electrode of the DSC in the single- and co-sensitized DSC; the evidence for this is that the scattering layer only becomes coloured when the electrode is exposed to **SQ2**. Because of the cell architecture, **SQ2** adsorbed on the scattering layer can come in contact with the electrolyte and this may be a reason why R_{rec} is lower for the DSC containing the **SQ2**. In conclusion, an optimal electron transport in the DSC is promoted by an interplay of the parameters discussed above and as a consequence, the highest J_{sc} is observed for the co-sensitized DSC. Additionally, L_d (Table 38) is almost twice the magnitude of L which is an appropriate value for a well performing DSC.

Light filter tests were performed in order to investigate whether the two dyes in the co-sensitized DSC work independently or via an electron or energy transfer mechanism.⁵¹ The J - V curves and EQE spectra were recorded with filters in place to block light in particular wavelength ranges. Two filters with specific light transmittance were chosen: a 500 nm short-pass filter and a 550 nm long-pass filter (Fig. 141).

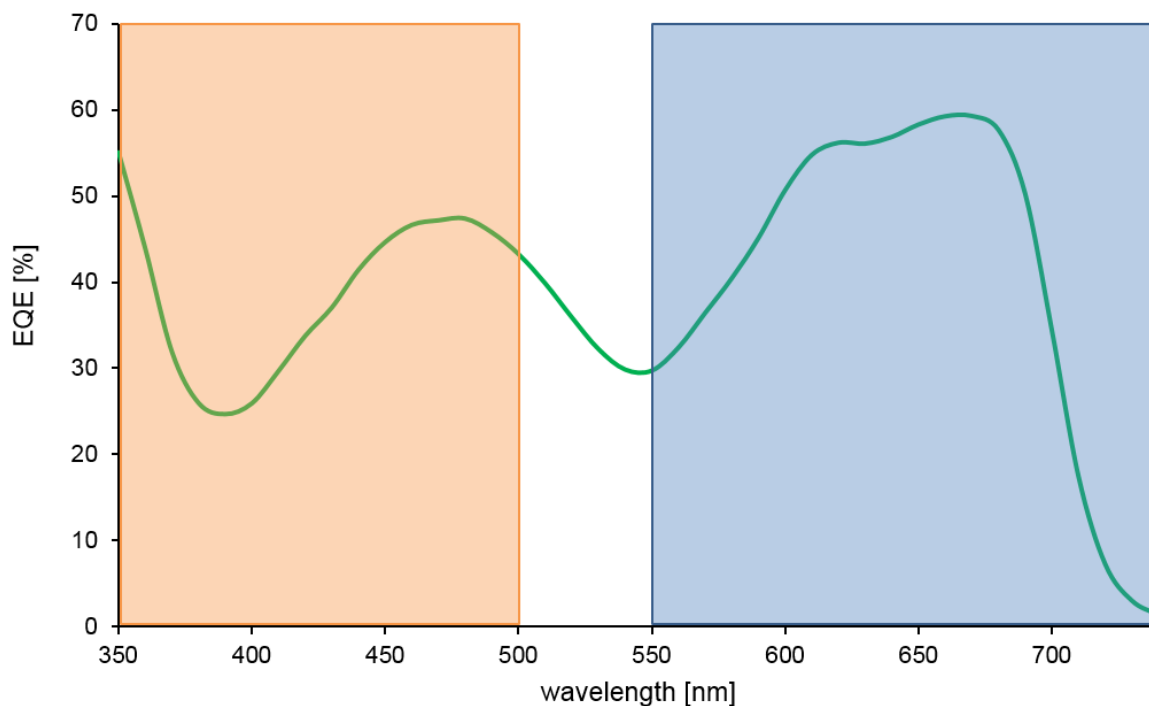


Fig. 141 Transmittance range of the 500 nm short-pass (orange rectangle) and 550 nm long-pass (blue rectangle) filters with respect to the EQE spectrum of the measured co-sensitized DSC.

The 500 nm short-pass filter blocks light with a wavelength longer than 500 nm. The 550 nm long-pass filter blocks light with a wavelength shorter than 550 nm. Additional measurements with a 41% transmittance filter were performed to investigate the performance at reduced light intensities; a 41% transmittance filter was the available filter closest to 50%. For the filter tests, the best-performing **SQ2** cell (dipping time of 4 hours, Table 29) and a co-sensitized DSC assembled by the procedure in *DP D* (Table 30) with 0.0001 mM **SQ2** (Table 36) were used. The measurements were performed by placing the corresponding filters on top of the DSCs. The 500 nm short-pass filter was from THORLABS (25 mm sputtered edgepass filter, short-pass 500 nm), the 550 nm long-pass filter from Reichmann Feinoptik (Farbglasfilter OG 550, long-pass 550 nm) and the 41% transmittance filter from Andover Corporation. The light intensity was measured by placing the filter on top of a fully-masked reference Si photodiode.

Table 39 summarizes the DSC performance data with applied filters. The different irradiances were obtained by placing the respective filters on top of a fully-masked Si reference photodiode. Fig. 142 displays the *J-V* curves of the DSCs without or with the filters.

Table 39 Performance parameters and EQE maxima of a co-sensitized DSC assembled by the dipping procedure D and of a single-dye DSCs containing the dye **SQ2** with a dipping time of 4 hours without a filter, a 550 nm long-pass filter with or without additional 41% transmittance filter and a 500 nm short-pass filter.

dye	filter	irradiance ^a [mW cm ⁻²]	J_{sc} [mA cm ⁻²]	V_{oc} [mV]	ff [%]	η [%]	EQE_{max} [nm, %]
co-sens. DSC	no filter	1000	9.71	552	70	3.75	460, 37.3 660, 42.6
SQ2	no filter	1000	8.37	563	71	3.36	550, 43.2
co-sens. DSC	550	692	4.97	536	72	2.78	670, 41.6
SQ2	550	692	5.07	556	72	2.93	550, 43.9
co-sens. DSC	550/41% light	308	2.12	516	72	2.57	670, 15.7
SQ2	550/41% light	308	2.11	534	73	2.66	570, 15.5
co-sens. DSC	500	83	1.30	468	74	5.46	460, 35.7

a) irradiance values obtained with a fully-masked Si reference cell and the corresponding filters placed on top.

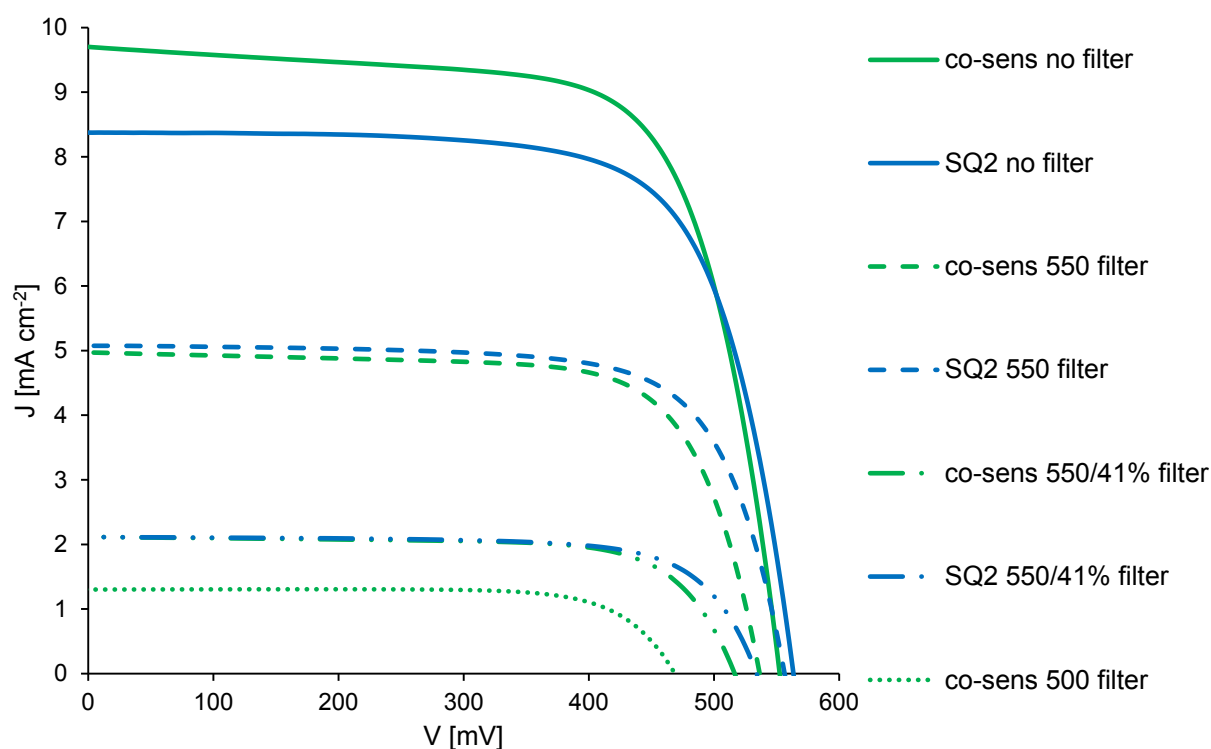


Fig. 142 J - V curves of a co-sensitized DSC and a single-dye **SQ2** DSC without filter, with a 550 nm long-pass filter with and without additional 41% transmittance filter and with a 500 nm short-pass filter.

Both DSCs have a value of $\eta > 3\%$ without a filter (3.75% for the co-sensitized DSC and 3.36% for the single-dye **SQ2** DSC, Table 39). Inspection of Fig. 142 and Table 39 demonstrates that both DSCs have comparable J_{sc} values with a 550 nm long-pass filter (4.97 mA cm⁻² for the co-sensitized DSC and 5.07 mA cm⁻² for the single-dye **SQ2** DSC, Table 39). At reduced light intensity achieved by placing a 41% transmittance filter on top of the 550 nm long-pass filter (Table 39), the same J_{sc} values were observed for the co-sensitized DSC (2.12 mA cm⁻²) and the single-dye **SQ2** DSC (2.11 mA cm⁻²). This demonstrates that a dipping time of 20 minutes with respect to 4 hours for the single-dye DSC are adequate to obtain optimal performance of the **SQ2** dye in the co-sensitized DSC.

The performance of the co-sensitized DSC with a 500 nm short-pass filter shows that the copper(I)-dye performs well under reduced light intensity (Table 39). The impact of the light intensity on the overall efficiency η is presented in Equation 14. The key parameters leading to improved efficiency at lower light intensities are J_{sc} , V_{oc} and ff .

$$\eta = \frac{P_{out}}{P_{in}} = \frac{J_{sc} \cdot V_{oc} \cdot ff}{P_{in}}$$

Equation 14 Definition of the overall efficiency η .

The impact of the light intensity on V_{oc} is observed in the filter measurements. The lower the light intensity, the lower the V_{oc} , consistent with previous investigations.²¹¹⁻²¹⁶ The co-sensitized DSC without a filter has $V_{oc} = 552$ mV (Table 39) which decreases at lower light intensity: at a light intensity of 69.2 mW cm⁻², $V_{oc} = 536$ mV, while at 30.8 mW cm⁻², $V_{oc} = 516$ mV and at 8.3 mW cm⁻² it is 486 mV. This is consistent with the linear relationship between V_{oc} and the logarithm of the light intensity (Fig. 143).²¹¹⁻²¹³

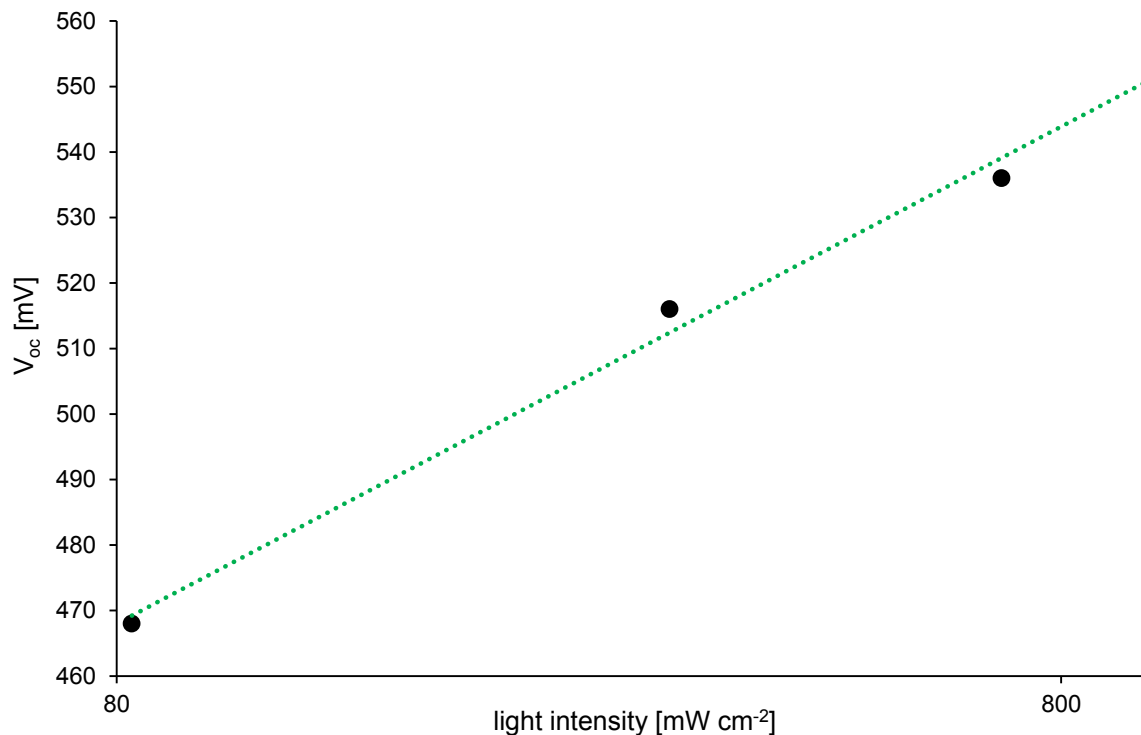


Fig. 143 The dependence of V_{oc} on the light-intensity (plotted on a logarithmic scale). Data are from Table 39.

As a control experiment, the EQE spectra of a single-dye **SQ2** cell with and without a 550 nm long-pass filter were measured and are shown in Fig. 144. Within the transmittance range of the filter, identical EQE responses are obtained in both experiments. The same filter tests were performed with the co-sensitized DSC (Fig. 145).

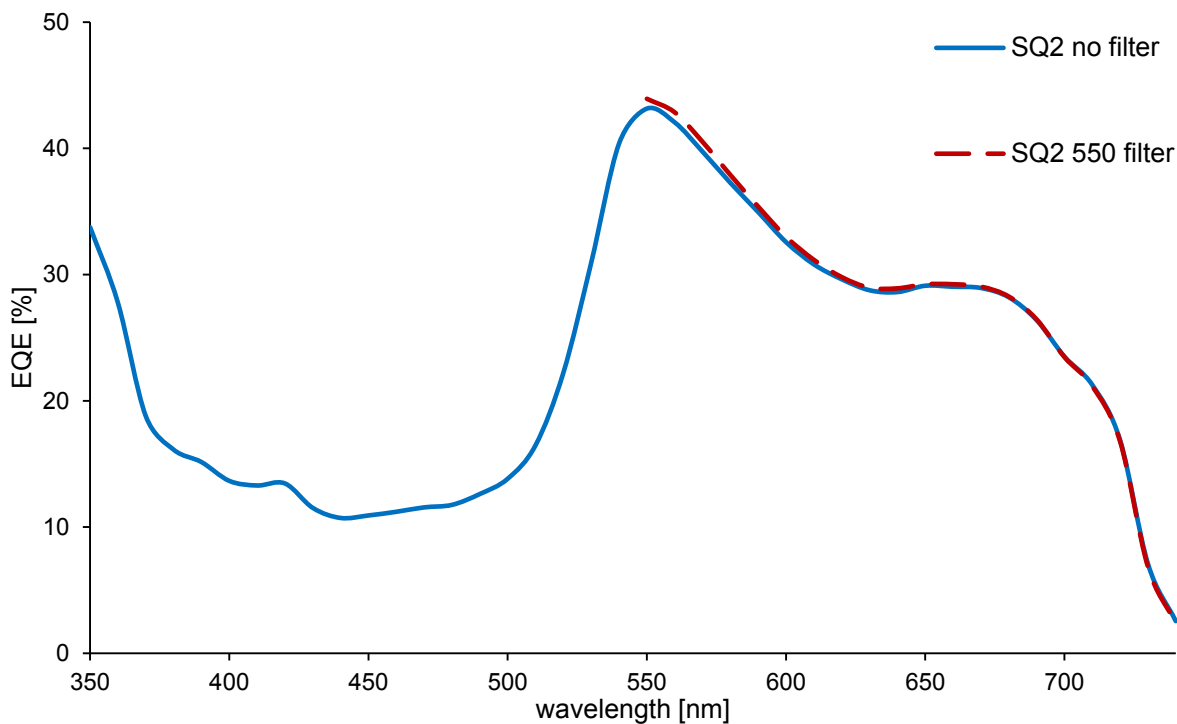


Fig. 144 EQE curve of a single-dye **SQ2** DSC with and without a 550 nm long-pass filter at the transmittance range of the filter.

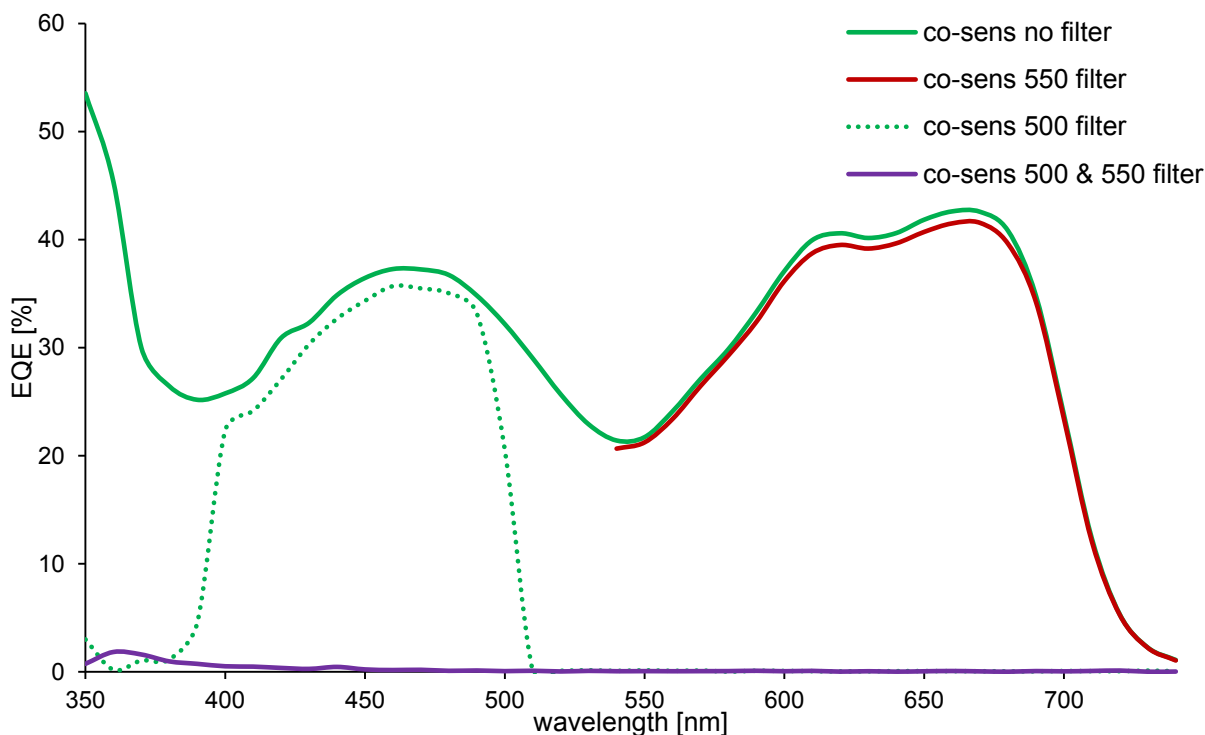


Fig. 145 EQE curve of a co-sensitized DSC without a filter, with a 550 nm long-pass filter at the transmittance range of the filter, with a 500 nm short-pass filter and with both filters.

Firstly, the EQE measurement with a 500 nm short-pass filter resulted in a slightly lower EQE response than without the filter. This is mainly due to the lower number of incident photons. Because of the properties of the filters, an EQE measurement with a reference to the 500 nm short-pass filter was not possible. A measurement with a 550 nm long-pass filter gave a comparable EQE spectrum with respect to that without the filter (Fig. 145). Differences between values of EQE_{max} with and without the filter were $\leq 1\%$. The validation of the measurements was obtained using both the 500 nm short-pass and the 550 nm long-pass filters which gave a negligible EQE response (purple trace in Fig. 145), confirming that there was no background response due to the bias light.

The results of EQE measurements carried out with the filters are consistent with the two dyes operating independently. For efficient electron injection, the lowest unoccupied orbitals (LUMOs) should be localized on the anchoring domain of the dye. DFT calculations for **SQ2** fit to the previously reported²⁰⁰. They show that **SQ2** has a LUMO localized on the anchoring unit (Fig. 146).

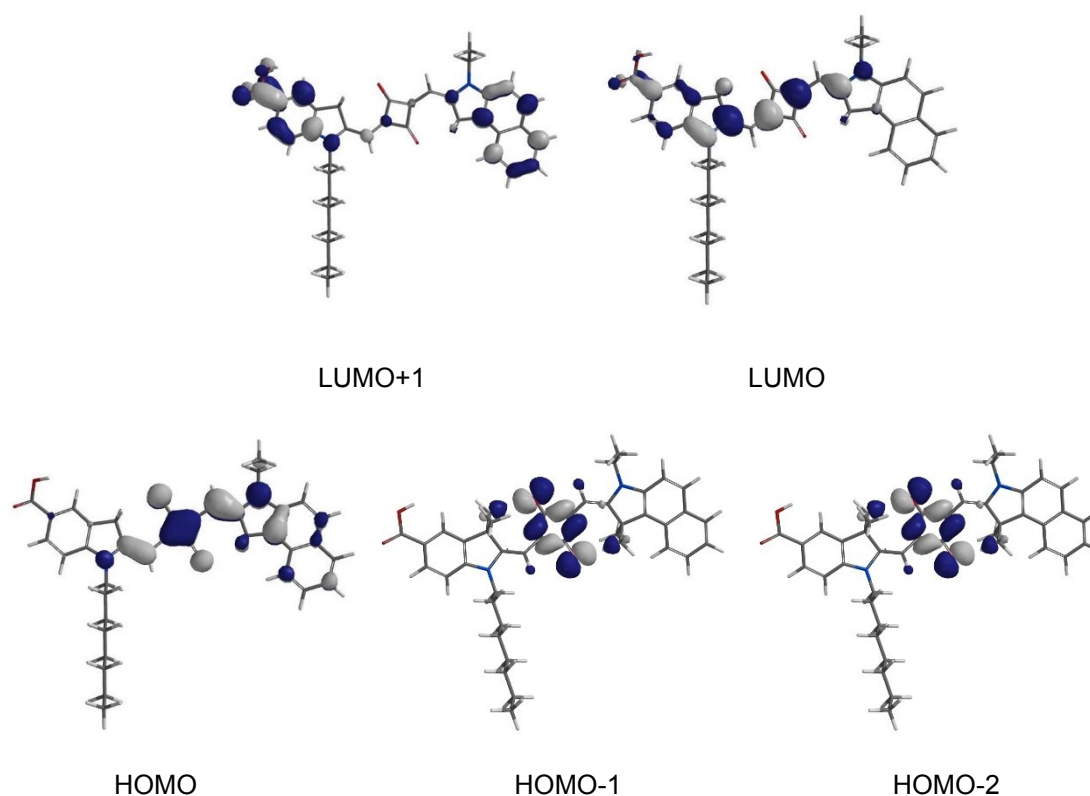


Fig. 146 The frontier molecular orbitals of **SQ2** fully optimized at B3LYP/6-31G* level.

Ground state DFT calculations were carried out on $[\text{Cu}(\text{ALP1})(\text{N}^{\wedge}\text{NS})]^+$ with the geometry optimized at the PM3 level. A 6-31G* basis set on all atoms was chosen, since it was previously demonstrated that the orbital characteristics are basically unaltered by using larger basis sets, even though calculated absorption spectra are significantly influenced.¹³⁴ The highest occupied and lowest unoccupied orbitals of $[\text{Cu}(\text{ALP1})(\text{N}^{\wedge}\text{NS})]^+$ are shown in Fig. 147, and show that the LUMO manifold contains orbitals with significant anchor character. Thus, the orbital characteristics are compatible with both dyes being able to inject electrons in contrast to other investigated co-sensitized DSCs where an electron transfer mechanism may be operative.⁵¹

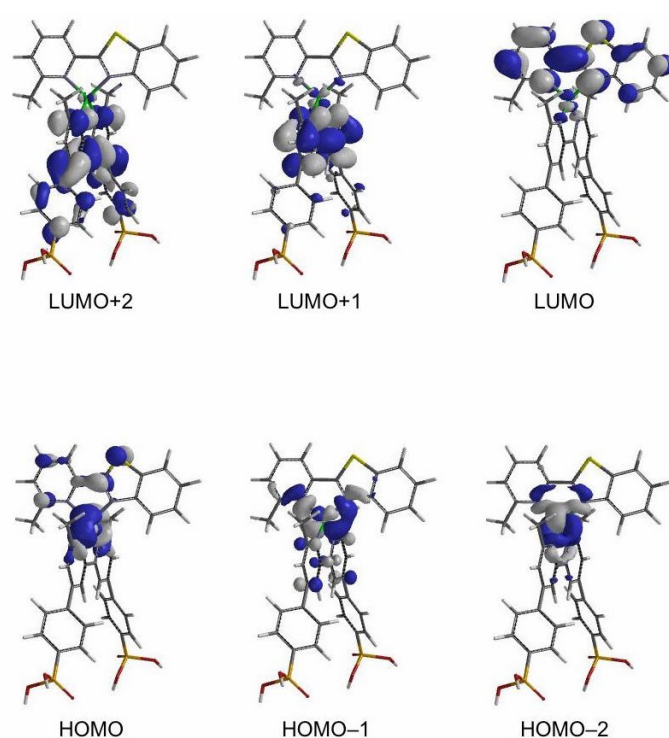


Fig. 147 The frontier molecular orbitals of $[\text{Cu}(\text{ALP1})(\text{N}^{\wedge}\text{NS})]^+$ at B3LYP/6-31G* level (gas phase, ground state) (reprint with permission of Royal Society of Chemistry).

In conclusion, this is the first example of co-sensitization in DSCs using a copper(I)-based sensitizer and a commercially available organic dye. The investigation has shown that the sequences in which the photoanodes of the n-type DSCs are exposed to $[\text{Cu}(\text{ALP1})(\text{N}^{\wedge}\text{NS})]^+$ and **SQ2**, and the times that the electrodes are immersed in the respective dye baths, critically influence the overall performance of the DSCs. Aggregation of the **SQ2** molecules on the electrode surface is important in terms of achieving panchromatic light-harvesting of the

co-sensitized DSCs, but excessive aggregation is detrimental. The results of EQE measurements carried out with different wavelength-range filters are consistent with the two dyes operating independently. By judicious matching of the EQE maxima arising from the heteroleptic copper(I) dye [Cu(ALP1)(N^{NS})]⁺ and from organic dye SQ2 in complementary parts of the visible spectrum, the highest photoconversion efficiency reported for a copper(I)-based DSC (65.6% relative to N719 set at 100%) were achieved.

EXPERIMENTAL PART

18. General Instruments and Methods

Chemicals were purchased from *Acros*, *Alpha Aesar*, *Flourochem*, *Fluka*, *Merck*, *Sigma-Aldrich* and *Solaronix*.

A *Biotage Initiator 8* reactor was used for microwave reactions.

^1H and ^{13}C NMR spectra were recorded at 295 K using a *Bruker Avance III-250*, *400* or *500* NMR spectrometer with chemical shifts referenced to residual solvent peaks with respect to $\delta(\text{TMS}) = 0$ ppm.

Solution and solid state absorption spectra were recorded on an *Agilent Cary 5000* UV-Vis-NIR spectrophotometer.

Electrospray ionization (ESI) mass spectra were recorded on a *Bruker Esquire 3000plus* or a *Shimadzu LCMS-2020* instrument.

MALDI TOF mass spectra were recorded on a *Bruker Daltonics Inc. microflex* instrument.

HR ESI-MS were recorded on a *Bruker maXis 4G* instrument.

Electrochemical measurements were made on a *CH Instruments 900B* potentiostat using glassy carbon, platinum wire and silver wire or a leakless AgCl/Ag^+ electrode (eDAQ ET069) as the working, counter, and reference electrodes, respectively. Samples were dissolved in HPLC grade CH_2Cl_2 (10^{-4} to 10^{-5} mol dm^{-3}) containing 0.1 mol dm^{-3} $[\text{Bu}_4\text{N}][\text{PF}_6]$ as the supporting electrolyte; all solutions were degassed with argon. Fc was used as the internal reference. The scan rate was 0.1 V s^{-1} .

Crystallography Data were collected on either a *Bruker--Nonius KappaAPEX* diffractometer with data collection and data reduction, structure solution and refinement using the programs *APEX2*²¹⁷, *SIR92*²¹⁸ and *CRYSTALS*²¹⁹, or on a *Stoe StadiVari* diffractometer with data collection and data reduction, structure solution and refinement using the programs *X-Area*²²⁰, *Superflip*²²¹ and *CRYSTALS*²¹⁹. Structures were analysed using *Mercury* v. 3.8^{222,223}.

Ground state density functional theory (DFT) calculations were performed using *Spartan 14* (v. 1.1.3) or *Spartan 16* (v. 1.1.1, *Wavefunction Inc.*) at the B3LYP level with a 6-31G* basis set in vacuum. Initial energy optimization was carried out at a semi-empirical (PM3) level.

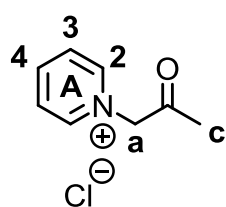
19. Ancillary Ligand Synthesis

19.1. 2,2'-Bipyridine-Based Ligands

$R\text{-L-Br}$ ligands with $R = n\text{-Bu, iso-Bu, n-Hex, Ph}$ and $L\text{-X}$ ligands with $X = F, Cl$ have been synthesized according to literature.^{129,133}

19.1.1. 4,4'-Di-(4-bromophenyl)-6,6'-dimethyl-2,2'-bipyridine (**L-Br**)

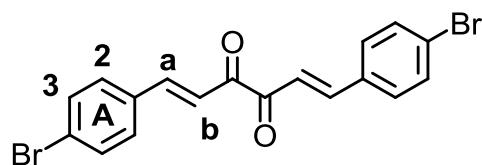
Precursors:



Chloroacetone (25.0 mL, 313 mmol, 1.0 eq.) and pyridine (25.3 mL, 313 mmol, 1.0 eq.) were added to Et₂O (200 mL) and heated to reflux overnight. The reaction mixture was slowly cooled to room temperature over 1 h while stirring. The precipitate was filtered and washed with Et₂O. The

filtrate was concentrated under reduced pressure and cooled in a freezer for several hours. The precipitate was filtered and washed with Et₂O. 1-(2-Oxopropyl)pyridin-1-ium chloride (8.48 g, 49.4 mmol, 15.8%) was isolated as a white crystalline solid.

¹H NMR (400 MHz, CDCl₃) δ / ppm: 9.34 (dd, $J = 6.6, 1.2$ Hz, 2H, H^{A2}), 8.45 (tt, $J = 7.9, 1.3$ Hz, 1H, H^{A4}), 8.03 (dd, $J = 7.6, 6.8$ Hz, 2H, H^{A3}), 6.70 (s, 2H, H^a), 2.50 (s, 3H, H^c).



To a vigorously stirred solution of 4-bromobenzaldehyde (20.0 g, 108 mmol, 2.0 eq.) and piperidine (1.07 mL, 10.8 mmol, 0.2 eq.) in MeOH (100 mL), a solution of 2,3-butanedione (4.72 mL,

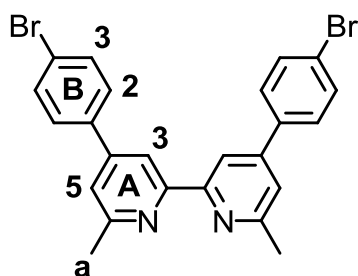
54 mmol, 1.0 eq.) in MeOH (20 mL) was added dropwise using a dropping funnel over 30 min. Then, the dropping funnel was rinsed through with MeOH (30 mL). The reaction mixture was stirred at room temperature for 100 min and heated to reflux overnight. Under stirring, the solution was slowly cooled to room temperature over 1 h. The precipitate was removed by

filtration, washed with Et₂O and dried on airstream. (1*E*,5*E*)-1,6-bis(4-bromophenyl)hexa-1,5-diene-3,4-dione (5.84 g, 13.9 mmol, 25.7%) was isolated as an orange solid.

The ¹H NMR spectrum fits to the literature¹⁰⁰:

¹H NMR (400 MHz, CDCl₃) δ / ppm: 7.81 (d, *J* = 16.2 Hz, 2H, H^a), 7.57 (d, *J* = 8.6 Hz, 4H, H^{A2}), 7.52 (d, *J* = 8.5 Hz, 4H, H^{A3}), 7.49 (d, *J* = 16.2 Hz, 2H, H^b).

Ligand:



Under vigorous stirring 1-(2-oxopropyl)pyridin-1-ium chloride (10.0 g, 58.3 mmol, 2.5 eq.) was solved in EtOH (100 mL). (1*E*,5*E*)-1,6-bis(4-bromophenyl)hexa-1,5-diene-3,4-dione (9.79 g, 23.3 mmol, 1.0 eq.) and ammonium acetate (26.9 g, 350 mmol, 15 eq.) were added. Additional EtOH (100 mL) was added. Then the reaction mixture was heated to reflux overnight. Under stirring

the reaction mixture was cooled to room temperature. Afterwards the precipitate was filtered and washed with cold Et₂O. The precipitate was dried on airstream. The remaining solid was recrystallized in MeOH. 4,4'-Di-(4-bromophenyl)-6,6'-dimethyl-2,2'-bipyridine (**L-Br**, 7.08 g, 14.3 mmol, 61.5%) was isolated as a white solid.

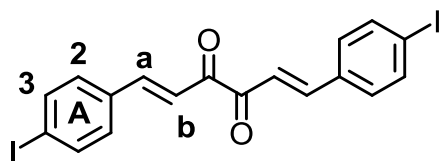
The ¹H NMR spectrum fits to the literature¹⁰⁰:

¹H NMR (400 MHz, CDCl₃) δ / ppm: 8.57 (s, 2H, H^{A3}), 7.73 – 7.57 (overlapping m, 8H, H^{B2+B3}), 7.42 (d, *J* = 0.9 Hz, 2H, H^{A5}), 2.77 (s, 6H, H^a).

19.1.2. 4,4'-Di-(4-iodophenyl)-6,6'-dimethyl-2,2'-bipyridine (**L-I**)

Precursors:

Kröhnke salt see 19.1.1 **L-Br**



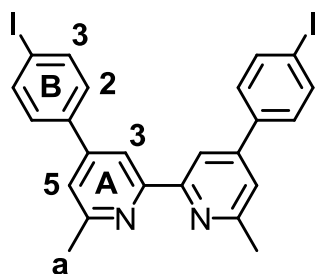
To a vigorously stirred solution of 4-iodobenzaldehyde (3.00 g, 12.9 mmol, 2.0 eq.) and piperidine (0.13 mL, 1.29 mmol, 0.2 eq.) in MeOH (25 mL), a solution of 2,3-butanedione (0.57 mL, 6.46 mmol, 1.0 eq.) in MeOH (8.0 mL) was added dropwise using a dropping funnel over 20 min. Then, the dropping funnel was rinsed through with MeOH (5.0 mL). The reaction mixture was stirred at room temperature over 1 h and heated to reflux overnight. Under stirring, the solution was slowly cooled to room temperature over 1 h and put into the fridge for several minutes. The precipitate was removed by filtration, washed with cold Et₂O and dried under an airstream. The remaining solid was recrystallized in MeOH. (1*E*,5*E*)-1,6-bis(4-iodophenyl)hexa-1,5-diene-3,4-dione (1.02 g, 1.98 mmol, 30.7%) was isolated as a brown solid.

¹H NMR (500 MHz, CDCl₃) δ / ppm: 7.78 (d, *J* = 16.1 Hz, 2H, H^a), 7.78 (d, *J* = 8.4 Hz, 4H, H^{A2}), 7.50 (d, *J* = 16.2 Hz, 2H, H^b), 7.37 (d, *J* = 8.4 Hz, 4H, H^{A3}).

¹³C NMR (126 MHz, CDCl₃) δ / ppm: 188.2 (C^{C=O}), 146.6 (C^a), 138.3 (C^{A2}), 133.7 (C^{A1}), 130.3 (C^{A3}), 119.8 (C^b), 98.1 (C^{A4}).

Found: C, 40.57, H, 2.48; C₁₈H₁₂I₂O₂ · H₂O requires C, 40.63, H, 2.65%.

Ligand:



Under vigorous stirring 1-(2-oxopropyl)pyridin-1-ium chloride (668 mg, 3.89 mmol, 2.5 eq.) was solved in EtOH (10.0 mL). (1*E*,5*E*)-1,6-bis(4-iodophenyl)hexa-1,5-diene-3,4-dione (800 mg, 1.56 mmol, 1.0 eq.) and ammonium acetate (1.80 g, 23.3 mmol, 15 eq.) were added. Additional EtOH (10 mL) was added. Then the reaction mixture was heated to reflux overnight. Under stirring the reaction mixture was cooled to room temperature. Afterwards the precipitate was filtered and washed with cold EtOH and cold Et₂O. The precipitate was dried under an airstream. For purification, the solid was recrystallized in MeOH and afterwards in CHCl₃/Et₂O. A suspension in CHCl₃ was

filtered and 4,4'-di-(4-iodophenyl)-6,6'-dimethyl-2,2'-bipyridine (**L-I**, 93.3 mg, 0.160 mmol, 10.3%) was isolated by column chromatography (SiO₂, 4 x 20 cm, CH₂Cl₂ : EtOAc, 4 : 1) as an off-white solid.

¹H NMR (500 MHz, CDCl₃) δ / ppm: 8.81 (broadened s, 2H, H^{A3}), 7.87 (m, 4H, H^{B3}), 7.66 (m, 4H, H^{B2}), 7.52 (s, 2H, H^{A5}), 2.90 (s, 6H, H^a).

¹³C NMR (126 MHz, CDCl₃) δ / ppm: 158.0 (C^{A6}), 155.3 (C^{A4}), 153.5 (C^{A2}), 138.4 (C^{B3}), 136.2 (C^{B1}), 129.2 (C^{B3}), 122.6 (C^{A5}), 121.9 (C^{B4}), 119.4 (C^{A3}), 23.2 (C^{Me}).

ESI MS *m/z* positive mode 589.2 [M + H]⁺ (calc. 589.0).

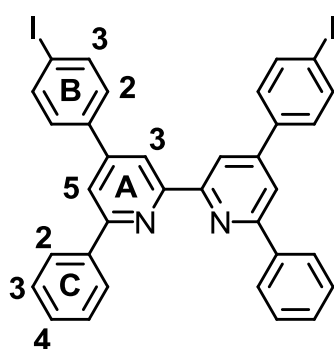
Found: C, 48.87, H, 3.34, N, 4.27; C₂₄H₁₈I₂N₂ requires C, 49.00, H, 3.08, N, 4.76%.

19.1.3. 4,4'-Di-(4-iodophenyl)-6,6'-diphenyl-2,2'-bipyridine (**PhL-I**)

Precursors: commercial available 1-(2-oxo-2-phenyl-ethyl)pyridin-1-ium bromide was used

Diketone see 19.1.2 **L-I**

Ligand:



Under vigorous stirring 1-(2-oxo-2-phenyl-ethyl)pyridin-1-ium bromide (0.814 g, 2.93 mmol, 2.5 eq.) was solved in EtOH (30.0 mL). (1*E*,5*E*)-1,6-bis(4-iodophenyl)hexa-1,5-diene-3,4-dione (0.600 g, 1.17 mmol, 1.0 eq.) and ammonium acetate (1.35 g, 17.6 mmol, 15 eq.) were added. Additional EtOH (10 mL) was added. Then the reaction mixture was heated to reflux. After 3 h, the reaction mixture was filtered and the bittern was heated to reflux

overnight. The precipitate was dried under an airstream. Under stirring the reaction mixture was cooled to room temperature. Afterwards the precipitate was filtered and washed with cold EtOH. The precipitate was dried under an airstream. For purification, both solid were resolved in CH₂Cl₂. By adding EtOH a white precipitate was formed that was filtered and washed with a little CH₂Cl₂ until the bittern was colourless. The solid was dried under vacuum.

4,4'-Di-(4-iodophenyl)-6,6'-diphenyl-2,2'-bipyridine (**^{Ph}L-I**, 194 mg, 0.272 mmol, 23.3%) was isolated as an off-white solid.

¹H NMR (500 MHz, CDCl₃) δ / ppm: 8.81 (d, *J* = 1.6 Hz, 2H, H^{A3}), 8.20 (m, 4H, H^{C2}), 7.96 (d, *J* = 1.4 Hz, 2H, H^{A5}), 7.91 (m, 4H, H^{B3}), 7.58 (m, 4H, H^{B2}), 7.55 (m, 4H, H^{C3}), 7.49 (m, 2H, H^{C4}).

¹³C NMR (126 MHz, CDCl₃) δ / ppm: 157.4 (C^{A6}), 156.1 (C^{A2}), 149.4 (C^{A4}), 139.0 (C^{C1}), 138.2 (C^{B3}), 129.3 (C^{C4}), 129.1 (C^{B1}), 128.9 (C^{B2}), 128.9 (C^{C3}), 127.2 (C^{C2}), 118.6 (C^{A5}), 117.8 (C^{A3}), 95.2 (C^{B4}).

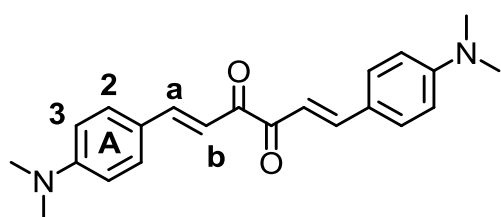
ESI MS *m/z* positive mode 713.3 [M + H]⁺ (calc. 713.0).

Found: C, 55.97, H, 3.20, N, 3.97; C₃₄H₂₂I₂N₂ · H₂O requires C, 55.91, H, 3.31, N, 3.84%.

19.1.4. 4,4'-Di-(4-dimethylaminophenyl)-6,6'-diphenyl-2,2'-bipyridine (**L-NMe₂**)

Precursors:

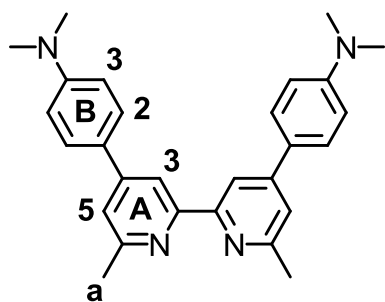
Kröhnke salt see 19.1.1 **L-Br**



To a vigorously stirred solution of 4-dimethylaminobenzaldehyde (5.00 g, 33.2 mmol, 2.0 eq.) and piperidine (0.33 mL, 3.32 mmol, 0.2 eq.) in MeOH (80 mL), a solution of 2,3-butanedione (1.45 mL, 16.6 mmol, 1.0 eq.) in MeOH (10 mL) was added dropwise using a dropping funnel over 30 min. Then, the dropping funnel was rinsed through with MeOH (5 mL). The reaction mixture was stirred at room temperature over 1 h and heated to reflux overnight. Under stirring, the solution was slowly cooled to room temperature over 1 h. The precipitate was removed by filtration, washed with Et₂O and dried on airstream. (1*E*,5*E*)-1,6-bis(4-dimethylaminophenyl)hexa-1,5-diene-3,4-dione (0.458 g, 1.32 mmol, 7.92%) was isolated as an orange solid.

^1H NMR (400 MHz, CDCl_3) δ / ppm: 7.79 (d, $J = 16.0$ Hz, 2H, H^{a}), 7.56 (d, $J = 8.9$ Hz, 4H, H^{A2}), 7.24 (d, $J = 16.3$ Hz, 2H, H^{b}), 6.74 (d, $J = 8.6$ Hz, 4H, H^{A3}), 3.06 (s, 12H, H^{NMe}).

Ligand:



Under vigorous stirring 1-(2-oxopropyl)pyridin-1-ium chloride (369 mg, 2.15 mmol, 2.5 eq.) was solved in EtOH (40 mL).

(1*E*,5*E*)-1,6-bis(4-dimethylaminophenyl)hexa-1,5-diene-3,4-dione (300 mg, 0.861 mmol, 1.0 eq.) and ammonium acetate (995 mg, 12.9 mmol, 15 eq.) were added. Additional EtOH (10 mL) was added. Then the reaction mixture was heated to

reflux overnight. Under stirring the reaction mixture was cooled to room temperature. Afterwards the precipitate was filtered and washed with cold MeOH and cold Et₂O. The precipitate was dried under an airstream. 4,4'-Di-(4-dimethylaminophenyl)-6,6'-dimethyl-2,2'-bipyridine (**L-NMe₂**, 166 mg, 0.393 mmol, 45.6%) was isolated as an off-white solid.

^1H NMR (500 MHz, CDCl_3) δ / ppm: 8.40 (s, 2H, H^{A3}), 7.71 (d, $J = 8.5$ Hz, 4H, H^{B2}), 7.36 (s, 2H, H^{A5}), 6.81 (d, $J = 8.5$ Hz, 4H, H^{B3}), 3.03 (s, 12H, H^{NMe}), 2.69 (s, 6H, H^{a}).

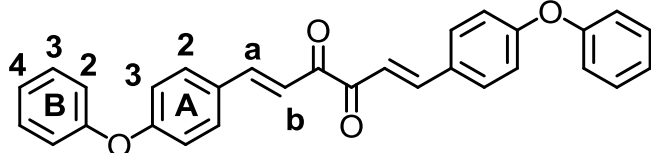
^{13}C NMR (126 MHz, CDCl_3) δ / ppm: 158.1 (C^{A6}), 151.0 (C^{B4}), 127.8 (C^{B2}), 126.0 (C^{A4}), 119.6 (C^{A5}), 115.5 (C^{A3}), 112.6 (C^{B3}), 40.4 (C^{NMe2}), 24.8 (C^{a}).

ESI MS m/z positive mode 423.3 [$\text{M} + \text{H}$]⁺ (calc. 423.3).

19.1.5. 4,4'-Di-(4-phenoxyphenyl)-6,6'-diphenyl-2,2'-bipyridine (**L-OPh**)

Precursors:

Kröhnke salt see 19.1.1 **L-Br**

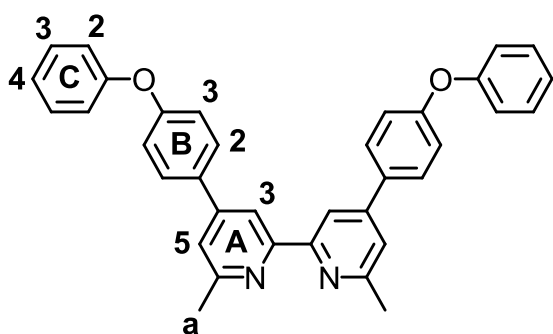


To a vigorously stirred solution of 4-phenoxybenzaldehyde (2.50 mL, 14.3 mmol, 2.0 eq.) and piperidine (0.70 mL, 7.09 mmol, 1.0 eq.) in MeOH

(80 mL), a solution of 2,3-butanedione (0.62 mL, 7.13 mmol, 1.0 eq.) in MeOH (10 mL) was added dropwise using a dropping funnel over 30 min. Then, the dropping funnel was rinsed through with MeOH (5 mL). The reaction mixture was stirred at room temperature over 1 h and heated to reflux overnight. Under stirring, the solution was slowly cooled to room temperature over 1 h. The precipitate was removed by filtration, washed with Et₂O and dried on airstream. (1*E*,5*E*)-1,6-bis(4-phenoxyphenyl)hexa-1,5-diene-3,4-dione (883 mg, 1.98 mmol, 27.7%) was isolated as an orange solid.

¹H NMR (500 MHz, CDCl₃) δ / ppm: 7.83 (d, *J* = 16.2 Hz, 2H, H^a), 7.62 (d, *J* = 8.7 Hz, 4H, H^{A2}), 7.40 (m, 4H, H^{B3}), 7.38 (d, *J* = 16.1 Hz, 2H, H^b), 7.19 (tt, *J* = 7.1, 1.1 Hz, 2H, H^{B4}), 7.09 - 7.04 (m, 4H, H^{B2}), 7.01 (d, *J* = 8.7 Hz, 4H, H^{A3}).

Ligand:



Under vigorous stirring 1-(2-oxopropyl)pyridin-1-ium chloride (384 mg, 2.24 mmol, 2.5 eq.) was solved in EtOH (40 mL). (1*E*,5*E*)-1,6-bis(4-phenoxyphenyl)hexa-1,5-diene-3,4-dione (400 mg, 0.896 mmol, 1.0 eq.) and ammonium acetate (1.04 g, 13.4 mmol, 15 eq.) were added. Additional EtOH (10 mL) was added.

Then the reaction mixture was heated to reflux overnight. Under stirring the reaction mixture was cooled to room temperature. Afterwards the precipitate was filtered and washed with cold MeOH and cold Et₂O. The precipitate was dried under an airstream. 4,4'-Di-(4-phenoxyphenyl)-6,6'-dimethyl-2,2'-bipyridine (**L-OPh**, 161 mg, 0.309 mmol, 34.5%) was isolated as an off-white solid.

^1H NMR (400 MHz, CDCl_3) δ / ppm: 8.46 (s, 2H, $\text{H}^{\text{A}3}$), 7.74 (d, $J = 8.4$ Hz, 4H, $\text{H}^{\text{B}2}$), 7.40 - 7.36 (m, 6H, $\text{H}^{\text{A}5+\text{C}3}$), 7.16 (t, $J = 7.4$ Hz, 2H, $\text{H}^{\text{C}4}$), 7.12 (d, $J = 8.4$ Hz, 4H, $\text{H}^{\text{B}3}$), 7.08 (d, $J = 8.4$ Hz, 4H, $\text{H}^{\text{C}2}$), 2.70 (s, 6H, H^{a}).

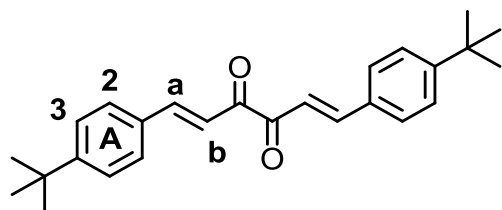
^{13}C NMR (126 MHz, CDCl_3) δ /ppm: 158.9 ($\text{C}^{\text{A}6}$), 158.2 ($\text{C}^{\text{B}4}$), 156.9 ($\text{C}^{\text{C}1}$), 156.4 ($\text{C}^{\text{A}2}$), 148.8 ($\text{C}^{\text{B}1}$), 133.7 ($\text{C}^{\text{A}4}$), 129.9 ($\text{C}^{\text{C}3}$), 128.6 ($\text{C}^{\text{B}2}$), 123.7 ($\text{C}^{\text{C}4}$), 120.7 ($\text{C}^{\text{A}5}$), 119.1 ($\text{C}^{\text{C}2}$), 119.0 ($\text{C}^{\text{B}3}$), 116.3 ($\text{C}^{\text{A}3}$), 24.8 (C^{a}).

ESI MS m/z positive mode 521.2 $[\text{M} + \text{H}]^+$ (calc. 521.2).

19.1.6. 4,4'-Di-(4-*tert*-butylphenyl)-6,6'-diphenyl-2,2'-bipyridine (**L-t-Bu**)

Precursors:

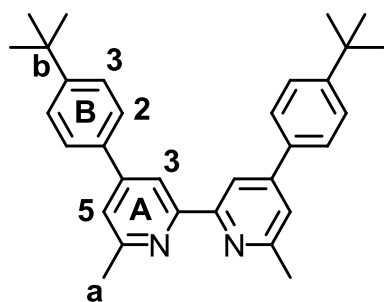
Kröhnke salt see 19.1.1 **L-Br**



To a vigorously stirred solution of 4-*tert*-Butylbenzaldehyde (5.00 mL, 29.0 mmol, 2.0 eq.) and piperidine (0.29 mL, 2.90 mmol, 0.2 eq.) in MeOH (80 mL), a solution of 2,3-butanedione (1.27 mL, 14.5 mmol, 1.0 eq.) in MeOH (10 mL) was added dropwise using a dropping funnel over 30 min. Then, the dropping funnel was rinsed through with MeOH (5 mL). The reaction mixture was stirred at room temperature over 1 h and heated to reflux overnight. Under stirring, the solution was slowly cooled to room temperature over 1 h. The precipitate was removed by filtration, washed with cold MeOH and dried on airstream. (1*E*,5*E*)-1,6-bis(4-*tert*-butylphenyl)hexa-1,5-diene-3,4-dione (782 mg, 2.09 mmol, 14.4%) was isolated as an orange solid.

^1H NMR (400 MHz, CDCl_3) δ / ppm: 7.85 (d, $J = 16.2$ Hz, 2H, H^{a}), 7.60 (d, $J = 8.3$ Hz, 4H, $\text{H}^{\text{A}2}$), 7.45 (d, $J = 8.0$ Hz, 4H, $\text{H}^{\text{A}3}$), 7.44 (d, $J = 16.5$ Hz, 2H, H^{b}), 1.34 (s, 18H, H^{Bu}).

Ligand:



Under vigorous stirring 1-(2-oxopropyl)pyridin-1-ium chloride (575 mg, 3.35 mmol, 2.5 eq.) was solved in EtOH (40 mL). (1*E*,5*E*)-1,6-bis(4-tert-butylphenyl)hexa-1,5-diene-3,4-dione (500 mg, 1.34 mmol, 1.0 eq.) and ammonium acetate (1.55 g, 20.1 mmol, 15 eq.) were added. Additional EtOH (10 mL) was added. Then the reaction mixture was heated to reflux

overnight. Under stirring the reaction mixture was cooled to room temperature. Afterwards the precipitate was filtered and washed with cold MeOH and cold Et₂O. The precipitate was dried under an airstream. 4,4'-Di-(4-tert-butylphenyl)-6,6'-dimethyl-2,2'-bipyridine (**L-t-Bu**, 650 mg, 1.52 mmol, 67.1%) was isolated as an off-white solid.

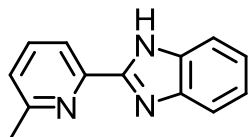
¹H NMR (500 MHz, CDCl₃) δ / ppm: 8.47 (s, 2H, H^{A3}), 7.71 (d, *J* = 8.2 Hz, 4H, H^{B2}), 7.52 (d, *J* = 8.2 Hz, 4H, H^{B3}), 7.39 (s, 2H, H^{A5}), 2.70 (s, 6H, H^a), 1.38 (s, 18H, H^{tBu}).

¹³C NMR (126 MHz, CDCl₃) δ / ppm: 158.2 (C^{A6}), 156.6 (C^{A2}), 152.0 (C^{B4}), 149.3 (C^{A4}), 135.9 (C^{B1}), 126.9 (C^{B2}), 125.8 (C^{B3}), 120.7 (C^{A5}), 116.5 (C^{A3}), 34.7 (C^b), 31.2 (C^{tBu}), 24.7 (C^a).

ESI MS *m/z* positive mode 449.2 [M + H]⁺ (calc. 449.3).

19.2. Heterocyclic N[^]NX Ancillary Ligands

19.2.1. 2-(6-Methylpyridin-2-yl)-1*H*-benzo[*d*]imidazole (N[^]NNH)



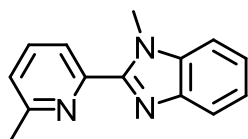
2-(6-Methylpyridin-2-yl)-1*H*-benzo[*d*]imidazole (N[^]NNH) was synthesized adapting the literature procedure.¹²⁶

O-Phenylenediamine (2.25 g, 20.8 mmol, 1.0 eq.) and 6-methyl-picolinic acid (3 g, 20.8 mmol, 1.0 eq.) were dissolved in polyphosphoric acid and stirred at 175 °C for 3 h. The reaction mixture was cooled to room temperature and poured into ice water. After filtration the solid is washed with dilute sodium bicarbonate solution and dried at the high vacuum. 2-(6-Methylpyridin-2-yl)-1*H*-benzo[*d*]imidazole (N[^]NNH, 2.69 g, 12.8 mmol, 61.7%) was isolated as off-white solid.

The ¹H NMR spectrum fits to the literature¹³⁰:

¹H NMR (500 MHz, CDCl₃) δ / ppm: 10.72 (s, 1H), 8.24 (d, *J* = 7.8 Hz, 1H), 7.86 - 7.82 (m, 1H), 7.76 - 7.71 (m, 1H), 7.49-7.45 (m, 1H), 7.31 - 7.26 (m, 2H), 7.22 (d, *J* = 7.7 Hz, 1H), 2.61 (s, 3H).

19.2.2. 1-Methyl-2-(6-methylpyridin-2-yl)-1*H*-benzo[*d*]imidazole (N[^]NNMe)



1-Methyl-2-(6-methylpyridin-2-yl)-1*H*-benzo[*d*]imidazole (N[^]NNMe) was synthesized according to the literature.¹²⁶

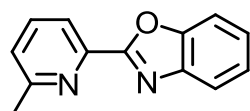
Potassium hydroxide (268 mg, 4.78 mmol, 2.0 eq.) was added to N[^]NNH (500 mg, 2.39 mmol, 1.0 eq.) in dimethylformamide (20 mL) and stirred at room temperature for 20 min. Afterwards, iodomethane (0.149 mL, 2.39 mmol, 1.0 eq.) was added dropwise under vigorous stirring. The reaction mixture was stirred at room temperature for 1 h and at 35 °C overnight. After letting the reaction mixture cool down to room temperature, H₂O and EtOAc were added and the layers were separated. The aqueous layer was extracted with EtOAc (3 x 100 mL) and the combined organic layers were washed with brine (100 mL), dried over Na₂SO₄ and the solvent was removed under reduced pressure. Remaining dimethylformamide

was removed with the help of toluene. The product was dried under high vacuum. **N[^]NNMe** was isolated as a yellow-white solid (502 mg, 2.25 mmol, 94.1%).

The ¹H NMR spectrum fits to the literature²²⁴:

¹H NMR (400 MHz, CDCl₃) δ / ppm: 8.17 (d, *J* = 7.8 Hz, 1H), 7.84 - 7.82 (m, 1H), 7.73 (t, *J* = 7.8, 7.8 Hz, 1H), 7.45 - 7.43 (m, 1H), 7.36-7.28 (m, 2H), 7.21 (d, *J* = 7.7 Hz, 1H), 4.29 (s, 3H), 2.65 (s, 3H).

19.2.3. 2-(6-Methylpyridin-2-yl)benzo[*d*]oxazole (**N[^]NO**)

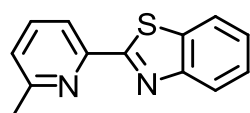


2-(6-Methylpyridin-2-yl)benzo[*d*]oxazole (**N[^]NO**) was synthesized adapting the literature procedure¹²⁵.

A Nitrogen-flushed microwave vial equipped with a magnetic stir bar was charged with benzoxazole (0.500 mL, 4.95 mmol, 1.0 eq.), 6-bromo-2-picoline (1.13 mL, 9.90 mmol, 2.0 eq.), copper(I) iodide (91.3 mg, 0.479 mmol, 0.1 eq.), 1,10-phenanthroline monohydrate (97.3 mg, 0.491 mmol, 0.1 eq.) and tribasic potassium phosphate (2.10 g, 9.90 mmol, 2.0 eq.). Dimethylformamide (7 mL) was added and the microwave vial was sealed. The reaction mixture was heated to 120 °C for 18 h. Afterwards, H₂O and EtOAc were added and the layers were separated. The aqueous layer was extracted with EtOAc (3 x 100 mL) and the combined organic layers were washed with brine (100 mL), dried over Na₂SO₄ and the solvent was removed under reduced pressure. The crude product was purified by column chromatography (SiO₂; cyclohexane : EtOAc 1:2). **N[^]NO** was isolated as a yellow-white solid (454 mg, 2.16 mmol, 43.6%).

The ¹H NMR spectrum fits to the literature¹³¹:

¹H NMR (500 MHz, CDCl₃) δ / ppm: 8.16 (d, *J* = 7.8 Hz, 1H), 7.85 - 7.80 (m, 1H), 7.79 - 7.73 (m, 1H), 7.67 - 7.65 (m, 1H), 7.42 - 7.35 (m, 2H), 7.31 (d, *J* = 7.7 Hz, 1H), 2.72 (s, 3H).

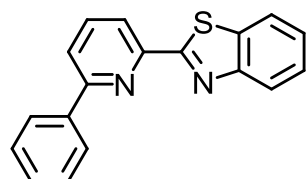
19.2.4. 2-(6-Methylpyridin-2-yl)benzo[d]thiazole (**N[^]NS**)

2-(6-Methylpyridin-2-yl)benzo[d]thiazole (**N[^]NS**) was synthesized adapting the literature procedure¹²⁵.

Benzothiazole (0.3 mL, 2.65 mmol, 1.0 eq.), 2-bromo-6-methylpyridine (0.6 mL, 5.30 mmol, 2.0 eq.), copper(I) iodide (48.9 mg, 0.257 mmol, 0.1 eq.), 1,10-phenanthroline monohydrate (52.1 mg, 0.263 mmol, 0.1 eq.), K₃PO₄ (1.13 g, 5.30 mmol, 2.0 eq.) and dry dimethylformamide (4 mL) were added to a microwave vial, purged with N₂ and heated at 120 °C overnight. Afterwards, H₂O and EtOAc were added and the layers were separated. The aqueous layer was extracted with EtOAc (3 x 50 mL) and the combined organic layers were washed with brine (100 mL), dried over Na₂SO₄ and the solvent was removed under reduced pressure. The crude product was purified by column chromatography (SiO₂; cyclohexane : EtOAc 3:1). **N[^]NS** was isolated as an off-white solid (165 mg, 0.729 mmol, 27.5%).

The ¹H NMR spectrum fits to the literature¹³²:

¹H NMR (400 MHz, CDCl₃) δ / ppm: 8.17 (d, *J* = 7.8 Hz, 1H), 8.09 (ddd, *J* = 8.2, 1.1, 0.6 Hz, 1H), 7.95 (ddd, *J* = 7.9, 1.2, 0.6 Hz, 1H), 7.76 - 7.70 (m, 1H), 7.50 (ddd, *J* = 8.3, 7.2, 1.3 Hz, 1H), 7.41 (ddd, *J* = 8.3, 7.2, 1.2 Hz, 1H), 7.24 (d, *J* = 7.5 Hz, 1H), 2.65 (s, 3H).

19.2.5. 2-(6-Phenylpyridin-2-yl)benzo[d]thiazole (**PhN[^]NS**)

2-(6-Phenylpyridin-2-yl)benzo[d]thiazole (**PhN[^]NS**) was synthesized according to the literature.²²⁵

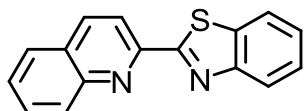
Benzothiazole (0.11 mL, 0.971 mmol, 1.0 eq.), 2-bromo-6-phenylpyridine (455 mg, 1.94 mmol, 2.0 eq.), copper(I) iodide (17.9 mg, 0.094 mmol, 0.1 eq.), 1,10-phenanthroline monohydrate (19.1 mg, 0.096 mmol, 0.1 eq.), K₃PO₄ (412 mg, 1.94 mmol, 2.0 eq.) and dry dimethylformamide (1 mL) were added to a microwave vial, purged with N₂ and heated at 120 °C overnight. Afterwards, H₂O and EtOAc were added and the layers were separated. The aqueous layer was extracted with EtOAc (3 x 50 mL) and the combined organic layers were washed with brine (100 mL), dried over Na₂SO₄ and the solvent was removed under reduced pressure. The crude product was purified by column chromatography (SiO₂;

cyclohexane : EtOAc 6:1), the solvent removed and the residue washed with *n*-pentane. **PhN^{NS}** was isolated as an off-white solid (143 mg, 0.496 mmol, 51.1%).

The ¹H NMR spectrum fits to the literature²²⁵:

¹H NMR (500 MHz, CDCl₃) δ / ppm: 8.31 (dd, *J* = 7.6, 1.0 Hz, 1H), 8.20–8.15 (m, 2H), 8.12 (m, 1H), 7.97 (ddd, *J* = 8.0, 1.1, 0.6 Hz, 1H), 7.92 (m, 1H), 7.85 (dd, *J* = 7.9, 1.0 Hz, 1H), 7.56–7.50 (m, 3H), 7.50–7.45 (m, 1H), 7.43 (ddd, *J* = 8.2, 7.2, 1.2 Hz, 1H).

19.2.6. 2-(Quinolin-2-yl)benzo[*d*]thiazole (**quiN^{NS}**)

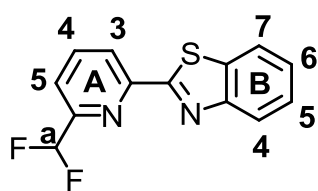


2-(Quinolin-2-yl)benzo[*d*]thiazole (**quiN^{NS}**) was synthesized adapting the literature procedure¹²⁵.

Benzothiazole (0.30 mL, 2.65 mmol, 1.0 eq.), 2-bromoquinoline (404 mg, 1.94 mmol, 2.0 eq.), copper(I) iodide (17.9 mg, 0.094 mmol, 0.1 eq.), 1,10-phenanthroline monohydrate (19.1 mg, 0.096 mmol, 0.1 eq.), K₃PO₄ (412 mg, 1.94 mmol, 2.0 eq.) and dry dimethylformamide (5 mL) were added to a microwave vial, purged with N₂ and heated at 120 °C overnight. Afterwards, H₂O and EtOAc were added and the layers were separated. The aqueous layer was extracted with EtOAc (3 x 50 mL) and the combined organic layers were washed with brine (100 mL), dried over Na₂SO₄ and the solvent was removed under reduced pressure. The crude product was purified by column chromatography (SiO₂; cyclohexane : EtOAc 5:3). All fractions with the product were combined and the solvent removed. The crude product was used for the complexation with [Cu(MeCN)₄][PF₆].

The ¹H NMR spectrum fits to the literature²²⁶:

¹H NMR (400 MHz, CDCl₃) δ / ppm: 8.50 (d, *J* = 8.5 Hz, 1H), 8.31 (d, *J* = 8.5 Hz, 1H), 8.21 (d, *J* = 7.7 Hz, 1H), 8.14 (d, *J* = 8.1 Hz, 1H), 8.00 (d, *J* = 8.1 Hz, 1H), 7.88 (d, *J* = 8.1 Hz, 1H), 7.80 - 7.75 (m, 1H), 7.63–7.57 (m, 1H), 7.55 - 7.49 (m, 1H), 7.48 - 7.42 (m, 1H).

19.2.7. 2-(6-(Difluoromethyl)pyridin-2-yl)benzo[*d*]thiazole ($^{CH_2F_2}N^{\wedge}NS$)

2-(6-(Difluoromethyl)pyridin-2-yl)benzo[*d*]thiazole ($^{CH_2F_2}N^{\wedge}NS$) was synthesized adapting the literature procedure¹²⁵.

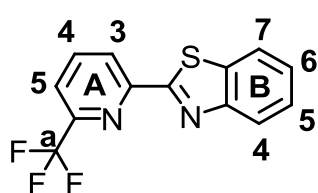
Benzothiazole (0.109 mL, 0.962 mmol, 1.0 eq.), 2-bromo-6-difluoromethylpyridine (0.235 mL, 1.92 mmol, 2.0 eq.), copper(I) iodide (18.3 mg, 0.0962 mmol, 0.1 eq.), 1,10-phenanthroline monohydrate (19.1 mg, 0.0962 mmol, 0.1 eq.), K_3PO_4 (408 mg, 1.92 mmol, 2.0 eq.) and dry dimethylformamide (7 mL) were added to a microwave vial, purged with N_2 and heated at 120 °C overnight. Afterwards, H_2O and EtOAc were added and the layers were separated. The aqueous layer was extracted with EtOAc (3 x 50 mL) and the combined organic layers were washed with brine (100 mL), dried over Na_2SO_4 and the solvent was removed under reduced pressure. The crude product was purified by column chromatography (EtOAc). The solvent was removed and the residue was washed with n-pentane. $^{CH_2F_2}N^{\wedge}NS$ was isolated as a white solid (59 mg, 0.225 mmol, 23.4%).

1H NMR (500 MHz, $CDCl_3$) δ / ppm: 8.48 (dd, $J = 7.9, 1.0$ Hz, Hz, 1H, H^{A3}), 8.11 (ddd, $J = 8.1, 1.1, 0.6$ Hz, 1H, H^{B7}), 8.01 (dd, $J = 7.8, 7.8$ Hz, 1H, H^{A4}), 7.97 (ddd, $J = 7.9, 1.3, 0.7$ Hz, 1H, H^{B4}), 7.74 (dd, $J = 7.7, 1.0$ Hz, 1H, H^{A5}), 7.53 (ddd, $J = 8.3, 7.2, 1.3$ Hz, 1H, H^{B6}), 7.45 (ddd, $J = 8.2, 7.2, 1.2$ Hz, 1H, H^{B5}), 6.73 (t, $J = 55.2$ Hz, 1H, H^a).

^{13}C NMR (126 MHz, $CDCl_3$) δ / ppm: 168.1 (C^{B2}), 154.2 (C^{B7}), 152.9 (C^{A6}), 151.2 (C^{A2}), 138.4 (C^{A4}), 136.3 (C^{B3}), 126.4 (C^{B6}), 126.0 (C^{B5}), 123.8 (C^{B7}), 122.3 (C^{A3}), 122.0 (C^{B4}), 121.4 (C^{A5}), 113.7 (C^a).

^{19}F NMR (471 MHz, $CDCl_3$) δ / ppm: - 117.8 (F^a).

ESI MS m/z positive mode 263.0 $[M + H]^+$ (calc. 263.0).

19.2.8. 2-(6-(Trifluoromethyl)pyridin-2-yl)benzo[*d*]thiazole ($^{CF_3}N^{\wedge}NS$)

2-(6-(Trifluoromethyl)pyridin-2-yl)benzo[*d*]thiazole ($^{CF_3}N^{\wedge}NS$) was synthesized adapting the literature procedure¹²⁵.

Benzothiazole (0.164 mL, 1.5 mmol, 1.0 eq.), 2-bromo-6-trifluoromethylpyridine (678 mg, 3.0 mmol, 2.0 eq.), copper(I) iodide (28.0 mg, 0.15 mmol, 0.1 eq.), 1,10-phenanthroline monohydrate (27.0 mg, 0.15 mmol, 0.1 eq.), K₃PO₄ (637 mg, 3.0 mmol, 2.0 eq.) and dry dimethylformamide (6 mL) were added to a microwave vial, purged with N₂ and heated at 120 °C overnight. Afterwards, H₂O and EtOAc were added and the layers were separated. The aqueous layer was extracted with EtOAc (3 x 50 mL) and the combined organic layers were washed with brine (100 mL), dried over Na₂SO₄ and the solvent was removed under reduced pressure. The crude product was purified by column chromatography (SiO₂; CH₂Cl₂). ^{CF}₃N[^]NS was isolated as a white solid (157 mg, 0.56 mmol, 37.3%).

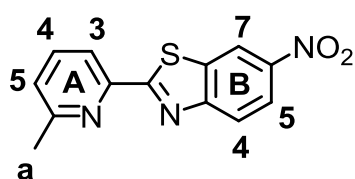
¹H NMR (500 MHz, CDCl₃) δ / ppm: 8.56 (d, *J* = 8.0 Hz, 1H, H^{A3}), 8.11 (d, *J* = 8.2 Hz, 1H, H^{B7}), 8.04 (t, *J* = 7.8 Hz, 1H, H^{A4}), 7.97 (d, *J* = 8.0 Hz, 1H, H^{B4}), 7.76 (d, *J* = 7.7 Hz, 1H, H^{A5}), 7.53 (t, *J* = 7.7 Hz, 1H, H^{B6}), 7.46 (t, *J* = 7.6 Hz, 1H, H^{B5}).

¹³C NMR (126 MHz, CDCl₃) δ / ppm: 154.1 (C^{B7}), 151.9 (C^{A2}), 148.4 (C^{A6}), 138.5 (C^{A4}), 136.5 (C^{B3}), 126.4 (C^{B6}), 126.1 (C^{B5}), 124.0 (C^{B7}), 123.2 (C^{A3}), 122.1 (C^{B4}), 121.6 (C^{A5}).

¹⁹F NMR (471 MHz, CDCl₃) δ / ppm: - 68.1 (F^a).

ESI MS *m/z* positive mode 281.0 [M + H]⁺ (calc. 281.0).

19.2.9. 2-(6-Methylpyridin-2-yl)-6-nitrobenzo[*d*]thiazole (N[^]NS(NO₂))



2-(6-Methylpyridin-2-yl)-6-nitrobenzo[*d*]thiazole (N[^]NS(NO₂)) was synthesized adapting the literature procedure¹²⁵.

6-Nitrobenzothiazole (995 mg, 5.53 mmol, 1.0 eq.), 2-Bromo-6-methylpyridine (1.26 mL, 1.90 g, 1.23 mmol, 2.0 eq.), 1,10-Phenanthroline (106.5 mg, 0.592 mmol, 0.1 eq.), CuI (103.3 mg, 0.544 mmol, 0.1 eq.) and K₃PO₄ (2.49 mg, 11.7 mmol, 2.1 eq.) were dissolved in dry DMF (20 mL) under N₂-atmosphere in a microwave vial. The reaction mixture was heated to 120 °C for 2 d. H₂O was added and the aqueous phase was extracted with EtOAc. The organic phase was washed with brine and dried over Na₂SO₄. It was filtered and dried under reduced pressure. The crude was purified by

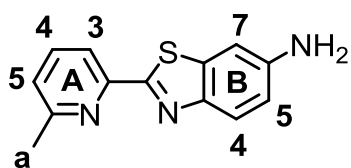
column chromatography (SiO₂; cyclohexane : EtOAc, 3 : 1; a few drops of Et₃N) yielding the pure product (855 mg, 3.15 mmol, 57%) as a pale yellow solid.

¹H NMR (500 MHz, CDCl₃) δ / ppm: 8.88 (d, *J* = 2.3 Hz, 1H, H^{B7}), 8.37 (dd, *J* = 9.0, 2.3 Hz, 1H, H^{B5}), 8.19 (d, *J* = 7.7 Hz, 1H, H^{A3}), 8.15 (d, *J* = 9.0 Hz, 1H, H^{B4}), 7.78 (dd, *J* = 7.7, 7.7 Hz, 1H, H^{A4}), 7.32 (d, *J* = 7.7 Hz, 1H, H^{A5}), 2.67 (s, 3H, H^a).

¹³C NMR (126 MHz, CDCl₃) δ / ppm: 176.1 (C^{A2}), 159.4 (C^{A6}), 158.2 (C^{B6}), 149.9 (C^{B7}), 137.5 (C^{A4}), 136.7 (C^{B2}), 126.2 (C^{A5}), 123.8 (C^{B4}), 121.8 (C^{B5}), 118.7 (C^{B7}), 118.4 (C^{A3}), 24.5 (C^a).

ESI MS *m/z* positive mode 272.1 [M + H]⁺ (calc. 272.0).

19.2.10. 2-(6-Methylpyridin-2-yl)benzo[*d*]thiazole-6-amine (N^ANS(NH₂))



Zinc powder was dissolved in aq. HCl (3 : 1 H₂O : HCl 37%). It was stirred for 20 minutes, filtered and dried under high vacuum. 2-(6-Methylpyridin-2-yl)-6-nitrobenzo[*d*]thiazole (N^ANS(NO₂), 60.0 mg, 0.221 mmol, 1.0 eq.) and the activated Zinc powder

(58.0 mg, 1.16 mmol, 5.2 eq.) were dissolved in dry MeOH (10 mL). Hydrazine monohydrate (0.27 mL, 278 mg, 4.28 mmol, 19 eq.) was added slowly. It was heated to 70 °C and stirred for 3 d. It was extracted with CH₂Cl₂ and the organic phase was washed with brine. The solvent was removed under reduced pressure. The crude was purified by column chromatography (SiO₂; cyclohexane : EtOAc, 1 : 1; a few drops of Et₃N) yielding the pure product (16.4 mg, 0.0681 mmol, 31%) as a pale yellow solid.

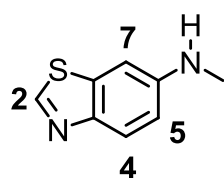
¹H NMR (500 MHz, CDCl₃) δ / ppm: 8.07 (d, *J* = 7.8 Hz, 1H, H^{A3}), 7.84 (d, *J* = 8.7 Hz, 1H, H^{B4}), 7.67 (dd, *J* = 7.8, 7.8 Hz, 1H, H^{A4}), 7.20 - 7.13 (m, 2H, H^{A5+B7}), 6.84 (dd, *J* = 8.7, 2.3 Hz, 1H, H^{B5}), 3.87 (s, 1H, H^{NH2}), 2.62 (s, 1H, H^a).

¹³C NMR (126 MHz, CDCl₃) δ / ppm: 165.9 (C^{A2}), 158.7 (C^{A6}), 151.2 (C^{B2}), 148.0 (C^{B6}), 145.0 (C^{B7}), 138.2 (C^{B3}), 137.1 (C^{A4}), 124.4 (C^{B4}), 124.2 (C^{A5}), 117.4 (C^{A3}), 115.9 (C^{B5}), 106.0 (C^{B7}), 24.5 (C^a).

ESI MS m/z positive mode 242.1 $[M + H]^+$ (calc. 242.1).

19.2.11. *N*-Methyl-2-(6-methylpyridin-2-yl)benzo[*d*]thiazole-6-amine
($N^{\wedge}NS(NHMe)$)

Precursor:



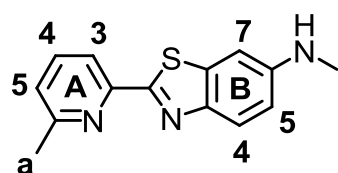
Benzothiazol-6-amine (566 mg, 3.77 mmol, 1.0 eq.) was dissolved in DMF (20 mL) and KOH (880 mg, 15.7 mmol, 4.2 eq.) was added. The reaction mixture was stirred for 1 h at room temperature and heated to 50 °C for 1 h.

It was cooled to room temperature and methyl iodide (0.47 mL, 1.07 g, 7.54 mmol, 2.0 eq.) was added. The reaction mixture was heated to 35 °C and stirred for 5 h. It was allowed to cool to room temperature and H₂O was added. It was extracted with EtOAc and the organic phase was washed with aq. sat. NaCl. It was dried over Na₂SO₄ and filtered. The solvent was removed under reduced pressure and the product was purified by column chromatography (SiO₂; cyclohexane : EtOAc, 2 : 1; a few drops of Et₃N) yielding *N,N*-dimethylbenzothiazol-6-amine (173 mg, 0.971 mmol, 26%) as a yellow solid and *N*-methylbenzothiazol-6-amine (73.9 mg, 0.451 mmol, 12%) as a yellow oil.

The ¹H NMR spectrum fits to the literature²²⁷:

¹H NMR (500 MHz, CDCl₃) δ / ppm: 8.66 (s, 1H, H²), 7.91 - 7.85 (m, 1H, H⁷), 7.04 (d, $J = 2.4$ Hz, 1H, H⁴), 6.82 (dd, $J = 8.8, 2.4$ Hz, 1H, H⁶), 2.91 (s, 3H, H^{NMe}).

Ligand:



N-Methyl-2-(6-methylpyridin-2-yl)benzo[*d*]thiazole-6-amine ($N^{\wedge}NS(NHMe)$) was synthesized adapting the literature procedure¹²⁵.

N-Methylbenzo[*d*]thiazol-6-amine (31.7 mg, 0.193 mmol, 1.0 eq.), 2-Bromo-6-methylpyridine (0.04 mL, 60.4 mg, 0.351 mmol, 1.8 eq.), 1,10-Phenanthroline (6.30 mg, 0.0350 mmol, 0.18 eq.),

CuI (4.70 mg, 0.0247 mmol, 0.13 eq.) and K₃PO₄ (91.4 mg, 0.431 mmol, 2.2 eq.) were dissolved in dry DMF (1.0 mL) under N₂-atmosphere in a microwave vial. The reaction mixture was heated to 120 °C and stirred overnight. H₂O was added and the aqueous phase was extracted with EtOAc. The organic phase was washed with brine and dried over Na₂SO₄. It was filtered and the solvent was removed under reduced pressure. The crude was purified by column chromatography (SiO₂; cyclohexane : EtOAc, 1 : 1; a few drops of Et₃N) yielding the pure product (5.6 mg, 0.0220 mmol, 12%) as a pale yellow solid.

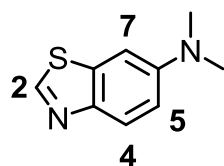
¹H NMR (500 MHz, CDCl₃) δ / ppm: 8.07 (d, *J* = 7.8 Hz, 1H, H^{A3}), 7.84 (d, *J* = 8.8 Hz, 1H, H^{B4}), 7.67 (dd, *J* = 7.7, 7.7 Hz, 1H, H^{A4}), 7.16 (d, *J* = 7.6 Hz, 1H, H^{A5}), 7.03 (d, *J* = 2.4 Hz, 1H, H^{B7}), 6.78 (dd, *J* = 8.8, 2.4 Hz, 1H, H^{B5}), 2.92 (s, 3H, H^{NMe}), 2.63 (s, 3H, H^a).

¹H NMR (126 MHz, CDCl₃) δ / ppm: 164.7 (C^{B2}), 158.6 (C^{A6}), 151.3 (C^{A2}), 147.8 (C^{B6}), 147.0 (C^{B7}), 138.6 (C^{B3}), 136.9 (C^{A4}), 124.1 (C^{A5}), 123.8 (C^{B4}), 117.2 (C^{A3}), 114.5 (C^{B5}), 101.6 (C^{B7}), 30.9 (C^{NMe}), 24.4 (C^a).

ESI MS *m/z* positive mode 256.1 [M + H]⁺ (calc. 256.1).

19.2.12. *N,N*-Dimethyl-2-(6-methylpyridin-2-yl)benzo[*d*]thiazole-6-amine (N[^]NS(NMe₂))

Precursor:



Benzothiazol-6-amine (566 mg, 3.77 mmol, 1.0 eq.) was dissolved in DMF (20 mL) and KOH (880 mg, 15.7 mmol, 4.2 eq.) was added. The reaction mixture was stirred for 1 h at room temperature and heated to 50 °C for 1 h. It was cooled to room temperature and methyl iodide (0.47 mL, 1.07 g, 7.54 mmol, 2.0 eq.) was added. The reaction mixture was heated to 35 °C and stirred for 5 h. It was allowed to cool to room temperature and H₂O was added. It was extracted with EtOAc and the organic phase was washed with aq. sat. NaCl. It was dried over Na₂SO₄ and filtered. The solvent was removed under reduced pressure and the product was purified by column chromatography (SiO₂; cyclohexane : EtOAc, 2 : 1; a few drops of Et₃N) yielding

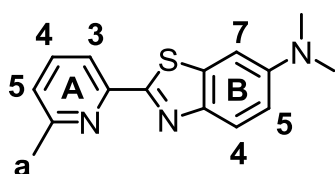
EXPERIMENTAL PART

N,N-dimethylbenzothiazol-6-amine (173 mg, 0.971 mmol, 26%) as a yellow solid and *N*-methylbenzothiazol-6-amine (73.9 mg, 0.451 mmol, 12%) as a yellow oil.

The ^1H NMR spectrum fits to the literature²²⁷:

^1H NMR (500 MHz, CDCl_3) δ / ppm: 8.68 (s, 1H, H^2), 7.95 (d, $J = 9.1$ Hz, 1H, H^7), 7.16 (s, 1H, H^4), 7.01 (d, $J = 9.1$ Hz, 1H, H^6), 3.04 (s, 6H, $\text{H}^{\text{N}(\text{Me})_2}$).

Ligand:



N,N-Dimethyl-2-(6-methylpyridin-2-yl)benzo[*d*]thiazole-6-amine ($\text{N}^{\wedge}\text{NS}(\text{NMe}_2)$) was synthesized adapting the literature procedure¹²⁵.

N,N-Dimethylbenzo[*d*]thiazol-6-amine (111 mg, 0.624 mmol, 1.0 eq.), 2-Bromo-6-methylpyridine (0.14 mL, 211 mg, 1.23 mmol, 2.0 eq.), 1,10-Phenanthroline (11.2 mg, 0.0622 mmol, 0.10 eq.), CuI (15.9 mg, 0.0836 mmol, 0.13 eq.) and K_3PO_4 (286 mg, 1.35 mmol, 2.2 eq.) were dissolved in dry DMF (2.0 mL) under N_2 -atmosphere in a microwave vial. The reaction mixture was heated to 120 °C and stirred overnight. H_2O was added and the aqueous phase was extracted with EtOAc. The organic phase was washed with brine and dried over Na_2SO_4 . It was filtered and dried under reduced pressure. The crude was purified by column chromatography (AlOx; cyclohexane : EtOAc, 5 : 1; a few drops of Et_3N) yielding the product as a pale yellow solid (44.1 mg, 0.164 mmol, 26%).

^1H NMR (500 MHz, CDCl_3) δ / ppm: 8.08 (d, $J = 7.7$ Hz, 1H, $\text{H}^{\text{A}3}$), 7.90 (d, $J = 9.1$ Hz, 1H, $\text{H}^{\text{B}4}$), 7.67 (dd, $J = 7.7, 7.7$ Hz, 1H, $\text{H}^{\text{A}4}$), 7.17 (d, $J = 7.7$ Hz, 1H, $\text{H}^{\text{A}5}$), 7.14 (d, $J = 2.6$ Hz, 1H, $\text{H}^{\text{B}7}$), 6.97 (dd, $J = 9.1, 2.6$ Hz, 1H, $\text{H}^{\text{B}5}$), 3.05 (s, 6H, $\text{H}^{\text{N}(\text{Me})_2}$), 2.63 (s, 3H, H^{a}).

^{13}C NMR (126 MHz, CDCl_3) δ / ppm: 164.9 ($\text{C}^{\text{B}2}$), 158.5 ($\text{C}^{\text{A}6}$), 151.3 ($\text{C}^{\text{A}2}$), 149.0 ($\text{C}^{\text{B}6}$), 146.3 ($\text{C}^{\text{B}7}$), 138.4 ($\text{C}^{\text{B}3}$), 136.9 ($\text{C}^{\text{A}4}$), 124.0 ($\text{C}^{\text{A}5}$), 123.6 ($\text{C}^{\text{B}4}$), 117.2 ($\text{C}^{\text{A}3}$), 113.4 ($\text{C}^{\text{B}5}$), 103.0 ($\text{C}^{\text{B}7}$), 41.0 ($\text{C}^{\text{N}(\text{Me})_2}$), 24.4 (C^{a}).

ESI MS m/z positive mode 270.1 [$\text{M} + \text{H}$] $^+$ (calc. 270.1).

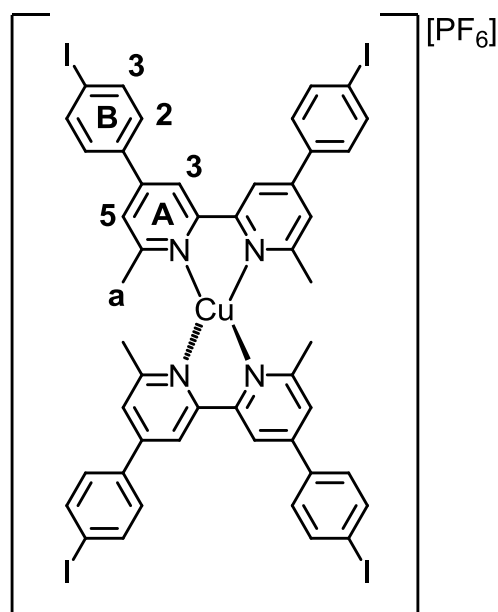
20. Copper(I) Complex Synthesis

The copper(I) source for the copper(I) complex synthesis $[\text{Cu}(\text{MeCN})_4][\text{PF}_6]$ was synthesised according to literature.²²⁸

20.1. 2,2'-Bipyridine-Ligand-Based Complexes

$[\text{Cu}(\text{R-L-Br})_2][\text{PF}_6]$ complexes with R = n-Bu, iso-Bu, n-Hex, Ph and $[\text{Cu}(\text{L-X})_2][\text{PF}_6]$ complexes with X = F, Cl, Br have been synthesized according to literature.^{129,133}

20.1.1. $[\text{Cu}(\text{L-I})_2][\text{PF}_6]$



4,4'-Di-(4-iodophenyl)-6,6'-dimethyl-2,2'-bipyridine (**L-I**, 50 mg, 0.085 mmol, 2.0 eq.) was dissolved in CH_2Cl_2 (16 mL) and MeCN (4 mL) and tetrakis(acetonitrile)copper(I) hexafluorophosphate (15.8 mg, 0.043 mmol, 1.0 eq.) was added under stirring. The reaction mixture was stirred at room temperature for 43 h. Then, CH_2Cl_2 was removed under reduced pressure and MeCN was reduced under reduced pressure to a minimum volume that the product is still in solution. The product was precipitated with Et_2O , filtered off, washed with cold Et_2O and dried on airstream. For purification the

product was dissolved in MeCN. The solution was filtered and the solvent was reduced under reduced pressure to a minimum that the product is still in solution. The product was precipitated with Et_2O , filtered off, washed with cold Et_2O and dried on airstream. Afterwards, the product was dissolved in MeCN and split into 4 vials. Addition of Et_2O resulted in the precipitation of a white solid. The solid was sedimented in each vial and the red solution was decanted carefully. The solution was left to rest over the weekend. In each vial, orange needles occurred and were separated. The isolated orange needles were confirmed by X-ray crystallography to be

[Cu(**L-I**)(MeCN)₂][PF₆]. The remaining red solutions were combined and solvent removed. A mixture of [Cu(**L-I**)(MeCN)₂][PF₆] and [Cu(**L-I**)₂][PF₆] (9.3 mg total mass) was isolated as a dark red solid.

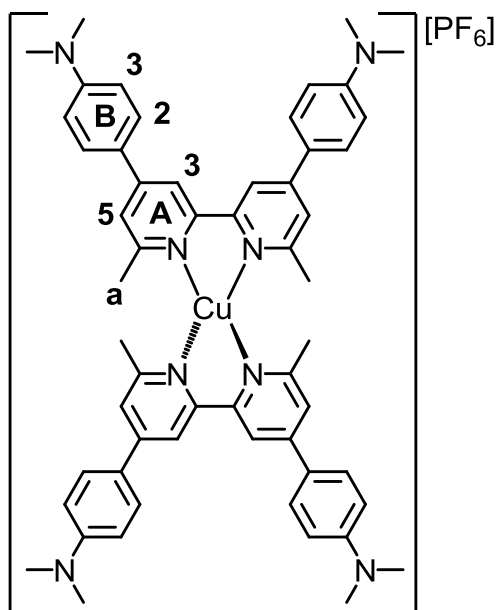
¹H NMR (500 MHz, CD₃CN, 295 K cations in exchange) δ / ppm: 8.61 (broad, H^{A3}), 7.97 (d, *J* = 7.6 Hz, 8H, H^{B3}), 7.85 (broad, H^{A5}), 7.71 (d, *J* = 7.3 Hz, 8H, H^{B2}), 2.52 (v br, FWHM ~145 Hz, H^a).

¹³C NMR (126 MHz, CD₃CN, 295 K cations in exchange) δ / ppm: 150.0 (C^{A4}), 137.6 (C^{B1}), 130.2 (C^{B3}), 130.2 (C^{B2}), 124.5 (C^{A5}), 118.6 (C^{A3}), 96.7 (H^{B4}), signals for C^{A6}, C^{A2} and C^a not resolved.

ESI MS *m/z* positive mode 1239.3 [M - PF₆]⁺ (calc. 1238.8), 692.2 [Cu(**L-I**)(MeCN)]⁺ (calc. 691.9), 589.2 [**L-I** + H]⁺ (calc. 589.0) (base peak); negative mode 144.9 [PF₆]⁻ (calc. 145.0).

For crystals of [Cu(**L-I**)(MeCN)₂][PF₆]: found: C, 38.09, H, 3.02, N, 5.84; C₂₈H₂₄CuF₆I₂N₄P requires C, 38.27, H, 2.75, N, 6.38%.

20.1.2. [Cu(**L-NMe**)₂][PF₆]



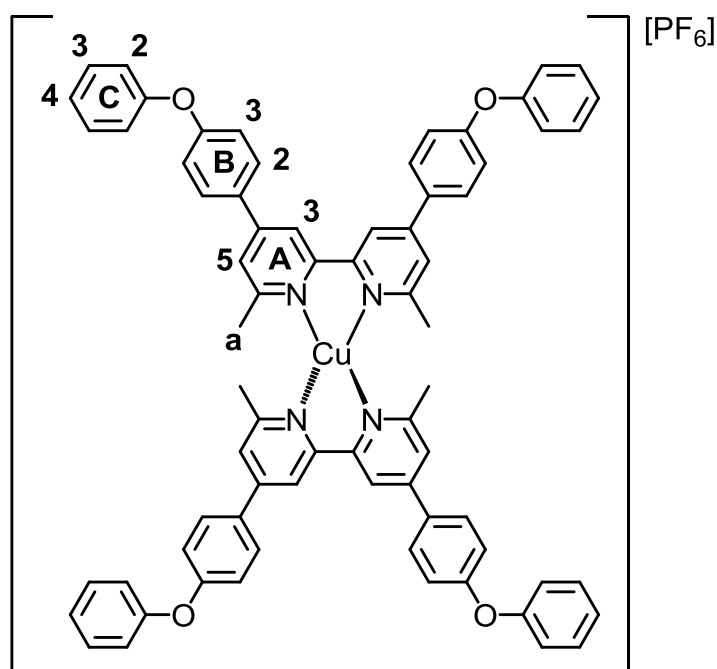
4,4'-Di-(4-dimethylaminophenyl)-6,6'-dimethyl-2,2'-bipyridine (**L-NMe**, 80.0 mg, 0.189 mmol, 2.0 eq.) was dissolved in CH₂Cl₂ (16 mL) and MeCN (8 mL) and tetrakis(acetonitrile)copper(I) hexafluoridophosphate (35.3 mg, 0.0947 mmol, 1.0 eq.) was added under stirring. The reaction mixture was stirred at room temperature overnight. Then, CH₂Cl₂ was removed under reduced pressure and MeCN was reduced under reduced pressure to a minimum volume that the product is still in solution. The product was precipitated with Et₂O, filtered off, washed with cold Et₂O and dried on airstream. [Cu(**L-NMe**)₂][PF₆]

(27.0 mg, 0.0260 mmol, 27.1%) was isolated as a dark red solid.

^1H NMR (400 MHz, CD_3CN) δ / ppm: 8.60 (s, 4H, $\text{H}^{\text{A}3}$), 7.91 (d, $J = 9.0$ Hz, 8H; $\text{H}^{\text{B}2}$), 7.76 (s, 4H, $\text{H}^{\text{A}5}$), 6.93 (d, $J = 9.0$ Hz, 8H, $\text{H}^{\text{B}3}$), 3.07 (s, 24H, H^{NMe}), 2.34 (s, 12H, H^{a}).

ESI MS m/z positive mode 907.4 $[\text{M} - \text{PF}_6]^+$ (calc. 907.4); negative mode 144.9 $[\text{PF}_6]^-$ (calc. 145.0).

20.1.3. $[\text{Cu}(\text{L-OPh})_2][\text{PF}_6]$



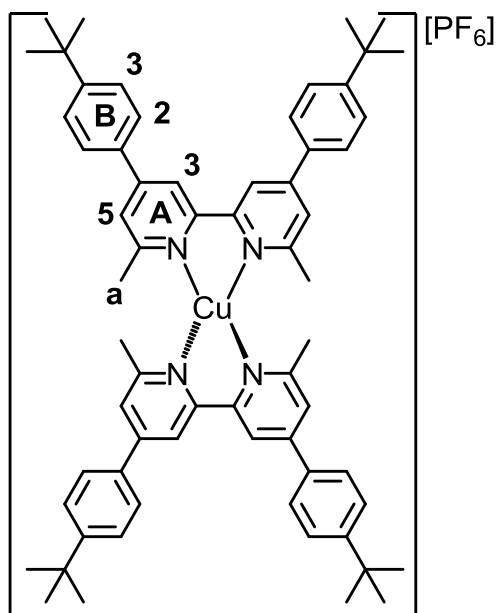
4,4'-Di-(4-diphenoxyphenyl)-6,6'-dimethyl-2,2'-bipyridine (**L-OPh**, 80.0 mg, 0.154 mmol, 2.0 eq.) was dissolved in CH_2Cl_2 (20 mL) and MeCN (10 mL) and tetrakis(acetonitrile)copper(I) hexafluoridophosphate (28.6 mg, 0.0768 mmol, 1.0 eq.) was added under stirring. The reaction mixture was stirred at room temperature overnight. Then, CH_2Cl_2 and MeCN were removed under reduced pressure. $[\text{Cu}(\text{L-OPh})_2][\text{PF}_6]$

(96.2 mg, 0.0770 mmol, 100%) was isolated as a dark red solid.

^1H NMR (500 MHz, CDCl_3) δ / ppm: 8.62 (s, 4H, $\text{H}^{\text{A}3}$), 7.97 (d, $J = 8.1$ Hz, 8H, $\text{H}^{\text{B}2}$), 7.81 (s, 4H, $\text{H}^{\text{A}5}$), 7.45 (t, $J = 7.7$ Hz, 8H, $\text{H}^{\text{C}3}$), 7.23 (t, $J = 7.4$ Hz, 4H, $\text{H}^{\text{C}4}$), 7.18 (d, $J = 8.2$ Hz, 8H, $\text{H}^{\text{B}3}$), 7.12 (d, $J = 8.0$ Hz, 8H, $\text{H}^{\text{C}2}$), 2.41 (s, 12H, H^{a}).

^{13}C NMR (126 MHz, CD_3CN) δ / ppm: 160.3 ($\text{C}^{\text{B}4}$), 157.2 ($\text{C}^{\text{C}1}$), 150.2 ($\text{C}^{\text{A}4}$), 132.6 ($\text{C}^{\text{B}1}$), 131.1 ($\text{C}^{\text{C}3}$), 130.1 ($\text{C}^{\text{B}2}$), 125.2 ($\text{C}^{\text{C}4}$), 124.0 ($\text{C}^{\text{A}5}$), 120.5 ($\text{C}^{\text{C}2}$), 119.7 ($\text{C}^{\text{B}3}$), 118.3 ($\text{C}^{\text{A}3}$).

ESI MS m/z positive mode 1103.3 $[\text{M} - \text{PF}_6]^+$ (calc. 1103.4); negative mode 144.9 $[\text{PF}_6]^-$ (calc. 145.0).

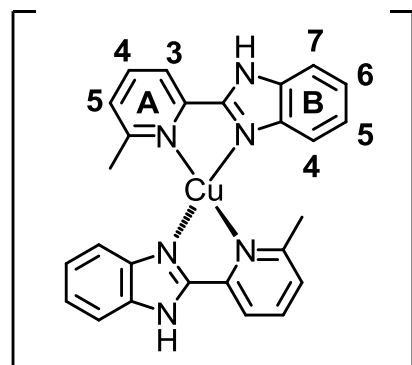
20.1.4. $[\text{Cu}(\text{L-t-Bu})_2][\text{PF}_6]$ 

4,4'-Di-(4-tert-butylphenyl)-6,6'-dimethyl-2,2'-bipyridine (**L-t-Bu**, 100 mg, 0.222 mmol, 2.0 eq.) was dissolved in CH_2Cl_2 (16 mL) and MeCN (8 mL) and tetrakis(acetonitrile)copper(I) hexafluoridophosphate (25.3 mg, 0.111 mmol, 1.0 eq.) was added under stirring. The reaction mixture was stirred at room temperature for 4.5 h. Then, CH_2Cl_2 and MeCN were removed under reduced pressure. $[\text{Cu}(\text{L-t-Bu})_2][\text{PF}_6]$ (121 mg, 0.109 mmol, 98.6%) was isolated as a dark red solid.

^1H NMR (500 MHz, CD_3CN) δ / ppm: 8.69 (s, 4H, $\text{H}^{\text{A}3}$), 7.91 (d, $J = 8.1$ Hz, 8H; $\text{H}^{\text{B}2}$), 7.82 (s, 4H, $\text{H}^{\text{A}5}$), 7.65 (d, $J = 8.0$ Hz, 8H, $\text{H}^{\text{B}3}$), 2.35 (s, 12H, H^{a}), 1.39 (s, 36H, H^{tBu}).

^{13}C NMR (126 MHz, CD_3CN) δ / ppm: 158.5 ($\text{C}^{\text{A}6}$), 154.3 ($\text{C}^{\text{B}4}$), 153.4 ($\text{C}^{\text{A}2}$), 150.8 ($\text{C}^{\text{A}4}$), 135.0 ($\text{C}^{\text{B}1}$), 128.0 ($\text{C}^{\text{B}2}$), 127.1 ($\text{C}^{\text{B}3}$), 124.0 ($\text{C}^{\text{A}5}$), 118.2 ($\text{C}^{\text{A}3}$), 34.7 (C^{b}), 31.2 (C^{tBu}), 25.2 (C^{a}).

ESI MS m/z positive mode 959.6 $[\text{M} - \text{PF}_6]^+$ (calc. 959.5); negative mode 144.9 $[\text{PF}_6]^-$ (calc. 145.0).

20.2. Heterocyclic N[^]NNX Ancillary Ligands-Based Complexes20.2.1. [Cu(N[^]NNH)₂][PF₆]

[PF₆] In a Nitrogen flushed flask, N[^]NNH (100 mg, 0.478 mmol, 2.0 eq.) and [Cu(MeCN)₄][PF₆] (89.1 mg, 0.239 mmol, 1.0 eq.) were stirred in MeCN (5 mL). After 20 min the reaction mixture was filtered with a syringe filter and the solvent was removed in a warm water bath under Nitrogen stream. [Cu(N[^]NNH)₂][PF₆] was isolated as a red solid

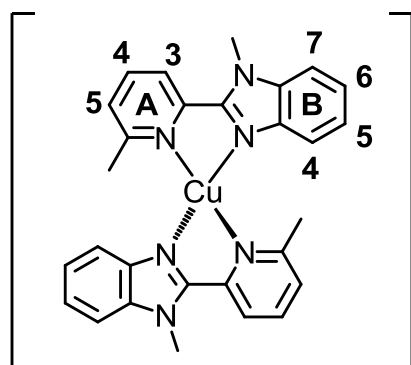
(147 mg, 0.234 mmol, 97.9%). The product is air-sensible and was stored under Argon.

¹H NMR (500 MHz, CD₃CN) δ / ppm: 13.45 (s, 1H, H^{NH}), 8.26 (d, *J* = 8.0 Hz, 1H, H^{A3}), 8.13 (t, *J* = 7.7 Hz, 1H, H^{A4}), 7.70 (d, *J* = 8.0 Hz, 1H, H^{B4/B7}), 7.57 (d, *J* = 7.5 Hz, 1H, H^{A5}), 7.48 (d, *J* = 8.1 Hz, 1H, H^{B4/B7}), 7.35 (t, *J* = 7.5 Hz, 1H, H^{B5/B6}), 7.20 (t, *J* = 7.7 Hz, 1H, H^{B5/B6}), 2.12 (s, 3H, H^{Me}).

¹³C NMR (126 MHz, CD₃CN) δ / ppm: 139.8 (C^{A4}), 127.3 (C^{A5}), 126.0 (C^{B5/B6}), 124.5 (C^{B5/B6}), 119.6 (C^{A3}), 119.3 (C^{B4/B7}), 113.5 (C^{B4/B7}), 24.3 (C^{Me}).

ESI MS *m/z* positive mode 481.1 [M - PF₆]⁺ (calc. 481.1), 240.4 [M - 2PF₆]²⁺ (calc. 240.6); negative mode 144.7 [PF₆]⁻ (calc. 145.0).

HR-ESI MS *m/z* positive mode 481.1198 [M - PF₆]⁺ (calc. 481.1196).

20.2.2. $[\text{Cu}(\text{N}^{\wedge}\text{NNMe})_2][\text{PF}_6]$ 

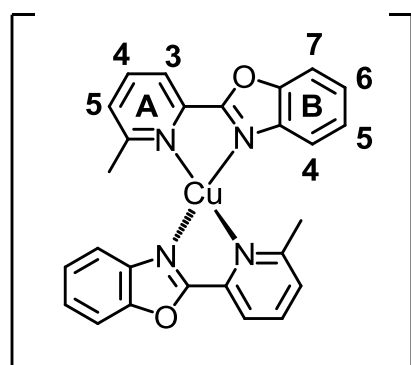
$\text{N}^{\wedge}\text{NNMe}$ (500 mg, 2.24 mmol, 2.0 eq.) and $[\text{Cu}(\text{MeCN})_4][\text{PF}_6]$ (417 mg, 1.12 mmol, 1.0 eq.) were stirred in MeCN (20 mL). After 20 min the reaction mixture was filtered and the solvent was removed under reduced pressure. $[\text{Cu}(\text{N}^{\wedge}\text{NNMe})_2][\text{PF}_6]$ was isolated as a red solid (691 mg, 1.06 mmol, 94.6%).

^1H NMR (500 MHz, CD_3CN) δ / ppm: 8.07 - 8.03 (m, 1H, $\text{H}^{\text{A}4}$), 7.94 - 7.90 (m, 2H, $\text{H}^{\text{B}4/\text{B}7}$), 7.79 - 7.76 (m, 2H, $\text{H}^{\text{B}5/\text{B}6}$), 7.74 (d, $J = 7.8$ Hz, 1H, $\text{H}^{\text{A}3}$), 7.64 (d, $J = 7.9$ Hz, 1H, $\text{H}^{\text{A}5}$), 4.01 (s, 3H, H^{NMe}), 2.68 (s, 3H, H^{Me}).

^{13}C NMR (126 MHz, CD_3CN) δ / ppm: 161.8 ($\text{C}^{\text{A}6}$), 148.6 ($\text{C}^{\text{B}2}$), 141.0 ($\text{C}^{\text{A}2}$), 139.1 ($\text{C}^{\text{A}4}$), 133.0 ($\text{C}^{\text{B}7\text{a}}$), 128.2 ($\text{C}^{\text{B}5/\text{B}6}$), 127.9 ($\text{C}^{\text{A}5}$), 126.2 ($\text{C}^{\text{A}3}$), 114.1 ($\text{C}^{\text{B}4/\text{B}7}$), 32.8 (C^{NMe}), 24.4 (C^{Me}).

ESI MS m/z positive mode 509.1 $[\text{M} - \text{PF}_6]^+$ (calc. 509.1); negative mode 144.9 $[\text{PF}_6]^-$ (calc. 145.0).

HR-ESI MS m/z positive mode 509.1516 $[\text{M} - \text{PF}_6]^+$ (calc. 509.1509).

20.2.3. $[\text{Cu}(\text{N}^{\wedge}\text{NO})_2][\text{PF}_6]$ 

$\text{N}^{\wedge}\text{NO}$ (100 mg, 0.476 mmol, 2.0 eq.) and $[\text{Cu}(\text{MeCN})_4][\text{PF}_6]$ (88.7 mg, 0.238 mmol, 1.0 eq.) were stirred in MeCN (20 mL). After 20 min the reaction mixture was filtered and the solvent was removed under reduced pressure. $[\text{Cu}(\text{N}^{\wedge}\text{NO})_2][\text{PF}_6]$ was isolated as a red solid (150 mg, 0.238 mmol, 100%).

^1H NMR (500 MHz, CD_3CN) δ / ppm: 8.18 (d, $J = 7.6$ Hz, 1H, $\text{H}^{\text{A}3}$), 8.00 - 7.94 (m, 1H, $\text{H}^{\text{A}4}$), 7.82 (d, $J = 8.3$ Hz, 1H, $\text{H}^{\text{B}7}$), 7.79 (d, $J = 9.3$ Hz, 1H, $\text{H}^{\text{B}4}$), 7.55 (d, $J = 7.6$ Hz, 1H, $\text{H}^{\text{A}5}$), 7.53 (ddd, $J = 7.8, 7.6, 1.0$ Hz, 1H, $\text{H}^{\text{B}5}$), 7.47 (ddd, $J = 7.7, 7.5, 1.0$ Hz, 1H, $\text{H}^{\text{B}6}$), 2.66 (s, 3H, H^{Me}).

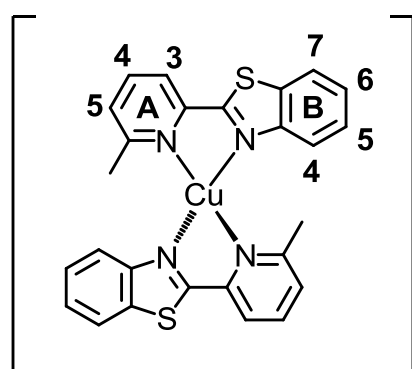
^{13}C NMR (126 MHz, CD_3CN) δ / ppm: 161.5 ($\text{C}^{\text{B}2}$), 160.3 ($\text{C}^{\text{A}6}$), 152.3 ($\text{C}^{\text{B}3\text{a}}$), 144.7 ($\text{C}^{\text{A}2}$), 141.1 ($\text{C}^{\text{B}7\text{a}}$), 139.3 ($\text{C}^{\text{A}4}$), 127.7 ($\text{C}^{\text{A}5}$), 127.6 ($\text{C}^{\text{B}5}$), 126.5 ($\text{C}^{\text{B}6}$), 121.6 ($\text{C}^{\text{A}3}$), 120.9 ($\text{C}^{\text{B}7}$), 112.4 ($\text{C}^{\text{B}4}$), 24.7 (C^{Me}).

ESI MS m/z positive mode 483.1 [$\text{M} - \text{PF}_6$] $^+$ (calc. 483.1); negative mode 144.9 [PF_6] $^-$ (calc. 145.0).

HR-ESI MS m/z positive mode 483.0881 [$\text{M} - \text{PF}_6$] $^+$ (calc. 483.0877).

Found: C, 50.03, H, 3.63, N, 9.22%; $\text{C}_{26}\text{H}_{20}\text{CuF}_6\text{N}_4\text{PO}_2 \cdot 0.25\text{MeCN}$ requires C, 49.79, H, 3.27, N, 9.31%.

20.2.4. $[\text{Cu}(\text{N}^{\wedge}\text{NS})_2][\text{PF}_6]$



$[\text{PF}_6]$ $\text{N}^{\wedge}\text{NS}$ (50.0 mg, 0.221 mmol, 2.0 eq.) and $[\text{Cu}(\text{MeCN})_4][\text{PF}_6]$ (41.0 mg, 0.110 mmol, 1.0 eq.) were stirred in MeCN (20 mL). After 20 min the reaction mixture was filtered and the solvent was removed under reduced pressure. $[\text{Cu}(\text{N}^{\wedge}\text{NS})_2][\text{PF}_6]$ was isolated as a red solid (72.7 mg, 0.110 mmol, 100%).

^1H NMR (500 MHz, CD_3CN) δ / ppm: 8.10 (d, $J = 7.7$ Hz, 1H, $\text{H}^{\text{A}3}$), 8.09 (d, $J = 7.5$ Hz, 1H, $\text{H}^{\text{B}7}$), 8.06 (d, $J = 8.2$ Hz, 1H, $\text{H}^{\text{B}4}$), 7.94 - 7.88 (m, 1H, $\text{H}^{\text{A}4}$), 7.58 (ddd, $J = 8.2, 7.0, 1.2$ Hz, 1H, $\text{H}^{\text{B}5}$), 7.52 (ddd, $J = 8.1, 7.1, 1.1$ Hz, 1H, $\text{H}^{\text{B}6}$), 7.47 (d, $J = 7.7$ Hz, 1H, $\text{H}^{\text{A}5}$), 2.64 (s, 3H, H^{Me}).

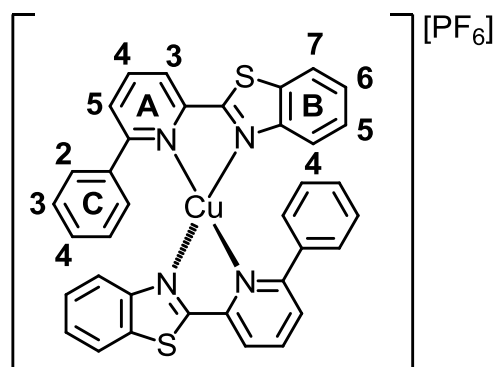
^{13}C NMR (126 MHz, CD_3CN) δ / ppm: 169.8 ($\text{C}^{\text{B}2}$), 160.0 ($\text{C}^{\text{A}6}$), 153.8 ($\text{C}^{\text{B}3\text{a}}$), 150.3 ($\text{C}^{\text{A}2}$), 139.2 ($\text{C}^{\text{A}4}$), 136.5 ($\text{C}^{\text{B}7\text{a}}$), 127.9 ($\text{C}^{\text{B}5}$), 127.3 ($\text{C}^{\text{B}6}$), 127.2 ($\text{C}^{\text{A}5}$), 124.0 ($\text{C}^{\text{B}4}$), 123.5 ($\text{C}^{\text{B}7}$), 119.8 ($\text{C}^{\text{A}3}$), 24.6 (C^{Me}).

ESI MS m/z positive mode 515.1 [$\text{M} - \text{PF}_6$] $^+$ (calc. 515.1); negative mode 144.6 [PF_6] $^-$ (calc. 145.0).

HR-ESI MS m/z positive mode 515.0429 [$\text{M} - \text{PF}_6$] $^+$ (calc. 515.0420).

Found: C, 46.05, H, 3.32, N, 9.23; $C_{26}H_{20}CuF_6N_4PS_2 \cdot H_2O \cdot 0.5MeCN$ requires C, 46.35, H, 3.39, N, 9.01%.

20.2.5. $[Cu(PhN^{\wedge}NS)_2][PF_6]$



$PhN^{\wedge}NS$ (50.0 mg, 0.173 mmol, 2.0 eq.) and $[Cu(MeCN)_4][PF_6]$ (32.3 mg, 0.0867 mmol, 1.0 eq.) were stirred in CH_2Cl_2 (20 mL) and MeCN (10 mL) for 20 min. Then, CH_2Cl_2 was removed under reduced pressure and MeCN was reduced under reduced pressure to a minimum volume with the product still in solution. The product was precipitated with Et_2O ,

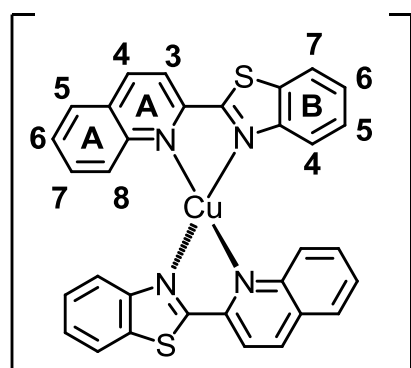
filtered off, washed with cold Et_2O and dried on airstream. $[Cu(PhN^{\wedge}NS)_2][PF_6]$ was isolated as a red solid (68.1 mg, 0.086 mmol, 100%).

1H NMR (500 MHz, acetone- d_6) δ / ppm: 8.35 (d, $J = 8.2$ Hz, 1H, H^{B4}), 8.23 (pseudo-t, $J = 7.8$ Hz, 1H, H^{A4}), 8.19 (d, $J = 7.8$ Hz, 1H, H^{A3}), 7.92 - 7.84 (m, 2H, H^{A5+B7}), 7.67 (ddd, $J = 8.2, 7.1, 1.1$ Hz, 1H, H^{B5}), 7.56 (ddd, $J = 8.2, 7.1, 1.2$ Hz, 1H, H^{B6}), 7.39 (d, $J = 7.5$ Hz, 2H, H^{C2}), 7.10 (t, $J = 7.5$ Hz, 1H, H^{C4}), 6.84 (t, $J = 7.6$ Hz, 2H, H^{C3}).

^{13}C NMR (126 MHz, acetone- d_6) δ / ppm: 168.4 (C^{B2}), 159.6 (C^{A6}), 150.7 (C^{B3}), 149.5 (C^{A2}), 140.3 (C^{A4}), 139.4 (C^{C1}), 136.0 (C^{B7}), 130.3 (C^{C4}), 128.7 (C^{B6}), 128.3 (C^{B5}), 128.2 (C^{C3}), 128.0 (C^{C2}), 127.1 (C^{A5}), 124.0 (C^{B4}), 123.4 (C^{A3}), 123.3 (C^{B7}).

ESI MS m/z positive mode 639.1 $[M - PF_6]^+$ (calc. 639.1); negative mode 144.9 $[PF_6]^-$ (calc. 145.0).

HR-ESI MS m/z positive mode 639.0734 $[M - PF_6]^+$ (calc. 639.0733).

20.2.6. $[\text{Cu}(\text{qu}^{\text{i}}\text{N}^{\wedge}\text{NS})_2][\text{PF}_6]$ 

$[\text{PF}_6]^-$ $\text{qu}^{\text{i}}\text{N}^{\wedge}\text{NS}$ (280 mg, 1.07 mmol, 2.0 eq.) and $[\text{Cu}(\text{MeCN})_4][\text{PF}_6]$ (200 mg, 0.534 mmol, 1.0 eq.) were stirred in CH_2Cl_2 (20 mL) for 20 min. Then, CH_2Cl_2 was reduced under reduced pressure to a minimum volume with the product still in solution. The product was precipitated with Et_2O , filtered off, washed with cold Et_2O and dried on airstream. $[\text{Cu}(\text{qu}^{\text{i}}\text{N}^{\wedge}\text{NS})_2][\text{PF}_6]$

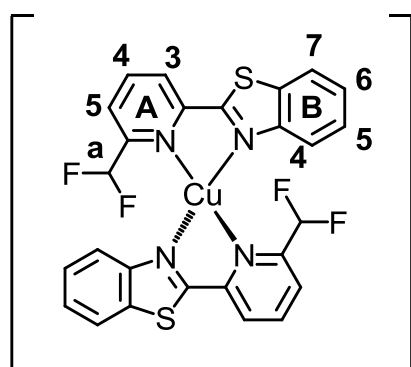
was isolated as a red solid (382 mg, 0.521 mmol, 97.6%).

^1H NMR (500 MHz, acetone- d_6) δ / ppm: 9.02 (d, J = 8.5 Hz, 1H, $\text{H}^{\text{A}4}$), 8.68 (t, J = 8.6 Hz, 1H, $\text{H}^{\text{A}3}$), 8.39 (d, J = 8.2 Hz, 1H, $\text{H}^{\text{B}4}$), 8.23 (d, J = 8.2 Hz, 1H, $\text{H}^{\text{A}5}$), 8.03 (d, J = 8.5 Hz, 1H, $\text{H}^{\text{A}8}$), 7.78 (d, J = 8.3 Hz, 1H, $\text{H}^{\text{B}7}$), 7.70 (t, J = 7.5 Hz, 1H, $\text{H}^{\text{A}6}$), 7.61 (t, J = 7.6 Hz, 1H, $\text{H}^{\text{B}5}$), 7.56 (t, J = 7.8 Hz, 1H, $\text{H}^{\text{A}7}$), 7.43 (t, J = 7.7 Hz, 1H, $\text{H}^{\text{B}6}$).

^{13}C NMR (126 MHz, acetone- d_6) δ / ppm: 151.1 ($\text{C}^{\text{B}7}$), 146.9 ($\text{C}^{\text{A}8}$), 140.8 ($\text{C}^{\text{A}4}$), 133.0 ($\text{C}^{\text{A}7}$), 131.6 ($\text{C}^{\text{A}4}$), 130.0 ($\text{C}^{\text{A}6}$), 129.3 ($\text{C}^{\text{A}5}$), 128.8 ($\text{C}^{\text{A}8}$), 128.7, ($\text{C}^{\text{B}6}$), 125.8 ($\text{C}^{\text{B}5}$), 124.0 ($\text{C}^{\text{B}4}$), 123.4 ($\text{C}^{\text{B}7}$), 121.5 ($\text{C}^{\text{A}3}$).

ESI MS m/z positive mode 587.0 $[\text{M} - \text{PF}_6]^+$ (calc. 587.0); negative mode 144.9 $[\text{PF}_6]^-$ (calc. 145.0).

HR-ESI MS m/z positive mode 587.0421 $[\text{M} - \text{PF}_6]^+$ (calc. 587.0420).

20.2.7. $[\text{Cu}(\text{CHF}_2\text{N}^{\wedge}\text{NS})_2][\text{PF}_6]$ 

$[\text{PF}_6]^-$ $\text{CHF}_2\text{N}^{\wedge}\text{NS}$ (20.0 mg, 0.0762 mmol, 2.0 eq.) and $[\text{Cu}(\text{MeCN})_4][\text{PF}_6]$ (14.2 mg, 0.0381 mmol, 1.0 eq.) were stirred in MeCN (4 mL). After 20 min the reaction mixture was filtered and the solvent was removed under reduced pressure. $[\text{Cu}(\text{CHF}_2\text{N}^{\wedge}\text{NS})_2][\text{PF}_6]$ was isolated as an orange solid (27.9 mg, 0.0381 mmol, 100%).

^1H NMR (500 MHz, CD_3CN) δ / ppm: 8.47 (d, $J = 7.8$ Hz, 1H, $\text{H}^{\text{A}3}$), 8.14 (t, $J = 7.8$ Hz, 1H, $\text{H}^{\text{A}4}$), 8.12 – 8.06 (m, 2H, $\text{H}^{\text{B}4+\text{B}7}$), 7.80 (d, $J = 7.6$ Hz, 1H, $\text{H}^{\text{A}5}$), 7.58 (t, $J = 7.7$ Hz, 1H, $\text{H}^{\text{B}6}$), 7.51 (t, $J = 7.6$ Hz, 1H, $\text{H}^{\text{B}5}$), 6.84 (t, $J_{\text{HF}} = 55.0$ Hz, 1H, H^{a}).

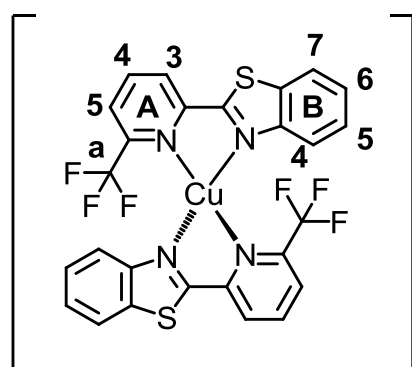
^{13}C NMR (126 MHz, CD_3CN) δ / ppm: 154.9 ($\text{C}^{\text{B}7}$), 153.5 ($\text{C}^{\text{A}6}$), 152.2 ($\text{C}^{\text{A}2}$), 140.2 ($\text{C}^{\text{A}4}$), 136.9 ($\text{C}^{\text{B}3}$), 127.6 ($\text{C}^{\text{B}6}$), 127.2 ($\text{C}^{\text{B}5}$), 124.4 ($\text{C}^{\text{B}4/\text{B}7}$), 123.4 ($\text{C}^{\text{A}3}$), 123.2 ($\text{C}^{\text{B}4/\text{B}7}$), 122.9 ($\text{C}^{\text{A}5}$), 114.4 (C^{a}).

^{19}F NMR (471 MHz, CD_3CN) δ / ppm: -72.7 (d, $J = 707$ Hz, $\text{F}^{\text{PF}6}$), -117.4 (F^{a}).

ESI MS m/z positive mode 587.0 $[\text{M} - \text{PF}_6]^+$ (calc. 587.0); negative mode 144.9 $[\text{PF}_6]^-$ (calc. 145.0).

HR-ESI MS m/z positive mode 587.0051 $[\text{M} - \text{PF}_6]^+$ (calc. 587.0043).

20.2.8. $[\text{Cu}(\text{CF}_3\text{N}^{\wedge}\text{NS})_2][\text{PF}_6]$



$[\text{PF}_6]$ $\text{CF}_3\text{N}^{\wedge}\text{NS}$ (23.3 mg, 0.0832 mmol, 2.0 eq.) and $[\text{Cu}(\text{MeCN})_4][\text{PF}_6]$ (15.5 mg, 0.0416 mmol, 1.0 eq.) were stirred in CH_2Cl_2 (8 mL). After 20 min the reaction mixture was filtered and the solvent was removed under reduced pressure. $[\text{Cu}(\text{CF}_3\text{N}^{\wedge}\text{NS})_2][\text{PF}_6]$ was isolated as a red solid (13.0 mg, 0.0170 mmol, 20.3%).

^1H NMR (500 MHz, CD_3CN) δ / ppm: 8.82 (d, $J = 7.9$ Hz, 1H, $\text{H}^{\text{A}3}$), 8.60 (t, $J = 7.6$ Hz, 1H, $\text{H}^{\text{A}4}$), 8.36 (d, $J = 7.9$ Hz, 1H, $\text{H}^{\text{B}7}$), 8.24 (d, $J = 7.5$ Hz, 1H, $\text{H}^{\text{B}4}$), 8.07 (d, $J = 8.2$ Hz, 1H, $\text{H}^{\text{A}5}$), 7.67 (t, $J = 7.5$ Hz, 1H, $\text{H}^{\text{B}6}$), 7.60 (t, $J = 7.7$ Hz, 1H, $\text{H}^{\text{B}5}$).

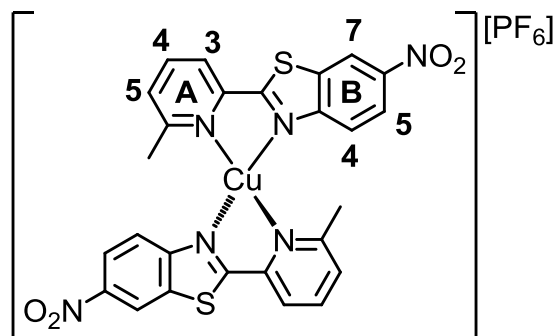
^{13}C NMR (126 MHz, CD_3CN) δ / ppm: 127.8 ($\text{C}^{\text{B}5}$), 127.7 ($\text{C}^{\text{B}6}$), 126.5 ($\text{C}^{\text{A}3}$), 124.1 ($\text{C}^{\text{B}4}$), 123.2 ($\text{C}^{\text{A}5}$), 123.1 ($\text{C}^{\text{B}7}$).

^{19}F NMR (471 MHz, CD_3CN) δ / ppm: -68.7 (F^{a}), -72.7 (d, $J = 707$ Hz, $\text{F}^{\text{PF}6}$).

ESI MS m/z positive mode 623.0 $[\text{M} - \text{PF}_6]^+$ (calc. 623.0); negative mode 145.0 $[\text{PF}_6]^-$ (calc. 145.0).

HR-ESI MS m/z positive mode 622.9859 $[M - PF_6]^+$ (calc. 622.9855).

20.2.9. $[Cu(N^A NS(NO_2))_2][PF_6]$



2-(6-Methylpyridin-2-yl)-6-nitrobenzo[d]thiazole ($N^A NS(NO_2)$, 919 mg, 3.39 mmol, 2.0 eq.) was dissolved in 1 : 1 CH_2Cl_2 : MeCN (200 mL).

Tetrakis(acetonitrile)copper(I) hexafluorophosphate (569 mg, 1.53 mmol, 0.90 eq.) was added. The solution turned dark red.

The reaction mixture was stirred at room temperature overnight. It was precipitated in Et_2O , filtered and dried under air stream yielding the product (684 mg, 0.911 mmol, 54%) as a red powder.

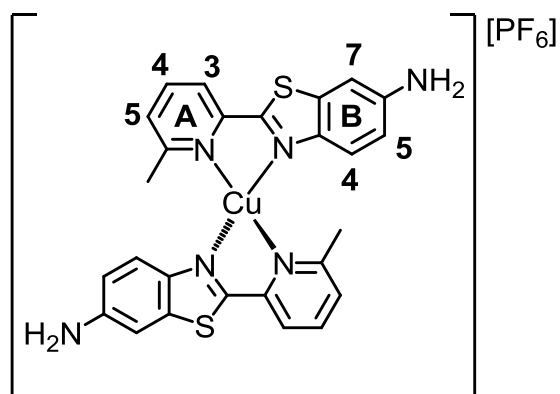
1H NMR (500 MHz, CD_3CN) δ / ppm: 8.97 (d, $J = 2.4$ Hz, 2H, H^{B7}), 8.35 (dd, $J = 9.0, 2.4$ Hz, 2H, H^{B5}), 8.22-8.10 (m, 4H, H^{B4+A3}), 7.88 (dd, $J = 7.7, 7.7$ Hz, 2H, H^{A4}), 7.44 (d, $J = 7.7$ Hz, 2H, H^{A5}), 2.62 (s, 6H, H^a).

^{13}C NMR (126 MHz, acetone- d_6) δ / ppm: 160.3 (C^{A6}), 154.3 ($C^{B3'}$), 148.2 (C^{B2}), 174.3 (C^{B6}), 140.5 (C^{B4}), 129.8 (C^{A5}), 123.8 (C^{A4}), 123.6 (C^{A3}), 123.5 (C^{B5}), 121.0 (C^{B7}), 25.2 (C^a).

ESI MS m/z positive mode 605.0 $[M - PF_6]^+$ (calc. 605.0); negative mode 144.9 $[PF_6]^-$ (calc. 145.0).

HR-ESI MS m/z positive mode 605.0112 $[M - PF_6]^+$ (calc. 605.0121).

20.2.10. $[\text{Cu}(\text{N}^{\wedge}\text{NS}(\text{NH}_2))_2][\text{PF}_6]$



2-(6-Methylpyridin-2-yl)benzothiazol-6-amine ($\text{N}^{\wedge}\text{NS}(\text{NH}_2)$, 15.0 mg, 0.0622 mmol, 2.0 eq.) was dissolved in 1:1 MeCN : CH_2Cl_2 .

Tetrakis(acetonitrile)copper(I) hexafluorophosphate (12.2 mg, 0.0327 mmol, 1.1 eq.) was added and the solution turned red. It was stirred at room temperature for 2 d. The solvent was removed until the product was still in

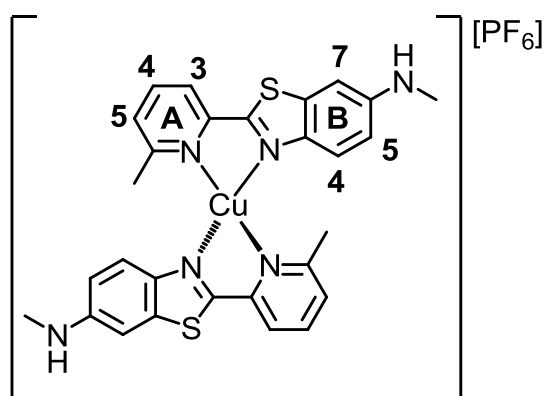
solution and it was precipitated in Et_2O yielding the pure product (20.9 mg, 0.0302 mmol, 97%) as a dark yellow solid.

^1H NMR (500 MHz, CD_3CN) δ / ppm: 8.00 - 7.84 (m, 4H, $\text{H}^{\text{A}3+\text{A}4}$), 7.80 - 7.72 (m, 2H, $\text{H}^{\text{B}4}$), 7.43 (s, 2H, $\text{H}^{\text{A}5}$), 7.20 (s, 2H, $\text{H}^{\text{B}7}$), 6.97 - 6.87 (m, 2H, $\text{H}^{\text{B}5}$), 2.63 (s, 6H, H^{Me}).

ESI MS m/z positive mode 545.1 $[\text{M} - \text{PF}_6]^+$ (calc. 545.1); negative mode 144.9 $[\text{PF}_6]^-$ (calc. 145.0).

HR-ESI MS m/z positive mode 545.0623 $[\text{M} - \text{PF}_6]^+$ (calc. 545.0638).

20.2.11. $[\text{Cu}(\text{N}^{\wedge}\text{NS}(\text{NHMe}))_2][\text{PF}_6]$



N-Methyl-2-(6-methylpyridin-2-yl)benzothiazol-6-amine ($\text{N}^{\wedge}\text{NS}(\text{NHMe})$, 5.6 mg, 0.0220 mmol, 2.0 eq.) was dissolved in 1:1 MeCN : CH_2Cl_2 .

Tetrakis(acetonitrile)copper(I) hexafluorophosphate (4.1 mg, 0.0110 mmol, 1.0 eq.) was added and the solution turned red. It was stirred at room temperature for 3 d. The solvent was removed until the product was still in

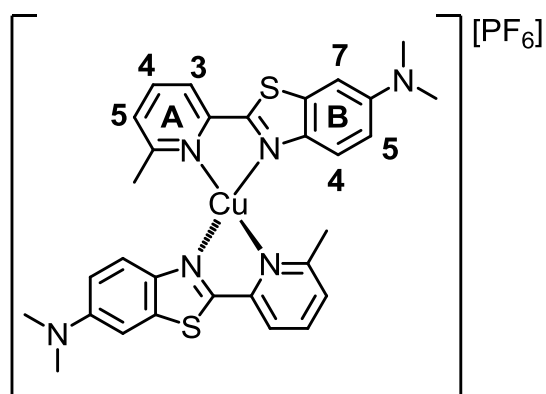
solution and it was precipitated in Et_2O yielding the pure product as a red solid in quantitative yield.

^1H NMR (500 MHz, CD_3CN) δ / ppm: 8.01 - 7.92 (m, 2H, $\text{H}^{\text{A}3}$), 7.89 - 7.80 (m, 2H, $\text{H}^{\text{A}4}$), 7.79 - 7.70 (m, 2H, $\text{H}^{\text{B}4}$), 7.41 - 7.33 (m, 2H, $\text{H}^{\text{A}5}$), 7.09 (s, 2H, $\text{H}^{\text{B}7}$), 6.91 - 6.83 (m, 2H, $\text{H}^{\text{B}5}$), 4.89 (broad s, 2H H^{NH}), 2.84 (s, 6H, H^{NMe}), 2.60 (s, 6H, H^{Me}).

ESI MS m/z positive mode 573.1 $[\text{M} - \text{PF}_6]^+$ (calc. 573.1); negative mode 144.9 $[\text{PF}_6]^-$ (calc. 145.0).

HR-ESI MS m/z positive mode 573.0954 $[\text{M} - \text{PF}_6]^+$ (calc. 573.0951).

20.2.12. $[\text{Cu}(\text{N}^{\wedge}\text{NS}(\text{NMe}_2))_2][\text{PF}_6]$



N,N -Dimethyl-2-(6-methylpyridin-2-yl)benzo[*d*]thiazole-6-amine ($\text{N}^{\wedge}\text{NS}(\text{NMe}_2)$, 34.7 mg, 0.129 mmol, 2.0 eq.) was dissolved in 1:1 CH_2Cl_2 : MeCN . Tetrakis(acetonitrile)copper(I) hexafluorophosphate (26.2 mg, 0.0702 mmol, 1.1 eq.) was added and the reaction mixture turned red. It was stirred at room temperature for 2 d. It was precipitated in Et_2O yielding the product

(40.5 mg, 0.0542 mmol, 84%) as an orange solid.

^1H NMR (500 MHz, CD_3CN) δ / ppm: 8.00 - 7.86 (m, 4H, $\text{H}^{\text{A}3+\text{A}4}$), 7.81 (d, $J = 9.3$ Hz, 2H, $\text{H}^{\text{B}4}$), 7.46 (s, 2H, $\text{H}^{\text{A}5}$), 7.28 (s, 2H, $\text{H}^{\text{B}7}$), 7.07 (d, $J = 9.3$ Hz, 2H, $\text{H}^{\text{B}5}$), 3.05 (s, 12H, H^{NMe_2}), 2.62 (s, 6H, H^{Me}).

^{13}C NMR (126 MHz, CD_3CN) δ / ppm: 159.5 ($\text{C}^{\text{A}5}$), 151.0 ($\text{C}^{\text{B}3'}$), 150.9 ($\text{C}^{\text{B}6}$), 139.4 ($\text{C}^{\text{A}4}$), 138.6 ($\text{C}^{\text{B}7}$), 126.8 ($\text{C}^{\text{A}5}$), 123.9 ($\text{C}^{\text{B}4}$), 120.0 ($\text{C}^{\text{A}3}$), 114.9 ($\text{C}^{\text{B}5}$), 103.7 ($\text{C}^{\text{B}7}$), 40.9 (C^{NMe_2}), 24.9 (C^{Me}).

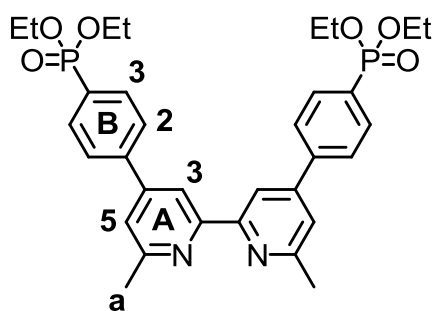
ESI MS m/z positive mode 601.1 $[\text{M} - \text{PF}_6]^+$ (calc. 601.1); negative mode 144.9 $[\text{PF}_6]^-$ (calc. 145.0).

HR-ESI MS m/z positive mode 601.1276 $[\text{M} - \text{PF}_6]^+$ (calc. 601.1264).

21. Anchoring Ligand Synthesis

21.1. ((6,6'-Dimethyl-[2,2'-bipyridine]-4,4'-diyl)-bis(4,1-phenylene))bis(phosphonic acid) (ALP1)

((6,6'-Dimethyl-[2,2'-bipyridine]-4,4'-diyl)-bis(4,1-phenylene))bis(phosphonic acid) (**ALP1**) was synthesized according to literature.¹³³



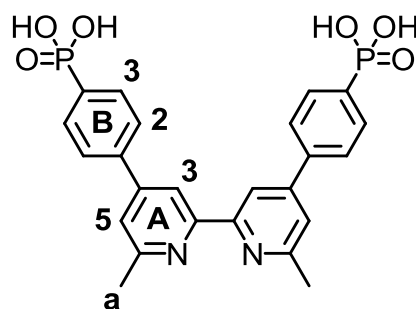
4,4'-Di-(4-bromophenyl)-6,6'-dimethyl-2,2'-bipyridine (**L-Br**, 1.00 g, 2.02 mmol, 1.0 eq.), Pd(PPh₃)₄ (213 mg, 0.182 mmol, 0.1 eq.) and Cs₂CO₃ (1.43 g, 4.39 mmol, 2.2 eq.) were combined in anhydrous THF (15 mL) in a 10 or 20 mL microwave vial equipped with a stirrer bar under argon. Diethylphosphite (1.03 mL, 8.06 mmol, 4.0 eq.) was

added by syringe before the vial was sealed and the reaction mixture heated to 110 °C for 90 min in the microwave. The remaining pressure was reduced carefully with a needle under stirring. Under stirring the reaction mixture was cooled to room temperature. The reaction mixture was filtered and flushed with THF (2 x 10 mL) to give a yellow solution. Then the solvent was evaporated under reduced pressure. The resulting brown residue was dissolved in CH₂Cl₂ (20 mL) and stirred with decolourising charcoal for 30 minutes. The suspension was filtered over celite and flushed with CH₂Cl₂ (100 mL). The solvent was evaporated under reduced pressure to produce an oily bright yellow residue. The residue was dissolved in dry acetone (5.0 mL) what resulted in precipitation of a white solid. The liquid was decanted and the precipitate was dried under reduced pressure. The precipitate was purified by column chromatography (SiO₂, 4 x 11 cm, EtOAc). The liquid was evaporated under reduced pressure. The residue was purified by column chromatography (b-AlOx, 4 x 10 cm, CH₂Cl₂ : EtOAc, 1 : 1). Tetraethyl 4,4'-(6,6'-dimethyl-2,2'-bipyridine-4,4'-diyl)bis(4,1-phenylene)diphosphonate (0.330 g, 0.542 mmol, 26.8%) was isolated as a white solid.

EXPERIMENTAL PART

The ^1H NMR spectrum fits to the literature¹³³:

^1H NMR (400 MHz, CD_3CN) δ / ppm: 8.56 (d, $J = 1.0$ Hz, 2H, $\text{H}^{\text{A}3}$), 8.01 – 7.78 (overlapping m, 8H, $\text{H}^{\text{B}2+\text{B}3}$), 7.58 (d, $J = 1.2$ Hz, 2H, $\text{H}^{\text{A}5}$), 4.24 – 3.86 (m, 8H, $\text{H}^{\text{Et}(\text{CH}_2)}$), 2.67 (s, 6H, H^{a}), 1.30 (t, $J = 7.0$ Hz, 12H, $\text{H}^{\text{Et}(\text{CH}_3)}$).



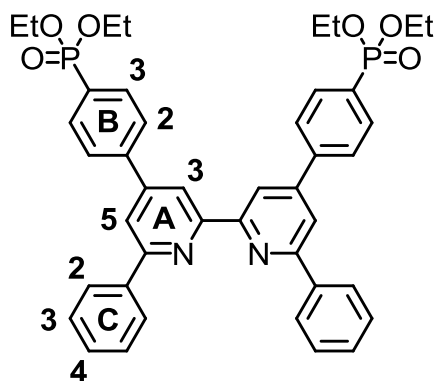
Tetraethyl 4,4'-(6,6'-dimethyl-2,2'-bipyridine-4,4'-diyl)bis(4,1-phenylene)diphosphonate (250 mg, 0.411 mmol, 1.0 eq.) was dissolved in aqueous HCl (6 M, 20 mL) and the solution was heated at reflux for 48 h. The solvent was removed under reduced pressure to leave a pale yellow residue. The residue was treated with AcOH (25 mL) at reflux in the presence of

5 drops of concentrated aqueous HCl for 6 h at 120 °C. Under stirring the reaction mixture was cooled to room temperature. Water (50 mL) was added. This resulted in the precipitation of ((6,6'-Dimethyl-[2,2'-bipyridine]-4,4'-diyl)-bis(4,1-phenylene))bis(phosphonic acid) as a white powder. The solid was dried on high vacuum for 2 d. ((6,6'-Dimethyl-[2,2'-bipyridine]-4,4'-diyl)-bis(4,1-phenylene))bis(phosphonic acid) (**ALP1**, 171 mg, 83.9%) was isolated as a white solid.

The ^1H NMR spectrum fits to the literature¹³³:

^1H NMR (400 MHz, DMSO-d_6) δ / ppm: 11.28 (broad s, 4H, $\text{H}^{-\text{OH}}$), 8.52 (s, 2H, $\text{H}^{\text{A}3}$), 7.95 (dd, $J = 6.8, 1.7$ Hz, 4H, $\text{H}^{\text{B}2}$), 7.85 (dd, $J = 12.0, 7.8$ Hz, 4H, $\text{H}^{\text{B}3}$), 7.72 (s, 2H, $\text{H}^{\text{A}5}$), 2.68 (s, 6H, H^{a}).

21.2. ((6,6'-Diphenyl-[2,2'-bipyridine]-4,4'-diyl)-bis(4,1-phenylene))bis(phosphonic acid) (^{Ph}ALP1)



4,4'-Di-(4-bromophenyl)-6,6'-diphenyl-2,2'-bipyridine (^{Ph}L-Br, 247 mg, 0.399 mmol, 1.0 eq.), [Pd(PPh₃)₄] 138 mg, 0.12 mmol, 0.3 eq.) and Cs₂CO₃ (325 mg, 0.999 mmol, 2.5 eq.) were combined in anhydrous THF (20 mL) in a 10–20 mL microwave vial equipped with a stirrer bar under argon. Diethylphosphite (0.12 g, 0.11 mL, 0.880 mmol, 2.2 eq.) was added by syringe before the vial was sealed and the reaction mixture was heated under microwave irradiation to 110 °C for 150 min. The reaction mixture was filtered to yield a yellow solution prior to evaporation of the solvent under reduced pressure. The resulting yellow residue was then dissolved in CH₂Cl₂ (20 mL) and stirred with decolourising charcoal for 10 min then filtered over celite prior to removal of solvent under reduced pressure to produce an oily yellow residue which crystallized quickly. Upon addition of acetone (20 mL), a white precipitate formed. The white solid was collected by filtration, washed with Et₂O (20 mL) and dried under a stream of air, yielding Tetraethyl 4,4'-(6,6'-diphenyl-2,2'-bipyridine-4,4'-diyl)bis(4,1-phenylene)diphosphonate as a white solid (161 mg, 0.220 mmol, 55.1%).

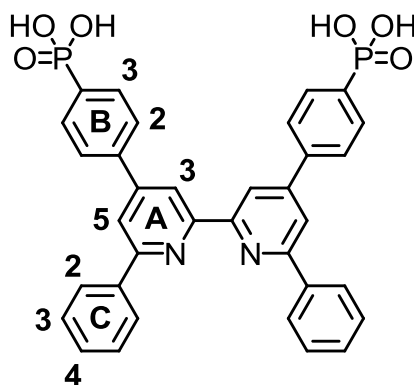
¹H NMR (500 MHz, CDCl₃) δ / ppm: 8.91 (d, *J* = 1.5 Hz, 2H, H^{A3}), 8.22 (m, 4H, H^{C2}), 8.04 (m, 6H, H^{A5+B3}), 7.97 (m, 4H, H^{B2}), 7.57 (m, 4H, H^{C3}), 7.51 (m, 2H, H^{C4}), 4.18 (m, 8H, H^{Et(CH2)}), 1.38 (t, *J* = 7.1 Hz, 12H, H^{Et(CH3)}).

¹³C NMR (126 MHz, CDCl₃) δ / ppm: 157.6 (C^{A6}), 156.0 (C^{A2}), 149.8 (C^{A4}), 142.8 (C^{B1}), 138.8 (C^{C1}), 132.8 (d, *J*_{PC} = 11.0 Hz, C^{B3}), 129.7 (C^{C4}), 129.1 (C^{C3}), 128.6 (C^{B4}), 127.7 (d, *J*_{PC} = 15.5 Hz, C^{B2}), 127.5 (C^{C2}), 119.3 (C^{A5}), 118.8 (C^{A3}), 62.5 (d, *J*_{PC} = 5.5 Hz, C^{Et(CH2)}), 16.6 (d, *J*_{PC} = 6.5 Hz, C^{Et(CH3)}).

ESI MS *m/z* 733.6 [M + H]⁺ (calc. 733.3).

Found: C, 68.83, H, 5.83, N, 3.96; C₄₂H₄₂N₂O₆P₂ requires C, 68.84, H, 5.78, N, 3.82%.

EXPERIMENTAL PART



Tetraethyl 4,4'-(6,6'-diphenyl-2,2'-bipyridine-4,4'-diyl)bis(4,1-phenylene)diphosphonate (121 mg, 0.165 mmol, 1.0 eq.) was dissolved in concentrated aqueous HCl and the solution was heated at reflux for 48 h. Solvent was removed under reduced pressure leaving an off-white residue. This was added to glacial acetic acid (35 mL) and concentrated aqueous HCl (1 mL) and the mixture was heated at reflux for 24 h. After cooling to room temperature and standing for 24 h, a pale

yellow powder precipitated and this was collected by filtration. After washing with water (10 mL), acetone (10 mL) and Et₂O (20 mL), ((6,6'-Diphenyl-[2,2'-bipyridine]-4,4'-diyl)-bis(4,1-phenylene))bis(phosphonic acid) was isolated as off-white solid (**^{Ph}ALP1**, 65.9 mg, 0.108 mmol, 65.5%).

¹H NMR (500 MHz, DMSO-*d*₆) δ / ppm: 8.82 (d, *J* = 1.6 Hz, 2H, H^{A3}), 8.40 (d, *J* = 7.3 Hz, 4H, H^{C2}), 8.38 (d, *J* = 1.7 Hz, 2H, H^{A5}), 8.13 (dd, *J*_{HH} = 8.2 Hz, *J*_{PH} = 3.1 Hz, 4H, H^{B2}), 7.90 (dd, *J*_{PH} = 12.6 Hz, *J*_{HH} = 7.8 Hz, 4H, H^{B3}), 7.60 (t, *J* = 7.6 Hz, 4H, H^{C3}), 7.53 (m, 2H, H^{C4}).

¹³C NMR (126 MHz, DMSO-*d*₆) δ / ppm: 156.6 (C^{A6}), 155.8 (C^{A2}), 149.0 (C^{A4}), 139.9 (C^{B1}), 138.4 (C^{C1}), 135.1 (d, *J*_{PC} = 178 Hz, C^{B4}), 131.4 (C^{B3}), 129.4 (C^{C4}), 128.8 (C^{C3}), 127.1 (C^{B2+C2}), 118.7 (C^{A5}), 117.2 (C^{A3}).

ESI MS *m/z* 621.4 [M + H]⁺ (calc. 621.1).

CONCLUSION
&
OUTLOOK

Photovoltaics play a key role in the energy transition to renewable energy sources and are the only devices that convert the energy of sunlight directly into electricity. Research has to be done in every area of photovoltaics where the systems in place have to be optimized and new generations have to be developed. This thesis shows the exciting potential of copper(I) dye-sensitized solar cells and the development of strategies to improve the economical part of the fabrication of solar cells, to regenerate destroyed dye and to boost copper(I)-based DSC performance to the next level.

After it has been shown that bpy-based ancillary ligands with phenyl substituents in the 6,6'-positions and iodo as peripheral halogen in the 4,4'-positions give the highest photoconversion efficiency in their series of different alkyl- and aryl-substituents or peripheral halogens, the combination of both lead to the **^{Ph}L-I** ancillary ligand. Another dye-assembly process than the general ligand-exchange dye-assembly process has to be used because the homoleptic copper(I) complex cannot be isolated. The new 1:1 dye-assembly process is developed especially for cases like this. One step in the synthesis is not needed and the excess of ancillary ligand is minimized what improves the total economical part of the fabrication of the device. However, it has to be noted that the dye-assembly process has to be adjusted to the ligand combination in order to achieve the highest possible performance. The introduction of the co-adsorbent **Cheno** to the copper(I) dye [Cu(**ALP1**)(**L-I**)]⁺ does not improve the photoconversion efficiency. The addition of **Cheno** to the anchoring ligand solution has an unfavourable effect, resulting in lower J_{sc} values and overall efficiencies. Similar parameters to those without co-adsorbent are observed when **Cheno** is added to the ancillary ligand solution in the 1:1 dye-assembly process. For some ligand combinations in copper(I) dyes a destruction of the dye under exposure to the I⁻/I₃⁻ electrolyte is observed. The dye is readily regenerated by dipping the electrode into a [Cu(MeCN)₄][PF₆]-solution and an ancillary ligand solution. This could improve the lifetime of the device. The investigations of additional 2,2'-bipyridine-based ancillary ligands with different functional groups resulted in no further improvement of the cell performance and showed the absolute necessity of a new family of ancillary ligands. The new families are the **N[^]N^X** ancillary ligands. The investigations of the influence of the heteroatom resulted in DSCs with comparable photoconversion performance to the best-performing bpy-based ancillary ligands. These simple unmodified ligands surpass the threshold values for bpy-based ancillary ligands. Initial optimizations of the **N[^]NS** ligand lead to the copper(I) dye [Cu(**ALP1**)(^{CHF₂}**N[^]NS**)]⁺, which

is the best-performing single-dye copper(I) DSC with an overall efficiency of 3.20% with respect to 7.55% for **N719**. Co-sensitization of the dyes $[\text{Cu}(\text{ALP1})(\text{N}^{\wedge}\text{NNH})]^+$ and $[\text{Cu}(\text{ALP1})(\text{N}^{\wedge}\text{NS})]^+$ showed that the dipping procedure is important in order to achieve an impact of both dyes. This is the first time that co-sensitization including a copper(I) dye has been examined and is an important development as it opens the way to a strategy for harvesting the full solar energy spectrum without the need for designing new panchromatic complexes.

The new families of $\text{N}^{\wedge}\text{NX}$ ancillary ligands lead to panchromatic light harvesting. Pre-tests with the ruthenium dye **N719** show that the anchoring of a phosphonic acid- and a carboxylic acid anchoring group can take place simultaneously on the semiconductor surface. The order of the dipping steps and the dipping time have an impact on the anchoring as well as on the influence of both dyes on the performance of the DSC. These results are taken into account for the investigations of panchromatic co-sensitized copper(I) dye-sensitized solar cells. This is the first example of co-sensitization in DSCs using a copper(I)-based dye and a commercial available organic dye. **SQ2** has a complementary absorption range with respect to $[\text{Cu}(\text{ALP1})(\text{N}^{\wedge}\text{NS})]^+$ and by judicious matching of the EQE maxima of both dyes by tuning the order of the dipping steps, the dipping time and the dye-bath concentration panchromatic light-harvesting is achieved. The optimum dipping procedure leads to a DSC with the highest photoconversion efficiency reported for copper(I)-based DSCs (65.6% relative to **N719** set to 100%).

The new families of $\text{N}^{\wedge}\text{NX}$ ancillary ligands and the co-sensitization with **SQ2** increase the photoconversion efficiency from around 2% to 4.5%. New strategies could improve the economical part of the fabrication of the solar cells or the lifetime of the device. These results confirm the exciting potential of low-cost Earth-abundant dye-sensitized solar cells. Therefore, the investigations of all parts of the DSC have to be combined in order to improve the photoconversion efficiency of copper(I) DSCs. Optimized iodine-based²²⁹, cobalt-based¹⁰⁶ or new copper-based electrolytes²³⁰ have to be combined with the best performing copper(I) dyes. Co-sensitization should become a standard test for all new copper(I) dyes and the tuning of the semiconductor as well as the counter electrode has to be taken into account. The boost in photoconversion efficiency in this thesis is extremely promising and shows that even greater improvement in the performance of copper(I)-based DSC can be achieved in the near future.

ACKNOWLEDGEMENTS

ACKNOWLEDGEMENTS

First of all, I want to thank my supervisors Prof. Dr. Edwin C. Constable and Prof. Dr. Catherine E. Housecroft for giving me the opportunity to do my PhD thesis in their research group. Thank you very much for your support during the last four years. Whenever I had a question, you had an open ear and gave the answers and advices which lead to these successful results. Your inquisitiveness and widespread scientific knowledge act as a model in my life as a chemist.

I also thank Prof. Dr. Marcel Mayor for being my co-examiner and co-referee.

A big thank you to Prof. Dr. Catherine E. Housecroft for proof reading this thesis and her immense support with all of her experience as a scientific writer.

I must give a big thank you to Dr. Sven Y. Brauchli for the introduction to the exciting research area of dye-sensitized solar cells, the supervision and completion of the investigations during my Master studies and the development and synthesis of the anchoring ligand **^{Ph}ALP1**.

I want to thank all the Wahlpraktikum- and Master students who worked under my supervision: Cedric Wobill, Jasmin A. Kübler (synthesis of **N^{NS(X)}** ligands and complexes), Guglielmo Risi (synthesis of **^{CF3}N^{NS}** ligand)

Big thanks to all current and former members of the DSC subgroup for their help and fruitful discussions about the topic DSCs: Annika Büttner, Cedric Wobill, Maximilian Klein, Nathalie Marinakis, Mariia Karpacheva, Dr. Markus Willgert, Dr. Alexander Stephens, Dr. Sebastian Fürer, Dr. Sven Brauchli, Dr. Ewald Schönhofer, Dr. Nik Hostettler, Dr. Colin Martin, Dr. Iain Wright, Dr. Biljana Bozic-Weber and Liselotte Siegfried.

Additionally, I want to thank Dr. Nik Hostettler, Dr. Cathrin Ertl, Dr. Roché Walliser, Maximilian Klein and Dr. Sarah Keller for measuring 500 MHz NMR spectra, 2D NMR spectra and variable-temperature NMR experiments and the team of Dr. Daniel Häussinger for the technical support; Maximilian Klein and Dr. Steffen Müller for the MALDI-TOF MS measurements; Heinz Nadig, Sylvie Mittelheiser and Michael Pfeffer for HR ESI-MS measurements; Dr. Markus Neuburger and Dr. Alessandro Prescimone for measuring X-ray diffraction; Sylvie Mittelheiser for the measurements of the elemental analysis and Prof. Dr. Catherine Housecroft for the DFT calculations. I would like to thank Dr. Markus Willgert for the introduction to EIS, the first EIS measurements and the great support during all of my EIS measurements.

Thank you to all Constable/Housecroft group members that accompanied my time in this productive group (in alphabetical order): Dr. Biljana Bozic-Weber, Dr. Sven Brauchli, Fabian

ACKNOWLEDGEMENTS

Brunner, Dr. Andreas Bünzli, Annika Büttner, Dr. Cathrin Ertl, Dr. Sebastian Fürer, Dr. Nik Hostettler, Mariia Karpacheva, Dr. Sarah Keller, Maximilian Klein, Dr. Angelo Lanzilotto, Nathalie Marinakis, Dr. Colin Martin, Dr. Collin Morris, Dr. Steffen Müller, Dr. Niamh Murray, Isaak Nohara, Dr. Gabriel Schneider, Dr. Ewald Schönhofer, Dr. Jonas Schönle, Liselotte Siegfried, Dr. Marketa Smidkova, Dr. Alexander Stephens, Dr. Srboljub Vujovic, Dr. Roché Walliser, Alexandra Wiesler, Dr. Markus Willgert, Cedric Wobill, Dr. Iain Wright, Dr. Jennifer Zampese and Dr. Davood Zare.

I want to thank the whole staff of the Department of Chemistry who guarantee that all the scientific work can be done under best possible conditions. Especially, I want to thank Beatrice Erismann for administrative support, Markus Hauri for organization of orders and keeping the system of the buildings running, Dr. Bernhard Jung for IT support and Markus Ast and the Werkstatt-Team for their great support.

For financial support the European Research Council, the Swiss National Science Foundation and the University of Basel are acknowledged.

Thank you for fruitful discussions with all the chemists I've met all over the world (Switzerland, Turkey, Canada, Italy, Denmark, Great Britain, Sweden) and the Reisefonds of the University of Basel to make it possible.

My dream to become a chemist started about 15 years ago and my chemistry teachers Dietmar Ahrens, Dr. Michael Reck and Dr. Ulrich Finke were the persons who showed me the beautiful world of chemistry and all professors of chemistry at the University of Basel gave me an insight into chemistry. Thank you very much for your enthusiastic teaching and sharing your knowledge with interested students!

I want to thank all my friends inside and outside the lab who make my life worthy to live. Thank you to the whole Hug family who admit me in their brilliant family with open arms.

And last but not least, a great thank you to my family. A big thank you to my parents who gave me the freedom to create my life and supported me on my way to become a chemist. The connection to my sister Annika helps me in every condition of life and I'm very proud of us.

The last and biggest thank you goes to the girl of my life.

At the beginning there's always a dream.

ACKNOWLEDGEMENTS

REFERENCES

- 1 B. O'Regan and M. Grätzel, *Nature*, 1991, **353**, 737.
- 2 <http://www.worldometers.info/world-population/>; 10.01.2018.
- 3 United Nations, Department of Economic and Social Affairs, Population Division (2017). World Population Prospects 2017 – Data Booklet (ST/ESA/SER.A/401).
- 4 K. Bithas and P. Kalimeris, *Revisiting the Energy-Development Link*, SpringerBriefs in Economics, DOI 10.1007/978-3-319-20732-2_2.
- 5 ftp://afmp.cmdl.noaa.gov/products/trends/co2/co2_annmean_mlo.txt; 25.03.2018.
- 6 <http://cdiac.ess-dive.lbl.gov/ftp/trends/co2/siple2.013>; 25.03.2018.
- 7 <https://www.theatlantic.com/technology/archive/2015/11/a-brief-history-of-human-energy-use/415749/>; 21.03.2018.
- 8 V. Smil, *Energy in world history*, Westview Press, Boulder, 1994.
- 9 D. M. Bowman, J. K. Balch and P. Artaxo, *Science*, 2009, **324**, 481.
- 10 R. Fouquet and P. J. Pearson, *The Energy Journal*, 2006, **27**, 139.
- 11 J. Goudsblom, *Journal of World History*, 1992, **3**, 1.
- 12 R. Heinberg, *The end of growth: Adapting to our new economic reality*, New Society Publishers Gabriola Island, 2011.
- 13 A. Lucas, *Wind, Water, Work. Ancient and Medieval Milling Technology*, Brill Academic Publishers, 2006.
- 14 F. Krausmann, *Social Ecology Working Paper 131*, 2011.
- 15 J. R. McNeill, *Something new under the sun: An environmental history of the twentieth-century world (the global century series)*, WW Norton and Company, New York, 2000.
- 16 <http://famreit.com/20-james-watt-steam-engine-diagram/james-watt-steam-engine-diagram-parts-compliant-concept-nor-s/>; 25.03.2018.
- 17 https://inflationdata.com/Inflation/Inflation_Rate/Historical_Oil_Prices_Table.asp; 25.03.2018.
- 18 www.welt.e/wirtschaft/article136741255/Das-Maerchen-von-der-grossen-Oelpreisverschwoerung.html; 25.03.2018.
- 19 V. Smil, *Scientific American*, 2014, **310**, 52.
- 20 see for example: Bundesministerium für Umwelt, Naturschutz und Reaktorsicherheit (BMU), Erneuerbare-Energien-Gesetz (EEG) 2012, Berlin, 2012; Bundesministerium für Umwelt, Naturschutz und Reaktorsicherheit (BMU), Erneuerbare-Energien-Gesetz (EEG) 2017, Bundesgesetzblatt Jahrgang 2016 Teil I Nr. 49, Bonn, 2016.
- 21 BP, *BP Statistical Review of World Energy 2017*, London, 2017.
- 22 H. Weigt, *Game of Electrons - A Song of Water and Sun*, talk, Basel, 04.12.2017.
- 23 V. Smil, *Energy Transitions*, talk, Equinox Summit Energy 2030, Waterloo, June 2011.
- 24 <http://www.sueddeutsche.de/wirtschaft/oekostrom-an-neujahr-versorgte-sich-deutschland-erstmal-nur-mit-oekostrom-1.3813875>; 23.03.2018.
- 25 S. Pain, *Nature*, 2017, **551**, 134.
- 26 <http://www.rwe.com/web/cms/de/1439286/rwe-power-ag/energietraeger/wasserkraft/wasserkraft-bei-rwe/geschichte-der-wasserkraft/>; 23.03.2018.
- 27 convertnews.com/wp-content/uploads/2015/09/niagara-falls-first-power-plant.jpg; 25.03.2018.
- 28 A. A. Coskun and Y. Ö. Türker, *Environ Monit Assess*, 2012, **184**, 1265.
- 29 <https://www.leifiphysik.de/uebergreifend/regenerative-energieversorgung/geschichte/geschichte-der-windenergie>; 23.03.2018.
- 30 <http://www.zeit.de/2012/06/Windkraft/komplettansicht>; 23.03.2018.
- 31 <http://www.history.alberta.ca/energyheritage/energy/wind-power/wind-power-in-north-america-and-the-development-of-windpumps/the-halladay-and-jacobs-windmills.aspx>; 25.03.2018.

- 32 M. A. M. Al-Alwani, A. B. Mohamad, N. A. Ludin, A. A. H. Kadhum and K. Sopian, *Renewable and Sustainable Energy Reviews*, 2016, **65**, 183.
- 33 M. Pagliaro, G. Palmisano and R. Ciriminna, *Flexible Solar Cells*, Wiley-VCH, Weinheim, 2008.
- 34 G. Likhtenshtein, *Solar Energy Conversion*, Wiley-VCH, Weinheim, 2012.
- 35 M. Magni, P. Biagini, A. Colombo, C. Dragonetti, D. Roberto and A. Valore, *Coordination Chemistry Reviews*, 2016, **322**, 69.
- 36 P. P. Kumavat, P. Sonar and D. S. Dalal, *Renewable and Sustainable Energy Reviews*, 2017, **78**, 1262.
- 37 C. Clement Raj and R. Prasanth, *Journal of Power Sources*, 2016, **317**, 120.
- 38 <http://www.meteoweb.eu/2015/04/accadde-oggi-nel-1954-la-prima-batteria-solare/434111/>; 25.03.2018.
- 39 M. A. Green, Y. Hishikawa, E. D. Dunlop, D. H. Levi, J. Hohl-Ebinger and A. W. Y. Ho-Baillie, *Prog Photovolt Res Appl*, 2018, **26**, 3.
- 40 K. Yoshikawa, H. Kawasaki and W. Yoshida, *Nat Energy*, 2017, **2**, 17032.
- 41 B. M. Kayes, H. Nie, R. Twist, S. G. Spruytte, F. Reinhardt, I.C. Kizilyalli and G. S. Higashi, *Proceedings of the 37th IEEE Photovoltaic Specialists Conference*, 2011.
- 42 T. Kato, A. Handa, T. Yagioka, T. Matsuura, K. Yamamoto, S. Higashi, J.-L. Wu, K. F. Tai, H. Hiroi, T. Yoshiyama, T. Sakai and H. Sugimoto, *44th IEEE Photovoltaic Specialists Conference*, Washington DC, June 2017.
- 43 P. T. Chiu, D. L. Law, R. L. Woo, S. Singer, D. Bhusari, W. D. Hong, A. Zakaria, J. C. Boisvert, S. Mesropian, R. R. King and N. H. Karam, *Proc. 40th IEEE Photovoltaic Specialist Conference*, Denver, June 2014.
- 44 R. Komiya, A. Fukui, N. Murofushi, N. Koide, R. Yamanaka and H. Katayama, *Technical Digest, 21st International Photovoltaic Science and Engineering Conference*, Fukuoka, November 2011.
- 45 S. Mori, H. Oh-oka, H. Nakao, T. Gotanda, Y. Nakano, H. Jung, A. Iida, R. Hayase, N. Shida, M. Saito, K. Todorii, T. Asakura, A. Matsui and M. Hosoya, *MRS Proceedings*, 2015, **1737**.
- 46 W. S. Yang, J. H. Noh and N. J. Jeon, *Science*, 2015, **348**, 1234.
- 47 T. Skotheim, Dye sensitized solar-cells, US patent: 4190950, 1980.
- 48 <https://factorynet.at/a/master-of-photosynthesis-sfl-technologies>; 25.03.2018.
- 49 M. L. Parisi, S. Maranghi and R. Basosi, *Renewable and Sustainable Energy Reviews*, 2014, **39**, 124.
- 50 H. J. Snaith, *Adv Funct Mater*, 2010, **20**, 13.
- 51 K. Kakiage, Y. Aoyama, T. Yano, K. Oya, J.-I. Fujisawa and M. Hanaya, *Chem. Commun.*, 2015, **51**, 15894.
- 52 <https://www.sn.at/schlagzeilen/science-tower-ein-leuchtturm-der-innovationen-1002919>; 25.03.2018.
- 53 <http://www.exeger.com/applications/#breakthrough-application>; 25.03.2018.
- 54 <http://gcell.com/product/solar-keyboard>; 25.03.2018.
- 55 F. Odobel, L. Le Pleux, Y. Pellegrin and E. Blart, *Acc. Chem. Res.*, 2010, **43**, 1063.
- 56 F. Brunner, N. Marinakis, C. Wobill, M. Willgert, C. D. Ertl, T. Kosmalski, M. Neuburger, B. Bozic-Weber, T. Glatzel, E. C. Constable and C. E. Housecroft, *J. Mater. Chem.C*, 2016, **4**, 9823.
- 57 N. Marinakis, M. Willgert, E. C. Constable and C. E. Housecroft, *Sustainable Energy Fuels*, 2017, **1**, 626.
- 58 N. Marinakis, C. Wobill, E. C. Constable and C. E. Housecroft, *Polyhedron*, 2018, **140**, 122.

- 59 S. Yun, Y. Qin, A. R. Uhl, N. Vlachopoulos, M. Yin, D. Li, X. Hanf and A. Hagfeldt, *Energy Environ. Sci.*, 2018, **11**, 476.
- 60 D. R. McMillin, M. T. Buckner and B. T. Ahn, *Inorg. Chem.*, 1977, **16**, 943.
- 61 N. Armaroli, *Chem. Soc. Rev.*, 2001, **30**, 113.
- 62 B. Bozic-Weber, E. C. Constable and C. E. Housecroft, *Coordination Chemistry Reviews*, 2013, **257**, 3089.
- 63 <https://education.jlab.org/itselemental/index.html>; 25.03.2018.
- 64 <https://www.quandl.com/collections/markets/copper>; 25.03.2018.
- 65 <https://www.quandl.com/collections/markets/rare-metals>; 25.03.2018.
- 66 ICSG, The World Copper Factbook 2017, Lisbon, 2017.
- 67 <http://www.asm-recycling.co.uk/blog/the-world-of-metal-recycling-the-facts/>; 6.2.2018.
- 68 C. E. Housecroft and A. G. Sharpe, *Inorganic chemistry*, 4th edition, Pearson, Essex, 2012.
- 69 J. Wu, Z. Lan, J. Lin, M. Huang, Y. Huang, L. Fan, G. Luo, Y. Lin, Y. Xie and Y. Wei, *Chem. Soc. Rev.*, 2017, **46**, 5975.
- 70 K. Kalyanasundaram, A. Hagfeldt, G. Boschloo, L. Sun, L. Kloo and H. Pettersson, *Chem. Rev.*, 2010, **110**, 6595.
- 71 U. Sulaeman and A. Z. Abdullah, *Renewable and Sustainable Energy Reviews*, 2017, **74**, 438.
- 72 F. W. Low and C. W. Lai, *Renewable and Sustainable Energy Reviews*, 2018, **82**, 103.
- 73 K. Fan, J. Yu and W. Ho, *Mater. Horiz.*, 2017, **4**, 319.
- 74 M.-E. Yeoh and K.-Y. Chan, *Int. J. Energy Res.*, 2017, **41**, 2446.
- 75 J. Gong, K. Sumathy, Q. Qiao and Z. Zhou, *Renewable and Sustainable Energy Reviews*, 2017, **68**, 234.
- 76 S. Sharma, B. Siwach, S. K. Ghoshal and D. Mohan, *Renewable and Sustainable Energy Reviews*, 2017, **70**, 529.
- 77 <http://ruby.colorado.edu/~smyth/min/tio2.html>; 12.03.2018.
- 78 <http://rredc.nrel.gov/solar/spectra/am1.5/>; 25.03.2018.
- 79 A. Di Paola, M. Bellardita, R. Ceccato, L. Palmisano and F. Parrino, *J. Phys. Chem. C*, 2009, **113**, 15166.
- 80 A. Hagfeldt, G. Boschloo, L. Sun, L. Kloo and H. Pettersson, *Chem. Rev.*, 2010, **110**, 6595.
- 81 M. K. Nazeeruddin, A. Kay, I. Rodicio, R. Humphry-Baker, E. Mueller, P. Liska, N. Vlachopoulos and M. Grätzel, *J. Am. Chem. Soc.*, 1993, **115**, 6382.
- 82 M. K. Nazeeruddin, P. Péchy and M. Grätzel, *Chem. Commun.*, 1997, **1**, 1705.
- 83 M. K. Nazeeruddin, S. M. Zakeeruddin, R. Humphry-Baker, M. Jirousek, P. Liska, N. Vlachopoulos, V. Shklover, C.-H. Fischer and M. Grätzel, *Inorg. Chem.*, 1999, **38**, 6298.
- 84 M. K. Nazeeruddin, F. De Angelis, S. Fantacci, A. Selloni, G. Viscardi, P. Liska, S. Ito, B. Takeru and M. Grätzel, *J. Am. Chem. Soc.*, 2005, **127**, 16835.
- 85 C.-Y. Lin, C.-F. Lo, M.-H. Hsieh, S.-J. Hsu, H.-P. Lu and E.W.-G. Diau, *J. Chin. Chem. Soc.*, 2010, **57**, 1136.
- 86 Y. Shen, F. Zheng, W. Cheng, F. Gu, J. Zhang and Y. Xia, *Semicond. Sci. Technol.*, 2010, **25**, 065016.
- 87 L.-L. Li and E. W.-G. Diau, *Chem. Soc. Rev.*, 2013, **42**, 291.
- 88 T. Higashino and H. Imahori, *Dalton Trans.*, 2015, **44**, 448.
- 89 A. Yella, H.-W. Lee, H. N. Tsao, C. Yi, K. Chandiran, M. K. Nazeeruddin, E. W.-G. Diau, C.-Y. Yeh, S. M. Zakeeruddin and M. Grätzel, *Science*, 2011, **334**, 629.
- 90 B. Bozic-Weber, E.C. Constable, N. Hostettler, C.E. Housecroft, R. Schmitt and E. Schönhofer, *Chem. Commun.*, 2012, **48**, 5727.

- 91 J. Deng, L. Guo, Q. Xiu, L. Zhang, G. Wen and C. Zhong, *Mater. Chem. Phys.*, 2012, **133**, 452.
- 92 N. Alonso-Vante, J.-F. Nierengarten and J.-P. Sauvage, *J. Chem. Soc., Dalton Trans.*, 1994, 1649.
- 93 T. Bessho, E. C. Constable, M. Grätzel, A. Hernandez Redondo, C.E. Housecroft, W. Kylberg, M. K. Nazeeruddin, M. Neuburger and S. Schaffner, *Chem. Commun.*, 2008, 3717.
- 94 H. J. Snaith, *Energy Environ. Sci.*, 2012, **5**, 6513.
- 95 H. J. Snaith, *Nat. Photonics*, 2012, **6**, 337.
- 96 C. Dragonetti, M. Magni, A. Colombo, F. Melchiorre, P. Biagini and D. Roberto, *ACS Appl. Energy Mater.*, 2018, **1**, 751.
- 97 M. Magni, P. Biagini, A. Colombo, C. Dragonetti, D. Roberto and A. Valore, *Coord. Chem. Rev.*, 2016, **322**, 69.
- 98 L. Zhang and J. M. Cole, *ACS Appl. Mater. Interfaces*, 2015, **7**, 3427.
- 99 M. Sandroni, Y. Pellegrin and F. Odobel, *C. R. Chimie*, 2016, **19**, 79.
- 100 B. Bozic-Weber, S. Y. Brauchli, E. C. Constable, S. O. Furer, C. E. Housecroft and I. A. Wright, *Phys. Chem. Chem. Phys.*, 2013, **15**, 4500.
- 101 Y. M. Klein, M. Willgert, A. Prescimone, E. C. Constable and C. E. Housecroft, *Dalton Trans.*, 2016, **45**, 4659.
- 102 Y. Baumgartner, Y. M. Klein, E. C. Constable, C. E. Housecroft and M. Willgert, *RSC Adv.*, 2016, **6**, 86220.
- 103 M. Wagstaffe, A. G. Thomas, M. J. Jackman, M. Torres-Molina, K. L. Syres and K. Handrup, *J. Phys. Chem. C*, 2016, **120**, 1693.
- 104 M. Schmittel, U. Lüning, M. Meder, A. Ganz, C. Michel, M. Herderich, *Heterocycl. Commun.*, 1997, **3**, 493.
- 105 M. Sandroni, L. Favereau, A. Planchat, H. Akdas-Kilig, N. Szuwarski, Y. Pellegrin, E. Blart, H. Le Bozec, M. Boujtita and F. Odobel, *J. Mater. Chem. A*, 2014, **2**, 9944.
- 106 S. O. Furer, B. Bozic-Weber, T. Schefer, C. Wobill, E. C. Constable, C. E. Housecroft and M. Willgert, *J. Mater. Chem. A*, 2016, **4**, 12995.
- 107 A. Mahmood, *Solar Energy*, 2016, **123**, 127.
- 108 Y.-C. Chen and J. T. Lin, *Sustainable Energy Fuels*, 2017, **1**, 969.
- 109 C.-P. Lee, C.-T. Li and K.-C. Ho, *Materials Today*, 2017, **20**, 267.
- 110 S. Chaurasia and J. T. Lin, *Chem. Rec.*, 2016, **16**, 1311.
- 111 <http://www.finanzen.ch/rohstoffe/platinpreis>; 05.03.2018.
- 112 S. Mozaffari, M. R. Nateghi and M. B. Zarandi, *Renewable and Sustainable Energy Reviews*, 2017, **71**, 675.
- 113 G. Boschloo and A. Hagfeldt, *Acc. Chem. Res.*, 2009, **42**, 1819.
- 114 D. D. Macdonald, *Electrochimica Acta*, 2006, **51**, 1376.
- 115 B.-Y. Chang and S.-M. Park, *Annu. Rev. Anal. Chem.*, 2010, **3**, 207.
- 116 F. Fabregat-Santiago, G. Garcia-Belmonte, I. Mora-Sero and J. Bisquert, *Phys. Chem. Chem. Phys.*, 2011, **13**, 9083.
- 117 J. Bisquert, *Journal of Electroanalytical Chemistry*, 2010, **646**, 43.
- 118 F. Fabregat-Santiago, J. Bisquert, E. Palomares, L. Otero, D. Kuang, S. M. Zakeeruddin and M. Grätzel, *J. Phys. Chem. C*, 2007, **111**, 6550.
- 119 Q. Wang, J.-E. Moser and M. Grätzel, *J. Phys. Chem. B*, 2005, **109**, 14945.
- 120 Q. Wang, S. Ito, M. Grätzel, F. Fabregat-Santiago, I. Mora-Sero, J. Bisquert, T. Bessho and H. Imai, *J. Phys. Chem. B*, 2006, **110**, 25210.
- 121 M. Liberatore, F. Decker, L. Burtone, V. Zardetto, T. M. Brown, A. Reale and A. Di Carlo, *J. Appl. Electrochem.*, 2009, **39**, 2291.

- 122 M. R. Shoar Abouzari, F. Berkemeier, G. Schmitz and D. Wilmer, *Solid State Ionics*, 2009, **180**, 922
- 123 J. Bisquert, F. Fabregat-Santiago, I. Mora-Seró, G. Garcia-Belmonte and S. Giménez, *J. Phys. Chem. C*, 2009, **113**, 17278.
- 124 F. Kröhnke, *Synthesis*, 1976, 1.
- 125 H.-Q. Do, R. M. Kashif Khan and O. Daugulis, *J. Am. Chem. Soc.*, 2008, **130**, 15185.
- 126 C. Rai and J.B. Braunwarth, *J. Org. Chem.*, 1961, **26**, 3434.
- 127 M. J. Saif and K. R. Flower, *Transition Met Chem*, 2013, **38**, 113.
- 128 S. Gowda and D. C. Gowda, *Indian J. Chem. Sect B*, 2003, **42**, 180.
- 129 F. J. Malzner, S. Y. Brauchli, E. C. Constable, C. E. Housecroft and M. Neuburger, *RSC Adv.*, 2014, **4**, 48712.
- 130 H. A. Elagab, H. G. Alt, *Inorg. Chim. Acta*, 2015, **431**, 266.
- 131 R. Gao, L. Xiao, X. Hao, W.-H. Sun and F. Wang, *Dalton Trans.*, 2008, **41**, 5645.
- 132 F. Derridj, J. Roger, F. Geneste, S. Djebbar and H. Doucet, *Journal of Organometallic Chemistry*, 2009, **694**, 455.
- 133 B. Bozic-Weber, S. Y. Brauchli, E. C. Constable, S. O. Furer, C. E. Housecroft, F. J. Malzner, I. A. Wright and J. A. Zampese, *Dalton Trans.*, 2013, **42**, 12293.
- 134 B. Bozic-Weber, V. Chaurin, E. C. Constable, C. E. Housecroft, M. Meuwly, M. Neuburger, J. A. Rudd, E. Schönhofer and L. Siegfried, *Dalton Trans.*, 2012, **41**, 14157.
- 135 M. Nishio, *CrystEngComm*, 2004, **6**, 130.
- 136 F. J. Malzner, S. Y. Brauchli, E. Schönhofer, E. C. Constable and C. E. Housecroft, *Polyhedron*, 2014, **82**, 116.
- 137 B. Wenger, M. Grätzel and J.-E. Moser, *Chimia*, 2005, **59**, 123.
- 138 B. Wenger, M. Grätzel and J.-E. Moser, *J. Am. Chem. Soc.*, 2005, **127**, 12150.
- 139 V. K. Thorsmolle, B. Wenger, J. Teuscher, C. Bauer and J.-E. Moser, *Chimia*, 2007, **61**, 631.
- 140 T. E. Hewat, L. J. Yellowlees and N. Robertson, *Dalton Trans.*, 2014, **43**, 4127.
- 141 S. Y. Brauchli, B. Bozic-Weber, E. C. Constable, N. Hostettler, C. E. Housecroft and J. A. Zampese, *RSC Adv.*, 2014, **4**, 34801.
- 142 S. O. Furer, B. Bozic-Weber, M. Neuburger, E. C. Constable and C. E. Housecroft, *RSC Adv.*, 2015, **5**, 69430.
- 143 F. J. Malzner, C. E. Housecroft and E. C. Constable, *Inorganics*, 2018, **6**, 57.
- 144 N. R. Neale, N. Kopidakis, J. van de Lagemaat, M. Grätzel and A. J. Frank, *J. Phys. Chem. B*, 2005, **109**, 23183.
- 145 Q. Wang, W. M. Campbell, E. E. Bonfantani, K. W. Jolley, D. L. Officer, P. J. Walsh, K. Gordon, R. Humphry-Baker, M. K. Nazeeruddin and M. Grätzel, *J. Phys. Chem. B*, 2005, **109**, 15397.
- 146 C.-W. Lee, H.-P. Lu, C.-M. Lan, Y.-L. Huang, Y.-R. Liang, W.-N. Yen, Y.-C. Liu, Y.-S. Lin, E. W.-G. Diau and C.-Y. Yeh, *Chem.-Eur. J.*, 2009, **115**, 1403.
- 147 C. L. Linfoot, P. Richardson, T. E. Hewat, P. Moudam, M. M. Forde, A. Collins, F. White and N. Robertson, *Dalton Trans.*, 2010, **39**, 8945.
- 148 T. B. Nguyen, L. Ermolenko and A. Al-Mourabit, *Org. Lett.*, 2013, **15**, 4218.
- 149 X. Chen, X. Cui, F. Yang and Y. Wu, *Org. Lett.*, 2015, **17**, 1445.
- 150 A. Sarkar, S. Bhattacharyya and A. Mukherjee, *Dalton Trans.*, 2016, **45**, 1166.
- 151 A. Labrunie, Y. Jiang, F. Baert, A. Leliège, J. Roncali, C. Cabanetos and P. Blanchard, *RSC Adv.*, 2015, **5**, 102550.
- 152 Y. T. Azar and M. Payami, *Phys. Chem. Chem. Phys.*, 2015, **17**, 29574.
- 153 P. Savarino, G. Viscardi, P. Quagliotto and E. Barne, *Spectrochimica Acta.*, 1993, **49A**, 1379.

- 154 P. Savarino, G. Viscardi, P. Quagliotto, P. Perracino and E. Barni, *J. Heterocyclic Chem.*, 1997, **34**, 1479.
- 155 T. Swetha, S. Niveditha, K. Bhanuprakash, A. Islam, L. Han, I. M. Bedja, R. Fallahpour and S. P. Singh, *Inorganic Chemistry Communications*, 2015, **51**, 61.
- 156 T. Jella, M. Srikanth, R. Bolligarla, Y. Soujanya, S. P. Singh and L. Giribabu, *Dalton Trans.*, 2015, **44**, 14697.
- 157 F. Derridj, A. L. Gottumukkala, S. Djebbar and H. Doucet, *Eur. J. Inorg. Chem.*, 2008, 2550.
- 158 Y. Liu, A. Hagfeldt, X.-R. Xiao and S.-E. Lindquist, *Sol. Energy Mater. Sol. Cells*, 1998, **55**, 267.
- 159 F. Brunner, Y. M. Klein, S. Keller, C. D. Morris, A. Prescimone, E. C. Constable and C. E. Housecroft, *RSC Adv.*, 2015, **5**, 58694.
- 160 C. S. K. Ranasinghe, W. M. N. M. B. Wanninnayake, G. R. A. Kumara, R. M. G. Rajapakshe and P. M. Sirimanne, *Optik*, 2014, **125**, 813.
- 161 S. Gao, R. Q. Fan, X. M. Wang, L. S. Qiang, L. G. Wei, P. Wang, Y. L. Yang and Y. L. Wang, *Dalton Trans.*, 2015, **44**, 18187.
- 162 R. Yadav, M. Trivedi, G. Kociok-Köhn, R. Chauhan, A. Kumar and S. W. Gosavi, *Eur. J. Inorg. Chem.*, 2016, 1013.
- 163 J. Luo, Z. Wan, C. Jia, Y. Wang, X. Wu and X. Yao, *Electrochimica Acta*, 2016, **211**, 364.
- 164 Y. Wang, P. Sun, J. Zhao, M. Gao, Q. Yi, Y. Su, L. Gao and G. Zou, *Electrochimica Acta*, 2016, **194**, 67.
- 165 D. D. Babu, R. Su, A. El-Shafei and A. V. Adhikari, *Electrochimica Acta*, 2016, **198**, 10.
- 166 Y. Ogomi, S. S. Pandey, S. Kimura and S. Hayase, *Thin Solid Films*, 2010, **519**, 1087.
- 167 L. Wei, Y. Yang, R. Fan, Y. Na, P. Wang and Y. Dong, *Thin Solid Films*, 2015, **592**, 14.
- 168 D. D. Babu, D. Elsherbiny, H. Cheema, A. El-Shafei and A. V. Adhikari, *Dyes and Pigments*, 2016, **132**, 316.
- 169 L. Wei, Y. Yang, R. Fan, P. Wang, Y. Dong, W. Zhou and T. Luan, *J. Power Sources*, 2015, **293**, 203.
- 170 Y. Xu, L.-S. Qiang, Y.-L. Yang, L.-G. Wei, P. Wang and R.-Q. Fan, *Chinese Chemical Letters*, 2016, **27**, 127.
- 171 R. Elangovan and P. Venkatachalam, *J. Inorg. Organomet. Polym.*, 2015, **25**, 823.
- 172 L. Wei, Y. Na, Y. Yang, R. Fan, P. Wang and L. Li, *Phys. Chem. Chem. Phys.*, 2015, **17**, 1273.
- 173 P. Salvatori, S. Agrawal, C. Barreddi, C. Malapaka, M. de Borniol and F. De Angelis, *RSC Adv.*, 2014, **4**, 57620.
- 174 L. Wei, Y. Yang, Z. Zhu, R. Fan, P. Wang, Y. Dong and S. Chen, *RSC Adv.*, 2015, **5**, 96934.
- 175 U. Mehmood, I. A. Hussein, K. Harrabi, N. Tabete and G. R. Berdiyrov, *RSC Adv.*, 2016, **6**, 7897.
- 176 R. Cisneros, M. Beley and F. Lopicque, *Phys. Chem. Chem. Phys.*, 2016, **18**, 9645.
- 177 G. H. Rao, A. Venkateswararao, L. Giribabu, L. Han, I. Bedja, R. K. Gupta, A. Islam and S. P. Singh, *Phys. Chem. Chem. Phys.*, 2016, **18**, 14279.
- 178 D. D. Babu, R. Su, A. El-Shafei and A. V. Adhikari, *RSC Adv.*, 2016, **6**, 30205.
- 179 G. Koyyada, S. Shome, M. Chandrasekharam, G. D. Sharmac and S. P. Singh, *RSC Adv.*, 2016, **6**, 41151.
- 180 G. D. Sharma, P. A. Angaridis, S. Pipou, G. E. Zervaki, V. Nikolaou, R. Misra and A. G. Coutsolelos, *Organic Electronics*, 2015, **25**, 295.
- 181 S. Fan, X. Lu, H. Sun, G. Zhou, Y. J. Chang and Z.-S. Wang, *Phys. Chem. Chem. Phys.*, 2016, **8**, 932.

- 182 S. Y. Brauchli, F. J. Malzner, E. C. Constable and C. E. Housecroft, *RSC Adv.*, 2015, **5**, 48516.
- 183 S. Zhu, Z. An, X. Sun, Z. Wu, X. Chen and P. Chen, *Dyes and Pigments*, 2015, **120**, 85.
- 184 T. H. Nguyen, T. Suresh and J. H. Kim, *Organic Electronics*, 2016, **30**, 40.
- 185 F. Risplendi and G. Cicero, *J. Phys. Chem. C*, 2015, **119**, 27348.
- 186 A. Islam, Md. Akhtaruzzaman, T. H. Chowdhury, C. Qin, L. Han, I. M. Bedja, R. Stalder, K. S. Schanze and J. R. Reynolds, *ACS Appl. Mater. Interfaces*, 2016, **8**, 4616.
- 187 X. Lu, T. Lan, Z. Qin, Z.-S. Wang and G. Zhou, *ACS Appl. Mater. Interfaces*, 2014, **6**, 19308.
- 188 C. Magne, M. Urien and T. Pauporté, *RSC Adv.*, 2013, **3**, 6315.
- 189 H. Li, Y. Wu, Z. Geng, J. Liu, D. Xua and W. Zhu, *J. Mater. Chem. A*, 2014, **2**, 14649.
- 190 K. Kakiage, Y. Aoyama, T. Yano, K. Oya, T. Kyomenb and M. Hanaya, *Chem. Commun.*, 2015, **51**, 6315.
- 191 M. Fang, H. Li, Q. Li and Z. Li, *RSC Adv.*, 2016, **6**, 40750.
- 192 Y. Wei, Z. Wu, Z. An, X. Chen, P. Chen and Q. Liu, *Chin. J. Chem.* 2014, **32**, 474.
- 193 S. Y. Brauchli, F. J. Malzner, E. C. Constable and C. E. Housecroft, *RSC Adv.*, 2014, **4**, 62728.
- 194 M. K. Nazeeruddin, R. Humphry-Baker, P. Liska and M. Grätzel, *J. Phys. Chem. B*, 2003, **107**, 8981.
- 195 L.-Y. Lin, M.-H. Yeh, C.-P. Lee, J. Chang, A. Baheti, R. Vittal, K. R. J. Thomas and K.-C. Ho, *J. Power Sources*, 2014, **247**, 906.
- 196 R. Y.-Y. Lin, H.-W. Lin, Y.-S. Yen, C.-H. Chang, H.-H. Chou, P.-W. Chen, C.-Y. Hsu, Y.-C. Chen, J. T. Lin and K.-C. Ho, *Energy Environ. Sci.*, 2013, **6**, 2477.
- 197 Z. Xue, L. Wang and B. Liu, *Nanoscale*, 2013, **5**, 2269.
- 198 M. Rudolph, T. Yoshida, H. Miura and D. Schlettwein, *J. Phys. Chem. C*, 2015, **119**, 1298.
- 199 R. Y.-Y. Lin, Y.-S. Yen, Y.-T. Cheng, C.-P. Lee, Y.-C. Hsu, H.-H. Chou, C.-Y. Hsu, Y.-C. Chen, J. T. Lin, K.-C. Ho and C. Tsai, *Org. Lett.*, 2012, **14**, 3612.
- 200 T. Geiger, S. Kuster, J.-H. Yum, S.-J. Moon, M. K. Nazeeruddin, M. Grätzel and F. Nüesch, *Adv. Funct. Mater.*, 2009, **19**, 2720.
- 201 J. Chang, C.-P. Lee, D. Kumar, P.-W. Chen, L.-Y. Lin, K. R. J. Thomas and K.-C. Ho, *J. Power Sources*, 2013, **240**, 779.
- 202 A. Abate, R. Pérez-Tejada, K. Wojciechowski, J. M. Foster, A. Sadhanala, U. Steiner, H. J. Snaith, S. Franco and J. Orduna, *Phys. Chem. Chem. Phys.*, 2015, **17**, 18780.
- 203 C. O'Rourke and D. R. Bowler, *J. Phys.: Condens. Matter*, 2014, **26**, 195302.
- 204 R. Luschtinetz, S. Gemming and G. Seifert, *Eur. Phys. J. Plus*, 2011, **126**, 98.
- 205 A. Mishra, M. K. R. Fischer and P. Bäuerle, *Angew. Chem. Int. Ed.*, 2009, **48**, 2474.
- 206 S. Ito, T. N. Murakami, P. Comte, P. Liska, C. Grätzel, M. K. Nazeeruddin and M. Grätzel, *Thin Solid Films*, 2008, **516**, 4613.
- 207 M. Miyashita, K. Sunahara, T. Nishikawa, Y. Uemura, N. Koumura, K. Hara, A. Mori, T. Abe, E. Suzuki and S. Mori, *J. Am. Chem. Soc.*, 2008, **130**, 17874.
- 208 E. M. Barea, C. Zafer, B. Gultekin, B. Aydin, S. Koyuncu, S. Icli, F. Fabregat Santiago and J. Bisquert, *J. Phys. Chem. C*, 2010, **114**, 19840.
- 209 A. J. Huckaba, A. Yella, P. Brogdon, J. S. Murphy, M. K. Nazeeruddin, M. Grätzel and J. H. Delcamp, *Chem. Commun.*, 2016, **52**, 8424.
- 210 H.-H. Chou, C.-H. Yang, J. T. Lin and C.-P. Hsu, *J. Phys. Chem. C*, 2017, **121**, 983.
- 211 C. M. Ramsdale, J. A. Barker, A. C. Arias, J. D. MacKenzie, R. H. Friend and N. C. Greenham, *J. Appl. Phys.*, 2002, **92**, 4266.
- 212 L. J. A. Koster, V. D. Mihailetschi, R. Ramaker and P. W. M. Blom, *Appl. Phys. Lett.*, 2005, **86**, 123509.

- 213 P. Salvador, M. G. Hidalgo, A. Zaban and J. Bisquert, *J. Phys. Chem. B*, 2005, **109**, 15915.
- 214 P. R. F. Barnes, A. Y. Anderson, J. R. Durrant and B. C. O'Regan, *Phys. Chem. Chem. Phys.*, 2011, **13**, 5798.
- 215 J. A. Barker, C. M. Ramsdale and N. C. Greenham, *Phys. Rev. B: Condens. Matter Mater. Phys.*, 2003, **67**, 075205.
- 216 H. J. Snaith, L. Schmidt-Mende and M. Grätzel, *Phys. Rev. B: Condens. Matter Mater. Phys.*, 2006, **74**, 045306.
- 217 APEX2, version 2 User Manual, M86--E01078, Bruker Analytical X--ray Systems, Inc., Madison, WI, 2006.
- 218 A. Altomare, G. Cascarano, G. Giacovazzo, A. Guagliardi, M. C. Burla, G. Polidori and M. Camalli, *J. Appl. Crystallogr.*, 1994, **27**, 435.
- 219 P. W. Betteridge, J. R. Carruthers, R. I. Cooper, K. Prout and D. J. Watkin, *J. Appl. Crystallogr.*, 2003, **36**, 1487.
- 220 Stoe & Cie, X-area Software, 2011.
- 221 L. Palatinus and G. Chapuis, *J. Appl. Cryst.*, 2007, **40**, 786.
- 222 I. J. Bruno, J. C. Cole, P. R. Edgington, M. K. Kessler, C. F. Macrae, P. McCabe, J. Pearson and R. Taylor, *Acta Crystallogr., Sect. B: Struct. Sci.*, 2002, **58**, 389.
- 223 C. F. Macrae, I. J. Bruno, J. A. Chisholm, P. R. Edgington, P. McCabe, E. Pidcock, L. Rodriguez-Monge, R. Taylor, J. Van de Streek and P. A. Wood, *J. Appl. Crystallogr.*, 2008, **41**, 466.
- 224 W.-H. Sun, P. Hao, S. Zhang, Q. Shi, W. Zuo, X. Tang, *Organometallics*, 2007, **26**, 2720.
- 225 C. D. Ertl, C. Momblona, A. Pertegas, J. M. Junquera-Hernandez, M.-G. La-Placa, A. Prescimone, E. Ortí, C. E. Housecroft, E. C. Constable and H. J. Bolink, *J. Am. Chem. Soc.*, 2017, **139**, 3237.
- 226 A. Rahim, S. Pasha Shaik, M. Feroz Baig, A. Alarific and A. Kamal, *Org. Biomol. Chem.*, 2018, **16**, 635.
- 227 K. Serdons, K. Van Laere, P. Janssen, H. F. Kung, G. Bormans and A. Verbruggen, *J. Med. Chem.*, 2009, **52**, 7090.
- 228 G. J. Kubas, *Inorg. Synth.*, 1990, **28**, 68.
- 229 S. O. Fürer, L. Y. N. Luu, B. Bozic-Weber, E. C. Constable, C. E. Housecroft, *Dyes and Pigments*, 2016, **132**, 72.
- 230 M. Karpacheva, F. J. Malzner, C. Wobill, A. Büttner, E. C. Constable and C. E. Housecroft, *Dyes and Pigments*, 2018, **156**, 410.

CURRICULUM VITAE

Frederik J. Malzner

Home:

[REDACTED]

[REDACTED]

[REDACTED]

Tel.: [REDACTED]

Mobile: [REDACTED]

University:

Department of Chemistry

University of Basel

BPR 1096

Mattenstrasse 24a

CH-4058 Basel

Switzerland

Tel.: [REDACTED]

[REDACTED]

Education:

1999-2008

Allgemeine Hochschulreife

Klettgau-Gymnasium Tiengen, Tiengen, Germany

2009-2012

Bachelor of Science in Chemistry

University of Basel, Basel, Switzerland

2012-2014

Master of Science in Chemistry

University of Basel, Basel, Switzerland

Thesis: Achieving Record Levels Of Efficiency With Copper(I) Dye-Sensitized Solar Cells

Prof. Dr. Edwin C. Constable and Prof. Dr. Catherine E. Housecroft

2014-2018

Doctor of Philosophy in Chemistry

University of Basel, Basel, Switzerland

Thesis: Catch the Sun: New Ancillary Ligands in Copper(I) Dye-Sensitized Solar Cells Lead to Panchromatic Light Harvesting

Prof. Dr. Edwin C. Constable and Prof. Dr. Catherine E. Housecroft

Research Experience:

2012-2014

Master's Researcher

University of Basel, Basel Switzerland

Department of Chemistry

Topic: Synthesis of Copper(I) Complexes of 4,4'-Bis(4-bromophenyl)-6,6'-dialkyl-2,2'-bipyridine Ligands and their Applications in Dye-Sensitized Solar Cells

Prof. Dr. Edwin C. Constable and Prof. Dr. Catherine E. Housecroft

Department of Physics, Paul Scherrer Institut (PSI)

Topic: Switching of Bonding Motifs through On-Surface Reactions

Prof. Dr. Thomas A. Jung

Department of Chemistry

Topic: Achieving Record Levels Of Efficiency With Copper(I) Dye-Sensitized Solar Cells

Prof. Dr. Edwin C. Constable and Prof. Dr. Catherine E. Housecroft

2014-2018

PhD Researcher

University of Basel, Basel, Switzerland

Department of Chemistry

Topic: Catch the Sun: New Ancillary Ligands in Copper(I) Dye-Sensitized Solar Cells Lead to Panchromatic Light Harvesting

Prof. Dr. Edwin C. Constable and Prof. Dr. Catherine E. Housecroft

2018

Postdoctoral Researcher

University of Basel, Basel, Switzerland

Department of Chemistry

Prof. Dr. Edwin C. Constable and Prof. Dr. Catherine E. Housecroft

Publications:

- [1] B. Bozic-Weber, S. Y. Brauchli, E. C. Constable, S. O. Fürer, C. E. Housecroft, F. J. Malzner, I. A. Wright and J. A. Zampese, *Dalton Trans.*, 2013, **42**, 12293.
- [2] F. J. Malzner, S. Y. Brauchli, E. Schönhofer, E. C. Constable and C. E. Housecroft, *Polyhedron*, 2014, **82**, 116.
- [3] F. J. Malzner, S. Y. Brauchli, E. C. Constable, C. E. Housecroft and M. Neuburger, *RSC Advanced*, 2014, **4**, 48712.
- [4] S. Y. Brauchli, F. J. Malzner, E. C. Constable and C. E. Housecroft, *RSC Advanced*, 2014, **4**, 62728.
- [5] S. Y. Brauchli, F. J. Malzner, E. C. Constable and C. E. Housecroft, *RSC Advanced*, 2015, **5**, 48516.
- [6] T. Nijs, F. J. Malzner, S. Fatayer, A. Wäckerlin, S. Nowakowska, E. C. Constable, C. E. Housecroft and T. A. Jung, *Chem. Comm.*, 2015, **51**, 12297.
- [7] F. J. Malzner, A. Prescimone, E. C. Constable, C. E. Housecroft and M. Willgert, *J. Mater. Chem. A*, 2017, **5**, 4671.
- [8] F. J. Malzner, M. Willgert, E. C. Constable and C. E. Housecroft, *J. Mater. Chem. A*, 2017, **5**, 13717. [REGI Key Scientific Article 01/2018]
- [9] A. J. Stephens, F. J. Malzner, E. C. Constable and C. E. Housecroft, *Sustainable Energy Fuels*, 2018, **2**, 786.
- [10] M. Karpacheva, F. J. Malzner, C. Wobill, A. Büttner, E. C. Constable and C. Housecroft, *Dyes and Pigments*, 2018, **156**, 410. (MK, FJM, CW and AB contributed equally to this work)
- [11] F. J. Malzner, C. E. Housecroft and E. C. Constable, *Inorganics*, 2018, **6**, 57.

Conferences attended:

- 2014 5th EuCheMS Chemistry Congress, Istanbul, Turkey (Poster)
- 2015 Swiss Chemical Society Fall Meeting 2015, Lausanne, Switzerland (Poster)
- 2016 99th Canadian Chemistry Conference and Exhibition, Halifax, Canada (Poster)
- 2016 Swiss Chemical Society Fall Meeting 2016, Zurich, Switzerland (Poster)
- 2016 Clariant Chemistry Day 2016, Basel, Switzerland (Poster)
- 2017 4th EuCheMS Inorganic Chemistry Conference, Copenhagen, Denmark (Oral)
- 2017 Swiss Chemical Society Fall Meeting 2017, Bern, Switzerland (Poster)
- 2017 1st Dyenamo DSSC Conference, Uppsala, Sweden (Poster)

Workshops attended:

- 2016 10th International School on Hybrid and Organic Photovoltaics, Roccamare, Italy
- 2017 Bath Electrochemical Summer School, Bath, United Kingdom
- 2017 Dyenamo Training and Coaching Day, Uppsala, Sweden

Awards:

- 2014 Top poster award, EuCheMS Working party on Chemistry and Energy
- 2018 Key Scientific Article, Renewable Energy global innovations

Professional Memberships:

Swiss Chemical Society

Professional References:

Prof. Dr. Edwin C. Constable

Department of Chemistry

University of Basel

BPR 1096

Mattenstrasse 24a

CH-4058 Basel

Switzerland

edwin.constable@unibas.ch

Prof. Dr. Catherine E. Housecroft

Department of Chemistry

University of Basel

BPR 1096

Mattenstrasse 24a

CH-4058 Basel

Switzerland

catherine.housecroft@unibas.ch